Εθνικο Μετσοβιο Πολυτεχνειο
Σχολη Ηλεκτρολογων Μηχανικων
και Μηχανικων Υπολογιστων
Τομεας Ηλεκτρικης Ισχυος

Μέθοδοι στατικής και δυναμικής εκτίμησης κατάστασης συστημάτων ηλεκτρικής ενέργειας με χρήση ετερογενών μετρητικών δεδομένων

Power system static and dynamic state estimation methods using heterogeneous measurements

ΔΙΔΑΚΤΟΡΙΚΗ ΔΙΑΤΡΙΒΗ

Ορέστης Α. Δαρμής

Αθήνα, Ιούλιος 2025

ΕΘΝΙΚΟ ΜΕΤΣΟΒΙΟ ΠΟΛΥΤΕΧΝΕΙΟ
ΣΧΟΛΗ ΗΛΕΚΤΡΟΛΟΓΩΝ ΜΗΧΑΝΙΚΩΝ
ΚΑΙ ΜΗΧΑΝΙΚΩΝ ΥΠΟΛΟΓΙΣΤΩΝ
ΤΟΜΕΑΣ ΗΛΕΚΤΡΙΚΗΣ ΙΣΧΥΟΣ

Μέθοδοι στατικής και δυναμικής εκτίμησης κατάστασης συστημάτων ηλεκτρικής ενέργειας με χρήση ετερογενών μετρητικών δεδομένων

Power system static and dynamic state estimation methods using heterogeneous measurements

ΔΙΔΑΚΤΟΡΙΚΗ ΔΙΑΤΡΙΒΗ

Ορέστης Α. Δαρμής

Συμβουλευτική Επιτροπή : Γεώργιος Ν. Κορρές
Σταύρος Α. Παπαθανασίου
Παύλος Σ. Γεωργιλάκης

Εγκρίθηκε από την επταμελή εξεταστική επιτροπή την $2^{η}$ Ιουλίου 2025.

.... Γεώργιος Κορρές Καθηγητής Ε.Μ.Π	.... Σταύρος Παπαθανασίου Καθηγητής Ε.Μ.Π.	.... Παύλος Γεωργιλάκης Καθηγητής Ε.Μ.Π.
.... Άρης Δημέας Επίκουρος Καθηγητής Ε.Μ.Π.	.... Ιωάννης Προυσαλίδης Καθηγητής Ε.Μ.Π.	.... Φώτιος Κανέλλος Αναπληρωτής Καθηγητής Πολυτεχνείο Κρήτης
	.... Ελευθέριος Κόντης Επίκουρος Καθηγητής Πανεπιστήμιο Θεσσαλίας	

Αθήνα, Ιούλιος 2025

....
Ορέστης Α. Δαρμής

Διδάκτωρ Ηλεκτρολόγος Μηχανικός και Μηχανικός Υπολογιστών Ε.Μ.Π.

ΠΕΡΙΛΗΨΗ

Η εκτίμηση κατάστασης (State Estimation – SE) αποτελεί θεμελιώδες εργαλείο των συστημάτων διαχείρισης ενέργειας, παρέχοντας ένα ακριβές στιγμιότυπο των λειτουργικών συνθηκών του συστήματος με βάση μετρήσεις συλλεγόμενες από το πεδίο. Η παρούσα διατριβή εστιάζει στην ανάπτυξη καινοτόμων μεθόδων υβριδικής εκτίμησης κατάστασης (Hybrid State Estimation – HSE), για την αξιοποίηση ετερογενών μετρητικών δεδομένων προερχόμενων από τα μετρητικά συστήματα εποπτικού ελέγχου και συλλογής δεδομένων (SCADA) και από μονάδες μέτρησης φασιθετών (PMU).

Ο πρώτος ερευνητικός άξονας της διατριβής εστιάζει στις στατικές μεθόδους HSE. Αρχικά, προτείνεται ένας εκτιμητής σταθμισμένων ελαχίστων τετραγώνων που αποτελείται από δύο διαδοχικά στάδια εκτίμησης, ένα για κάθε μετρητικό σύστημα, κατάλληλος για αναβάθμιση του υπάρχοντος λογισμικού SE με ελάχιστες τροποποιήσεις. Στη συνέχεια, αναπτύσσεται ένα ισοδύναμο μοντέλο για κλασικές συνδέσεις HVDC με μετατροπείς πηγής ρεύματος κατάλληλο για στατική HSE, το οποίο επαληθεύεται μέσω αριθμητικών προσομοιώσεων που αξιοποιούν ετερογενείς μετρήσεις εναλλασσόμενου ρεύματος (AC), μαζί με μετρήσεις στην πλευρά του συνεχούς ρεύματος (DC). Τέλος, γίνεται μια πρώτη διερεύνηση της επίδρασης των διαφορετικών πιθανών σχημάτων μέτρησης φασιθετών ρεύματος μέσω PMU – με τη μορφή ροών ή εγχύσεων – στη σύγκλιση και την ακρίβεια της HSE, ζήτημα που δεν έχει μελετηθεί επαρκώς στη βιβλιογραφία.

Ο δεύτερος ερευνητικός άξονας της διατριβής εστιάζει στην ανάπτυξη μιας μεθόδου HSE υποστηριζόμενης από πρόβλεψη (Forecasting-Aided State Estimation – FASE). Στο πλαίσιο της μεθόδου, διαμορφώνεται ένα μοντέλο μετάβασης καταστάσεων (state transition model) που ενημερώνεται συνεχώς με δεδομένα πραγματικού χρόνου από PMU, βασιζόμενο στη θεωρία βέλτιστης σύντηξης δεδομένων από πολλαπλούς αισθητήρες (multi-sensor data fusion theory). Για την αντιμετώπιση του ζητήματος της έλλειψης συγχρονισμού μεταξύ των μετρήσεων SCADA και PMU, ενσωματώνεται ένα επιπλέον βήμα εξομάλυνσης στη διαδικασία FASE, βασισμένο στον αλγόριθμο εξομάλυνσης σταθερού διαστήματος (fixed-interval smoothing algorithm) Bryson-Frazier.

Στη συνέχεια, καθώς ο εντοπισμός και η ανίχνευση εσφαλμένων μετρήσεων (bad data) αποτελούν αναπόσπαστο κομμάτι των εκτιμητών κατάστασης, γίνεται ανάπτυξη αλγορίθμων επεξεργασίας εσφαλμένων δεδομένων, στο πλαίσιο των προτεινόμενων μεθόδων HSE, με χρήση του ελέγχου μεγίστων κανονικοποιημένων υπολοίπων (Largest Normalized Residual Test – LNRT).

Τέλος, πρακτικές πτυχές της παρούσας έρευνας αναδεικνύονται μέσω της υλοποίησης εργαστηριακής διάταξης στο Εργαστήριο ΣΗΕ του Τομέα Ηλεκτρικής Ισχύος του ΕΜΠ, η οποία αποτελείται από εμπορικές συσκευές PMU, PMU χαμηλού κόστους και ψηφιακό προσομοιωτή ηλεκτρικών δικτύων, και καθιστά δυνατή τη δοκιμή και αξιολόγηση εφαρμογών εποπτείας και ελέγχου που βασίζονται σε συγχρονισμένα δεδομένα φασιθετών.

Λέξεις-Κλειδιά

Ακρίβεια, Ανίχνευση εσφαλμένων δεδομένων, Βελτιστοποίηση, Εκτίμηση κατάστασης υποστηριζόμενη από πρόβλεψη, Επεκτεταμένο φίλτρο Kalman, Μέθοδος σταθμισμένων ελαχίστων τετραγώνων, Μονάδες μέτρησης φασιθετών, Μοντέλα μετάβασης καταστάσεων, Σύγκλιση, Σύντηξη δεδομένων, Συστήματα εποπτείας ευρείας περιοχής, Συστήματα μεταφοράς συνεχούς ρεύματος υψηλής τάσης, Υβριδική εκτίμηση κατάστασης, Ψηφιακή προσομοίωση συστημάτων ηλεκτρικής ενέργειας.

Abstract

Power system state estimation (SE) constitutes an essential function of energy management systems, enabling operators to maintain a comprehensive awareness of system operating conditions through available field measurements. This dissertation introduces several contributions to the research domain of hybrid state estimation (HSE), aimed at optimally integrating heterogeneous supervisory control and data acquisition (SCADA) and phasor measurement unit (PMU) data.

Initially, fundamental concepts of static and dynamic SE are elaborated from both mathematical and practical implementation perspectives, followed by an introduction to the principles of HSE. Subsequently, key challenges associated with HSE implementations are identified, accompanied by a comprehensive literature review focusing on novel static and dynamic HSE methods designed to overcome these challenges. Furthermore, a classification of existing methods is proposed based on their scope and underlying mathematical formulations.

The contributions of this thesis first focus on static HSE methods. A weighted least squares (WLS)-based static HSE formulation is developed, separately handling SCADA and WAMS measurements. The principal advantages of the proposed method include its modular design and practical applicability, making it particularly suitable for PMU integration into existing SE software through minimal modifications. Moreover, considering the widespread adoption of high-voltage direct current (HVDC) transmission technology, a model suitable for current source converter (CSC)-HVDC links in static HSE implementations is proposed and validated via numerical simulations involving both SCADA and PMU measurements on the AC side, along with diverse combinations of DC-side measurements. Additionally, the thesis investigates the inclusion of current injection phasors from PMUs in static HSE algorithms, examining how various current measurement configurations – whether flows or injections – influence HSE performance, a topic inadequately addressed in prior literature.

Recognizing the increasing complexity and stochastic behavior of contemporary power systems, transitioning toward advanced SE algorithms capable of providing enhanced system visibility and situational awareness becomes imperative. In response, this thesis proposes a hybrid forecasting-aided state estimation (FASE) approach leveraging an extended Kalman filter (EKF) framework. The method supplements existing static state estimators by incorporating additional information derived from the temporal evolution of system states through multi-sensor data fusion, employing a transition model that combines dense, real-time PMU measurements with forecasted state estimates. To address synchronization discrepancies between SCADA and PMU data, a post-processing correction step based on the modified Bryson-Frazier fixed-interval smoothing algorithm is implemented.

In the final two chapters, algorithms dedicated to detecting and suppressing bad data within the context of the proposed HSE approaches are formulated. Additionally, practical aspects of the research are demonstrated using a laboratory-scale experimental setup that integrates both commercial and low-cost PMUs with a digital real-time power system simulator, thereby enabling comprehensive testing and validation of synchrophasor-based monitoring and control algorithms.

Keywords

Accuracy, Bad data analysis, Convergence, Data fusion, Digital real-time simulation, Extended Kalman filter, Forecasting-aided state estimation, High voltage direct current, Hybrid state estimation, Optimization, Phasor measurement unit, State transition models, Weighted least squares, Wide area monitoring systems.

ΠΡΟΛΟΓΟΣ

Το 2020, ορμώμενος από τα ομολογουμένως ενθαρρυντικά σχόλια που έλαβα κατά την παρουσίαση της διπλωματικής μου εργασίας, αποφάσισα να απευθυνθώ στον επιβλέποντά μου, Καθηγητή κ. Γεώργιο Κορρέ, με σκοπό να εμβαθύνω περαιτέρω στο πεδίο της εργασίας μου μέσω της εκπόνησης διδακτορικής διατριβής. Όπως προκύπτει και από τον τίτλο του παρόντος συγγράμματος, το ερευνητικό αυτό πεδίο εστιάζει στους εκτιμητές κατάστασης συστημάτων ηλεκτρικής ενέργειας.

Η εκτίμηση κατάστασης αποτελεί, για περίπου μισό αιώνα, καθιερωμένη διαδικασία εποπτείας των συστημάτων ηλεκτρικής ενέργειας και προκύπτει ως σύζευξη εννοιών και εργαλείων από τη γραμμική άλγεβρα, τη στατιστική, τη θεωρία πιθανοτήτων και τη βελτιστοποίηση. Ο διεπιστημονικός αυτός χαρακτήρας καθιστά το αντίστοιχο ερευνητικό πεδίο πρόσφορο για βελτιώσεις και καινοτομίες σε πολλαπλές πτυχές του, προσφέροντας αντίστοιχα ποικίλες ερευνητικές προκλήσεις για τους ενεργειακούς μηχανικούς. Παράλληλα, η ανάπτυξη και διάδοση νέων τεχνολογιών μέτρησης στο πλαίσιο των σύγχρονων ευφυών δικτύων ηλεκτρισμού, η ραγδαία αύξηση του όγκου των μετρητικών δεδομένων πραγματικού χρόνου και η αύξηση της συνολικής πολυπλοκότητας των σημερινών συστημάτων ηλεκτρικής ενέργειας σε επίπεδο μεταφοράς και διανομής, μετατρέπει τη σχετική έρευνα σε πολυεπίπεδο πρόβλημα που συνενώνει τους τομείς της πληροφορικής, των τηλεπικοινωνιών και της ανάλυσης ηλεκτρικών δικτύων. Κατά την εξαετία 2020–2025, η ερευνητική μου δραστηριότητα επικεντρώθηκε στην αναβάθμιση επιμέρους λειτουργιών των εκτιμητών κατάστασης, ώστε να ανταποκρίνονται στις απαιτήσεις των τεχνολογικά αναπτυσσόμενων δικτύων ηλεκτρικής ενέργειας. Το παρόν πόνημα αποσκοπεί στην αναλυτική παρουσίαση των μεθόδων και τεχνικών που αναπτύχθηκαν, καθώς και στην τεκμηρίωση των αποτελεσμάτων και της συνεισφοράς τους.

Ακολούθως, θεωρώ υποχρέωσή μου να εκφράσω την ευγνωμοσύνη μου προς όσους συνέβαλαν ουσιαστικά στην ολοκλήρωση της παρούσας έρευνας. Αρχικά, θα ήθελα να ευχαριστήσω τα μέλη της τριμελούς συμβουλευτικής επιτροπής, τους κ.κ. Καθηγητές Σ. Παπαθανασίου και Π. Γεωργιλάκη, για την αδιάλειπτη υποστήριξη και καθοδήγησή τους καθ’ όλη τη διάρκεια των σπουδών μου. Επιπλέον, οφείλω ιδιαίτερες ευχαριστίες στους κ.κ. Α. Δημέα, Ι. Προυσαλίδη, Φ. Κανέλλο και Ε. Κόντη, οι οποίοι με τίμησαν με τη συμμετοχή τους στις επιτροπές κρίσης της διατριβής και η συνδρομή τους στην ποιοτική ενίσχυση του ερευνητικού μου έργου υπήρξε πολύτιμη.

Όσον αφορά τους συνεργάτες και φίλους που γνώρισα στη διάρκεια αυτής της πορείας, οφείλω εγκάρδιες ευχαριστίες στον διδάκτορα μηχανικό ΕΜΠ Θ. Ξύγκη, καθώς και στους υποψήφιους διδάκτορες ΕΜΠ Γ. Καρβέλη, Β. Γιωτόπουλο και Μ. Αποστολίδη, για τις γόνιμες συζητήσεις, τις συμβουλές και τη συμμετοχή τους στη συγγραφή επιστημονικών δημοσιεύσεών μου. Θα ήθελα να ευχαριστήσω επίσης τον διδάκτορα μηχανικό ΕΜΠ Δ. Λαγό, για την πολύτιμη βοήθειά του στην υλοποίηση της εργαστηριακής διάταξης που αξιοποιήθηκε στο πλαίσιο της διατριβής.

Η οικογένειά μου στάθηκε αρωγός σε κάθε βήμα μου. Εκφράζω την ευγνωμοσύνη μου στους γονείς μου, Αντώνη και Ηρώ, για την αδιάκοπη στήριξη και ενθάρρυνσή τους. Από καρδιάς ευχαριστώ και τη σύντροφό μου, Δήμητρα, για την κατανόηση, τις προτροπές της και την αντοχή που μου προσέδωσε σε απαιτητικές περιστάσεις, τόσο πνευματικά όσο και ηθικά. Ιδιαίτερες ευχαριστίες οφείλω και σε όλους τους φίλους μου για την έμπρακτη υποστήριξή τους όλα αυτά τα χρόνια.

Το μεγαλύτερο «ευχαριστώ» το οφείλω εκ βάθους καρδίας στον επιβλέποντά μου, Καθηγητή Γ. Κορρέ, ως ελάχιστη ένδειξη ευγνωμοσύνης για την καθοδήγηση, την ακατάπαυστη υποστήριξη και την καλοσύνη που επέδειξε απέναντι μου. Η ευθυκρισία, η επιστημονική του οξυδέρκεια και οι ατελείωτες παραινέσεις του υπήρξαν καθοριστική πηγή έμπνευσης και στήριξης καθ’ όλη την εκπόνηση της διδακτορικής διατριβής.

Ορέστης Α. Δαρμής
Αθήνα, Ιούλιος 2025

TABLE OF CONTENTS

CATALOG OF FIGURES

CATALOG OF TABLES

CATALOG OF ALGORITHMS

TABLE OF ACRONYMS

A/D	Analog to digital	MAE	Mean absolute error
ADN	Active distribution network	MBF	Modified Bryson-Frazier
AGC	Automatic generation control	MC	Monte Carlo
AMI	Advanced metering infrastructure	ML	Machine learning
ANN	Artificial neural network	MLE	Maximum likelihood estimation
BD	Bad data	MMS	Manufacturing message specifications
CFE	Communication front end	MS	Measurement set
CIOC	Communication input/output controllers	MU	Merging unit
CKF	Cubature Kalman filter	NE	Normal equations
CSC	Current source converter	PDC	Phasor data concentrator
CSE	Conventional state estimation	PDF	Probability density function
CT	Current transformer	PF	Particle filter
DER	Distributed or decentralized energy resources	PLC	Programmable logic controller
DFR	Digital fault recorder	PMU	Phasor measurement unit
DMS	Distribution management system	PSE	Post-processing hybrid state estimation
DRTS	Digital real-time simulation	RES	Renewable energy sources
DSE	Dynamic state estimation	RMS	Root mean square
DSSE	Distribution system state estimation	ROCOF	Rate of change of frequency
ECC	Energy control center	RTDS	Real-time digital simulator
EnKF	Ensemble Kalman filter	RTS	Rauch-Tung-Striebel
EKF	Extended Kalman filter	RTU	Remote terminal unit
EMS	Energy management system	SA	Substation automation
FACTS	Flexible AC transmission systems	SCADA	Supervisory control and data acquisition
FASE	Forecasting-aided state estimation	SE	State estimation
FIDVR	Fault-induced delayed voltage recovery	SIL	Software-in-the-loop
FSE	Fusion hybrid state estimation	SOL	System operating limit
GPS	Global positioning system	SPDC	Super phasor data concentrator
HDSE	Hybrid dynamic state estimation	SSE	Static state estimation
HIL	Hardware-in-the-loop	TSE	Tracking state estimation
HMI	Human-machine interface	TSO	Transmission system operator
HSE	Hybrid state estimation	TVE	Total vector error
HSSE	Hybrid static state estimation	UKF	Unscented Kalman filter
HVDC	High voltage direct current	UT	Unscented transform
IED	Intelligent electronic device	UTC	Universal coordinated time
ISE	Integrated hybrid state estimation	VSC	Voltage source converter
ISR	Information storage and retrieval	VT	Voltage transformer
IT	Instrument transformer	WAM-PAC	Wide area monitoring, protection, and control
KF	Kalman filter	WAMS	Wide area monitoring system
LAN	Local area network	WAN	Wide area network
LAV	Least absolute value	WLAV	Weighted least absolute values
LCC	Line-commutated converter	WLS	Weighted least squares

Εκτενής ελληνική περίληψη

Η εκτίμηση κατάστασης (SE) ενός Συστήματος Ηλεκτρικής Ενέργειας (ΣΗΕ) αποτελεί θεμελιώδες εργαλείο των συστημάτων διαχείρισης ενέργειας (EMS). Κύριος στόχος της είναι η απόδοση μιας σαφούς και ολοκληρωμένης απεικόνισης των πραγματικών συνθηκών λειτουργίας του συστήματος, αξιοποιώντας δεδομένα πραγματικού χρόνου, τα οποία προέρχονται από μετρητικές διατάξεις εγκατεστημένες στους υποσταθμούς. Στα σύγχρονα συστήματα μεταφοράς ηλεκτρικής ενέργειας επικρατούν δύο βασικές τεχνολογίες συλλογής μετρήσεων: το Σύστημα Εποπτικού Ελέγχου και Συλλογής Δεδομένων (SCADA) και το Σύστημα Εποπτείας Ευρείας Περιοχής (WAMS). Τα πολλαπλά πλεονεκτήματα της ενσωμάτωσης συγχρονισμένων μετρήσεων φασιθετών (synchrophasors) από μονάδες μέτρησης φασιθετών (PMUs) – οι κατεξοχήν χρησιμοποιούμενες μετρητικές συσκευές στα συστήματα WAMS – στους συμβατικούς αλγορίθμους SE που βασίζονται σε μετρήσεις SCADA, είναι ευρέως αναγνωρισμένα από την διεθνή επιστημονική κοινότητα. Το γεγονός αυτό έχει οδηγήσει στην ανάπτυξη πληθώρας μεθόδων υβριδικής εκτίμησης κατάστασης (HSE), οι οποίες αποσκοπούν στην βέλτιστη αξιοποίηση αμφότερων των μετρητικών συστημάτων, για τη συνολικά πιο αποτελεσματική εκτίμηση της λειτουργικής κατάστασης του συστήματος. Στο πλαίσιο αυτό, η παρούσα διδακτορική διατριβή εστιάζει στην ανάπτυξη καινοτόμων μεθόδων υβριδικής στατικής και δυναμικής εκτίμησης κατάστασης ΣΗΕ, οι οποίες συμβάλουν στην αποτελεσματικότερη χρήση μετρήσεων SCADA και PMU, εξετάζοντας την οιονεί στατική (quasi-steady) κατάσταση λειτουργίας τους.

Κέντρα Ελέγχου Ενέργειας & Εκτίμηση κατάστασης ΣΗΕ

Τον ρόλο του κεντρικού σημείου επεξεργασίας και ανάλυσης του συνόλου των διαθέσιμων μετρητικών δεδομένων, και, ακολούθως, της έκδοσης κατάλληλων εντολών ελέγχου, αναλαμβάνουν σύγχρονα υπολογιστικά συστήματα και προηγμένες εφαρμογές λογισμικού που είναι εγκατεστημένα στα Κέντρα Ελέγχου Ενέργειας (ΚΕΕ) και βασίζονται στην τεχνολογία πληροφοριών και επικοινωνιών. Δεδομένου ότι η σύσταση των ΚΕΕ χρονολογείται από τη δεκαετία του 1950, η κυριότερη και πιο σύνθετη πρόκληση που έχουν να αντιμετωπίσουν οι σχετικές λειτουργίες των ΚΕΕ τον $21^{ο}$ αιώνα, είναι η αλματώδης επέκταση της γεωγραφικής κάλυψης των ηλεκτρικών δικτύων και, συνεπακόλουθα, η αξιοσημείωτη αύξηση των εμπλεκόμενων φορέων και χρηστών. Η υποστήριξη αγορών ηλεκτρικής ενέργειας, δημοσίων και ιδιωτικών διαχειριστών, ανεξάρτητων παραγωγών, καθώς και διαφόρων κατηγοριών καταναλωτών, δημιουργεί αυξημένες απαιτήσεις ως προς την υπολογιστική ισχύ και την αξιοπιστία των εργαλείων των σύγχρονων ΚΕΕ.

Θεωρώντας το ΣΗΕ ως ένα ενιαίο σύνολο επιμέρους υποσυστημάτων (σύστημα μεταφοράς, δίκτυο διανομής, καταναλωτές), καθίσταται απαραίτητη η διατήρηση μιας ολοκληρωμένης επίγνωσης της κατάστασης (situational awareness) σε όλη την έκτασή του, ώστε αυτό να λειτουργεί αποτελεσματικά και με ασφάλεια, ή, ισοδύναμα, η κατάστασή του να βρίσκεται εντός προκαθορισμένων ορίων, δεδομένων συγκεκριμένων ενδογενών και εξωγενών παραμέτρων. Η κατάσταση ενός ΣΗΕ, καθώς και ο βαθμός επάρκειάς της, προσδιορίζονται μέσω μαθηματικών μεθόδων, με βάση τη μελέτη συγκεκριμένων χαρακτηριστικών μεγεθών του. Γενικά, ο πλήρης προσδιορισμός της κατάστασης του δικτύου σε μια δεδομένη χρονική στιγμή, μπορεί να επιτευχθεί εάν είναι γνωστό το μοντέλο του, δηλαδή η διάταξη όλων των κόμβων και των κλάδων που το αποτελούν και οι τιμές των σχετικών τους παραμέτρων, καθώς και οι φασιθέτες (phasors) τάσης σε κάθε κόμβο του.

Η έννοια της εκτίμησης κατάστασης ΣΗΕ εισήχθη από τους Schweppe et al. το 1970, με σκοπό τον βέλτιστο έλεγχο της λειτουργίας τους σε πραγματικό χρόνο, αναγνωρίζοντας την εγγενή αδυναμία των διαθέσιμων τότε μετρητικών συστημάτων να αποδώσουν αξιόπιστα την πραγματική λειτουργική κατάστασή τους. Το μαθηματικό μοντέλο της εκτίμησης κατάστασης βασίζεται στη θεωρία εκτίμησης, έναν κλάδο της στατιστικής με ευρεία εφαρμογή στη μελέτη των συστημάτων αυτομάτου ελέγχου, και χρησιμοποιεί στοιχεία από τη θεωρία πιθανοτήτων. Το πρόβλημα της εκτίμησης κατάστασης ανάγεται στον προσδιορισμό των φασιθετών τάσης σε όλους τους κόμβους του υπό μελέτη συστήματος, οι οποίοι αποτελούν, στη γενική περίπτωση, τις μεταβλητές κατάστασής του, αξιοποιώντας τις διαθέσιμες μετρήσεις από το πεδίο. Ο εκτιμητής κατάστασης (state estimator) έχει παγιωθεί ως η μοναδική υπολογιστική διαδικασία των ΚΕΕ που εξασφαλίζει την καλύτερη δυνατή απεικόνιση της τρέχουσας κατάστασης του συστήματος σε συνθήκες πραγματικού χρόνου. Επομένως, γίνεται αντιληπτό ότι η επίγνωση κατάστασης στα ΣΗΕ είναι μια έννοια που συνδέεται άμεσα με τα ΚΕΕ, όπου λαμβάνει χώρα η συγκέντρωση, η επεξεργασία και η ανάλυση των μετρητικών δεδομένων από τις εγκατεστημένες μονάδες μέτρησης. Ως εκ τούτου, η εύρυθμη λειτουργία των πρώτων είναι άρρηκτα συνδεδεμένη με την ύπαρξη αποτελεσματικών και εύρωστων μηχανισμών εποπτείας και διαχείρισης στα τελευταία.

Μονάδες Μέτρησης Φασιθετών

Τα τελευταία χρόνια, ο τομέας των ΣΗΕ διανύει μια περίοδο ριζικών και ταχέων μεταβολών, οι οποίες υπαγορεύονται από διάφορους παράγοντες, όπως η συνεχής αύξηση της ζήτησης ηλεκτρικής ενέργειας, οι πολυάριθμες διασυνδέσεις δικτύων σε παγκόσμια κλίμακα, η απελευθέρωση της αγοράς ηλεκτρικής ενέργειας, και η υψίστης σημασίας μετάβαση από την υφιστάμενη παραγωγή ενέργειας από ορυκτά καύσιμα προς τις ανανεώσιμες πηγές ενέργειας (ΑΠΕ). Οι εν λόγω αλλαγές καθιστούν αναγκαίο τον εκσυγχρονισμό των υποδομών των ΣΗΕ, καθώς και την ανάπτυξη και ενσωμάτωση καινοτόμων λύσεων και τεχνολογιών διαχείρισής τους, ώστε να δύνανται να ανταποκριθούν στις νέες λειτουργικές απαιτήσεις.

Σε αυτό το πλαίσιο, γίνεται επιτακτική η ανάγκη για πιο αξιόπιστα και εκτενή συστήματα εποπτείας και ελέγχου, τα οποία είναι ζωτικής σημασίας για τη διασφάλιση της επαρκούς, ασφαλούς και οικονομικής παροχής ηλεκτρικής ενέργειας στους καταναλωτές. Οι αυξανόμενες απαιτήσεις απομακρυσμένης εποπτείας και ελέγχου εξυπηρετούνται από τον σταδιακό εκσυγχρονισμό του σχετικού εξοπλισμού, ο οποίος αποτελείται από μονάδες αισθητήρων (sensors) και επενεργητών (actuators) που υπόκεινται σε τηλεχειρισμό. Η ανάπτυξη προηγμένων συστημάτων μέτρησης και αυτοματισμών σε όλο το εύρος των ΣΗΕ αποτελεί κρίσιμο βήμα για τη μετάβαση στα ευφυή δίκτυα ηλεκτρισμού (smart grids).

Μια κομβικής σημασίας εξέλιξη σε αυτόν τον τομέα είναι η μετάβαση από αναλογικές και ηλεκτρομηχανικές διατάξεις σε ψηφιακές συσκευές, γεγονός που επιτρέπει την ανάπτυξη και υιοθέτηση νέων τεχνολογιών μέτρησης και ελέγχου. Ειδικότερα, στο επίπεδο των συστημάτων μεταφοράς, την τελευταία δεκαετία βρίσκεται σε εξέλιξη η ευρεία εγκατάσταση μετρητικών συσκευών υψηλής ακρίβειας με προηγμένες δυνατότητες. Παράδειγμα αποτελούν οι μονάδες PMU, οι οποίες καταγράφουν το πλάτος και τη φασική γωνία των ημιτονοειδών ηλεκτρικών μεγεθών με υψηλή ακρίβεια, ενώ προσφέρουν κατά πολύ υψηλότερους ρυθμούς αναφοράς σε σχέση με τις συμβατικές απομακρυσμένες τερματικές μονάδες (Remote Terminal Units – RTUs) του συστήματος SCADA. Οι φασιθέτες που καταγράφονται από τα PMU υπολογίζονται και σημαίνονται χρονικά ως προς μια σταθερή αναφορά χρόνου, η οποία τυπικά προέρχεται από το παγκόσμιο σύστημα εντοπισμού θέσης (GPS). Στο ίδιο πνεύμα, τα διακοπτικά μέσα ζεύξης (αποζεύκτες, διακόπτες φορτίου και ισχύος) και προστασίας (διακόπτες οδηγούμενοι από ηλεκτρονόμους) αναβαθμίζονται μέσω της δυνατότητας λήψης συγχρονισμένων μετρήσεων φασιθετών, δηλαδή αποκτούν δυνατότητες PMU. Η ευρεία χρήση της νέας αυτής τεχνολογίας μέτρησης έχει οδηγήσει σήμερα στην ανάπτυξη των συστημάτων εποπτείας ευρείας περιοχής (WAMS), δηλαδή δικτύων διασυνδεδεμένων PMU που παρέχουν στους διαχειριστές επίγνωση της λειτουργικής κατάστασης του συστήματος σε επίπεδο κλασμάτων του δευτερολέπτου. Συνεπώς, οι μονάδες PMU και το ευρύτερο πλαίσιο των συστημάτων WAMS αποτελούν πλέον αναπόσπαστο μέρος των σύγχρονων μηχανισμών εποπτείας των συστημάτων μεταφοράς ηλεκτρικής ενέργειας.

Αναμφίβολα, η εξέλιξη των μετρητικών υποδομών έχει συμβάλλει αποφασιστικά στη βελτίωση της λειτουργίας των εκτιμητών κατάστασης. Ιστορικά, η εποπτεία των ΣΗΕ βασίζεται σε αλγόριθμους εκτίμησης κατάστασης που χρησιμοποιούν μετρήσεις του συστήματος SCADA, οι οποίες συλλέγονται από μονάδες RTU. Υπό αυτές τις συνθήκες, η κατάσταση του συστήματος εξάγεται από μετρήσεις ροών και εγχύσεων ισχύος και μέτρων τάσης ζυγών, μέσω μη γραμμικών μοντέλων βελτιστοποίησης. Ωστόσο, η ποιότητα των εκτιμήσεων επηρεάζεται από διάφορες πηγές σφάλματος, συμπεριλαμβανομένης της χρονικής ασυμφωνίας (έλλειψης χρονικής συνάφειας) των μετρήσεων, του θορύβου επικοινωνίας που εισάγεται κατά τη μετάδοση των δεδομένων μέσω παρωχημένων διαύλων επικοινωνίας, καθώς και της υπόθεσης ότι το δίκτυο βρίσκεται σε μόνιμη κατάσταση λειτουργίας. Με την ενσωμάτωση των μονάδων PMU στις μετρητικές υποδομές των ΣΗΕ, γίνονται πλέον διαθέσιμες συγχρονισμένες μετρήσεις με υψηλούς ρυθμούς δειγματοληψίας και αναφοράς, επιπλέον των μη συγχρονισμένων συμβατικών μετρήσεων SCADA. Έτσι, τα χρονικά παράθυρα λειτουργίας των εκτιμητών κατάστασης αναμένεται να μειωθούν σε τάξεις των λίγων δευτερολέπτων, ενώ η συμβολή των PMU στην εξασφάλιση της παρατηρησιμότητας και στη βελτίωση της ακρίβειας της εκτίμησης είναι σημαντική. Επιπλέον, καθώς οι μονάδες PMU είναι ικανές να καταγράφουν τους φασιθέτες ροών ρευμάτων εκπεφρασμένους σε Καρτεσιανές συντεταγμένες, το μοντέλο μετρήσεων της εκτίμησης κατάστασης απλοποιείται σημαντικά και, μάλιστα, υπό ορισμένες συνθήκες, μπορεί να γραμμικοποιηθεί πλήρως, προσφέροντας σημαντική βελτίωση της επίδοσης της υπολογιστικής διαδικασίας του εκτιμητή. Τέλος, μία από τις πιο σημαντικές εφαρμογές της τεχνολογίας των PMU είναι η επιτήρηση της κατάστασης του ΣΗΕ υπό μεταβαλλόμενες συνθήκες λειτουργίας, μέσω τεχνικών δυναμικής εκτίμησης κατάστασης (DSE) και μεθόδων εκτίμησης κατάστασης υποστηριζόμενων από πρόβλεψη (FASE).

Υβριδική Εκτίμηση Κατάστασης ΣΗΕ

Παρά τα αδιαμφισβήτητα αυτά πλεονεκτήματα, η πλήρης αντικατάσταση των συμβατικών συσκευών μέτρησης με PMU (ή, γενικότερα, με ευφυείς ηλεκτρονικές συσκευές με δυνατότητες PMU) παραμένει ανέφικτη, κυρίως λόγω οικονομικών και τεχνικών περιορισμών – η διαλειτουργικότητα με παλαιότερα υποσυστήματα του ΚΕΕ και τα κόστη που σχετίζονται με τον εξοπλισμό, την εγκατάστασή του και τις σχετικές υποδομές επικοινωνιών αποτελούν σημαντικούς παράγοντες. Συνεπώς, στα περισσότερα συστήματα μεταφοράς, οι συγχρονισμένες μετρήσεις φασιθετών δεν επαρκούν για την επίτευξη της πλήρους παρατηρησιμότητας του δικτύου, καθιστώντας τα συστήματα SCADA απαραίτητα για την επίλυση της εκτίμησης κατάστασης, με τα PMU να λειτουργούν ως συμπληρωματική πηγή μετρήσεων. Ως εκ τούτου, η συνύπαρξη των δύο συστημάτων εποπτείας SCADA και WAMS παραμένει προς το παρόν πρακτική αναγκαιότητα, με τις μεθόδους υβριδικής εκτίμησης κατάστασης (HSE) να αξιοποιούν ταυτόχρονα μετρήσεις προερχόμενες από RTU και PMU. Οι συγκεκριμένες τεχνικές έχουν προσελκύσει σημαντικό ερευνητικό ενδιαφέρον, όπως αντικατοπτρίζεται από την πληθώρα σχετικών δημοσιεύσεων την τελευταία δεκαετία.

Όπως προαναφέρθηκε, αναμφίβολα η ενσωμάτωση δεδομένων από πολλαπλά μετρητικά συστήματα ενισχύει σημαντικά την απόδοση του εκτιμητή κατάστασης, βελτιώνοντας τόσο την ακρίβεια της εκτίμησης, όσο και την ευρωστία απέναντι σε εσφαλμένα δεδομένα, λόγω της υψηλής περίσσειας μετρήσεων. Ωστόσο, ο συνδυασμός δεδομένων από διαφορετικές πηγές δεν αποτελεί απλή διαδικασία, με τη σχετική βιβλιογραφία να εντοπίζει δύο βασικές κατηγορίες προκλήσεων:

1) *Διαφορετικοί ρυθμοί αναφοράς και χρονικά ασυνεπή δεδομένα*: Τα PMU καταγράφουν μετρήσεις με σημαντικά υψηλότερους ρυθμούς από ό,τι τα συστήματα SCADA. Επιπλέον, τα μετρητικά δεδομένα εισάγονται στον εκτιμητή κατάστασης χωρίς να εξασφαλίζεται η χρονική συνάφειά τους. Αυτή η χρονική δυσαρμονία σημαίνει ότι οι μετρήσεις από το πεδίο δεν αντιπροσωπεύουν απαραίτητα μία συγκεκριμένη χρονική στιγμή της λειτουργικής κατάστασης του ΣΗΕ. Πέρα από την απουσία συγχρονισμένων χρονικών σημάνσεων (timestamps) στα δεδομένα SCADA, επιπρόσθετες χρονικές ασυνέπειες προκύπτουν λόγω τυχαίων καθυστερήσεων μεταφοράς (propagation delays) των μετρητικών δεδομένων, μέσω των διαύλων επικοινωνίας, από το πεδίο προς το ΚΕΕ.

2) *Διαφορετικά μετρούμενα μεγέθη και επίπεδα ακρίβειας*: Τα δύο μετρητικά συστήματα συλλέγουν διαφορετικού τύπου δεδομένα, δημιουργώντας προκλήσεις στην υλοποίηση εφαρμογών υβριδικής εκτίμησης κατάστασης, καθώς συχνά απαιτούνται ριζικές τροποποιήσεις και προσαρμογές στο υπάρχον λογισμικό του ΚΕΕ. Επιπλέον, ενδέχεται να προκύψουν αριθμητικά ζητήματα, για παράδειγμα κατά την αρχικοποίηση του αλγορίθμου εκτίμησης κατάστασης, σε περίπτωση που οι μετρήσεις μιγαδικών ρευμάτων από PMU εκφράζονται σε πολικές συντεταγμένες. Επιπλέον, οι διαφορές στην ακρίβεια των αισθητήρων περιπλέκουν την ανάθεση βαρών στις μετρήσεις, ενώ σημαντικές αποκλίσεις στα επίπεδα ακρίβειας μπορούν να επηρεάσουν αρνητικά την κατάσταση (condition) της μήτρας κέρδους και, επομένως, την αξιοπιστία των αποτελεσμάτων της εκτίμησης.

Για την αντιμετώπιση αυτών των προκλήσεων, έχουν προταθεί διάφορες μέθοδοι στη βιβλιογραφία. Οι τεχνικές στατικής εκτίμησης κατάστασης (SSE) κατηγοριοποιούνται με βάση το εύρος εφαρμογής και τις αλγοριθμικές τους διαδικασίες, σε συνάρτηση με τις προαναφερθείσες προκλήσεις. Τα PMU λειτουργούν με σαφώς υψηλότερους ρυθμούς αναφοράς συγκριτικά με τα συστήματα SCADA, παρέχοντας έτσι πολλαπλά σύνολα μετρήσεων μεταξύ διαδοχικών ενημερώσεων των δεδομένων από RTU. Ωστόσο, η αποκλειστική χρήση μετρήσεων PMU σε αυτά τα χρονικά διαστήματα, πιθανότατα δεν θα επαρκεί για την επίτευξη της παρατηρησιμότητας του ΣΗΕ, καθιστώντας το πρόβλημα της εκτίμησης κατάστασης μη επιλύσιμο. Για την αντιμετώπιση αυτού του ζητήματος, έχουν αναπτυχθεί μέθοδοι που μετριάζουν την επίδραση της χρονικής ασυμφωνίας στην ακρίβεια της εκτίμησης ή, εναλλακτικά, αποκαθιστούν την παρατηρησιμότητα του συστήματος μεταξύ διαδοχικών αφίξεων μετρήσεων SCADA, μέσω τεχνικών πρόβλεψης και αξιοποίησης των στατιστικών χαρακτηριστικών των μετρήσεων. Ειδικότερα, οι προτεινόμενες προσεγγίσεις περιλαμβάνουν τεχνικές ανακατασκευής μετρήσεων (measurement reconstruction) με αξιοποίηση ιστορικών δεδομένων από το σύστημα SCADA, καθώς και προσωρινή αποθήκευση (buffering) των μετρήσεων PMU. Οι τελευταίες χρησιμοποιούνται για την επίλυση της εκτίμησης κατάστασης κατά την άφιξη νέων δεδομένων από τα RTU, καθιστώντας την προσέγγιση αυτή ιδιαίτερα αποτελεσματική για περιοδικές εκτιμήσεις κατάστασης σε διαστήματα μεγαλύτερα της περιόδου αναφοράς του SCADA. Επιπροσθέτως, οι διάφορες μέθοδοι που έχουν προταθεί για την αξιοποίηση ετερογενών μετρητικών δεδομένων μπορούν να κατηγοριοποιηθούν σε τρεις κύριες ομάδες:

1) Οι μέθοδοι υβριδικής εκτίμησης κατάστασης ενός σταδίου (ISE) διαμορφώνουν ένα ενιαίο μοντέλο μετρήσεων προερχόμενων από RTU και PMU, το οποίο αξιοποιείται για την επίλυση της εκτίμησης κατάστασης. Οι μέθοδοι ISE οδηγούν στη βέλτιστη λύση της HSE, υπό την έννοια ότι αυτή προσαρμόζεται βέλτιστα και στα δύο σύνολα μετρήσεων.
2) Μέθοδοι υβριδικής εκτίμησης κατάστασης πολλών σταδίων (PSE): Αυτές οι μέθοδοι διαχωρίζουν τις μετρήσεις RTU και PMU, επιλύοντας διαφορετικά προβλήματα εκτίμησης κατάστασης για κάθε υποσύνολο δεδομένων. Συνήθως, περιλαμβάνουν μια αρχική εκτίμηση βασισμένη σε μετρήσεις SCADA, ακολουθούμενη από μία γραμμική εκτίμηση κατάστασης με δεδομένα PMU – ή το αντίστροφο – διασφαλίζοντας έτσι ότι τα δύο σύνολα δεδομένων αντιστοιχούν σε ξεχωριστά μοντέλα μετρήσεων. Ο διαχωρισμός αυτός επιτρέπει την ενσωμάτωση δεδομένων φασιθετών με ελάχιστες τροποποιήσεις στο υπάρχον λογισμικό εκτίμησης κατάστασης. Εντούτοις, πρέπει να σημειωθεί ότι οι συγκεκριμένες μέθοδοι είναι προσεγγιστικές και η σύγκλισή τους, στην ίδια λύση που παρέχεται από τις (βέλτιστες) μεθόδους ISE, δεν είναι εγγυημένη.
3) Μέθοδοι σύντηξης δεδομένων σε συστήματα επιτηρούμενα από πολλαπλούς αισθητήρες (FSE): Οι συγκεκριμένες μέθοδοι παρουσιάζουν δομικές ομοιότητες με τους αλγορίθμους PSE, καθώς και οι δύο αξιοποιούν ξεχωριστούς εκτιμητές για διαφορετικές πηγές μετρήσεων. Σε αντίθεση με τις μεθόδους PSE, οι μέθοδοι FSE υπολογίζουν τις εκτιμήσεις αυτές παράλληλα, συνδυάζοντας τα αποτελέσματά τους μέσω ενός τελικού σχήματος βέλτιστης εκτίμησης ελάχιστης διακύμανσης. Αξίζει να σημειωθεί ότι η εφαρμογή των μεθόδων FSE καθιστά απαραίτητη προϋπόθεση την

πλήρη παρατηρησιμότητα (complete observability) του ΣΗΕ μέσω μετρήσεων PMU, κάτι το οποίο δεν είναι πρακτικά εφικτό για την πλειονότητα των δικτύων. Αυτό έχει ως αποτέλεσμα την αναγκαιότητα χρήσης ψευδομετρήσεων ή εκτιμήσεων/προβλέψεων μετρητικών δεδομένων PMU, για την επίτευξη πλήρους παρατηρησιμότητας.

Παράλληλα, η πλειονότητα των εκτιμητών κατάστασης που χρησιμοποιούνται ακόμα στα ΚΕΕ βασίζονται στην υπόθεση της μόνιμης κατάστασης λειτουργίας του συστήματος, παραβλέποντας την χρονική μεταβολή των συνθηκών λειτουργίας και την ύπαρξη δυναμικών φαινομένων. Οι μέθοδοι που προαναφέρθηκαν ονομάζονται «στατικές», υπό την έννοια ότι κάθε εκτίμηση του διανύσματος κατάστασης παρέχεται βάσει ενός και μοναδικού συνόλου μετρήσεων, η εκτέλεση του εκτιμητή γίνεται με ρυθμούς που δεν υπερβαίνουν τους ρυθμούς αναφοράς του SCADA, ενώ δεν αξιοποιούνται ισοδύναμα μοντέλα που να περιγράφουν τη δυναμική συμπεριφορά των στοιχείων του ΣΗΕ σε μεταβατική κατάσταση λειτουργίας. Αυτές οι παραδοχές αποτελούν απόρροια της χρήσης αποκλειστικά μη συγχρονισμένων και «αραιών» μετρητικών δεδομένων παρεχόμενων από τα συστήματα SCADA. Σήμερα, η εξάπλωση των PMU επιτρέπει την ανάπτυξη τεχνικών υβριδικής δυναμικής εκτίμησης κατάστασης (DSE), οι οποίες επιτρέπουν την θεώρηση του ΣΗΕ ως ενός χρονικά μεταβαλλόμενου συστήματος, καθώς και τη μελέτη αυτού υπό ποικίλες συνθήκες λειτουργίας.

Εν γένει, η στατική εκτίμηση κατάστασης αποδίδει ικανοποιητικά υπό συνθήκες οιονεί στατικής κατάστασης λειτουργίας, όπου το ΣΗΕ επιδέχεται ομαλές και σταδιακές μεταβολές. Σε αυτή την περίπτωση, οι μετρήσεις από το σύστημα SCADA επαρκούν για την επίλυση της εκτίμησης κατάστασης, με τις μετρήσεις PMU να ενισχύουν την περίσσεια μετρήσεων. Εντούτοις, η αυξανόμενη πολυπλοκότητα των σύγχρονων ΣΗΕ λόγω της εκτεταμένης διείσδυσης διεσπαρμένης παραγωγής, της αμφίδρομης ροής ισχύος και των νέων τεχνολογιών που ενσωματώνονται στην πλευρά της ζήτησης έχει αναδείξει τους περιορισμούς των στατικών μοντέλων εκτίμησης κατάστασης. Οι στοχαστικές διακυμάνσεις στη ζήτηση και την παραγωγή των ΑΠΕ εισάγουν σημαντική αβεβαιότητα στη λειτουργία του συστήματος, καθιστώντας τις στατικές μεθόδους συχνά μη βέλτιστες για την αποτύπωση της λειτουργικής κατάστασης σε πραγματικό χρόνο. Σε ταχέως μεταβαλλόμενες ή μεταβατικές συνθήκες λειτουργίας, τα PMU αποτελούν προς το παρόν τη μόνη κατάλληλη πηγή μετρήσεων για την αξιόπιστη εκτίμηση κατάστασης, ενώ τα δεδομένα του συστήματος SCADA μπορούν να αξιοποιηθούν μόνο ως συμπληρωματικές πληροφορίες.

Οι πιθανές καταστάσεις λειτουργίας ενός ΣΗΕ μπορούν γενικά να διαχωριστούν σε δύο αμοιβαία αποκλειόμενες συνθήκες: την οιονεί στατική (quasi-steady) και τη μεταβατική (transient) κατάσταση. Οι μεταβατικές συνθήκες λειτουργίας προκύπτουν όταν το σύστημα υφίσταται μια ξαφνική διαταραχή, όπως είναι τα σφάλματα, οι διακοπτικές λειτουργίες και οι απότομες μεταβολές στην παραγωγή και στην ζήτηση. Κατά την οιονεί στατική λειτουργία, το σύστημα υφίσταται μόνο αργές και σταδιακές μεταβολές στην παραγωγή και στην ζήτηση, προκαλώντας αμελητέες μεταβολές στις δυναμικές μεταβλητές κατάστασης, όπως είναι η ταχύτητα και η γωνία περιστροφής των δρομέων στις σύγχρονες γεννήτριες.

Όταν η δυναμική εκτίμηση κατάστασης (DSE) εφαρμόζεται σε συνθήκες οιονεί στατικής λειτουργίας, ο όρος «δυναμική» ενδέχεται να είναι παραπλανητικός, καθώς θεωρείται ότι η μεταβολή της δυναμικής κατάστασης του ΣΗΕ στον χρόνο, όπως αυτή σχετίζεται με την έννοια της ευστάθειας, είναι ανύπαρκτη ή αμελητέα. Σημασιολογικές διαφωνίες σχετικά με την έννοια και την εφαρμογή των μεθόδων DSE οδήγησαν τους ερευνητές στη διαμόρφωση του όρου «εκτίμηση κατάστασης υποστηριζόμενη από πρόβλεψη» (FASE). Καθώς το σύστημα εξελίσσεται με την πάροδο του χρόνου, οι διαδοχικές καταστάσεις δεν είναι ανεξάρτητες, αλλά αποτελούν σημεία μιας χρονοσειράς. Η μέθοδος FASE εκμεταλλεύεται αυτή τη συσχέτιση, χρησιμοποιώντας ένα γραμμικό μοντέλο που περιγράφει την εξέλιξη των μεταβλητών κατάστασης στον χρόνο, αγνοώντας τα μεταβατικά φαινόμενα.

Η εφαρμογή των μεθόδων υβριδικής δυναμικής εκτίμησης κατάστασης (DSE) παρουσιάζει προκλήσεις παρόμοιες με εκείνες που συναντώνται στην ανάπτυξη μεθόδων SSE, όπως η αξιοποίηση μη συγχρονισμένων μετρήσεων με διαφορετικούς ρυθμούς αναφοράς, η ανθεκτικότητα έναντι εσφαλμένων ή ελλιπών μετρήσεων, καθώς και η διαχείριση ετερογενών μετρητικών δεδομένων.

Συνεισφορές της Διδακτορικής Διατριβής

Το ερευνητικό έργο που περιγράφεται στην παρούσα διδακτορική διατριβή κινείται σε δύο βασικούς άξονες. Ο πρώτος άξονας αφορά τη διαμόρφωση υβριδικών μεθόδων στατικής εκτίμησης κατάστασης (SSE) με περιορισμένο αριθμό μετρήσεων από PMU, ενώ ο δεύτερος επικεντρώνεται στην ανάπτυξη μιας μεθόδου εκτίμησης κατάστασης υποστηριζόμενης από πρόβλεψη (FASE), υπό την παρουσία ετερογενών μετρητικών δεδομένων με διαφορετικούς ρυθμούς αναφοράς. Η αποτελεσματικότητα όλων των προτεινόμενων προσεγγίσεων διερευνάται μέσω εκτενών προσομοιώσεων σε πρότυπα ηλεκτρικά δίκτυα.

Αρχικά, παρουσιάζεται η ανάπτυξη μιας υβριδικής στατικής μεθόδου SE βασισμένης στη βελτιστοποίηση σταθμισμένων ελαχίστων τετραγώνων (WLS) με περιορισμούς ισότητας. Η προτεινόμενη προσέγγιση απορρέει από την ευρέως γνωστή μέθοδο επίλυσης Hachtel (Hachtel's augmented matrix) και προσφέρει τα ακόλουθα πλεονεκτήματα:

1) Ανεξάρτητη διαμόρφωση των μοντέλων μετρήσεων SCADA και PMU, η οποία καθιστά τη μέθοδο ευέλικτη και κατάλληλη για τις υλοποιήσεις ISE, PSE και FSE, ανάλογα με τις δυνατότητες του συστήματος διαχείρισης ενέργειας (EMS) και τις απαιτήσεις του ΚΕΕ.
2) Η προτεινόμενη διατύπωση του προβλήματος HSE παρακάμπτει ορισμένους περιορισμούς που σχετίζονται με τη λειτουργία των αλγορίθμων PSE και FSE. Συγκεκριμένα, μέσω αναλυτικών υπολογισμών και εκτενών προσομοιώσεων, αποδεικνύεται ότι ο αλγόριθμος PSE διατηρεί στην πράξη την ιδιότητα της βέλτιστης αμερόληπτης εκτίμησης, παρέχοντας αποτελέσματα συγκρίσιμα με του αλγορίθμου ISE. Επιπλέον, ο αλγόριθμος FSE είναι εφαρμόσιμος σε συστήματα με μερική παρατηρησιμότητα (partial observability) από PMU, χωρίς να απαιτείται η ανακατασκευή ή πρόβλεψη μετρήσεων ή η χρήση ψευδομετρήσεων. Τέλος, οι αλγόριθμοι PSE και FSE είναι κατάλληλοι για την αναβάθμιση του ήδη υπάρχοντος λογισμικού εκτίμησης κατάστασης των ΚΕΕ με μετρήσεις PMU με ελάχιστες τροποποιήσεις.
3) Η προτεινόμενη μέθοδος αποδίδει εξαιρετικά αποτελέσματα, υπερτερώντας παρόμοιων μεθόδων PSE και FSE όσον αφορά την ακρίβεια, χωρίς να αυξάνει σημαντικά τις υπολογιστικές απαιτήσεις. Η εφαρμοσιμότητα και η αποτελεσματικότητά της επαληθεύονται μέσω εκτενών αριθμητικών προσομοιώσεων σε πρότυπα δίκτυα IEEE, χρησιμοποιώντας ευρέως καθιερωμένους δείκτες επίδοσης εκτιμητών κατάστασης.
4) Η διατύπωση του μοντέλου μετρήσεων PMU σε Καρτεσιανές συντεταγμένες μειώνει τη μη γραμμικότητα και τη μη κυρτότητα (non-convexity) του προβλήματος βελτιστοποίησης, συμβάλλοντας στην αύξηση της υπολογιστικής απόδοσης των προτεινόμενων αλγορίθμων.

Επιπλέον, με γνώμονα την εκτεταμένη ενσωμάτωση τεχνολογιών μεταφοράς υψηλής τάσης συνεχούς ρεύματος (HVDC), ιδίως για τη διασύνδεση ανανεώσιμων πηγών ενέργειας και την ανάπτυξη υποθαλάσσιων διασυνδέσεων, οι σύγχρονοι αλγόριθμοι εκτίμησης κατάστασης καλούνται να ενσωματώνουν ισοδύναμα μοντέλα για την ακριβή αναπαράσταση των εν λόγω στοιχείων. Ως εκ τούτου, αναπτύχθηκε ένα ισοδύναμο μοντέλο για κλασικές συνδέσεις HVDC με μετατροπείς πηγής ρεύματος (CSC HVDC) κατάλληλο για στατική υβριδική εκτίμηση κατάστασης. Η εγκυρότητά του επαληθεύεται μέσω προσομοιώσεων, θεωρώντας μετρήσεις εναλλασσόμενου ρεύματος (AC) από το σύστημα SCADA και από PMU, καθώς και ποικίλους συνδυασμούς μετρήσεων στην πλευρά του συνεχούς ρεύματος (DC). Οι κύριες συνεισφορές του προτεινόμενου αλγορίθμου ISE για δίκτυα HVAC/HVDC είναι οι εξής:

1) Ανεξάρτητη διαμόρφωση των συνόλων μετρήσεων AC και DC, εκπεφρασμένων ως συναρτήσεις των AC και DC μεταβλητών κατάστασης αντιστοίχως, και ταυτόχρονος υπολογισμός όλων των μεταβλητών κατάστασης μέσω ενιαίου εκτιμητή.
2) Διαμόρφωση των μαθηματικών εξισώσεων που συσχετίζουν τις μεταβλητές κατάστασης των υποσυστημάτων AC και DC, αξιοποιώντας τις σχέσεις που περιγράφουν τους μετασχηματιστές ζεύξης (coupling transformers) και τη λειτουργία των μετατροπέων σε κάθε πλευρά της ζεύξης HVDC, οι οποίες συμπεριλαμβάνονται στο πρόβλημα εκτίμησης κατάστασης μέσω ενός συνόλου μη γραμμικών περιορισμών ισότητας.
3) Επίτευξη παρατηρησιμότητας των ζεύξεων CSC-HVDC με λιγότερες μετρήσεις, συγκριτικά με σχετικές μεθόδους της βιβλιογραφίας.

Ακολούθως, στο πλαίσιο της διατριβής έγινε μια πρώτη διερεύνηση της επίδρασης των διαφορετικών πιθανών διατάξεων μέτρησης φασιθετών ρεύματος μέσω PMU – με τη μορφή ροών ή εγχύσεων – στην υβριδική μέθοδο εκτίμησης κατάστασης ISE, αξιολογώντας την απόδοσή της ως προς τη σύγκλιση και την ακρίβεια, ζήτημα που δεν έχει μελετηθεί επαρκώς στη βιβλιογραφία. Επιπλέον, εξετάστηκαν πρακτικά ζητήματα που σχετίζονται με το τεχνικό μέρος της εγκατάστασης των PMU, όπως η επιλογή των σημείων μέτρησης σε επίπεδο κυκλώματος τόσο σε δίκτυα διανομής, όσο και σε συστήματα μεταφοράς. Τα ευρήματα αυτής της ανάλυσης καταδεικνύουν ότι η κατάλληλη επιλογή των σημείων μέτρησης των μιγαδικών ρευμάτων από PMU είναι κρίσιμης σημασίας για την αποτελεσματική εφαρμογή των μεθόδων ISE.

Λόγω της αυξημένης πολυπλοκότητας και στοχαστικότητας των σύγχρονων ΣΗΕ, η μετάβαση σε προηγμένους αλγόριθμους εκτίμησης κατάστασης που προσφέρουν βελτιωμένη επίγνωση των συνθηκών λειτουργίας του συστήματος, δεν αποτελεί απλώς μια αναμενόμενη εξέλιξη, αλλά αναγκαιότητα. Υπό αυτό το πρίσμα, ο δεύτερος ερευνητικός άξονας της παρούσας διατριβής εστιάζει στην ανάπτυξη μιας μεθόδου εκτίμησης κατάστασης πολλών σταδίων (multi-stage) υποστηριζόμενης από πρόβλεψη (FASE) βασισμένης στο επεκτεταμένο μαθηματικό φίλτρο Kalman (EKF), η οποία είναι εφαρμόσιμη σε συστήματα που δεν είναι πλήρως παρατηρήσιμα από PMU. Η προτεινόμενη μέθοδος συμβάλει στην αποτελεσματική διαχείριση ετερογενών μετρητικών δεδομένων με διαφορετικούς ρυθμούς αναφοράς, ενώ παράλληλα απαιτεί ελάχιστες τροποποιήσεις στο υφιστάμενο λογισμικό SSE. Οι κύριες συνεισφορές της συνοψίζονται ως εξής:

1) Βήμα πρόβλεψης (time update step): Η χρήση του EKF στις κλασικές μεθόδους FASE βασίζεται σε μοντέλα μετάβασης καταστάσεων (state transition models), των οποίων οι παράμετροι έχουν υπολογιστεί εκ των προτέρων με βάση ιστορικά δεδομένα και οι τιμές τους διατηρούνται σταθερές κατά την διεξαγωγή εκτίμησης κατάστασης σε πραγματικό χρόνο, περιορίζοντας έτσι την ικανότητά τους να προσαρμόζονται σε ταχέως μεταβαλλόμενες συνθήκες. Επομένως, αντί ενός μοντέλου μετάβασης που να βασίζεται αποκλειστικά σε πρόβλεψη (forecasting), η προτεινόμενη μέθοδος FASE αξιοποιεί τη γραμμική σχέση μεταξύ των μεταβλητών κατάστασης παρατηρήσιμων από PMU και των αντίστοιχων μετρήσεων, για τη διαμόρφωση ενός μοντέλου μετάβασης που ενημερώνεται συνεχώς με δεδομένα που αντιπροσωπεύουν την τρέχουσα λειτουργική κατάσταση του ΣΗΕ. Η συγκεκριμένη προσέγγιση βασίζεται στη θεωρία βέλτιστης σύντηξης δεδομένων από πολλαπλούς αισθητήρες (multi-sensor data fusion theory), ώστε να παρέχει μια αξιόπιστη εκ των προτέρων (*a priori*) εκτίμηση των μεταβλητών κατάστασης παρατηρήσιμων από PMU.
2) Βήμα διόρθωσης (forward correction / measurement update step): Η πλειονότητα των μεθόδων FASE στη βιβλιογραφία, αφορά υλοποιήσεις ISE, στις οποίες οι μετρήσεις SCADA και PMU αναμειγνύονται σε κοινό μοντέλο μετρήσεων, απαιτώντας έτσι σημαντικές τροποποιήσεις ή αντικατάσταση του υπάρχοντος λογισμικού στο ΚΕΕ. Στην προτεινόμενη προσέγγιση, οι *a priori* εκτιμήσεις που παρέχονται από το μοντέλο μετάβασης, μαζί με τις συγχρονισμένες μετρήσεις φασιθετών, υποβάλλονται σε ξεχωριστή επεξεργασία από τις μετρήσεις SCADA, σε δύο διακριτά

στάδια της διαδικασίας εκτίμησης. Έτσι αποφεύγονται πιθανές παρεμβάσεις στο συμβατικό λογισμικό SSE, το οποίο παραμένει ως έχει, ενώ παράλληλα ελαχιστοποιείται η ανταλλαγή δεδομένων μεταξύ των σταδίων της εκτίμησης, γεγονός που διευκολύνει την ενσωμάτωση της μεθόδου στο υφιστάμενο λογισμικό του EMS.

3) Βήμα εξομάλυνσης (backward correction / smoothing step): Με σκοπό την αντιμετώπιση του ζητήματος της έλλειψης χρονικής συνάφειας μεταξύ των μετρήσεων, η προτεινόμενη μέθοδος ενσωματώνει ένα βήμα εξομάλυνσης στη διαδικασία EKF, βασισμένο στον αλγόριθμο εξομάλυνσης σταθερού διαστήματος (fixed-interval smoothing algorithm) Bryson-Frazier (MBF). Ο αλγόριθμος MBF αξιοποιεί μελλοντικά σύνολα μετρήσεων, και, μέσω των στατιστικών τους χαρακτηριστικών, επανεκτιμά βέλτιστα το διάνυσμα κατάστασης προηγούμενων χρονικών στιγμών. Η χρήση αντίστοιχων αλγορίθμων δεν έχει διερευνηθεί ευρέως στο πλαίσιο των μεθόδων FASE, ενώ η μέθοδος Rauch-Tung-Striebel (RTS) που έχει προταθεί σε προηγούμενες εργασίες επιβάλλει πολλαπλές και αυστηρές υποθέσεις όσον αφορά την οιονεί στατική κατάσταση λειτουργίας του ΣΗΕ και απαιτεί υπολογιστικά ασύμφορες αντιστροφές πινάκων. Σε σύγκριση με τον αλγόριθμο RTS, η προτεινόμενη μέθοδος είναι υπολογιστικά αποδοτικότερη, ενώ η εφαρμοσιμότητά της είναι λιγότερο περιορισμένη από τις διάφορες παραδοχές ως προς την λειτουργική κατάσταση του ΣΗΕ. Επιπλέον, στην προτεινόμενη προσέγγιση, οι παράμετροι του μοντέλου μετάβασης καταστάσεων ενημερώνονται μετά από κάθε εκτέλεση της μεθόδου FASE, μέσω του αλγορίθμου MBF. Με αυτόν τον τρόπο, ενσωματώνεται διαρκώς πληροφορία από μελλοντικές μετρήσεις στην εκτίμηση (διόρθωση) των παραμέτρων του μοντέλου μετάβασης, μειώνοντας έτσι τα σφάλματα εκτίμησης που οφείλονται στην ελλιπή προσαρμογή των υφιστάμενων μοντέλων πρόβλεψης του EKF στις πραγματικές συνθήκες λειτουργίας.

Καθώς ο εντοπισμός και η ανίχνευση εσφαλμένων μετρήσεων (bad data) αποτελούν αναπόσπαστο κομμάτι των εκτιμητών κατάστασης, γίνεται ανάπτυξη αλγορίθμων επεξεργασίας εσφαλμένων δεδομένων, στο πλαίσιο των προτεινόμενων μεθόδων ISE, PSE και FASE, με χρήση του ελέγχου μεγίστων κανονικοποιημένων υπολοίπων, βασιζόμενοι σε συνήθεις πρακτικές της σχετικής βιβλιογραφίας.

Τέλος, πρακτικές πτυχές της παρούσας έρευνας παρουσιάζονται αξιοποιώντας εργαστηριακή διάταξη του Εργαστηρίου ΣΗΕ του ΕΜΠ, η οποία αποτελείται από συσκευές PMU του εμπορίου, PMU χαμηλού κόστους, και ψηφιακό προσομοιωτή ηλεκτρικών δικτύων πραγματικού χρόνου, και καθιστά δυνατή τη δοκιμή και αξιολόγηση αλγορίθμων εποπτείας που βασίζονται σε συγχρονισμένα δεδομένα φασιθετών. Η ανάπτυξη και ρύθμιση του εξοπλισμού και του λογισμικού της πειραματικής διάταξης περιγράφονται λεπτομερώς, ενώ το σχετικό Κεφάλαιο ολοκληρώνεται με εκτενείς προσομοιώσεις αλγορίθμων εκτίμησης κατάστασης σε πραγματικό χρόνο και την αξιολόγηση της επίδοσής τους, τόσο σε συστήματα μεταφοράς, όσο και σε ακτινικά δίκτυα διανομής.

Η διδακτορική διατριβή ολοκληρώνεται με μια ανακεφαλαίωση των σημαντικότερων συμπερασμάτων που προέκυψαν από την πολυετή αυτή έρευνα, ενώ παρέχονται και ενδεχόμενες κατευθύνσεις για μελλοντική μελέτη, γύρω από τις τεχνικές εκτίμησης κατάστασης που αξιοποιούν ετερογενή μετρητικά δεδομένα.

1. INTRODUCTION

The global power systems landscape is undergoing a period of substantial and rapid change, driven by various factors that necessitate the modernization of infrastructure to meet contemporary operational demands [1]. The demand for high-quality power has been steadily increasing, particularly in developing countries, while global grid interconnections have expanded significantly. Additionally, deregulation has led to increased separation of power producers and consumers. Finally, a pivotal factor is the transition from the existing fossil fuel and nuclear generation towards an increasing reliance on renewables, or more generally, Decentralized Energy Resources (DERs), leading to the assimilation of more and varied energy sources into the grid [2]. This is particularly true in Europe, where the targets set by the European Commission are promoting ambitious plans, in the member states, for the renovation of the generation portfolio [1].

Power grids are overall shifting from a load-driven paradigm to a generation-driven system, wherein generation dictates the operational dynamics of the system. This shift, in turn, introduces several challenges to power system operation [1]:

- The location of generation sites is determined by the availability of Renewable Energy Resources (RES) rather than the proximity to major consumption centers.
- The inherent variability of renewable energy sources introduces substantial stochasticity in the electric network operation, as traditional dispatchable power sources are supplanted by probabilistic generation patterns. This necessitates the use of advanced prediction tools and complicates the alignment of generation with demand compared to conventional energy sources.
- Integrating DERs into the existing grid requires significant modifications to transmission infrastructure. The regulatory environment surrounding transmission development is complex, involving multiple federal, state, and local regulations. This complexity can delay the construction of new transmission lines and make it difficult to plan for future needs.

Consequently, power systems have expanded in size, their planning and operation have become more complex, and they are pushed increasingly close to their operating limits, with the European Network of Transmission System Operators for Electricity (ENTSO-E) interconnected system exemplifying this trend of stressed power systems [2]. Addressing these challenges requires more robust and flexible power systems, which, in turn, demands the development and integration of innovative technological solutions.

In this context, the need for more accurate and extensive monitoring and control mechanisms, supported by effective and resilient information and communication technologies, becomes imperative, as they have become vital for sustaining power system reliability and ensuring an adequate and secure electricity supply to consumers [2], [3].

Consequently, the synergy between secure, efficient, and economical operation of the power grid and advanced information technologies is paramount for addressing future challenges. Electric transmission systems have been at the forefront of this evolution. Notable research initiatives have focused on the development and deployment of innovative approaches to enhance transmission system visibility, facilitated by State Estimation (SE) – an essential tool of the Energy Management System (EMS) that enables a reliable assessment of the power system's current operational state, thereby supporting real-time operation and control. Additionally, ongoing research efforts seek to integrate recent technological advancements in metering infrastructure, such as Wide Area Monitoring, Protection, and Control (WAMPAC) schemes, as well as advanced network controllers such as Flexible AC Transmission Systems (FACTS) and High Voltage Direct Current (HVDC) technologies, into the existing monitoring frameworks. In summary, research in advanced monitoring methods for transmission systems can be categorized into two main areas [4]: new algorithms and new measurement technologies.

1.1 Motivation

This Section presents the motivation for this thesis by drawing upon recent developments in the two core aspects of power transmission system monitoring, that is, algorithms and measurement technologies. Specifically, it highlights the importance of advanced power system SE algorithms and the advantages of synchrophasor measurement systems. It also underscores the necessity of validating the efficacy of such innovative SE algorithms and measurement configurations, both through offline simulations and online laboratory-scale test beds.

1.1.1 Energy control centers and power system state estimation

As transmission networks continue to expand, the complexity of their operation has increased. The growing distance between bulk generation and load centers, coupled with the integration of large-scale renewables, introduces additional operating constraints. These factors have drawn heightened attention to the Energy Control Center (ECC) and the methods employed for monitoring and control of transmission systems [5]. Advanced computing systems and software tools within ECCs play a central role in processing and analyzing field data, managing the vast volume of available information, and issuing appropriate control commands. Given that ECCs date back to the 1950s, the primary challenge faced by modern ECCs, as opposed to earlier iterations, is the rapid expansion of power grid geographic coverage and, consequently, the substantial increase in stakeholders and users they must manage. Serving electricity markets, public system operators, private electricity providers, independent producers, large consumers, and low-voltage (LV) consumers imposes increased demands on the computational power and reliability of ECC tools to ensure their effective operation.

Viewing the power system infrastructure as an integration of several subsystems (e.g., transmission, distribution networks, and consumers), it is essential to maintain a sufficient level of situational awareness throughout its entirety to ensure proper operation. This means that system conditions must remain within predefined limits based on specific endogenous and exogenous parameters. The system's state is assessed by studying key characteristics and is determined using rigorous mathematical tools. Generally, the complete state of a power system at a given moment can be established if the system model – comprising all nodes, branches, and their respective parameters – is known, along with the voltage phasors at each node.

Before the introduction of power system SE, the Transmission System Operator (TSO) was tasked with performing most of the real-time functions within the ECC, including generation and interchange scheduling, outage monitoring and scheduling, frequency and time corrections, bias setting coordination, and emergency system restoration. These activities were guided by operational procedures established by the planning department, which were informed by comprehensive load flow studies. However, operators frequently encountered unforeseen circumstances not encompassed by the planning scenarios.

To address this, load flow software was installed in the ECC, allowing operators to input manually collected data that reflected real-time conditions. Although this constituted an improvement, the operator's load flow solutions were often compromised due to inadequate or inconsistent data, as well as occasional gross errors in both measurements and the network model [6]. This revealed a disconnect between the planning-based load flow analyses and the practical requirements of the TSO, establishing a clear need for a process that could utilize various imprecise field measurements to accurately estimate the real-time state of the system.

State estimation aims to determine the system's state based on available measurements, effectively assigning values to all voltage phasors across the network, which constitute the system's state variables. The state estimator has now been solidified as the only computational process within ECCs capable of producing an accurate real-time representation of a network's condition. Thus, situational awareness in power systems is directly linked to ECCs, where measurement data from installed metering devices are aggregated, processed, and analyzed. Consequently, the reliable operation of power systems is inextricably tied to the existence of effective and robust monitoring mechanisms within ECCs.

Traditional Supervisory Control and Data Acquisition (SCADA) systems rely on Remote Terminal Unit (RTU) devices for power system monitoring, which provide scalar information from the field at intervals of several seconds. In AC systems, RTUs typically report the Root Mean Square (RMS) values of active and reactive power, voltages and currents. Early SE algorithms relied on measurements of line power flows to infer bus voltage angles and magnitudes (i.e., the state variables of the system) [7]. Direct measurement of the state was infeasible; instead, it was inferred from the low-resolution, unsynchronized SCADA data, via nonlinear optimization models. This limitation, coupled with the necessity of gathering a substantial volume of measurements within the ECC, compelled the initial state estimators to make compromises that persist to this day [6]. Furthermore, SE accuracy was often compromised due to various error sources, including temporal measurement inconsistencies, communication noise, and the assumption of steady-state operating conditions.

1.1.2 Phasor measurement units and hybrid state estimation

The development of advanced measurement and automation systems across the entirety of power systems is a critical step toward the transition to smart grids. The demands for enhanced remote monitoring and control are being addressed through the gradual modernization of the relevant equipment, which consists of sensor units and actuators that are subject to remote control. A significant development in this field has been the shift from analog and electromechanical devices to digital implementations, paving the way for more advanced measurement technologies [4]. The past decade has seen the widespread installation of high-precision measurement units with advanced capabilities, such as Phasor Measurement Units (PMUs). PMUs are measurement devices capable of measuring not only the amplitude but also the phase of sinusoidal quantities, while offering significantly higher reporting rates compared to RTUs. The phasors recorded by PMUs are calculated and timestamped with respect to a global time reference, typically derived from the Global Positioning System (GPS). In the same vein, switching and protection devices are being upgraded through their capability to receive synchronized phasor measurements, effectively gaining PMU functionalities. The advent of this novel measurement technology has led to the development of Wide Area Monitoring Systems (WAMS), which are networks of interconnected PMUs that provide situational awareness of the power system operating conditions with sub-second granularity [4].

Undoubtedly, advancements in metering infrastructure have significantly improved state estimator performance. Specifically, the integration of PMUs into power system measurement configurations now enables the use of precise, synchronized phasor measurements with high sampling and reporting rates, in addition to conventional SCADA measurements, significantly enhancing network observability and SE accuracy. Additionally, as PMUs can record complex branch currents in Cartesian coordinates, the SE measurement model is significantly simplified. Under certain conditions, it can even be fully linearized, greatly improving the computational efficiency of the state estimator. Consequently, state estimator execution times are expected to decrease to a few seconds.

Additionally, one of the most important applications of PMUs is *dynamic state estimation*, which enables real-time power system monitoring under rapidly changing or transient conditions. With the increasing importance of system dynamics and the need to operate transmission grids closer to their capacity, it has become clear that conventional SCADA systems are insufficient for effective monitoring during critical events. Furthermore, direct measurement of bus voltage phase angles is essential for assessing overall system stability. Consequently, a prominent application of PMUs, and the broader WAMS framework, is the dynamic monitoring of the system operating conditions, through Dynamic State Estimation (DSE) methods [5]. In essence, PMUs serve as the enabling technology for DSE to achieve extensive real-time system visibility and situational awareness, and provide reliable information to downstream control and operation functions within the ECC [8].

Despite the coexistence of SCADA and WAMS monitoring systems being a practical necessity, incorporating multi-rate, heterogeneous measurements into SE is complicated by issues such as the absence of synchronized timing of measurements (the "time skewness" problem) and the diversity of recorded electrical quantities. These factors often necessitate modifications to existing SE software to handle PMU data, and can lead to algorithmic convergence issues due to large discrepancies in measurement accuracy among measurement systems [9]. Research into addressing these issues has resulted in the formulation of various Hybrid State Estimation (HSE) methods that aim to optimally combine PMU measurements with the existing conventional measurements, and investigates the following main topics:

1) Different mathematical models for integrating PMU and SCADA measurements into the SE problem,
2) HSE implementation considerations and feasibility studies,
3) HSE-based power system monitoring and control applications, and
4) Optimal PMU placement for HSE.

This thesis aims to contribute to the first three aspects of HSE research, by proposing novel HSE approaches designed to enable integration of diverse measurement sources into SE, as well as demonstrate the effectiveness of HSE in power system monitoring, as will be detailed in the following Section.

1.1.3 Laboratory-scale platforms for PMU-based application studies

The critical importance of synchronized PMU measurements has been widely recognized across a range of power system applications, which is reflected in the accelerating deployment of PMUs worldwide. Beyond SE, PMUs are also used for fault location, inter-area oscillation monitoring, model parameter tuning and validation, as well as many other WAMPAC functions. A proven method for developing and validating these applications is the use of Hardware-in-the-Loop (HIL) simulation, which enables the creation of proof-of-concept for new devices and software tools, the evaluation of the accuracy and reliability of integrated solutions and the conduction of certification or pre-commissioning tests. This thesis further illustrates practical examples and laboratory-scale configurations where HIL simulations have been utilized to develop synchrophasor applications and validate their performance under different scenarios [10].

1.2 Thesis outline

This Section summarizes the primary contributions and structure of the thesis, referencing the corresponding publications of the author.

Chapter 2 – Energy management systems and SCADA

Chapter 2 traces the historical progression and functional evolution of the EMS, highlighting how SCADA has played a pivotal role in real-time data gathering, network monitoring, and control. The Chapter examines the critical hardware and software components of SCADA and discusses how EMS platforms have evolved to accommodate larger, more complex power networks. By reviewing standard EMS applications, the Chapter establishes the context for how modern power system operations strongly rely on the SCADA infrastructure.

Chapter 3 – Synchrophasor measurement systems

Chapter 3 provides a historical overview of time-synchronized measurements and their applications in power systems. It describes the key components of the synchrophasor measurement system, including PMUs, PMU-enabled devices, time synchronization sources, and phasor data concentrators. The Chapter elaborates on the role of each component and demonstrates their collaborative operation as part of a comprehensive technological solution. These foundational insights introduce the reader to the fundamentals of synchrophasor technology and its intended uses.

Chapter 4 – Power system monitoring and state estimation

Chapter 4 emphasizes the significance of continuous, real-time power system monitoring and its close relationship with SE, a crucial function for ensuring system security and reliability. It introduces the fundamental mathematical formulation of SE, focusing on how real-time measurements – from both traditional SCADA and synchrophasor technologies – are leveraged to derive an estimate of the current state. This Chapter also delves into dynamic state estimation methods, which extend the traditional static SE framework to account for rapidly changing system conditions and transient events. It introduces the framework of Kalman filters and explains their importance in capturing system dynamics and utilizing state forecasting techniques in enhancing SE performance.

Chapter 5 – Hybrid power system state estimation [R1]

This Chapter offers a new perspective on categorizing hybrid SE approaches, detailing various methods for integrating synchronized phasor measurements into power system SE. The material presented sets the stage for the subsequent Chapters.

[R1] O. Darmis and G. Korres, "A survey on hybrid SCADA/WAMS state estimation methodologies in electric power transmission systems," *Energies*, vol. 16, no. 2, Jan. 2023.

Chapter 6 – Hybrid static state estimation under limited PMU availability [R2]–[R4]

This Chapter introduces an equality-constrained hybrid static SE algorithm that combines data from SCADA and WAMS systems. The proposed method is founded on the widely adopted Weighted Least Squares (WLS) approach and is applicable to both single- and multi-stage SE architectures. A key advantage of this approach is its non-intrusive implementation, which preserves the core functions of conventional SE software within the EMS, while improving the efficacy of existing SCADA-based estimators.

This Chapter also presents a hybrid state estimation algorithm for AC power systems with integrated classic HVDC links. The proposed nonlinear WLS-based method models the AC system zero injections and AC/DC coupling equations as equality constraints and calculates both AC and DC states simultaneously.

The Chapter finally aims to assess the impact of PMU current measurement schemes on SE, by investigating its performance (convergence and accuracy) in the presence of current flow or injection data, as well as a combination of both. Moreover, practical considerations on technical installation issues, e.g., the circuit-level measurement point and the utilization of instrument transformers, are discussed. The findings from the proposed analysis show that the configuration of available current measurements strongly affect the SE quality, thus, explicit planning of relevant metering schemes is required.

After elaborating on the derivation and the different formulations of the proposed methods, Chapter 6 concludes with extensive numerical simulations on several IEEE benchmark systems, to evaluate their performance and effectiveness.

[R2] O. A. Darmis and G. N. Korres, "A hybrid power system state estimator under limited PMU availability," *IEEE Trans. Power Syst.*, vol. 39, no. 6, pp. 7166–7177, Nov. 2024.

[R3] O. Darmis, G. Karvelis, and G. N. Korres, "PMU-based state estimation for networks containing LCC-HVDC Links," *IEEE Trans. Power Syst.*, vol. 37, no. 3, pp. 2475–2478, May 2022.

[R4] T. Xygkis, O. Darmis, and G. Korres, “Impact of current measurement configuration on power system state estimation,” in *14th Mediterranean Conference on Power Generation Transmission, Distribution and Energy Conversion (MEDPOWER)*, Athens, Greece, 2024, pp. 1–6.

Chapter 7 – Forecasting-aided state estimation using multi-source, multi-rate measurements [R5]

Chapter 7 presents a multi-stage forecasting-aided SE framework with equality constraints, utilizing the extended Kalman filter to independently process SCADA and PMU data. The conventional SCADA-based state estimator remains unaltered and is augmented with synchronized PMU data and a priori state information derived from the extended Kalman filter. To enhance the accuracy of the forecasting model, an estimation fusion technique is developed, leveraging real-time PMU measurements. To address measurement asynchronization and random delays, the modified Bryson-Frazier fixed-interval smoothing algorithm is applied, combining current state information with a series of prior FASE solutions to optimally infer the system states. Extensive numerical simulations on the IEEE 14-, 118-, and 300-bus benchmark systems demonstrate the efficacy and practical applicability of the proposed method.

[R5] O. Darmis and G. N. Korres, “Forecasting-aided power system state estimation using multisource multirate measurements,” *IEEE Trans. Instrum. Meas.*, vol. 74, pp. 1–15, 2025.

Chapter 8 – Bad data processing in state estimation

As the identification and detection of erroneous measurements (bad data) constitute an integral part of state estimators, algorithms for bad data processing are developed within the framework of the proposed HSE methods, using the largest normalized residual test, in accordance with standard practices in the relevant literature.

Chapter 9 – Laboratory-scale PMU-based power system monitoring platform [R6]–[R9]

Chapter 9 outlines a laboratory setup for simulations in power system monitoring, using PMUs. The setup integrates a real-time power system simulation platform with hardware PMUs and software PDCs, and is used to replicate realistic grid conditions and monitor system behavior under various scenarios. The key components of the experimental environment, including the power system simulator, PMU devices, data acquisition systems, and time-synchronization sources, are detailed. The Chapter also covers the configuration process, which includes interfacing PMUs with the simulator and the utilization of phasor data concentrators for real-time data aggregation and filtering. Case studies on an IEEE benchmark system and a reduced version of the Kythnos distribution network, demonstrate the effectiveness of HSE and PMU-based SE methods.

[R6] O. Darmis, G. N. Korres, D. Lagos, and N. D. Hatziargyriou, “A hardware-in-the-loop configuration for real-time power system monitoring,” in *2022 IEEE PES Innovative Smart Grid Technologies Conference Europe (ISGT-Europe)*, Novi Sad, Serbia, 2022, pp. 1–5.

[R7] O. Darmis and G. N. Korres, “RTDS-supported software-in-the-loop test bed for synchrophasor applications,” in *2022 2nd International Conference on Energy Transition in the Mediterranean Area (SyNERGY MED)*, Thessaloniki, Greece, 2022, pp. 1–6.

[R8] V. Giotopoulos, O. Darmis, and G. Korres, “A comprehensive scheme of open-source tools and low-cost PMUs for the deployment of synchrophasor applications,” presented in *Protection, Automation & Control World Conference 2024 (PAC World 2024)*, Athens, Greece, 2024, pp. 1–8.

[R9] T. Xygkis, O. Darmis, G. Karvelis, A. Dimeas, G. Korres, and N. Hatziargyriou, “D-PMU based state estimation and fault analysis in active distribution grids: a case study for Kythnos Island, Greece,” in *27th International Conference on Electricity Distribution (CIRED 2023)*, Rome, Italy, 2023, pp. 3108–3113.

Chapter 10 – Conclusions and prospects

The final Chapter summarizes the main findings of this research, emphasizing the effectiveness of the methods that have been proposed for enhancing HSE performance and applicability. It also acknowledges the limitations encountered during the study and proposes potential future research directions.

2. ENERGY MANAGEMENT SYSTEMS AND SCADA

The electric power system is a vast, geographically dispersed network that delivers energy to critical sectors, including residential, commercial, and industrial facilities. As more sectors, such as transportation, are increasingly electrified, the complexity of power systems has grown significantly. To effectively manage this complexity, the power system relies on computer-assisted systems for its monitoring, control, and overall operation. Over time, these systems have evolved in tandem with advancements in computing and communication technologies and are now known as the *Energy Management System*, a term used to collectively refer to the functions of the ECC [8].

2.1 Energy management system overview

The EMS integrates hardware and software that enables power system monitoring and control, using sensors and meters in a digital network. The core functionalities of an EMS include real-time data acquisition, system parameter validation, execution of EMS software functions for predictive and diagnostic purposes, issuance of control commands to operational equipment, and support for operator decision-making through advanced analytics and visualization tools. Overall, the primary objective of an EMS is to guarantee stable, reliable, secure, and optimized power delivery across the grid [5], [11].

Historically, EMSs originated from manual dispatcher operations in the 1940s, where control relied heavily on empirical knowledge and communication with local field operators. Early EMS designs were based on proprietary and analog technologies, with significant reliance on manual processes for remote data acquisition and control, facilitating automatic generation, interchange, and frequency control. The post-1970 period witnessed substantial progress in state estimation and optimal power flow theory, particularly in response to major blackouts such as the 1977 U.S. event and similar European incidents, which reinforced the necessity of network security assessment, dispatcher training simulators, emergency corrective actions, and voltage stability monitoring. The increasing need for economic dispatch and load management drove the evolution of optimal power flow techniques within the EMS, incorporating security constraints to ensure operational stability (minimization of real power losses, maintenance of a voltage profile, ensuring a predefined short-circuit capacity) [5], [11], [12].

The advent of microprocessors, enhanced communication technologies, and advancements in power system hardware enabled the transition to digital systems. The introduction of fast, efficient algorithms for EMS applications and advances in computing hardware have enabled the real-time implementation of these procedures, equipping ECCs with advanced data acquisition, processing, and visualization capabilities. As a result, contemporary EMS functionalities have significantly expanded in scope, encompassing the following processes [8], [12]:

1. *Monitoring systems*, which have evolved from legacy SCADA to digital systems that include state estimation, bad data detection and rejection, real-time model validation, and advanced visualization tools. These advancements ensure accurate representation of system operations and enhance situational awareness.
2. *Dispatch operations* are now managed by fully digital Automatic Generation Control (AGC). AGC integrates load frequency control, power interchange management, and power system optimization.
3. System security functions are embedded within a hierarchical *control framework* that supports both monitoring and control activities. This integration strengthens the system's resilience to disturbances and enhances operational reliability.
4. Advanced *economy scheduling*, including functionalities that enable power market participation. This integration reflects the increasing importance of market dynamics in system operations.

2.1.1 *The EMS framework*

The EMS framework, illustrated in Figure 2.1, integrates transmission and generation operation management, simulation tools, and data acquisition/control systems. Its individual components include [5], [12]:

- *Generation operation management*: Load forecasting, unit commitment, economic dispatch, and AGC.
- *Transmission operations management*: Network configuration, state estimation, contingency analysis, and optimal power flow.
- *Study mode simulations*: Power flow studies and short-circuit analysis.
- *Energy services*: Services such as event analysis, scheduling, and energy accounting support both operational and market-related aspects of the grid.
- *Dispatcher Training Simulator (DTS)*: Simulators designed to replicate real-life scenarios, allowing operators to practice and improve their response to various system conditions and contingencies.

A crucial element of the EMS is the SCADA system, which acts as a vital link between the physical power system and the computational functions of the EMS., as demonstrated in Figure 2.1.

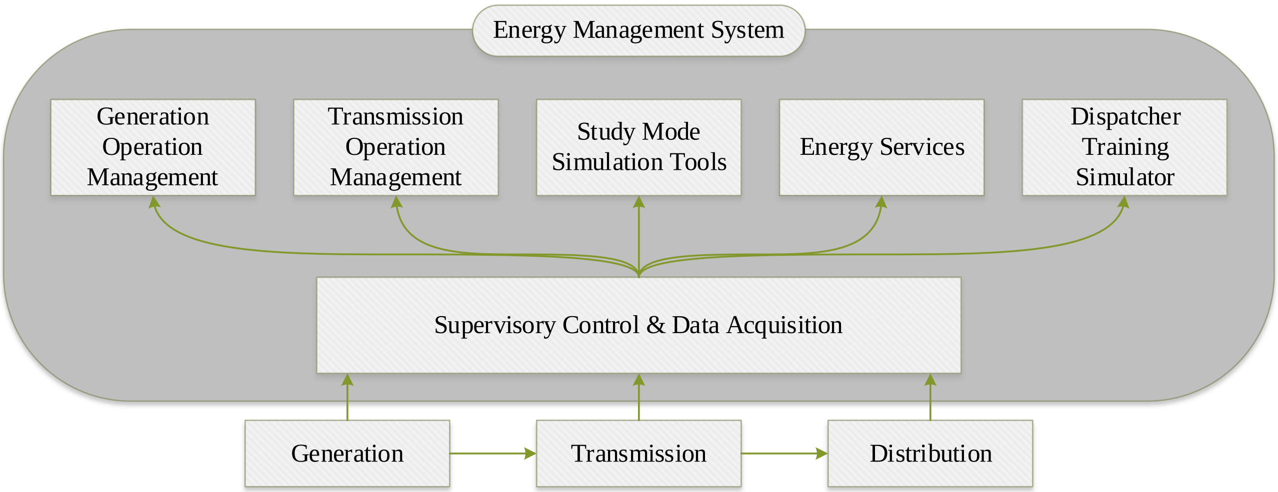

Figure 2.1: The typical energy management system framework [5].

The EMS functions can also be categorized based on the required response times, as depicted in Figure 2.2, including real-time operations, pre-event planning, and post-event analysis [5], [12]:

- *SCADA telemetry*: Data is polled approximately every 2 seconds for the near-real-time monitoring of operating conditions.
- *AGC*: Data is collected every 2-4 seconds to enable adjustments in generation output and frequency control.
- *SE and Contingency Analysis (CA)*: These functions typically run every 60 seconds to ensure system stability and preparedness for potential disturbances.
- *Optimal power flow and economic dispatch*: These functions are executed at intervals of approximately 30 minutes to ensure the cost-effective and efficient operation of the grid.
- *PMUs* provide high-resolution data at 25-120 scans per second, significantly enhancing the monitoring process with millisecond-level granularity.

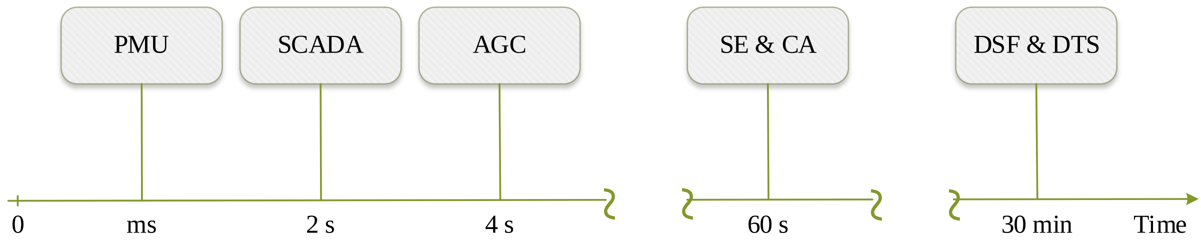

Figure 2.2: Different energy management system time frames [5].

2.1.2 Data flow in the EMS

The schematic diagram of the hardware setup of the EMS within the modern ECC is illustrated in Figure 2.3. The SCADA system, as will be extensively discussed in the following, plays a pivotal role in collecting and transmitting real-time telemetered data from the field.

Field devices such as wattmeters, voltmeters, current meters, and breaker status indicators are connected to RTUs, which serve as intermediaries between field equipment and the ECC. RTUs transmit data through communication channels to Communication Input/Output Controllers (CIOCs) located at the ECC. This real-time data is then utilized to construct the current network topology and is processed by the SE algorithm, which provides a reliable representation of the current system state, forming the basis for advanced analyses [8]. The outputs of the SE algorithm serve as inputs for key EMS functions, including power flow, optimal power flow, contingency analysis, and economic dispatch, which collectively ensure the grid operates securely, reliably, and efficiently under varying conditions. Processed information is then presented to operators through advanced visualization tools, such as screens, dynamic mimic boards (interactive displays representing the real-time status of the power system), or computer-generated projections [5], [8]. Additionally, computers at the ECC are capable of issuing control commands to field devices. These commands may be executed automatically by the EMS or manually upon operator instruction. Commands are transmitted back to field equipment via CIOCs, communication links, and RTUs for actions such as tripping breakers, adjusting transformer tap positions, or changing generator outputs.

2.2 The SCADA system

Generation and transmission automation systems are commonly referred to as “SCADA/EMS” systems, wherein the data acquisition and control are SCADA-specific functions. Although the terms “SCADA” and “EMS” are often used interchangeably, it is crucial to distinguish between the components and functionalities of a modern SCADA system to understand its unique role. SCADA is an integrated technology comprising the following elements: the RTUs or Intelligent Electronic Devices (IEDs), the data concentrators and Merging Units (MUs), the communication system, the master station and the Human-Machine Interface (HMI) [5].

2.2.1 Remote terminal units (RTUs)

RTUs serve as the “eyes, ears, and hands” of the SCADA system. They are responsible for acquiring data from field devices, processing it, and transmitting relevant information to the EMS. Simultaneously, RTUs relay control signals from the ECC to field devices to execute operational actions [5], [11].

Historically, RTUs operated as passive devices functioning as slaves to the master station (ECC). However, modern RTUs are equipped with advanced computational and optimization capabilities, significantly enhancing their role in the SCADA system. The evolution of RTUs began with the introduction of microprocessor-based logic in the 1980s. Subsequent advancements in communication technologies and processing power have enhanced their efficiency, flexibility, and reliability while reducing manufacturing costs. Modern RTUs are modular in design, allowing for ease of assembly and customization. They feature menu-driven user interfaces that can be adapted to specific processes, preprogrammed control algorithms to handle a variety of tasks, and high-speed communication networks with built-in redundancy for improved performance and reliability. Additionally, RTUs now adhere to standardized communication protocols, such as IEEE 1815/DNP3 and IEC 60870-5-101/103, ensuring interoperability [5], [13].

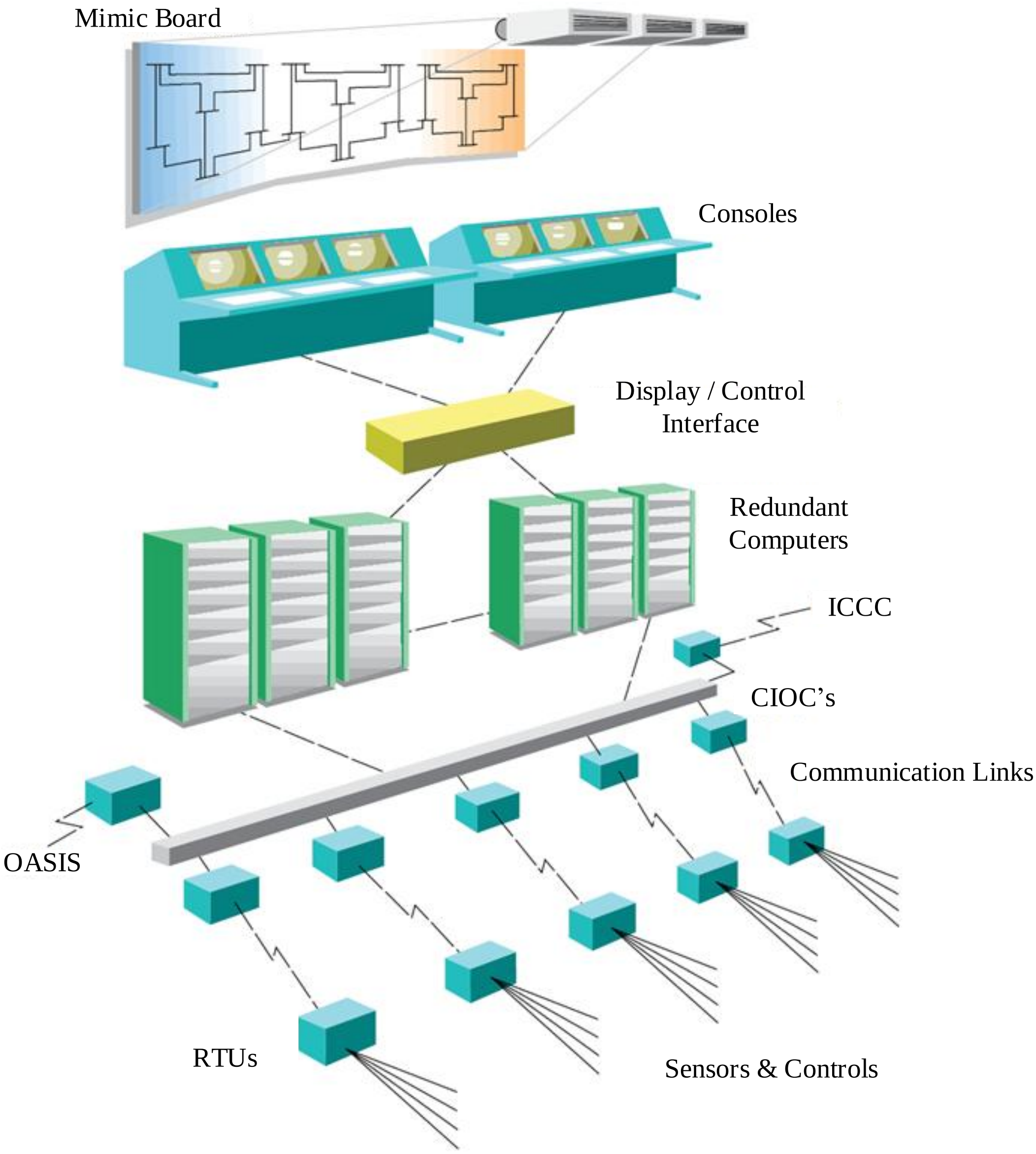

Figure 2.3: Hardware configuration of the energy management system [8].

A simplified view of the field deployment of RTUs is illustrated in Figure 2.4. Modern RTUs are tasked with collecting a comprehensive set of data for each sampling period. Analog data is typically scanned every few seconds, triggered by requests from the ECC, while status data is often compressed by transmitting only changes in status to reduce communication traffic. The collected data – critical for real-time system operation and control – includes breaker status, disconnect switch status, transformer tap settings, MW and MVAr flow measurements, voltage and current magnitudes, and phase angle differences [5].

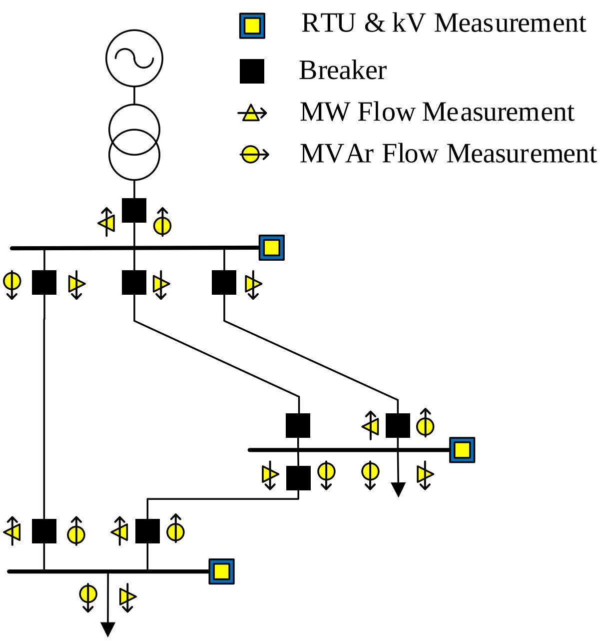

Figure 2.4: SCADA measurement system deployment.

The main components of an RTU, illustrated in Figure 2.5, are elaborated as follows [5]:

- *Communication subsystem*: The communication subsystem links the SCADA network to the RTU's internal logic. In contemporary bidirectional communication networks, this subsystem interprets commands from the ECC, initiates RTU operations, and relays control instructions to field devices while also processing field data for transmission to the EMS. To ensure data integrity, modern RTUs employ advanced error-checking techniques, such as parity checks or the more robust Cyclic Redundancy Check (CRC). Most modern devices also support multi-port communication, allowing for interaction with multiple master stations, peer RTUs and/or IEDs.
- *Logic subsystem*: At the heart of the RTU lies the logic subsystem, which is responsible for processing data, managing analog-to-digital conversions, and executing control actions. The Central Processing Unit (CPU) within this subsystem is responsible for acquiring and processing data, executing control functions, and managing time synchronization, which is essential for accurate event logging. Analog data, such as voltage and current measurements, is digitized using A/D converters, while binary data is used to monitor and control the status of field devices. High-speed scanning and microprocessor interrupts enable precise sequence-of-events logging with millisecond-level accuracy. By filtering signals and reporting only exceptions, the logic subsystem also minimizes communication traffic, aiding in efficient data handling.
- *Termination subsystem*: The termination subsystem forms the physical interface between the RTU and external equipment, protecting it from environmental factors such as voltage surges, electromagnetic interference, and lightning strikes. Isolation techniques, including interposing relays and optical isolators, safeguard digital inputs, while transducers and sensors provide electrical isolation for analog signals. Low-level (4–20 mA) analog signal inputs are fed to the A/D converter through fuses. Analog outputs control process variables like motor speeds, and digital outputs manage switches like circuit breakers.
- *Power supply subsystem*: RTUs have dedicated DC power supplies, commonly using 24 V, 48 V, or 125 V, with combinations of different DC voltage levels frequently implemented to enhance redundancy. In transmission and distribution systems, RTUs are powered by the substation battery, which is designed to prevent malfunctions or safety risks from ground faults.

- *Testing and HMI subsystem*: Provides built-in hardware and firmware tests, visual indicators, and maintenance panels for diagnostics and testing. RTUs at remote locations are usually unmanned but have built-in diagnostics and LED indicators to convey system status. Some RTUs also have low-cost LCD/LED displays to show real-time data. Diagnostic routines monitor the hardware and software, with faults reported to the master station. Additionally, technicians can use plug-in test sets to simulate master station operations, enabling effective troubleshooting and maintenance.

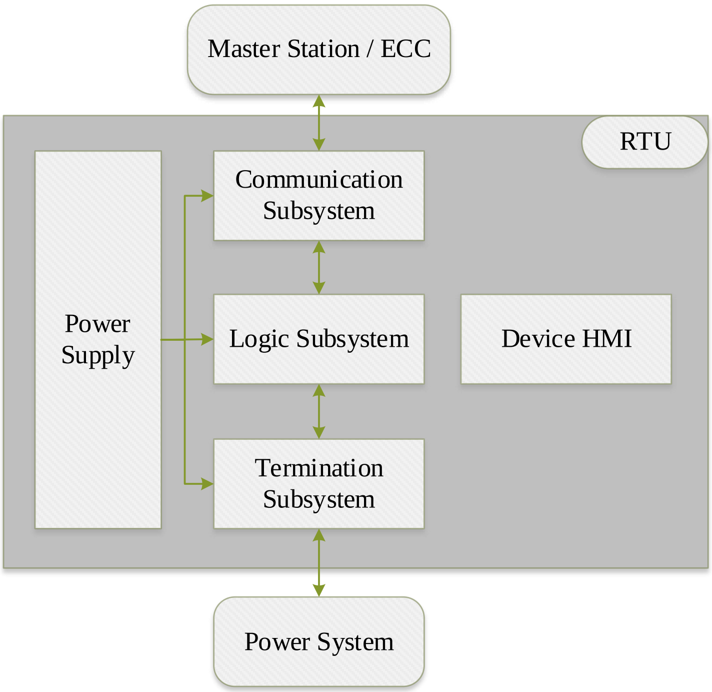

Figure 2.5: Remote terminal unit subsystems [5].

2.2.2 *Intelligent electronic devices (IEDs)*

By industry standards, an IED is defined as “any device incorporating one or more processors with the capability to receive or send data/control from or to an external source, such as electronic multi-function meters, digital relays, and controllers.” The adoption of IEDs has become increasingly widespread due to advancements in communication infrastructure, the establishment of standardized protocols, and enhanced interoperability. These developments have enabled substations to operate with minimal human intervention while simultaneously improving system reliability and preventing maloperations. Thus, to appreciate the transformative impact of IEDs on power system automation, it is important to explore their functionality in detail [5].

First introduced in the early 1980s with microprocessor-based controls, IEDs have significantly changed power utility operations by integrating protection, automation, and data analysis capabilities into a single platform. In contrast to traditional single-function electromechanical relays, IEDs consolidate multiple protection functions within one device. This integration not only lowers associated costs but also reduces the physical footprint of relay panels and switchgear. Over time, IEDs have expanded their functionality to include advanced features such as phasor measurement and waveform capture, further increasing their value to modern power systems [5].

The adoption of IEDs brings numerous benefits to power utilities [5]:

- Reduction in installation and panel costs, combined with faster commissioning and maintenance processes.
- Quicker recovery times after disturbances, minimizing downtime and operational disruptions.

- By automating critical functions and incorporating adaptive settings, IEDs enhance system reliability and capacity utilization while reducing losses due to incorrect settings or malfunctions.

From a design perspective, IEDs are structured for ease of programming, commissioning, and maintenance. The versatility of IEDs is illustrated in Figure 2.6, which depicts the functional blocks composing a typical IED. The modular hardware allows for the convenient replacement of components, such as draw-out cards, minimizing repair times and complexity. On the software side, IEDs are designed to independently manage protection, control, metering, and communication functions. The device architecture supports analog and digital inputs and outputs, while also providing waveform capture and disturbance analysis capabilities, essential for detailed event investigations. Moreover, built-in self-monitoring and external circuit monitoring features enhance the reliability of the device, allowing it to detect potential issues and prevent failures, thus significantly reducing downtime.

The deployment of IEDs in the field is illustrated Figure 2.7, which provides a comprehensive view of their integration with connected devices and the diverse functionalities they handle. More specifically [5]:

- One of the most significant functionalities of IEDs is their role in *protection*, particularly through the use of phasor estimation. As primary protection devices, relay IEDs offer significant improvements over traditional microprocessor-based relays by reducing the need for auxiliary equipment. For instance, modern transformer differential relays can automatically correct Current Transformer (CT) mismatches, eliminating the need for external devices. Furthermore, the concept of open system relaying enables software-based reconfiguration to achieve various relay functions. IEDs employ generalized numerical relay designs with specialized modules for data processing, signal scaling, filtering, and A/D conversion. Event reporting and fault diagnosis are further strengths of modern IEDs, as they can capture fault waveforms and record events such as pick-ups, trips, and reclosures, eliminating the need for separate Digital Fault Recorders (DFRs). Events are stored in nonvolatile memory with precise timestamps synchronized via GPS, enabling accurate event sequencing. Even after a blackout, IEDs facilitate fault diagnosis by retaining critical data for post-event analysis, significantly improving restoration times and operational insights.
- IEDs also integrate *metering* and *power quality analysis*, offering significant cost savings by combining protection and metering functionalities within one device. These metering capabilities allow IEDs to measure parameters such as voltage, current, real and reactive power, and perform load profiling. This functionality helps utilities monitor long-term system performance, supporting commissioning, testing, and control of capacitor banks. Another standout feature of modern IEDs is their ability to perform phasor estimation, calculating voltage and current phasors synchronized via GPS. This capability enables the IED to function as a PMU.
- Another critical functionality is the *programmable logic* and *breaker control* integrated within IEDs. By handling logical inputs and outputs for protection directly within the device, IEDs eliminate the need for external Programmable Logic Controllers (PLCs). This built-in capability allows users to create custom logic configurations tailored to specific applications. The relay algorithms and internal trip logic of the IED ensure precise control over circuit breakers, enhancing both operational accuracy and reliability in protection calculations.
- In addition, IEDs are equipped with *self- and external circuit monitoring* capabilities. Self-monitoring functions diagnose internal issues such as hardware failures or power supply interruptions, ensuring device reliability. Simultaneously, IEDs monitor external circuits, such as current inputs, breaker coils, and transformer conditions, detecting potential issues and preventing false tripping, enhancing the reliability and safety of substation operations.

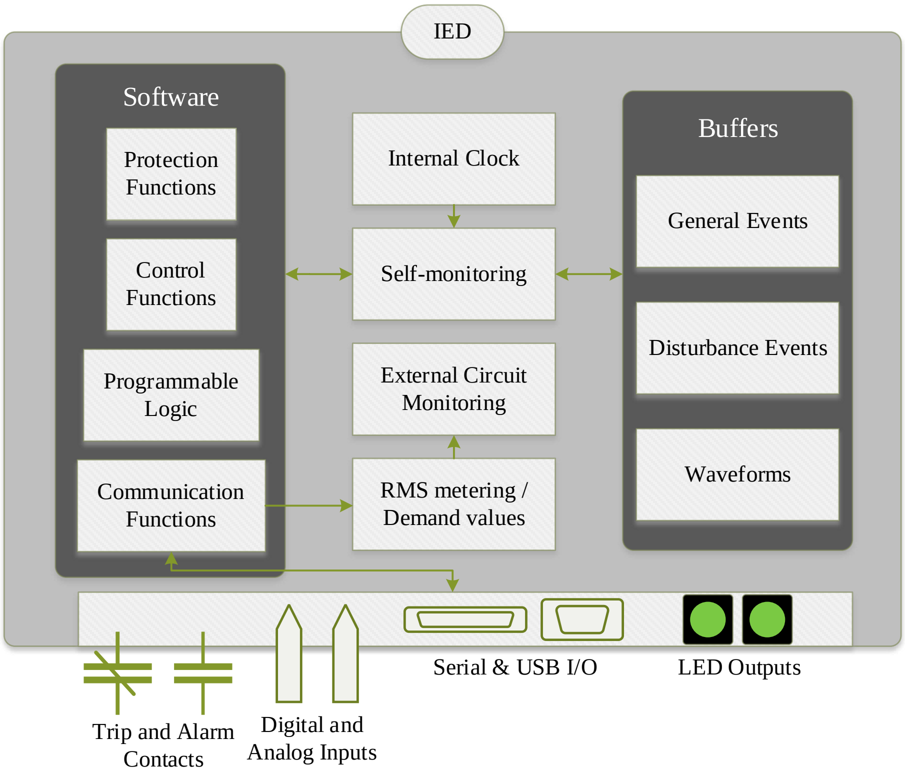

Figure 2.6: Typical IED structure.

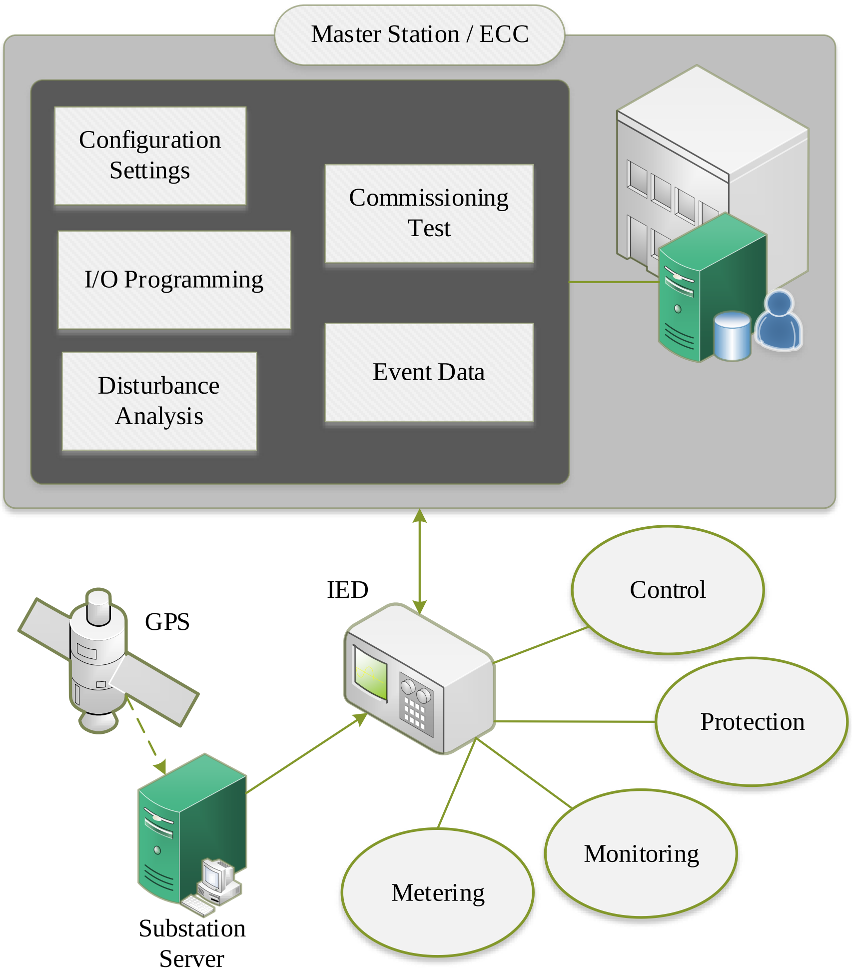

Figure 2.7: Functional view of modern IEDs [5].

Finally, the communication capabilities of IEDs are essential for their role in modern utilities. Supporting protocols such as MODBUS, DNP3, and IEC 61850, IEDs offer multi-port communication and an open communication architecture. These features enable integration with higher-level systems and allow easy upgrades through plug-and-play modules. Communication is supported via optical or electrical ports, with remote access enabled through modems, allowing interaction with other IEDs and substations [13].

2.2.3 Data concentrators and merging units (MUs)

Data concentrators play a critical role in substation automation by aggregating data from IEDs and other field inputs, streamlining the flow of information to higher-level systems. Traditional RTUs rely on hardwired connections to collect analog signals and status points, which are then converted into digital form for processing. In contrast, IEDs use standardized communication protocols to transmit the required data directly to data concentrators, which communicate within the substation via a Local Area Network (LAN). This architecture significantly enhances scalability and reduces wiring complexity [5]. Figure 2.8 illustrates the transition from traditional RTUs to modern IEDs with data concentrators in a substation.

MUs further advance the data acquisition process by introducing the concept of a process bus. Unlike data concentrators that rely on LANs to aggregate information, MUs connect directly to field equipment, digitizing signals at the source and transmitting them over the process bus LAN to IEDs using communication protocols such as the IEC 61850-9-2 [13]. This design eliminates the need for extensive hardwiring and simplifies substation configurations.

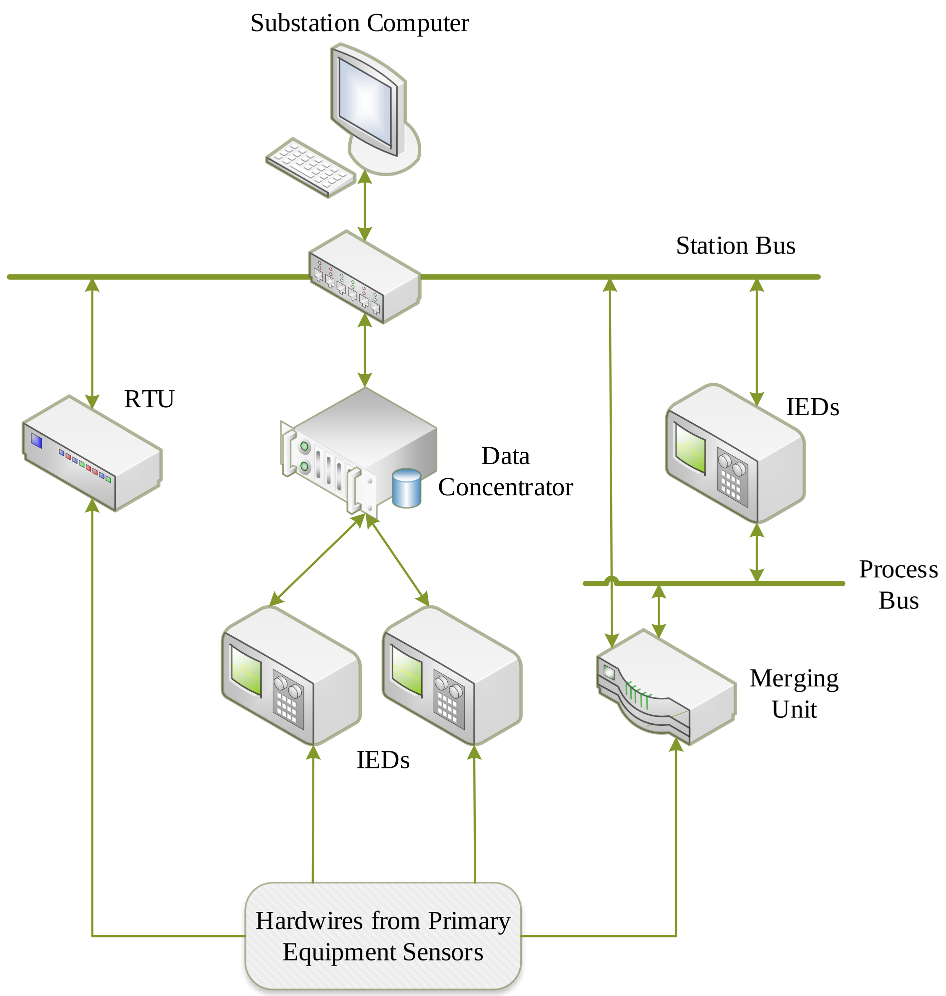

Figure 2.8: Migration from RTUs, to IEDs and data concentrators, to MUs and IEDs [5].

2.2.4 SCADA communication system

The SCADA communication system acts as the nervous system of the power grid, facilitating the transfer of data between field equipment and the ECC. It enables real-time monitoring of parameters such as generation levels, voltage and current magnitudes, system load, and the status of circuit breakers and isolators. Additionally, it transmits control commands from the control center to field equipment. Initially limited to major equipment and critical buses, SCADA communication now extends to end customers with the implementation of smart grids and home automation, allowing two-way communication from generation to distribution [13], [5].

Communication protocols form the foundation of SCADA systems, defining the format for data exchange between devices. These protocols ensure interoperability by establishing rules for data packaging, addressing, and error detection. Initially, proprietary protocols limited compatibility, prompting international organizations to standardize formats. The Open System Interconnection (OSI) model, issued by the International Organization for Standardization (ISO) in 1984, provides a structured framework for communication processes. SCADA systems often use Transmission Control Protocol/Internet Protocol (TCP/IP), with the OSI model adopted by the International Electrotechnical Commission (IEC) [5]. Several widely used SCADA and smart grid protocols are illustrated in Figure 2.9, with the most important ones briefly discussed in the following [5], [13]:

- *Modbus*: Originally developed for PLC communication, Modbus has become widely used in SCADA systems, particularly between master stations and RTUs. It operates on a master-slave model, using OSI layers 1, 2, and 7, with a CRC for error detection.
- *Inter-Control Center Protocol (ICCP)*: Defined under IEC 60870-6, ICCP enables real-time telecontrol communication between control centers using Wide Area Networks (WANs). It is widely adopted by utilities and system operators, employing Manufacturing Message Specifications (MMS) for messaging.
- *IEC 60870-5-101/103/104*: IEC 60870-5 is an open protocol for SCADA telemetry. It follows a hierarchical structure with six parts and companion standards, supporting telecontrol equipment in industry-level SCADA systems.
- *Distributed Network Protocol 3 (DNP3)*: DNP3 is an open protocol developed in Canada, using the EPA architecture and FT3 frame format from IEC 60870-5. It supports larger data frames and robust error detection, commonly used for communication between field devices and control systems.
- *IEEE C37.118: Synchrophasor Standard*: Designed for synchronized phasor and frequency measurements, this standard enables precise real-time data transmission with timestamping. It has been superseded by IEEE/IEC 60255-118-1, which supports enhanced features for synchrophasor communication.
- *IEC 61850*: Developed for comprehensive substation automation, IEC 61850 ensures interoperability across vendor systems and supports logical node modeling, advanced features such as GOOSE messaging, and standardized configuration language. It integrates communication at process, bay, and station levels.

The evolution of SCADA communication systems aligns with the growing complexity of smart grids, introducing new challenges in robustness, efficiency, security, and grid reliability:

1) *Robustness*: Modern SCADA systems demand a robust communication and information infrastructure capable of meeting performance metrics such as low latency, high bandwidth, and fast response times. These requirements are critical for reliable automation and control.

2) *Efficiency*: The bidirectional flow of information in smart grids, spanning from domestic devices to substations and ECCs, necessitates efficient communication. Technologies with rapid data acquisition, such as PMUs, play a vital role in optimizing system controls and computing capabilities.
3) *Security*: The security of the communication system is paramount, given the sensitive and time-critical nature of the data it transmits. Secure communication protocols and robust cybersecurity measures must protect infrastructure across domains such as power plants, substations, and real-time systems, addressing emerging threats while safeguarding privacy.
4) *Impact on grid reliability*: The integration of RES, demand response mechanisms, and the proliferation of electric vehicles introduces significant challenges to grid reliability. Renewable energy sources, such as wind and solar, are inherently intermittent and unpredictable, requiring sophisticated forecasting and real-time adjustments to maintain balance between generation and demand. Communication systems play a crucial role in enabling these adjustments by providing accurate, time-sensitive data to control centers and field devices.

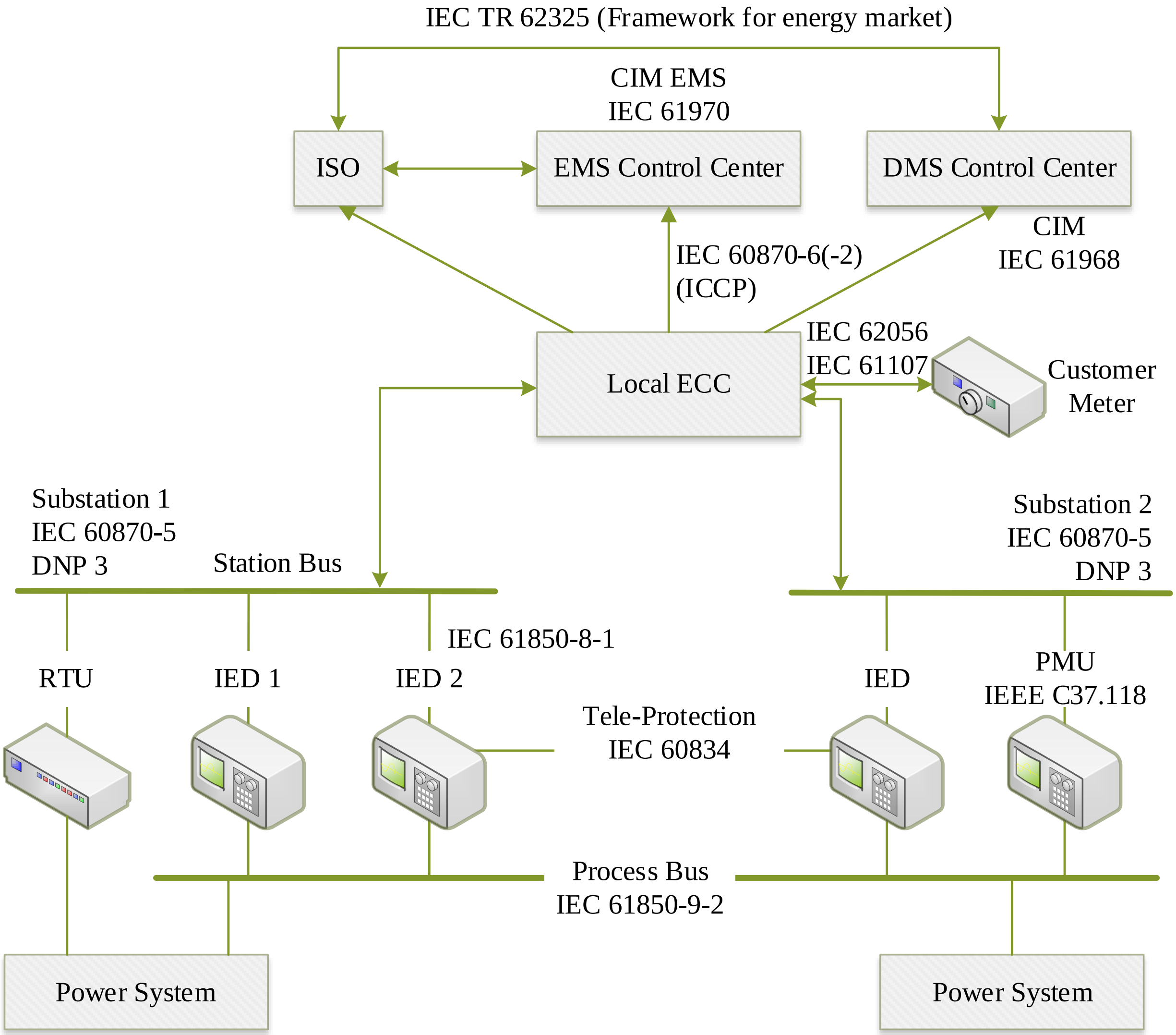

Figure 2.9: SCADA and smart grid protocols [5].

2.2.5 SCADA master stations [5]

The SCADA master station serves as the central hub for monitoring and controlling the power grid, consisting of interconnected computers, servers, peripherals, and input/output (I/O) systems. These stations vary in scale, from small substation control rooms to large national transmission ECCs. Small master stations, typically found in sub-load dispatch centers, handle a limited number of RTUs and provide basic control and monitoring. Medium-sized stations incorporate multiple servers – such as SCADA/EMS, Information Storage and Retrieval (ISR), and development servers – with operator terminals for extensive system supervision. Large-scale master stations feature redundant systems, enhanced security, and often a fully redundant backup station at a remote location, ensuring uninterrupted operation during emergencies.

The hardware of a master station includes dedicated servers connected through high-speed, dual-redundant LANs, each tasked with specific roles within a client-server environment. Key components include the SCADA server for core functions like data collection and control command execution, application servers for specialized tasks such as generation or distribution SCADA applications, and ISR servers for historical data archiving and report generation. Other essential hardware includes Communication Front Ends (CFEs) for data transfer, ICCP servers for inter-center communication, and Dispatcher Training Simulator (DTS) servers for operator training. Advanced visualization systems, like video projection systems, support large control rooms by driving dynamic mimic board displays.

The software components of a master station support both basic SCADA functions and advanced applications tailored to specific system needs, such as generation, transmission, or distribution. Basic SCADA functions include data acquisition, remote control, historical data analysis, database management, reporting, and HMI functionalities. For instance, data acquisition involves collecting analog, digital, and pulse inputs from field equipment, while remote control capabilities enable operators to manage circuit breakers and isolators. Historical data analysis provides critical insights into post-event scenarios, aiding in system planning and operational improvements.

Advanced SCADA applications expand these basic functionalities into domain-specific roles. Generation SCADA, often implemented as SCADA/AGC, incorporates complex energy management applications, including AGC, economic dispatch calculation, interchange transaction scheduling, unit commitment, short-term load forecasting, and hydrothermal coordination.

Transmission SCADA builds on basic functions by integrating advanced EMS applications. These include:

- *State estimation*: Processes redundant data to determine system state variables, enabling accurate real-time monitoring.
- *Contingency analysis*: Simulates outages to assess potential impacts on system stability, bus voltages, and power flows.
- *Network configuration processor*: Automatically determines system topology based on breaker statuses and measurements.
- *Optimal power flow*: Solves for optimal system configurations to achieve objectives like cost minimization or power loss reduction under operational constraints.

Distribution automation and Distribution Management Systems (DMS) focus on enhancing reliability and operational efficiency at the distribution level. Key functionalities include fault identification, isolation, and service restoration, network reconfiguration to optimize distribution paths, load management and demand response to balance consumption, integration with customer and geographical information systems, power factor and reactive power control to optimize voltage profiles, short-term load forecasting, and three-phase unbalanced power flow studies.

Figure 2.10 illustrates the evolution of SCADA systems from basic functionalities to advanced applications such as SCADA/AGC for generation, SCADA/EMS for transmission, and SCADA/DMS for distribution, according to [5]. As SCADA systems incorporate these advanced features, their complexity and cost increase, reflecting their expanded capabilities to meet modern grid demands.

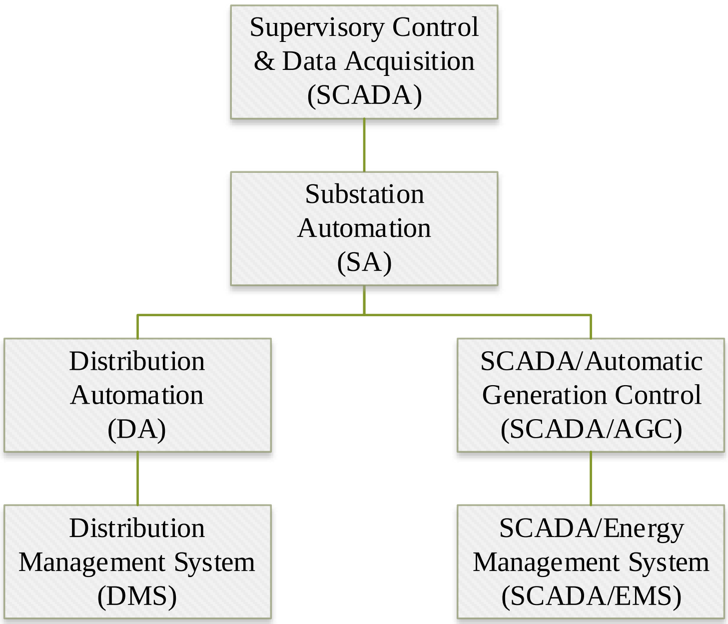

Figure 2.10: SCADA functions in power systems.

2.2.6 Human-machine interface (HMI) [5]

The HMI serves as an interactive platform where operators monitor and control the power system. Its design emphasizes user-friendliness, efficiency, and error reduction, allowing operators to manage complex systems with minimal effort. Over time, operator tools have evolved from manual devices to sophisticated computer-based systems. In modern SCADA systems, the HMI integrates hardware and software to provide an interface for controlling generation, transmission, and distribution systems.

The hardware components of the HMI include operator consoles equipped with multiple displays, which offer diagnostic and graphical views tailored to industry-specific needs, enabling operators to visualize system conditions in real-time. Alarms are incorporated into the interface with visual and auditory notifications, ensuring operators are promptly informed of system events. Mimic diagrams, a core feature of ECCs, offer a comprehensive visual overview of the system, displayed on LCD/LED panels or dynamic map boards that update automatically based on system changes. Various peripheral devices are used for generating event logs and reports.

The software components of the HMI complement the hardware by providing advanced visualization and control capabilities. Access control mechanisms ensure system security, requiring user authentication through IDs and passwords. Real-time and historical data visualization helps operators track variables such as voltage, current, frequency, and power flow, supporting informed decision-making. Forecasting capabilities that track historical data, and real-time changes may also be available, to predict future system states and evaluate performance over time. Alarm processing systems compare incoming data against predefined thresholds, triggering alarms when deviations occur, so that operators can acknowledge and filter alarms, avoiding information overload while ensuring critical issues are addressed promptly. Logs and reports generated by the HMI system serve various organizational needs, supporting both operational insights and regulatory compliance.

2.2.7 Data flow in the SCADA system [5]

The data flow in a SCADA system reflects the sequential processes required to transform raw field measurements into actionable information displayed on an operator's console. This flow can be examined through the example of displaying a 150 kV bus bar voltage on a mimic diagram, involving several steps, as illustrated in Figure 2.11:

1) *Field measurement*: A Voltage Transformer (VT) at the substation steps the 150 kV voltage down to a manageable level (e.g., 300 V) for further processing. In addition to reducing the voltage, the PT provides electrical isolation, protecting sensitive measurement and control equipment from the high-voltage system.
2) *Signal conversion*: A voltage transducer converts the 300 V output from the PT into a 4–20 mA analog signal. This standardized current range is less susceptible to interference over long distances, so that data transmitted to the RTU remains accurate.
3) *A/D conversion*: The RTU's analog input module digitizes the 4–20 mA signal for transmission.
4) *Data packaging*: The digitized measurement is encapsulated into data packets according to the communication protocol used between the RTU and the master station.
5) *Transmission*: The data packets are transmitted from the RTU to the master station via the established communication network, which may include wired connections (e.g., fiber optics, Ethernet) or wireless systems (e.g., microwave, cellular networks).
6) *Processing at master station*: A front-end processor or communication front-end decodes the incoming data packets to extract the relevant measurement information.
7) *Display*: The decoded data is rescaled to represent the original 150 kV value and displayed on the mimic diagram at the corresponding bus bar, thus completing the monitoring cycle.

2.3 Substation automation [5], [14]

Substation automation (SA) has become a cornerstone of modern power systems, transforming traditional substations into intelligent, interconnected hubs of operation. By integrating advanced technologies – such as IEDs, process buses, and standardized communication protocols – SA delivers substantial benefits in operational efficiency, reliability, and scalability. Its growing adoption reflects a critical role in meeting the demands of modern utilities, including enhanced grid resilience, reduced operational costs, and support for RES integration. This Section explores the evolution of SA, its technical underpinnings, the transition from conventional to digital substations, and the challenges encountered during its implementation.

2.3.1 Evolution of substation automation

Historically, substations relied heavily on manual operations. Electromechanical relays and extensive hardwiring formed the backbone of traditional control systems, necessitating frequent human intervention for maintenance, fault isolation, and reconfiguration, and leading to operational inefficiencies and prolonged outages. The advent of SCADA systems marked the first step toward automation by enabling remote monitoring and control, albeit with limited functionality and a strong dependence on centralized control systems.

The introduction of microprocessor-based devices in the 1980s spurred the transition from manual systems to semi-automated and later fully automated substations. IEDs revolutionized substation design by integrating protection, control, and monitoring functions into a single platform. The adoption of digital communication, e.g., through IEC 61850, further accelerated automation by enabling seamless interoperability between devices from different manufacturers. These technological advances laid the foundation for fully integrated digital substations capable of self-diagnosis, adaptive control, and real-time data exchange.

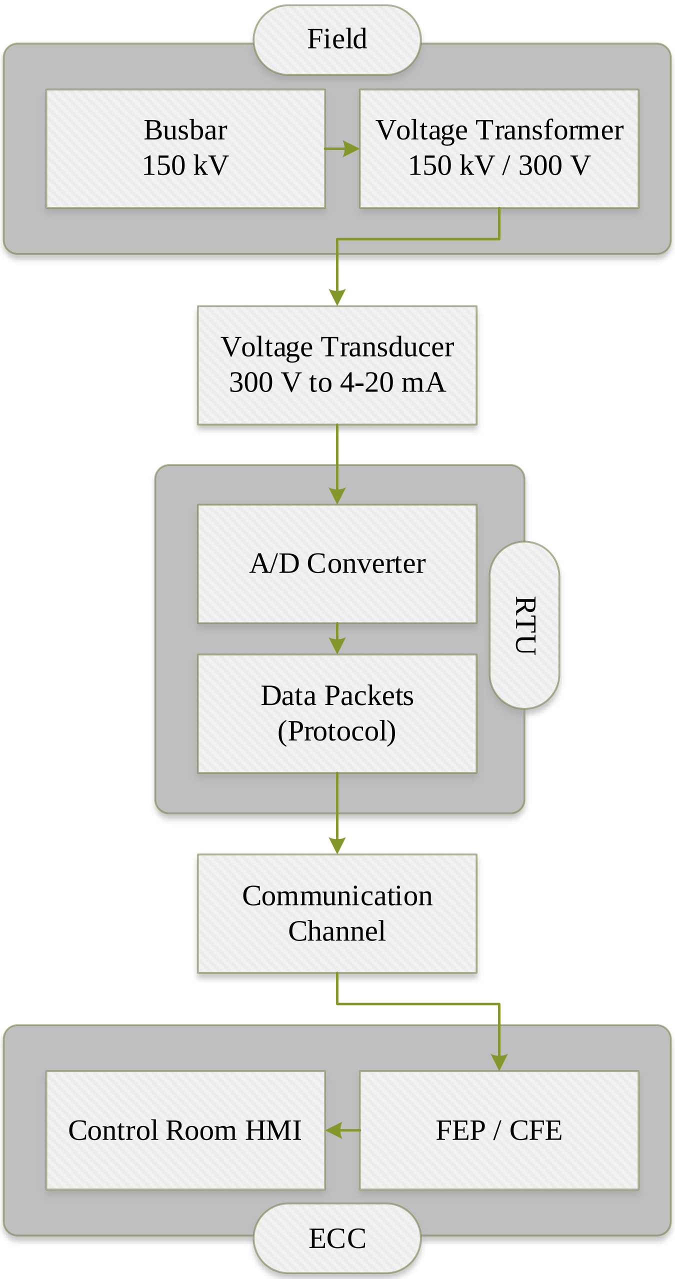

Figure 2.11: Data transfer from the busbar to the control center HMI [5].

2.3.2 Components of substation automation systems

A modern substation automation system typically comprises several interconnected components:

- *IEDs* consolidate multiple functionalities within a single device, reducing hardware requirements and improving system responsiveness. Advanced IEDs may also support phasor measurement, waveform capture, and real-time fault analysis.
- The *process bus* manages communication between field devices (e.g., sensors, actuators) and IEDs. By digitizing signals at the source, the process bus reduces wiring complexity and minimizes signal degradation.

- The *station bus* connects IEDs, HMIs, and external systems, enabling centralized monitoring and control. It also supports the flow of operational data across different levels of the substation.
- Serving as the primary user interface, the *HMI* allows operators to oversee system performance and respond to critical events in real-time. Modern HMIs feature graphical interfaces, alarm management systems, and historical data analysis tools.
- *Standardized protocols* (IEC 61850, DNP3, and Modbus) enable continuous communication among devices. IEC 61850, in particular, offers real-time peer-to-peer messaging and wide-ranging interoperability, making it a pivotal standard for modern SA.
- *Digital instrument transformers and MUs* provide highly accurate measurements and aggregate data from multiple sensors, ensuring reliable input to protection and control systems.

2.3.3 Transition from conventional to digital substations

Conventional substations rely on extensive hardwiring for control and protection, with devices operating largely in isolation. Analog signal transmission over long distances often leads to interference, compromising reliability. Additionally, these systems frequently lack scalability, to costly and time-consuming expansions or modifications. Digital substations overcome these limitations by incorporating advanced automation technology, characterized by:

1) *Scalability* – Modular design strategies allow for effortless addition of new devices and functions.
2) *Flexibility* – Digital communication protocols enable integration with broader utility systems.
3) *Reliability* – Self-diagnostic capabilities and real-time fault detection minimize downtime and boost system resilience.
4) *Interoperability* – Standardized protocols ensure compatibility across devices and vendors.

Overall, by replacing analog signals with digital interfaces, digital substations substantially simplify wiring, improve data fidelity, and establish a layered architecture for efficient data flow across the process, bay, and station levels.

2.3.4 Challenges in implementing substation automation

Implementing substation automation presents several challenges that utilities must address to fully realize its potential. One of the most significant difficulties lies in integrating modern technologies with legacy systems. Many substations still operate with outdated equipment and infrastructure, and retrofitting these with advanced automation components requires meticulous planning. Compatibility issues can arise, particularly when older systems lack the flexibility to interface seamlessly with modern IEDs and digital communication networks. Utilities must invest time and resources to ensure smooth interoperability and avoid operational disruptions during the transition.

Cybersecurity is another pressing concern as increased digitalization introduces vulnerabilities in the communication and control infrastructure. Automated substations depend on real-time data exchange, making them potential targets for cyberattacks that could compromise critical operations. Utilities need to implement robust security measures – encryption, intrusion detection, and role-based access control – to protect critical assets and continuously adapt to emerging cyber threats.

Financial constraints also pose a significant barrier, especially for utilities operating in regulated markets with tight budgets. While implementing SA promises long-term cost savings, the initial investment required for new equipment, installation costs, and personnel training can be substantial. For many utilities, this financial burden is compounded by the need to maintain uninterrupted operations during upgrades, which may necessitate temporary solutions that increase overall costs.

Another challenge lies in the skill gap associated with adopting advanced technologies. SA systems require specialized knowledge for installation, operation, and maintenance, and the existing workforce may lack the necessary expertise. Utilities need comprehensive training initiatives to ensure that engineers and operators can manage, maintain, and troubleshoot these systems.

Despite these challenges, utilities often adopt a phased approach to SA implementation, beginning with incremental upgrades, such as gradually integrating IEDs or digital communication into selected areas, while retaining some legacy components. This strategy helps spread costs over time and allows for an overall smoother transition.

3. Synchrophasor Measurement Systems

Phasor measurement units (PMUs) are measurement devices designed to record bus voltage and line current phasors, as well as the frequency and the Rate of Change of Frequency (ROCOF) of these signals. By employing precise time synchronization – commonly achieved through a GPS-based clock – each measurement is tagged with its corresponding time instant, thereby enabling the concept of *synchronized phasor measurements*, or *synchrophasors*. These high-resolution measurements have become the preferred means to monitoring and analyzing modern electric power systems [4]. Over the years, extensive research and development in PMU technology have led to a wide range of emerging applications, including advanced situational awareness, real-time control, and dynamic stability assessment. This Chapter explores the evolution of PMU technology, and the wide range of emerging applications based on synchrophasor measurements.

3.1 Basic definitions

The concept of the phasor was introduced in 1893 by Charles Proteus Steinmetz [15]. A phasor represents a sinusoidal signal as a complex number, encapsulating both its RMS value and phase angle. This representation is particularly effective for analyzing power systems under steady-state conditions at nominal frequencies, typically 50 or 60 Hz [15]. Consider a pure sinusoidal signal described by:

$$x(t) = X_m \cos(\omega t + \varphi) \tag{3.1}$$

where $\omega = 2\pi f$ is the angular frequency in radians per second, φ is the phase angle in radians, X_m is the amplitude of the signal, and $X_m / \sqrt{2}$ is its RMS value. Eq. (3.1)can also be written as:

$$x(t) = \mathrm{Re}\{X_m e^{j(\omega t+\varphi)}\} = \mathrm{Re}\{X_m e^{j\varphi} e^{j\omega t}\} \tag{3.2}$$

By suppressing the time-varying exponential term $e^{j\omega t}$ the sinusoidal signal $x(t)$ can be represented as the complex number:

$$x(t) \leftrightarrow \tilde{X} = (X_m / \sqrt{2}) e^{j\varphi} = (X_m / \sqrt{2})(\cos\varphi + j\sin\varphi) \tag{3.3}$$

This complex number is the phasor representation of the sinusoid, with its magnitude equal to the RMS value and its angle corresponding to the phase offset. Figure 3.1 illustrates the relationship between a sinusoid and its phasor representation. The length of the phasor equals the RMS value of the sinusoid, and its phase angle is relative to a chosen reference axis, making the phase angle arbitrary based on the coordinate system [8].

In addition to phasor representation, the frequency *f* of the sinusoidal signal is a fundamental parameter in AC systems. PMUs measure *f* in Hz and the ROCOF, defined as:

$$ROCOF = \frac{df}{dt} \tag{3.4}$$

ROCOF, expressed in Hz/s, provides critical insights into system dynamics, particularly during transient events. Both frequency and ROCOF measurements, along with synchrophasor data, are referenced to Coordinated Universal Time (UTC), ensuring precise temporal alignment across all measurement points [4].

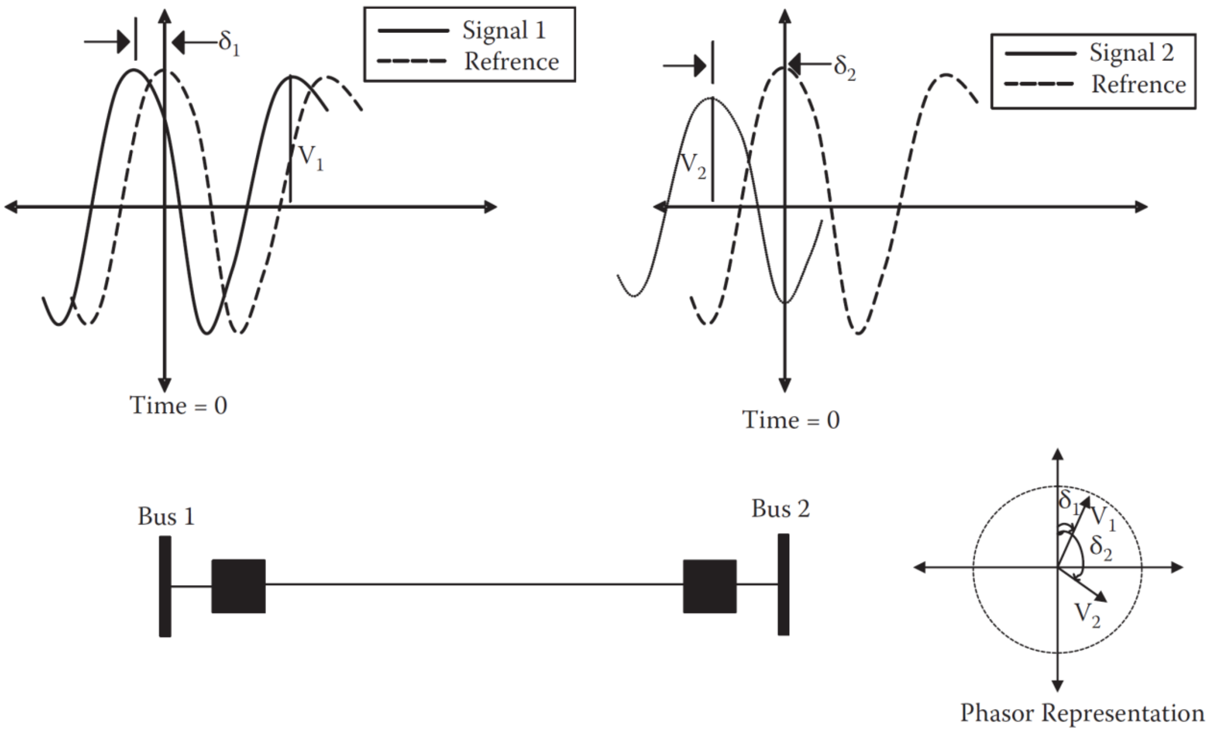

Figure 3.1: A sinusoid and its representation as a phasor [6].

3.2 Short history of the PMU

The concept of synchronized sampling first emerged in protection systems, where measurements were collected at substations separated by considerable distances. Important strides were made in the 1970s and 1980s with the development of computer relaying algorithms. A notable development was the Symmetrical Component Distance Relay (SCDR), specifically designed for protecting HV transmission lines, which led to the Symmetrical Component Discrete Fourier Transform (SCDFT) – a recursive algorithm for computing symmetrical components of voltages and currents [16]. This work underscored the value of measuring positive sequence voltages and currents over one cycle of the fundamental frequency, provided that such measurements could be synchronized across the power system [6]. Concurrently, the deployment of the GPS was gaining momentum, revealing its potential as an effective means for achieving precise synchronization of power system measurements over wide geographical areas [4].

This groundwork culminated in the development of the first prototype PMU utilizing GPS technology by a research team at Virginia Tech in 1988 [16]. At that time, the GPS receiver clock was external to the PMU, and due to the limited number of GPS satellites available, the clock was equipped with a high-precision internal oscillator to ensure timekeeping in the absence of visible satellites [6]. These prototype PMUs were subsequently deployed in several substations operated by the Bonneville Power Administration, the American Electric Power Service Corporation, and the New York Power Authority [17]. Macrodyne Co. was the first industrial adopter, initiating numerous demonstration projects focusing on PMU use at the transmission level. Over the years, the number of manufacturers has grown to tens of mass producers nowadays, while deployment of PMUs in power systems is being carried out in earnest in many countries worldwide [4].

It is noteworthy that synchrophasor measurement capability need not be the sole function or purpose of a device; many relay manufacturers now include PMU functionalities protective relays, meters, and fault recorders. Any device offering synchrophasor measurement can be considered a PMU (e.g., a PMU-enabled IED), provided that its PMU functionality does not compromise other device functions and vice versa. Because each manufacturer employs its own phasor calculation algorithms, variations in accuracy and latency can exist among different PMU or PMU-enabled IED models [8]. Figure 3.2 and Figure 3.3 illustrate examples of PMU-enabled IEDs from different manufacturers.

Figure 3.2: GE RPV311 digital fault recorders with PMU functionality.

Figure 3.3: SEL-351A protection relays with PMU functionality.

Most recently, utilities and regional market operators have turned to large-scale synchrophasor technology deployments in substations, following two main strategies: (a) use of dedicated PMUs and (b) use of PMU-enabled IEDs, including DFRs, digital protective relays, digital disturbance recorders. As the industry begins to leverage this technology, making it a mainstream choice for enhancing system monitoring, protection, and control, the total number of PMUs and PMU-enabled IEDs is anticipated to grow significantly over the next five to ten years.

Maximizing the benefits of this technology will require substantial labor for substation installation, communication standardization, data integration, and the development of appropriate visualization tools [4]. To ensure device interoperability, the IEEE has led extensive standardization efforts. The first PMU standard, IEEE Standard 1344, was published in 1995 [18]. Subsequent refinements produced IEEE C37.118 (2005) [19] and IEEE C37.118.1 (2011) [20], with its amendment IEEE C37.118.1a (2014) [21], followed by IEEE C37.118.2 [22]. As of 2024, the current version, IEEE/IEC 60255-118-1-2018, was released in 2018 [23]. The IEEE standard permits PMU manufacturers to select their design approaches, providing only specifications under steady-state and dynamic testing conditions. It also defines the primary performance metric, the Total Vector Error (TVE), for PMU accuracy evaluation and comparison. The standard IEEE C37.118.1-2011 first introduced two performance classes: a P-class, designed for applications requiring rapid responses, such as protection, and an M-class, offering higher accuracy for measurement applications [22]. Another important standardization milestone is the IEEE standard C37.242-2021 [24], initially released in 2013 and revised in 2021, which serves as a guide for the synchronization, calibration, testing, and installation of PMUs.

3.3 PMU architecture

The architecture of PMUs varies across manufacturers, leading to differences in design and implementation. Despite these variations, identifying the fundamental components of a generic PMU is essential for understanding its core architecture and operational principles. This Section examines certain practical considerations in PMU design and provides an overview of its hardware modules, emphasizing how each component influences the overall accuracy and performance of the PMU. A typical PMU, with its block diagram illustrated in Figure 3.4, is composed of four different modules: the data acquisition system, the computation module, the synchronization sources, and the communication interface [4].

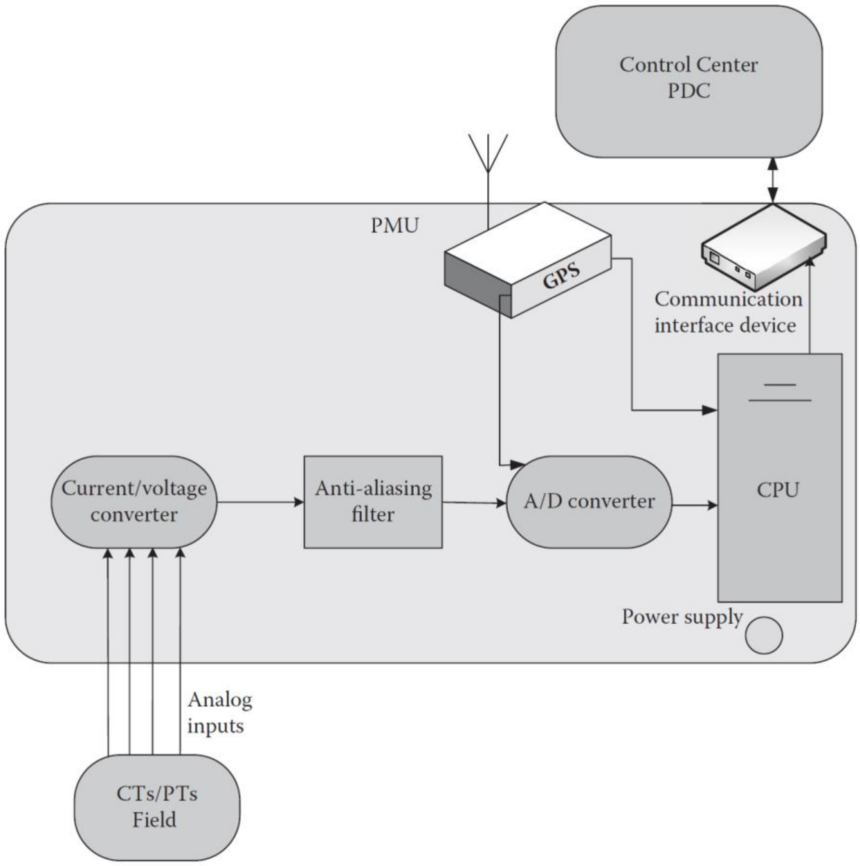

Figure 3.4: PMU architecture block diagram [5].

3.3.1 Data acquisition system

The data acquisition module comprises the Instrument Transformers (ITs) and current/voltage converters, which adapt power system signals to the PMU's rated input levels. Voltage and current signals are transformed to standard input levels – typically 300 V/5A – via appropriate CTs and PTs, ensuring compatibility with the specifications of the signal processing stage of the device. These transformed signals are further converted into voltage levels suitable for processing, usually within a 10V range [5].

The signal conditioning module is responsible for adapting analog input signals for digital acquisition circuits. This module includes an anti-aliasing (low-pass) filter, which is intended to isolate the fundamental power frequency signal from unwanted high-frequency components before A/D conversion [4], [5]. The sampling rate of the A/D converter dictates the frequency response of the anti-aliasing filters, which typically have a cut-off frequency less than half the sampling frequency to satisfy the Nyquist criterion [4].

A high-resolution A/D converter digitizes the analog signals. The number of A/D channels depends on the number of signals being measured. In most PMU implementations, at least six channels are required to accommodate three-phase voltage and current measurements. The sampling clock pulse, provided by a crystal oscillator within the GPS module, is phase-locked with the GPS clock, ensuring precise synchronization during A/D conversion. To optimize digital signal processing, decimation filtering is applied, reducing the sampling rate while preserving measurement accuracy [5].

3.3.2 Computation module

The computation module, typically a CPU, is responsible for real-time computation of phasor estimates from acquired voltage and current signals. It determines the positive sequence phasor of the power system quantities and assigns a UTC timestamp to each measurement, obtained from the GPS module.

Importantly, the processing capability of a PMU depends strongly on the number of input channels processed simultaneously and on the computational complexity of the real-time algorithm used to calculate (or, more appropriately, estimate) synchrophasors, frequency, and ROCOF. As it is necessary to minimize PMU latency while maximizing its reporting rate, the choice of an estimation algorithm and hardware suitable for the specific needs and sought performance is a critical factor. In addition, the choice of hardware depends on several other factors such as programmability, reconfigurability, and parallelization features. In fact, hardware for PMU implementation can range from general-purpose processors to specialized chipsets, such as digital signal processors, graphical processing units, or application-specific integrated circuits, which offer higher performance but may compromise programmability [4].

3.3.3 Synchronization sources

The time synchronization module is the basis of the synchrophasor concept and the defining feature of a PMU, distinguishing it from conventional digital measurement devices. It enables the acquisition of a precise time reference, used to disseminate the current time throughout the system and discipline the synchronization of internal clocks and of the recorded measurements. Consequently, data transmission speed is no longer a critical factor in the utilization of phasor data across multiple PMUs in a WAMS [4], [6].

The synchronization source may be either internal or external to the PMU, typically relying on a satellite receiver either directly or indirectly. External synchronization is often achieved via established time protocols, such as the IRIG-B and the Precision Time Protocol (PTP, IEEE 1588), which relay time information to the device. The synchronization module performs multiple critical functions [4]:

- It provides a common UTC time reference for measurement timestamps.
- It indicates the exact reporting instant of PMU measurements.
- It can be used to trigger data acquisition, depending on the chosen architecture.
- It supplies time quality indicators that must accompany the measurement data.

The IEEE C37.118.1 standard specifies a maximum allowable timing error of 1 μs for PMUs. For synchrophasor-based power system monitoring, this timing accuracy is generally considered sufficient, as it corresponds to a phase angle error of approximately 0.02° in 50 Hz systems. However, for certain high-speed protection applications, stricter timing accuracy (e.g., 100 ns or better) may be required to ensure precise event localization and fault detection [8].

3.3.4 Communication interface

The communication interface enables the transmission of measurement data to any synchrophasor-enabled device (PMU or PDC), thereby facilitating integration of the device into a broader WAMS architecture. PMUs support contemporary communication technologies, with Ethernet being the predominant communication medium. PMU data is transferred over TCP or UDP over IP. Besides copper cables, state-of-the-art PMUs incorporate fiber optic and/or wireless network interfaces.

The IEEE C37.118.2 standard defines PMU data frame structure and specifies the format of communication messages [22]. The measurement frame must include the phasor values (magnitude and angle or real and imaginary parts) from all the PMU input channels, the frequency and ROCOF, along with the corresponding UTC timestamp. Each frame also contains various fields to identify the data streams, assess the quality of synchronization and signify erroneous data, as well as additional fields typical of packet communications, such as synchronization frames, packet sizes, correction bits, and other protocol-specific information. Message types defined in IEEE C37.118.2 include data frames (measurement reports), configuration frames (device setup information), and command frames (control messages for PMUs).

3.3.5 Performance and design considerations

PMU design requires a balance between cost, performance, and hardware constraints. As several hardware elements collaborate within the PMU, their individual specifications significantly influence the overall performance of the device. For instance, it is crucial that the anti-aliasing filter does not introduce distortions or excessive delays in the signals being measured, especially in the passband around the nominal system frequency. Attenuation or phase distortion can directly impact measurement accuracy, while delays may influence both the synchronization of measurements and the latency in reporting results. At the same time, the choice of real-time phasor estimation algorithms directly impacts latency and reporting rates. Furthermore, a PMU must relay measurements at a high reporting frequency to other PMUs or PDCs, depending on the chosen monitoring scheme. In compliance with IEEE C37.118.2, PMU reporting rates are typically set as integer multiples of the nominal power system cycle (20 ms for 50 Hz, 16.67 ms for 60 Hz) [19]. While traditional PMUs operate up to 120 fps, newer high-speed PMUs following IEEE 60255-118-1 allow reporting rates exceeding 120 fps, which must be supported without overwhelming the available network infrastructure [4].

3.4 Instrument transformers

ITs provide reduced voltage and current signals to the PMU analog inputs in the substation. Since 2010, the IEC 60044 standard series has been gradually replaced by the IEC 61869 series, which introduces a structured classification of ITs into two primary categories [25]:

- Conventional ITs, which include inductive CTs, inductive VTs, combined CT-VT units and capacitive VTs.
- Low-power Instrument Transformers (LPITs), which output low-power analog or digital signals to measuring devices, meters, and protective or control systems. LPITs are further classified into active and passive types based on their dependency on an external power source.

Secondary voltage and current RMS levels are typically standardized at 100 V for voltage transformers and either 1 A or 5 A for current transformers, as specified in IEC 61869 and IEEE C57.13. However, variations exist in LPITs, which may produce low-power secondary signals in the 10V range or direct digital outputs.

The IEC 61869 series also establishes accuracy requirements for ITs based on their intended application, whether for measurement or protection. These requirements apply equally to conventional ITs and LPITs. The standard defines accuracy classes for CTs as 0.1, 0.2, 0.5, and 1, while for VTs, the classes include 0.1, 0.2, 0.5, 1, and 3. Compliance with a specific accuracy class requires meeting prescribed limits for ratio error (the percentage deviation of the transformed voltage/current ratio from its nominal value) and phase displacement (the angular deviation between primary and secondary signals) under specified operating conditions. For instance, a class 0.5 CT, commonly used in medium-and high-voltage networks, must maintain a ratio error within 0.5% of the rated current and a maximum phase displacement of 9 milliradians (mrad) [4].

In usual practice, magnetic-core VTs and CTs are employed, typically rated at class 0.5, which allows for a maximum ratio error of 0.5% and a phase error of 6 mrad at full scale. To mitigate the effect of the ratio and phase errors introduced by ITs, compensation algorithms are usually integrated into commercial PMUs. However, such compensations assume accurate knowledge of IT characteristics, which is often impractical and may not be reliable due to uncertainties in metrological assessments and the impact of actual network and environmental conditions on the transducers. Therefore, transducers are a major source of uncertainty in synchrophasor measurements [4].

3.5 Phasor data concentrators (PDCs)

The Phasor Data Concentrator (PDC) is an essential component of the WAMS infrastructure, responsible for collecting, processing, and routing synchrophasor data from multiple PMUs. Any device capable of receiving PMU measurement packets formatted according to IEEE C37.118.2 can function as a PDC [22]. The primary role of a PDC is to merge and time-align multiple PMU data streams into a unified dataset that can be forwarded to a higher-level synchrophasor-enabled device, such as a Super PDC (SPDC), or stored for post-event analyses. Since each PMU dataset is timestamped, the aggregation process is relatively straightforward, as measurements with identical timestamps can be aligned across multiple data streams [4].

3.5.1 Role of PDCs in WAMS

As illustrated in Figure 3.5, PDCs and SPDCs operate at different levels within the WAMS hierarchy, with specific roles depending on the application [4], [26]:

- In post-event analysis and offline applications, the PDC serves primarily as a data validation and archival unit. It gathers synchrophasor data from various PMUs, verifies the integrity of measurement packets, and stores the information in a database for future use. This function is particularly useful for forensic analysis of grid disturbances, oscillation events, and blackouts, where archived PMU data allows for detailed event reconstruction and diagnostics.
- In real-time applications, such as State Estimation (SE) and real-time grid monitoring, the PDC aligns PMU measurements based on their timestamps. In such cases, latency and reliability are critical factors, requiring the PDC to possess high computational capability. To ensure minimal processing delays, modern PDC implementations integrate efficient data queuing mechanisms and low-latency networking protocols.

3.5.2 Challenges in PDC implementation

Despite their essential role in WAMS, PDCs face several challenges that can impact performance and reliability [26]–[28]:

- Packet loss and data inconsistency: Network congestion, jitter, or hardware failures can lead to missing or out-of-order data packets, affecting time alignment and reliability. Advanced error correction and redundancy mechanisms must be implemented to mitigate these issues.
- Scalability issues: As the number of deployed PMUs increases, data processing loads on PDCs grow exponentially. Efficient data compression and distributed computing architectures can help address scalability concerns.
- Cybersecurity vulnerabilities: Since PDCs serve as centralized data hubs, they can be targets for cyberattacks, such as data injections, denial-of-service, and GPS spoofing. Robust encryption and authentication mechanisms must be integrated to ensure secure data exchange.

The increasing adoption of software-defined networking and cloud-based PDC architectures offers new opportunities for improving PDC performance. Future research is focusing on decentralized data aggregation, utilizing edge computing to reduce dependence on centralized PDCs, thereby improving resilience and fault tolerance. AI-driven data quality analysis leverages machine learning algorithms to automatically detect and filter out erroneous PMU data, improving system reliability, and blockchain-based data security explores blockchain technology to enhance the integrity and authenticity of synchrophasor data exchanges in large-scale WAMS networks [26], [28].

3.6 Structure of the wide area monitoring system

WAMS are synchrophasor-based networks designed to provide real-time monitoring of both steady-state and dynamic conditions across large-scale power transmission and sub-transmission networks. These systems serve as an early warning mechanism against grid instabilities, playing a crucial role in preventing cascading failures, optimizing asset utilization, and enhancing overall grid reliability [4], [26], [29].

The architecture of a typical WAMS is illustrated in Figure 3.5. At the core of this system are PMUs, which function as measurement nodes deployed at critical substations. PMUs provide timestamped measurements from all monitored buses and feeders, which can be stored locally and accessed remotely for post-event analysis or diagnostic purposes. However, in most applications, the phasor data is used at locations remote from the PMUs, where continuous data streams from multiple PMUs are aggregated. This data transfer necessitates a communication network that comprises PMUs, communication links, PDCs to ensure the reliable transmission of field measurements to monitoring applications, conventionally located at the ECC. Individual PMU data streams are first transmitted to upper-level PDCs, i.e., SPDCs, which mediate data sharing between ECCs or even across utilities [4], [26], [29].

3.7 Integration of PMU-based applications in the EMS

When commercial PMUs first became available, their primary application was limited to post-event analysis, given the high cost of the devices and the limitations of communication networks for real-time data transmission. However, with the rapid expansion of PMU deployment and advancements in communication infrastructure, research has increasingly focused on leveraging phasor and frequency measurements for real-time monitoring, control, and protection of power systems [4], [5]. Overall, WAMS are expected to revolutionize the EMS functionalities as they offer significant advantages over the legacy SCADA system, as illustrated in Table 3.1.

One of the frequently cited advantages of WAMS is the enhancement of situational awareness by providing operators with synchronized phasor data from critical grid nodes. However, situational awareness alone does not sufficiently justify the significant financial investment required for deploying WAMS. Consequently, research has concentrated on exploring PMU-based applications that provide actionable insights for grid operation and stability. These applications include state estimation, voltage stability monitoring, oscillation detection, transient stability assessment, and fault location [8], [30]. A brief description of available real-time and offline production-grade phasor data applications is given in Table 3.2 and Table 3.3, respectively, followed by their analytical description in the following Subsections.

3.7.1 Power system monitoring and control [6], [8], [31]

Historically, *power system monitoring* depends on SE algorithms that use SCADA measurements collected by RTUs to estimate the voltage phasors at all system buses. Using this approach, the system state is inferred from unsynchronized power flow and injection measurements using a nonlinear state estimator. However, the quality of the state estimates is affected by several sources of error, including measurement asynchronization, communication noise introduced during data transmission through outdated communication channels, and the assumption of steady-state grid operation. The integration of PMU technology addresses many of these issues by providing higher reporting rates, direct observation of state variables, and synchronization of measurements to a precise time source. Furthermore, as PMUs are capable of recording branch current phasors, the SE measurement model is simplified and, under certain conditions, may become fully linear, offering significant advantages over conventional nonlinear methods.

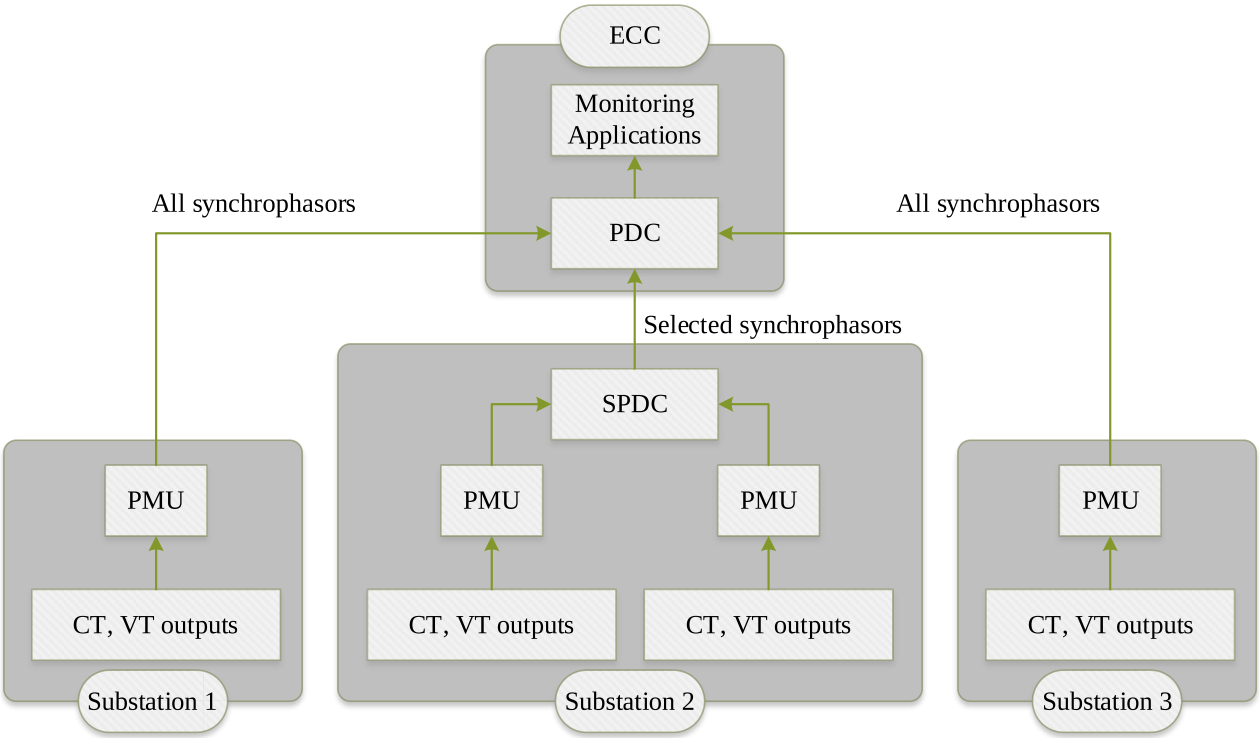

Figure 3.5: Hierarchy of the phasor measurement systems [4].

Table 3.1: Comparison of SCADA and WAMS measurement systems.

Aspect	SCADA	WAMS
Measurement type	Voltage and current magnitudes, power flows and injections	Voltage and current phasors, frequency and ROCOF
Reporting rate	0.1-1 fps, due to bandwidth and processing limitations	25-120, or even higher fps
Synchronization	No time synchronization	Synchronized using GPS timestamps
Accuracy	Lower: low-resolution A/D converters, errors during data transmission	High: high-resolution A/D converters, reliable data transmission, strict calibration standards and error-correction algorithms
Latency	High latency due to legacy communication systems	Compatible with modern high-speed communication protocols
Application focus	Steady-state monitoring and control	Dynamic monitoring, real-time control, and protection
Event detection	Limited to slow, large-scale events	Capable of detecting fast, localized events

Table 3.2: Description of real-time PMU applications [30].

Real-time applications	Functionality
Setting system operating limits (SOLs); Event detection and avoidance	• Data-informed identification of normal range of operation • Alerts to indicate abnormal operating conditions; Presentation and decision support tools for event identification and correction
Congestion management	Real-time calculation of line ratings with feed through to online monitoring tools
Fault location	• Geo-spatial display of event location • Near real-time and historical data presentation capability • Event type identification and display (phase-ground vs. phase-phase fault, loss of load, loss of generation, etc.)
Power oscillations	• Oscillation detection and mode meter • Display estimates of oscillation damping and oscillation energy • Decision support tools to deal with poorly dampened oscillations
Outage restoration	• Assist in re-synchronizing of islands • Quicker restoration by expediting forensics and event identifications
Special protection schemes and islanding	• Identify precursors to events that would necessitate islanding • Ensure proper generation controls are in place to manage the island, once created
State estimation	Integrate high-fidelity synchronized phasor measurements in state estimators
Voltage stability	• Voltage stability indicators defined with relation to current operating point • Long and short-term trending to help operators identify changes in system conditions
Wide-area controls	• Response-based wide-area reactive switching when wide-area voltage instability is detected • Response-based inter-area oscillation damping using power modulation controls
Wide-area situational awareness	Trending displays • Display trends of system frequency at multiple locations (long and short timeframe) • Display trends of major path flows • Operator training for disturbance identification Phase angle alarms and displays • Displays that show angular separation between critical areas in the system, with alarms • Decision support tools to deal with alarms • Reactive reserve monitors

Table 3.3: Description of offline PMU applications [30].

Offline applications	**Functionality**
Baselining	Baselining tools • Integrate system performance indicators (damping, voltage stability, etc.) into EMS • Provide seasonal reports Use baselines • To improve planning models • For pattern recognition and early diagnosis of abnormal grid events • To set alert and alarming thresholds
Alarming and SOL evaluation and design	• Wide area phasor angles may be better indicators limiting conditions and SOLs • Alarms and SOLs based on system damping
Forensic event analysis	• Mechanisms for collecting data from PMUs • Tools to identify significant operational parameters involved (modes of oscillation, frequency excursions, voltage impacts, etc.)
Generator model validation	Power plant model and performance validation • Validate power plant models • Track power plant performance with respect to voltage, frequency and oscillations • Detect control failures
Load model derivation	• Estimate system load sensitivity to frequency • Estimate real-time load sensitivity to voltages • Measure and analyze dynamic load response during FIDVR events
Power oscillations	• Oscillation detection and mode meter • Baseline oscillation damping with respect to system operating conditions
Frequency stability	• Analysis and baselining of system frequency performance and governor response distribution in interconnections
System model calibration and validation	• Adopt processes for system model validation using tools to compare actual event data to study results

In power systems, *control* is typically localized, with generators managed based on local measurements and a model of the rest of the power system. In contrast, wide-area control, enabled by PMUs, provides system-wide visibility, allowing operators to detect and mitigate disturbances in real-time. By combining local and global control strategies, PMUs enable advanced stability control measures, including adaptive islanding, which prevents cascading failures by intelligently separating unstable grid sections, real-time generator rescheduling, and dynamically adjusting voltage support via reactive power compensation.

Traditional methods for *transient stability assessment* involve time-domain simulations and direct methods, which, while effective, lack the speed and adaptability required for real-time operation. Synchronized PMU measurements address these limitations by offering a more accurate representation of system dynamics. One significant advancement enabled by PMUs is the use of decision trees (DTs) for transient stability assessment. DT-based methods involve offline training using historical data and simulations, creating a model that can classify real-time system conditions as stable or unstable based on PMU measurements. This approach significantly enhances the accuracy and speed of stability assessments, as PMU data provides up-to-date system conditions that improve the reliability of DT classifications. Additionally, preventive control strategies have been developed that continuously monitor system stability margins. If instability is detected, automated corrective measures, such as generation redispatch, controlled load shedding, and dynamic reactive power compensation, can be triggered to prevent system collapse. These capabilities are particularly valuable in deregulated power markets, where real-time security assessments are crucial.

Real-time stability monitoring is a crucial aspect of modern power system operation, enabling operators to detect and mitigate potential instabilities before they escalate into cascading failures. PMUs contribute to real-time stability monitoring in several areas:

1) *Voltage stability monitoring*: PMUs help assess voltage stability by providing real-time voltage magnitude and phase angle data from across the grid. These measurements are used to compute voltage security indices, which indicate proximity to voltage collapse. Unlike conventional methods that rely on offline model-based simulations, PMU-based approaches enable dynamic voltage stability analysis by continuously monitoring grid conditions and identifying weak areas prone to voltage instability.
2) *Oscillation monitoring*: PMUs assist in identifying poorly damped low-frequency (0.2 to 2 Hz) inter-area oscillations, which can degrade power quality and lead to system instability. Real-time oscillation monitoring systems utilize ringdown analysis and ambient data methods to identify electromechanical oscillatory modes. By processing PMU data with algorithms such as Prony analysis and frequency domain decomposition, system operators can detect oscillations early and implement damping measures to prevent instability.
3) *Angle stability monitoring*: Maintaining angle stability is essential for preventing loss of generator synchronism and system-wide blackouts. PMUs provide phase angle measurements that allow real-time tracking of angular deviations across the network. These measurements support the implementation of wide-area feedback control strategies, where corrective actions such as generator rescheduling or controlled islanding are triggered based on real-time stability assessments.

Additionally, historical PMU data can be effectively used in conjunction with the operations planning model to determine operating limits for rotor angle stability, voltage stability, and small signal stability.

PMUs have also been instrumental in grid integration of renewable energy sources, where their high-precision measurements aid in monitoring and controlling variable generation from wind and solar plants. They assist in managing voltage and frequency stability challenges associated with high penetration of renewables, thereby enhancing grid adaptability to fluctuating power injections. Additionally, PMUs contribute to load modeling and demand response by capturing real-time voltage and frequency fluctuations, which helps in refining load models and improving demand-side management strategies, enhancing grid flexibility and efficiency.

Adaptive system restoration is also a critical aspect of power system resilience, aiming to minimize downtime and economic losses following blackouts. Traditional restoration strategies, based on precomputed simulations, often fail due to discrepancies between assumed and actual system conditions. In contrast, PMU-based restoration leverages real-time wide-area measurements to dynamically adjust restoration actions. The integration of PMU data enables precise monitoring of phase angles at key buses, allowing for optimized reconnection of system islands while preventing excessive angular differences that could destabilize the network. Additionally, PMUs support real-time generation-load rescheduling within system islands, ensuring synchronization before reclosing attempts.

3.7.2 Power system protection [6], [8]

Synchronized phasor measurements have significantly advanced power system protection by addressing longstanding challenges, including the protection of series-compensated and multi-terminal lines, as well as the limitations in setting out-of-step relays. In many situations the capability to measure a remote voltage or current on the same reference as local variables has greatly enhanced the accuracy and reliability of protection functions. In some cases, communication of synchronized measurements between line terminals suffices, while in others, wide-area data exchange is necessary to ensure effective fault detection. Phasor measurements are particularly beneficial for protection functions with inherently slower response times, where measurement latency does not compromise performance. This is particularly relevant for backup protection functions of distance relays and protection functions concerned with managing angular or voltage stability of networks, which can effectively utilize PMU measurements with propagation delays of up to several hundred milliseconds.

Differential protection, a well-established principle for buses, transformers, and generators, has historically lacked direct application to long transmission lines due to the absence of synchronized measurements. Transmission lines incorporating series compensation, FACTS devices, or multi-terminal configurations pose unique protection challenges, which have traditionally been addressed using differential-like schemes such as phase comparison. However, the increasing availability of synchronized phasor measurements and advanced communication infrastructure now enables the implementation of true differential protection for such complex network configurations. PMUs also enable *distance protection* schemes by offering synchronized fault detection and location capabilities. By accurately identifying fault locations, PMUs contribute to faster restoration times and reduced operational disruptions.

Moreover, PMUs have expedited the development of *adaptive out-of-step protection*, which adjusts relay settings dynamically based on real-time grid conditions, thereby enhancing protection system reliability and selectivity. Out-of-step conditions, where a group of generators loses synchronism with the rest of the system, can precipitate large-scale grid failures. Traditional out-of-step relays use predefined impedance relay zones, determined through extensive transient stability simulations, to distinguish between stable and unstable power swings. However, in highly interconnected power systems, these settings quickly become outdated, leading to misoperations that may exacerbate cascading failures. By leveraging time-series analysis, PMU-based out-of-step relays can dynamically assess evolving angular swings and predict stability outcomes. This approach enables timely corrective actions, such as controlled islanding or generator tripping, to prevent widespread system collapse. Initially, adaptive out-of-step protection can be applied to known system separation points, with gradual expansion to more complex network configurations as experience and data availability improve.

The performance of *backup protection*, particularly in distance relays, has been a subject of debate due to the risk of unnecessary tripping caused by load encroachment during system disturbances. Zone 3 of distance relays, traditionally used for remote backup protection, has been identified as particularly susceptible to misoperation, leading to proposals advocating its removal. However, a complete elimination of remote backup protection could compromise system security in scenarios where no other protection mechanism is available. Instead, a more refined approach is required to ensure that backup protection remains effective while avoiding unintended tripping under high-load conditions. PMU measurements offer a viable solution to mitigate this issue by providing real-time data that can differentiate between actual faults and load encroachment. In scenarios where a distance relay's Zone 3 is triggered, PMU data can be utilized to assess whether the event corresponds to a genuine fault or a load-induced condition. If a significant negative-sequence current is detected, indicating an unbalanced fault, the relay trip is justified. Conversely, if the currents remain balanced, the event may either correspond to a three-phase fault on an adjacent circuit or a loadability violation. To further refine the decision-making process, PMUs installed at the terminals of the lines backed up by the relay in question can analyze the ratio of positive-sequence voltage to current. If none of these PMUs detect a fault in their primary protection zones, the Zone 3 pickup must be attributed to a loadability violation rather than an actual fault. In such cases, supervisory control can dynamically block the operation of the backup relay, preventing unnecessary tripping.

3.7.3 Commercial synchrophasor applications

In the early 2010s, commercial synchrophasor applications were primarily focused on offline analysis, model validation, post-event diagnostics, and limited real-time visualization. At that time, commercial software such as SEL-3378 Synchrophasor Vector Processor (SVP), now superseded by the SEL-3555 Real-Time Automation Controller (RTAC), combined with the SEL SynchroWave Monitoring software, ABB PSGuard, Alstom Psymetrix's PhasorPoint (later integrated into GE Vernova), and Electric Power Group's (EPG) Real-Time Dynamics Monitoring System (RTDMS) had begun enabling applications such as wide-area situational awareness, voltage and frequency stability monitoring, power swing and oscillation detection, and event-driven data archiving. However, these tools were still considered to be under development and lacked the maturity required for production-grade deployment. Over the past decade, the increased deployment of PMUs and the expansion of their applications have been driven by advancements in both communication infrastructures (e.g., optical fiber, Gbps networks, and 5G) and embedded microprocessor technology, enabling enhanced real-time processing and data exchange capabilities. Modern PMU-enabled devices now support low-latency control actions, advanced analytics, and integration with AI-driven decision support systems. Widespread deployment has improved, notably through initiatives like NASPI in North America, which continues to coordinate stakeholders in developing robust applications and promoting deployment strategies. In Europe, ENTSO-E and various national TSOs have expanded synchrophasor integration into WAMS, supporting cross-border coordination and renewable integration. Although challenges remain, particularly in data quality assurance, cybersecurity, and organizational adoption, synchrophasor applications are increasingly recognized by TSOs as essential tools for real-time grid reliability, resilience, and control. Table 3.4 indicates the relative priorities for phasor application development, according to report [30].

Implementation of synchrophasor applications is also facing various challenges. First, even though phasor technology hardware is mature, there is the challenge of how to build PMUs that can perform effectively and consistently at sampling rates upwards of 120 frames per second, to meet oscillation monitoring needs, and the challenge of developing and maintaining a secure communications system dedicated to transfer of phasor data that can deliver data and control directives fast enough to support interconnection-wide monitoring, analysis and automated controls. In terms of application-specific research, the most pressing need is for baselining analyses, since good baselining feeds a wealth of other real-time and planning priorities including event diagnosis, alarm-setting, system operating limits setting, smarter real-time trending, validation of dynamic power system and power plant models, and development of intelligent operator decision support tools. As with all new technologies, extensive end user training will be needed to successfully transition phasor technology into full use as a real-time operational tool. Operations personnel need to see how phasor data and applications can improve their ability to reliably operate the system. Applications and interfaces must be developed that make terabytes of data easy to visualize and interpret, including measures such as phasor-informed alerts and alarms, so that when operators need to deal with an emerging grid situation, they can access tools to use the data constructively, or receive intelligent decision support options based on phasor system-enabled options. The experimental synchrophasor network developed in Chapter 9 of this thesis contributes to the necessity of developing more reliable and useful applications to improve power system operation and reliability, as well as providing education and training to relevant personnel.

Table 3.4: Priority of PMU-based application integration [30].

Application	Priority		
	Real-time operations	**Day-ahead operations**	**Asset management**
Alarming and setting SOLs	High	Low	Low
Baselining	High	High	High
Congestion management	Medium	High	Medium
Fault location	Medium	Low	Low
Power oscillations	High	Medium	Medium
Frequency stability	High	Low	High
Operations planning	Low	High	Medium
Outage restoration	High	Low	Low
Resource integration	Medium	Low	High
Special protection schemes and islanding	Low	Medium	High
State estimation	High	Low	Low
Voltage stability	High	Low	Low
Wide-area controls	High	Low	High
Forensic analysis	Medium	Medium	High
Generator and load model validation	Low	High	High
System model validation	Low	High	High

4. Power System Monitoring and State Estimation

Power system monitoring is one of the most fundamental responsibilities of a system operator, who must continuously assess system conditions to ensure grid operation remains within predefined safety and reliability thresholds. Ideally, operators would have complete visibility of system attributes, such as bus voltages, line power flows, and frequency deviations. However, due to the significant cost of extensive measurement infrastructures, ECCs typically rely on a limited set of critical measurements [12].

State estimation (SE) is the process of determining the values of unknown state variables within a system by using available real-time measurements and predefined criteria. This technique is widely employed in contexts where measurement errors could affect data integrity. Historically, SE was used to predict the positions of aerospace vehicles via noisy radar data and other imprecise sensor inputs. In power systems, SE is regarded as a fundamental function of the ECC, essential for real-time monitoring, control, and contingency analysis in the EMS.

4.1 Power system monitoring and security

Power system monitoring involves continuous assessment of system conditions to ensure that all operational parameters remain within acceptable limits. Typical parameters monitored in power systems include substation voltages, transmission power flows, generator active and reactive power output, total system load, interchange schedules, system frequency, and the status of circuit breakers and switches. These parameters are critical for evaluating system performance and identifying potential violations that may necessitate preventive or corrective control actions [12].

4.1.1 Security concepts and contingency analysis

Power system security refers to the system's ability to withstand disturbances while maintaining a reliable electricity supply. A higher level of security corresponds to a lower likelihood of load loss or widespread blackouts. Security-driven control actions are therefore designed to [32]:

1) Prevent cascading failures by ensuring the system can withstand disturbances.
2) Mitigate risks to critical grid infrastructure, protecting transmission lines, generators, and substations from damage.

A fundamental tool for assessing system security is contingency analysis, which evaluates the system's response to potential equipment failures or generator outages. A contingency is defined as the unexpected loss of transmission lines, transformers, or generation units, which could push the system into an insecure or emergency state. To determine whether the current operating state is secure, a set of single and multiple contingency scenarios must be simulated. These simulations utilize steady-state power flow analysis, where system constraints, such as transmission line thermal limits and voltage stability margins, are evaluated under different contingency conditions. If a contingency threatens system security, two main strategies can be implemented [11], [32]:

1) *Preventive* control actions: Modify the system's operating state before the contingency occurs.
2) *Corrective* control actions: Implement real-time responses to mitigate the impact of the contingency after it occurs.

The power system security levels are defined based on the economy-security functions of the EMS, which use the SE results to determine real-time security conditions. Figure 4.1 illustrates the hierarchical classification of security levels, which guides appropriate control (C) and preventive (P) actions, while transitions caused by operations, contingencies, or accidental actions are indicated by arrows [11], [32]:

- *Secure* (Level 1): All loads are supplied without violating operating limits, and the system can withstand any contingency without requiring post-event corrective action.
- *Correctively Secure* (Level 2): Similar to Level 1, all loads are supplied without operating limit violations. However, in this case, potential violations from contingencies can be corrected with control actions, primarily focused on active power control. This level is more cost-effective but relies on post-contingency corrections, determined in advance using optimal power flow with security constraints.
- *Alert* (Level 3): All loads are supplied, but some contingency-related violations cannot be corrected without load loss. Preventive generation rescheduling and network reconfiguration, based on optimal power flow with contingency constraints, are necessary to restore security.
- *Correctable Emergency* (Level 4): Some operating limits are exceeded, but corrections can be applied without load loss. Emergency control actions restore system security to Level 3 or higher.
- *Noncorrectable Emergency* (Level 5): Operating limits are violated, and load shedding is required to maintain stability. The optimal amount and location of load curtailment are determined using security-constrained optimal power flow.
- *Restorative* (Level 6): While operating limits are no longer exceeded, load shedding has occurred. Restorative control measures aim to return the system to a more secure state, ideally Levels 1 or 2.

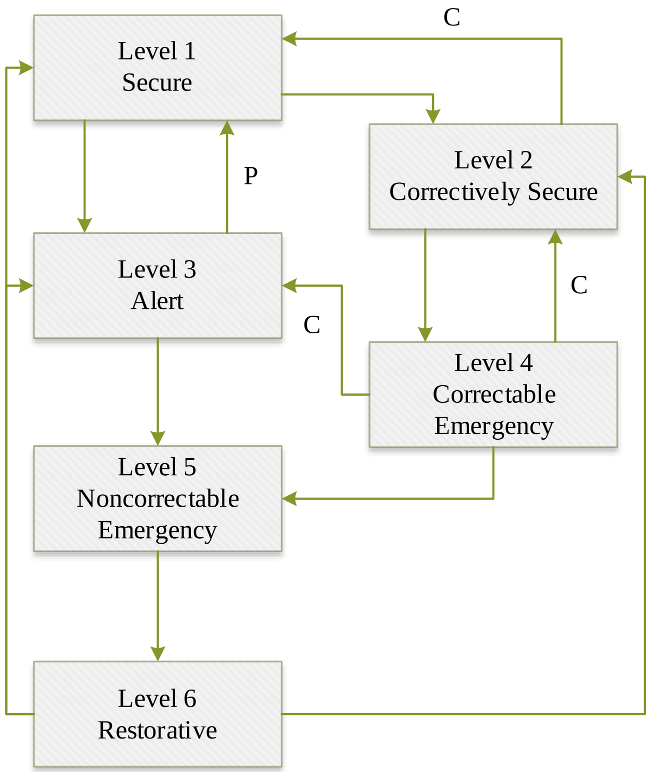

Figure 4.1: Power network static security levels.

4.1.2 Situational awareness [33]

A widely accepted definition of situational awareness is “the *perception* of elements in the environment within a certain time and space, the *comprehension* of their significance, and the *projection* of their status into the near future.” More specifically, the three levels of situational awareness are:

- *Perception*: The operator must accurately perceive the status, attributes, and dynamics of environmental variables.

- *Comprehension*: The information gathered from perception needs to be synthesized through interpretation, pattern recognition, and evaluation.
- *Projection*: The operator must be able to extrapolate this data to anticipate future states and develop an appropriate action plan.

These principles are widely applied in critical decision-making environments such as aviation, air traffic control, military operations, and power system control rooms. In the context of a control room in the ECC, operators rely on advanced visualization and decision-support tools like SE to enhance situational awareness. Errors made by operators often stem from gaps in situational awareness, where critical information is overlooked (perception failure), system conditions are misinterpreted (comprehension failure), future contingencies are underestimated (projection failure). Therefore, the goal is to enhance control room environments with visualization tools to aid perception, provide robust data analysis systems for comprehension, and support operators in making and executing decisions effectively at the projection level.

4.2 Power system state estimation fundamentals

In 1970, Schweppe et al., having recognized the inherent inability of measurement systems to capture the actual state of a power system, introduced *power system state estimation* into their study, with the ultimate goal of optimally controlling their operation in real time [34]. The mathematical model they proposed derives from estimation theory – a branch of statistics with broad application in the study of Automatic Control Systems – and incorporates elements of probability theory. The purpose of state estimation is to define the system state based on the available measurements; in other words, to assign values to the voltage phasors of all the nodes in the system under study, which in the general case constitute its state variables. SE has become established as the computational procedure capable of producing the most faithful possible depiction of a network's current state under real-time conditions in the ECC.

4.2.1 The role of power system state estimation in the EMS

The usefulness of SE is typically juxtaposed with that of power flow analysis, which in the 1950s was the first computational tool for depicting the steady state of a power system corresponding to a given operating point at which the system generates, transfers, and distributes electric power [32]. In power flow analysis, one calculates the voltage phasors of all the nodes, as well as the active and reactive power flows in all the branches of the system. Although both SE and power flow analysis computationally rely on the same electrical quantities – that is, on the solution of the same mathematical equations – and represent the system state using static analysis models, their qualitative differences are quite significant. Generally, power flow analysis computes the operating state of the system for a snapshot of its steady state, based on available values of electrical quantities. On the other hand, SE provides the most probable state of the system, treating the available data as measurements with their corresponding accuracies. In other words, SE is a real-time computational tool for processing measurements, whereas power flow analysis is a computational procedure that cannot function reliably in real time, given that it is not designed to detect and filter the errors realistically present in any measurement data [35].

More specifically, unlike power flow analysis, the available values of electrical quantities are treated as measurements within the context of state estimation. They are therefore associated with specific errors and modeled as random variables whose variances depend on these errors. A direct consequence of this modeling is that the state estimator functions as a filter for the available "raw" data, as it can assess their quality, identify potential gross measurement errors, and reduce the noise that distorts them. Power flow analysis does not offer any of these capabilities, since its modeling does not support evaluating input values and does not exhibit adaptability with respect to them. Finally, SE is formulated as an optimization problem whose solution is based on examining an overdetermined system of equations, i.e., it is designed to manage a surplus of data. Power flow analysis, in contrast, is about finding the unique solution to a system of algebraic equations, where surplus data are not desirable. State estimators were already being used in ECCs in the 1970s, aiming to ensure the reliable operation of transmission systems through real-time measurements obtained from the terminal units of SCADA systems [36]. Over the years, the specific functions have evolved in terms of both their computational core and the algorithms used, while alternative methods have been proposed for the optimization problem upon which SE is based. Historically, the chief difficulties impeding state estimators arose from the inability to obtain synchronized measurements from distributed terminal units and from inadequate measurement infrastructure in distribution networks [37]. As a result of these shortcomings, only transmission systems were sufficiently monitored – synchronization was dismissed because of the slowly varying conditions of power systems during steady-state operation – while distribution networks were effectively unmonitored due to a lack of measurement data, which made running state estimators impossible. The need to monitor distribution networks led to gradually introducing pseudo-measurements into the set of available data so that the condition of sufficient data redundancy could be met. Pseudo-measurements refer to values that have not actually been measured but are products of forecasting or of processing historical data.

In Figure 4.2, the data flow diagram of a typical SE implementation in the ECC is presented. More specifically, state estimators generally comprise the following functions [5], [38]:

- *Topology processor*: the status of switches and circuit breakers are processed to determine the current network topology, and the system model is updated in real-time to reflect network reconfigurations.
- *Observability analysis*: determines whether the available set of field measurements is sufficient to uniquely estimate the system state. If full observability is not achieved due to insufficient measurements, the system may be divided into observable islands where SE can be applied separately, or observability can be reinstated using pseudo-measurements, that is, estimated measurement values based on historical or forecasted data.
- *State estimation algorithm*: uses an optimization process to derive the estimated state of the network from available real-time measurements over a specific time frame.
- *Bad Data (BD) detection and identification*: an algorithm that detects, identifies, and eliminates gross measurements in the dataset, based on the statistical properties of measurements. Depending on the employed SE algorithm, this step may be integrated directly in the estimation process, or it can be a postprocessing step; in the latter case, if BD are detected and eliminated, the SE process is repeated.
- *Topology error identification & system parameter estimation*: detects topology errors caused by incorrect reporting of switching component statuses, and diagnoses incorrect line impedances or transformer tap settings that affect SE accuracy. Finally, parameter estimation is executed, updating the network model with the most probable system parameters based on the SE solution.

The outputs of the state estimator serve as critical inputs for multiple downstream EMS applications, including contingency analysis and security monitoring, economic dispatch and optimal power flow, as well as voltage stability assessment and control [5], [38].

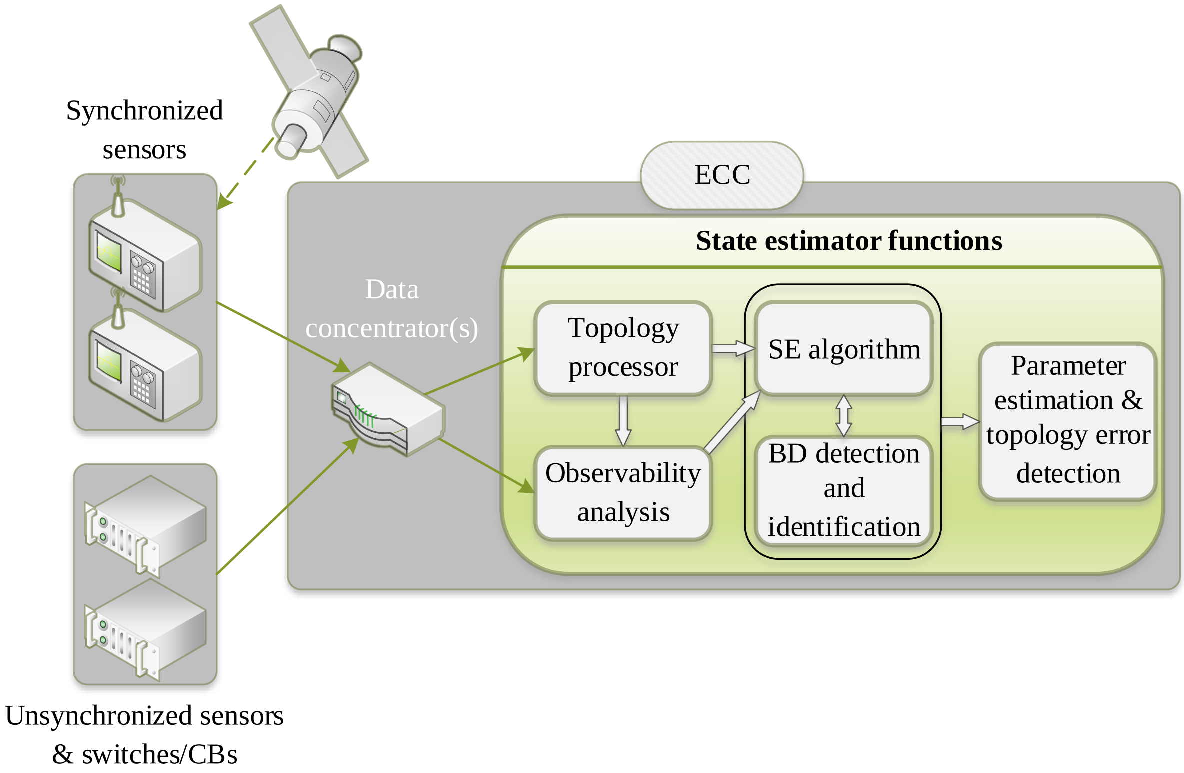

Figure 4.2: Data flow diagram of SE, from the field sensors to the ECC.

4.2.2 SCADA measurements and state estimation

Accurate SE results are directly correlated to the quality and reliability of the measurement data available. SCADA-based SE primarily relies on the following types of real-time measurements: bus voltage magnitudes, bus voltage angle differences between buses, active and reactive power injections into buses, active and reactive power flows in branches, and branch current flow magnitudes. In cases where direct measurements are unavailable or insufficient, pseudo-measurements are usually considered in the form of target bus voltage magnitudes and/or angles, target active-reactive branch power flows, and estimated or forecasted active-reactive power injections. Each measuring device of course introduces some level of random error; thus, SCADA measurements typically contain errors due to [32]:

- *Instrument transformers*: ITs are the primary field measurement devices that introduce errors stemming from saturation, nonlinearity, and hysteresis effects, leading to distorted signal outputs. Over time, instrument transformers degrade due to exposure to temperature variations, humidity, mechanical stress, and transient phenomena. Poor precision classes of CTs/VTs also exacerbate measurement inaccuracies
- *Measurement transducers*: Measurement transducers exhibit nonlinear behavior under extreme operating conditions, such as light load conditions (low current values cause nonlinearities in CTs), while wiring issues can cause voltage drops and signal attenuation.
- *Communication noise*: Communication links introduce random noise due to electromagnetic interference from nearby equipment, harmonics affecting sensor readings, and inductive or capacitive coupling between measurement circuits.
- *Data loss and random communication delays*: SCADA data transmission occurs over various network types (serial, IP-based, fiber-optic, or microwave). Failures in communication channels can cause measurement loss and random propagation delays affecting measurement synchronization.

- *Time skewness*: SCADA measurements are not inherently synchronized, leading to time skewness among different sensors.

4.3 Evolution of power system state estimation algorithms

The state estimator has served as an integral computational and operational unit of ECCs ever since the introduction of digital computers for the development of the EMS in the mid-1960s. The first proposals for monitoring transmission systems using estimation theory had already appeared in the late 1960s. From 1970 onward, and for at least four decades, the static state estimation model proposed by Schweppe et al. constituted the main field of study for transmission-system state estimation. Under the static model, initially formulated in 1968 [34], the time parameter is excluded from the study of the system state; effectively, the estimation process handles measurement sets as snapshots, owing to the lack of measurement synchronization and the delays involved in data transmission. In parallel, a concise description of an equivalent dynamic model was provided. Finally, organizing the static model as an optimization problem solved via the WLS method [39] emerged as the most popular technique for studying SE in electric power systems.

A significant contribution to the evolution of the WLS static model came from the research led by Monticelli on the development of the fast decoupled method for solving the problem [40] and on the formulation of generalized state estimation, which treats analog measurements, switch states, and the electrical parameters of lines as a single set of interacting measurement data [41]. Within the context of generalized state estimation, both digital and analog measurement data were jointly processed, and in essence, topology processing was integrated in such a way as to permit the detection of unacceptable data. This methodology was founded on modeling sections of the system/network at the level of physical linkage – namely, by considering unknown line impedance values or switch states as additional state variables.

Comparative studies led by Wu on numerical stability, computational efficiency, and implementation complexity for various methods proposed over time for solving the WLS static model [42], [43] helped address the problem of ill-conditioned matrices arising during model solution. These matrices possess eigenvalues close to zero, making it difficult to solve the system of equations. These studies included the normal equations method, orthogonal factorization, the hybrid method, the use of equality constraints in the normal equations, and the Hachtel augmented matrix method. Critical factors influencing the solution of the WLS static model include virtual measurements for zero injection nodes and current measurements. The combination of zero-injection measurements with high weighting factors is one of the main causes of ill-conditioned matrices. Modeling such virtual measurements as equality constraints during model solution has contributed to mitigating this issue. Moreover, introducing current magnitude measurements – primarily studied in [44], [45] – represents a notable advancement in the development of the WLS static model, as these require special handling relative to other measurement types. Finally, incorporating inequality constraints into the model [46] has ensured compliance with prevailing system operating limits.

One of the most important features of state estimators is robustness with respect to measurement sets that exhibit large variations in individual accuracies and in cases of outliers containing unacceptable errors (bad data). WLS SE has an inherent weakness in handling such measurement sets [32], leading to the proposal of various solution-method variants under these conditions [47], [48]. To ensure robustness, several alternative formulations of the SE problem have been developed, with the most notable being Least Absolute Value (LAV) estimation, nonquadratic estimators, and the least median of squares estimator, all evaluated post-hoc in [49]. In conjunction with any SE method, the projection statistics technique has been proposed as a means of enhancing estimator robustness in power systems by identifying leverage points in the measurement set – i.e., points corresponding to outlier measurements in the Cartesian coordinate system [50]. A reference point for state estimator robustness is the work of Huber [51], who systematized the generalized maximum likelihood estimation for minimizing the general Huber function. The corresponding generalized estimator (Huber M-estimator) aided in implementing generalized estimator models in power systems [52]–[54].

4.4 Weighted least squares state estimation

The objective of SE is to determine the most likely state of the system based on the quantities that are measured. One way to accomplish this is by Maximum Likelihood Estimation (MLE), a method widely used in statistics [55]. The measurement errors are assumed to have a known probability distribution with unknown parameters. The joint probability density function for all the measurements can then be written in terms of these unknown parameters. This function is referred to as the likelihood function and will attain its peak value when the unknown parameters are chosen to be closest to their actual values. Hence, an optimization problem can be formulated to maximize the likelihood function as a function of these unknown parameters. The solution will give the maximum likelihood estimates for the parameters of interest [32], [38].

4.4.1 The measurement model

The fundamental problem of SE, solved using the SE algorithm, is essentially solving an overdetermined system of nonlinear equations. This problem is mathematically represented using the *measurement model*, which describes the relationship between the state variables and the measurements, generally given by [32], [38]:

$$\boldsymbol{z} = \boldsymbol{h}(\boldsymbol{x}) + \boldsymbol{e} \tag{4.1}$$

where $\boldsymbol{h}(\cdot) \in \mathbb{R}^n \to \mathbb{R}^m$ is the vector of nonlinear functions relating the measurement vector $\boldsymbol{z} \in \mathbb{R}^m$ to the true (unknown) state vector $\boldsymbol{x} \in \mathbb{R}^n$, and $\boldsymbol{e} \in \mathbb{R}^m$ is the random vector of measurement errors. The random vector $\boldsymbol{e}$ is primarily used to model the errors of the measuring instruments that record the quantities, while it may also include errors arising during data transmission, as well as any introduced communication noise, according to Section 4.2.2. Note that vectors and matrices shall be henceforth denoted by boldface throughout the thesis.

The measurement set $\boldsymbol{z} \in \mathbb{R}^m$ can thus be represented in terms of the state vector $\boldsymbol{x} \in \mathbb{R}^n$ of the system via the measurement model (4.1). Generally, as far as non-dynamic state estimators are concerned, the state vector comprises either bus voltage magnitudes and phase angles or the real and imaginary parts of bus voltage phasors, depending on whether it is expressed in polar or rectangular coordinates, respectively. Thus, assuming a power system with N buses, the bus voltage phasors are $\tilde{V}_k = V_k \angle \delta_k = V_{\mathrm{R},k} + jV_{\mathrm{I},k}$, $k = 1, 2, ..., N$, and the state vector is defined as:

$$\boldsymbol{x} := \begin{bmatrix} V_1 & V_2 & \cdots & V_N & \delta_1 & \delta_2 & \cdots & \delta_N \end{bmatrix}^T \tag{4.2}$$

in polar coordinates, or:

$$\boldsymbol{x} := \begin{bmatrix} V_{\mathrm{R},1} & V_{\mathrm{R},2} & \cdots & V_{\mathrm{R},N} & V_{\mathrm{I},1} & V_{\mathrm{I},2} & \cdots & V_{\mathrm{I},N} \end{bmatrix}^T \tag{4.3}$$

in rectangular coordinates. When phase angle measurements are included in the measurement vector, the state vector comprises $n = 2N$ state variables, that is, N voltage magnitudes (or real parts) and N voltage angles (or imaginary parts). When the measurement set does not contain phase angle data, one bus is chosen as reference, and its angle is set equal to an arbitrary value, such as zero. In this case, the state vector will have $n = 2N - 1$ elements, N bus voltage magnitudes (or real parts) and N – 1 phase angles (or imaginary parts).

4.4.2 Maximum likelihood estimation

The normal Probability Density Function (PDF) for a scalar random variable z is defined as:

$$p(z) = \frac{1}{\sqrt{2\pi\sigma^2}} \exp\left(-\frac{1}{2}\left(\frac{z-\mu}{\sigma} \right)^2 \right) \tag{4.4}$$

where $\mu = E(z)$ is the expected or mean value of *z*, and σ is the standard deviation of *z*. The shape of the PDF $p(z)$ is dependent on the parameters μ and σ.

Defining random variable $u = \dfrac{z-\mu}{\sigma}$, yields:

$$\mathrm{E}(u) = \frac{1}{\sigma}\left(E(z)-\mu\right) = 0 \tag{4.5}$$

$$Var(u) = \frac{1}{\sigma^2} Var(z-\mu) = \frac{\sigma^2}{\sigma^2} = 1 \tag{4.6}$$

Hence, the new PDF can be written as:

$$\Phi(u) = \frac{1}{\sqrt{2\pi}} e^{-\frac{u^2}{2}} \tag{4.7}$$

Figure 4.3 illustrates the plot of $\Phi(u)$, which is referred to as the standard normal PDF.

Next, the study is specified for the case of electric power systems. Suppose there is a set of measurement data $\boldsymbol{z}$ for a sample of electrical quantities, which consists of voltages, currents, and powers. According to measurement theory, the random vector of measurement errors $\boldsymbol{e} \in \mathbb{R}^m$ follows a multivariate normal distribution with mean $E(\boldsymbol{e}) = \boldsymbol{0}$ and covariance $Cov(\boldsymbol{e}) = \boldsymbol{R}$, i.e., $\boldsymbol{e} \sim \mathcal{N}(\boldsymbol{0}, \boldsymbol{R})$, then, via (4.1), it holds that:

$$\boldsymbol{z} \sim \mathcal{N}(\boldsymbol{h}(\boldsymbol{x}), \boldsymbol{R}) \tag{4.8}$$

We now consider a joint PDF that represents the probability of observing *m* independent normally distributed measurements $z_1, z_2, \cdots, z_m$, with $z_i \sim \mathcal{N}\left(h_i(\boldsymbol{x}), \sigma_i^2\right)$. Assuming that the measurement errors are independent random variables, $\boldsymbol{R}$ is a diagonal matrix with elements σ_i^2, and the joint PDF of the random measurement vector $\boldsymbol{z} = [z_1 \ z_2 \ \cdots \ z_m]^T$ can be expressed as the product of the individual PDFs:

$$\begin{aligned} p(\boldsymbol{z} \mid \boldsymbol{x}) &= \prod_{i=1}^{m} p(z_i \mid \boldsymbol{x}) = \prod_{i=1}^{m} \left(\frac{1}{\sqrt{2\pi\sigma_i^2}} \right) \exp\left(-\frac{1}{2} \sum_{i=1}^{m} \left(\frac{z_i - h_i(\boldsymbol{x})}{\sigma_i} \right)^2 \right) \\ &= \frac{1}{\sqrt{(2\pi)^m |\boldsymbol{R}|}} \exp\left(-\frac{1}{2} (\boldsymbol{z} - \boldsymbol{h}(\boldsymbol{x}))^T \boldsymbol{R}^{-1} (\boldsymbol{z} - \boldsymbol{h}(\boldsymbol{x})) \right) \end{aligned} \tag{4.9}$$

where $|\boldsymbol{R}| = \prod_{i=1}^{m} \sigma_i^2$. Function $p(\boldsymbol{z} \mid \boldsymbol{x}) = L(\boldsymbol{x})$ is referred to as the likelihood function for the measurement vector $\boldsymbol{z}$, which quantifies the probability of observing the particular set of measurements, i.e., the elements of $\boldsymbol{z}$, for a given state vector $\boldsymbol{x}$.

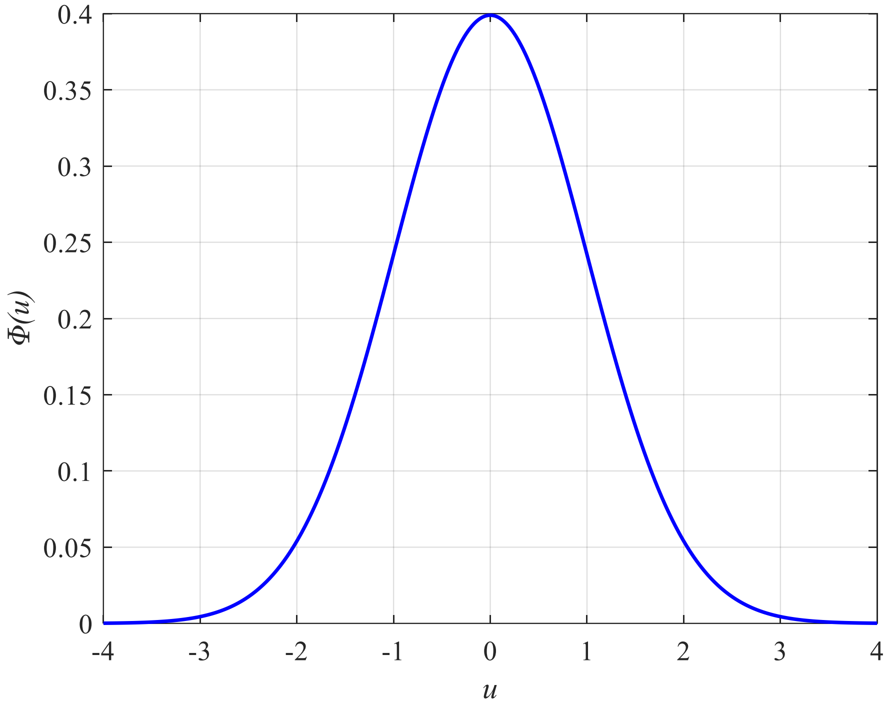

Figure 4.3: Standard normal Gaussian distribution PDF.

The objective of MLE is to calculate the values of the distribution parameters θ, which maximize the likelihood function. For the Gaussian distribution it holds that $\theta = (\mu, \sigma)$, so in our case the MLE aims to maximize the likelihood $L(\boldsymbol{\mu}, \boldsymbol{R}) = p(z \mid \boldsymbol{\mu}, \boldsymbol{R})$. Considering that $\boldsymbol{\mu} = \boldsymbol{h}(\boldsymbol{x})$ and assuming that $Cov(\boldsymbol{z}) = \boldsymbol{R}$ is a known constant matrix, this is equivalent to maximizing (4.9):

$$\hat{\boldsymbol{x}} := \arg\max_{\boldsymbol{x} \in \mathbb{R}^n} L(\boldsymbol{x}) \tag{4.10}$$

In solving optimization problem (4.10) it is common to replace the likelihood function with its natural logarithm, the so-called log-likelihood function $\ell(\boldsymbol{x})$, which simplifies the differentiation involved in the optimization process. This function is expressed as:

$$\ell(\boldsymbol{x}) = \ln L(\boldsymbol{x}) = -\frac{m}{2}\ln(2\pi) - \frac{1}{2}\ln|\boldsymbol{R}| - \frac{1}{2}\left(\boldsymbol{z} - \boldsymbol{h}(\boldsymbol{x})\right)^T \boldsymbol{R}^{-1}\left(\boldsymbol{z} - \boldsymbol{h}(\boldsymbol{x})\right) \tag{4.11}$$

Thus, the problem of maximizing the log-likelihood function is equivalent to minimizing the term $J(\boldsymbol{x}) = \left(\boldsymbol{z} - \boldsymbol{h}(\boldsymbol{x})\right)^T \boldsymbol{R}^{-1}\left(\boldsymbol{z} - \boldsymbol{h}(\boldsymbol{x})\right)$, yielding the following formulation of the SE problem:

$$\hat{\boldsymbol{x}} := \arg\min_{\boldsymbol{x} \in \mathbb{R}^n} J(\boldsymbol{x}) = \left(\boldsymbol{z} - \boldsymbol{h}(\boldsymbol{x})\right)^T \boldsymbol{R}^{-1}\left(\boldsymbol{z} - \boldsymbol{h}(\boldsymbol{x})\right) \tag{4.12}$$

The term $J(\boldsymbol{x})$ is referred to as the WLS objective function, as it represents the weighted sum of the squared residuals, where $\boldsymbol{R}^{-1}$ provides the weights. By expanding $J(\boldsymbol{x})$ into individual measurement terms, (4.12) yields:

$$\hat{\boldsymbol{x}} := \arg\min_{\boldsymbol{x} \in \mathbb{R}^n} J(\boldsymbol{x}) = \sum_{i=1}^{m} w_i \left(z_i - h_i(\boldsymbol{x})\right)^2 \tag{4.13}$$

where $w_i = \dfrac{1}{\sigma_i^2}$.

4.5 Power system modeling for state estimation

Regarding the modeling of the electric grid and its individual components in the context of the classic Static State Estimation (SSE) problem, the power system is assumed to operate in a steady-state condition. This implies that all loads, power flows, transmission lines, and shunt admittances within the network are three-phase and symmetric quantities. These assumptions justify the use of the single-phase positive-sequence equivalent circuit for system modeling and greatly simplify the mathematical formulation of SE, although their universal validity is not entirely guaranteed. All quantities are henceforth expressed in per-unit (pu) values. The following Sections describe the most common component models used in SE.

4.5.1 AC transmission line

Transmission lines are represented by the two-port π equivalent model. The model of such a transmission line, which connects from bus *i* to bus *j*, consists of a series complex admittance $\tilde{y}_{ij} = g_{ij} + jb_{ij}$ and two shunt complex admittances $\tilde{y}_{sij} = g_{sij} + jb_{sij}$ and $\tilde{y}_{sji} = \tilde{y}_{sij}$, one connected to bus *i* and the other to bus *j*. The structure of the model is illustrated in Figure 4.4.

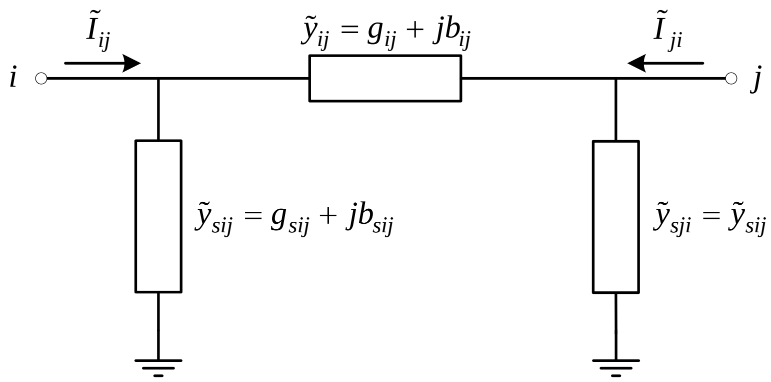

Figure 4.4: Transmission line pi-equivalent model.

The complex currents $\tilde{I}_{ij}$ and $\tilde{I}_{ji}$ can be expressed as functions of the complex voltages $\tilde{V}_i$ and $\tilde{V}_j$ at the terminal buses:

$$\begin{bmatrix} \tilde{I}_{ij} \\ \tilde{I}_{ji} \end{bmatrix} = \begin{bmatrix} \tilde{y}_{ij} + \tilde{y}_{sij} & -\tilde{y}_{ij} \\ -\tilde{y}_{ij} & \tilde{y}_{ij} + \tilde{y}_{sij} \end{bmatrix} \begin{bmatrix} \tilde{V}_i \\ \tilde{V}_j \end{bmatrix} \tag{4.14}$$

4.5.2 Transformers

The actual transformer located at bus i of branch $i - j$ is modeled as an ideal transformer with complex tap ratio $\tilde{n}_{ij} = t_{ij} e^{j\varphi_{ij}}$, where t_{ij} is the tap ratio magnitude in p.u. and φ_{ij} is the phase shift angle, in series with an equivalent admittance $\tilde{y}_{ij} = g_{ij} + jb_{ij}$, as illustrated in Figure 4.5. The terminals of the actual transformer correspond to buses *i* and *j*, and *k* is an intermediate virtual bus. The node equations for the two-port network are obtained by appropriately expressing the currents $\tilde{I}_{kj}$ and $\tilde{I}_{ji}$ in terms of the admittance matrix of branch $k - j$ and voltages $\tilde{V}_k$ and $\tilde{V}_j$:

$$\begin{bmatrix} \tilde{I}_{kj} \\ \tilde{I}_{jk} \end{bmatrix} = \begin{bmatrix} \tilde{y}_{ij} & -\tilde{y}_{ij} \\ -\tilde{y}_{ij} & \tilde{y}_{ij} \end{bmatrix} \begin{bmatrix} \tilde{V}_k \\ \tilde{V}_j \end{bmatrix} \tag{4.15}$$

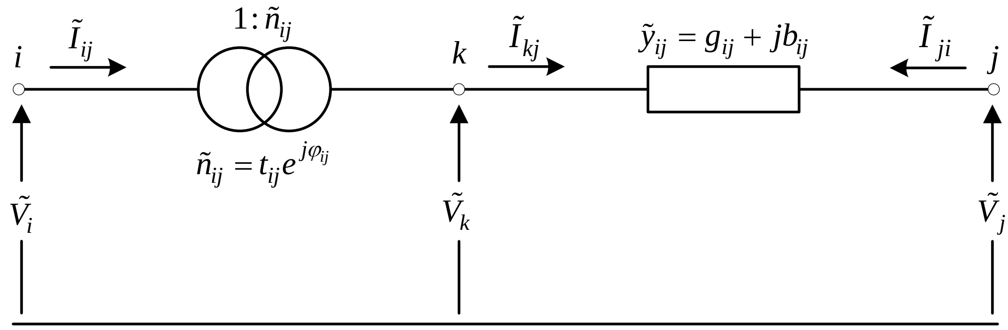

Figure 4.5: Phase-shifting transformer equivalent model.

Substituting $\tilde{I}_{kj}=\dfrac{\tilde{I}_{ij}}{\tilde{n}_{ij}^*}$ and $\tilde{V}_k=\tilde{n}_{ij}\tilde{V}_i$ in (4.15) gives the complex current flows $\tilde{I}_{ij}$ and $\tilde{I}_{ji}$, at the sending and receiving ends of the actual transformer respectively, expressed in terms of the 2×2 admittance matrix and the respective terminal voltages:

$$\begin{bmatrix}\tilde{I}_{ij}\\ \tilde{I}_{ji}\end{bmatrix}=\begin{bmatrix}t_{ij}^2\tilde{y}_{ij} & -\tilde{n}_{ij}^*\tilde{y}_{ij}\\ -\tilde{n}_{ij}\tilde{y}_{ij} & \tilde{y}_{ij}\end{bmatrix}\begin{bmatrix}\tilde{V}_i\\ \tilde{V}_j\end{bmatrix} \tag{4.16}$$

4.5.3 General branch model

The AC transmission lines, transformers and phase shifters, or any combination of such components connected in series, can be modeled using a common branch model. This consists of a standard π-model, with total series admittance $\tilde{y}_{ij}=g_{ij}+jb_{ij}$ and two shunt complex admittances $\tilde{y}_{sij}=g_{sij}+jb_{sij}$ and $\tilde{y}_{sji}=g_{sji}+jb_{sji}$, connecting the two ideal phase-shifting transformers existing at each end of the branch, as shown in Figure 4.6. The complex current flows $\tilde{I}_{ij}$ and $\tilde{I}_{ji}$, at the *i* and *j* ends of the branch respectively, can then be expressed in terms of the 2×2 branch admittance matrix and the respective terminal voltages:

$$\begin{bmatrix}\tilde{I}_{ij}\\ \tilde{I}_{ji}\end{bmatrix}=\begin{bmatrix}t_{ij}^2\left(\tilde{y}_{sij}+\tilde{y}_{ij}\right) & -\tilde{n}_{ij}^*\tilde{n}_{ji}\tilde{y}_{ij}\\ -\tilde{n}_{ji}^*\tilde{n}_{ij}\tilde{y}_{ij} & t_{ji}^2\left(\tilde{y}_{sji}+\tilde{y}_{ij}\right)\end{bmatrix}\begin{bmatrix}\tilde{V}_i\\ \tilde{V}_j\end{bmatrix} \tag{4.17}$$

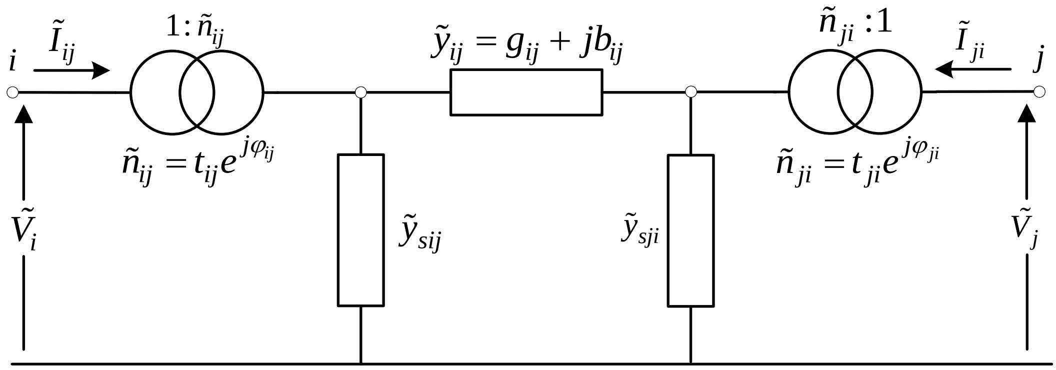

Figure 4.6: General branch model.

Thus, for instance, if $\tilde{n}_{ij} = \tilde{n}_{ji} = 1.0$, the result is an equivalent π-model of a transmission line; if $\tilde{n}_{ij} = 1.0$ and $\tilde{n}_{ji} = t_{ji} e^{j\varphi_{ji}}$, then the result is a phase-shifting transformer with tap located on the *j* bus side in series with a transmission line.

4.5.4 Shunt elements

Shunt elements can be either capacitors or inductors and are used to control voltage or reactive power. They are represented by a shunt imaginary admittance $\tilde{y}_i = jb_i$. The sign of the admittance value determines the type of shunt element: if $b_i > 0$, $\tilde{y}_i$ corresponds to a shunt capacitor, while if $b_i < 0$, it corresponds to a shunt inductor. The model structure is illustrated in Figure 4.7.

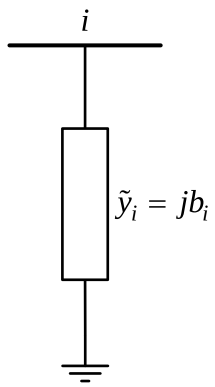

Figure 4.7: Shunt element equivalent model.

4.5.5 Loads and generators

Constant power loads and generators connected to a bus *i* are represented as equivalent complex power injections and, therefore, have no impact on the network model. A generator has a complex injection $\tilde{S}_{Gi} = P_{Gi} + jQ_{Gi}$ with positive active power, while a constant power load has a complex injection $\tilde{S}_{Di} = P_{Di} + jQ_{Di}$ with negative active power. In contrast, constant admittance loads affect the network model and are represented as shunt complex admittances $\tilde{y}_i = g_i + jb_i$. Table 4.1 illustrates the models for constant admittance loads, constant power loads, and generators, respectively.

Table 4.1: Active and reactive power injection conventions.

Element	Injected active power (P)	Injected reactive power (Q)
Constant admittance load	$P > 0$ or $P < 0$	$Q > 0$ or $Q < 0$
Constant power load	$P < 0$	
Generator	$P > 0$	

4.6 The SCADA measurement function

Let us assume a power system with N buses and M branches, and consider a generalized bus *i* of this system with complex voltage $\tilde{V}_i = V_i e^{j\delta_i}$, as illustrated in Figure 4.8. An equivalent shunt admittance $\tilde{y}_i$ is connected to bus *i*, representing any combination of capacitors, inductors, or constant admittance loads. The generator connected to bus *i* injects a complex power $\tilde{S}_{Gi}$, while the corresponding constant power load absorbs a complex power $\tilde{S}_{Di}$.

Now, we assume that branch b connects bus i to bus j, with the complex voltage at bus j denoted by $\tilde{V}_j = V_j e^{j\delta_j}$. Branch b could be a transformer, a transmission line, or a transformer in series with a transmission line, represented in general by (4.17).

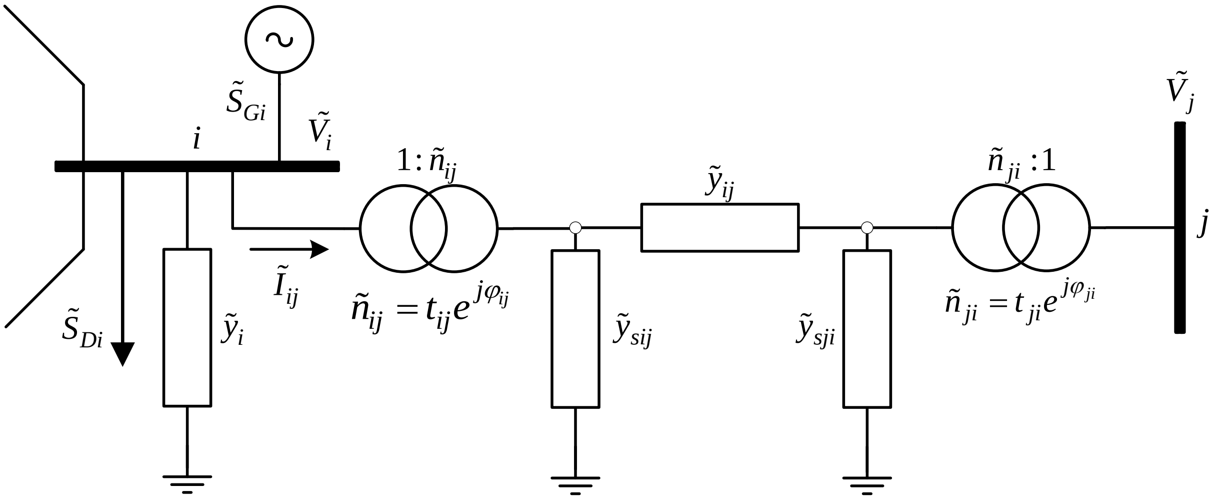

Figure 4.8: General bus-branch model.

4.6.1 State vector in polar coordinates

When expressing the state vector $\boldsymbol{x} \in \mathbb{R}^n$ in polar coordinates, i.e., $\boldsymbol{x} := [V_1\ V_2\ \cdots\ V_N\ \ \delta_1\ \delta_2\ \cdots\ \delta_N]^T$, the conventional SCADA measurements derived from each measurement point, which include branch power flows, bus power injections and bus voltage and branch current magnitudes, need to be expressed via the measurement function $\boldsymbol{h}(\boldsymbol{x})$ in terms of these state variables, i.e. the bus voltage magnitudes V_k and angles δ_k, $k = 1, 2, ..., N$.

To formulate the measurement function for each measurement type, let us consider the general bus i of Figure 4.8, along with the measured quantities deriving from this bus: the voltage magnitude V_i, the branch current magnitude I_{ij}, the active P_{ij} and reactive Q_{ij} power flow on branch $i-j$, and the active and reactive power injections at bus i, denoted by P_i and Q_i, respectively.

According to (4.17), the expression of complex current $\tilde{I}_{ij}$ is:

$$\tilde{I}_{ij} = t_{ij}^2 \left(\tilde{y}_{sij} + \tilde{y}_{ij}\right)\tilde{V}_i - \tilde{n}_{ij}^* \tilde{n}_{ji} \tilde{y}_{ij} \tilde{V}_j \tag{4.18}$$

where $\tilde{n}_{ij} = t_{ij} e^{j\varphi_{ij}}$ and $\tilde{n}_{ji} = t_{ji} e^{j\varphi_{ji}}$.

The real and imaginary parts of current flow phasors are obtained as:

$$\begin{aligned} I_{\mathrm{R},ij} := \mathrm{Re}\left(\tilde{I}_{ij}\right) = t_{ij}^2 V_i &\left((g_{sij} + g_{ij})\cos\delta_i - (b_{sij} + b_{ij})\sin\delta_i\right) \\ &- t_{ij} t_{ji} V_j \left(g_{ij}\cos(\delta_j - \Delta\varphi_{ij}) - b_{ij}\sin(\delta_j - \Delta\varphi_{ij})\right) \end{aligned} \tag{4.19}$$

$$\begin{aligned} I_{\mathrm{I},ij} := \mathrm{Im}\left(\tilde{I}_{ij}\right) = t_{ij}^2 V_i &\left((g_{sij} + g_{ij})\sin\delta_i + (b_{sij} + b_{ij})\cos\delta_i\right) \\ &- t_{ij} t_{ji} V_j \left(g_{ij}\sin(\delta_j - \Delta\varphi_{ij}) + b_{ij}\cos(\delta_j - \Delta\varphi_{ij})\right) \end{aligned} \tag{4.20}$$

with $\Delta\varphi_{ij} = \varphi_{ij} - \varphi_{ji}$.

The magnitude of current $\tilde{I}_{ij} = I_{ij}\angle\theta_{ij}$ in terms of V_i, V_j, δ_i and δ_j is then given by:

$$h_{I_{ij}}(\boldsymbol{x}) = I_{ij} = \sqrt{I_{\mathrm{R},ij}^2 + I_{\mathrm{I},ij}^2} = \sqrt{C_{ij}V_i^2 + D_{ij}V_j^2 + 2V_iV_j\left(E_{ij}\cos\delta_{ij} + F_{ij}\sin\delta_{ij}\right)} \tag{4.21}$$

where:

$$C_{ij} = t_{ij}^4\left((g_{sij} + g_{ij})^2 + (b_{sij} + b_{ij})^2\right)$$

$$D_{ij} = t_{ij}^2 t_{ji}^2\left[\left(g_{ij}\cos(\Delta\varphi_{ij}) + b_{ij}\sin(\Delta\varphi_{ij})\right)^2 + \left(b_{ij}\cos(\Delta\varphi_{ij}) - g_{ij}\sin(\Delta\varphi_{ij})\right)^2\right]$$

$$E_{ij} = -t_{ij}^3 t_{ji}\left[(g_{sij} + g_{ij})\left(g_{ij}\cos(\Delta\varphi_{ij}) + b_{ij}\sin(\Delta\varphi_{ij})\right) + (b_{sij} + b_{ij})\left(b_{ij}\cos(\Delta\varphi_{ij}) - g_{ij}\sin(\Delta\varphi_{ij})\right)\right]$$

$$F_{ij} = -t_{ij}^3 t_{ji}\left[(g_{sij} + g_{ij})\left(b_{ij}\cos(\Delta\varphi_{ij}) - g_{ij}\sin(\Delta\varphi_{ij})\right) - (b_{sij} + b_{ij})\left(g_{ij}\cos(\Delta\varphi_{ij}) + b_{ij}\sin(\Delta\varphi_{ij})\right)\right]$$

We now consider the complex power flow on branch $i-j$, from bus i to bus j, given by $\tilde{S}_{ij} := \tilde{V}_i\tilde{I}_{ij}^* = P_{ij} + jQ_{ij}$. Substituting $\tilde{V}_i = V_i(\cos\delta_i + j\sin\delta_i)$, $\tilde{I}_{ij} = I_{\mathrm{R},ij} + jI_{\mathrm{I},ij}$ and using (4.19), (4.20) we obtain:

$$h_{P_{ij}}(\boldsymbol{x}) = P_{ij} = t_{ij}^2(g_{sij} + g_{ij})V_i^2 - t_{ij}t_{ji}V_iV_j\left(g_{ij}\cos(\delta_{ij} + \Delta\varphi_{ij}) + b_{ij}\sin(\delta_{ij} + \Delta\varphi_{ij})\right) \tag{4.22}$$

$$h_{Q_{ij}}(\boldsymbol{x}) = Q_{ij} = -t_{ij}^2(b_{sij} + b_{ij})V_i^2 + t_{ij}t_{ji}V_iV_j\left(b_{ij}\cos(\delta_{ij} + \Delta\varphi_{ij}) - g_{ij}\sin(\delta_{ij} + \Delta\varphi_{ij})\right) \tag{4.23}$$

where P_{ij} and Q_{ij} denote the active and reactive power flow on branch $i-j$, and $\delta_{ij} = \delta_i - \delta_j$.

Using (4.18), the complex current injection at bus *i*, can be written as:

$$\tilde{I}_i = \left(\tilde{y}_i + \sum_{j\in a(i)} t_{ij}^2\left(\tilde{y}_{sij} + \tilde{y}_{ij}\right)\right)\tilde{V}_i - \sum_{j\in a(i)} \tilde{n}_{ij}^*\tilde{n}_{ji}\tilde{y}_{ij}\tilde{V}_j \tag{4.24}$$

for $i = 1,...,N$, where $a(i)$ is the set of buses adjacent to bus i. This expression can be rewritten in matrix form as:

$$\boldsymbol{I} = \boldsymbol{Y}\boldsymbol{V} \tag{4.25}$$

where $\boldsymbol{I}$ is the vector of nodal current injections, with elements $\tilde{I}_i$, $i = 1,...,N$, $\boldsymbol{V}$ is the vector of nodal voltages $\tilde{V}_i$, $i = 1,...,N$, and $\boldsymbol{Y} = \boldsymbol{G} + j\boldsymbol{B}$ is the bus admittance matrix, with elements:

$$\tilde{Y}_{ij} = G_{ij} + jB_{ij} = -\tilde{n}_{ij}^*\tilde{n}_{ji}\tilde{y}_{ij} \tag{4.26}$$

$$\tilde{Y}_{ii} = G_{ii} + jB_{ii} = \tilde{y}_i + \sum_{j\in a(i)} t_{ij}^2\left(\tilde{y}_{sij} + \tilde{y}_{ij}\right) \tag{4.27}$$

and:

$$G_{ij} = -t_{ij}t_{ji}\left(g_{ij}\cos(\Delta\varphi_{ij}) + b_{ij}\sin(\Delta\varphi_{ij})\right) \tag{4.28}$$

$$B_{ij} = -t_{ij}t_{ji}\left(b_{ij}\cos(\Delta\varphi_{ij}) - g_{ij}\sin(\Delta\varphi_{ij})\right) \tag{4.29}$$

$$G_{ii} = g_i + \sum_{j\in a(i)} t_{ij}^2(g_{sij} + g_{ij}) \tag{4.30}$$

$$B_{ii} = b_i + \sum_{j\in a(i)} t_{ij}^2(b_{sij} + b_{ij}) \tag{4.31}$$

The complex power injection at bus *i* is given by:

$$\tilde{S}_i = \tilde{V}_i \tilde{I}_i^* = P_i + jQ_i \tag{4.32}$$

Applying (4.24) to (4.32) yields the equations of the active and reactive power injection at bus *i*, denoted by P_i and Q_i, respectively:

$$h_{P_i}(\boldsymbol{x}) = P_i = g_i V_i^2 + \sum_{j \in a(i)} P_{ij} = G_{ii} V_i^2 + V_i \sum_{j \in a(i)} V_j \left(G_{ij} \cos \delta_{ij} + B_{ij} \sin \delta_{ij} \right) \tag{4.33}$$

$$h_{Q_i}(\boldsymbol{x}) = Q_i = -b_i V_i^2 + \sum_{j \in a(i)} Q_{ij} = -B_{ii} V_i^2 + V_i \sum_{j \in a(i)} V_j \left(G_{ij} \sin \delta_{ij} - B_{ij} \cos \delta_{ij} \right) \tag{4.34}$$

Finally, the voltage magnitude measurement measures the state variable V_i directly:

$$h_{V_i}(\boldsymbol{x}) = V_i \tag{4.35}$$

4.6.2 State vector in rectangular coordinates

When the state vector is in rectangular form, i.e., $\boldsymbol{x} := \left[V_{\mathrm{R},1} \ V_{\mathrm{R},2} \ \cdots \ V_{\mathrm{R},N} \ V_{\mathrm{I},1} \ V_{\mathrm{I},2} \ \cdots \ V_{\mathrm{I},N} \right]^T$, then, considering again the general bus of Figure 4.8, we can calculate the elements of the measurement function $\boldsymbol{h}(\boldsymbol{x})$ in terms of the real and imaginary parts of bus voltage phasors, $V_{\mathrm{R},k}$ and $V_{\mathrm{I},k}$ respectively, with $k = 1, 2, ..., N$.

Via (4.19), (4.20) we have:

$$\begin{aligned} I_{\mathrm{R},ij} = {} & t_{ij}^2 \left((g_{sij} + g_{ij}) V_{\mathrm{R},i} - (b_{sij} + b_{ij}) V_{\mathrm{I},i} \right) \\ & - t_{ij} t_{ji} \left[\left(g_{ij} \cos(\Delta\varphi_{ij}) + b_{ij} \sin(\Delta\varphi_{ij}) \right) V_{\mathrm{R},j} - \left(b_{ij} \cos(\Delta\varphi_{ij}) - g_{ij} \sin(\Delta\varphi_{ij}) \right) V_{\mathrm{I},j} \right] \end{aligned} \tag{4.36}$$

$$\begin{aligned} I_{\mathrm{I},ij} = {} & t_{ij}^2 \left[(g_{sij} + g_{ij}) V_{\mathrm{I},i} + (b_{sij} + b_{ij}) V_{\mathrm{R},i} \right] \\ & - t_{ij} t_{ji} \left[\left(g_{ij} \cos(\Delta\varphi_{ij}) + b_{ij} \sin(\Delta\varphi_{ij}) \right) V_{\mathrm{I},j} + \left(b_{ij} \cos(\Delta\varphi_{ij}) - g_{ij} \sin(\Delta\varphi_{ij}) \right) V_{\mathrm{R},j} \right] \end{aligned} \tag{4.37}$$

The magnitude of current $\tilde{I}_{ij} = I_{ij} \angle \theta_{ij}$ in terms of $V_{\mathrm{R},i}$, $V_{\mathrm{I},i}$, $V_{\mathrm{R},j}$ and $V_{\mathrm{I},j}$ is then given by:

$$\begin{aligned} & h_{I_{ij}}(\boldsymbol{x}) = I_{ij} = \sqrt{I_{\mathrm{R},ij}^2 + I_{\mathrm{I},ij}^2} = \\ & \sqrt{C_{ij} \left(V_{\mathrm{R},i}^2 + V_{\mathrm{I},i}^2 \right) + D_{ij} \left(V_{\mathrm{R},j}^2 + V_{\mathrm{I},j}^2 \right) + 2E_{ij} \left(V_{\mathrm{R},i} V_{\mathrm{R},j} + V_{\mathrm{I},i} V_{\mathrm{I},j} \right) + 2F_{ij} \left(V_{\mathrm{I},i} V_{\mathrm{R},j} - V_{\mathrm{R},i} V_{\mathrm{I},j} \right)} \end{aligned} \tag{4.38}$$

We now consider the complex power flow on branch $i - j$, $\tilde{S}_{ij} := \tilde{V}_i \tilde{I}_{ij}^* = P_{ij} + jQ_{ij}$. Substituting $\tilde{V}_i = V_{\mathrm{R},i} + jV_{\mathrm{I},i}$, $\tilde{I}_{ij} = I_{\mathrm{R},ij} + jI_{\mathrm{I},ij}$ and using (4.36), (4.37) we obtain:

$$\begin{aligned} h_{P_{ij}}(\boldsymbol{x}) = P_{ij} = {} & t_{ij}^2 (g_{sij} + g_{ij}) \left(V_{\mathrm{R},i}^2 + V_{\mathrm{I},i}^2 \right) \\ & - t_{ij} t_{ji} V_{\mathrm{R},i} \left[\left(g_{ij} \cos(\Delta\varphi_{ij}) + b_{ij} \sin(\Delta\varphi_{ij}) \right) V_{\mathrm{R},j} - \left(b_{ij} \cos(\Delta\varphi_{ij}) - g_{ij} \sin(\Delta\varphi_{ij}) \right) V_{\mathrm{I},j} \right] \\ & - t_{ij} t_{ji} V_{\mathrm{I},i} \left[\left(b_{ij} \cos(\Delta\varphi_{ij}) - g_{ij} \sin(\Delta\varphi_{ij}) \right) V_{\mathrm{R},j} + \left(g_{ij} \cos(\Delta\varphi_{ij}) + b_{ij} \sin(\Delta\varphi_{ij}) \right) V_{\mathrm{I},j} \right] \end{aligned} \tag{4.39}$$

$$\begin{aligned} h_{Q_{ij}}(\boldsymbol{x}) = Q_{ij} = {} & -t_{ij}^2 (b_{sij} + b_{ij}) \left(V_{\mathrm{R},i}^2 + V_{\mathrm{I},i}^2 \right) \\ & + t_{ij} t_{ji} V_{\mathrm{R},i} \left[\left(b_{ij} \cos(\Delta\varphi_{ij}) - g_{ij} \sin(\Delta\varphi_{ij}) \right) V_{\mathrm{R},j} + \left(g_{ij} \cos(\Delta\varphi_{ij}) + b_{ij} \sin(\Delta\varphi_{ij}) \right) V_{\mathrm{I},j} \right] \\ & - t_{ij} t_{ji} V_{\mathrm{I},i} \left[\left(g_{ij} \cos(\Delta\varphi_{ij}) + b_{ij} \sin(\Delta\varphi_{ij}) \right) V_{\mathrm{R},j} - \left(b_{ij} \cos(\Delta\varphi_{ij}) - g_{ij} \sin(\Delta\varphi_{ij}) \right) V_{\mathrm{I},j} \right] \end{aligned} \tag{4.40}$$

where P_{ij} and Q_{ij} denote the active and reactive power flow on branch $i - j$.

The equations of the active and reactive power injection at bus *i*, denoted by P_i and Q_i respectively, can be expressed using P_{ij} and Q_{ij} as follows:

$$
\begin{aligned}
&h_{P_i}(\boldsymbol{x}) = P_i = g_i\left(V_{\mathrm{R},i}^2 + V_{\mathrm{I},i}^2\right) + \sum_{j\in a(i)} P_{ij} = \\
&G_{ii}\left(V_{\mathrm{R},i}^2 + V_{\mathrm{I},i}^2\right) + V_{\mathrm{R},i}\sum_{j\in a(i)}\left(G_{ij}V_{\mathrm{R},j} - B_{ij}V_{\mathrm{I},j}\right) + V_{\mathrm{I},i}\sum_{j\in a(i)}\left(B_{ij}V_{\mathrm{R},j} + G_{ij}V_{\mathrm{I},j}\right)
\end{aligned}
\tag{4.41}
$$

$$
\begin{aligned}
&h_{Q_i}(\boldsymbol{x}) = Q_i = -b_i\left(V_{\mathrm{R},i}^2 + V_{\mathrm{I},i}^2\right) + \sum_{j\in a(i)} Q_{ij} = \\
&-B_{ii}\left(V_{\mathrm{R},i}^2 + V_{\mathrm{I},i}^2\right) + V_{\mathrm{R},i}\sum_{j\in a(i)}\left(-B_{ij}V_{\mathrm{R},j} - G_{ij}V_{\mathrm{I},j}\right) + V_{\mathrm{I},i}\sum_{j\in a(i)}\left(G_{ij}V_{\mathrm{R},j} - B_{ij}V_{\mathrm{I},j}\right)
\end{aligned}
\tag{4.42}
$$

Finally, the measured voltage magnitude of bus i is expressed as:

$$
h_{V_i}(\boldsymbol{x}) = V_i = \sqrt{V_{\mathrm{R},i}^2 + V_{\mathrm{I},i}^2} \tag{4.43}
$$

4.6.3 Measurement model formulation

Using (4.21)–(4.35) and (4.38)–(4.43) for the polar and rectangular formulation of the state vector, respectively, the SCADA measurements may be expressed with respect to the state variables. If we consider the general bus *i* of Figure 4.8, we can write the elements of $\boldsymbol{z}$ that correspond to the measured quantities (denoted by superscript *m*) deriving from bus *i*, as follows:

$$
\begin{bmatrix} V_i^m \\ I_{ij}^m \\ P_{ij}^m \\ Q_{ij}^m \\ P_i^m \\ Q_i^m \end{bmatrix} = \begin{bmatrix} h_{V_i}(\boldsymbol{x}) \\ h_{I_{ij}}(\boldsymbol{x}) \\ h_{P_{ij}}(\boldsymbol{x}) \\ h_{Q_{ij}}(\boldsymbol{x}) \\ h_{P_i}(\boldsymbol{x}) \\ h_{Q_i}(\boldsymbol{x}) \end{bmatrix} + \begin{bmatrix} e_{V_i} \\ e_{I_{ij}} \\ e_{P_{ij}} \\ e_{Q_{ij}} \\ e_{P_i} \\ e_{Q_i} \end{bmatrix} \tag{4.44}
$$

where e_z represents the additive random Gaussian noise of measurement z. By generalizing (4.44) for each measured bus *i* and branch $i-j$, the complete measurement model of the SE problem for the entire power system is derived as:

$$
\begin{bmatrix} \boldsymbol{z}_V \\ \boldsymbol{z}_I \\ \boldsymbol{z}_{P_f} \\ \boldsymbol{z}_{Q_f} \\ \boldsymbol{z}_{Q_i} \\ \boldsymbol{z}_{P_i} \end{bmatrix} = \begin{bmatrix} \boldsymbol{h}_V(\boldsymbol{x}) \\ \boldsymbol{h}_I(\boldsymbol{x}) \\ \boldsymbol{h}_{P_f}(\boldsymbol{x}) \\ \boldsymbol{h}_{Q_f}(\boldsymbol{x}) \\ \boldsymbol{h}_{Q_i}(\boldsymbol{x}) \\ \boldsymbol{h}_{P_i}(\boldsymbol{x}) \end{bmatrix} + \begin{bmatrix} \boldsymbol{e}_V \\ \boldsymbol{e}_I \\ \boldsymbol{e}_{P_f} \\ \boldsymbol{e}_{Q_f} \\ \boldsymbol{e}_{Q_i} \\ \boldsymbol{e}_{P_i} \end{bmatrix} \tag{4.45}
$$

where $\boldsymbol{z}_V$ is the vector of voltage magnitude measurements, $\boldsymbol{z}_I$ is the vector of current magnitude measurements, $\boldsymbol{z}_{P_f}$, $\boldsymbol{z}_{Q_f}$ are the vectors of active and reactive power flow measurements, and $\boldsymbol{z}_{P_i}$, $\boldsymbol{z}_{Q_i}$ are the vectors of active and reactive power injection measurements.

4.7 PMU-based state estimation

Following the derivation of the measurement functions $\boldsymbol{h}(\boldsymbol{x})$ and the Jacobian matrix $\boldsymbol{H}(\boldsymbol{x})$ for the conventional SCADA measurements, this section presents their corresponding elements when only PMU measurements are incorporated in the SE measurement vector.

As previously discussed, the SCADA-based SE techniques use bus voltage and current magnitude measurements, along with active and reactive power flows and injections in lines and buses, respectively. In this case, the measurement function is a vector of nonlinear functions based on the power flow analysis model, as demonstrated in Section 4.6. In contrast, since PMUs can directly measure voltage and current phasors, it becomes possible to formulate a linear measurement model, when the state vector is expressed in Cartesian coordinates. Thus, the exclusive usage of synchronized phasor measurements enables the formulation of the SE problem into a linear form, essentially expressed as a linear regression problem with a noniterative solution.

4.7.1 State vector in polar coordinates

To make this Chapter of the thesis comprehensive and self-sufficient, it is important to include the derivation of the nonlinear PMU-based SE measurement model. When expressing the state vector in polar coordinates, the synchrophasor measurements derived from each measurement point, which typically include bus voltage and branch current phasors, need to be expressed via the measurement function $\boldsymbol{h}(\boldsymbol{x})$ in terms of the bus voltage magnitudes V_k and angles δ_k, with $k = 1, 2, ..., N$.

Let us consider the general bus *i* of Figure 4.8, along with the measured phasors deriving from bus *i*: the voltage phasor $\tilde{V}_i = V_i \angle \delta_i$ and the current phasor $\tilde{I}_{ij} = I_{ij} \angle \theta_{ij}$ on branch $i - j$. These two phasors yield a total of four measurands, that is, the voltage magnitude V_i, the voltage phase angle δ_i, the branch current magnitude I_{ij}, and the branch current phase angle θ_{ij}.

Via (4.21) we already have the current magnitude equation, and via (4.35) we have the voltage magnitude equation, as these measurements also exist in the SCADA measurement systems. As the voltage angles are state variables, we simply write:

$$h_{\delta_i}(\boldsymbol{x}) = \delta_i \tag{4.46}$$

Finally, the current phase angle θ_{ij} can be expressed as:

$$\begin{gathered} h_{\theta_{ij}}(\boldsymbol{x}) = \theta_{ij} = \arctan\left(\frac{I_{\mathrm{I},ij}}{I_{\mathrm{R},ij}}\right) = \\ \arctan\left(\frac{t_{ij}^2 V_i\left((g_{sij}+g_{ij})\sin\delta_i + (b_{sij}+b_{ij})\cos\delta_i\right) - t_{ij}t_{ji}V_j\left(g_{ij}\sin(\delta_j - \Delta\varphi_{ij}) + b_{ij}\cos(\delta_j - \Delta\varphi_{ij})\right)}{t_{ij}^2 V_i\left((g_{sij}+g_{ij})\cos\delta_i - (b_{sij}+b_{ij})\sin\delta_i\right) - t_{ij}t_{ji}V_j\left(g_{ij}\cos(\delta_j - \Delta\varphi_{ij}) - b_{ij}\sin(\delta_j - \Delta\varphi_{ij})\right)}\right) \end{gathered} \tag{4.47}$$

It should also be noted that both voltage and current phasor measurements can be expressed in rectangular coordinates, that is, as $\tilde{V}_i = V_{\mathrm{R},i} + jV_{\mathrm{I},i}$ and $\tilde{I}_{ij} = I_{\mathrm{R},ij} + jI_{\mathrm{I},ij}$, respectively. In this case, we can write:

$$h_{V_{\mathrm{R},i}}(\boldsymbol{x}) = V_{\mathrm{R},i} = V_i \cos\delta_i \tag{4.48}$$

$$h_{V_{\mathrm{I},i}}(\boldsymbol{x}) = V_{\mathrm{I},i} = V_i \sin\delta_i \tag{4.49}$$

$$\begin{gathered} h_{I_{\mathrm{R},ij}}(\boldsymbol{x}) = I_{\mathrm{R},ij} = \\ t_{ij}^2 V_i\left((g_{sij}+g_{ij})\cos\delta_i - (b_{sij}+b_{ij})\sin\delta_i\right) - t_{ij}t_{ji}V_j\left(g_{ij}\cos(\delta_j - \Delta\varphi_{ij}) - b_{ij}\sin(\delta_j - \Delta\varphi_{ij})\right) \end{gathered} \tag{4.50}$$

$$h_{I_{\mathrm{I},ij}}(\boldsymbol{x}) = I_{\mathrm{I},ij} = \\ t_{ij}^2 V_i \left((g_{sij} + g_{ij}) \sin\delta_i + (b_{sij} + b_{ij}) \cos\delta_i \right) - t_{ij} t_{ji} V_j \left(g_{ij} \sin(\delta_j - \Delta\varphi_{ij}) + b_{ij} \cos(\delta_j - \Delta\varphi_{ij}) \right) \tag{4.51}$$

Given that (4.47) can be undefined when the denominator is zero, and, (4.48), (4.49) introduce non-linearities to $\boldsymbol{h}(\boldsymbol{x})$, it is a well-established practice to consider voltage phasor measurements in polar coordinates and current phasor measurements in rectangular coordinates [9]. Thus, using (4.35), (4.46) , (4.50) and (4.51) the PMU measurements may be expressed with respect to the state vector in polar coordinates. If we consider again the general bus i of Figure 4.8, we can write the elements of $\boldsymbol{z}$ that correspond to the measured quantities (denoted by superscript m) deriving from bus i, as follows:

$$V_i^m = h_{V_i}(\boldsymbol{x}) + e_{V_i} = V_i + e_{V_i} \tag{4.52}$$

$$\delta_i^m = h_{\delta_i}(\boldsymbol{x}) + e_{\delta_i} = \delta_i + e_{\delta_i} \tag{4.53}$$

$$I_{\mathrm{R},ij}^m = h_{I_{\mathrm{R},ij}}(\boldsymbol{x}) + e_{I_{\mathrm{R},ij}} = I_{\mathrm{R},ij} + e_{I_{\mathrm{R},ij}} \tag{4.54}$$

$$I_{\mathrm{I},ij}^m = h_{I_{\mathrm{I},ij}}(\boldsymbol{x}) + e_{I_{\mathrm{I},ij}} = I_{\mathrm{I},ij} + e_{I_{\mathrm{I},ij}} \tag{4.55}$$

where e_z denotes the additive random Gaussian noise of measurement z.

By generalizing (4.52)–(4.55) for each PMU-measured bus i and branch $i-j$, the complete PMU measurement model for the entire power system is derived as follows:

$$\begin{bmatrix} \boldsymbol{z}_V \\ \boldsymbol{z}_\delta \\ \boldsymbol{z}_{I_\mathrm{R}} \\ \boldsymbol{z}_{I_\mathrm{I}} \end{bmatrix} = \begin{bmatrix} \boldsymbol{h}_V(\boldsymbol{x}) \\ \boldsymbol{h}_\delta(\boldsymbol{x}) \\ \boldsymbol{h}_{I_\mathrm{R}}(\boldsymbol{x}) \\ \boldsymbol{h}_{I_\mathrm{I}}(\boldsymbol{x}) \end{bmatrix} + \begin{bmatrix} \boldsymbol{e}_V \\ \boldsymbol{e}_\delta \\ \boldsymbol{e}_{I_\mathrm{R}} \\ \boldsymbol{e}_{I_\mathrm{I}} \end{bmatrix} \tag{4.56}$$

where $\boldsymbol{z}_V$, $\boldsymbol{z}_\delta$ are the vectors of voltage magnitude and angle measurements, respectively, and $\boldsymbol{z}_{I_\mathrm{R}}$, $\boldsymbol{z}_{I_\mathrm{I}}$ are the vectors of current magnitude and angle measurements, respectively.

4.7.2 State vector in rectangular coordinates

By expressing the state vector in rectangular coordinates, the PMU measurement model is linearized, given that the voltage phasors are provided to the estimator in rectangular form. More specifically, we may write all measurement equations as linear functions of the real and imaginary parts of bus voltage phasors, $V_{\mathrm{R},k}$ and $V_{\mathrm{I},k}$ respectively, with $k = 1, 2, ..., N$.

The real and imaginary parts of bus voltage phasors are directly measured state variables, therefore:

$$h_{V_{\mathrm{R},i}}(\boldsymbol{x}) = V_{\mathrm{R},i} \tag{4.57}$$

$$h_{V_{\mathrm{I},i}}(\boldsymbol{x}) = V_{\mathrm{I},i} \tag{4.58}$$

Considering the current phasor measurements in rectangular coordinates, (4.50), (4.51), we obtain:

$$h_{I_{\mathrm{R},ij}}(\boldsymbol{x}) = I_{\mathrm{R},ij} = t_{ij}^2 \left((g_{sij} + g_{ij}) V_{\mathrm{R},i} - (b_{sij} + b_{ij}) V_{\mathrm{I},i} \right) \\ - t_{ij} t_{ji} \left[\left(g_{ij} \cos(\Delta\varphi_{ij}) + b_{ij} \sin(\Delta\varphi_{ij}) \right) V_{\mathrm{R},j} - \left(b_{ij} \cos(\Delta\varphi_{ij}) - g_{ij} \sin(\Delta\varphi_{ij}) \right) V_{\mathrm{I},j} \right] \tag{4.59}$$

$$h_{I_{\mathrm{I},ij}}(\boldsymbol{x}) = I_{\mathrm{I},ij} = t_{ij}^2 \left[(g_{sij} + g_{ij}) V_{\mathrm{I},i} + (b_{sij} + b_{ij}) V_{\mathrm{R},i} \right] \\ - t_{ij} t_{ji} \left[\left(g_{ij} \cos(\Delta\varphi_{ij}) + b_{ij} \sin(\Delta\varphi_{ij}) \right) V_{\mathrm{I},j} + \left(b_{ij} \cos(\Delta\varphi_{ij}) - g_{ij} \sin(\Delta\varphi_{ij}) \right) V_{\mathrm{R},j} \right] \tag{4.60}$$

Thus, using (4.57)–(4.60) the PMU measurements may be expressed through linear functions with respect to the state vector in rectangular coordinates. If we consider again the general bus *i* of Figure 4.8, we can write the elements of $\boldsymbol{z}$ that correspond to the measured quantities (denoted by superscript *m*) deriving from bus *i*, as follows:

$$V_{\mathrm{R},i}^{m} = h_{V_{\mathrm{R},i}}(\boldsymbol{x}) + e_{V_{\mathrm{R},i}} = V_{\mathrm{R},i} + e_{V_{\mathrm{R},i}} \tag{4.61}$$

$$V_{\mathrm{I},i}^{m} = h_{V_{\mathrm{I},i}}(\boldsymbol{x}) + e_{V_{\mathrm{I},i}} = V_{\mathrm{I},i} + e_{V_{\mathrm{I},i}} \tag{4.62}$$

$$I_{\mathrm{R},ij}^{m} = h_{I_{\mathrm{R},ij}}(\boldsymbol{x}) + e_{I_{\mathrm{R},ij}} = I_{\mathrm{R},ij} + e_{I_{\mathrm{R},ij}} \tag{4.63}$$

$$I_{\mathrm{I},ij}^{m} = h_{I_{\mathrm{I},ij}}(\boldsymbol{x}) + e_{I_{\mathrm{I},ij}} = I_{\mathrm{I},ij} + e_{I_{\mathrm{I},ij}} \tag{4.64}$$

where e_z denotes the additive random Gaussian noise of measurement z.

By generalizing (4.61)–(4.64) for each PMU-measured bus i and branch $i-j$, the complete PMU measurement model for the entire power system is derived as follows:

$$\begin{bmatrix} \boldsymbol{z}_{V_\mathrm{R}} \\ \boldsymbol{z}_{V_\mathrm{I}} \\ \boldsymbol{z}_{I_\mathrm{R}} \\ \boldsymbol{z}_{I_\mathrm{I}} \end{bmatrix} = \begin{bmatrix} \boldsymbol{h}_{V_\mathrm{R}}(\boldsymbol{x}) \\ \boldsymbol{h}_{V_\mathrm{I}}(\boldsymbol{x}) \\ \boldsymbol{h}_{I_\mathrm{R}}(\boldsymbol{x}) \\ \boldsymbol{h}_{I_\mathrm{I}}(\boldsymbol{x}) \end{bmatrix} + \begin{bmatrix} \boldsymbol{e}_{V_\mathrm{R}} \\ \boldsymbol{e}_{V_\mathrm{I}} \\ \boldsymbol{e}_{I_\mathrm{R}} \\ \boldsymbol{e}_{I_\mathrm{I}} \end{bmatrix} \tag{4.65}$$

where $\boldsymbol{z}_{V_\mathrm{R}}$, $\boldsymbol{z}_{V_\mathrm{I}}$ are the vectors of voltage magnitude and angle measurements, respectively, and $\boldsymbol{z}_{I_\mathrm{R}}$, $\boldsymbol{z}_{I_\mathrm{I}}$ are the vectors of current magnitude and angle measurements, respectively.

4.8 Solution of the SE problem

The SCADA and PMU measurement models can be used to formulate and solve the nonlinear and linear SE problems, respectively.

4.8.1 Nonlinear state estimation

As discussed in Section 4.4, the general SE problem can be formulated as the minimization of $J(\boldsymbol{x})$ via (4.12) or the equivalent expression (4.13). For the case of an overdetermined nonlinear measurement model, that is, $\boldsymbol{z} = \boldsymbol{h}(\boldsymbol{x}) + \boldsymbol{e}$ with $\boldsymbol{z}, \boldsymbol{e} \in \mathbb{R}^m$, $\boldsymbol{x} \in \mathbb{R}^n$ and $m > n$, the first order optimality conditions will have to be satisfied at the minimum of $J(\boldsymbol{x})$:

$$\nabla J(\boldsymbol{x}) = \frac{\partial J(\boldsymbol{x})}{\partial \boldsymbol{x}} = -\boldsymbol{H}^T(\boldsymbol{x})\boldsymbol{R}^{-1}\left(\boldsymbol{z} - \boldsymbol{h}(\boldsymbol{x})\right) = \boldsymbol{0} \tag{4.66}$$

where $\boldsymbol{H}(\boldsymbol{x}) = \dfrac{\partial \boldsymbol{h}(\boldsymbol{x})}{\partial \boldsymbol{x}}$ is the Jacobian matrix of $\boldsymbol{h}(\boldsymbol{x})$. Expanding the gradient $\nabla J(\boldsymbol{x})$ around a current estimate $\boldsymbol{x}^{(i)}$ using a first-order Taylor series expansion, yields:

$$\nabla J(\boldsymbol{x}) \approx \nabla J(\boldsymbol{x}^{(i)}) + \nabla^2 J(\boldsymbol{x}^{(i)})\left(\boldsymbol{x} - \boldsymbol{x}^{(i)}\right) \tag{4.67}$$

where $\nabla^2 J(\boldsymbol{x}) = \dfrac{\partial^2 J(\boldsymbol{x})}{\partial \boldsymbol{x} \partial \boldsymbol{x}^T}$. Ignoring the second-order derivatives of $\boldsymbol{h}(\boldsymbol{x})$ in calculating $\nabla^2 J(\boldsymbol{x})$ results in the following approximation:

$$\nabla^2 J(\boldsymbol{x}) \approx \boldsymbol{H}^T(\boldsymbol{x})\boldsymbol{R}^{-1}\boldsymbol{H}(\boldsymbol{x}) \tag{4.68}$$

Using the Gauss-Newton iterative solution scheme gives:

$$\boldsymbol{x}^{(i+1)} = \boldsymbol{x}^{(i)} - \left(\nabla^2 J(\boldsymbol{x}^{(i)})\right)^{-1} \nabla J(\boldsymbol{x}^{(i)}) \Leftrightarrow$$

$$\boldsymbol{x}^{(i+1)} = \boldsymbol{x}^{(i)} + \left(\boldsymbol{H}^T(\boldsymbol{x}^{(i)})\boldsymbol{R}^{-1}\boldsymbol{H}(\boldsymbol{x}^{(i)})\right)^{-1} \boldsymbol{H}^T(\boldsymbol{x}^{(i)})\boldsymbol{R}^{-1}\left(\boldsymbol{z} - \boldsymbol{h}(\boldsymbol{x}^{(i)})\right) \Leftrightarrow$$

$$\Delta\boldsymbol{x}^{(i)} = \boldsymbol{x}^{(i+1)} - \boldsymbol{x}^{(i)} = \left(\boldsymbol{H}^T(\boldsymbol{x}^{(i)})\boldsymbol{R}^{-1}\boldsymbol{H}(\boldsymbol{x}^{(i)})\right)^{-1} \boldsymbol{H}^T(\boldsymbol{x}^{(i)})\boldsymbol{R}^{-1}\left(\boldsymbol{z} - \boldsymbol{h}(\boldsymbol{x}^{(i)})\right) \tag{4.69}$$

where superscript (i) now denotes the iteration index, $\boldsymbol{x}^{(i)}$ is the estimated state vector at the i-th iteration, and $\Delta\boldsymbol{x}^{(i)}$ is the i-th incremental correction or update. $\boldsymbol{G}(\boldsymbol{x}) := \boldsymbol{H}^T(\boldsymbol{x})\boldsymbol{R}^{-1}\boldsymbol{H}(\boldsymbol{x})$ is called the gain matrix, which is sparse, positive definite and symmetric. Matrix $\boldsymbol{G}(\boldsymbol{x})$ is typically not inverted, but is instead decomposed into its triangular factors and the following sparse linear set of the so-called Normal Equations (NE) is solved using forward/back substitutions at each iteration (i):

$$\boldsymbol{G}(\boldsymbol{x}^{(i)})\Delta\boldsymbol{x}^{(i)} = \boldsymbol{H}^T(\boldsymbol{x}^{(i)})\boldsymbol{R}^{-1}\left(\boldsymbol{z} - \boldsymbol{h}(\boldsymbol{x}^{(i)})\right) \tag{4.70}$$

The iterative solution of (4.70) requires an initial guess to be made for the state vector $\boldsymbol{x}^{(0)}$. As in the case of the power flow solution, this guess typically corresponds to the flat voltage profile, where all bus voltages are assumed to be 1.0 pu and in-phase with each other. The iterative algorithm for solving the WLS SE problem is outlined in Algorithm 4.1.

4.8.1.1 The SCADA measurement Jacobian matrix

Given the measurement model (4.45), the structure of the SCADA measurement Jacobian can be derived for both polar and rectangular expressions of the state vector:

$$\boldsymbol{H}(\boldsymbol{x}) = \frac{\partial \boldsymbol{h}(\boldsymbol{x})}{\partial \boldsymbol{x}} = \begin{bmatrix} \frac{\partial \boldsymbol{h}_V}{\partial \boldsymbol{V}} & \frac{\partial \boldsymbol{h}_V}{\partial \boldsymbol{\delta}} \\ \frac{\partial \boldsymbol{h}_I}{\partial \boldsymbol{V}} & \frac{\partial \boldsymbol{h}_I}{\partial \boldsymbol{\delta}} \\ \frac{\partial \boldsymbol{h}_{P_f}}{\partial \boldsymbol{V}} & \frac{\partial \boldsymbol{h}_{P_f}}{\partial \boldsymbol{\delta}} \\ \frac{\partial \boldsymbol{h}_{Q_f}}{\partial \boldsymbol{V}} & \frac{\partial \boldsymbol{h}_{Q_f}}{\partial \boldsymbol{\delta}} \\ \frac{\partial \boldsymbol{h}_{P_i}}{\partial \boldsymbol{V}} & \frac{\partial \boldsymbol{h}_{P_i}}{\partial \boldsymbol{\delta}} \\ \frac{\partial \boldsymbol{h}_{Q_i}}{\partial \boldsymbol{V}} & \frac{\partial \boldsymbol{h}_{Q_i}}{\partial \boldsymbol{\delta}} \end{bmatrix} \quad \text{or} \quad \boldsymbol{H}(\boldsymbol{x}) = \frac{\partial \boldsymbol{h}(\boldsymbol{x})}{\partial \boldsymbol{x}} = \begin{bmatrix} \frac{\partial \boldsymbol{h}_V}{\partial \boldsymbol{V}_{\mathrm{R}}} & \frac{\partial \boldsymbol{h}_V}{\partial \boldsymbol{V}_{\mathrm{I}}} \\ \frac{\partial \boldsymbol{h}_I}{\partial \boldsymbol{V}_{\mathrm{R}}} & \frac{\partial \boldsymbol{h}_I}{\partial \boldsymbol{V}_{\mathrm{I}}} \\ \frac{\partial \boldsymbol{h}_{P_f}}{\partial \boldsymbol{V}_{\mathrm{R}}} & \frac{\partial \boldsymbol{h}_{P_f}}{\partial \boldsymbol{V}_{\mathrm{I}}} \\ \frac{\partial \boldsymbol{h}_{Q_f}}{\partial \boldsymbol{V}_{\mathrm{R}}} & \frac{\partial \boldsymbol{h}_{Q_f}}{\partial \boldsymbol{V}_{\mathrm{I}}} \\ \frac{\partial \boldsymbol{h}_{P_i}}{\partial \boldsymbol{V}_{\mathrm{R}}} & \frac{\partial \boldsymbol{h}_{P_i}}{\partial \boldsymbol{V}_{\mathrm{I}}} \\ \frac{\partial \boldsymbol{h}_{Q_i}}{\partial \boldsymbol{V}_{\mathrm{R}}} & \frac{\partial \boldsymbol{h}_{Q_i}}{\partial \boldsymbol{V}_{\mathrm{I}}} \end{bmatrix} \tag{4.71}$$

where $\boldsymbol{V} := \begin{bmatrix} V_1 & V_2 & \cdots & V_N \end{bmatrix}^T$, $\boldsymbol{\delta} := \begin{bmatrix} \delta_2 & \cdots & \delta_N \end{bmatrix}^T$, $\boldsymbol{V}_{\mathrm{R}} := \begin{bmatrix} V_{\mathrm{R},1} & V_{\mathrm{R},2} & \cdots & V_{\mathrm{R},N} \end{bmatrix}^T$ and $\boldsymbol{V}_{\mathrm{I}} := \begin{bmatrix} V_{\mathrm{I},2} & \cdots & V_{\mathrm{I},N} \end{bmatrix}^T$. The non-zero derivatives of (4.71), i.e., the non-zero elements of $\boldsymbol{H}(\boldsymbol{x})$, can be calculated according to (4.21)–(4.35) and (4.38)–(4.43), for polar and rectangular coordinates, respectively, and are explicitly presented in Appendix A.

Algorithm 4.1: Nonlinear WLS state estimation.

1)	Initialize the iteration index $i \leftarrow 0$ and set the state vector $\boldsymbol{x}^{(0)}$ at flat start.
2)	Calculate the gain matrix $\boldsymbol{G}(\boldsymbol{x}^{(i)})$.
3)	Calculate the right-hand side of (4.70), $\boldsymbol{t}^{(i)} := \boldsymbol{H}^T(\boldsymbol{x}^{(i)})\boldsymbol{R}^{-1}\left(\boldsymbol{z} - \boldsymbol{h}(\boldsymbol{x}^{(i)})\right)$.
4)	Decompose $\boldsymbol{G}(\boldsymbol{x}^{(i)})$ and solve (4.70) for $\Delta\boldsymbol{x}^{(i)}$.
5)	Check for convergence: **If** $\left\|\Delta\boldsymbol{x}^{(i)}\right\|_\infty \le \varepsilon$, where ε is the convergence tolerance, **then** $\hat{\boldsymbol{x}} \leftarrow \boldsymbol{x}^{(i)} + \Delta\boldsymbol{x}^{(i)}$ and terminate the algorithm. **Else**, $\boldsymbol{x}^{(i+1)} \leftarrow \boldsymbol{x}^{(i)} + \Delta\boldsymbol{x}^{(i)}$, $i \leftarrow i+1$ and return to Step 2.

4.8.2 Linear state estimation

The linear nature of the PMU-based SE problem results in the formulation of a linear regression model. The MLE problem of maximizing the log-likelihood function is equivalent to minimizing the objective function $J(\boldsymbol{x}) = \left(\boldsymbol{z} - \boldsymbol{H}\boldsymbol{x}\right)^T \boldsymbol{R}^{-1}\left(\boldsymbol{z} - \boldsymbol{H}\boldsymbol{x}\right)$, yielding the following formulation of the state estimate:

$$\hat{\boldsymbol{x}} := \arg\min_{\boldsymbol{x}\in\mathbb{R}^n} J(\boldsymbol{x}) \tag{4.72}$$

The first order optimality conditions will have to be satisfied at the minimum of $J(\boldsymbol{x})$:

$$\nabla J(\boldsymbol{x}) = \frac{\partial J(\boldsymbol{x})}{\partial \boldsymbol{x}} = -\boldsymbol{H}^T\boldsymbol{R}^{-1}\left(\boldsymbol{z} - \boldsymbol{H}\boldsymbol{x}\right) = \boldsymbol{0} \tag{4.73}$$

Expanding the gradient $\nabla J(\boldsymbol{x})$ around the estimate $\boldsymbol{x}^{(i)}$ using a first-order Taylor series expansion as in (4.67), and ignoring the second-order derivatives of $\boldsymbol{h}(\boldsymbol{x})$ results in the following approximation of $\nabla^2 J(\boldsymbol{x})$:

$$\nabla^2 J(\boldsymbol{x}) \approx \boldsymbol{H}^T\boldsymbol{R}^{-1}\boldsymbol{H} \tag{4.74}$$

Using the Gauss-Newton numerical method yields:

$$\begin{gathered}
\boldsymbol{x}^{(i+1)} = \boldsymbol{x}^{(i)} - \left(\nabla^2 J(\boldsymbol{x}^{(i)})\right)^{-1}\nabla J(\boldsymbol{x}^{(i)}) \Leftrightarrow \\
\boldsymbol{x}^{(i+1)} = \boldsymbol{x}^{(i)} + \left(\boldsymbol{H}^T\boldsymbol{R}^{-1}\boldsymbol{H}\right)^{-1}\boldsymbol{H}^T\boldsymbol{R}^{-1}\left(\boldsymbol{z} - \boldsymbol{H}\boldsymbol{x}^{(i)}\right) \Leftrightarrow \\
\boldsymbol{G}\hat{\boldsymbol{x}} = \boldsymbol{H}^T\boldsymbol{R}^{-1}\boldsymbol{z}
\end{gathered} \tag{4.75}$$

In contrast to the iterative Gauss-Newton numerical method for solving the nonlinear WLS SE problem, the state estimate of the linear WLS problem is provided by the closed-form solution (4.75). Algorithm 4.2 presents the general solution of the linear SE.

Algorithm 4.2: Linear WLS state estimation.

1)	Calculate the gain matrix $\boldsymbol{G} = \boldsymbol{H}^T\boldsymbol{R}^{-1}\boldsymbol{H}$.
2)	Calculate $\boldsymbol{H}^T\boldsymbol{R}^{-1}\boldsymbol{z}$.
3)	Decompose $\boldsymbol{G}$ and solve (4.75) for $\hat{\boldsymbol{x}}$.

4.8.2.1 The PMU measurement Jacobian matrix

Given the measurement model (4.45), the structure of the PMU measurement Jacobian matrix can also be derived for both polar and rectangular expressions of the state vector:

$$\boldsymbol{H}(\boldsymbol{x}) = \frac{\partial \boldsymbol{h}(\boldsymbol{x})}{\partial \boldsymbol{x}} = \begin{bmatrix} \frac{\partial \boldsymbol{h}_V}{\partial \boldsymbol{V}} & \frac{\partial \boldsymbol{h}_V}{\partial \boldsymbol{\delta}} \\ \frac{\partial \boldsymbol{h}_\delta}{\partial \boldsymbol{V}} & \frac{\partial \boldsymbol{h}_\delta}{\partial \boldsymbol{\delta}} \\ \frac{\partial \boldsymbol{h}_{I_\mathrm{R}}}{\partial \boldsymbol{V}} & \frac{\partial \boldsymbol{h}_{I_\mathrm{R}}}{\partial \boldsymbol{\delta}} \\ \frac{\partial \boldsymbol{h}_{I_\mathrm{I}}}{\partial \boldsymbol{V}} & \frac{\partial \boldsymbol{h}_{I_\mathrm{I}}}{\partial \boldsymbol{\delta}} \end{bmatrix} \quad \text{or} \quad \boldsymbol{H} = \frac{\partial \boldsymbol{h}(\boldsymbol{x})}{\partial \boldsymbol{x}} = \begin{bmatrix} \frac{\partial \boldsymbol{h}_{V_\mathrm{R}}}{\partial \boldsymbol{V}_\mathrm{R}} & \frac{\partial \boldsymbol{h}_{V_\mathrm{R}}}{\partial \boldsymbol{V}_\mathrm{I}} \\ \frac{\partial \boldsymbol{h}_{V_\mathrm{I}}}{\partial \boldsymbol{V}_\mathrm{R}} & \frac{\partial \boldsymbol{h}_{V_\mathrm{I}}}{\partial \boldsymbol{V}_\mathrm{I}} \\ \frac{\partial \boldsymbol{h}_{I_\mathrm{R}}}{\partial \boldsymbol{V}_\mathrm{R}} & \frac{\partial \boldsymbol{h}_{I_\mathrm{R}}}{\partial \boldsymbol{V}_\mathrm{I}} \\ \frac{\partial \boldsymbol{h}_{I_\mathrm{I}}}{\partial \boldsymbol{V}_\mathrm{R}} & \frac{\partial \boldsymbol{h}_{I_\mathrm{I}}}{\partial \boldsymbol{V}_\mathrm{I}} \end{bmatrix} \tag{4.76}$$

where $\boldsymbol{V} := \begin{bmatrix} V_1 & V_2 & \cdots & V_N \end{bmatrix}^T$, $\boldsymbol{\delta} := \begin{bmatrix} \delta_1 & \delta_2 & \cdots & \delta_N \end{bmatrix}^T$, $\boldsymbol{V}_\mathrm{R} := \begin{bmatrix} V_{\mathrm{R},1} & V_{\mathrm{R},2} & \cdots & V_{\mathrm{R},N} \end{bmatrix}^T$ and $\boldsymbol{V}_\mathrm{I} := \begin{bmatrix} V_{\mathrm{I},2} & \cdots & V_{\mathrm{I},N} \end{bmatrix}^T$. For the case of polar coordinates, the non-zero elements of $\boldsymbol{H}(\boldsymbol{x})$ can be calculated according to (4.35), (4.46), (4.50) and (4.51), and are analytically presented in Appendix A. For rectangular coordinates, the PMU measurement model becomes linear and can be written as:

$$\boldsymbol{z} = \boldsymbol{H}\boldsymbol{x} + \boldsymbol{e} \tag{4.77}$$

where the Jacobian matrix $\boldsymbol{H}$ is now constant, with the following structure:

$$\boldsymbol{H} = \left(\begin{array}{cccccc|c} \cdots & V_{\mathrm{R},i} & V_{\mathrm{I},i} & \cdots & V_{\mathrm{R},j} & V_{\mathrm{I},j} & \cdots \\ \hline \cdots & 1 & 0 & \cdots & 0 & 0 & \cdots & V_{\mathrm{R},i}^m \\ \cdots & 0 & 1 & \cdots & 0 & 0 & \cdots & V_{\mathrm{I},i}^m \\ \cdots & t_{ij}^2(g_{sij}+g_{ij}) & -t_{ij}^2(b_{sij}+b_{ij}) & \cdots & -t_{ij}t_{ji}D_{ij} & t_{ij}t_{ji}E_{ij} & \cdots & I_{\mathrm{R},ij}^m \\ \cdots & t_{ij}^2(b_{sij}+b_{ij}) & t_{ij}^2(g_{sij}+g_{ij}) & \cdots & -t_{ij}t_{ji}E_{ij} & -t_{ij}t_{ji}D_{ij} & \cdots & I_{\mathrm{I},ij}^m \end{array}\right), \; j \in a(i) \tag{4.78}$$

$$D_{ij} = g_{ij}\cos(\Delta\varphi_{ij}) + b_{ij}\sin(\Delta\varphi_{ij})$$
$$E_{ij} = b_{ij}\cos(\Delta\varphi_{ij}) - g_{ij}\sin(\Delta\varphi_{ij})$$

4.8.3 Observability concepts

The feasibility of a system-wide SE solution depends on the number and distribution of measurement points within the network. This concept is known as observability: a system is considered observable only when it has sufficient measurements to reconstruct the complete system state. Since the steady state of a power system is defined by two independent variables (voltage magnitude and angle) at each bus, at least twice the number of nodes must be measured to achieve observability, as discussed in Table 4.2.

In an underdetermined system, the SE problem is not solvable, as there are insufficient measurements to uniquely determine the system state. In a determined system, while a solution is feasible, the absence of redundant measurements means that there is no capacity to account for measurement accuracy (weights) or detect erroneous measurements. By contrast, an overdetermined system, which contains more measurements than necessary, enhances the robustness of SE by enabling bad data detection and elimination.

Table 4.2: Levels of system observability [56].

System classification	Number of measurement points	Ramification
Underdetermined	Less than twice the number of system buses	Infinite solutions: not enough information is available to solve the SE problem
Determined	Approximately equal to twice the number of system buses	One exact solution: no measurement redundancy means the SE is prone to bad data. Measurements must be distributed across the system to achieve observability
Overdetermined	Greater than twice the number of system buses	Redundancy: measurements are weighted based on their accuracy to calculate the SE solution. SE is resilient to erroneous measurements

Generally, numerical models of observability analysis constitute the mathematical expression of the corresponding topological approaches; however, their equivalence cannot be guaranteed. According to the IEEE institute's technical report [57], two types of observability are distinguished. *Topological observability* is verified through graph theory without considering the parameters of the actual model of the system under study and the weighting coefficients of the measurements, and it does not include floating-point arithmetic operations. In contrast, *numerical observability* is verified through numerical calculations related to the triangulation of the gain matrix or the Jacobian matrix of the system under study.

Observability in power systems is rigorously defined within both the topological and numerical frameworks [32], [38]. According to the topological approach, a system is called observable when a *spanning tree* can be formed, consisting of branches of the system for which power flow measurements are available, which is of full degree, that is, it includes all the nodes of the system. If this condition cannot be fulfilled, the system is considered unobservable and is partitioned into observable islands, which may even degenerate into isolated nodes.

According to the numerical approach, a system is observable when its Jacobian matrix is of full rank or, equivalently, its gain matrix is of full rank or, equivalently, is invertible. The rank of a matrix is defined as the dimension of the vector space that can be generated by its column vectors – that is, it equals the number of its linearly independent columns (it is proven that this is equal to the corresponding number of its rows). Consequently, for a full-rank Jacobian matrix, it holds that:

$$\operatorname{rank}\{\boldsymbol{H}\} = \min\{m, n\} \tag{4.79}$$

that is, the rank of the matrix is equal to the smaller of its two dimensions. For overdetermined systems $m > n$, and thus $\operatorname{rank}\{\boldsymbol{H}\} = n$. Generally, the invertibility of the gain matrix $\boldsymbol{G}$ is the most common condition for checking the observability status of a system [35].

4.8.4 Properties of the gain matrix

Apart from numerical observability analysis methods relying on its study, the gain matrix $\boldsymbol{G}$ represents a critical structure of the WLS SE model, with the following properties [35], [38]:

1) In general, it is a non-negative definite matrix, i.e., its eigenvalues are non-negative. It is positive definite for fully observable networks.
2) It is structurally and numerically symmetric and sparse, yet less sparse compared to $\boldsymbol{H}$.
3) It is characterized as an ill-conditioned matrix, making its factorization a necessary procedure for reliably solving the SE problem.

4) It quantifies the accuracy of the state estimation results.
5) It contains all relevant information about the type, location, and accuracy of the available measurements.

$\boldsymbol{G}$ can be built and stored as a sparse matrix for computational efficiency and memory considerations. Consider the measurement Jacobian $\boldsymbol{H}$ and the covariance matrix $\boldsymbol{R}$ for a set of m measurements, each one corresponding to a single row, as shown below:

$$\boldsymbol{H} = \begin{bmatrix} \boldsymbol{H}_1 \\ \boldsymbol{H}_2 \\ \vdots \\ \boldsymbol{H}_m \end{bmatrix}, \quad \boldsymbol{R} = \begin{bmatrix} R_{11} & 0 & \cdots & 0 \\ 0 & R_{22} & 0 & 0 \\ 0 & 0 & \ddots & 0 \\ 0 & 0 & \cdots & R_{mm} \end{bmatrix}$$

Then, the gain matrix can be written as:

$$\boldsymbol{G} = \sum_{i=1}^{m} \boldsymbol{G}_i = \sum_{i=1}^{m} \boldsymbol{H}_i^T R_{ii}^{-1} \boldsymbol{H}_i \tag{4.80}$$

Since $\boldsymbol{H}_i$ in (4.80) are very sparse row vectors, their product will also yield a sparse matrix, and nonzero terms in $\boldsymbol{G}$ can thus be calculated and stored in sparse form. The sparsity pattern of $\boldsymbol{G}$ depends on the type of available measurements. When only power flow measurements are present, the gain matrix shares the same sparsity pattern as the corresponding admittance matrix $\boldsymbol{Y}$, which represents the branches where power flow measurements exist. However, the inclusion of SCADA-based bus injection measurements alters this pattern, as an injection measurement introduces additional nonzero elements in the gain matrix structure. These elements correspond to all branches connected to the measured node. In an extreme case where injection measurements are available at every node, the gain matrix has a sparsity pattern similar to the square of the network admittance matrix. Note that although the gain matrix is generally less sparse than the $\boldsymbol{Y}$ matrix, it is still very sparse for large networks, justifying the use of sparse matrix techniques [38].

The factorization of the gain matrix has been the subject of extensive study, as will be discussed extensively in Subsection 4.9, because it is less sparse compared to the Jacobian matrix. The gain matrix $\boldsymbol{G}$ can be written as a product of a lower triangular sparse matrix and its transpose. This is called the Cholesky decomposition of $\boldsymbol{G}$, details of which are given in [38]. The decomposed form of $\boldsymbol{G}$ will be:

$$\boldsymbol{G} = \boldsymbol{L}\boldsymbol{L}^T \tag{4.81}$$

Note that this decomposition may not exist for systems which are not fully observable, and as a result, an SE solution cannot be obtained for such (unobservable) systems. Triangular factors of $\boldsymbol{G}$ are not unique, and extracting these factors must be carried out in a manner that preserves their sparsity as much as possible. There are several methods for optimizing the sparsity of the resulting $\boldsymbol{L}$ factors, through elementary row operations, which yield row-equivalent forms of $\boldsymbol{G}$ prior to factorization, as well as through appropriate algorithms during the factorization process [58]. Specifically, for the Cholesky method, the sparsity of $\boldsymbol{L}$ is preserved via the minimum-degree or Tinney-2 ordering algorithm – so named after its proponent [35].

An especially important property of the matrix is that its inverse $\boldsymbol{G}^{-1}(\hat{\boldsymbol{x}})$ coincides with the covariance matrix of the WLS SE solution. Since the nonlinear WLS static model provides an *asymptotically unbiased* estimator of the state vector $\boldsymbol{x}$, we have:

$$E(\hat{\boldsymbol{x}}) = \boldsymbol{x} \tag{4.82}$$

In other words, the mean value of the WLS state estimates one would obtain for different realizations (in terms of measurement values) of the same set of available measurements equals the actual system state [39]. Furthermore, by solving (4.66) after linearizing $\boldsymbol{h}(\boldsymbol{x})$ in the neighborhood of the estimate $\hat{\boldsymbol{x}}$, it can be shown that the covariance matrix $Cov(\hat{\boldsymbol{x}})$ is given by [34]:

$$Cov(\hat{\boldsymbol{x}}) := E\left[(\boldsymbol{x}-\hat{\boldsymbol{x}})(\boldsymbol{x}-\hat{\boldsymbol{x}})^T\right] = \boldsymbol{G}^{-1}(\hat{\boldsymbol{x}}) \tag{4.83}$$

Consequently, the i-th diagonal element of $\boldsymbol{G}^{-1}(\hat{\boldsymbol{x}})$ coincides with the variance of the estimated state variable $\hat{x}_i$, i.e.,

$$Var(\hat{x}_i) = \left[\boldsymbol{G}^{-1}(\hat{\boldsymbol{x}})\right]_{ii} \tag{4.84}$$

Finally, the information content of the gain matrix is sufficient to provide full knowledge regarding the available measurements in a system under study. It can be shown that within the DC model framework, the Jacobian matrix $\boldsymbol{H}$ – and therefore the gain matrix – can be expressed as a function of its incidence matrix, which encodes how branches and nodes are interconnected. Hence, in numerous studies the i-th row of the Jacobian matrix uniquely encodes the type and topological characteristics of the i-th measurement [35]. Furthermore, based on (4.80), the matrix $\boldsymbol{G}_i$, corresponding to the measurement z_i, also incorporates its accuracy through the weighting factor $R_{ii}^{-1} = \sigma_i^{-2}$. Consequently, the gain matrix, expressed as the sum of the individual terms $\boldsymbol{G}_i$, $i = 1, 2, ..., m$, contains all the pertinent information. This property makes it a valuable tool for optimizing the design of measurement infrastructures in electric power systems [35].

4.8.5 Forward/back substitutions [38]

Assuming that the gain matrix is properly decomposed into its Cholesky factors $\boldsymbol{L}$ and $\boldsymbol{L}^T$, the next step is to solve the NE for $\Delta\boldsymbol{x}^{(i)}$:

$$\boldsymbol{L}\boldsymbol{L}^T\Delta\boldsymbol{x}^{(i+1)} = \boldsymbol{t}^{(i)} \tag{4.85}$$

where $\boldsymbol{t}^{(i)} = \boldsymbol{H}^T(\boldsymbol{x}^{(i)})\boldsymbol{R}^{-1}\left(\boldsymbol{z}-\boldsymbol{h}(\boldsymbol{x}^{(i)})\right)$. This solution is obtained in two steps:

1) *Forward substitution*: Let $\boldsymbol{L}^T\Delta\boldsymbol{x}^{(i+1)} = \boldsymbol{u}$, and obtain the elements of $\boldsymbol{u}$ starting from u_1 by using substitutions in the transformed equation $\boldsymbol{L}\boldsymbol{u} = \boldsymbol{t}^{(i)}$. The top row will yield the solution for $u_1 = t_1/L_{11}$. Substituting for u_1 in the rest of the rows will reduce the set of equations by one. Repeating the same procedure for u_i, $i = 2, 3, ..., n$ sequentially, will yield the entire solution for $\boldsymbol{u}$.
2) *Back substitution*: Now that $\boldsymbol{u}$ is available, use $\boldsymbol{L}^T\Delta\boldsymbol{x}^{(i+1)} = \boldsymbol{u}$ to back-substitute and solve for the entries of $\Delta\boldsymbol{x}^{(i+1)}$. This time, the substitutions should start at the bottom row, where the last element of the solution vector is obtained as $\Delta x_n^{(i+1)} = u_n/L_{nn}$. Substituting for it in the remaining rows, the back substitution process can continue until all entries are calculated.

Note that both the forward and back substitution steps proceed very efficiently due to the sparse structure of the triangular factor $\boldsymbol{L}$.

4.9 Alternative formulations of the WLS state estimator [38]

The WLS SE problem can typically be solved efficiently using the NE, as outlined in the previous Section, particularly with modern computational capabilities. However, it is well established that under certain conditions – commonly encountered in practice – the NE approach may suffer from numerical instabilities. These instabilities can prevent the solution algorithm from converging to an acceptable solution or, in some cases, lead to divergence. In this Section, the limitations of NE are first discussed, along with well-established alternative techniques that offer improved numerical robustness.

4.9.1 Numerical weaknesses of the NE formulation

Let us first recall, from the previous chapter, that the WLS SE leads to the iterative solution of the so-called NE:

$$\boldsymbol{G}(\boldsymbol{x}^{(i)})\Delta\boldsymbol{x}^{(i)} = \boldsymbol{H}^T(\boldsymbol{x}^{(i)})\boldsymbol{R}^{-1}\left(\boldsymbol{z}-\boldsymbol{h}(\boldsymbol{x}^{(i)})\right) \tag{4.86}$$

Equation (4.86) is solved by Cholesky factorization of $\boldsymbol{G}$ and forward/backward substitutions. Since $\boldsymbol{G}$ is positive definite for observable systems, pivoting is not necessary; however, prior to its decomposition, $\boldsymbol{G}$ must first be symmetrically permuted to preserve sparsity. As $\boldsymbol{G}$ is, in general, less sparse than the bus admittance matrix, solving the NE requires significantly more computations than the corresponding power flow solution for the same network [38].

Another important property of $\boldsymbol{G}$, mentioned in Subsection 4.8.4, is the numerical ill-conditioning of the NE. A linear equation system is said to be ill-conditioned if small errors in the entries of the coefficient matrix and/or the right-hand side vector translate into significant errors in the solution vector. The more singular a matrix is, the more ill-conditioned its associated system will be [38]. The degree to which a system is ill-conditioned can be quantified by a measure called the condition number, which is defined as:

$$\kappa(\boldsymbol{A}) = \|\boldsymbol{A}\|\cdot\left\|\boldsymbol{A}^{-1}\right\| \tag{4.87}$$

This value is equal to unity for identity matrices and tends to infinity for matrices approaching singularity. Condition numbers are typically approximately computed, due to the high computing cost of κ as evident from its definition. One such approximation which yields a good estimate of the condition number is the ratio $\lambda_{\max}/\lambda_{\min}$ where $\lambda_{\max}$ and $\lambda_{\min}$ are the largest and smallest absolute eigenvalues, respectively, of a normalized matrix. It can also be shown that:

$$\kappa(\boldsymbol{A}^T\boldsymbol{A}) = \left(\kappa(\boldsymbol{A})\right)^2 \tag{4.88}$$

which means that the NE are intrinsically ill-conditioned [38].

Although such cases are rarely found in practice, a combination of too low a termination threshold and severe ill-conditioning may cause convergence problems or even divergence. Given expression (4.80) of the gain matrix, it becomes clear that the coexistence of measurements with large variations in their accuracy leads to extreme values (both negative and positive) in the elements of $\boldsymbol{G}$. An example of this is the use of very large weighting factors to enforce virtual measurements. Consequently, this is cited as the principal reason for its generally ill-conditioned nature [43]. Another cause of this inherent property is the frequent presence of lines/branches with low series impedance, as well as short and long lines simultaneously present at the same bus [59]. Finally, a large proportion of injection measurements can create (or nearly create) linear dependencies of the rows of $\boldsymbol{G}$ among those measurements. As those dependencies accumulate, the gain matrix inherits these near-linear relationships, which significantly degrades its numerical conditioning [38].

In the following sections, several alternative techniques which try to circumvent the shortcomings of the NE by avoiding the use of $\boldsymbol{G}$ and/or handling virtual measurements in a more effective manner, are discussed.

4.9.2 Alternative methods of gain matrix factorization [38]

In addition to the widely used Cholesky factorization, there are alternative methods that provide improved numerical stability. These approaches can be particularly beneficial in handling ill-conditioned systems and minimizing the risk of computational errors.

4.9.2.1 Orthogonal factorization

Orthogonal factorization (or *QR* decomposition) provides a numerically stable alternative to Cholesky factorization. In this method, matrix $\boldsymbol{H}' := \boldsymbol{W}^{1/2}\boldsymbol{H}$, with $\boldsymbol{W} := \boldsymbol{R}^{-1}$, is decomposed into two matrices: an orthogonal matrix $\boldsymbol{Q}$ and an upper trapezoidal matrix $\boldsymbol{\mathcal{R}}$:

$$\boldsymbol{H}' = \boldsymbol{Q}\boldsymbol{\mathcal{R}} = \begin{bmatrix}\boldsymbol{Q}_n & \boldsymbol{Q}_0\end{bmatrix}\begin{bmatrix}\boldsymbol{U} \\ \boldsymbol{0}\end{bmatrix} = \boldsymbol{Q}_n\boldsymbol{U} \tag{4.89}$$

Applying this factorization to the NE, yields:

$$\boldsymbol{U}\Delta\boldsymbol{x} = \boldsymbol{Q}_n^T\boldsymbol{W}^{1/2}\left(\boldsymbol{z} - \boldsymbol{h}(\boldsymbol{x})\right) \tag{4.90}$$

which is the key equation in this approach and is solved for $\Delta\boldsymbol{x}$ via back substitution.

The main advantages of orthogonal factorization lie in avoiding the explicit computation and factorization of $\boldsymbol{G} = \boldsymbol{H}'^T\boldsymbol{H}'$, while being more numerically robust than the *LU* factorization, since it does not rely on scalar pivots. Although constructing the orthogonal matrix $\boldsymbol{Q}$ can be computationally expensive, optimizations such as square-root-free implementations of the Givens rotations make the process viable for large systems.

4.9.2.2 Hybrid factorization

The hybrid factorization method combines elements of both the Cholesky and orthogonal factorizations. The key observation here is that the matrix $\boldsymbol{U}$ obtained from the orthogonal factorization corresponds to the same Cholesky factor of the gain matrix $\boldsymbol{G}$. Thus, instead of computing $\boldsymbol{G}$ explicitly, $\boldsymbol{U}$ can be obtained using orthogonal transformations on $\boldsymbol{H}'$, and then $\Delta\boldsymbol{x}$ is obtained via $\boldsymbol{U}^T\boldsymbol{U}\Delta\boldsymbol{x} = \boldsymbol{H}'^T\boldsymbol{W}^{1/2}\left(\boldsymbol{z} - \boldsymbol{h}(\boldsymbol{x})\right)$. This hybrid method leverages the numerical stability of orthogonal transformations while retaining computational efficiency, since there is no need to keep track of $\boldsymbol{Q}$.

4.9.2.3 Peters and Wilkinson

The *Peters and Wilkinson* method introduces another alternative by performing an *LU* decomposition on the matrix $\boldsymbol{H}'$, transforming the NE into $\boldsymbol{L}^T\boldsymbol{L}\Delta\boldsymbol{y} = \boldsymbol{L}^T\boldsymbol{W}^{1/2}\left(\boldsymbol{z} - \boldsymbol{h}(\boldsymbol{x})\right)$ with $\Delta\boldsymbol{y} = \boldsymbol{U}\Delta\boldsymbol{x}$. Vector $\Delta\boldsymbol{y}$ is first computed by Cholesky factorization of $\boldsymbol{L}^T\boldsymbol{L}$ and forward/backward substitution, and then $\Delta\boldsymbol{x}$ is obtained by backward substitution. The main advantage of this scheme is the fact that $\boldsymbol{L}^T\boldsymbol{L}$ is less ill-conditioned than $\boldsymbol{G} = \boldsymbol{H}'^T\boldsymbol{H}'$.

4.9.3 Equality-constrained WLS state estimation

As already stated in Section 4.2, usage of virtual measurements is commonly implemented into SE. As already discussed, very accurate virtual measurements, such as zero injections, can be included directly in the measurement vector $\boldsymbol{z}$, with very high weights (very low variances) in the covariance matrix $\boldsymbol{R}$. This, however, may lead to ill-conditioning of the gain matrix. A straightforward method for avoiding the usage of large weighting factors is to model these measurements as explicit constraints in the WLS problem, as follows:

$$\hat{\boldsymbol{x}} := \arg\min_{\boldsymbol{x}} J(\boldsymbol{x}) = \sum_{i=1}^{m} \left(\frac{z_i - h_i(\boldsymbol{x})}{\sigma_i} \right)^2 = \boldsymbol{e}^T \boldsymbol{R}^{-1} \boldsymbol{e}$$
$$\text{s.t. } \boldsymbol{c}(\boldsymbol{x}) = \boldsymbol{0} \tag{4.91}$$

where $\boldsymbol{c}(\boldsymbol{x}) = \boldsymbol{0}$ represents accurate virtual measurements, such as zero power or current injections that are now excluded from $\boldsymbol{z}$ and $\boldsymbol{h}(\boldsymbol{x})$. This problem is solved using the method of Lagrange multipliers, with Lagrangian function:

$$\mathcal{L}(\boldsymbol{x}, \boldsymbol{\lambda}) = J(\boldsymbol{x}) + \boldsymbol{\lambda}^T \boldsymbol{c}(\boldsymbol{x}) \tag{4.92}$$

The first-order optimality conditions are written as:

$$\begin{aligned} \frac{\partial \mathcal{L}(\boldsymbol{x}, \boldsymbol{\lambda})}{\partial \boldsymbol{x}} &= \boldsymbol{0} \Leftrightarrow -\boldsymbol{H}^T(\boldsymbol{x}) \boldsymbol{R}^{-1} (\boldsymbol{z} - \boldsymbol{h}(\boldsymbol{x})) + \boldsymbol{C}^T(\boldsymbol{x}) \boldsymbol{\lambda} = \boldsymbol{0} \\ \frac{\partial \mathcal{L}(\boldsymbol{x}, \boldsymbol{\lambda})}{\partial \boldsymbol{\lambda}} &= \boldsymbol{0} \Leftrightarrow \boldsymbol{c}(\boldsymbol{x}) = \boldsymbol{0} \end{aligned} \tag{4.93}$$

where $\boldsymbol{C}(\boldsymbol{x}) = \dfrac{\partial \boldsymbol{c}(\boldsymbol{x})}{\partial \boldsymbol{x}}$ is the Jacobian of $\boldsymbol{c}(\boldsymbol{x})$.

Following a similar procedure to Section 4.8.1 in order to solve the nonlinear equations (4.93), the Gauss-Newton method yields the following linear system:

$$\begin{bmatrix} \boldsymbol{G}(\boldsymbol{x}^{(i)}) & \boldsymbol{C}^T(\boldsymbol{x}^{(i)}) \\ \boldsymbol{C}(\boldsymbol{x}^{(i)}) & \boldsymbol{0} \end{bmatrix} \begin{bmatrix} \Delta \boldsymbol{x}^{(i)} \\ \boldsymbol{\lambda}^{(i+1)} \end{bmatrix} = \begin{bmatrix} \boldsymbol{H}^T(\boldsymbol{x}^{(i)}) \boldsymbol{R}^{-1} \left(\boldsymbol{z} - \boldsymbol{h}(\boldsymbol{x}^{(i)}) \right) \\ -\boldsymbol{c}(\boldsymbol{x}^{(i)}) \end{bmatrix} \tag{4.94}$$

Note that the matrix $\boldsymbol{R}^{-1}$ no longer has large values, which eliminates one of the main sources of ill-conditioning. However, the drawback of (4.94) lies in its coefficient matrix being indefinite. This means that row pivoting to preserve numerical stability must be combined with sparsity-oriented techniques during *LU* factorization, destroying the initial symmetry. More sophisticated techniques, capable of resorting on-the-fly to 2x2 pivots to preserve the symmetry have been developed to deal with indefinite matrices. Other block-pivot approaches have been presented in which the pivot size is decided in advance based on available measurements [38].

It is worth mentioning that the condition number of the coefficient matrix in (4.94) can be further improved by simply scaling the term of the Lagrangian corresponding to the objective function, yielding:

$$\mathcal{L}(\boldsymbol{x}, \boldsymbol{\lambda}_s) = aJ(\boldsymbol{x}) + \boldsymbol{\lambda}_s^T \boldsymbol{c}(\boldsymbol{x}) \tag{4.95}$$

It is easy to show that the scaling factor a has no influence on the estimated state and that $\boldsymbol{\lambda}_s = a\boldsymbol{\lambda}$. The equation system that must be solved at each iteration is:

$$\begin{bmatrix} a\boldsymbol{G}(\boldsymbol{x}^{(i)}) & \boldsymbol{C}^T(\boldsymbol{x}^{(i)}) \\ \boldsymbol{C}(\boldsymbol{x}^{(i)}) & \boldsymbol{0} \end{bmatrix} \begin{bmatrix} \Delta \boldsymbol{x}^{(i)} \\ \boldsymbol{\lambda}_s^{(i+1)} \end{bmatrix} = \begin{bmatrix} a\boldsymbol{H}^T(\boldsymbol{x}^{(i)}) \boldsymbol{R}^{-1} \left(\boldsymbol{z} - \boldsymbol{h}(\boldsymbol{x}^{(i)}) \right) \\ -\boldsymbol{c}(\boldsymbol{x}^{(i)}) \end{bmatrix} \tag{4.96}$$

Very low condition numbers are obtained when a is chosen as [38]:

$$a = \frac{1}{\max(R_{ii}^{-1})} \quad \text{or} \quad a = \frac{m}{\sum_{i=1}^{m} R_{ii}^{-1}} \tag{4.97}$$

It should be noted that $a = 1$ might lead to condition numbers which are actually worse than that of the conventional $\boldsymbol{G}$, because the values R_{ii}^{-1} are usually very large compared to the coefficients of $\boldsymbol{C}$. This flexibility is not possible in the conventional approach, where scaling the objective function has no effect on $\kappa(\boldsymbol{G})$. Hence, this is another advantage of modeling virtual measurements as equality constraints.

4.9.4 Hachtel's augmented matrix approach

Similar to virtual measurements, regular measurement equations can be written as equality constraints if the associated residuals are retained as explicit variables. In this approach, the WLS problem can be restated as:

$$
\begin{aligned}
&\hat{\boldsymbol{x}} := \arg\min_{\boldsymbol{x}} J(\boldsymbol{x}) = \boldsymbol{r}^T \boldsymbol{R}^{-1} \boldsymbol{r} \\
&\text{s.t. } \boldsymbol{r} = \boldsymbol{z} - \boldsymbol{h}(\boldsymbol{x}) \\
&\qquad \boldsymbol{c}(\boldsymbol{x}) = \boldsymbol{0}
\end{aligned}
\tag{4.98}
$$

The resulting Lagrangian will have two sets of Lagrange multipliers, $\boldsymbol{\lambda}$ and $\boldsymbol{\mu}$:

$$
\mathcal{L}(\boldsymbol{x}, \boldsymbol{r}, \boldsymbol{\lambda}, \boldsymbol{\mu}) = J(\boldsymbol{r}) + \boldsymbol{\lambda}^T \boldsymbol{c}(\boldsymbol{x}) + \boldsymbol{\mu}^T \left(\boldsymbol{r} - \boldsymbol{z} + \boldsymbol{h}(\boldsymbol{x}) \right) \tag{4.99}
$$

Linearizing the first order optimality conditions and using $\boldsymbol{r} = -\boldsymbol{R}\boldsymbol{\mu}$, the following system of equations will be obtained:

$$
\begin{bmatrix} \boldsymbol{0} & \boldsymbol{C}^T(\boldsymbol{x}^{(i)}) & \boldsymbol{H}^T(\boldsymbol{x}^{(i)}) \\ \boldsymbol{C}(\boldsymbol{x}^{(i)}) & \boldsymbol{0} & \boldsymbol{0} \\ \boldsymbol{H}(\boldsymbol{x}^{(i)}) & \boldsymbol{0} & -\boldsymbol{R} \end{bmatrix}
\begin{bmatrix} \Delta \boldsymbol{x}^{(i)} \\ \boldsymbol{\lambda}^{(i+1)} \\ \boldsymbol{\mu}^{(i+1)} \end{bmatrix}
=
\begin{bmatrix} \boldsymbol{0} \\ -\boldsymbol{c}(\boldsymbol{x}^{(i)}) \\ \boldsymbol{z} - \boldsymbol{h}(\boldsymbol{x}^{(i)}) \end{bmatrix}
\tag{4.100}
$$

The coefficient matrix in (4.100) is called the *Hachtel's matrix*. Note that (4.100) will become identical to (4.94) if $\boldsymbol{\mu}$ is eliminated. Hence, this is the most primitive or augmented formulation and, according to the theory discussed above, lower condition numbers are expected. On the other hand, since the Hachtel's matrix is very sparse, solving the above system is not particularly expensive in terms of arithmetic operations, but a more involved logic is needed to control and track the required row pivoting [38]. As in the case of (4.94), the condition number of the Hachtel's matrix can be further improved if the residual weights are properly scaled. This is achieved simply by using a scaling factor as in (4.95) , yielding:

$$
\begin{bmatrix} \boldsymbol{0} & \boldsymbol{C}^T(\boldsymbol{x}^{(i)}) & \boldsymbol{H}^T(\boldsymbol{x}^{(i)}) \\ \boldsymbol{C}(\boldsymbol{x}^{(i)}) & \boldsymbol{0} & \boldsymbol{0} \\ \boldsymbol{H}(\boldsymbol{x}^{(i)}) & \boldsymbol{0} & -a^{-1}\boldsymbol{R} \end{bmatrix}
\begin{bmatrix} \Delta \boldsymbol{x}^{(i)} \\ \boldsymbol{\lambda}_s^{(i+1)} \\ \boldsymbol{\mu}_s^{(i+1)} \end{bmatrix}
=
\begin{bmatrix} \boldsymbol{0} \\ -\boldsymbol{c}(\boldsymbol{x}^{(i)}) \\ \boldsymbol{z} - \boldsymbol{h}(\boldsymbol{x}^{(i)}) \end{bmatrix}
\tag{4.101}
$$

4.10 Power System Dynamic State Estimation

Power systems, by design, operate under hierarchical monitoring and control systems to manage a wide range of dynamic phenomena, varying across multiple time scales. As discussed in the previous Chapter, historically, SSE models and methods have formed the backbone of the EMS for power system visibility and situational awareness, assuming the system operates in a steady state. However, the increasing complexity of power grids due to the large-scale DER integration, complex loads, and new demand-side technologies has exposed the limitations of these traditional static models. Dynamic characteristics – such as variations in demand and renewable energy supply – cause frequent and unpredictable shifts in the system's state. These stochastic variations in generation and load introduce uncertainties, often rendering SSE methods insufficient for real-time operation. To address these challenges, Dynamic State Estimation (DSE) has emerged as a critical tool, enabling the accurate tracking of power system dynamics. DSE not only helps capture fast-changing states like rotor angles and generator speeds but also enhances control and protection strategies, particularly under scenarios of high system uncertainty [60].

4.10.1 Dynamic state estimation motivations and background

The power grid is experiencing profound changes in generation mixes and load compositions, particularly due to the increasing penetration of intermittent, stochastic and power electronics-interfaced non-synchronous renewable generation and DERs [60]. These changes manifest as new types of system dynamics that static models fail to capture. For example, stochastic fluctuations in renewable generation, driven by variations in weather conditions, can cause rapid changes in system states, such as voltage and rotor speed. These fast dynamics present a challenge for traditional EMS, which rely on SCADA systems that update data only every few seconds or minutes, making them inadequate for capturing real-time system fluctuations [60], [61]. Thus, DSE offers several compelling benefits in this evolving landscape. With the proliferation of PMUs, capable of providing synchronized measurements across the power grid at much higher resolutions, DSE tools can now be implemented to significantly enhance system monitoring, control, and protection [61]. Some of the key applications of DSE include [60], [62]:

- *Power system monitoring*: By providing accurate estimates of dynamic state variables and dynamic state trajectory tracking, DSE enables real-time modal analysis, crucial for identifying system oscillations, as well as bus frequency, ROCOF and center of inertia frequency estimation, data quality detection and correction – e.g., against cyber-attacks – and anomaly detection.
- *Improved control strategies*: DSE supports both local and wide-area control by accurately estimating dynamic states, such as rotor speeds and voltage angles. These states can then be used as inputs for more precise control of excitation systems in generators or FACTS, improving the system's overall response to disturbances.
- *Enhanced protection systems*: One of the most significant contributions of DSE is its ability to improve the reliability of power system protection schemes. Traditional protection systems rely on pre-set relay settings, which may not be robust against fast-changing conditions. DSE, on the other hand, allows for real-time fault detection by cross-referencing PMU data with dynamic models. This enables more adaptive protection mechanisms, which can prevent blackouts and better manage generator stability during out-of-step events.
- *Model validation and parameter calibration*: Online tracking and identification of system model parameters, including those for synchronous machines, dynamic loads, wind farms, and other power electronics-interfaced DERs, has been an important application of DSE. By continuously validating and updating these models, DSE contributes to more reliable dynamic security assessments, allowing operators to predict and react to potential system instabilities.

Under this premise, in parallel with the development of the WLS SSE model, DSE models have also been studied, albeit to a lesser extent. Despite being initially mentioned in the 1970s [63], [64], it was only in recent years that the power system community has picked up the momentum in DSE research. Part of the reason was the lack of appropriate metering infrastructure, like PMUs and MUs that are being widely deployed to capture the appropriate dynamics in power systems. Feasibility studies using PMU measurements for DSE are reported in [65], and, subsequently, various Kalman filter (KF)-based techniques, such as Extended Kalman Filter (EKF), Unscented Kalman Filter (UKF) [66], Ensemble

Kalman Filter (EnKF), Particle Filter (PF) and their variants [67] have been applied to DSE. Data-driven DSE [68], observability analysis to guide measurement selection [69], and the enhancement of robustness against bad data and parameter errors are also developed in [70], [71].

4.10.2 Dynamic state estimation framework

To address the diverse operational conditions in power systems, this section presents the unified DSE framework that integrates various SE techniques. These methods differ in their ability to handle fully dynamic versus quasi-steady conditions and their applicability under specific operating scenarios.

4.10.2.1 Quasi-steady state vs. transient conditions

Power system states can generally be classified into two mutually exclusive primary operating conditions: quasi-steady and transient. Transient operating conditions occur when the system experiences a sudden disturbance (e.g., faults, switching events, or rapid changes in generation/load). During these events, the dynamic states evolve according to differential equations. The system's behavior under transient conditions is captured by the following set of differential-algebraic equations [62]:

$$\frac{\partial \boldsymbol{x}(t)}{\partial t} = \boldsymbol{f}\left(\boldsymbol{x}(t), \boldsymbol{u}(t), \boldsymbol{p}\right) \tag{4.102}$$

$$\mathbf{0} = \boldsymbol{c}\left(\boldsymbol{x}(t), \boldsymbol{u}(t), \boldsymbol{p}\right) \tag{4.103}$$

where $\boldsymbol{x} \in \mathbb{R}^n$ denotes the state vector comprising algebraic state variables, such as voltage and current phasors, as well as dynamic states, such as rotor angles and speeds, $\boldsymbol{u}$ is the input vector (e.g., control inputs), $\boldsymbol{p}$ represents system parameters, and $\boldsymbol{f}(\cdot)$, $\boldsymbol{c}(\cdot)$ are nonlinear functions representing the system's differential and algebraic equations, respectively. In this case, (4.102) captures the rapid evolution of the dynamic states over time, and (4.103) consists of the algebraic constraints of the system (e.g., power flow equations) that must be satisfied.

During quasi-steady operation, the system experiences slow and gradual changes in load or renewable generation. In this case, generators and controllers respond effectively to maintain system balance, with negligible variations in the dynamic states (e.g., rotor speed and angle). Mathematically, the quasi-steady state is described by the following set of algebraic equations, where dynamic state changes are assumed to be minimal [62]:

$$\mathbf{0} \approx \boldsymbol{f}\left(\boldsymbol{x}(t), \boldsymbol{u}(t), \boldsymbol{p}\right) \tag{4.104}$$

$$\mathbf{0} = \boldsymbol{g}\left(\boldsymbol{x}(t), \boldsymbol{u}(t), \boldsymbol{p}\right) \tag{4.105}$$

Under quasi-steady conditions, changes in state variables over time are slow, so $\frac{\partial \boldsymbol{x}(t)}{\partial t} \approx \mathbf{0}$. This justifies the use of static or quasi-dynamic state estimators, which assume that the system is approximately at equilibrium, with no rapid changes in dynamic states, as will be discussed in the following.

4.10.2.2 Discrete-time models

Both quasi-steady and transient operating conditions are expressed in continuous-time models via (4.102)–(4.105), which are then discretized for practical use in SE. The state-space representation in discrete time is given by [62]:

$$\boldsymbol{x}_{k+1} = \boldsymbol{f}\left(\boldsymbol{x}_k, \boldsymbol{u}_k, \boldsymbol{p}\right) + \boldsymbol{w}_k \tag{4.106}$$

$$\boldsymbol{z}_k = \boldsymbol{h}\left(\boldsymbol{x}_k, \boldsymbol{u}_k, \boldsymbol{p}\right) + \boldsymbol{e}_k \tag{4.107}$$

where $\boldsymbol{x}_k$ represents the discrete-time state vector at time step *k*, $\boldsymbol{w}_k$, is the error vector accounting for model approximation and time discretization errors, $\boldsymbol{e}_k$ is the measurement error vector, and the algebraic constraints $\boldsymbol{c}(\cdot)$ are processed together with the incoming measurement vector $\boldsymbol{z}_k$ via the nonlinear measurement function $\boldsymbol{h}(\cdot)$. The random vectors $\boldsymbol{w}_k$ and $\boldsymbol{e}_k$ are usually assumed to be normally distributed with zero mean and covariance matrices $\boldsymbol{Q}_k$ and $\boldsymbol{R}_k$ respectively. Note that they are the superposition of different sources of noise/errors (e.g. from sensors, communication channels, or models) and may not follow a Gaussian distribution in practice [72].

4.10.2.3 Dynamic state estimation methods

DSE in general is a nonlinear filtering problem that can be formulated using recursive state-space models. In DSE, the goal is to estimate the state vector $\boldsymbol{x}_k$ given all available measurements up to the current time step *k*. This is typically accomplished using the *Kalman filter* (KF) framework, through a combination of prediction (or time update) and filtering (or measurement update) steps:

1) *Prediction step*: This step predicts the state at the next time step based on past data. Using the state estimates from the previous time step $k-1$, i.e., $\hat{\boldsymbol{x}}_{k-1}$, with the corresponding covariance matrix $\boldsymbol{P}_{k-1}$, the predicted state at time *k* is calculated via (4.106) directly, or through a set of points drawn from the probability distribution of the estimated state vector, which is dependent on the assumed probability distribution of $\boldsymbol{w}_k$.
2) *Update step*: Once measurements $\boldsymbol{z}_k$ become available, the predicted state is updated using the measurements at time step *k* to estimate the state vector $\hat{\boldsymbol{x}}_k$ and the covariance matrix $\boldsymbol{P}_k$.

Several variants of the KF can be used depending on the level of nonlinearity in the system and on how the state statistics are propagated, such as [65], [73], [74]:

- The EKF linearizes the system's nonlinear equations around the current operating point, via a Taylor series expansion. It is a common method for implementing SE in mildly nonlinear systems, but its accuracy and applicability are limited by the quality of the linearization.
- The UKF, originally derived from the Unscented Transform (UT), improves upon the EKF by using deterministic sampling techniques to select a set of samples – referred to as sigma points – which represent the *a priori* state statistics to be propagated through the nonlinear system. UKF provides a more accurate approximation of the state probability distribution, particularly for highly nonlinear systems, while avoiding calculation of the derivatives of the nonlinear equations.
- The EnKF leverages a Monte Carlo-based sampling technique, where an ensemble of possible states is maintained, and each member of the ensemble is updated based on the system dynamics and available measurements. This method is particularly effective for large-scale systems with significant uncertainties, as it estimates the covariance of the states through the ensemble, providing a more computationally feasible solution than other KF variants for high-dimensional systems.
- Similar to EnKF, PFs approximate the state probability distribution using a set of particles, each representing a possible system state. These particles are propagated through the system's nonlinear dynamics, and their distribution is updated based on new measurements. PFs are very flexible and can handle highly nonlinear systems and non-Gaussian noise, but they can be computationally intensive.

4.10.3 Dynamic state estimation under quasi-steady operation

When DSE is applied to quasi-steady state operating conditions, the "dynamic" denomination may be misleading, as the system dynamics associated with the stability concept are assumed to be absent/negligible. Semantic arguments in the SE context over the meaning of DSE have led researchers to coin the terms Forecasting-Aided State Estimation (FASE) and Tracking State Estimation (TSE) [62], [75].

4.10.3.1 Forecasting-aided and tracking state estimation principles

In SSE methods, each measurement set is processed independently, disregarding any temporal correlation between successive states. However, as the system evolves over time, successive snapshots are not independent but are part of a continuous time evolution of the system. FASE takes advantage of this fact by constructing a dynamic model that links consecutive states through a forecasted state trajectory. The assumption of quasi-steady operating conditions in power systems leads to the concept of static-state dynamics, that is, the time evolution (or sequence) of steady-state bus voltage phasors, while disregarding transients [75]. In normal operation, power systems remain in a steady-state regime, with variables such as bus voltages, power flows, and transformer taps changing incrementally. FASE is designed to estimate this static-state dynamic behavior, incorporating the system's natural time evolution and providing more accurate state estimates, when the system undergoes small but continuous changes.

FASE is a particular application of DSE under quasi-steady conditions, where system states evolve slowly and are driven primarily by stochastic changes in demand and generation, simplifying the transition model to a linear equation. The typical FASE state-space model is written as [62]:

$$\boldsymbol{x}_{k+1} = \boldsymbol{F}_k \boldsymbol{x}_k + \boldsymbol{g}_k + \boldsymbol{w}_k \tag{4.108}$$

$$\boldsymbol{z}_k = \boldsymbol{h}(\boldsymbol{x}_k, \boldsymbol{p}) + \boldsymbol{e}_k \tag{4.109}$$

where $\boldsymbol{x}_k$ now represents only the algebraic state variables that specifically refer to bus voltage magnitudes and angles, $\boldsymbol{F}_k$ is the state transition matrix representing the linear evolution of states between time steps, and $\boldsymbol{g}_k$ is a trend vector, which incorporates the effects of control inputs $\boldsymbol{u}_k$.

TSE is an oversimplified version of FASE, where the state transitions are assumed to be minimal, represented by small random fluctuations. The TSE state-space model is expressed as:

$$\boldsymbol{x}_{k+1} = \boldsymbol{x}_k + \boldsymbol{w}_k \tag{4.110}$$

$$\boldsymbol{z}_k = \boldsymbol{h}(\boldsymbol{x}_k) + \boldsymbol{e}_k \tag{4.111}$$

TSE works well for systems that remain relatively unchanged over time but struggles to track any significant changes to state variables. With the increasing penetration of DERs and flexible loads, the evolution of states over time cannot be simply replaced by a white Gaussian noise [12], [52]. This scenario is further aggravated in the presence of changes in network topology and parameters owing to line or transformer switching or switching of capacitor banks or shunt reactors. As a result, it becomes a challenge to adopt TSE for practical applications.

4.10.3.2 Evolution of forecasting-aided state estimation

The concept of FASE emerged in the late 20th century as an extension of traditional SE methods. Early efforts began in the 1970s, with the aim of tracking the time evolution of the power system state using relatively simple models [63], [76]–[78]. These naive models lacked any genuine forecasting ability and used the most recent state estimate as a prediction for the next time step, assuming minimal state variation between consecutive time steps.

Despite the limitations of these early models, they established the foundation for further work in FASE. In particular, the need for a more sophisticated dynamic estimation process became evident, leading to the development of models that could better capture the time-varying nature of power systems. By the 1980s, innovation analysis was incorporated into FASE, where the difference between predicted and actual measurements (the innovation vector) was used to detect anomalies, including sudden variation of system states, bad data, and errors in network topology [79], [80]. More sophisticated dynamic models were proposed in [81], [82]; these models were adaptative in the sense that their parameters are estimated online – using exponential smoothing and KF techniques – according to identifiable patterns of system state temporal evolution. This led to improved forecasting accuracy and more efficient handling of anomalies.

In the late 1990s and early 2000s, significant strides were made with the introduction of Artificial Neural Networks (ANNs) and pattern analysis techniques in FASE [83]–[86]. The advances made, pertained to real-time topology identification through the pattern analysis of raw measurements – both analog and binary – and the utilization of normalized innovations in the form of ANN input variables for data debugging (identification of bad data and misconfigured network branches). Researchers have also explored the combination of fuzzy logic with FASE, particularly for handling rapid, large-scale load changes [87], [88]. Finally, improvements in bad data processing and pseudo-measurements provision were achieved by means of FASE: the solution to the open problem of bad data detection/identification in critical measurements and sets via innovation analysis [89]; the use of forecasted values as pseudo-measurements together with respective error covariances (weights in the WLS SE), automatically generated at the forecasting step [90].

4.10.3.3 FASE mathematical framework

The mathematical formulation of FASE is based on the state space model involving (4.108) and (4.109): the state transition (or state) and the measurement (or observation) equations, respectively. Eliminating the parameter vector $\boldsymbol{p}$ from the unknown variables and assuming that the states refer to only voltage phasors, the FASE state-space model becomes [62], [75], [81]:

$$\boldsymbol{x}_{k+1} = \boldsymbol{F}_k \boldsymbol{x}_k + \boldsymbol{g}_k + \boldsymbol{w}_k \tag{4.112}$$

$$\boldsymbol{z}_k = \boldsymbol{h}(\boldsymbol{x}_k) + \boldsymbol{e}_k \tag{4.113}$$

where subscript k denotes the discrete time instant t_k, $\boldsymbol{F}_k \in \mathbb{R}^{n \times n}$ is the diagonal state transition matrix for transition $t_k \to t_{k+1}$, vector $\boldsymbol{g}_k \in \mathbb{R}^n$ captures the trend of the state trajectory, $\boldsymbol{h}_k : \mathbb{R}^n \to \mathbb{R}^m$ is the vector of nonlinear functions relating the measurement vector $\boldsymbol{z}_k \in \mathbb{R}^m$ to the state vector $\boldsymbol{x}_k \in \mathbb{R}^n$, with $n < m$, random vectors $\boldsymbol{e}_k$ and $\boldsymbol{w}_k$ are the independent Gaussian measurement and transition errors, respectively, with $E(\boldsymbol{w}_k) = E(\boldsymbol{e}_k) = \boldsymbol{0}$, $Cov(\boldsymbol{w}_k) = \boldsymbol{Q}_k$ and $Cov(\boldsymbol{e}_k) = \boldsymbol{R}_k$.

To establish the FASE model, some important considerations on power system operations are usually assumed [75]:

- the time frame of interest is considered small, of the order of few minutes;
- a linear function properly represents the transition trajectory between consecutive states;
- control variables are not included in $\boldsymbol{g}_k$, since their effect is much faster than the adopted time frame.

Generally, the elements of the forecasting model parameters $\boldsymbol{F}_k$, $\boldsymbol{g}_k$ and $\boldsymbol{Q}_k$ are not known *a priori* and need to be estimated. FASE methods typically rely on historical time-series data to estimate these parameters. The most widely used forecasting techniques in FASE are time-series methods and statistical models, which have been adapted from general forecasting applications to fit the specific needs of power systems [75].

The exponential smoothing method, often employed in FASE, generates forecasts by taking weighted averages of past observations, with weights that decrease exponentially as the observations get older. A key advantage of exponential smoothing is its simplicity and ability to be converted into a state-space form, where the state transition matrix is derived from the smoothing parameters. Widely used approaches are exponential smoothing regression or recursive least squares [81], [82], [87], [91], [92]. The FASE algorithms that have been proposed so far and rely on exponential smoothing methods have considered the state transition matrix as diagonal. This means that no correlation between state variables is assumed. Further research is required to evaluate whether correlation contributes to a better state forecasting capability, and in view of the increase in computational burden, a possible inclusion of correlation should be carefully examined. Various FASE methods have also employed ANNs for state forecasting [85], [86], [89], [93]. ANNs are capable of modeling complex, nonlinear relationships between system states, which can be useful for predicting the state trajectory under quasi-steady conditions. However, the practical benefits of ANNs over traditional linear models have been limited, and further research is required to justify their computational complexity in real-time FASE applications.

The one-step ahead state forecast, denoted by $\hat{\boldsymbol{x}}_{k+1|k}$, is obtained using information on the system behavior up to time step *k*; this is also known as *a priori* state estimate. The parameters $\boldsymbol{F}_k$ and $\boldsymbol{g}_k$ are usually defined according to the Holt's two-parameter linear exponential smoothing method, due to its simple implementation [75]:

$$\begin{cases} \hat{\boldsymbol{x}}_{k+1|k} = \boldsymbol{A}_k + \boldsymbol{B}_k \\ \boldsymbol{A}_k = \alpha \hat{\boldsymbol{x}}_{k|k} + (1-\alpha)\hat{\boldsymbol{x}}_{k|k-1} \\ \boldsymbol{B}_k = \beta(\boldsymbol{A}_k - \boldsymbol{A}_{k-1}) + (1-\beta)\boldsymbol{B}_{k-1} \end{cases} \tag{4.114}$$

where $\boldsymbol{A}_k$ and $\boldsymbol{B}_k$ are the estimates of the level and the trend of the state variables, respectively, and α and β are the corresponding scalar smoothing parameters, with $(\alpha,\beta) \in [0,1]^2$. The level $\boldsymbol{A}_k$ is the weighted average of the *a posteriori* $\hat{\boldsymbol{x}}_{k|k}$ and *a priori* $\hat{\boldsymbol{x}}_{k|k-1}$ state estimates. The trend $\boldsymbol{B}_k$ is a weighted average of the estimated trend based on the level change $\boldsymbol{A}_k - \boldsymbol{A}_{k-1}$ and the previous estimate of the trend $\boldsymbol{B}_{k-1}$. Via mathematical manipulations (4.114) becomes [81]:

$$\begin{cases} \hat{\boldsymbol{x}}_{k+1|k} = \boldsymbol{F}_k \hat{\boldsymbol{x}}_{k|k} + \boldsymbol{g}_k \\ \boldsymbol{F}_k = \alpha(1+\beta)\boldsymbol{I} \\ \boldsymbol{g}_k = (1+\beta)(1-\alpha)\hat{\boldsymbol{x}}_{k|k-1} - \beta\boldsymbol{A}_{k-1} + (1-\beta)\boldsymbol{B}_{k-1} \\ \boldsymbol{A}_k = \alpha \hat{\boldsymbol{x}}_{k|k} + (1-\alpha)\hat{\boldsymbol{x}}_{k|k-1} \\ \boldsymbol{B}_k = \beta(\boldsymbol{A}_k - \boldsymbol{A}_{k-1}) + (1-\beta)\boldsymbol{B}_{k-1} \end{cases} \tag{4.115}$$

4.10.3.4 Extended Kalman filter-based FASE

FASE can be perceived as an extended WLS estimation, in the sense that the received measurements are processed together with the available *a priori* estimated (forecasted) state to produce the *a posteriori* estimated (filtered) state [75], [81].

We consider again the nonlinear FASE state space model of (4.112) and (4.113). The initial state vector $\boldsymbol{x}_0$, with mean $\boldsymbol{\mu}_0 = E\left[\boldsymbol{x}_0\right] = \hat{\boldsymbol{x}}_0$ and covariance $\boldsymbol{P}_0 = Cov(\boldsymbol{x}_0) = E[(\boldsymbol{x}_0 - \hat{\boldsymbol{x}}_0)(\boldsymbol{x}_0 - \hat{\boldsymbol{x}}_0)^T]$ needs to be provided by the conventional SSE. In the following we assume that the random vectors $\boldsymbol{w}_k$ and $\boldsymbol{e}_k$ are temporally uncorrelated (white noise), zero-mean random sequences with known covariances and both of them are uncorrelated with the initial state $\boldsymbol{x}_0$.

1) Prediction step:

Let $\hat{\boldsymbol{x}}_k$ and $\boldsymbol{P}_k$ be the *a posteriori* estimates of the state vector and its covariance matrix, respectively, at time t_k. By applying the conditional expectation operator on (4.112), the *a priori* estimate of the state vector $\tilde{\boldsymbol{x}}_{k+1} := \hat{\boldsymbol{x}}_{k+1|k}$ and its covariance matrix $\tilde{\boldsymbol{P}}_{k+1}$ are calculated as follows:

$$\tilde{\boldsymbol{x}}_{k+1} \equiv E[\boldsymbol{x}_{k+1} \,|\, \boldsymbol{z}_k] = E[\boldsymbol{F}_k \boldsymbol{x}_k + \boldsymbol{g}_k + \boldsymbol{w}_k \,|\, \boldsymbol{z}_k] = E[\boldsymbol{F}_k \boldsymbol{x}_k + \boldsymbol{g}_k \,|\, \boldsymbol{z}_k] = \boldsymbol{F}_k \hat{\boldsymbol{x}}_k + \boldsymbol{g}_k \tag{4.116}$$

Thus, the forecasting error is calculated as:

$$\boldsymbol{e}_{k+1}^f \equiv \boldsymbol{x}_{k+1} - \tilde{\boldsymbol{x}}_{k+1} = \boldsymbol{F}_k \boldsymbol{x}_k + \boldsymbol{g}_k + \boldsymbol{w}_k - (\boldsymbol{F}_k \hat{\boldsymbol{x}}_k + \boldsymbol{g}_k) = \boldsymbol{F}_k (\boldsymbol{x}_k - \hat{\boldsymbol{x}}_k) + \boldsymbol{w}_k \tag{4.117}$$

and the forecast error covariance is expressed as:

$$\tilde{\boldsymbol{P}}_{k+1} = E[\boldsymbol{e}_{k+1}^f (\boldsymbol{e}_{k+1}^f)^T] = \boldsymbol{F}_k E[(\boldsymbol{x}_k - \hat{\boldsymbol{x}}_k)(\boldsymbol{x}_k - \hat{\boldsymbol{x}}_k)^T] \boldsymbol{F}_k^T + E[\boldsymbol{w}_k \boldsymbol{w}_k^T] = \boldsymbol{F}_k \boldsymbol{P}_k \boldsymbol{F}_k^T + \boldsymbol{Q}_k \tag{4.118}$$

2) Correction step:

Using the measurement set $\boldsymbol{z}_k$ and the *a priori* state vector $\tilde{\boldsymbol{x}}_k$, the *a posteriori* estimated state vector $\hat{\boldsymbol{x}}_k$ may be obtained by solving the following WLS optimization problem with objective function $J(\boldsymbol{x}_k)$, at time instant t_k [81]:

$$\hat{\boldsymbol{x}}_k := \arg\min_{\boldsymbol{x}_k} J(\boldsymbol{x}_k) = \left(\boldsymbol{z}_k - \boldsymbol{h}_k(\boldsymbol{x}_k)\right)^T \boldsymbol{R}_k^{-1} \left(\boldsymbol{z}_k - \boldsymbol{h}_k(\boldsymbol{x}_k)\right) + \left(\tilde{\boldsymbol{x}}_k - \boldsymbol{x}_k\right)^T \tilde{\boldsymbol{P}}_k^{-1} \left(\tilde{\boldsymbol{x}}_k - \boldsymbol{x}_k\right) \tag{4.119}$$

For the case of an overdetermined nonlinear measurement model, that is, $\boldsymbol{z}_k = \boldsymbol{h}(\boldsymbol{x}_k) + \boldsymbol{e}_k$ with $\boldsymbol{z}_k, \boldsymbol{e}_k \in \mathbb{R}^m$, $\boldsymbol{x}_k \in \mathbb{R}^n$ and $m > n$, the first order optimality conditions will have to be satisfied at the minimum of $J(\boldsymbol{x}_k)$:

$$\nabla J(\boldsymbol{x}_k) = \frac{\partial J(\boldsymbol{x}_k)}{\partial \boldsymbol{x}_k} = -\boldsymbol{H}^T(\boldsymbol{x}_k) \boldsymbol{R}_k^{-1} \left(\boldsymbol{z}_k - \boldsymbol{h}(\boldsymbol{x}_k)\right) - \tilde{\boldsymbol{P}}_k^{-1} \left(\tilde{\boldsymbol{x}}_k - \boldsymbol{x}_k\right) = \boldsymbol{0} \tag{4.120}$$

where $\boldsymbol{H}(\boldsymbol{x}) = \dfrac{\partial \boldsymbol{h}(\boldsymbol{x})}{\partial \boldsymbol{x}}$ is the Jacobian matrix of $\boldsymbol{h}(\boldsymbol{x})$. Expanding the gradient $\nabla J(\boldsymbol{x}_k)$ around a current estimate $\boldsymbol{x}_k^{(i)}$ using a first-order Taylor series expansion, yields:

$$\nabla J(\boldsymbol{x}_k) \approx \nabla J(\boldsymbol{x}_k^{(i)}) + \nabla^2 J(\boldsymbol{x}_k^{(i)}) \left(\boldsymbol{x}_k - \boldsymbol{x}_k^{(i)}\right) \tag{4.121}$$

where $\nabla^2 J(\boldsymbol{x}) = \dfrac{\partial^2 J(\boldsymbol{x})}{\partial \boldsymbol{x}^2}$ is the Hessian matrix of $J(\boldsymbol{x})$. Ignoring the second-order derivatives of $\boldsymbol{h}(\boldsymbol{x})$ in calculating $\nabla^2 J(\boldsymbol{x})$ results in the following approximation:

$$\nabla^2 J(\boldsymbol{x}_k) \approx \boldsymbol{H}^T(\boldsymbol{x}_k) \boldsymbol{R}_k^{-1} \boldsymbol{H}(\boldsymbol{x}_k) + \tilde{\boldsymbol{P}}_k^{-1} \tag{4.122}$$

Using the Gauss-Newton iterative solution scheme, yields:

$$\left(\boldsymbol{G}(\boldsymbol{x}_k^{(i)}) + \tilde{\boldsymbol{P}}_k^{-1}\right) \Delta \boldsymbol{x}_k^{(i+1)} = \boldsymbol{H}^T(\boldsymbol{x}_k^{(i)}) \boldsymbol{R}^{-1} \left(\boldsymbol{z} - \boldsymbol{h}(\boldsymbol{x}_k^{(i)})\right) + \tilde{\boldsymbol{P}}_k^{-1} \left(\tilde{\boldsymbol{x}}_k - \boldsymbol{x}_k^{(i)}\right) \tag{4.123}$$

where superscript (i) denotes the iteration index, subscript k denotes the current time instant, $\boldsymbol{x}_k^{(i)}$ is the estimated state vector at the i-th iteration, $\Delta\boldsymbol{x}_k^{(i+1)} = \boldsymbol{x}_k^{(i+1)} - \boldsymbol{x}_k^{(i)}$ is the i-th incremental correction, and $\boldsymbol{G}(\boldsymbol{x}_k^{(i)}) := \boldsymbol{H}^T(\boldsymbol{x}_k^{(i)})\boldsymbol{R}_k^{-1}\boldsymbol{H}(\boldsymbol{x}_k^{(i)})$ is the SSE gain matrix.

Equation (4.123) corresponds to the Iterated Extended Kalman Filter (IEKF). The complete IEKF correction process for solving the FASE problem is presented in Algorithm 4.3. The Kalman gain $\boldsymbol{K}_k \in \mathbb{R}^{n\times m}$ and the covariance matrix of $\hat{\boldsymbol{x}}_k$, $\boldsymbol{P}_k = E[(\boldsymbol{x}_k - \hat{\boldsymbol{x}}_k)(\boldsymbol{x}_k - \hat{\boldsymbol{x}}_k)^T]$, are obtained post-estimation by:

$$\left(\boldsymbol{G}(\hat{\boldsymbol{x}}_k) + \tilde{\boldsymbol{P}}_k^{-1}\right)\boldsymbol{K}_k = \boldsymbol{H}^T(\hat{\boldsymbol{x}}_k)\boldsymbol{R}_k^{-1} \tag{4.124}$$

$$\boldsymbol{P}_k = \left(\boldsymbol{I} - \boldsymbol{K}_k\boldsymbol{H}(\hat{\boldsymbol{x}}_k)\right)\tilde{\boldsymbol{P}}_k \tag{4.125}$$

Algorithm 4.3: Iterated extended Kalman filter correction step at instant t_k.

1) Initialize the iteration index $i \leftarrow 0$ and use $\boldsymbol{x}_k^{(0)} \leftarrow \tilde{\boldsymbol{x}}_k$ as initial guess.

2) Calculate the inverse of the sparse *a priori* covariance matrix $\tilde{\boldsymbol{P}}_k^{-1}$

3) Calculate matrix $\boldsymbol{G}(\boldsymbol{x}_k^{(i)}) + \tilde{\boldsymbol{P}}_k^{-1}$

4) Calculate the right-hand side of (4.123), $\boldsymbol{H}^T(\boldsymbol{x}_k^{(i)})\boldsymbol{R}^{-1}\left(\boldsymbol{z} - \boldsymbol{h}(\boldsymbol{x}_k^{(i)})\right) + \tilde{\boldsymbol{P}}_k^{-1}\left(\tilde{\boldsymbol{x}}_k - \boldsymbol{x}_k^{(i)}\right)$.

5) Decompose $\boldsymbol{G}(\boldsymbol{x}_k^{(i)}) + \tilde{\boldsymbol{P}}_k^{-1}$ and solve (4.123) for $\Delta\boldsymbol{x}_k^{(i+1)}$.

6) Check for convergence:

If $\left\|\Delta\boldsymbol{x}_k^{(i+1)}\right\|_\infty \le \varepsilon$, where ε is the convergence tolerance, **then** $\hat{\boldsymbol{x}}_k \leftarrow \boldsymbol{x}_k^{(i)} + \Delta\boldsymbol{x}_k^{(i+1)}$ and terminate the algorithm. **Else**, $\boldsymbol{x}_k^{(i+1)} \leftarrow \boldsymbol{x}_k^{(i)} + \Delta\boldsymbol{x}_k^{(i+1)}$, $i \leftarrow i+1$ and return to Step 3.

7) Calculate the Kalman gain by solving (4.124) for $\boldsymbol{K}_k$.

8) Use (4.125) to calculate the a posteriori covariance matrix $\boldsymbol{P}_k$.

5. HYBRID POWER SYSTEM STATE ESTIMATION

In contemporary electric power transmission systems, the primary data sources for SE are the SCADA and WAMS systems. As outlined in Chapter 4, Conventional State Estimation (CSE) algorithms utilize voltage and current magnitude, as well as active and reactive power injection/flow measurements, gathered by the SCADA system via RTUs deployed at substations across the grid. While SCADA systems have relatively long data update intervals by today's standards and offer moderate measurement accuracy, their maturity, reliability, and widespread deployment make them a cornerstone of ECC operations [5], [94].

WAMS generally comprise dispersed PMUs and PDCs. Since their emergence in the 1980s, PMUs have evolved into indispensable tools for WAMS, delivering high-resolution GPS-synchronized snapshots of bus voltage and branch current phasors, along with measurements of frequency and ROCOF. The reporting rates of PMUs, which range from 10 to 240 frames per second depending on system specifications and manufacturer, far exceed those of SCADA systems [6], [95]. The inclusion of synchrophasor data in SE has been transformative, enhancing accuracy and performance for several reasons [95]:

- *Improved state estimate quality*: PMUs provide exceptionally accurate measurements, with magnitude errors around 0.1% and phase angle errors of approximately 0.001 radians, in steady-state conditions [4]. This precision enhances the reliability of SE results, offering operators better confidence in security assessments and providing higher-quality data for downstream control functions within the EMS.
- *Direct measurement of state variables*: Unlike RTUs, PMUs directly measure state variables, that is, the bus voltage phasors. This capability simplifies the mathematical formulation of the SE problem into a linear model, thereby reducing computational complexity and improving algorithmic efficiency.
- *Measurement synchronization*: GPS-synchronized timestamps ensure that measurements from different regions align temporally, enabling precise system-wide snapshots of operating conditions.
- *High reporting rates*: By leveraging advanced communication protocols, PMUs offer reporting rates up to 100 times faster than traditional RTUs. This rapid reporting is essential for monitoring fast-evolving system dynamics and improving operator responsiveness.

Despite these undisputable advantages, the deployment of PMUs or PMU-enabled IEDs remains somewhat limited, primarily due to economic and technical constraints – interoperability with legacy systems and costs related to hardware, installation, and communication infrastructure are all significant factors. Consequently, in most transmission systems, synchrophasor measurements alone are insufficient to attain full network observability for linear PMU-based SE. This has led to a continued reliance on SCADA systems, with synchrophasor data serving as complementary information. The coexistence of SCADA and WAMS thus remains a practical necessity, with hybrid approaches integrating RTU and PMU measurements to develop viable SE algorithms [9].

In this context, Hybrid State Estimation (HSE) techniques, which merge SCADA and PMU data, have garnered substantial research interest, reflected in an extensive body of literature. This Chapter provides an in-depth examination of the arising challenges and recent research advancements in the development and implementation of HSE algorithms for transmission systems. Furthermore, it identifies key research gaps and explores future opportunities in this evolving field.

5.1 Challenges in integrating multi-source data into state estimation

Integrating measurements from multiple systems notably improves the performance of SE, enhancing both precision and the handling of erroneous measurements, due to increased measurement redundancy. However, combining data from diverse sources is far from straightforward. Research on HSE identifies two primary categories of challenges:

1) *Different reporting rates and time-inconsistent data*: PMUs report measurements at significantly higher rates than SCADA systems. Moreover, data from different sources often arrive unsynchronized, a phenomenon known as measurement asynchronization or time skewness. This misalignment means that field measurements typically fail to represent a single, consistent time instance. Beyond the lack of synchronized timestamps in SCADA data, additional timing inconsistencies arise from communication delays that vary among sensors [8], [9].
2) *Variability in measurement types and accuracy levels:* The two measurement systems collect different types of data, creating implementation challenges as existing SE software often requires modifications to accommodate these variations. Numerical issues may also occur, for example during the initialization of the SE algorithm, when current phasor measurements are expressed in polar coordinates [96]. Furthermore, differences in sensor accuracy complicate the assignment of measurement weights; significant discrepancies in accuracy levels can adversely affect gain matrix conditioning and SE reliability [97].

To address these challenges, a variety of methods have been proposed. The subsequent Sections delve into these methods, providing detailed discussions of their strategies and effectiveness. Figure 5.1 illustrates the hierarchical classification of HSE methodologies, as proposed in [98]. SSE methods are categorized based on their scope and algorithmic processes relative to the challenges discussed above. Meanwhile, DSE methods are primarily classified according to their state space models, with further subcategories reflecting their unique contributions and mathematical foundations.

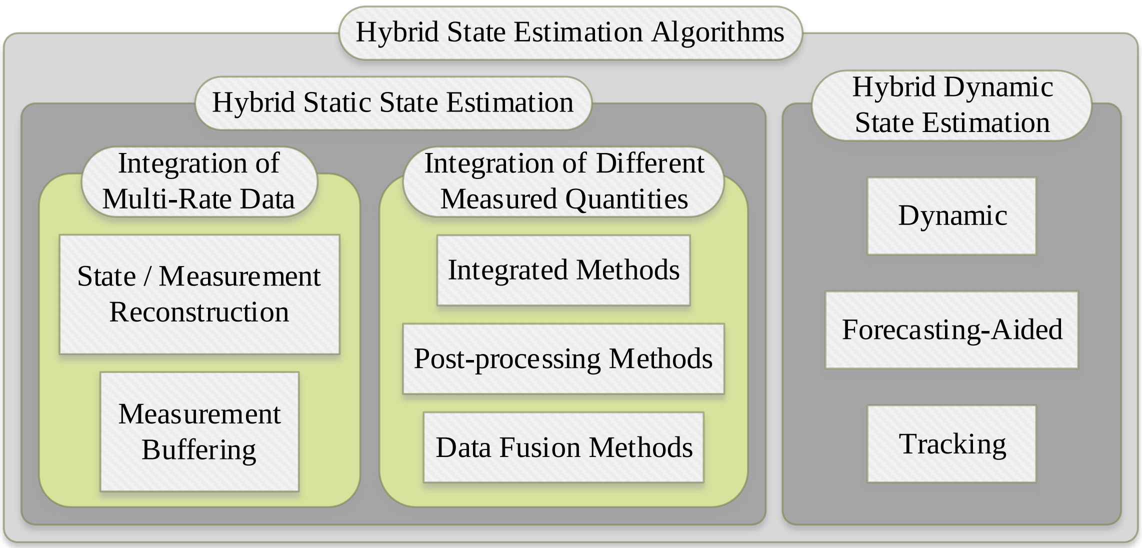

Figure 5.1: Proposed categorization of HSE methods.

5.2 Hybrid static state estimation

As discussed in Section 4.8.1, SCADA-based SSE remains the most widely implemented SE approach for transmission systems, being “static” in the sense that it disregards temporal correlations between measurements and states. By incorporating both SCADA and WAMS measurements, Hybrid Static State Estimation (HSSE) leverages RTUs as the primary data source, while the limited number of PMU measurements improves redundancy. Various HSSE methods have been developed to address the challenges highlighted in the previous Section, and these methods can be categorized based on their targeted issues.

5.2.1 Integration of asynchronous and multi-rate data

PMUs operate at significantly higher reporting rates than SCADA systems, resulting in multiple PMU scans being available between two consecutive SCADA updates, as illustrated in Figure 5.2. However, the system will likely be unobservable when only PMU measurements are available, on account of the limited number of PMUs installed. To address this, several methods have been proposed to mitigate the impact of measurement time skewness and restore system observability between successive SCADA measurement updates.

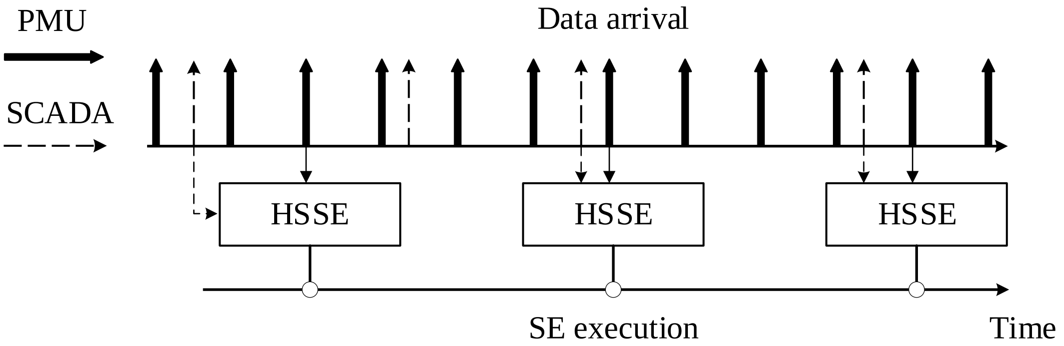

Figure 5.2: Effect of measurement asynchronization on state estimation.

5.2.1.1 Measurement reconstruction techniques

One common solution involves *measurement reconstruction*, wherein linear PMU-based SE is employed to track network states between SCADA updates, while nonlinear SE is executed when data from both PMUs and RTUs become available [99]–[103]. For instance, in [99], a linear SE approach combines refreshed synchrophasor data with power and voltage pseudo-measurements. These pseudo-measurements are derived from either fixed values – obtained during the last HSSE execution with both PMU and SCADA information – or recursively calculated values from the most recent PMU-based SE. In [100] and [101] PMU measurements are processed alongside voltage and current phasor pseudo-measurements from the PMU-unobservable subnetwork, calculated using the most recent state estimates. An alternative approach, proposed in [102], employs a hybrid estimation strategy that alternates between a WLS estimator (for simultaneous SCADA and PMU updates) and a robust Weighted Least Absolute Value (WLAV) estimator (for PMU-only updates). This method leverages PMU data and a minimal set of reconstructed RTU measurements to ensure full observability, similar to the strategies in [100] and [101]. To further enhance SE performance, [103] proposes a decentralized framework that partitions the network into phasor measurement islands – with a common GPS reference – and SCADA-observable sub-islands, comprising critical RTU measurements. This setup streamlines the application of robust HSSE methods to counter bad data and cyberattacks.

Alternative methods for addressing the limited PMU data between SCADA scans are presented in [104]–[107]. Work [104], introduces a distributed compressive sensing method to reconstruct RTU measurements using spatial and temporal correlations among recent state estimates. A classic WLS-based SE algorithm is then used to solve the SE problem, incorporating PMU-derived power flows, PMU-measured voltage magnitudes, and RTU data. In a robust HSSE approach uses processed PMU data as *a priori* information in a modified WLS-based SE. During intervals without SCADA updates, PMU-unobservable bus states are inferred using an interpolation matrix, while measurement weights dynamically adjust to changes in system conditions. In [106], a real-time recursion-correction linear

HSSE method processes asynchronous RTU and PMU data in a continuous stream. Between SCADA updates, PMU data and the latest SE results are recursively corrected, using multithreaded processing to optimize performance for large-scale systems. Another innovative method, proposed in [107], applies Sequential Quadratic Programming (SQP) to HSSE, leveraging reconstructed line-current pseudo-measurements from recent SE results to maintain observability when only PMU data are refreshed. By efficiently managing nonlinearities, SQP demonstrates strong performance in high-dimension, equality-constrained SE problems.

5.2.1.2 PMU data buffering

Buffering PMU measurements offers another solution to the challenges posed by multi-rate data. By leveraging the statistical properties of a set of consecutive PMU measurements, this approach aims to "sanitize" the PMU data within a specific time window (buffer), reducing the impact of noise and deviations caused by variations in system states on the processed measurements. The filtered PMU data is then used to perform SE upon receiving new SCADA measurements, making buffering particularly effective for periodic HSSE executions with intervals longer than the SCADA reporting period [108]–[111].

Recent studies have explored optimization strategies for PMU data buffering. In [108], the optimal buffer length is determined using hypothesis testing, while [109] evaluates three methods for optimizing buffer length by analyzing mean and variance shifts in PMU measurements. In [110], a procedure for considering temporal and spatial correlations in PMU measurement datasets for HSSE is proposed. Time series of PMU data are modeled using stationary vector autoregressive (VAR) models to filter out measurement noise. Similarly, [111] introduces a robust HSSE method that considers correlations among diverse measurement types to improve SE accuracy. This method applies the UT to calculate both self- and cross-correlations among SCADA measurements, with PMU correlations modeled as in [110].

5.2.2 Integration of different measured quantities

A crucial aspect of HSSE formulations involves the integration of phasors and conventional measurements into a unified estimator. Due to the inherent differences in the characteristics of each measurement type, directly incorporating phasor data into existing state estimators necessitates substantial modifications to EMS software. The various methods proposed for integrating data from different sensor types are generally categorized into three main groups, as outlined in [9] and illustrated in Figure 5.1: *Integrated HSSE methods (ISE), Post-processing HSSE methods (PSE)*, and *Fusion HSSE methods (FSE)*.

5.2.2.1 Integrated hybrid methods

ISE methods directly combine SCADA and PMU measurements into a single measurement model, as shown in Figure 5.3. Beyond the necessary modifications to existing SE algorithms within the EMS to incorporate phasor measurements, ISE approaches introduce several additional challenges, as detailed in the following.

The inclusion of current phasor measurements and substantial variations between SCADA and PMU measurement weights may lead to ill-conditioning of the gain matrix at flat start and cause poor algorithm convergence, or even divergence in extreme cases [97]. Various methods have been proposed to address these numerical issues [100], [112]–[115]:

- *Processing current phasors in rectangular coordinates*: In [112], SCADA and PMU measurements are jointly processed, with branch current phasors converted from polar to rectangular coordinates, thereby improving the conditioning of the gain matrix. This approach includes detailed descriptions of the employed state space model and covariance matrix calculation for current measurements based on error propagation theory. Similarly, a nonlinear WLS formulation of the ISE problem is presented in [113], which avoids numerical problems encountered at flat start or for lightly loaded lines, by representing current measurements in rectangular coordinates when necessary. Building on these works, [100] applies the matrix inversion lemma (Sherman-Morrison-Woodbury formula) to retain the structure of the conventional SCADA-based state estimator, while representing current phasors in rectangular form.

- *Conversion of current phasors to voltage phasor measurements*: In [114], the authors propose an approach of including only voltage phasor measurements, by expressing current measurement functions in terms of bus voltage phasors adjacent to PMU-measured buses. The state vector comprises bus voltage phasors and the branch currents measured by PMUs in polar form, while equality constraints are used to link PMU buses to their respective neighboring buses.
- *Regularization techniques*: To address numerical instability in WLS, [115] employs a regularization method based on least squares optimization, using the L-curve method for parameter selection, providing robustness and correlation management across measurements. Zero injections are treated as equality constraints in a post-estimation step.

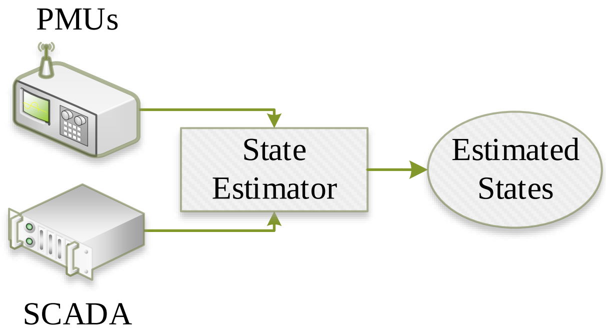

Figure 5.3: Structure of integrated hybrid state estimation methods.

Numerous formulations contribute to the applicability of ISE and improve its performance by leveraging linear models, decentralized approaches, or solutions in the complex domain:

- *Linear models*: Work [116] proposes converting power measurements into equivalent current phasors, forming a linear iterative WLS-based ISE with constant Jacobian and gain matrices, thereby reducing SE execution time. A non-iterative linear WLS approach in [117] transforms SCADA measurements into voltages and currents in rectangular form, with equality constraints modeling zero injections. Robust linear methods have also appeared, such as those in [118]–[120]. In [118] a robust, linear LAV-based ISE is presented, solved non-iteratively through linear programming. Work [119] also introduces a linear robust ISE, employing a Schweppe-type M-estimator with Huber loss function. The method of iteratively reweighted least squares (IRLS) is used to maximize the likelihood function in the M-estimator. In [120], the authors propose two LAV-based robust ISE methods, both leveraging linear measurement models. The first method is formulated as a single linear programming problem, while the second builds upon an alternative LAV-based estimator that can be solved by gradient-based methods. The equivalent circuit formulation (ECF) in [121] represents SCADA and PMU measurements using linear circuits, allowing SE to be calculated through a linear system of optimality conditions. Further enhancements of this method in terms of practical implementation are presented in [122], including circuit models for all possible combinations of RTU measurements, zero injections, and cases with unmonitored buses.
- *Multi-area approaches*: Decentralized methods like [123] propose multi-area ISE, in which boundary bus state estimates are obtained through PMU-based SE, and are then incorporated as constraints in the local SCADA-based SE of each area. A decentralized solution using the gossip-

based Gauss-Newton algorithm is proposed in [124], enabling parallel computation across subareas, with dynamic adjustment of measurement weights to improve robustness against bad data. In [125] the authors propose a fully distributed Gauss-Newton approach, in which each area carries out the SE locally and independently, relying on local measurements and limited communication with neighboring areas. Alternatively, [126] proposes an iterative multi-area ISE, which executes SE sequentially across subareas, addressing the problem of slack bus angle referencing with pseudo-measurements from boundary bus state estimates.

- *Complex domain solution*: Various papers have also addressed the solution of the ISE problem in the complex domain, which has been proven to be computationally advantageous. Publication [127] first presents an implementation of the WLS-based ISE problem using complex Taylor series expansion, based on Wirtinger calculus. It is worth noting that current measurements do not require any special handling, unlike ISE implementations over the real domain. Subsequent works [128] and [129] extend these formulations to include equality constraints and nonlinear least-squares methods.

5.2.2.2 Post-processing hybrid methods

Post-processing HSSE (PSE) methods strategically decouple RTU and PMU measurements in the SE problem. This typically involves executing a conventional SCADA-based SE followed by a linear, PMU-based SE – or vice versa – ensuring the two datasets are represented in distinct measurement models (Figure 5.4). By separating the different measurement sets, PSE approaches enable the incorporation of phasor measurements with minimal modification to existing SE frameworks.

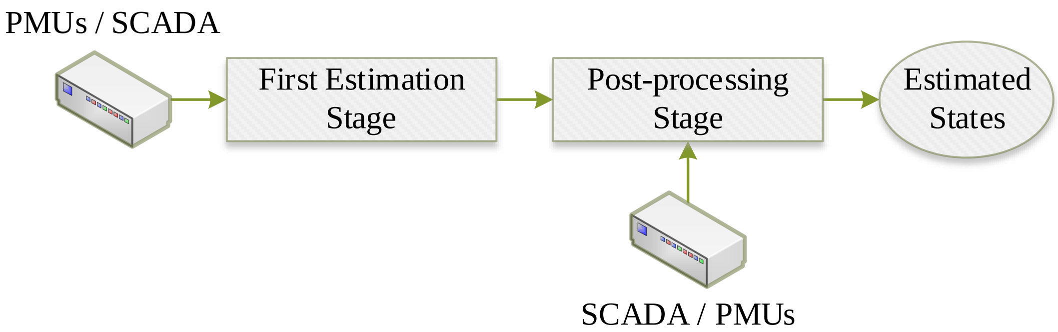

Figure 5.4: Structure of post-processing hybrid state estimation methods.

Several studies propose innovative ways to integrate phasor data into a post-processing SE phase [130]–[135]. Works [130]–[133]suggest embedding the estimated states from SCADA-based SE into the measurement vector of a subsequent PMU-based linear SE, using rectangular coordinates for phasor measurements. Building on this concept, [134] experiments with hybrid configurations that mix polar and rectangular representations for measurements and states. In [135], a similar cascaded architecture is employed, where the initial SE results serve as *a priori* state information for the post-processing PMU-based estimation phase.

An alternative approach in [136] proposes a PSE scheme, in which a linear state estimator first processes only synchrophasors in rectangular coordinates to estimate the states of the PMU-observable subnetwork. These results are then incorporated as either highly accurate measurements or equality constraints, along with available RTU data, into a nonlinear WLS SE in polar form to compute the system-wide state vector. Expanding on this framework, [137] directly incorporates PMU-observable bus states into the final estimated state vector. Additionally, [97] addresses potential numerical challenges by executing a LAV-based SE with PMU measurements only, and then a WLS-based post-processing step, as in [136].

A decentralized approach to PSE is explored in [138] partitioning the network into "linear" and "nonlinear" areas based on the prevalence of PMUs and RTUs, respectively. For "linear" areas, a linear WLS PMU-based SE is employed to estimate local states, leveraging the faster reporting rate of PMUs. Conversely, conventional SCADA-based SE methods are applied in "nonlinear" areas. As the linear SE is solved at a higher rate, the estimated states of boundary buses in "linear" areas are treated as highly weighted pseudo-measurements for the nonlinear SE.

5.2.2.3 Fusion hybrid methods

The fusion HSSE (FSE) share structural similarities with PSE algorithms, as both utilize separate SE modules for different measurement sources. However, unlike PSE, FSE executes these estimators in parallel and combines their outputs through a post-estimation fusion scheme to derive the final state estimate (Figure 5.5). The two state estimates are typically fused using the Bar-Shalom-Campo formula [139]:

$$\hat{\boldsymbol{x}} = \boldsymbol{W}_S \hat{\boldsymbol{x}}_S + \boldsymbol{W}_P \hat{\boldsymbol{x}}_P \tag{5.1}$$

where $\hat{\boldsymbol{x}}_S$ and $\hat{\boldsymbol{x}}_P$ are the estimated state vectors from the SCADA- and PMU-based modules, respectively; $\boldsymbol{W}_S$ and $\boldsymbol{W}_P$ are the weighting factors derived from the covariance matrices of SCADA and PMU measurements, respectively, and $\hat{\boldsymbol{x}}$ is the fused state vector. The primary advantage of FSE formulations lies in the ability to execute both modules in parallel, thereby reducing SE execution times. However, the approach is contingent on complete PMU observability, a condition that remains impractical in most power systems.

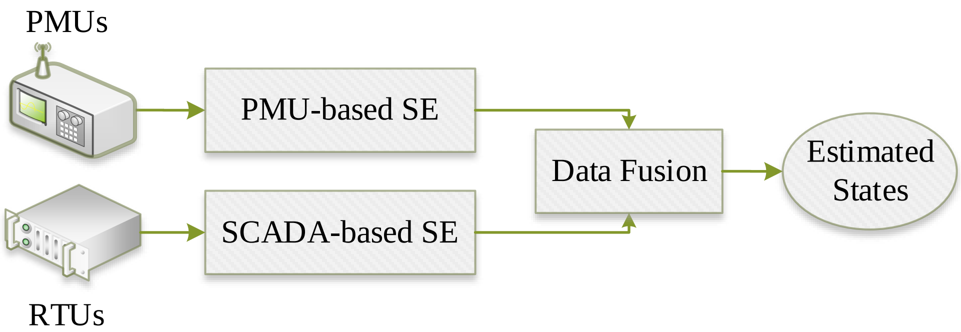

Figure 5.5: Structure of data fusion-based hybrid state estimation methods.

Work [140] introduces a multi-stage parallel SE architecture that optimally combines SCADA- and PMU-based estimation outputs using (5.1) that incorporates *a priori* information to attain complete PMU observability. Work [141] builds on this approach, presenting an accelerated FSE algorithm that improves execution times by leveraging parallel processing of RTU and PMU measurements and expediting the bad data handling process. References [142], [143] propose robust FSE methods. In [142], a data fusion architecture is developed where SCADA and PMU measurements are separately processed by BD-resilient maximum correntropy-based estimators. Work [143] has devised a robust FSE framework that accounts for non-Gaussian measurement noise and the issue of measurement time skewness. This method employs robust Mahalanobis distances in conjunction with a statistical test to optimize buffering length and weight assignment for PMU measurements. A Schweppe-type Huber generalized MLE is then used to filter out non-Gaussian noise and suppress the effects of measurement outliers. In [144], a distributed FSE strategy is introduced using a multi-stage approach, where SCADA- and PMU-based SE modules compute local state vectors separately and in parallel. To address PMU-observability limitations, a local state vector extension is applied, enabling both SCADA- and PMU-based estimators to obtain SE results for the same bus sets within each sub-area. Consistency in SE results is maintained across overlapping regions through state estimate exchanges between neighboring estimators.

5.2.3 Summary

This Subsection reviewed the development and implementation of various HSSE methods. One of the primary challenges addressed by these methods is the issue of incomplete observability, which arises from the limited availability of PMU measurements, between successive SCADA scans. To enable rapid SE execution, most approaches leverage either linear WLS-based algorithms or alternative non-WLS methods optimized for faster processing. When gaps in observability arise, predictions or reconstructions of unobservable states and SCADA measurements from prior SE executions are employed to restore full system observability, thus ensuring that SE results remain accessible within the EMS. Additionally, measurement buffering methods can be applied when both SCADA and PMU data are available.

The various HSSE techniques have also been categorized based on their mathematical modeling and strategies for integrating different measurement types, into ISE, PSE and FSE methods. Although ISE methods may encounter numerical instability under certain conditions and require significant modifications to existing SE software, extensive research has produced formulations that are easier to implement, numerically stable, and computationally efficient. PSE approaches effectively process PMU measurements separately from SCADA-based SE algorithms, using pre- or post-processing estimation modules. These methods are well-suited for decentralized implementations, although challenges related to data exchange between estimation stages or across substations and ECCs can hinder their efficiency. FSE approaches integrate outputs from SCADA- and PMU-based modules via a post-estimation fusion process. While these methods demonstrate strong potential for parallel processing, their reliance on complete PMU observability – a condition rarely achieved in practice – presents a significant limitation. To mitigate this, historical (*a priori*) data or pseudo-measurements are often employed to fill observability gaps, though this can complicate implementation.

5.3 Hybrid dynamic state estimation

The majority of state estimators currently used in modern ECCs rely on steady-state power system models, which do not account for time-dependent system operating conditions and dynamics. This constraint stems largely from the unsynchronized and low-resolution data provided by traditional SCADA systems [62]. However, the growing deployment of PMUs now enables the development of Hybrid Dynamic State Estimation (HDSE) techniques that combine both conventional SCADA and synchrophasor measurements, while capturing the temporal dependencies of system states [145].

The HSSE methods examined in Section 5.2 are static in the sense that a) each estimate of the state vector corresponds to a single system-wide measurement set, b) they are executed no faster than the SCADA reporting rates, and c) they neglect dynamic modelling of power system components. HSSE is generally effective under quasi-steady conditions, where system changes occur gradually; in these scenarios, conventional SCADA measurements are sufficient for SE, with PMU measurements enhancing accuracy and robustness as needed [60]. However, under transient or rapidly changing conditions, PMUs often become the primary reliable measurement source for SE, while low-resolution SCADA data can still be integrated to enhance measurement redundancy [61].

Implementing HDSE methods presents several challenges similar to those encountered in HSSE, namely the integration of asynchronous measurements with varying reporting rates, robustness against corrupted or delayed data, and the handling of heterogeneous and potentially correlated data sources. In the following, HDSE methods have been divided with respect to the inclusion of power system dynamics in their adopted state space model into the three major categories, according to Chapter 4.10: DSE, FASE and TSE methods.

5.3.1 Hybrid dynamic state estimation methods

DSE aims to model and track the internal state dynamics of power system components, particularly under transient operating conditions. To achieve this, the DSE framework employs a state transition model that captures the electromechanical or electromagnetic processes involved in these dynamics. PMUs play a critical role in DSE due to their high reporting rates, which are ideal for observing electromechanical transients [145].

In typical DSE approaches, the state vector is augmented to include the internal states of various system components, such as synchronous machines and dynamic loads. The continuous-time nonlinear state space model used in DSE is commonly employed in transient stability analysis and incorporates control inputs, network parameters, and (in)equality constraints. The discretized DSE state-space model is rewritten here for convenience:

$$\boldsymbol{x}_{k+1} = \boldsymbol{f}\left(\boldsymbol{x}_k, \boldsymbol{u}_k, \boldsymbol{p}\right) + \boldsymbol{w}_k \tag{5.2}$$

$$\boldsymbol{z}_k = \boldsymbol{h}\left(\boldsymbol{x}_k, \boldsymbol{u}_k, \boldsymbol{p}\right) + \boldsymbol{e}_k \tag{5.3}$$

where the quantities in (5.2) and (5.3) have already been defined in Subsection 4.10.2.2.

The estimation of dynamic states and system parameters in DSE frequently relies on the KF framework. UKF-based approaches [146]–[149] have established DSE frameworks under the presence of multi-rate data from RTUs and PMUs for tracking the dynamic system state during transient operating conditions. In [146], the dynamic state space model is discretized with sampling periods tailored to the reporting rates of each measurement system. The SCADA and PMU measurement models are then decoupled, allowing distinct estimators to be applied to each model, and the final estimated state is derived using a fusion process, such as (5.1). In [147], a UKF-based covariance intersection method is utilized to perform multi-rate data fusion.

Reference [148] introduces a discrete-time state transition model derived from an ANN trained for short-term load forecasting. Here, the DSE problem is solved using a dual-UKF approach, considering the interactions between the state vector and the dynamic power system model. The different reporting rates of SCADA and PMUs are addressed using a parameterized process model and a state reconstruction technique. Extending this method, [149] incorporates the dynamic state variables of synchronous machines and distributes the DSE solution across a multi-agent system, to improve scalability for large-scale power systems.

In [150], a multi-scale SE framework is proposed, which effectively enables the integration of SSE and DSE in EMS. The system is monitored in real-time through Singular Spectrum Analysis (SSA)-based change point detection, enabling the dynamic transition between static and dynamic estimation processes. A robust HSSE algorithm is initially applied for baseline monitoring, and, if a disturbance is detected by the SSA, the HSSE results are used to initialize a PMU-based DSE algorithm for real-time monitoring of transient conditions.

5.3.2 Hybrid forecasting-aided state estimation methods

Although they share mathematical foundations with DSE, FASE methods are designed to analyze quasi-steady operating conditions rather than capturing dynamic states, as elaborated in Section 4.10.3. The primary objective of FASE is to incorporate temporal correlations between state estimates into the SE problem. Pioneering work on hybrid FASE methods is presented in [151], combining the concepts of unscented filtering and SE. This derivative-free FASE approach updates the state transition model parameters using Holt's linear exponential smoothing algorithm and applies the UT to improve estimation accuracy.

Papers [152]–[156] address the synchronization of diverse data sources in FASE methods. Ref. [152] proposes a robust UKF algorithm that combines maximum correlation and interpolation techniques to synchronize PMU and SCADA data and leverages a strong tracking UT algorithm to handle gross measurement errors. In [153], an EKF-based time-alignment algorithm addresses irregular sampling and random delays. In [154], the unscented Rauch–Tung–Striebel (URTS) optimal smoothing algorithm is used to mitigate the effects of time skewness by efficiently re-estimating past states based on more recent measurements. Paper [155] introduces a two-stage framework where an initial SCADA-based SE provides a baseline state estimate, followed by the update of posterior distributions with PMU data, based on Bayesian inference. In [156], random delays between SCADA updates are handled by fusing unsynchronized SE outputs through a covariance intersection approach.

Papers [157]–[160] address FASE methods designed to handle missing data. In [157], an EKF-based FASE framework is proposed to handle missing RTU data. The SE problem is formulated as a constrained optimization task, with PMU measurements treated as inequality constraints, and solved using the Particle Swarm Optimization (PSO) algorithm. A multi-area FASE approach for large power grids is proposed in [158], where a modified distributed KF independently estimates local states while accounting for missing measurements. Inter-subsystem communication is achieved through internodal transformation theory. Work [159] presents a CKF-based FASE for state prediction during periods of missing PMU data, employing Holt's smoothing technique. In [160], spherical cubature and Gaussian quadrature rules are applied to estimate prior and posterior probability densities of state and measurement spaces. Between SCADA scans, state forecasting is conducted similarly to [159].

Efficient computational strategies for large-scale systems are discussed in [161]–[163]. In [161], a GPU-based massively parallel FASE is introduced to expedite FASE solution for large-scale systems, applying a two-level EKF approach. Work [162], presents an ANN-assisted dual-UKF FASE algorithm using a multi-agent framework, where a dynamic ANN develops a discrete-time state transition model for short-term load forecasting. The UKF estimates both the state vector and dynamic ANN parameters. Similarly, [163] proposes a distributed CKF algorithm for FASE in large-scale systems, enabling parallel SE execution in non-overlapping sub-areas to reduce computational and communication demands, eliminating the need for a central coordinator.

Post-processing FASE methods are explored in [164], [165]. In [164], a KF-aided sequential FASE method is proposed, where a PMU-based linear SE serves as the first stage, followed by an iterative stage combining SCADA data with pseudo-measurements from the first stage. A recursive KF uses consecutive PMU scans to increase pseudo-measurement accuracy. Likewise, [165] proposes a two-stage FASE, where PMU data along with a UKF-based prediction of SCADA measurements are utilized to obtain the SE solution at intervals between two successive SCADA scans.

5.3.3 Hybrid tracking state estimation methods

Tracking SE (TSE), often discussed alongside FASE, is a simplified variant that assumes minimal random deviations in the state vector over time. In [166] the effects of time skewness between simultaneously processed RTU and PMU data are addressed for TSE implementation. This approach comprises three main steps: prediction, innovation analysis, and correction. Predicted SCADA measurements are employed to ensure system observability, while a combined analysis of PMU measurement variations and innovation vectors distinguishes abrupt system state changes from gross measurement errors. The correction step then solves a constrained least-squares optimization problem to refine state estimates.

Parallelization and performance improvements for TSE are explored in [167], presents a decentralized UKF-based method incorporating a consensus algorithm for multi-area TSE. The UKF performs TSE locally within each non-overlapping power system subarea, while the consensus algorithm enables information exchange between neighboring subareas, ensuring cohesive SE results across the entire system.

A TSE approach considering the temporal aspects on the estimation process within a maximum correntropy-based EKF is proposed in [168]. Using a nonparametric probabilistic model to represent state variables within the kernel density estimation framework, this method incorporates sudden state transitions as non-Gaussian process noise. To mitigate the impact of suspect BD, a novel strategy to adjust the size of Parzen windows in the kernel estimation is introduced.

The issue of correlated prediction and measurement errors is addressed in [169], which proposes a KF-based TSE method for joint state and parameter estimation, This approach uses adaptive filtering to enhance its adaptability in dynamic conditions. The estimation problem is formulated as two inter-linked linear subproblems focused on state and parameter tracking, respectively.

5.4 Overview of literature gaps

This Section identifies key challenges in current hybrid static and dynamic SE research and suggests potential directions for future advancements.

1) *Numerical stability and convergence*: Despite significant progress in HSE methods, critical challenges remain in ensuring numerical stability and convergence. Differences in data fidelity and measurement variances can affect HSE algorithms, particularly under low-observability or weak redundancy scenarios. Decoupling SCADA and PMU measurement models – within static or dynamic SE frameworks – has shown to enhance convergence and numerical conditioning. However, this introduces trade-offs in terms of optimality, increased inter-process communication, and complexity in maintaining system observability. There is a pressing need to develop robust HSE frameworks that address these trade-offs holistically, particularly for multi-area grids with limited PMU penetration.
2) *Diverse reporting rates*: The fusion of multi-rate SCADA and PMU measurements remains a pivotal challenge. Since SCADA and other unsynchronized data sources (e.g., from FACTS controllers and DERs) rarely provide updates at regular intervals, SE methods must adapt to unsynchronized, multi-rate, and multi-sensor environments. Existing HSE algorithms are largely developed for either synchronized or uniformly sampled data streams, making them unsuitable for such applications. Promising approaches include designing HSE algorithms that operate independently of reporting rates or utilizing measurement buffering and statistical trend analysis to integrate low-resolution data into real-time SE. Foundational work leveraging extreme learning machines and Bayesian SE offers a strong starting point [170], [171].
3) *Robustness*: The increasing reliance on HSE frameworks introduces heightened vulnerability to Bad Data (BD), cyberattacks, and communication failures. Traditional WLS-based estimators are ill-equipped to handle such anomalies, often resulting in incorrect or divergent estimates. [172]. While robust estimation methods and anomaly detection techniques – such as LAV, Huber estimators, and machine learning classifiers – offer promising results, they often face scalability, latency, and integration issues within the EMS [102], [115]. There is a critical need for lightweight, real-time-capable robust HSE frameworks that maintain compatibility with existing WLS architectures while providing strong resilience against malicious data injection and systemic sensor failures [173]–[175].
4) *Performance optimization*: Real-time SE in modern power systems must scale to handle massive measurement volumes generated by SCADA and PMU deployments. Centralized HSE frameworks often struggle with computational delays and fail to meet timing constraints in large-scale or multi-area systems. Distributed SE architectures offer a promising solution by parallelizing estimation across subareas, yet face challenges in maintaining estimation quality under communication delays, missing data, and subarea observability constraints. Future research should focus

on developing effective coordination at boundary buses, resilient data exchange protocols, and adaptive subarea communication schemes [176], [177].

5) *Measurement model*: Enhancing the HSE measurement model is a key area for future research. Traditional measurement models assume Gaussian, stationary, and uncorrelated noise, which is often invalid in real-world settings, with noise statistics becoming even more complex when multiple data sources are integrated [178]–[180]. Additionally, the increasing integration of FACTS, HVDC, and DERs introduces new network modeling challenges, necessitating adjustments in both measurement models and parameter estimation techniques. Advanced mathematical formulations are needed to accommodate diverse combinations of system components and measurement data, broadening the scope of current SE modeling frameworks.

6) *State transition models*: DSE methods should evolve with more accurate and detailed state transition models. To obtain more reliable state estimates, state prediction and filtering must be made robust against the uncertainties inherent in power systems. Techniques like pattern recognition could help capture the effects of stochastic components, such as DERs. Multi-area, numerically robust, and efficient data-driven DSE methods represent promising directions for future exploration [181], [182]. Testing and validating DSE methods with real-world field data is also imperative, particularly under transient conditions where PMU accuracy can decline. Existing static state estimators could benefit significantly in terms of measurement redundancy by incorporating simple state space models, derived from TSE or FASE methods. To improve upon such methods, future research could consider the simultaneous topology and parameter estimation, the correlation between different PMU channels and successive measurement scans, as well as more advanced techniques for state forecasting and state transition modeling.

6. Hybrid Static State Estimators under Limited PMU Availability

According to Chapter 5, it has now been well-established that the enrichment of the existing measurement profile of SE with PMU data significantly enhances its performance by improving precision and measurement redundancy. However, integrating data from diverse sensors is a non-trivial process. The integration of SCADA and WAMS measurements in HSE algorithms has been extensively researched, resulting in a variety of formulations designed to combine phasor measurements with conventional data. These methods can be broadly classified into three categories, as outlined in Subsection 5.2.2, namely *integrated SE (ISE), post-processing SE (PSE)*, and *fusion SE (FSE) methods*.

ISE methods directly combine SCADA and PMU measurements into a single SE problem [112]. The concept of PSE is often employed as an alternative to ISE, aiming to decouple the RTU and PMU measurements using a cascaded SE architecture, which usually requires minimal modification of the existing SE software. However, PSE methods yield suboptimal results compared to their ISE counterparts, as they do not process SCADA and PMU measurements simultaneously. Similar to PSE, the FSE algorithms also utilize separate SE modules for each measurement type, and their estimates are combined in a post-estimation fusion scheme to produce the final solution. The main advantage of these methods is the ability to execute the two modules in parallel, leading to reduced computation times. Nevertheless, these methods operate under the assumption that the network is entirely observable through PMU measurements, otherwise the inclusion of pseudo-measurements or *a priori* state information is necessary to attain PMU-observability.

This Chapter first presents an equality-constrained WLS-based HSSE algorithm that focuses on addressing the challenge of simultaneous utilization of diverse measurement types. The method builds on the well-established Hachtel's augmented matrix approach [183], and the SE framework of [100], offering several notable advantages [184]:

1) The SCADA and PMU measurement models are formulated independently; thus, the proposed method is flexible in the sense that it is suitable for ISE, PSE, and FSE implementations, depending on the capabilities and requirements of the EMS.
2) Certain assumptions regarding the optimality and practical implementation of PSE and FSE methods are alleviated by using the proposed formulation of the HSE problem: the PSE algorithm retains its optimal estimation property, as it derives directly from the ISE algorithm, and the FSE algorithm is viable even in partially PMU-observable systems, without necessitating the inclusion of forecasts, pseudo-measurements or any changes to the existing conventional state estimators.
3) The devised method delivers promising results, on par with the optimal ISE methods [112], [113], in terms of accuracy and convergence, while providing state estimates of the highest quality among recently proposed WLS-based PSE and FSE methods, without significantly increasing computational demands.
4) The FSE implementation can leverage the linear formulation of the PMU measurement model in rectangular coordinates to reduce the nonlinearity and nonconvexity of the problem.

Subsequently, with respect to power system modeling and measurement model refinement, this Chapter discusses:

- A unified equality-constrained HSSE algorithm that explicitly models classic HVDC links and integrates them into the measurement model, using SCADA and PMU measurements from the AC network and measurements from the DC link [185].
- The impact of including different current phasor measurement schemes on the equality-constrained WLS HSSE method, by investigating its performance in terms of convergence and accuracy when

using current flow or injection data, as well as a mix of both. Additionally, practical considerations related to technical installation issues, such as the circuit-level measurement point and the utilization of instrument transformers, are elaborated [186].

6.1 Classic hybrid state estimation state space model

Assuming an N-bus power system and a measurement set (MS) comprising m_s SCADA measurements (bus voltage magnitudes, branch power flows, and bus power injections), m_p PMU measurements (complex bus voltages and currents) provided by PMUs, and m_z zero injections, the HSE measurement model is formulated as [32], [38]:

$$\begin{bmatrix} \boldsymbol{z}_s \\ \boldsymbol{z}_p \end{bmatrix} = \begin{bmatrix} \boldsymbol{h}_s(\boldsymbol{x}) \\ \boldsymbol{h}_p(\boldsymbol{x}) \end{bmatrix} + \boldsymbol{e} \qquad \mathbf{0} = \boldsymbol{c}(\boldsymbol{x}) \tag{6.1}$$

where $\boldsymbol{z}_s \in \mathbb{R}^{m_s}$ $(\boldsymbol{z}_p \in \mathbb{R}^{m_p})$ represents the vector of SCADA (PMU) measurements, $\boldsymbol{h}_s(\boldsymbol{x})$ $(\boldsymbol{h}_p(\boldsymbol{x}))$ is the vector of functions relating SCADA (PMU) measurements to the unknown state vector $\boldsymbol{x} \in \mathbb{R}^n$, with $m = m_s + m_p > n = 2N$, $\boldsymbol{e} \in \mathbb{R}^m$ is the vector of normally distributed and uncorrelated measurement errors with $E(\boldsymbol{e}) = \mathbf{0}$ and $Cov(\boldsymbol{e}) = \boldsymbol{R} = \begin{bmatrix} \boldsymbol{R}_s & \mathbf{0} \\ \mathbf{0} & \boldsymbol{R}_p \end{bmatrix}$, where $\boldsymbol{R}_s$ $(\boldsymbol{R}_p)$ is the diagonal covariance matrix of the SCADA (PMU) measurements, and $\boldsymbol{c}: \mathbb{R}^n \to \mathbb{R}^{m_z}$ denotes the vector of functions modeling zero current injections.

Assuming additive Gaussian measurement noise, the solution of the SE problem, that is, the estimated state vector $\hat{\boldsymbol{x}}$, is obtained via maximization of the log-probability function of the observations $\boldsymbol{z}$, resulting in the following WLS optimization problem with objective function $J(\boldsymbol{x})$ [38]:

$$\begin{aligned} &\hat{\boldsymbol{x}} := \arg\min_{\boldsymbol{x}} J(\boldsymbol{x}) = \boldsymbol{e}^T \boldsymbol{R}^{-1} \boldsymbol{e} \\ &\text{s.t. } \boldsymbol{c}(\hat{\boldsymbol{x}}) = \mathbf{0} \end{aligned} \tag{6.2}$$

The state vector $\boldsymbol{x}$ is expressed in either polar or rectangular coordinates, with its i-th entry written as $\boldsymbol{x}_i = [V_i \ \ \delta_i]^T$ or $\boldsymbol{x}_i = [V_{\mathrm{R},i} \ \ V_{\mathrm{I},i}]^T = [V_i \cos\delta_i \ \ V_i \sin\delta_i]^T$, where $\tilde{V}_i = V_i \angle \delta_i$ is the voltage phasor at bus i, and subscripts R and I denote its real and imaginary parts, respectively.

6.2 Proposed hybrid static state estimation formulation

The classic HSE model (6.1) can be equivalently written as:

$$\begin{aligned} \boldsymbol{z}_s &= \boldsymbol{h}_s(\boldsymbol{x}) + \boldsymbol{e}_s \\ \boldsymbol{z}_p &= \boldsymbol{h}_p(\boldsymbol{x}) + \boldsymbol{e}_p \\ \mathbf{0} &= \boldsymbol{c}(\boldsymbol{x}) \end{aligned} \tag{6.3}$$

where vectors $\boldsymbol{e}_s \in \mathbb{R}^{m_s}$ and $\boldsymbol{e}_p \in \mathbb{R}^{m_p}$ are now the normally distributed SCADA and PMU measurement errors, with zero mean and diagonal covariance matrices $\boldsymbol{R}_s$ and $\boldsymbol{R}_p$, respectively.

The solution of estimation problem (6.3) can be obtained according to Section 4.8, as follows:

$$\hat{\boldsymbol{x}} := \arg\min_{\boldsymbol{x}\in\mathbb{R}^n} J(\boldsymbol{x}) = \left(\boldsymbol{z}_s - \boldsymbol{h}_s(\boldsymbol{x})\right)^T \boldsymbol{R}_s^{-1}\left(\boldsymbol{z}_s - \boldsymbol{h}_s(\boldsymbol{x})\right) + \left(\boldsymbol{z}_p - \boldsymbol{h}_p(\boldsymbol{x})\right)^T \boldsymbol{R}_p^{-1}\left(\boldsymbol{z}_p - \boldsymbol{h}_p(\boldsymbol{x})\right) \\ \text{s.t. } \boldsymbol{c}(\boldsymbol{x}) = \boldsymbol{0} \tag{6.4}$$

By applying the Hachtel's augmented matrix method [183] only for the PMU measurements, the objective function of (6.4) now includes the weighted sum of the squared PMU measurement residuals $\boldsymbol{r}_p$, while the constraints obeyed by $\boldsymbol{r}_p$ and $\boldsymbol{c}(\boldsymbol{x})$ are introduced, as follows:

$$\begin{aligned} \hat{\boldsymbol{x}} &:= \arg\min_{\boldsymbol{x}\in\mathbb{R}^n} J(\boldsymbol{x},\boldsymbol{r}_p) = \left(\boldsymbol{z}_s - \boldsymbol{h}_s(\boldsymbol{x})\right)^T \boldsymbol{R}_s^{-1}\left(\boldsymbol{z}_s - \boldsymbol{h}_s(\boldsymbol{x})\right) + \boldsymbol{r}_p^T \boldsymbol{R}_p^{-1}\boldsymbol{r}_p \\ \text{s.t. } & \boldsymbol{r}_P = \boldsymbol{z}_P - \boldsymbol{h}_P(\boldsymbol{x}) \\ & \boldsymbol{c}(\boldsymbol{x}) = \boldsymbol{0} \end{aligned} \tag{6.5}$$

According to Section 4.9.4, (6.5) is solved via the method of Lagrange multipliers. The corresponding Lagrangian function $\mathcal{L}(\boldsymbol{x},\boldsymbol{r}_p,\boldsymbol{\lambda},\boldsymbol{\mu})$ is defined as:

$$\mathcal{L}(\boldsymbol{x},\boldsymbol{r}_p,\boldsymbol{\lambda},\boldsymbol{\mu}) = aJ(\boldsymbol{x},\boldsymbol{r}_p) + \boldsymbol{\lambda}^T\boldsymbol{c}(\boldsymbol{x}) + \boldsymbol{\mu}^T\left(\boldsymbol{r}_p - \boldsymbol{z}_p + \boldsymbol{h}_p(\boldsymbol{x})\right) \tag{6.6}$$

where $\boldsymbol{\lambda}$ and $\boldsymbol{\mu}$ are the Lagrange multipliers, and coefficient a is the scaling factor of the objective function. The first order optimality conditions are obtained as follows:

$$\frac{\partial\mathcal{L}}{\partial\boldsymbol{x}} = -a\boldsymbol{H}_s^T(\boldsymbol{x})\boldsymbol{R}_s^{-1}\left(\boldsymbol{z}_s - \boldsymbol{h}_s(\boldsymbol{x})\right) + \boldsymbol{C}^T(\boldsymbol{x})\boldsymbol{\lambda} + \boldsymbol{H}_p^T(\boldsymbol{x})\boldsymbol{\mu} = \boldsymbol{0} \tag{6.7}$$

$$\frac{\partial\mathcal{L}}{\partial\boldsymbol{r}_p} = a\boldsymbol{R}_p^{-1}\boldsymbol{r}_p + \boldsymbol{\mu} = \boldsymbol{0} \Leftrightarrow \boldsymbol{r}_p = -a^{-1}\boldsymbol{R}_p\boldsymbol{\mu} \tag{6.8}$$

$$\frac{\partial\mathcal{L}}{\partial\boldsymbol{\lambda}} = \boldsymbol{c}(\boldsymbol{x}) = \boldsymbol{0} \tag{6.9}$$

$$\frac{\partial\mathcal{L}}{\partial\boldsymbol{\mu}} = \boldsymbol{r}_p - \boldsymbol{z}_p + \boldsymbol{h}_p(\boldsymbol{x}) = \boldsymbol{0} \tag{6.10}$$

where $\boldsymbol{H}_s$, $\boldsymbol{H}_p$, and $\boldsymbol{C}$ are the Jacobian matrices of $\boldsymbol{h}_s$, $\boldsymbol{h}_p$, and $\boldsymbol{c}$, respectively.

The system of nonlinear equations (6.7)–(6.10) are solved iteratively using the Gauss-Newton method, as follows:

$$\begin{bmatrix} a\boldsymbol{G}_s(\boldsymbol{x}^{(i)}) & \boldsymbol{C}^T(\boldsymbol{x}^{(i)}) & \boldsymbol{H}_p^T(\boldsymbol{x}^{(i)}) \\ \boldsymbol{C}(\boldsymbol{x}^{(i)}) & \boldsymbol{0} & \boldsymbol{0} \\ \boldsymbol{H}_p(\boldsymbol{x}^{(i)}) & \boldsymbol{0} & -a^{-1}\boldsymbol{R}_p \end{bmatrix} \begin{bmatrix} \Delta\boldsymbol{x}^{(i+1)} \\ \boldsymbol{\lambda}^{(i+1)} \\ \boldsymbol{\mu}^{(i+1)} \end{bmatrix} = \begin{bmatrix} a\boldsymbol{H}_s^T(\boldsymbol{x}^{(i)})\boldsymbol{R}_s^{-1}\Delta\boldsymbol{z}_s^{(i)} \\ -\boldsymbol{c}(\boldsymbol{x}^{(i)}) \\ \Delta\boldsymbol{z}_P^{(i)} \end{bmatrix} \tag{6.11}$$

where (i) is the iteration index, $\boldsymbol{G}_s = \boldsymbol{H}_s^T\boldsymbol{R}_s^{-1}\boldsymbol{H}_s$, $\Delta\boldsymbol{z}_s^{(i)} = \boldsymbol{z}_s - \boldsymbol{h}_s(\boldsymbol{x}^{(i)})$, $\Delta\boldsymbol{z}_p^{(i)} = \boldsymbol{z}_p - \boldsymbol{h}_p(\boldsymbol{x}^{(i)})$, $\Delta\boldsymbol{x}^{(i+1)} = \boldsymbol{x}^{(i+1)} - \boldsymbol{x}^{(i)}$. For convenience and consistency, we shall adopt this notation throughout the remainder of this thesis, wherein the superscript (i) indicates the value of each matrix at the i-th iteration. Hence, $\boldsymbol{G}_s^{(i)} := \boldsymbol{G}_s(\boldsymbol{x}^{(i)})$, $\boldsymbol{C}^{(i)} := \boldsymbol{C}(\boldsymbol{x}^{(i)})$, and so forth. Thus, (6.11) can be written as:

$$\left[\begin{array}{c|c} \boldsymbol{G}_{sz}^{(i)} & \left(\boldsymbol{H}_{pz}^{(i)}\right)^T \\ \hline \boldsymbol{H}_{pz}^{(i)} & -a^{-1}\boldsymbol{R}_p \end{array}\right]\left[\begin{array}{c} \Delta\boldsymbol{x}^{(i+1)} \\ \boldsymbol{\lambda}^{(i+1)} \\ \hline \boldsymbol{\mu}^{(i+1)} \end{array}\right] = \left[\begin{array}{c} a\left(\boldsymbol{H}_s^{(i)}\right)^T \boldsymbol{R}_s^{-1}\Delta\boldsymbol{z}_s^{(i)} \\ -\boldsymbol{c}(\boldsymbol{x}^{(i)}) \\ \hline \Delta\boldsymbol{z}_p^{(i)} \end{array}\right] \tag{6.12}$$

where $\boldsymbol{H}_{pz}^{(i)} = \left[\boldsymbol{H}_p^{(i)}\ \ \boldsymbol{0}\right]$, $\boldsymbol{G}_{sz}^{(i)} = \begin{bmatrix} a\boldsymbol{G}_s^{(i)} & \left(\boldsymbol{C}^{(i)}\right)^T \\ \boldsymbol{C}^{(i)} & \boldsymbol{0} \end{bmatrix}$.

Using (6.8) to eliminate $\boldsymbol{r}_p$ in (6.12) and solving for $\begin{bmatrix} \Delta\boldsymbol{x}^{(i+1)} \\ \boldsymbol{\lambda}^{(i+1)} \end{bmatrix}$, yields:

$$\left.\begin{array}{l} \boldsymbol{G}_{sz}^{(i)}\begin{bmatrix} \Delta\boldsymbol{x}^{(i+1)} \\ \boldsymbol{\lambda}^{(i+1)} \end{bmatrix} + \left(\boldsymbol{H}_{pz}^{(i)}\right)^T \boldsymbol{\mu}^{(i+1)} = \begin{bmatrix} a\left(\boldsymbol{H}_s^{(i)}\right)^T \boldsymbol{R}_s^{-1}\Delta\boldsymbol{z}_s^{(i)} \\ -\boldsymbol{c}(\boldsymbol{x}^{(i)}) \end{bmatrix} \\ \boldsymbol{H}_{pz}^{(i)}\begin{bmatrix} \Delta\boldsymbol{x}^{(i+1)} \\ \boldsymbol{\lambda}^{(i+1)} \end{bmatrix} - a^{-1}\boldsymbol{R}_p\boldsymbol{\mu}^{(i+1)} = \Delta\boldsymbol{z}_p^{(i)} \end{array}\right\} \Leftrightarrow$$

$$\left\{\begin{array}{l} \begin{bmatrix} \Delta\boldsymbol{x}^{(i+1)} \\ \boldsymbol{\lambda}^{(i+1)} \end{bmatrix} = \left(\boldsymbol{G}_{sz}^{(i)}\right)^{-1}\begin{bmatrix} a\left(\boldsymbol{H}_s^{(i)}\right)^T \boldsymbol{R}_s^{-1}\Delta\boldsymbol{z}_s^{(i)} \\ -\boldsymbol{c}(\boldsymbol{x}^{(i)}) \end{bmatrix} - \left(\boldsymbol{G}_{sz}^{(i)}\right)^{-1}\left(\boldsymbol{H}_{pz}^{(i)}\right)^T \boldsymbol{\mu}^{(i+1)} \\ \boldsymbol{H}_{pz}^{(i)}\begin{bmatrix} \Delta\boldsymbol{x}^{(i+1)} \\ \boldsymbol{\lambda}^{(i+1)} \end{bmatrix} - a^{-1}\boldsymbol{R}_p\boldsymbol{\mu}^{(i+1)} = \Delta\boldsymbol{z}_p^{(i)} \end{array}\right\} \Leftrightarrow$$

$$\left\{\begin{array}{l} \begin{bmatrix} \Delta\boldsymbol{x}^{(i+1)} \\ \boldsymbol{\lambda}^{(i+1)} \end{bmatrix} = \left(\boldsymbol{G}_{sz}^{(i)}\right)^{-1}\begin{bmatrix} a\left(\boldsymbol{H}_s^{(i)}\right)^T \boldsymbol{R}_s^{-1}\Delta\boldsymbol{z}_s^{(i)} \\ -\boldsymbol{c}(\boldsymbol{x}^{(i)}) \end{bmatrix} - \left(\boldsymbol{G}_{sz}^{(i)}\right)^{-1}\left(\boldsymbol{H}_{pz}^{(i)}\right)^T \boldsymbol{\mu}^{(i+1)} \\ \boldsymbol{H}_{pz}^{(i)}\left(\boldsymbol{G}_{sz}^{(i)}\right)^{-1}\left(\begin{bmatrix} a\left(\boldsymbol{H}_s^{(i)}\right)^T \boldsymbol{R}_s^{-1}\Delta\boldsymbol{z}_s^{(i)} \\ -\boldsymbol{c}(\boldsymbol{x}^{(i)}) \end{bmatrix} - \left(\boldsymbol{H}_{pz}^{(i)}\right)^T \boldsymbol{\mu}^{(i+1)}\right) - a^{-1}\boldsymbol{R}_p\boldsymbol{\mu}^{(i+1)} = \Delta\boldsymbol{z}_p^{(i)} \end{array}\right\} \Leftrightarrow$$

$$\left\{\begin{array}{l} \begin{bmatrix} \Delta\boldsymbol{x}^{(i+1)} \\ \boldsymbol{\lambda}^{(i+1)} \end{bmatrix} = \left(\boldsymbol{G}_{sz}^{(i)}\right)^{-1}\begin{bmatrix} a\left(\boldsymbol{H}_s^{(i)}\right)^T \boldsymbol{R}_s^{-1}\Delta\boldsymbol{z}_s^{(i)} \\ -\boldsymbol{c}(\boldsymbol{x}^{(i)}) \end{bmatrix} - \left(\boldsymbol{G}_{sz}^{(i)}\right)^{-1}\left(\boldsymbol{H}_{pz}^{(i)}\right)^T \boldsymbol{\mu}^{(i+1)} \\ \left(a^{-1}\boldsymbol{R}_p + \boldsymbol{H}_{pz}^{(i)}\left(\boldsymbol{G}_{sz}^{(i)}\right)^{-1}\left(\boldsymbol{H}_{pz}^{(i)}\right)^T\right)\boldsymbol{\mu}^{(i+1)} = \boldsymbol{H}_{pz}^{(i)}\left(\boldsymbol{G}_{sz}^{(i)}\right)^{-1}\begin{bmatrix} a\left(\boldsymbol{H}_s^{(i)}\right)^T \boldsymbol{R}_s^{-1}\Delta\boldsymbol{z}_s^{(i)} \\ -\boldsymbol{c}(\boldsymbol{x}^{(i)}) \end{bmatrix} - \Delta\boldsymbol{z}_p^{(i)} \end{array}\right. \tag{6.13}$$

Setting $\begin{bmatrix} \Delta\boldsymbol{y}^{(i+1)} \\ \boldsymbol{\lambda}_y^{(i+1)} \end{bmatrix} := \left(\boldsymbol{G}_{sz}^{(i)}\right)^{-1}\begin{bmatrix} a\left(\boldsymbol{H}_s^{(i)}\right)^T \boldsymbol{R}_s^{-1}\Delta\boldsymbol{z}_s^{(i)} \\ -\boldsymbol{c}(\boldsymbol{x}^{(i)}) \end{bmatrix}$ in (6.13) yields:

$$\begin{cases} \begin{bmatrix} \Delta \boldsymbol{x}^{(i+1)} \\ \boldsymbol{\lambda}^{(i+1)} \end{bmatrix} = \begin{bmatrix} \Delta \boldsymbol{y}^{(i+1)} \\ \boldsymbol{\lambda}_y^{(i+1)} \end{bmatrix} - \left(\boldsymbol{G}_{sz}^{(i)}\right)^{-1} \left(\boldsymbol{H}_{pz}^{(i)}\right)^T \boldsymbol{\mu}^{(i+1)} \\ \boldsymbol{\mu}^{(i+1)} = \left(a^{-1}\boldsymbol{R}_p + \boldsymbol{H}_{pz}^{(i)} \left(\boldsymbol{G}_{sz}^{(i)}\right)^{-1} \left(\boldsymbol{H}_{pz}^{(i)}\right)^T \right)^{-1} \left(\boldsymbol{H}_{pz}^{(i)} \begin{bmatrix} \Delta \boldsymbol{y}^{(i+1)} \\ \boldsymbol{\lambda}_y^{(i+1)} \end{bmatrix} - \Delta \boldsymbol{z}_p^{(i)} \right) \end{cases} \tag{6.14}$$

Finally, by setting:

$$\begin{bmatrix} \Delta \boldsymbol{u}^{(i+1)} \\ \boldsymbol{\lambda}_u^{(i+1)} \end{bmatrix} := -\left(\boldsymbol{G}_{sz}^{(i)}\right)^{-1} \left(\boldsymbol{H}_{pz}^{(i)}\right)^T \boldsymbol{\mu}^{(i+1)} \tag{6.15}$$

and simplifying $\boldsymbol{H}_{pz}^{(i)} \begin{bmatrix} \Delta \boldsymbol{y}^{(i+1)} \\ \boldsymbol{\lambda}_y^{(i+1)} \end{bmatrix} = \boldsymbol{H}_p^{(i)} \Delta \boldsymbol{y}^{(i+1)}$, (6.14) gives the following system of linear equations:

$$\begin{bmatrix} \Delta \boldsymbol{y}^{(i+1)} \\ \boldsymbol{\lambda}_y^{(i+1)} \end{bmatrix} = \left(\boldsymbol{G}_{sz}^{(i)}\right)^{-1} \begin{bmatrix} a\left(\boldsymbol{H}_s^{(i)}\right)^T \boldsymbol{R}_s^{-1} \Delta \boldsymbol{z}_s^{(i)} \\ -\boldsymbol{c}(\boldsymbol{x}^{(i)}) \end{bmatrix} \tag{6.16}$$

$$\begin{bmatrix} \Delta \boldsymbol{u}^{(i+1)} \\ \boldsymbol{\lambda}_u^{(i+1)} \end{bmatrix} = \left(\boldsymbol{G}_{sz}^{(i)}\right)^{-1} \left(\boldsymbol{H}_{pz}^{(i)}\right)^T \left(a^{-1}\boldsymbol{R}_p + \boldsymbol{H}_{pz}^{(i)} \left(\boldsymbol{G}_{sz}^{(i)}\right)^{-1} \left(\boldsymbol{H}_{pz}^{(i)}\right)^T \right)^{-1} \left(\Delta \boldsymbol{z}_p^{(i)} - \boldsymbol{H}_p^{(i)} \Delta \boldsymbol{y}^{(i+1)} \right) \tag{6.17}$$

$$\begin{bmatrix} \Delta \boldsymbol{x}^{(i+1)} \\ \boldsymbol{\lambda}^{(i+1)} \end{bmatrix} = \begin{bmatrix} \Delta \boldsymbol{y}^{(i+1)} \\ \boldsymbol{\lambda}_y^{(i+1)} \end{bmatrix} + \begin{bmatrix} \Delta \boldsymbol{u}^{(i+1)} \\ \boldsymbol{\lambda}_u^{(i+1)} \end{bmatrix} \tag{6.18}$$

Equations (6.16)–(6.18) define the iterative scheme employed in solving the proposed HSE formulation. It is worth noting that the SCADA and PMU measurement models appear separately; at each iteration, calculation of $\Delta \boldsymbol{y}^{(i+1)}$ relies only on the SCADA measurement vector $\boldsymbol{z}_s$, while $\Delta \boldsymbol{u}^{(i+1)}$ is then updated using vector $\Delta \boldsymbol{y}^{(i+1)}$ and the PMU measurement vector $\boldsymbol{z}_p$. The state estimate incremental correction $\Delta \boldsymbol{x}^{(i+1)}$ and the Lagrange multipliers $\boldsymbol{\lambda}^{(i+1)}$, corresponding to zero injection constraints, are updated using $\Delta \boldsymbol{y}^{(i+1)}$ and $\Delta \boldsymbol{u}^{(i+1)}$ until convergence. Convergence is generally attained when $\left\| \Delta \boldsymbol{x}^{(i+1)} \right\|_\infty < \varepsilon$, where ε is a predetermined convergence threshold.

It should also be noted that, as we deal with indefinite matrices, we utilize an $\boldsymbol{LDL}^T$ factorization algorithm using block decomposition with pivoting to ensure numerical stability. This approach decomposes a symmetric matrix $\boldsymbol{A}$ into three factors, represented as $\boldsymbol{A} = \boldsymbol{P}^T \boldsymbol{LDL}^T \boldsymbol{P}$, where $\boldsymbol{L}$ is a lower triangular matrix with unit diagonal elements, $\boldsymbol{D}$ is a block diagonal matrix containing 1×1 or 2×2 diagonal blocks, and $\boldsymbol{P}$ is a permutation matrix to manage row and column interchanges [187]. The decomposition is implemented through MATLAB software and is based on a combination of proprietary routines and well-established external libraries for matrix decompositions [188].

If we assume that the entire power system is SCADA-observable, then $\boldsymbol{G}_{sz}$ is of full rank. The reasoning behind this assumption lies in existing SCADA metering infrastructures providing high RTU measurement redundancy to satisfy complete system observability even under severe measurement loss. Then the indefinite matrix $\boldsymbol{G}_{sz}$ can be decomposed into $\boldsymbol{LDL}^T$ factors for solving the sparse linear equations (6.16) and (6.17). In (6.17), we set $\boldsymbol{G}_{sz}^{-1}\boldsymbol{H}_{pz}^{T}=\boldsymbol{D}^{-1}\left(\left(\boldsymbol{P}^{T}\boldsymbol{L}\right)^{-1}\boldsymbol{H}_{pz}^{T}\right)$ and calculate matrix $\left(\boldsymbol{P}^{T}\boldsymbol{L}\right)^{-1}\boldsymbol{H}_{pz}^{T}$ efficiently by applying sparse vector techniques [189], exploiting the very sparse structure of $\boldsymbol{H}_{pz}$. This also allows efficient calculation of $\boldsymbol{H}_{pz}\boldsymbol{G}_{sz}^{-1}\boldsymbol{H}_{pz}^{T}=\left(\left(\boldsymbol{P}^{T}\boldsymbol{L}\right)^{-1}\boldsymbol{H}_{pz}^{T}\right)^{T}\boldsymbol{D}^{-1}\left(\left(\boldsymbol{P}^{T}\boldsymbol{L}\right)^{-1}\boldsymbol{H}_{pz}^{T}\right)$. The indefinite matrix $a^{-1}\boldsymbol{R}_p+\boldsymbol{H}_{pz}\boldsymbol{G}_{sz}^{-1}\boldsymbol{H}_{pz}^{T}$ is dense and is also decomposed into $\boldsymbol{LDL}^T$ factors to solve $\left(a^{-1}\boldsymbol{R}_p+\boldsymbol{H}_{pz}\boldsymbol{G}_{sz}^{-1}\boldsymbol{H}_{pz}^{T}\right)\boldsymbol{\mu}^{(i+1)}=\left(\boldsymbol{H}_p\Delta\boldsymbol{y}^{(i+1)}-\Delta\boldsymbol{z}_p^{(i+1)}\right)$ for $\boldsymbol{\mu}^{(i+1)}$.

In the following, the iterative scheme (6.16)–(6.18) is used to formulate three different HSE algorithms classified into the three different HSE categories.

6.2.1 Proposed integrated hybrid state estimation algorithm

Based on (6.16)–(6.18) an ISE algorithm can be devised and is presented in Algorithm 6.1 and the respective flowchart of Figure 6.1. For the purposes of this work, SE is assumed to be solved upon arrival of SCADA measurements, utilizing the most recent PMU dataset available to the EMS, based on measurement timestamps. To mitigate errors stemming from measurement time skew, buffering techniques can be utilized [108], [109]. The SE software is to receive the m_s (m_p) SCADA-measured (PMU-measured) values $\boldsymbol{z}_s$ $(\boldsymbol{z}_p)$, along with the RTU (PMU) measurement locations and accuracies, from the SCADA system (PDC).

Incremental correction $\Delta\boldsymbol{y}^{(i+1)}$ of (6.16) is calculated by the conventional SE iterations, whereas the incremental correction $\Delta\boldsymbol{u}^{(i+1)}$ in (6.17) can be computed by modifying the existing SE software within the EMS. As both $\Delta\boldsymbol{y}^{(i+1)}$ and $\Delta\boldsymbol{u}^{(i+1)}$ are updated at each iteration, the ISE implementation retains its joint optimality property, that is, the calculation of the best solution that fits both measurement sets simultaneously.

6.2.2 Proposed sequential hybrid state estimation algorithm

Let us now examine the SCADA- and PMU-based SE stages separately. To accomplish this, we first write the incremental correction (6.17) assuming a nonlinear PMU measurement model, as follows:

$$\begin{bmatrix}\Delta\boldsymbol{u}^{(i+1)}\\ \boldsymbol{\lambda}_u^{(i+1)}\end{bmatrix}=\left(\boldsymbol{G}_{sz}^{(i)}\right)^{-1}\left(\boldsymbol{H}_{pz}^{(i)}\right)^{T}\left(a^{-1}\boldsymbol{R}_p+\boldsymbol{H}_{pz}^{(i)}\left(\boldsymbol{G}_{sz}^{(i)}\right)^{-1}\left(\boldsymbol{H}_{pz}^{(i)}\right)^{T}\right)^{-1}\left(\boldsymbol{z}_p-\boldsymbol{h}_p(\boldsymbol{x}^{(i)})-\boldsymbol{H}_p^{(i)}\Delta\boldsymbol{y}^{(i+1)}\right) \tag{6.19}$$

Expanding the – generally – nonlinear PMU measurement function $\boldsymbol{h}_p(\cdot)$ around the current estimate $\boldsymbol{x}^{(i)}$ using a Taylor series, yields:

$$\boldsymbol{h}_p(\boldsymbol{x})=\boldsymbol{h}_p(\boldsymbol{x}^{(i)})+\boldsymbol{H}_p(\boldsymbol{x}^{(i)})(\boldsymbol{x}-\boldsymbol{x}^{(i)})+\frac{1}{2}(\boldsymbol{x}-\boldsymbol{x}^{(i)})^T\boldsymbol{H}_p'(\boldsymbol{x}^{(i)})(\boldsymbol{x}-\boldsymbol{x}^{(i)})+\ldots \tag{6.20}$$

where $\boldsymbol{H}_p'$ is the Hessian matrix of $\boldsymbol{h}_p(\boldsymbol{x})$.

Considering that at each iteration (i) of the ISE algorithm the calculation of $\Delta\boldsymbol{y}^{(i+1)}$ relies only on the SCADA measurement vector $\boldsymbol{z}_s$ and the zero injection information according to (6.16), the state vector incorporating the SCADA-based incremental correction is defined as:

$$\boldsymbol{y}^{(i+1)} := \boldsymbol{x}^{(i)} + \Delta\boldsymbol{y}^{(i+1)} \tag{6.21}$$

and

$$\boldsymbol{h}_p(\boldsymbol{y}^{(i+1)}) = \boldsymbol{h}_p(\boldsymbol{x}^{(i)}) + \boldsymbol{H}_p(\boldsymbol{x}^{(i)})\Delta\boldsymbol{y}^{(i+1)} + \frac{1}{2}\left(\Delta\boldsymbol{y}^{(i+1)}\right)^T \boldsymbol{H}'_p(\boldsymbol{x}^{(i)})\Delta\boldsymbol{y}^{(i+1)} + \ldots \tag{6.22}$$

Algorithm 6.1: Proposed ISE algorithm.

1) Initialize the iteration index $i \leftarrow 0$ and set the state vector $\boldsymbol{x}^{(0)}$ at flat start.

2) Calculate the gain matrix $\boldsymbol{G}_{sz}^{(i)}$ and the augmented PMU Jacobian $\boldsymbol{H}_{pz}^{(i)}$.

3) Calculate the right-hand side of (6.16), $\begin{bmatrix} a\left(\boldsymbol{H}_s^{(i)}\right)^T \boldsymbol{R}_s^{-1}\Delta\boldsymbol{z}_s^{(i)} \\ -\boldsymbol{c}(\boldsymbol{x}^{(i)}) \end{bmatrix}$.

4) Decompose $\boldsymbol{G}_{sz}^{(i)}$ and solve (6.16) for $\begin{bmatrix} \Delta\boldsymbol{y}^{(i+1)} \\ \boldsymbol{\lambda}_y^{(i+1)} \end{bmatrix}$ using forward-backward substitution.

5) Calculate $\boldsymbol{G}_{sz}^{-1}\boldsymbol{H}_{pz}^T$, $a^{-1}\boldsymbol{R}_p + \boldsymbol{H}_{pz}\boldsymbol{G}_{sz}^{-1}\boldsymbol{H}_{pz}^T$ and $\boldsymbol{H}_p\Delta\boldsymbol{y}^{(i)} - \Delta\boldsymbol{z}_p^{(i)}$.

6) Solve $\left(a^{-1}\boldsymbol{R}_p + \boldsymbol{H}_{pz}\boldsymbol{G}_{sz}^{-1}\boldsymbol{H}_{pz}^T\right)\boldsymbol{\mu}^{(i+1)} = \left(\boldsymbol{H}_p\Delta\boldsymbol{y}^{(i)} - \Delta z_p^{(i)}\right)$ for $\boldsymbol{\mu}^{(i+1)}$.

7) Calculate $\begin{bmatrix} \Delta\boldsymbol{u}^{(i+1)} \\ \boldsymbol{\lambda}_u^{(i+1)} \end{bmatrix} \leftarrow -\boldsymbol{G}_{sz}^{-1}\boldsymbol{H}_{pz}^T\boldsymbol{\mu}^{(i+1)}$.

8) Calculate $\begin{bmatrix} \Delta\boldsymbol{x}^{(i+1)} \\ \boldsymbol{\lambda}^{(i+1)} \end{bmatrix} \leftarrow \begin{bmatrix} \Delta\boldsymbol{y}^{(i+1)} \\ \boldsymbol{\lambda}_y^{(i+1)} \end{bmatrix} + \begin{bmatrix} \Delta\boldsymbol{u}^{(i+1)} \\ \boldsymbol{\lambda}_u^{(i+1)} \end{bmatrix}$.

9) Check for convergence: **If** the convergence criteria are satisfied for all state variables, **then** $\hat{\boldsymbol{x}} \leftarrow \boldsymbol{x}^{(i)} + \Delta\boldsymbol{x}^{(i+1)}$ and terminate the algorithm. **Else**, $\boldsymbol{x}^{(i+1)} \leftarrow \boldsymbol{x}^{(i)} + \Delta\boldsymbol{x}^{(i+1)}$, $i \leftarrow i+1$, return to Step 2.

As the iterative process (6.16)–(6.18) converges $(\boldsymbol{x}^{(i)} \rightarrow \hat{\boldsymbol{x}})$, then incremental correction $\Delta\boldsymbol{y}^{(i+1)}$ becomes increasingly small. Thus, as $\boldsymbol{x}^{(i)} \rightarrow \hat{\boldsymbol{x}}$, higher-order terms in (6.22) become negligible and the measurement function can be approximated by a linear function of $\Delta\boldsymbol{y}^{(i+1)}$:

$$\boldsymbol{h}_p(\boldsymbol{y}^{(i+1)}) \simeq \boldsymbol{h}_p(\boldsymbol{x}^{(i)}) + \boldsymbol{H}_p(\boldsymbol{x}^{(i)})\Delta\boldsymbol{y}^{(i+1)} \tag{6.23}$$

Using (6.23), near convergence (6.19) is written as:

$$\begin{bmatrix} \Delta\boldsymbol{u}^{(i+1)} \\ \boldsymbol{\lambda}_u^{(i+1)} \end{bmatrix} = \left(\boldsymbol{G}_{sz}^{(i)}\right)^{-1}\left(\boldsymbol{H}_{pz}^{(i)}\right)^T\left(a^{-1}\boldsymbol{R}_p + \boldsymbol{H}_{pz}^{(i)}\left(\boldsymbol{G}_{sz}^{(i)}\right)^{-1}\left(\boldsymbol{H}_{pz}^{(i)}\right)^T\right)^{-1}\left(\boldsymbol{z}_p - \boldsymbol{h}_p(\boldsymbol{y}^{(i+1)})\right) \tag{6.24}$$

For the ISE algorithm it also holds that:

$$\Delta\boldsymbol{x}^{(i+1)} = \Delta\boldsymbol{y}^{(i+1)} + \Delta\boldsymbol{u}^{(i+1)} = \boldsymbol{y}^{(i+1)} - \boldsymbol{x}^{(i)} + \Delta\boldsymbol{u}^{(i+1)} \Leftrightarrow \boldsymbol{x}^{(i+1)} = \boldsymbol{y}^{(i+1)} + \Delta\boldsymbol{u}^{(i+1)} \tag{6.25}$$

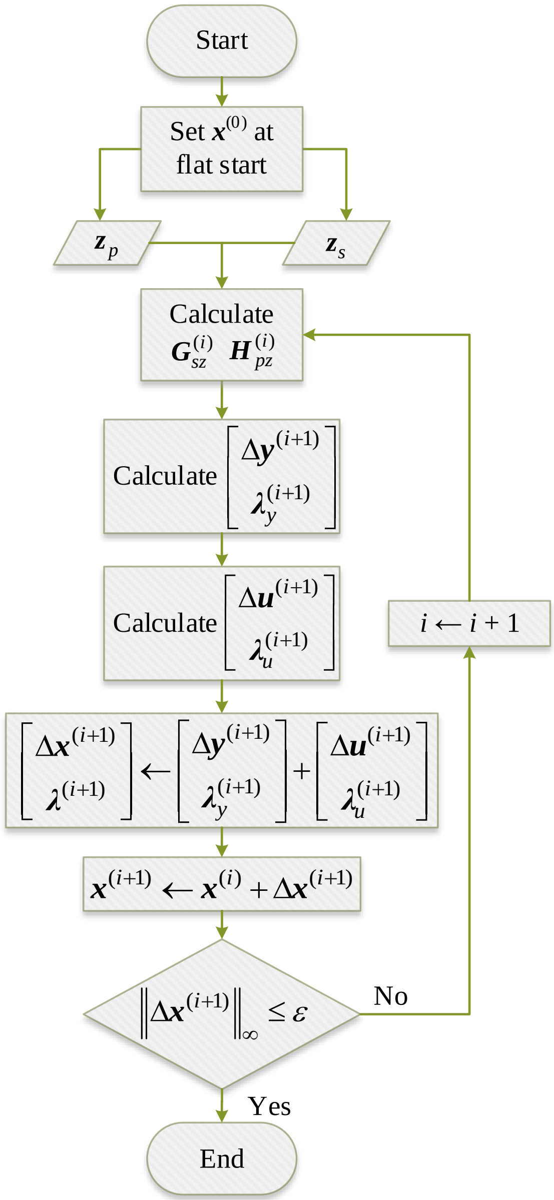

Figure 6.1: Flow diagram of the proposed ISE algorithm.

Thus, at the terminal iteration (t) where $\boldsymbol{y}^{(t)} := \hat{\boldsymbol{y}}$, $\boldsymbol{x}^{(t)} := \hat{\boldsymbol{x}}$ we can write:

$$\begin{bmatrix} \Delta\boldsymbol{u}^{(t)} \\ \boldsymbol{\lambda}_u^{(t)} \end{bmatrix} = \left(\boldsymbol{G}_{sz}^{(t-1)}\right)^{-1} \left(\boldsymbol{H}_{pz}^{(t-1)}\right)^T \left(a^{-1}\boldsymbol{R}_p + \boldsymbol{H}_{pz}^{(t-1)} \left(\boldsymbol{G}_{sz}^{(t-1)}\right)^{-1} \left(\boldsymbol{H}_{pz}^{(t-1)}\right)^T\right)^{-1} \left(\boldsymbol{z}_p - \boldsymbol{h}_p(\hat{\boldsymbol{y}})\right) \tag{6.26}$$

$$\hat{\boldsymbol{x}} = \hat{\boldsymbol{y}} + \Delta\boldsymbol{u}^{(t)} \tag{6.27}$$

Therefore, close to the SE solution, where (6.23) holds, a PSE scheme is applicable and is presented in Algorithm 6.2 and in the flowchart of Figure 6.2. Using i_s to denote the iterations of the SCADA-based stage, $\Delta\boldsymbol{y}^{(i_s)}$ and $\boldsymbol{\lambda}_y^{(i_s)}$ are calculated iteratively until convergence by the conventional SE iterations (6.16) (Step 1 of Algorithm 6.2), yielding $\hat{\boldsymbol{y}}$ and $\hat{\boldsymbol{\lambda}}_y$. Then, as the SCADA-based SE has converged to an optimal estimate $\hat{\boldsymbol{y}}$ of the system-wide state vector, we can formulate an iterative post-processing step to incorporate the PMU measurements $\boldsymbol{z}_p$ via Step 2 of Algorithm 6.2:

$$\begin{bmatrix} \Delta \boldsymbol{u}^{(i_p+1)} \\ \boldsymbol{\lambda}_u^{(i_p+1)} \end{bmatrix} = \left(\boldsymbol{G}_{sz}^{(i_p)}\right)^{-1} \left(\boldsymbol{H}_{pz}^{(i_p)}\right)^T \left(a^{-1}\boldsymbol{R}_p + \boldsymbol{H}_{pz}^{(i_p)} \left(\boldsymbol{G}_{sz}^{(i_p)}\right)^{-1} \left(\boldsymbol{H}_{pz}^{(i_p)}\right)^T\right)^{-1} \left(\boldsymbol{z}_p - \boldsymbol{h}_p(\boldsymbol{x}^{(i_p)})\right) \tag{6.28}$$

$$\boldsymbol{x}^{(i_p+1)} = \boldsymbol{x}^{(i_p)} + \Delta \boldsymbol{u}^{(i_p+1)} \tag{6.29}$$

with $\boldsymbol{x}^{(0)} = \hat{\boldsymbol{y}}$.

It is worth noting that in contrast to PSE methods found in literature, this PSE architecture keeps the existing SCADA-based SE module completely unmodified in the EMS and does not require augmenting the PMU measurement vector $\boldsymbol{z}_p$ with information from the SCADA-based stage. Hence, implementation of the proposed PSE in the EMS is significantly easier.

Even though the proposed PSE scheme is derived from the respective ISE algorithm as the iterative process converges, this is not proof that the ISE and PSE methods are equivalent. The final result is typically not the same local minimum of the WLS objective function as if both measurement sets were jointly processed in each iteration, as is the case with all PSE methods found in literature [130]. This becomes clear when considering that in the PSE the matrices of the SCADA-based iterations (6.16) and the PMU-based stage (6.28) are evaluated at $\boldsymbol{y}^{(i_s)} = \boldsymbol{y}^{(i_s-1)} + \Delta\boldsymbol{y}^{(i_s)}$ and $\boldsymbol{x}^{(i_p)} = \boldsymbol{x}^{(i_p-1)} + \Delta\boldsymbol{u}^{(i_p)}$, respectively, with $\boldsymbol{x}^{(0)} = \hat{\boldsymbol{y}}$. In iteration i of the ISE algorithm, when calculating $\boldsymbol{x}^{(i+1)} = \boldsymbol{x}^{(i)} + \Delta\boldsymbol{y}^{(i+1)} + \Delta\boldsymbol{u}^{(i+1)}$, the Jacobian and the gain matrices of (6.16) and (6.17) are evaluated at $\boldsymbol{x}^{(i)} = \boldsymbol{x}^{(i-1)} + \Delta\boldsymbol{y}^{(i)} + \Delta\boldsymbol{u}^{(i)}$. Thus, one can view the PSE formulation as an equivalent ISE, in which:

1) the effect of $\Delta\boldsymbol{u}^{(i)}$ on $\Delta\boldsymbol{x}^{(i)}$ is negligible for all iterations until $\left\|\Delta\boldsymbol{y}^{(i)}\right\|_\infty \le \varepsilon$, i.e., the SCADA-based SE has converged on its own, and
2) after this point, only $\Delta\boldsymbol{u}^{(i)}$ is calculated iteratively, until $\left\|\Delta\boldsymbol{x}^{(i)}\right\|_\infty = \left\|\Delta\boldsymbol{u}^{(i)}\right\|_\infty \le \varepsilon$.

For the PSE solution to be close to the optimal ISE solution, i.e., $\hat{\boldsymbol{x}}_{ISE} \simeq \hat{\boldsymbol{x}}_{PSE}$ (disregarding deviations caused by arithmetic operations), Step 1 of Algorithm 6.2 must converge unproblematically. If there are large discrepancies between the SCADA-based SE solution and the true state vector, e.g., in the presence of undetected bad data in the SCADA dataset that negatively affect the estimate of the first stage, then the PSE algorithm may provide suboptimal, or even unreliable results in extreme cases.

In this context, it is essential to prove that the resulting PSE optimal state estimate $\hat{\boldsymbol{x}}_{PSE}$ will generally be closer to the true state than $\hat{\boldsymbol{y}}$, i.e., that the proposed post-processing stage actually improves the quality of the state estimate of the SCADA-based stage. Ignoring zero injection constraints for convenience, at iteration i_s of the SCADA-based SE we can write:

$$\Delta\boldsymbol{y}^{(i_s+1)} = \left(\boldsymbol{G}_s^{(i_s)}\right)^{-1} \left(\boldsymbol{H}_s^{(i_s)}\right)^T \boldsymbol{R}_s^{-1} \Delta\boldsymbol{z}_s^{(i_s)} \Rightarrow$$

$$Cov(\Delta\boldsymbol{y}^{(i_s+1)}) = \left(\boldsymbol{G}_s^{(i_s)}\right)^{-1} \left(\boldsymbol{H}_s^{(i_s)}\right)^T \boldsymbol{R}_s^{-1}\boldsymbol{R}_s\boldsymbol{R}_s^{-1}\boldsymbol{H}_s^{(i_s)} \left(\boldsymbol{G}_s^{(i_s)}\right)^{-1} \Leftrightarrow$$

$$Cov(\Delta\boldsymbol{y}^{(i_s+1)}) = \left(\boldsymbol{G}_s^{(i_s)}\right)^{-1} \left(\boldsymbol{H}_s^{(i_s)}\right)^T \boldsymbol{R}_s^{-1}\boldsymbol{H}_s^{(i_s)} \left(\boldsymbol{G}_s^{(i_s)}\right)^{-1} = \left(\boldsymbol{G}_s^{(i_s)}\right)^{-1} \tag{6.30}$$

As the iterations progress and $\boldsymbol{y}^{(i_s)} \to \hat{\boldsymbol{y}}$, we can assume that the uncertainty in $\boldsymbol{y}^{(i_s)}$ is small relative to the uncertainty in $\Delta\boldsymbol{y}^{(i_s+1)}$, and that the errors in $\boldsymbol{y}^{(i_s)}$ and $\Delta\boldsymbol{y}^{(i_s+1)}$ are uncorrelated. Hence, according to Subsection 4.8.4, the covariance of $\boldsymbol{y}^{(i_s+1)}$ can be approximated as:

$$Cov(\boldsymbol{y}^{(i_s+1)}) = Cov\left(\boldsymbol{y}^{(i_s)} + \Delta\boldsymbol{y}^{(i_s+1)}\right) \approx Cov(\Delta\boldsymbol{y}^{(i_s+1)}) = \left(\boldsymbol{G}_s^{(i_s)}\right)^{-1} \tag{6.31}$$

Algorithm 6.2: Proposed PSE algorithm (nonlinear PMU measurement model).

1) SCADA-based estimation:

a. Initialize the iteration index $i_s \leftarrow 0$ and set the state vector $\boldsymbol{y}^{(0)}$ at flat start.

b. Calculate the augmented gain matrix $\boldsymbol{G}_{sz}^{(i_s)}$.

c. Calculate the right-hand side of (6.16), $\begin{bmatrix} a\left(\boldsymbol{H}_s^{(i_s)}\right)^T \boldsymbol{R}_s^{-1}\Delta\boldsymbol{z}_s^{(i_s)} \\ -\boldsymbol{c}(\boldsymbol{y}^{(i_s)}) \end{bmatrix}$.

d. Decompose $\boldsymbol{G}_{sz}^{(i_s)}$ and solve (6.16) for $\Delta\boldsymbol{y}^{(i_s+1)}$.

e. Check for convergence: **If** the convergence criteria are satisfied for all state variables, **then** $\hat{\boldsymbol{y}} \leftarrow \boldsymbol{y}^{(i_s)} + \Delta\boldsymbol{y}^{(i_s+1)}$ and terminate the algorithm. **Else**, $\boldsymbol{y}^{(i_s+1)} \leftarrow \boldsymbol{y}^{(i_s)} + \Delta\boldsymbol{y}^{(i_s+1)}$, $i_s \leftarrow i_s + 1$ and return to Step (b).

2) PMU-based post processing stage:

a. Initialize the iteration index $i_p \leftarrow 0$ and the state vector $\boldsymbol{x}^{(0)} \leftarrow \hat{\boldsymbol{y}}$.

b. Calculate $\boldsymbol{G}_{sz}^{(i_p)}$ and $\boldsymbol{H}_{pz}^{(i_p)}$.

c. Calculate $\Delta\boldsymbol{z}_p^{(i_p)}$, $\left(\boldsymbol{G}_{sz}^{(i_p)}\right)^{-1}\left(\boldsymbol{H}_{pz}^{(i_p)}\right)^T$ and $a^{-1}\boldsymbol{R}_p + \boldsymbol{H}_{pz}^{(i_p)}\left(\boldsymbol{G}_{sz}^{(i_p)}\right)^{-1}\left(\boldsymbol{H}_{pz}^{(i_p)}\right)^T$.

d. Solve $\left(a^{-1}\boldsymbol{R}_p + \boldsymbol{H}_{pz}^{(i_p)}\left(\boldsymbol{G}_{sz}^{(i_p)}\right)^{-1}\left(\boldsymbol{H}_{pz}^{(i_p)}\right)^T\right)\boldsymbol{\mu}^{(i_p+1)} = -\Delta\boldsymbol{z}_p^{(i_p)}$ for $\boldsymbol{\mu}^{(i_p+1)}$.

e. Calculate $\begin{bmatrix} \Delta\boldsymbol{u}^{(i_p+1)} \\ \boldsymbol{\lambda}_u^{(i_p+1)} \end{bmatrix} \leftarrow -\left(\boldsymbol{G}_{sz}^{(i_p)}\right)^{-1}\left(\boldsymbol{H}_{pz}^{(i_p)}\right)^T \boldsymbol{\mu}^{(i_p+1)}$.

f. Check for convergence: **If** the convergence criteria are satisfied for all state variables, **then** $\hat{\boldsymbol{x}} \leftarrow \boldsymbol{x}^{(i_p)} + \Delta\boldsymbol{u}^{(i_p+1)}$ and terminate the algorithm. **Else**, $\boldsymbol{x}^{(i_p+1)} \leftarrow \boldsymbol{x}^{(i_p)} + \Delta\boldsymbol{u}^{(i_p+1)}$, $i_p \leftarrow i_p + 1$ and return to Step (b).

At the terminal iteration t_s we have $Cov(\hat{\boldsymbol{y}}) = \left(\boldsymbol{G}_s^{(t_s)}\right)^{-1} = \boldsymbol{G}_s^{-1}$.

In the SCADA-based SE, the initial estimate $\boldsymbol{y}^{(0)}$ is set at the flat voltage profile and thus is considered to have negligible covariance. However, this is untrue for the PMU-based post-processing stage, as $\boldsymbol{x}^{(0)} = \hat{\boldsymbol{y}}$. Therefore using (6.31) may introduce significant errors in the calculation of $Cov(\boldsymbol{x}^{(i_p+1)})$. For a more accurate calculation of this covariance matrix, which propagates the uncertainties of $\boldsymbol{x}^{(i_p)}$ at each iteration, we employ the EKF-based calculation, which updates the covariance using:

$$Cov(\boldsymbol{x}^{(i_p+1)}) = \\ Cov(\boldsymbol{x}^{(i_p)}) - Cov(\boldsymbol{x}^{(i_p)})\left(\boldsymbol{H}_p^{(i_p)}\right)^T\left(\boldsymbol{R}_p + \boldsymbol{H}_p^{(i_p)}Cov(\boldsymbol{x}^{(i_p)})\left(\boldsymbol{H}_p^{(i_p)}\right)^T\right)^{-1}\boldsymbol{H}_p^{(i_p)}Cov(\boldsymbol{x}^{(i_p)}) \tag{6.32}$$

Considering that $Cov(\boldsymbol{x}^{(i_p)}) \simeq Cov(\hat{\boldsymbol{y}}) = \boldsymbol{G}_s^{-1}$, we write:

$$Cov(\boldsymbol{x}^{(i_p+1)}) = \boldsymbol{G}_s^{-1} - \boldsymbol{G}_s^{-1}\left(\boldsymbol{H}_p^{(i_p)}\right)^T \left(\boldsymbol{R}_p + \boldsymbol{H}_p^{(i_p)}\boldsymbol{G}_s^{-1}\left(\boldsymbol{H}_p^{(i_p)}\right)^T\right)^{-1} \boldsymbol{H}_p^{(i_p)}\boldsymbol{G}_s^{-1} \tag{6.33}$$

Using the matrix inversion lemma (Sherman-Morisson-Woodbury formula) [100], yields:

$$\left(\boldsymbol{R}_p + \boldsymbol{H}_p^{(i_p)}\boldsymbol{G}_s^{-1}\left(\boldsymbol{H}_p^{(i_p)}\right)^T\right)^{-1} = \boldsymbol{R}_p^{-1} - \boldsymbol{R}_p^{-1}\boldsymbol{H}_p^{(i_p)}\left(\boldsymbol{G}_s + \boldsymbol{G}_p^{(i_p)}\right)^{-1}\left(\boldsymbol{H}_p^{(i_p)}\right)^T \boldsymbol{R}_p^{-1} \tag{6.34}$$

where $\boldsymbol{G}_p^{(i_p)} = \left(\boldsymbol{H}_p^{(i_p)}\right)^T \boldsymbol{R}_p^{-1}\boldsymbol{H}_p^{(i_p)}$.

Substituting into (6.33) yields:

$$Cov(\boldsymbol{x}^{(i_p+1)}) = \boldsymbol{G}_s^{-1} - \boldsymbol{G}_s^{-1}\boldsymbol{G}_p^{(i_p)}\boldsymbol{G}_s^{-1} + \boldsymbol{G}_s^{-1}\boldsymbol{G}_p^{(i_p)}\left(\boldsymbol{G}_s + \boldsymbol{G}_p^{(i_p)}\right)^{-1}\boldsymbol{G}_p^{(i_p)}\boldsymbol{G}_s^{-1} \Leftrightarrow$$

$$Cov(\boldsymbol{x}^{(i_p+1)}) = \boldsymbol{G}_s^{-1} - \boldsymbol{G}_s^{-1}\boldsymbol{G}_p^{(i_p)}\left(\boldsymbol{G}_s + \boldsymbol{G}_p^{(i_p)}\right)^{-1} \tag{6.35}$$

Observing that $\left(\boldsymbol{G}_s^{-1} - \boldsymbol{G}_s^{-1}\boldsymbol{G}_p^{(i_p)}\left(\boldsymbol{G}_s + \boldsymbol{G}_p^{(i_p)}\right)^{-1}\right)\left(\boldsymbol{G}_s + \boldsymbol{G}_p^{(i_p)}\right) = \boldsymbol{I}$, we derive:

$$Cov(\boldsymbol{x}^{(i_p+1)}) = \left(\boldsymbol{G}_s + \boldsymbol{G}_p^{(i_p)}\right)^{-1} \tag{6.36}$$

For positive definite (PD) matrix $\boldsymbol{G}_s$ and positive semidefinite (PSD) $\boldsymbol{G}_p^{(i_p)}$, in the Loewner ordering sense it holds that:

$$\left(\boldsymbol{G}_s + \boldsymbol{G}_p^{(i_p)}\right)^{-1} \preceq \boldsymbol{G}_s^{-1} \tag{6.37}$$

and equivalently:

$$Cov(\boldsymbol{x}^{(i_p+1)}) \preceq Cov(\hat{\boldsymbol{y}}) \tag{6.38}$$

In the context of estimation theory, this ordering asserts that the estimator with covariance $Cov(\boldsymbol{x}^{(i_p+1)})$, and by extension $Cov(\hat{\boldsymbol{x}})$, is more accurate (or less uncertain) because it reduces or maintains the same variance for any linear combination of the estimated states, compared to the estimator with covariance $Cov(\hat{\boldsymbol{y}})$ [190].

Finally, we should note that the aforementioned PSE formulation holds for the nonlinear PMU measurement model. If the state vector is expressed in rectangular coordinates, then $\boldsymbol{h}_p(\cdot)$ is a vector of linear functions, and thus $\boldsymbol{H}_{pz}$ is a constant matrix. In this case, the post-processing stage is formulated as detailed in Algorithm 6.3. All the properties of the iterative PSE also hold for the linear PSE formulation.

6.2.3 Proposed data fusion-based state estimation algorithm

As discussed in Subsection 5.2.2.3, in FSE methods the SCADA- and PMU-based SE are solved separately and their outputs are combined using the Bar-Shalom-Campo formula [139] in a post-estimation fusion scheme to obtain the final state estimate. Even though such methods can be executed within a parallel computational framework to enhance efficiency and reduce processing time, they are only applicable under the assumption of complete PMU-observability of the network, which is still not feasible in most power systems.

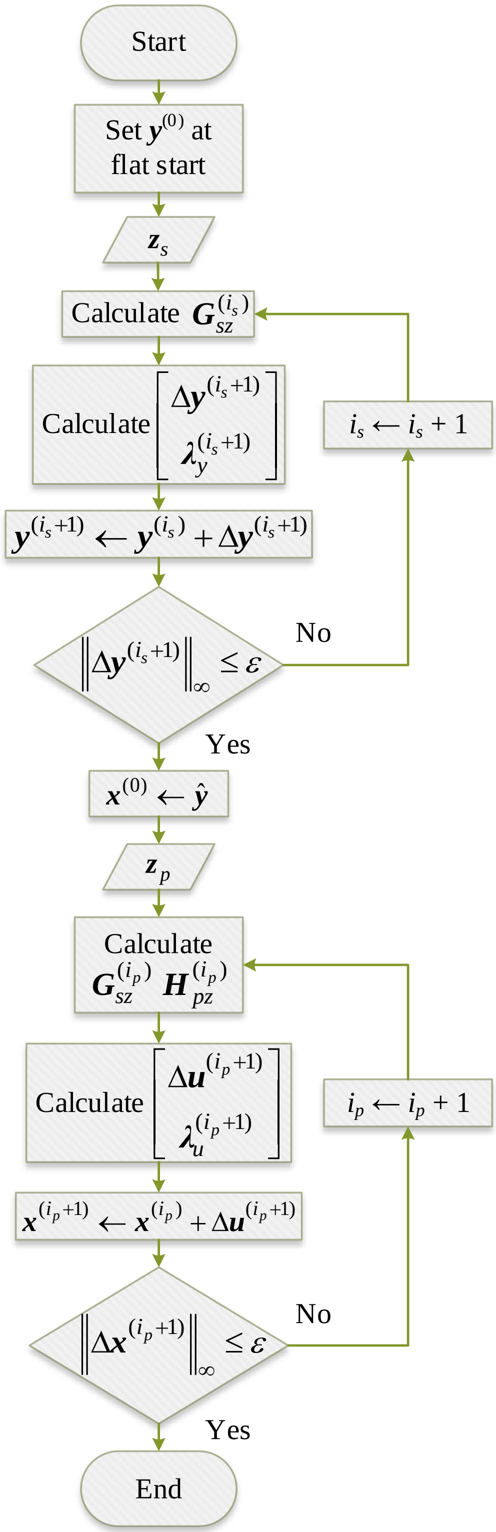

Figure 6.2: Flow diagram of the proposed PSE algorithm.

Algorithm 6.3: Linear post-processing stage of proposed PSE in rectangular coordinates.

1) PMU-based post processing stage:

a. Evaluate $\boldsymbol{G}_{sz}$ at $\hat{\boldsymbol{y}}$.

b. Calculate $\boldsymbol{G}_{sz}^{-1}\boldsymbol{H}_{pz}^{T}$, $a^{-1}\boldsymbol{R}_p + \boldsymbol{H}_{pz}\boldsymbol{G}_{sz}^{-1}\boldsymbol{H}_{pz}^{T}$ and $\boldsymbol{H}_p\hat{\boldsymbol{y}} - \boldsymbol{z}_p$.

c. Solve $\left(a^{-1}\boldsymbol{R}_p + \boldsymbol{H}_{pz}\boldsymbol{G}_{sz}^{-1}\boldsymbol{H}_{pz}^{T}\right)\hat{\boldsymbol{\mu}} = \left(\boldsymbol{H}_p\hat{\boldsymbol{y}} - \boldsymbol{z}_p\right)$ for $\hat{\boldsymbol{\mu}}$.

d. Calculate $\begin{bmatrix}\hat{\boldsymbol{u}} \\ \hat{\boldsymbol{\lambda}}_u\end{bmatrix} \leftarrow -\boldsymbol{G}_{sz}^{-1}\boldsymbol{H}_{pz}^{T}\hat{\boldsymbol{\mu}}$.

g. Calculate $\begin{bmatrix}\hat{\boldsymbol{x}} \\ \hat{\boldsymbol{\lambda}}\end{bmatrix} \leftarrow \begin{bmatrix}\hat{\boldsymbol{y}} \\ \hat{\boldsymbol{\lambda}}_y\end{bmatrix} + \begin{bmatrix}\hat{\boldsymbol{u}} \\ \hat{\boldsymbol{\lambda}}_u\end{bmatrix}$.

Let us assume a network with complete SCADA observability and limited PMU deployment and, thus, partial PMU observability. Figure 6.3 depicts an example of partitioning such a system into two overlapping observable subsystems: one that is both SCADA- and PMU-observable, and one that is observable using only SCADA measurements. A PMU-observable bus is termed as a PMU boundary bus if it is connected to at least one PMU-unobservable bus; otherwise, it is called a PMU internal bus.

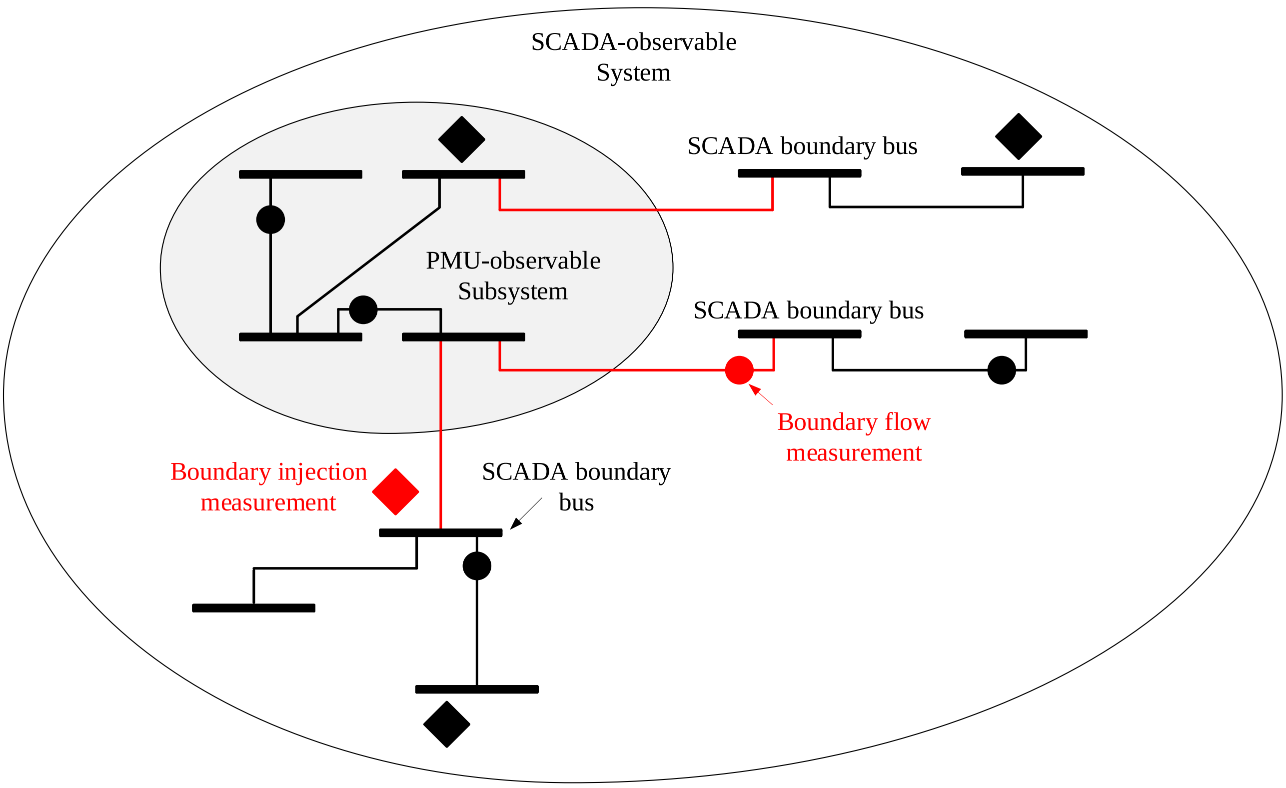

Figure 6.3: Power system partitioning according to SCADA and PMU observability.

Let $\boldsymbol{x}_s \in \mathbb{R}^n$ denote the state vector of the entire system obtained from the SCADA-based SE. The SCADA-based SE problem is solved via the following iterative scheme:

$$\begin{bmatrix} a\boldsymbol{G}_s^{(i)} & \left(\boldsymbol{C}^{(i)}\right)^T \\ \boldsymbol{C}^{(i)} & \boldsymbol{0} \end{bmatrix} \begin{bmatrix} \Delta\boldsymbol{x}_s^{(i+1)} \\ \boldsymbol{\lambda}_s^{(i+1)} \end{bmatrix} = \begin{bmatrix} a\left(\boldsymbol{H}_s^{(i)}\right)^T \boldsymbol{R}_s^{-1}\left(\boldsymbol{z}_s - \boldsymbol{h}(\boldsymbol{x}_s^{(i)})\right) \\ -\boldsymbol{c}(\boldsymbol{x}_s^{(i)}) \end{bmatrix} \tag{6.39}$$

The estimated state vector $\hat{\boldsymbol{x}}_s$ can be partitioned as:

$$\hat{\boldsymbol{x}}_s = \begin{bmatrix} \hat{\boldsymbol{x}}_{ss} \\ \hat{\boldsymbol{x}}_{sp} \end{bmatrix} \tag{6.40}$$

where $\hat{\boldsymbol{x}}_{ss} \in \mathbb{R}^{n_s}$ and $\hat{\boldsymbol{x}}_{sp} \in \mathbb{R}^{n_p}$ denote the estimated state vectors of the SCADA-only observable system and the PMU-observable subsystem, respectively.

If $\boldsymbol{x}_p \in \mathbb{R}^{n_p}$ is the state vector of the PMU-observable subsystem $(n_p < n)$, then the equality-constrained PMU-based linear SE is solved by:

$$\begin{bmatrix} a\boldsymbol{G}_p & \boldsymbol{C}_p^T \\ \boldsymbol{C}_p & \boldsymbol{0} \end{bmatrix} \begin{bmatrix} \hat{\boldsymbol{x}}_p \\ \hat{\boldsymbol{\lambda}}_p \end{bmatrix} = \begin{bmatrix} a\boldsymbol{H}_p^T \boldsymbol{R}_p^{-1} \boldsymbol{z}_p \\ \boldsymbol{0} \end{bmatrix} \tag{6.41}$$

where $\boldsymbol{G}_p = \boldsymbol{H}_p^T \boldsymbol{R}_p^{-1} \boldsymbol{H}_p$ and $\boldsymbol{C}_p$ is the constant Jacobian matrix of $\boldsymbol{c}_p(\cdot)$ modelling zero current injection constraints that pertain to PMU-observable zero injection buses.

A post-processing fusion stage is then employed to fuse the two SE solutions into a single state vector, which relies on a minimum variance criterion, thus providing an unbiased, minimum variance final estimate [140]:

$$\left(\boldsymbol{G}_{sp} + \boldsymbol{G}_p\right) \hat{\boldsymbol{x}}_f = \left(\boldsymbol{G}_{sp} \hat{\boldsymbol{x}}_{sp} + \boldsymbol{G}_p \hat{\boldsymbol{x}}_p\right) \tag{6.42}$$

where $\boldsymbol{G}_{sp}$ is the corresponding $n_p \times n_p$ submatrix of $\boldsymbol{G}_s(\hat{\boldsymbol{x}}_s)$, and $\hat{\boldsymbol{x}}_f$ is the fusion state vector with $\boldsymbol{R}_f = Cov(\hat{\boldsymbol{x}}_f) = \left(\boldsymbol{G}_{sp} + \boldsymbol{G}_p\right)^{-1}$. If $\boldsymbol{G}_{sp} + \boldsymbol{G}_p$ is invertible, then (6.42) can be solved by sparse triangular factorization and forward/back substitution. If inclusion of equality constraints $\boldsymbol{c}_p(\cdot)$ is mandatory to achieve observability, then $\boldsymbol{R}_f = Cov(\hat{\boldsymbol{x}}_f) = \boldsymbol{E}\left(\boldsymbol{G}_{sp} + \boldsymbol{G}_p\right)\boldsymbol{E}^T$ and $\hat{\boldsymbol{x}}_f$ is calculated according to:

$$\hat{\boldsymbol{x}}_f = \boldsymbol{E}\left(\boldsymbol{G}_{sp} + \boldsymbol{G}_p\right)\boldsymbol{E}^T \left(\boldsymbol{G}_{sp} \hat{\boldsymbol{x}}_{sp} + \boldsymbol{G}_p \hat{\boldsymbol{x}}_p\right) \tag{6.43}$$

where $\boldsymbol{E}$ is the $n_p \times n_p$ upper-left submatrix of $\begin{bmatrix} a\left(\boldsymbol{G}_{sp} + \boldsymbol{G}_p\right) + & \boldsymbol{C}_p^T \\ \boldsymbol{C}_p & \boldsymbol{0} \end{bmatrix}^{-1}$.

Now, a post-processing step can be formulated to propagate the refined state estimates of the PMU boundary buses contained in $\hat{\boldsymbol{x}}_{pb} \subset \hat{\boldsymbol{x}}_f$, as additional information to the SE problem of the subsystem that is not observable by PMUs. We use $\boldsymbol{z}_{ss} \subset \boldsymbol{z}_s$ to denote the vector that incorporates measurements from the SCADA-only observable subsystem. Using $\boldsymbol{x}_{ss}$ to denote the vector of the SCADA-only observable states, and $\boldsymbol{x}_{pb} \in \mathbb{R}^{n_{pb}}$ to denote the state vector of the PMU boundary buses, then the SE problem for the PMU-unobservable subsystem including information from the boundary PMU buses can be written as:

$$\begin{aligned} \boldsymbol{z}_{ss} &= \boldsymbol{h}_{ss}(\boldsymbol{x}_{spb}) + \boldsymbol{e}_{ss} \\ \hat{\boldsymbol{x}}_{pb} &= \boldsymbol{h}_{pb}(\boldsymbol{x}_{spb}) + \boldsymbol{e}_{pb} \\ \boldsymbol{0} &= \boldsymbol{c}_{ss}(\boldsymbol{x}_{spb}) \end{aligned} \tag{6.44}$$

where $\boldsymbol{x}_{spb} := \left[\boldsymbol{x}_{ss}^T \;\; \boldsymbol{x}_{pb}^T\right]^T$, $\boldsymbol{h}_{ss} \subset \boldsymbol{h}_s$ is the vector of functions modeling measurements $\boldsymbol{z}_{ss}$ with measurement error $\boldsymbol{e}_{ss}$, $\boldsymbol{h}_{pb}(\boldsymbol{x}_{spb}) = \boldsymbol{H}_{pb}\boldsymbol{x}_{spb}$ is the vector of linear functions mapping *a priori* information $\hat{\boldsymbol{x}}_{pb}$ to $\boldsymbol{x}_{spb}$, with $\boldsymbol{H}_{pb}$ a constant matrix of ones and zeros, and $\boldsymbol{e}_{pb}$ is the Gaussian estimation error of $\hat{\boldsymbol{x}}_{pb}$, with $\boldsymbol{R}_{pb} = Cov(\boldsymbol{e}_{pb})$ the corresponding $n_{pb} \times n_{pb}$ submatrix of $\boldsymbol{R}_f$. $\boldsymbol{c}_{ss}(\cdot)$ includes relevant zero current injection information from the SCADA-only observable network.

Noticing that problem (6.44) is similar to (6.3), using the same solution process and similar mathematical manipulations we can write:

$$\begin{bmatrix} a\boldsymbol{G}_{ss}^{(i)} & \left(\boldsymbol{C}_{ss}^{(i)}\right)^T & \boldsymbol{H}_{pb}^T \\ \boldsymbol{C}_{ss}^{(i)} & \boldsymbol{0} & \boldsymbol{0} \\ \boldsymbol{H}_{pb} & \boldsymbol{0} & -a^{-1}\boldsymbol{R}_{pb} \end{bmatrix} \begin{bmatrix} \Delta\boldsymbol{x}_{spb}^{(i+1)} \\ \boldsymbol{\lambda}^{(i+1)} \\ \boldsymbol{\mu}^{(i+1)} \end{bmatrix} = \begin{bmatrix} a\left(\boldsymbol{H}_{ss}^{(i)}\right)^T \boldsymbol{R}_{ss}^{-1}\Delta\boldsymbol{z}_{ss}^{(i)} \\ -\boldsymbol{c}_{ss}(\boldsymbol{x}_{spb}^{(i)}) \\ \Delta\boldsymbol{z}_{pb}^{(i)} \end{bmatrix} \Leftrightarrow$$

$$\begin{bmatrix} \Delta\boldsymbol{y}_{spb}^{(i+1)} \\ \boldsymbol{\lambda}_y^{(i+1)} \end{bmatrix} = \left(\boldsymbol{G}_{ssz}^{(i)}\right)^{-1} \begin{bmatrix} a\left(\boldsymbol{H}_{ss}^{(i)}\right)^T \boldsymbol{R}_{ss}^{-1}\Delta\boldsymbol{z}_{ss}^{(i)} \\ -\boldsymbol{c}_{ss}(\boldsymbol{x}_{spb}^{(i)}) \end{bmatrix} \tag{6.45}$$

$$\begin{bmatrix} \Delta\boldsymbol{u}_{spb}^{(i+1)} \\ \boldsymbol{\lambda}_u^{(i+1)} \end{bmatrix} = \left(\boldsymbol{G}_{ssz}^{(i)}\right)^{-1} \boldsymbol{H}_{pbz}^T \left(a^{-1}\boldsymbol{R}_{pb} + \boldsymbol{H}_{pbz}\left(\boldsymbol{G}_{ssz}^{(i)}\right)^{-1} \boldsymbol{H}_{pbz}^T\right)^{-1} \left(\Delta\boldsymbol{z}_{pb}^{(i)} - \boldsymbol{H}_{pb}\Delta\boldsymbol{y}_{spb}^{(i)}\right) \tag{6.46}$$

$$\begin{bmatrix} \Delta\boldsymbol{x}_{spb}^{(i+1)} \\ \boldsymbol{\lambda}^{(i+1)} \end{bmatrix} = \begin{bmatrix} \Delta\boldsymbol{y}_{spb}^{(i+1)} \\ \boldsymbol{\lambda}_y^{(i+1)} \end{bmatrix} + \begin{bmatrix} \Delta\boldsymbol{u}_{spb}^{(i+1)} \\ \boldsymbol{\lambda}_u^{(i+1)} \end{bmatrix} \tag{6.47}$$

where $\boldsymbol{G}_{ssz}^{(i)} = \begin{bmatrix} a\boldsymbol{G}_{ss}^{(i)} & \left(\boldsymbol{C}_{ss}^{(i)}\right)^T \\ \boldsymbol{C}_{ss}^{(i)} & \boldsymbol{0} \end{bmatrix}$, $\boldsymbol{H}_{pbz} = \left[\boldsymbol{H}_{pb} \;\; \boldsymbol{0}\right]$, $\Delta\boldsymbol{z}_{ss}^{(i)} = \boldsymbol{z}_{ss} - \boldsymbol{h}_{ss}(\boldsymbol{x}_{spb}^{(i)})$ and $\Delta\boldsymbol{z}_{pb}^{(i)} = \hat{\boldsymbol{x}}_{pb} - \boldsymbol{h}_{pb}(\boldsymbol{x}_{spb}^{(i)})$.

All the properties of the proposed ISE and PSE algorithms of the previous Sections, are retained for the iterative scheme (6.45)–(6.47). Hence, the post-processing stage of the proposed FSE can be solved using either Algorithm 6.1 or Algorithm 6.2 to calculate $\hat{\boldsymbol{x}}_{pb}$. The complete FSE scheme is presented in Algorithm 6.4

In implementing the proposed two-stage fusion SE process, the SCADA-based and PMU-based SE modules can be effectively executed within a parallel computational environment, as these two tasks are inherently independent. By exploiting the parallel computing capabilities available in modern multi-core processors, each estimation process can be allocated to distinct computational threads or processing units. This parallel implementation capitalizes on the modular nature of the estimation tasks, significantly reducing the total computation time compared to conventional sequential approaches. Upon completion of the parallel estimations, the individual results are synchronized, and the Bar-Shalom-Campo fusion formula is applied to integrate the estimates of the overlapping state variables associated with PMU-observable buses. The resultant fused estimate subsequently serves as input to the post-estimation refinement step to enhance the accuracy of the SCADA-only observable subsystem. The parallel execution framework thus enables efficient utilization of computational resources, improves scalability for large-scale power systems, and aligns with the overall objective of enhancing SE accuracy while minimizing additional computational overhead.

Algorithm 6.4: Proposed FSE algorithm (linear PMU measurement model).

1) SCADA-based estimation:

a. Initialize the iteration index $i_s \leftarrow 0$ and set the state vector $\boldsymbol{x}_s^{(0)}$ at flat start.

b. Calculate the augmented gain matrix $\boldsymbol{G}_{sz}^{(i_s)}$.

c. Calculate the right-hand side of (6.45), $\begin{bmatrix} a\left(\boldsymbol{H}_s^{(i_s)}\right)^T \boldsymbol{R}_s^{-1}\left(\boldsymbol{z}_s - \boldsymbol{h}(\boldsymbol{x}_s^{(i_s)})\right) \\ -\boldsymbol{c}(\boldsymbol{x}_s^{(i_s)}) \end{bmatrix}$.

d. Decompose $\boldsymbol{G}_{sz}^{(i_s)}$ and solve (6.45) for $\Delta\boldsymbol{x}_s^{(i_s+1)}$.

e. Check for convergence: **If** the convergence criteria are satisfied for all state variables, **then** $\hat{\boldsymbol{x}}_s \leftarrow \boldsymbol{x}_s^{(i_s)} + \Delta\boldsymbol{x}_s^{(i_s+1)}$ and terminate the algorithm. **Else**, $\boldsymbol{x}_s^{(i_s+1)} \leftarrow \boldsymbol{x}_s^{(i_s)} + \Delta\boldsymbol{x}_s^{(i_s+1)}$, $i_s \leftarrow i_s + 1$ and return to Step (b).

2) PMU-based estimation:

a. Calculate $\boldsymbol{G}_p = \boldsymbol{H}_p^T \boldsymbol{R}_p^{-1} \boldsymbol{H}_p$ and $\boldsymbol{C}_p$.

b. Solve $\begin{bmatrix} a\boldsymbol{G}_p & \boldsymbol{C}_p^T \\ \boldsymbol{C}_p & \boldsymbol{0} \end{bmatrix}\begin{bmatrix} \hat{\boldsymbol{x}}_p \\ \hat{\boldsymbol{\lambda}}_p \end{bmatrix} = \begin{bmatrix} a\boldsymbol{H}_p^T \boldsymbol{R}_p^{-1}\boldsymbol{z}_p \\ \boldsymbol{0} \end{bmatrix}$ for $\begin{bmatrix} \hat{\boldsymbol{x}}_p \\ \hat{\boldsymbol{\lambda}}_p \end{bmatrix}$.

3) Post-processing state fusion:

a. Form vector $\hat{\boldsymbol{x}}_{sp}$ and matrix $\boldsymbol{G}_{sp}$.

b. Solve $\left(\boldsymbol{G}_{sp} + \boldsymbol{G}_p\right)\hat{\boldsymbol{x}}_f = \left(\boldsymbol{G}_{sp}\hat{\boldsymbol{x}}_{sp} + \boldsymbol{G}_p\hat{\boldsymbol{x}}_p\right)$ for $\hat{\boldsymbol{x}}_f$.

c. Solve (6.45)–(6.47) using either Algorithm 6.1 or Algorithm 6.2.

6.2.4 Summary

This Section introduced an improved HSE method based on Hachtel's augmented matrix approach, designed to decouple and process independently the available SCADA and PMU data in the EMS. The modular architecture of the proposed HSE algorithm makes it suitable for ISE, PSE, and FSE implementations, with partially PMU-observable network, while dealing with the suboptimality of PSE formulations and eliminating the need for pseudo-measurements of FSE methods.

6.3 Hybrid state estimation for networks including classic HVDC links

While AC grids form the backbone of traditional power systems, HVDC transmission is an advanced technology that enables efficient bulk power transport with enhanced controllability [191]. The majority of SE research has focused on AC systems, with limited studies addressing AC/DC networks. The first integration of HVDC links into SE algorithms, using conventional RTU measurements on both AC and DC sides, dates back to the early 1980s [192].

SE algorithms for AC systems incorporating classic HVDC links − often referred to as Line Commutated Converter (LCC) or Current Source Converter (CSC)-HVDC− are well-documented. A PMU-only state estimator in polar coordinates for AC systems with LCC-HVDC links is introduced in [193], later expanded in [194] to accommodate various control modes. A PMU-based equality-constrained WLS state estimator in rectangular coordinates is described in [185], while [195] presents a robust two-stage least-trimmed squares-based SE algorithm for HVAC/HVDC systems.

With the rise of Voltage Source Converter (VSC) technology in HVDC transmission, SE models have evolved accordingly. Reference [196] introduces a PMU-based SE model for VSC-HVDC links, while [197] proposes an HSE combining SCADA and PMU measurements for HVAC/VSC-HVDC networks. A distributed SE algorithm for HVAC/VSC-HVDC grids is presented in [198], and a WLS-based SE model using pseudo-measurements for converter modeling is detailed in [199]. Reference [200] proposes the integration of multi-terminal VSC-HVDC links in a Hachtel-based SE framework incorporating SCADA and PMU measurements.

This Section introduces a unified HSE algorithm that simultaneously estimates AC and DC states by incorporating SCADA and PMU measurements from the AC network alongside DC link data. The main contributions of the proposed HSE algorithm are as follows:

1) AC and DC measurements are modeled independently and processed simultaneously as functions of AC and DC states, respectively. AC and DC states are also estimated simultaneously.
2) The relationship between AC and DC states is expressed by a set of three nonlinear equality constraints.
3) Fewer real-time measurements are required for the HVDC links to be observable, compared to similar methods found in the literature.

6.3.1 Proposed classic HVDC link model

A classic HVDC link between AC buses *i* and *j* is shown in Figure 6.4, where the subscripts *i* and *j* refer to the rectifier and inverter side of the DC link, respectively. In order to model the interconnection of the DC link with the AC system, a virtual AC bus *ci* (*cj*) is introduced between the converter transformer and the rectifier (inverter).

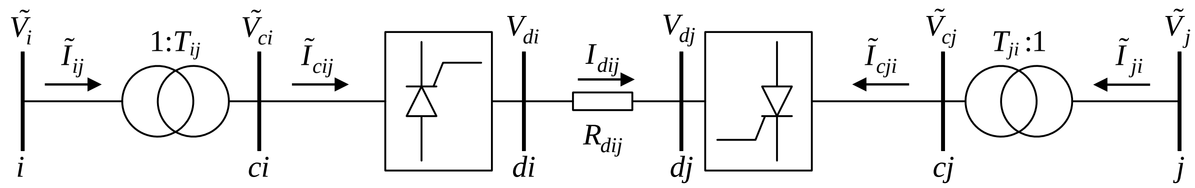

Figure 6.4: Single line diagram of a two-terminal classic HVDC link.

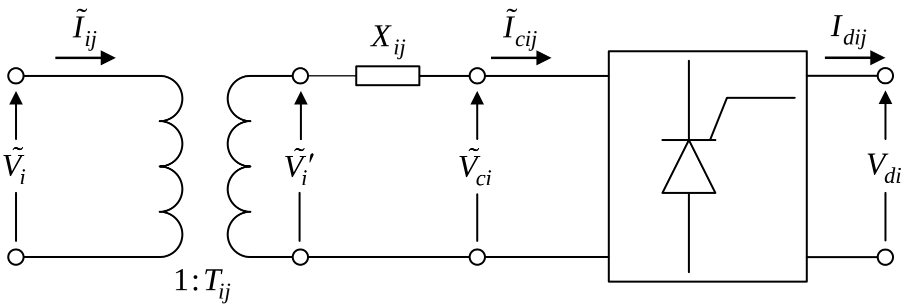

Figure 6.5: Transformer model at the rectifier side of the classic HVDC link.

The symbols appearing in Figure 6.4 are defined as follows: $\tilde{V}_k = V_k \angle \delta_k$, $k = i, ci, cj, j$ are AC line-to-line voltage phasors, $\tilde{I}_m = I_m \angle \theta_m$, $m = ij, cij, cji, ji$ are AC line current phasors, T_{ij}, T_{ji} and X_{ij}, X_{ji} are the off-nominal turns ratios and the reactance values of coupling transformers, respectively. V_{di} and V_{dj} are DC voltages, $I_{dij} = -I_{dji}$ is the DC current, and R_{dij} is the resistance of the DC line.

Based on the equivalent circuit of the transformer at the rectifier side (Figure 6.5) we obtain:

$$T_{ij} = \frac{\tilde{V}'_{ci}}{\tilde{V}_i} = \frac{V'_{ci}\angle\delta'_{ci}}{V_i\angle\delta_i} \Rightarrow \begin{cases} V'_{ci} = T_{ij}V_i \\ \delta'_{ci} = \delta_i \end{cases} \tag{6.48}$$

$$T_{ij} = \frac{\tilde{I}_{ij}}{\tilde{I}_{cij}} = \frac{I_{ij}\angle\theta_{ij}}{I_{cij}\angle\theta_{cij}} \Rightarrow \begin{cases} I_{ij} = T_{ij}I_{cij} \\ \theta_{ij} = \theta_{cij} \end{cases} \tag{6.49}$$

Using (6.48) and (6.49), the following AC/DC coupling equations can be derived:

$$V_{di} = k_1 B_{ij} V'_{ci} \cos(\delta'_{ci} - \theta_{cij}) = k_1 B_{ij} T_{ij} V_i \cos(\delta_i - \theta_{ij}) \tag{6.50}$$

$$V_{di} = k_1 B_{ij} V'_{ci} \cos a_{ij} - k_2 B_{ij} X_{ij} I_{dij} = k_1 B_{ij} T_{ij} V_i \cos a_{ij} - k_2 B_{ij} X_{ij} I_{dij} \tag{6.51}$$

$$I_{cij} = k_3 B_{ij} I_{dij} \tag{6.52}$$

where a_{ij} is the firing angle, B_{ij} represents the number of rectifier bridges, $k_1 = 3\sqrt{2}/\pi$, $k_2 = 3/\pi$, and $k_3 = \sqrt{6}/\pi$.

The relationship between current and voltages at the DC line is expressed by:

$$I_{dij} = \frac{V_{di} - V_{dj}}{R_{dij}} \tag{6.53}$$

Combining (6.50) with (6.51) yields:

$$P_{dij} = V_{di} I_{dij} = \sqrt{3} V_i I_{ij} \cos(\delta_i - \theta_{ij}) \tag{6.54}$$

$$P_{ij} = \sqrt{3} V_{ci} I_{cij} \cos(\delta_{ci} - \theta_{cij}) = P_{dij} \tag{6.55}$$

under the assumption that the active power losses at the rectifier and transformer are negligible. Combining (6.51) and (6.53) we obtain the following equality constraint:

$$V_{di} - k_1 B_{ij} T_{ij} V_i \cos a_{ij} + \frac{k_2 B_{ij} X_{ij}}{R_{dij}} (V_{di} - V_{dj}) = 0 \tag{6.56}$$

Given that $P_{ij} = P_{cij} = \dfrac{V'_{ci} V_{ci} \sin(\delta'_{ci} - \delta_{ci})}{X_{ij}} = P_{dij}$, combining (6.48), (6.49) with (6.53) yields:

$$\frac{V_{di}}{R_{dij}} (V_{di} - V_{dj}) - \frac{T_{ij} V_i V_{ci} \sin(\delta_i - \delta_{ci})}{X_{ij}} = 0 \tag{6.57}$$

Based on the transformer model of Figure 6.5 we obtain:

$$I_{cij}\angle\theta_{cij} = -\frac{j}{\sqrt{3} X_{ij}} (T_{ij} V_i \angle\delta_i - V_{ci}\angle\delta_{ci}) \tag{6.58}$$

Combination of (6.52) and (6.58) gives:

$$T_{ij}^2 V_i^2 + V_{ci}^2 - 2 T_{ij} V_i V_{ci} \cos(\delta_i - \delta_{ci}) - \frac{3 k_3^2 B_{ij}^2 X_{ij}^2}{R_{dij}^2} (V_{di} - V_{dj})^2 = 0 \tag{6.59}$$

To convert the equality constraints (6.56), (6.57) and (6.59) to the per unit system, the following base quantities are chosen, where actual and per unit variables are represented by capital and lowercase letters, respectively:

- For the AC side the base quantities chosen are: base impedances $Z_{b,i} = \dfrac{V_{b,i}^2}{S_b}$, $Z_{b,ci} = \dfrac{V_{b,ci}^2}{S_b}$ in Ω, and base currents $I_{b,i} = \dfrac{S_b}{\sqrt{3}V_{b,i}}$, $I_{b,ci} = \dfrac{S_b}{\sqrt{3}V_{b,ci}}$ in A, where S_b is the three-phase base power in MVA and $V_{b,i}$, $V_{b,ci}$ are the line-to-line base voltages in kV at buses *i* and *ci*, respectively.
- For the DC side the base quantities chosen are: base power $P_b = S_b$, base voltage $V_{b,di} = V_{b,ci}$ in kV, base current $I_{b,di} = \dfrac{P_b}{V_{b,di}} = \dfrac{S_b}{V_{b,ci}}$ in A, and base impedance $R_{b,di} = \dfrac{V_{b,di}}{I_{b,di}} = Z_{b,ci}$ in Ω.

After some algebraic transformations the AC/DC equality constraints (6.56), (6.57) and (6.59) are expressed in per unit as:

$$\frac{v_{di}}{r_{dij}}(v_{di} - v_{dj}) - \frac{t_{ij} v_i v_{ci} \sin(\delta_i - \delta_{ci})}{x_{ij}} = 0 \tag{6.60}$$

$$v_{di} - k_1 B_{ij} t_{ij} v_i \cos a_{ij} + \frac{k_2 B_{ij} x_{ij}}{r_{dij}}(v_{di} - v_{dj}) = 0 \tag{6.61}$$

$$t_{ij}^2 v_i^2 + v_{ci}^2 - 2 t_{ij} v_i v_{ci} \cos(\delta_i - \delta_{ci}) - \frac{3 k_3^2 B_{ij}^2 x_{ij}^2}{r_{dij}^2}(v_{di} - v_{dj})^2 = 0 \tag{6.62}$$

where t_{ij} is the off-nominal tap ratio in p.u.

Via similar mathematical manipulations, AC/DC coupling equality constraints are obtained for the inverter side:

$$\frac{v_{dj}}{r_{dij}}(v_{dj} - v_{di}) - \frac{t_{ji} v_j v_{cj} \sin(\delta_j - \delta_{cj})}{x_{ji}} = 0 \tag{6.63}$$

$$v_{dj} - k_1 B_{ji} t_{ji} v_j \cos \gamma_{ji} - \frac{k_2 B_{ji} x_{ji}}{r_{dij}}(v_{dj} - v_{di}) = 0 \tag{6.64}$$

$$t_{ji}^2 v_j^2 + v_{cj}^2 - 2 t_{ji} v_j v_{cj} \cos(\delta_j - \delta_{cj}) - \frac{3 k_3^2 B_{ji}^2 x_{ji}^2}{r_{dij}^2}(v_{dj} - v_{di})^2 = 0 \tag{6.65}$$

where γ_{ji} is the inverter extinction angle.

6.3.2 HVAC/HVDC state estimation formulation

Let $\boldsymbol{z} \in \mathbb{R}^m$ denote the measurement vector, $\boldsymbol{x} \in \mathbb{R}^n$ the vector of state variables, $\boldsymbol{h}(\cdot)$ the vector of non-linear functions relating measured and state variables, $\boldsymbol{c}(\cdot)$ the vector of non-linear functions modeling zero power injections and AC/DC coupling equality constraints (6.60)–(6.62) and (6.63)–(6.65) , and $\boldsymbol{e} \in \mathbb{R}^m$ the measurement error vector normally distributed with zero mean and diagonal covariance matrix $\boldsymbol{R}$.

As in Section 6.1, the equality-constrained nonlinear HSE problem is solved based on the WLS criterion:

$$\begin{aligned} &\hat{\boldsymbol{x}} := \arg\min_{\boldsymbol{x} \in \mathbb{R}^n} J(\boldsymbol{x}) = \left(\boldsymbol{z} - \boldsymbol{h}(\boldsymbol{x})\right)^T \boldsymbol{R}^{-1} \left(\boldsymbol{z} - \boldsymbol{h}(\boldsymbol{x})\right) \\ &\text{s.t. } \boldsymbol{c}(\boldsymbol{x}) = \boldsymbol{0} \end{aligned} \tag{6.66}$$

By applying the Gauss–Newton method to the first-order optimality conditions of the resulting Lagrangian function, the state estimate is obtained by iteratively solving:

$$\begin{bmatrix} \mathbf{G}^{(i)} & \left(\mathbf{C}^{(i)}\right)^T \\ \mathbf{C}^{(i)} & \mathbf{0} \end{bmatrix} \begin{bmatrix} \Delta \mathbf{x}^{(i+1)} \\ \boldsymbol{\lambda}^{(i+1)} \end{bmatrix} = \begin{bmatrix} \left(\mathbf{H}^{(i)}\right)^T \mathbf{R}^{-1}\left(\mathbf{z} - \mathbf{h}(\mathbf{x}^{(i)})\right) \\ -\mathbf{c}(\mathbf{x}^{(i)}) \end{bmatrix} \tag{6.67}$$

where i is the iteration index, $\boldsymbol{\lambda}$ is the vector of Lagrange multipliers, $\mathbf{H}^{(i)} = \partial \mathbf{h}(\mathbf{x}^{(i)})/\partial \mathbf{x}$ and $\mathbf{C}^{(i)} = \partial \mathbf{c}(\mathbf{x}^{(i)})/\partial \mathbf{x}$ are Jacobian matrices, and $\mathbf{G}^{(i)} = \left(\mathbf{H}^{(i)}\right)^T \mathbf{R}^{-1}\mathbf{H}^{(i)}$ is the gain matrix. The convergence of the iterative procedure is attained when $\left\|\Delta \mathbf{x}^{(i+1)}\right\|_\infty \leq \varepsilon$, where ε is a pre-specified convergence threshold.

When enough measurements are available so that $\operatorname{rank}\left\{\begin{bmatrix} \mathbf{H}^T & \mathbf{C}^T \end{bmatrix}^T\right\} = n$ at each iteration (i) to guarantee solvability of (6.67) for a state estimate, the system is said to be numerically observable, under the assumption that the rows of matrix $\mathbf{C}$ are linearly independent. If there are no phasor measurements, then an artificial zero valued phase angle measurement is introduced at reference bus to make column rank of $\begin{bmatrix} \mathbf{H}^T & \mathbf{C}^T \end{bmatrix}^T$ full.

The AC/DC measurement model can be expressed with respect to Figure 6.6, illustrating a generic AC bus i of the network, including generator, load, shunt, branch (transmission line or transformer), and converter (rectifier or inverter). In general, one or more branches and converters may be connected to bus i. A branch $i-j$ between any two AC buses i and $j \in \{k, l\}$ is represented with the two-port π-model, where $\tilde{y}_{ij} = g_{ij} + jb_{ij}$ is the series admittance, and $\tilde{y}_{sij} = g_{sij} + jb_{sij}$ $(\tilde{y}_{sji} = g_{sji} + jb_{sji})$ is the shunt admittance between bus i (j) and the ground.

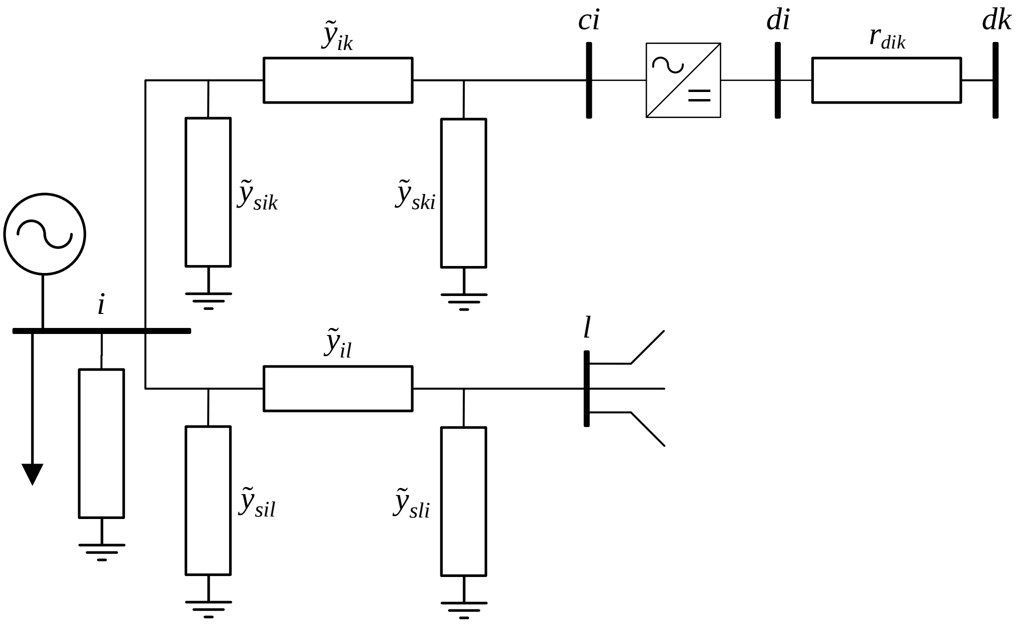

Figure 6.6: A generic AC bus connected to an AC branch and a DC link.

For a line $\tilde{y}_{sij} = \tilde{y}_{sji}$, and for a transformer $\tilde{y}_{sij} = t_{ij}(t_{ij} - 1)\tilde{y}_{ij}$ and $\tilde{y}_{sji} = (1 - t_{ij})\tilde{y}_{ij}$, where t_{ij} is the off-nominal p.u. tap ratio at side j of the transformer. A capacitor or reactor is represented with an admittance $\tilde{y}_i = g_i + jb_i$ connected to bus i. All electrical quantities are expressed in the per-unit system.

Consider that $\mathcal{B}_i$ is the set of AC buses connected to bus *i* through branches (lines or transformers), $\mathcal{C}_i$ is the set of secondary AC buses of the converter (rectifier or inverter) transformers connected to bus *i*, $\mathcal{N}_i = \mathcal{B}_i \cup \mathcal{C}_i$, $k \in \mathcal{B}_i$, $ci \in \mathcal{C}_i$, and di (dj) is the sending (receiving) end of the DC line $di - dj$. The AC measurements associated with bus *i* are described in detail in Sections 4.6 and 4.7, for the SCADA and PMU measurement systems, respectively. For a DC transmission line, the DC voltage is usually obtained using a resistive-capacitive (RC) voltage divider, while for the DC current various current sensor technologies can be used [201]. Generally, the respective DC measurements include:

- Voltage magnitude at bus *di*:

$$v_{di}^{m} = v_{di} + e_{v_{di}} \tag{6.68}$$

- Current magnitude from bus *di* to bus *dj*:

$$i_{dij}^{meas} = (v_{di} - v_{dj}) / r_{dij} + e_{i_{dij}} \tag{6.69}$$

- Active power from bus *di* to bus *dj*:

$$p_{dij}^{meas} = v_{di}(v_{di} - v_{dj}) / r_{dij} + e_{p_{dij}} \tag{6.70}$$

The subvector $\boldsymbol{x}_i$ of state vector $\boldsymbol{x}$ associated with generic bus *i* of Figure 6.6, includes the following AC and DC state variables in polar coordinates:

$$\boldsymbol{x}_i = \left[v_i \ \delta_i \ v_j \ \delta_j \ v_{ci} \ \delta_{ci} \ v_{di} \ v_{dj} \ \alpha_{ij} \ \gamma_{ij} \right]^T \tag{6.71}$$

6.4 Inclusion of current injection phasors in hybrid state estimators

The exploitation of synchronized phasor measurements for enhancing the capabilities of the modern EMS has been a topic of extensive research. In particular, the availability of both current magnitudes and angles is a differentiator for SE-based real-time situational awareness, as conventional metering systems typically provide only power and ampere measurements [38]. Current phasor data can be leveraged for various applications, including detecting reverse power flow, outage management, topology detection, model validation, fault location, as well as disturbance detection and classification [202].

The incorporation of line current flow phasors in HSE algorithms has been thoroughly investigated for transmission [9], [203], [204] and distribution systems [204]–[208]. Many works have also addressed the inclusion of current injections in SE, typically in the form of pseudo-measurements derived from forecasted SCADA (power injection) measurements, in order to linearize the measurement model [205]–[208]. However, currently, the option of utilizing PMUs to directly measure complex bus current injections for SE has received only rudimentary consideration and has not yet been adequately explored from either an algorithmic or practical perspective. Motivated by this literature gap, the main goal of this Section is to analyze the mathematical model and investigate the impact of both current flow and injection measurements on the performance of HSE. Furthermore, technical issues related to the implementation of the examined configurations, such as the measurement point in the circuit, the use of instrument transformers, and cost parameters, are discussed.

6.4.1 Current measurement configurations

Let us rewrite here the HSE measurement model as formulated in Section 6.1, for an N-bus power system and an MS comprising m_s SCADA measurements, m_p PMU measurements, and m_z zero injections:

$$\begin{bmatrix} \boldsymbol{z}_s \\ \boldsymbol{z}_p \end{bmatrix} = \begin{bmatrix} \boldsymbol{h}_s(\boldsymbol{x}) \\ \boldsymbol{h}_p(\boldsymbol{x}) \end{bmatrix} + \boldsymbol{e}$$
$$\boldsymbol{0} = \boldsymbol{c}(\boldsymbol{x}) \tag{6.72}$$

Assuming additive Gaussian measurement noise, the estimated state vector $\hat{\boldsymbol{x}}$, is obtained by solving the following WLS optimization problem with objective function $J(\boldsymbol{x})$:

$$\hat{\boldsymbol{x}} := \arg\min_{\boldsymbol{x}} J(\boldsymbol{x}) = \boldsymbol{e}^T \boldsymbol{R}^{-1} \boldsymbol{e}$$
$$\text{s.t. } \boldsymbol{c}(\hat{\boldsymbol{x}}) = \boldsymbol{0} \tag{6.73}$$

The state vector $\boldsymbol{x}$ is expressed in either polar or rectangular coordinates, with its i-th entry written as $\boldsymbol{x}_i = [V_i \;\; \delta_i]^T$ or $\boldsymbol{x}_i = [V_{\mathrm{R},i} \;\; V_{\mathrm{I},i}]^T = [V_i \cos\delta_i \;\; V_i \sin\delta_i]^T$, where $\tilde{V}_i = V_i \angle \delta_i$ is the voltage phasor at bus i, and subscripts R and I denote its real and imaginary parts, respectively.

Consider now a bus i with an installed PMU and the current measurement configurations illustrated in Figure 6.7, obtained via CTs. The term PMU is used here to refer to any device capable of recording phasors at either power transmission or distribution level, encompassing IEDs, micro-PMUs, or any other synchrophasor-enabled devices. In the following, the functions $h_{I_{\mathrm{R},ij}}(\boldsymbol{x})$, $h_{I_{\mathrm{I},ij}}(\boldsymbol{x})$, $h_{I_{\mathrm{R},i}}(\boldsymbol{x})$, and $h_{I_{\mathrm{I},i}}(\boldsymbol{x})$ of $\boldsymbol{h}_p(\boldsymbol{x})$, are used to model the current flow and injection phasors depicted in Figure 6.7.

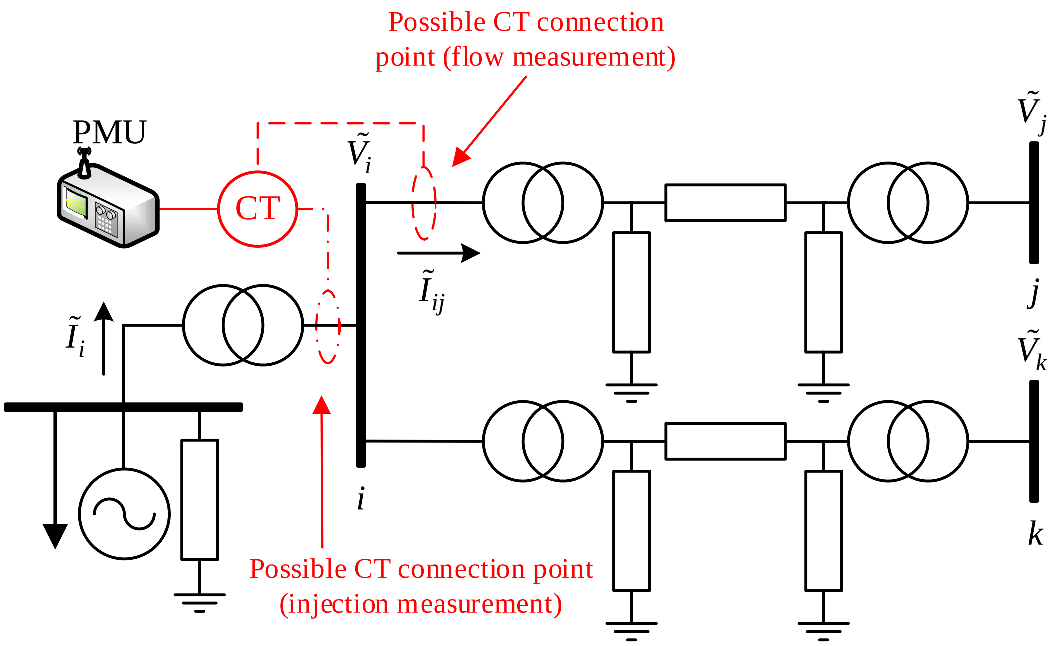

Figure 6.7: Different obtained current phasor measurements depending on CT configuration.

The complex current flow measurement is written as:

$$\tilde{I}_{ij}^m = I_{ij}^m \angle \theta_{ij}^m = I_{\mathrm{R},ij}^m + jI_{\mathrm{I},ij}^m \tag{6.74}$$

The respective measurement functions have already been defined in Section 4.7, as follows:

$$h_{I_{\mathrm{R},ij}}(\boldsymbol{x}) = t_{ij}^2 V_i \left((g_{sij} + g_{ij}) \cos\delta_i - (b_{sij} + b_{ij}) \sin\delta_i \right) - t_{ij} t_{ji} V_j \left(g_{ij} \cos(\delta_j - \Delta\varphi_{ij}) - b_{ij} \sin(\delta_j - \Delta\varphi_{ij}) \right) \tag{6.75}$$

$$h_{I_{\mathrm{I},ij}}(\boldsymbol{x}) = t_{ij}^2 V_i \left((g_{sij} + g_{ij}) \sin\delta_i + (b_{sij} + b_{ij}) \cos\delta_i \right) - t_{ij} t_{ji} V_j \left(g_{ij} \sin(\delta_j - \Delta\varphi_{ij}) + b_{ij} \cos(\delta_j - \Delta\varphi_{ij}) \right) \tag{6.76}$$

$$h_{I_{ij}}(\boldsymbol{x}) = \sqrt{h_{I_{\mathrm{R},ij}}^2(\boldsymbol{x}) + h_{I_{\mathrm{I},ij}}^2(\boldsymbol{x})} \tag{6.77}$$

$$h_{\theta_{ij}}(\boldsymbol{x}) = \arctan\left(\frac{h_{I_{\mathrm{I},ij}}(\boldsymbol{x})}{h_{I_{\mathrm{R},ij}}(\boldsymbol{x})}\right) \tag{6.78}$$

where g_{sij}, g_{ij}, b_{sij}, b_{ij}, t_{ij}, t_{ji}, and $\Delta\varphi_{ij} = \varphi_{ij} - \varphi_{ji}$ have been defined in Chapter 4. Therefore, the terms of (6.74) are written as:

$$I_{\mathrm{R},ij}^m = h_{I_{\mathrm{R},ij}}(\boldsymbol{x}) + e_{I_{\mathrm{R},ij}} \tag{6.79}$$

$$I_{\mathrm{I},ij}^m = h_{I_{\mathrm{I},ij}}(\boldsymbol{x}) + e_{I_{\mathrm{I},ij}} \tag{6.80}$$

$$I_{ij}^m = h_{I_{ij}}(\boldsymbol{x}) + e_{I_{ij}} \tag{6.81}$$

$$\theta_{ij}^m = h_{\theta_{ij}}(\boldsymbol{x}) + e_{\theta_{ij}} \tag{6.82}$$

The complex current injection measurement can be expressed as:

$$\tilde{I}_i^m = I_i^m \angle \theta_i^m = I_{\mathrm{R},i}^m + jI_{\mathrm{I},i}^m \tag{6.83}$$

According to (4.24), it holds that:

$$\tilde{I}_i = \tilde{Y}_{ii}\tilde{V}_i + \sum_{j\in a(i)} \tilde{Y}_{ij}\tilde{V}_j \tag{6.84}$$

where $\tilde{Y}_{ij} = G_{ij} + jB_{ij} = -\tilde{n}_{ij}^*\tilde{n}_{ji}\tilde{y}_{ij}$, $\tilde{Y}_{ii} = G_{ii} + jB_{ii} = \tilde{y}_i + \sum_{j\in a(i)} t_{ij}^2\left(\tilde{y}_{sij} + \tilde{y}_{ij}\right)$, $a(i)$ is the set of buses adjacent to bus i. The real and imaginary parts of $\tilde{I}_i$ are written as:

$$h_{I_{\mathrm{R},i}}(\boldsymbol{x}) = V_i\left(G_{ii}\cos\delta_i - B_{ii}\sin\delta_i\right) + \sum_{j\in a(i)} V_j\left(G_{ij}\cos\delta_j - B_{ij}\sin\delta_j\right) \tag{6.85}$$

$$h_{I_{\mathrm{I},i}}(\boldsymbol{x}) = V_i\left(B_{ii}\cos\delta_i + G_{ii}\sin\delta_i\right) + \sum_{j\in a(i)} V_j\left(B_{ij}\cos\delta_j + G_{ij}\sin\delta_j\right) \tag{6.86}$$

$$h_{I_i}(\boldsymbol{x}) = \sqrt{h_{I_{\mathrm{R},i}}^2(\boldsymbol{x}) + h_{I_{\mathrm{I},i}}^2(\boldsymbol{x})} \tag{6.87}$$

$$h_{\theta_i}(\boldsymbol{x}) = \arctan\left(\frac{h_{I_{\mathrm{I},i}}(\boldsymbol{x})}{h_{I_{\mathrm{R},i}}(\boldsymbol{x})}\right) \tag{6.88}$$

The terms of (6.83) are thus expressed as:

$$I_{\mathrm{R},i}^m = h_{I_{\mathrm{R},i}}(\boldsymbol{x}) + e_{I_{\mathrm{R},i}} \tag{6.89}$$

$$I_{\mathrm{I},i}^m = h_{I_{\mathrm{I},i}}(\boldsymbol{x}) + e_{I_{\mathrm{I},i}} \tag{6.90}$$

$$I_i^m = h_{I_i}(\boldsymbol{x}) + e_{I_i} \tag{6.91}$$

$$\theta_i^m = h_{\theta_i}(\boldsymbol{x}) + e_{\theta_i} \tag{6.92}$$

where subscripts R and I denote the real and imaginary parts of a phasor, respectively and variables e denote the additive random Gaussian noise of each measurement. The rest of the symbols shown in

Figure 6.7, $\tilde{V}_i = V_i \angle \delta_i$, $\tilde{V}_j = V_j \angle \delta_j$ and $\tilde{V}_k = V_k \angle \delta_k$, are the voltage phasors at buses *i*, *j* and *k*, respectively.

Assuming that at each PMU-monitored bus, a single device with one current measurement channel connected to a CT is installed, there are two possible current measurement configurations, according to Figure 6.7: $\boldsymbol{z}_f = \left[I_{\mathrm{R},ij}^m \;\; I_{\mathrm{I},ij}^m \right]^T$ and $\boldsymbol{z}_i = \left[I_{\mathrm{R},i}^m \;\; I_{\mathrm{I},i}^m \right]^T$. Each configuration contributes to the formation of the PMU measurement vector $\boldsymbol{z}_p = \left[\boldsymbol{z}_V^T \;\; \boldsymbol{z}_f^T \;\; \boldsymbol{z}_i^T \right]^T$, with $\boldsymbol{z}_V = \left[V_i^m \;\; \delta_i^m \right]^T$ or $\boldsymbol{z}_V = \left[V_{\mathrm{R},i}^m \;\; V_{\mathrm{I},i}^m \right]^T$ being the vector of voltage phasor measurements at bus *i* expressed in either polar or rectangular coordinates, respectively.

6.4.2 Impact of current injection information on the SE solution

Let us assume that the state vector is expressed in rectangular coordinates, with its entry pertaining to bus *i* written as $x_i = \left[V_{\mathrm{R},i} \;\; V_{\mathrm{I},i} \right]^T$. It is known that by expressing the state vector in rectangular coordinates, the functions $\boldsymbol{h}_p(\boldsymbol{x})$ and $\boldsymbol{c}(\boldsymbol{x})$ become linear, and their respective Jacobian matrices $\boldsymbol{H}_p \in \mathbb{R}^{m_p \times n}$ and $\boldsymbol{C} \in \mathbb{R}^{m_z \times n}$ are constant [113]. This is found to hold when incorporating current injection phasor measurements in $\boldsymbol{z}_p$, where $I_{\mathrm{R},i}^m$ and $I_{\mathrm{I},i}^m$ can be written as linear functions of the state variables, using (6.85), (6.86):

$$I_{\mathrm{R},i}^m = \left(G_{ii} V_{\mathrm{R},i} - B_{ii} V_{\mathrm{I},i} \right) + \sum_{j \in a(i)} \left(G_{ij} V_{\mathrm{R},j} - B_{ij} V_{\mathrm{I},j} \right) + e_{I_{\mathrm{R},i}} \tag{6.93}$$

$$I_{\mathrm{I},i}^m = \left(B_{ii} V_{\mathrm{R},i} + G_{ii} V_{\mathrm{I},i} \right) + \sum_{j \in a(i)} \left(B_{ij} V_{\mathrm{R},j} + G_{ij} V_{\mathrm{I},j} \right) + e_{I_{\mathrm{I},i}} \tag{6.94}$$

Table 6.1 demonstrates the structure of matrices $\boldsymbol{H}_p$ and $\boldsymbol{C}$, with $j,k \in a(i)$, where $\mathcal{Z}$ denotes the set of zero injection buses.

By applying the Gauss–Newton method to the first-order optimality conditions of the resulting Lagrangian function:

$$\mathcal{L}(\boldsymbol{x}, \boldsymbol{\lambda}) = J(\boldsymbol{x}) + \boldsymbol{\lambda}^T \boldsymbol{c}(\boldsymbol{x}) \tag{6.95}$$

and the solution is obtained by the iterative scheme:

$$\begin{bmatrix} \boldsymbol{G}^{(i)} & \left(\boldsymbol{C}^{(i)} \right)^T \\ \boldsymbol{C}^{(i)} & \boldsymbol{0} \end{bmatrix} \begin{bmatrix} \Delta \boldsymbol{x}^{(i+1)} \\ \boldsymbol{\lambda}^{(i+1)} \end{bmatrix} = \begin{bmatrix} \left(\boldsymbol{H}^{(i)} \right)^T \boldsymbol{R}^{-1} \Delta \boldsymbol{z}^{(i)} \\ -\boldsymbol{C} \boldsymbol{x}^{(i)} \end{bmatrix} \tag{6.96}$$

where superscript i is the iteration index, $\boldsymbol{H}^{(i)} = \begin{bmatrix} \boldsymbol{H}_s^{(i)} \\ \boldsymbol{H}_p \end{bmatrix} = \begin{bmatrix} \partial \boldsymbol{h}_s(\boldsymbol{x}) / \partial \boldsymbol{x} \big|_{\boldsymbol{x} = \boldsymbol{x}^{(i)}} \\ \partial \boldsymbol{h}_p(\boldsymbol{x}) / \partial \boldsymbol{x} \end{bmatrix}$, $\boldsymbol{C} = \partial \boldsymbol{c}(\boldsymbol{x}) / \partial \boldsymbol{x}$, $\boldsymbol{G}^{(i)} = \left(\boldsymbol{H}^{(i)} \right)^T \boldsymbol{R}^{-1} \boldsymbol{H}^{(i)}$, $\Delta \boldsymbol{z}^{(i)} = \begin{bmatrix} \boldsymbol{z}_s \\ \boldsymbol{z}_p \end{bmatrix} - \begin{bmatrix} \boldsymbol{h}_s(\boldsymbol{x}^{(i)}) \\ \boldsymbol{H}_p \boldsymbol{x}^{(i)} \end{bmatrix}$, and $\Delta \boldsymbol{x}^{(i+1)} = \boldsymbol{x}^{(i+1)} - \boldsymbol{x}^{(i)}$.

The state estimate $\boldsymbol{x}^{(i)}$ and Lagrange multipliers $\boldsymbol{\lambda}^{(i)}$ corresponding to zero injection constraints, are updated using (6.96) until convergence, which is attained when $\left\| \Delta \boldsymbol{x}^{(i)} \right\|_\infty < \varepsilon,$ where ε is the convergence threshold.

Table 6.1: Structure of Jacobian matrices $\boldsymbol{H}_p$ and $\boldsymbol{C}$ including current injection phasors.

$$
\boldsymbol{H}_p = \left(\begin{array}{ccccccccc:c}
\cdots & V_{\mathrm{R},i} & V_{\mathrm{I},i} & \cdots & V_{\mathrm{R},j} & V_{\mathrm{I},j} & \cdots & V_{\mathrm{R},k} & V_{\mathrm{I},k} & \\
\hdashline
\cdots & 1 & 0 & \cdots & 0 & 0 & \cdots & 0 & 0 & V_{\mathrm{R},i}^{m} \\
\cdots & 0 & 1 & \cdots & 0 & 0 & \cdots & 0 & 0 & V_{\mathrm{I},i}^{m} \\
\cdots & t_{ij}^{2}(g_{sij}+g_{ij}) & -t_{ij}^{2}(b_{sij}+b_{ij}) & \cdots & -t_{ij}t_{ji}D_{ij} & t_{ij}t_{ji}E_{ij} & \cdots & 0 & 0 & I_{\mathrm{R},ij}^{m} \\
\cdots & t_{ij}^{2}(b_{sij}+b_{ij}) & t_{ij}^{2}(g_{sij}+g_{ij}) & \cdots & -t_{ij}t_{ji}E_{ij} & -t_{ij}t_{ji}D_{ij} & \cdots & 0 & 0 & I_{\mathrm{I},ij}^{m} \\
\cdots & G_{ii} & -B_{ii} & \cdots & G_{ij} & -B_{ij} & \cdots & G_{ik} & -B_{ik} & I_{\mathrm{R},i}^{m} \\
\cdots & B_{ii} & G_{ii} & \cdots & B_{ij} & G_{ij} & \cdots & B_{ik} & G_{ik} & I_{\mathrm{I},i}^{m}
\end{array} \right), \; i \notin \mathcal{Z}
$$

$$
\boldsymbol{C} = \left(\begin{array}{ccccccccc:c}
\cdots & V_{\mathrm{R},i} & V_{\mathrm{I},i} & \cdots & V_{\mathrm{R},j} & V_{\mathrm{I},j} & \cdots & V_{\mathrm{R},k} & V_{\mathrm{I},k} & \\
\hdashline
\cdots & G_{ii} & -B_{ii} & \cdots & G_{ij} & -B_{ij} & \cdots & G_{ik} & -B_{ik} & I_{\mathrm{R},i}^{m}=0 \\
\cdots & B_{ii} & G_{ii} & \cdots & B_{ij} & G_{ij} & \cdots & B_{ik} & G_{ik} & I_{\mathrm{I},i}^{m}=0
\end{array} \right), \; i \in \mathcal{Z}
$$

$$
D_{ij} = g_{ij}\cos(\Delta\varphi_{ij}) + b_{ij}\sin(\Delta\varphi_{ij})
$$
$$
E_{ij} = b_{ij}\cos(\Delta\varphi_{ij}) - g_{ij}\sin(\Delta\varphi_{ij})
$$

6.4.3 Practical considerations

The majority of studies regarding the deployment of synchrophasors for SE purposes assume that the current measurements pertain to line current flows [4]. At power transmission level, all lines are equipped with switching devices at their ends, thus providing the necessary equipment, i.e., VTs, CTs and communication channels, for PMU installation. This setup is also applicable to all power system substations where the units can be installed at transformers or switchgear. In addition to commercially available dedicated PMU devices, existing digital relays and other IEDs, can be upgraded to integrate synchrophasor capability [202]. Overall, using a PMU to measure line current flows is indeed the most practical and economical solution for power transmission systems.

Contrariwise, measuring current phasors in distribution grids is a more complicated task. It is practically infeasible to obtain synchronized measurements of line current flows downstream primary substations, since the available switching and protection devices which could host PMUs, are limited. The required facilities must be constructed from scratch, thus, inferring high cost, mainly referring to the purchase of VTs/CTs, and unreasonable labor effort, that involves cabinet installation and space arrangements at overhead or underground locations, ad-hoc configuration of instrument transformers etc. [209].

As reported in [202], the most convenient option in case of distribution networks is to place PMUs at locations with pre-existing instrument transformers, such as the secondary, low voltage side of service transformers. In this case, low-cost PMU devices can be utilized, thus, reducing the related expenses. Further, by employing a unit with analog front-end interface as in [210], the use of VTs is not required, which not only eliminates the related cost but also mitigates the measurement errors. Therefore, by adopting this solution, the current measurements delivered by an installed PMU refer to bus injected/ absorbed currents.

Considering this analysis, the study of both current flow and injection phasor measurements is of major importance, since, currently, the latter are more easily acquirable in real-world deployment of PMUs at power distribution.

6.5 Numerical simulations

The accuracy, convergence properties, and computational efficiency of the proposed HSE methods of Sections 6.2–6.3 are investigated and compared to those of different HSE algorithms found in recent literature. This is accomplished via numerical simulations conducted using several IEEE test systems, with their data available in [211]. The networks under examination are simulated using the MATPOWER toolbox [212], and all the algorithms under investigation are implemented in MATLAB, on a computer with Intel Core i5-10400 processor and 16 GB of RAM.

6.5.1 *Measurement errors*

In the conducted simulations, the true values of states and measurements are derived by a power flow solution. The actual measurement values are generated by adding random Gaussian noise to the true measurements. The actual measured value of the i-th measurement is calculated as:

$$z_i = z_i^{true} + v \times \sigma_i \tag{6.97}$$

where z_i^{true} is the true value provided by the load flow solution, v is a $\mathcal{N}(0,1)$ random number, and σ_i is the standard deviation of z_i, $i = 1, 2, ..., m$.

Assuming that each metering device involves a maximum percentage error $e_{\max}$ around each measured value z_i, and given that $z_i \sim \mathcal{N}(z_i^{true}, \sigma_i^2)$ with a $\pm 3\sigma_i$ deviation around z_i^{true} covering more than 99.7% of the Gaussian curve, the standard deviation of the i-th measurement may be calculated as follows:

$$z_i^{true} - e_{\max} z_i^{true} < z_i < z_i^{true} + e_{\max} z_i^{true} \Rightarrow$$
$$\sigma_i \simeq \frac{e_{\max} z_i^{true}}{3} \tag{6.98}$$

The following $e_{\max}$ values are considered for each measurement type [8], [113]:

- for SCADA measurements, $e_{\max}^{s} = 2\%$,
- for PMU magnitude measurements, $e_{\max}^{pm} = 0.1\%$,
- for PMU angle measurements, $e_{\max}^{pa} = 0.35$ mrad.
- for HVDC-related measurements, $e_{\max}^{dc} = 5\%$.

In all cases where error-free measurements are considered, (6.97) becomes $z_i = z_i^{true}$. The values and standard deviations of phase angle measurements are expressed in radians, while for all other measurements they are expressed in per-unit.

6.5.2 *State estimation performance metrics*

Several well-established metrics are calculated to assess the performance of SE procedures in terms of convergence rate of the solution algorithm and accuracy of the state estimates, under controlled testing. Estimation errors can be compared separately for voltage magnitudes and phase angles, using the mean absolute errors MAE_V and MAE_A, respectively. Generally, the mean absolute error (MAE) is given by [213]:

$$MAE := \frac{1}{N} \sum_{i=1}^{N} | x_i^{true} - \hat{x}_i | \tag{6.99}$$

where x_i^{true} is the true value of voltage magnitude or phase angle of bus i obtained by the power flow solution, $\hat{x}_i$ is its corresponding estimation, and N is the total number of buses.

The $Macc_V$ metric is defined as the Euclidean norm of the difference between the true and estimated complex bus voltages, and is utilized to assess the combined effect of magnitude and angle errors on SE accuracy [213]:

$$Macc_V := \left\| \tilde{\boldsymbol{V}}^{true} - \tilde{\boldsymbol{V}}^{est} \right\|_2 = \sqrt{\sum_{i=1}^{N} \left| \tilde{V}_i^{true} - \tilde{V}_i^{est} \right|^2} \tag{6.100}$$

where $\tilde{\boldsymbol{V}}^{true}$ and $\tilde{\boldsymbol{V}}^{est}$ are the vectors of all true and estimated complex bus voltages in per-unit.

To evaluate the capability of the SE method to produce an estimate of the complex power flow on each branch, the $Macc_S$ metric can be calculated as [213]:

$$Macc_S := \sqrt{\sum_{i=1}^{M} \left| \tilde{S}_{f,i}^{true} - \tilde{S}_{f,i}^{est} \right|^2 + \left| \tilde{S}_{t,i}^{true} - \tilde{S}_{t,i}^{est} \right|^2} \tag{6.101}$$

where the summation index i ranges over all the M network branches, $\tilde{S}^{true}$ and $\tilde{S}^{est}$ are the true and estimated complex power flows, and the sending and receiving ends of each branch are denoted by subscripts f and t, respectively.

For assessing each estimator's ability to accurately calculate power system quantities that appear in the MS within the expected error margins indicated by the error variances σ_i^2, we introduce the error estimation index (*EEI*):

$$EEI := \sum_{i=1}^{m_p+m_s} \left(\frac{z_i^{true} - h_i(\hat{\boldsymbol{x}})}{\sigma_i} \right)^2 \tag{6.102}$$

The number of iterations and the execution time of each algorithm are used as convergence and timing metrics, respectively. Note that these metrics are used to assess the computational complexity of each method, and to indicate any convergence problems or numerical instability issues; they do not necessarily represent the actual performance of the estimator deployed in the EMS.

For the cases where the HSE solution is carried out using an iterative scheme, several indices can be calculated to quantify the estimator's ability to converge, by ascertaining that no significant changes in the state variables or the objective function occur at the terminal iteration [213]:

$$Mconv_J := \left| 1 - \frac{J(\boldsymbol{x}^{(t)})}{J(\boldsymbol{x}^{(t-1)})} \right| \tag{6.103}$$

$$Mconv_V := \max_{i \in N} \left| \frac{V_i^{(t)} - V_i^{(t-1)}}{V_i^{(t-1)}} \right| \tag{6.104}$$

$$Mconv_\delta := \max_{i \in N} \left| \delta_i^{(t)} - \delta_i^{(t-1)} \right| \tag{6.105}$$

where superscript t denotes the terminal iteration of the iterative scheme (6.96).The $Mconv_J$ metric calculates the relative change of the value of $J(\boldsymbol{x})$, while $Mconv_V$ ($Mconv_\delta$) measures the largest relative (absolute) change in bus voltage magnitude (angle) over all N buses, at the final iteration.

Finally, to investigate the degree of suboptimality of the proposed PSE (and by expansion, FSE) algorithm compared to the ISE approach, we can use the following suboptimality index, based on the objective function of the SE problem:

$$\mu_s = \frac{J_{PSE}(\hat{\boldsymbol{x}}) - J_{ISE}(\hat{\boldsymbol{x}})}{J_{ISE}(\hat{\boldsymbol{x}})} \tag{6.106}$$

where $J_{PSE}(\hat{\boldsymbol{x}})$ and $J_{ISE}(\hat{\boldsymbol{x}})$ are the optimal (minimum) values of the objective function, for the ISE and PSE implementations, respectively. By comparing the final objective function value (i.e., the sum of squared weighted residuals) for the ISE vs. that obtained by the PSE approach, we can quantify how well each approach fits the measurement data.

6.5.3 ISE, PSE and FSE numerical simulations

In the following, we compare the performance of the proposed algorithms of Section 6.2, with the ISE of [113], the PSE of [130], the FSE of [140], and the SCADA-based CSE of [183]. The ISE proposed in [113], is a conventional SE where the measurement vector is augmented to include all available phasor measurements in a unified estimator. The PSE algorithm of [130], treats the RTU-based estimates produced by the first SE stage as pseudo-measurements, jointly processed with PMU data in the second stage. The FSE method proposed in [140], involves a multistage architecture that combines results obtained from independent RTU- and PMU-based SE modules running in parallel, and a flat voltage profile $(1.0 \text{ pu}\angle 0^{\circ})$ is assigned to PMU-unobservable buses as *a priori* state information to guarantee complete PMU observability.

Regarding the FSE methods, the MATLAB Parallel Processing Toolbox was utilized to carry out all simulations by leveraging parallel computing resources on a multicore CPU, without relying on CUDA or MPI programming [214]. By dividing the SE task into smaller, independent subtasks (functions), the PMU-only and SCADA-based algorithms can be executed concurrently on multiple processing units. The Toolbox allows for synchronization and coordination of the two algorithms, as well as the propagation of the produced state vector estimates to the post-estimation fusion stage. More specifically, a parallel pool of three workers (MATLAB computational engines) is utilized, with each worker assigned to a physical CPU core. This guarantees that no two processes share the same floating-point unit, which would significantly hinder calculations. Two workers are utilized to compute Steps 1 and 2 of Algorithm 6.4 in parallel. The third worker waits to receive the state estimates and necessary matrices from Steps 1 and 2, to compute Step 3, thus producing the fused state vector.

6.5.3.1 Measurement configuration

The numerical studies are conducted on the IEEE 14-,118-, and 300-bus transmission systems. Tables 6.2 – 6.4 present the three different MSs considered for each test system. Each MS has a higher SCADA measurement redundancy m_s/n and contains a larger number of deployed PMUs than the previous MS. The RTU (PMU) measurements pertaining to a network bus consist of bus voltage magnitudes and power injections (bus voltage phasors), along with power flows (current phasors) recorded over all incident branches.

Modern PDCs can provide voltage and current phasors in both polar and rectangular forms to the EMS. For the numerical simulations, current phasors are always expressed in rectangular form, as this has been proven to be optimal for HSE implementations [96]. Voltage phasors can be processed in either form, depending on the employed SE method.

Assuming that (6.98) gives the standard deviations $\sigma_{m,i}$, $\sigma_{a,i}$ of the magnitude and angle measurements $z_{m,i}$, $z_{a,i}$ of a phasor expressed in polar form, then the standard deviations $\sigma_{r,i}$, $\sigma_{x,i}$ of the real and imaginary parts $z_{r,i}$, $z_{x,i}$ of the phasor transformed to rectangular form are calculated based on the uncertainty propagation theory [114]. The 2×2 covariance matrix of $z_{r,i} = z_{m,i}\cos(z_{a,i})$ and $z_{x,i} = z_{m,i}\sin(z_{a,i})$ is calculated as:

$$Cov\left(\begin{bmatrix} z_{r,i} & z_{x,i} \end{bmatrix}^T\right) = \boldsymbol{J}Cov\left(\begin{bmatrix} z_{m,i} & z_{a,i} \end{bmatrix}^T\right)\boldsymbol{J}^T \tag{6.107}$$

where $\boldsymbol{J} := \begin{bmatrix} \dfrac{\partial z_{r,i}}{\partial z_{m,i}} & \dfrac{\partial z_{r,i}}{\partial z_{a,i}} \\ \dfrac{\partial z_{x,i}}{\partial z_{m,i}} & \dfrac{\partial z_{x,i}}{\partial z_{a,i}} \end{bmatrix} = \begin{bmatrix} \cos(z_{a,i}) & -z_{m,i}\sin(z_{a,i}) \\ \sin(z_{a,i}) & z_{m,i}\cos(z_{a,i}) \end{bmatrix}$ and $Cov\left(\begin{bmatrix} z_{m,i} & z_{a,i} \end{bmatrix}^T\right) = \begin{bmatrix} \sigma_{m,i}^2 & 0 \\ 0 & \sigma_{a,i}^2 \end{bmatrix}$.

Thus:

$$Cov\left(\begin{bmatrix} z_{r,i} & z_{x,i} \end{bmatrix}^T\right) = \begin{bmatrix} \sigma_{m,i}^2\cos^2(z_{a,i}) + z_{m,i}^2\sigma_{a,i}^2\sin^2(z_{a,i}) & (\sigma_{m,i}^2 - z_{m,i}^2\sigma_{a,i}^2)\cos(z_{a,i})\sin(z_{a,i}) \\ (\sigma_{m,i}^2 - z_{m,i}^2\sigma_{a,i}^2)\cos(z_{a,i})\sin(z_{a,i}) & \sigma_{m,i}^2\sin^2(z_{a,i}) + z_{m,i}^2\sigma_{a,i}^2\cos^2(z_{a,i}) \end{bmatrix} \tag{6.108}$$

Table 6.2: Measurement configurations for the IEEE 14-bus test system.

	MS 1	**MS 2**	**MS 3**
SCADA buses	2, 6, 9	2, 4, 6, 9, 10	2, 4, 6, 8–10
PMU buses	3	5, 14	3, 5, 14
SCADA measurements	33	53	58
PMU measurements	6	16	22
m_s/n	1.179	1.893	2.071

Table 6.3: Measurement configurations for the IEEE 118-bus test system.

	MS 1	**MS 2**	**MS 3**
SCADA buses	3, 8, 11, 12, 17, 21, 22, 27, 31, 32, 34, 35, 40, 45, 49, 53, 56, 62, 65, 72, 73, 75, 77, 80, 85, 86, 91, 92, 94, 102, 105, 106, 110	3, 4, 7, 8, 11, 12, 17, 21, 22, 27, 28, 31, 32, 34, 35, 40, 44–46, 49, 53, 56, 62, 65, 72, 73, 75, 77, 78, 80, 85, 86, 91, 92, 94, 101, 102, 105–107	2–4, 7, 8, 11, 12, 16, 17, 21, 22, 27, 28, 31, 32, 34, 35, 40, 41, 44–46, 48–50, 53, 56, 57, 62, 65, 72, 73, 75, 77, 78, 80, 84–87, 91, 92, 94, 95, 101, 102, 105–107, 109–111
PMU buses	6, 23, 33, 59, 69, 89	19, 23, 33, 54, 59, 61, 69, 89, 100	1, 6, 19, 23, 33, 42, 51, 54, 59, 61, 69, 70, 89, 96, 100, 103
SCADA measurements	375	433	506
PMU measurements	66	112	176
m_s/n	1.59	1.835	2.144

Table 6.4: Measurement configurations for the IEEE 300-bus test system.

	MS 1	**MS 2**	**MS 3**
SCADA measurements	829	1063	1283
PMU measurements	148	270	420
m_s/n	1.382	1.772	2.138

6.5.3.2 State vector formulation

For all SE formulations, the state vector $\boldsymbol{x}$ can be expressed in either polar or rectangular coordinates. Table 6.5 provides the coordinates of the state vector and the solution method of each proposed SE formulation. As observed from Table 6.5, considering the state vector in rectangular coordinates for the PMU stage of FSE, along with phasors processed in rectangular form, linearizes the measurement model and results in non-iterative solution of the SE problem. In all the following simulations, rectangular coordinates were used to express the state vector.

Table 6.5: State vector and solution formulation for each proposed algorithm.

Proposed algorithm	Stage	State vector expression	Solution method
ISE	–	Polar or rectangular	Iterative
PSE	SCADA	Polar or rectangular	Iterative
	PMU	Same as SCADA	Iterative or non-iterative
FSE	SCADA	Polar or rectangular	Iterative
	PMU	Rectangular	Non-iterative
	Fusion	Same as SCADA	Iterative

6.5.3.3 Evaluation of simulation results

For each MS and test system, 1000 Monte Carlo (MC) trials were conducted to obtain an average of the performance metrics, which are provided in Table 6.6 for CSE, in Table 6.7 for ISE, in Table 6.8 for PSE, and in Table 6.9 for FSE. We refer to our proposed methods as ISE 1, PSE 1, and FSE 1. The ISE of [113], the PSE of [130], and the FSE of [140], are referred to as ISE 2, PSE 2, and FSE 2, respectively. The convergence tolerance for the SE iterations was set to $\varepsilon = 10^{-4}$ for all algorithms.

As regards PSE methods, the rows of Table 6.8 corresponding to the number of iterations have been omitted, as the SCADA-based module is the only iterative process, with the respective metrics provided in Table 6.6, while the PMU-based post-processing stage is non-iterative. For the same reason, only CPU times corresponding to the PMU-based stage are provided. As for FSE methods, we compare the convergence and timing metrics of the fusion stage of each method. The more computationally demanding iterative SCADA-based SE (running in parallel with the linear PMU-based SE of each method) is again the same for both methods.

Table 6.6: Conventional (SCADA-based) SE accuracy and performance metrics.

Metric	IEEE 14			IEEE 118			IEEE 300		
	MS 1	MS 2	MS 3	MS 1	MS 2	MS 3	MS 1	MS 2	MS 3
MAE_V ($\times 10^{-3}$ pu)	2.920	1.246	1.206	1.064	0.737	0.651	0.633	0.445	0.356
MAE_A ($\times 10^{-2}$ deg.)	8.035	2.683	2.601	11.550	10.950	9.811	6.791	4.375	3.739
$Macc_V$ (pu)	0.013	0.005	0.005	0.036	0.033	0.029	0.034	0.022	0.017
$Macc_S$ (pu)	0.045	0.013	0.012	0.582	0.420	0.375	0.771	0.542	0.439
EEI	23.95	24.90	24.27	211.93	210.13	210.92	458.05	456.02	458.19
Iterations	4	4	4	5	4.70	4.75	5	5	5
CPU time (ms)	4.00	3.70	4.10	11.00	10.70	13.00	114	120	135

Table 6.7: Proposed ISE accuracy and performance metrics.

Metric	SE method	IEEE 14			IEEE 118			IEEE 300		
		MS 1	MS 2	MS 3	MS 1	MS 2	MS 3	MS 1	MS 2	MS 3
MAE_V ($\times10^{-3}$ pu)	ISE 1	0.826	0.478	0.404	0.329	0.256	0.182	0.271	0.186	0.127
	ISE 2	0.827	0.487	0.434	0.324	0.225	0.173	0.260	0.179	0.129
MAE_A ($\times10^{-2}$ deg.)	ISE 1	3.231	0.687	0.378	1.467	1.063	0.570	2.189	1.275	0.782
	ISE 2	3.910	0.889	0.729	1.557	1.092	0.621	3.117	1.795	0.867
$Macc_V$ (pu)	ISE 1	0.005	0.002	0.001	0.007	0.005	0.003	0.015	0.009	0.005
	ISE 2	0.005	0.002	0.002	0.007	0.005	0.003	0.017	0.010	0.005
$Macc_S$ (pu)	ISE 1	0.027	0.007	0.004	0.125	0.096	0.067	0.411	0.312	0.139
	ISE 2	0.027	0.007	0.004	0.125	0.097	0.069	0.409	0.304	0.139
EEI	ISE 1	24.48	23.46	23.70	208.33	204.35	199.22	452.11	446.51	446.23
	ISE 2	25.09	24.07	24.10	209.41	205.29	204.75	451.91	452.82	449.81
Iterations	ISE 1	4	4	4	4	4	4	5	5	5
	ISE 2	4	4	4	4	4	4	5	5	5
Time (ms)	ISE 1	3.00	4.00	3.00	26.00	28.00	28.30	241	305	299
	ISE 2	3.10	3.20	4.30	16.00	17.00	17.00	149	161	204

Table 6.8: Proposed PSE accuracy and performance metrics.

Metric	SE method	IEEE 14			IEEE 118			IEEE 300		
		MS 1	MS 2	MS 3	MS 1	MS 2	MS 3	MS 1	MS 2	MS 3
MAE_V ($\times10^{-3}$ pu)	PSE 1	0.781	0.517	0.408	0.327	0.241	0.179	0.265	0.184	0.123
	PSE 2	1.613	0.552	0.504	0.622	0.424	0.338	0.359	0.299	0.216
MAE_A ($\times10^{-2}$ deg.)	PSE 1	3.214	0.691	0.379	1.506	1.056	0.569	2.169	1.285	0.774
	PSE 2	6.407	1.687	1.535	6.059	5.625	4.329	4.891	2.605	1.700
$Macc_V$ (pu)	PSE 1	0.005	0.002	0.001	0.007	0.005	0.003	0.015	0.009	0.005
	PSE 2	0.008	0.003	0.002	0.020	0.019	0.015	0.027	0.019	0.010
$Macc_S$ (pu)	PSE 1	0.027	0.007	0.004	0.127	0.096	0.068	0.413	0.310	0.142
	PSE 2	0.088	0.023	0.022	0.471	0.327	0.367	1.256	0.925	0.486
EEI	PSE 1	24.30	23.92	23.56	208.10	205.23	199.78	449.86	448.02	445.02
	PSE 2	26.81	26.32	26.81	223.15	244.75	245.08	595.14	556.93	541.53
PMU stage time (ms)	PSE 1	0.4	0.6	0.9	4.2	7.1	11	26	29	31
	PSE 2	1.2	1.4	1.7	1.5	1.4	1.3	2	5	10

Table 6.9: Proposed FSE accuracy and performance metrics.

Metric	SE method	IEEE 14			IEEE 118			IEEE 300		
		MS 1	MS 2	MS 3	MS 1	MS 2	MS 3	MS 1	MS 2	MS 3
MAE_V ($\times10^{-3}$ pu)	FSE 1	0.918	0.558	0.480	0.504	0.339	0.267	0.510	0.411	0.237
	FSE 2	0.879	0.549	0.483	0.531	0.351	0.273	0.534	0.435	0.318
MAE_A ($\times10^{-2}$ deg.)	FSE 1	3.329	1.719	1.357	2.280	1.830	1.540	2.805	2.047	1.616
	FSE 2	3.273	2.019	1.355	2.353	1.899	1.567	3.472	2.508	1.945
$Macc_V$ (pu)	FSE 1	0.007	0.003	0.002	0.013	0.009	0.006	0.045	0.033	0.010
	FSE 2	0.007	0.003	0.002	0.014	0.009	0.006	0.050	0.038	0.014
$Macc_S$ (pu)	FSE 1	0.057	0.015	0.009	0.270	0.204	0.159	1.479	1.368	0.441
	FSE 2	0.057	0.015	0.009	0.282	0.207	0.168	1.515	1.392	0.648
EEI	FSE 1	25.03	25.18	24.68	212.32	213.66	209.70	464.77	470.54	466.68
	FSE 2	24.42	26.61	24.73	214.59	217.68	214.07	487.84	482.37	473.24
Fusion stage iterations	FSE 1	1	1.6	1	2	2	2	2	2	2
	FSE 2	–	–	–	–	–	–	–	–	–
Fusion stage time (ms)	FSE 1	0.4	0.6	0.9	4.2	7.1	11	26	29	31
	FSE 2	1.2	1.4	1.7	1.5	1.4	1.3	2	5	10

From the results presented in Table 6.6–Table 6.9 we may deduce the following:

- All the proposed HSE methods provide more reliable state estimates versus the CSE approach, with higher RTU and PMU measurement redundancy leading to improvement in overall SE quality.
- Both ISE methods provide accurate state estimates with slight differences across all metrics. This is to be expected as the proposed ISE 1 has the same mathematical derivation as ISE 2, with the only difference being that ISE 2 does not include information from zero injections modeled in the form of equality constraints.
- The largest improvements can be found when comparing the PSE methods. Errors MAE_V , MAE_A , and $Macc_V$, show a decrease of 65.4%, 67.8%, and 68.9% on average, across all MSs and test systems. The proposed PSE 1 is also found superior in terms of its ability to produce an approximation of the power flow solution, when compared to PSE 2, as $Macc_S$ values are much lower for all simulations. Bearing in mind that PSE schemes only approach the optimal ISE solution near convergence and therefore generally provide suboptimal SE solutions compared to ISE methods, the metrics of PSE 1 are almost identical (within the margins of statistical error) compared to those of ISE 1, validating the effectiveness of the proposed PSE algorithm.
- The performance of the FSE approaches is almost equivalent, as far as the 14-bus system is concerned. For the 118-bus system there is a notable 6% improvement on average regarding MAE_A, as well as a 3.5% reduction in MAE_V and $Macc_V$ errors. For the 300-bus system, these improvements increase to 18.2%, 11.8%, and 17.2%, respectively. Convergence of the proposed FSE 1 is unproblematic, with any increase in execution time compared to FSE 2 being attributed to the iterative scheme implemented after calculating $\hat{\boldsymbol{x}}_f$.
- Generally, it is found that *EEI* values are lower for the proposed HSE methods. The calculated *EEI* values may be compared against a theoretical maximum value:

$$EEI_{\max} \simeq \sum_{i=1}^{m_p+m_s} \left(\frac{\pm 3\sigma_i}{\sigma_i} \right)^2 = 9\left(m_p + m_s\right) \tag{6.109}$$

  The simulations for all MSs return good (low) *EEI* values, which fall within 3.5%–7% of $EEI_{\max}$ for the 14-bus system, 3.5%–5.5% of $EEI_{\max}$ for the 118-bus system, and 3%–5.6% of $EEI_{\max}$ for the 300-bus system.
- The proposed methods return low $Macc_S$ values, proving the capability of the algorithms to deliver an estimation of the power flow solution. Note that the calculated $Macc_S$ values in p.u. correspond to a maximum deviation of 0.7% from the true total branch power flow for the 14-bus system, and around 0.2% for the 118- and 300-bus systems (base value of 100 MVA).
- As for the convergence rate, the required iterations are the same for ISE 1 and ISE 2. As expected, differences are observed between PSE 1 and PSE 2, as the latter employs a linear (non-iterative) post-processing stage, while the proposed PSE 1 requires an iterative procedure when the PMU measurement model is nonlinear. The same holds true for FSE methods, as FSE 1 performs an additional iterative process after calculating $\hat{\boldsymbol{x}}_f$. Note that for all PSE and FSE methods, convergence of each individual stage is required to achieve convergence to the optimal SE solution.

Additional remarks are also in order concerning the optimality of the multistage (PSE) estimator. In order to measure possible performance degradation over the proposed ISE algorithm, we make use of the degree of suboptimality μ_s . Via Table 6.10–Table 6.12 it is evident that the average value of μ_s

across all MC simulations is only 0.6%, with the highest value of 2.56% observed for the IEEE 14-bus network with a single deployed PMU. In terms of $Mconv_V$ and $Mconv_\delta$, the ISE algorithm is found to converge satisfactorily. The $Mconv_V$ and $Mconv_\delta$ values for the PSE algorithm are calculated using the difference between the SCADA-based and the final estimates, instead of the estimates from the last two iterations, as the post-processing stage is not necessarily iterative. Thus, the obtained values can be used to quantify the effect of the post-processing step on the SCADA-based state estimates.

Table 6.10: Convergence metrics for the ISE and PSE methods – IEEE 14-bus system.

MS	Metrics								
	J_{ISE}	J_{PSE}	μ_s	$Mconv_J$		$Mconv_V$		$Mconv_\delta$ (rad)	
				ISE	PSE	ISE	PSE	ISE	PSE
MS 1	13.66	13.72	0.0044	8.192×10^{-3}	–	1.584×10^{-5}	1.893×10^{-3}	9.482×10^{-6}	2.183×10^{-3}
MS 2	42.74	43.41	0.0157	2.565×10^{-6}	–	1.685×10^{-6}	1.188×10^{-3}	3.854×10^{-7}	6.650×10^{-4}
MS 3	53.52	53.55	0.0006	1.315×10^{-7}	–	9.543×10^{-7}	1.215×10^{-3}	1.926×10^{-7}	7.022×10^{-4}

Table 6.11: Convergence metrics for the ISE and PSE methods – IEEE 118-bus system.

MS	Metrics								
	J_{ISE}	J_{PSE}	μ_s	$Mconv_J$		$Mconv_V$		$Mconv_\delta$ (rad)	
				ISE	PSE	ISE	PSE	ISE	PSE
MS 1	218.6	218.7	0.0005	1.911×10^{-4}	–	5.681×10^{-6}	3.658×10^{-3}	1.099×10^{-5}	1.545×10^{-2}
MS 2	318.2	318.6	0.0013	1.399×10^{-6}	–	6.850×10^{-7}	2.328×10^{-3}	1.285×10^{-6}	8.931×10^{-3}
MS 3	449.7	451.2	0.0033	3.205×10^{-7}	–	3.692×10^{-7}	2.141×10^{-3}	6.457×10^{-7}	1.040×10^{-2}

Table 6.12: Convergence metrics for the ISE and PSE methods – IEEE 300-bus system.

MS	Metrics								
	J_{ISE}	J_{PSE}	μ_s	$Mconv_J$		$Mconv_V$		$Mconv_\delta$ (rad)	
				ISE	PSE	ISE	PSE	ISE	PSE
MS 1	491.6	491.7	0.0002	1.393×10^{-6}	–	5.236×10^{-7}	4.310×10^{-3}	2.710×10^{-6}	9.105×10^{-3}
MS 2	837.3	842.2	0.0059	2.884×10^{-6}	–	9.812×10^{-7}	2.228×10^{-3}	3.903×10^{-6}	6.440×10^{-3}
MS 3	1192	1194	0.0016	5.365×10^{-6}	–	5.934×10^{-6}	1.705×10^{-3}	6.160×10^{-6}	4.277×10^{-3}

It would also be useful to assess the system-wide accuracy of the proposed HSE algorithms. The mean absolute errors of voltage magnitudes and angles are calculated for each bus of the 118- and 300-bus systems, averaged from the same 1000 MC trials conducted for MS 3. The results are presented in the plots of Figure 6.8–Figure 6.9 for ISE, Figure 6.10–Figure 6.11 for PSE, and Figure 6.12–Figure 6.13 for FSE. In Figure 6.8–Figure 6.9, no noteworthy differences appear between ISE methods, as expected according to the results of Table 6.7. Figure 6.10 and Figure 6.11 demonstrate that the results of PSE 1 are closer to the power flow (true) values, than those of PSE 2 for all state variables. In Figure 6.12, one observes that the errors of FSE 2, which correspond to subareas with few or no PMU measurements (e.g., buses 103–112), are significantly increased. The same can be observed in Figure 6.13, for buses 170–230. In these parts of the network, the high density of complementary data used to artificially restore PMU-observability seems to negatively impact the accuracy of FSE 2. By avoiding usage of pseudo-measurements and by utilizing the post-estimation iterative scheme of Algorithm 6.4, FSE 1 manages to enhance SE quality in these subareas.

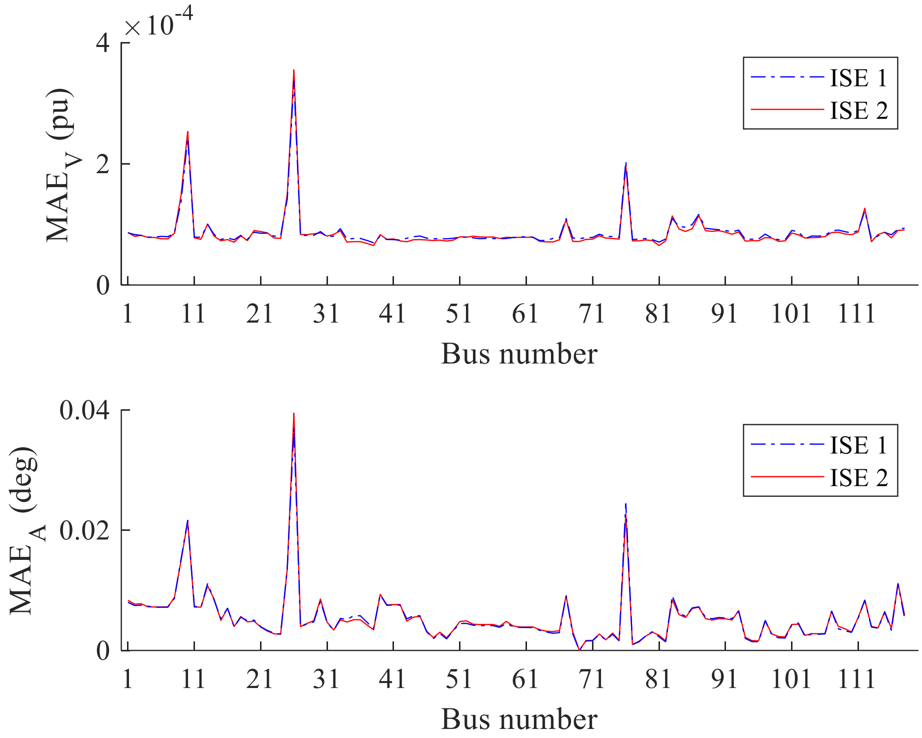

Figure 6.8: IEEE 118-bus system – Mean absolute errors of ISE methods.

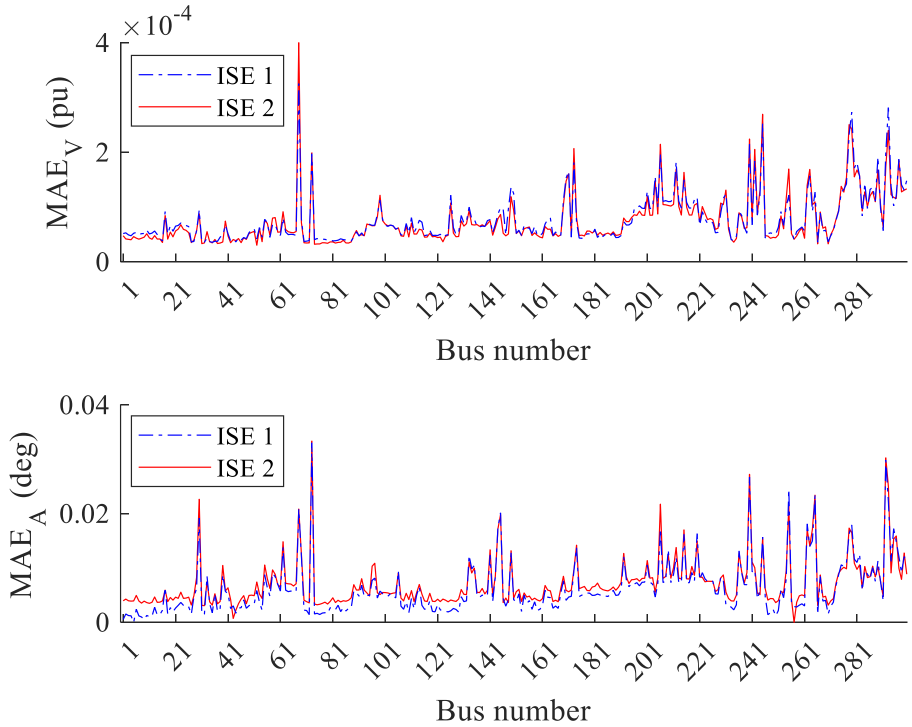

Figure 6.9: IEEE 300-bus system – Mean absolute errors of ISE methods.

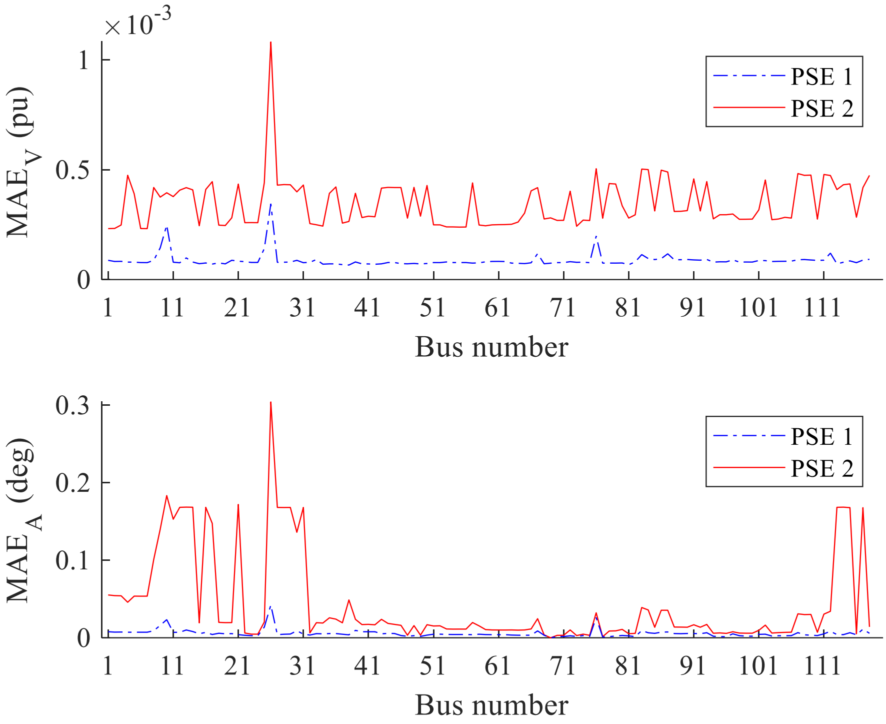

Figure 6.10: IEEE 118-bus system – Mean absolute errors of PSE methods.

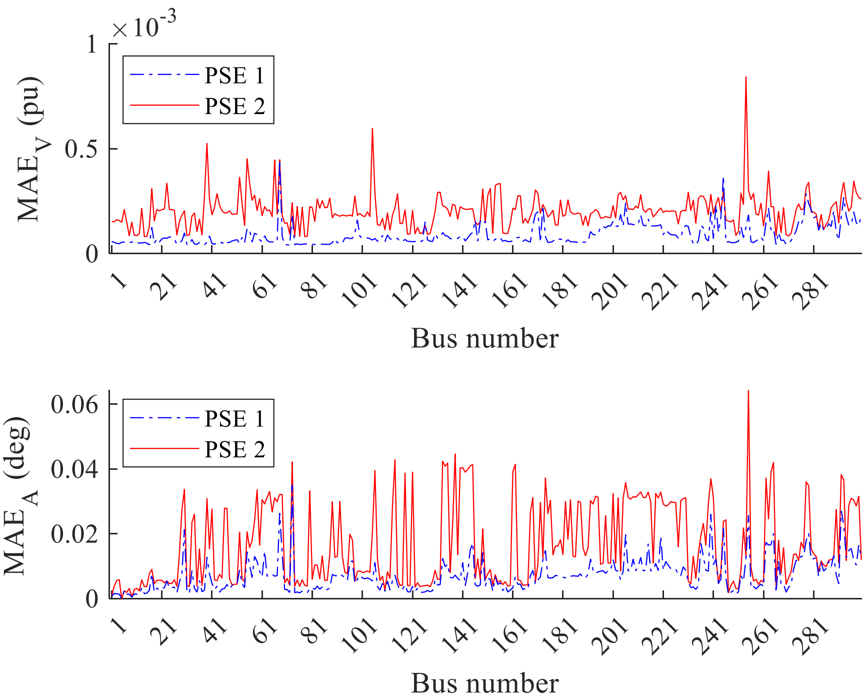

Figure 6.11: IEEE 300-bus system – Mean absolute errors of PSE methods.

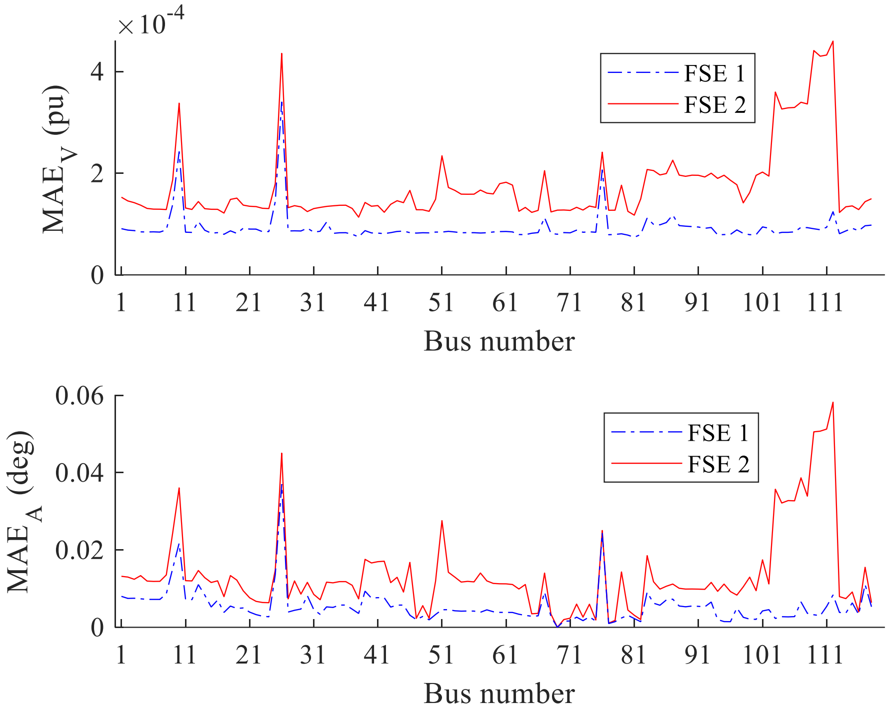

Figure 6.12: IEEE 118-bus system – Mean absolute errors of FSE methods.

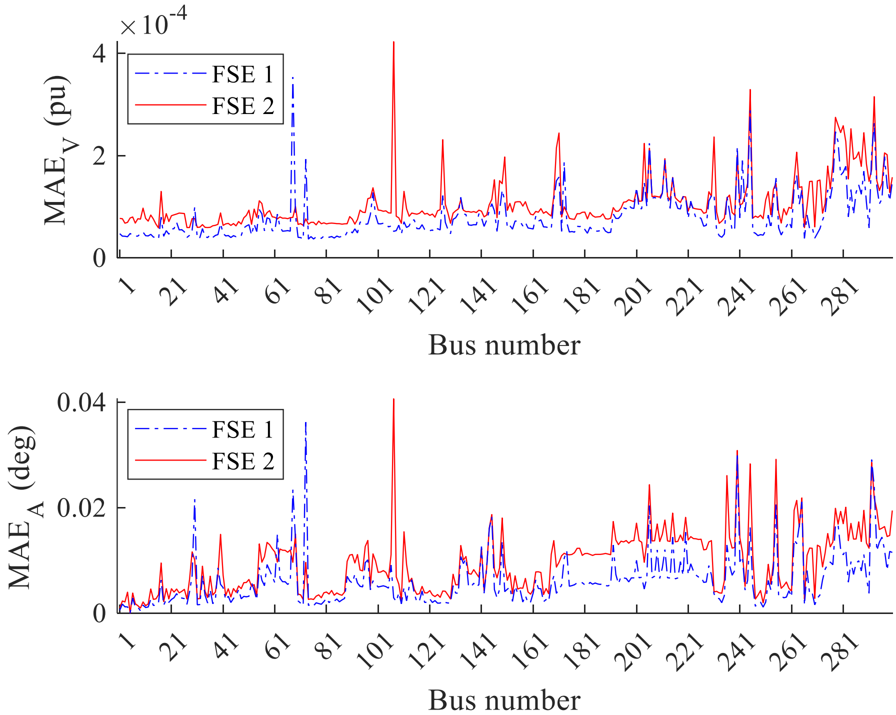

Figure 6.13: IEEE 300-bus system – Mean absolute errors of FSE methods.

6.5.3.4 Conclusions

Extensive numerical studies conducted on the 14-, 118-, and 300-bus IEEE test systems verify the reliability of the obtained SE results, while various performance metrics are compared with those obtained from similar approaches found in recent literature. The presented HSE scheme provides highly accurate results across all alternative formulations, while demonstrating improvements to SE quality over established PSE and FSE methods. In terms of convergence rate and execution time, the proposed algorithms are found to be well-performing and on par with the existing methods.

6.5.4 HVAC/HVDC network simulations

To demonstrate the performance and effectiveness of the proposed HVAC/HVDC SE methodology, simulation results obtained from the 14-bus and 30-bus IEEE benchmark systems are provided. The networks under examination were simulated in PSS®E [215], by integrating one CSC-HVDC link into the 14-bus system and two CSC-HVDC links into the 30-bus system. For the added HVDC links between AC buses i and j, the number of bridges is $B_{ij} = B_{ji} = 1$, the off-nominal turns ratios and reactance values of coupling transformers are $T_{ij} = T_{ji} = 0.975$ and $X_{ij} = X_{ji} = 5.95\ \Omega$, respectively, and $R_{dij} = 1.13\ \Omega$. Measurement data are generated using the power flow solutions obtained from PSS®E. Several scenarios are examined for each test network, including cases with error-free measurements and cases with measurements corrupted by random Gaussian noise. The performance evaluation focuses on the accuracy, convergence speed, and overall computational execution time of the proposed SE algorithm.

In the following, it is assumed that a single RTU (PMU) installed at a network bus can record the voltage magnitude (voltage phasor) of the respective bus and the power flows (current phasors) over all branches incident to that bus. For each simulation, the state vector is initialized at flat start, i.e., $V_i = v_{di} = 1$ pu, $\delta_i = \alpha_{ij} = \gamma_{ij} = 0° \ \forall i, j$, and the convergence threshold is set to 10^{-4}.

6.5.4.1 IEEE 14-bus test system

In the modified version of the IEEE 14-bus system (Figure 6.14), the AC transmission line between buses 1 and 2 has been replaced with a classic HVDC link. Buses 1, 2, 6, 8, and 9 are equipped with RTUs and buses 4, 11, 12, and 14 are equipped with PMUs. The AC measurement setup comprises 40 SCADA and 30 PMU measurements.

For the case of error-free measurements, the estimated states are compared to the power flow solution in Table 6.14 to validate the applicability of the proposed AC/DC measurement model and the associated coupling equality constraints. Here, the *MAE* index is given by:

$$MAE := \frac{1}{N}\sum_{i=1}^{N} | x_i^{true} - \hat{x}_i | \tag{6.110}$$

where x_i^{true} is the true value of AC (DC) voltage magnitude or voltage phase (firing/extinction) angle of AC (DC) bus *i* obtained by the power flow solution, $\hat{x}_i$ is its estimation, and *N* is the total number of AC and DC buses. In each scenario presented in Table 6.14, a different set of DC measurements is considered, as specified in Table 6.13. It should be noted that the coupling buses $c1$ and $c2$ of the proposed HVDC network model cannot be directly simulated within the PSS®E software. Therefore, the true values of v_{c1}, δ_{c1}, v_{c2}, and δ_{c2} were calculated using (6.49) and (6.58), combined with the power flow solution obtained from PSS®E. The largest deviations from the true states occur when only one DC measurement is utilized and progressively decrease with the incorporation of additional DC measurements (MS 2–MS 4). Additionally, it is important to emphasize that the SE problem is solvable provided there is at least one DC measurement along with RTU or PMU measurements available from both AC terminals of the HVDC link.

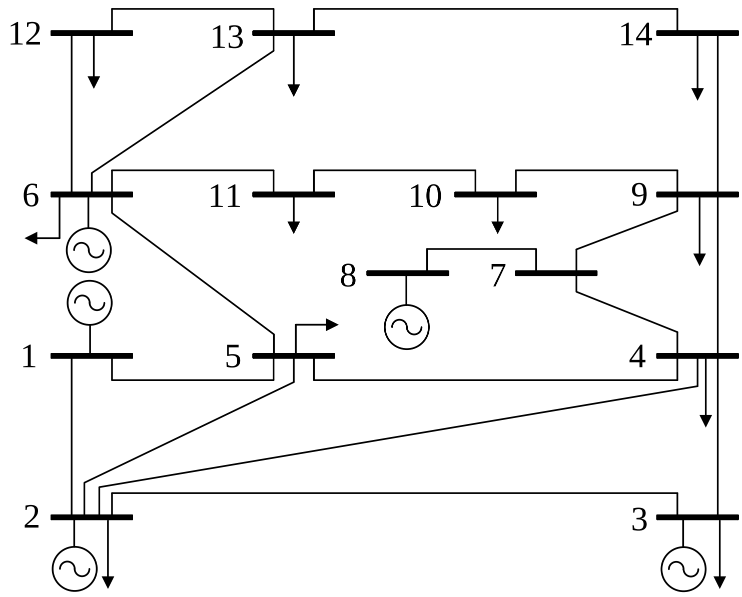

Figure 6.14: IEEE 14-bus test system single-line diagram.

Table 6.13: Sets of DC measurements for the IEEE 14-bus system.

MS	MS 1	MS 2	MS 3	MS 4
DC Measurements	v_{d1}	v_{d1}, v_{d2}	v_{d1}, i_{d1-2}	v_{d1}, v_{d2}, p_{d1-2}

Table 6.14: AC/HVDC ISE – Performance metrics for the IEEE 14-bus system (error-free measurements).

Metric	MS 1	MS 2	MS 3	MS 4
MAE_V (pu)	1.429×10^{-5}	4.358×10^{-9}	2.153×10^{-10}	5.321×10^{-12}
MAE_A (deg)	3.225×10^{-3}	1.635×10^{-8}	3.145×10^{-9}	6.223×10^{-11}

Subsequently, simulations with measurements contaminated with random Gaussian noise are carried out. The following three cases were examined, with the inclusion of only one DC measurement (v_{d1}):

- RTUs at buses 1, 2, 6, 8, and 9.
- PMUs at buses 1, 2, 4, 8, 11, 12, and 14.
- RTUs at buses 1, 2, 6, 8, 9 and PMUs at buses 4, 11, 12, and 14.

In Table 6.15, the number of iterations, the MAE, and the CPU time for each case are presented, calculated as an average from 500 MC simulations performed for each case. As is evident from the results, there are notable differences in the MAE among different estimation scenarios, with SCADA-based and PMU-based estimation solutions exhibiting the lowest and highest accuracy, respectively. The *MAE* values of voltage magnitude and angle achieved by the HSE method are approximately 27% and 40.5% times lower, respectively, than those obtained using SCADA-based estimation. This highlights the significant improvement in SE accuracy provided by the additional PMU measurements, albeit with a slight increase in computational burden. Moreover, minor differences in the average execution times of the three cases are observed, with the PMU-based estimation being the fastest. Given that RTU measurements typically have sampling periods of several seconds, the HSE execution time of approximately 20 ms does not impede the estimation process.

Table 6.15: AC/HVDC ISE – Performance metrics for the IEEE 14-bus system (Gaussian noise).

	SCADA-based		**PMU-based**		**Hybrid**	
MAE	Magnitudes (pu)	Angles (°)	Magnitudes (pu)	Angles (°)	Magnitudes (pu)	Angles (°)
	0.0015	0.028	0.0007	0.002	0.0011	0.019
Iterations	4		2		3	
Time (ms)	12.90		8.62		17.64	

Following the validation of the proposed method, its robustness against bad data is further examined. The subsequent tests rely on the principle that, in the presence of single or multiple non-interacting bad data, the largest normalized residual typically corresponds to the erroneous measurement [38]. Thus, the Largest Normalized Residual Test (LNRT) is conducted iteratively using successive cycles of the proposed HSE, progressively removing suspect measurements from the MS, until all normalized residuals fall below a predefined threshold, indicating no remaining bad data (see Chapter 8). This threshold is set to 3, corresponding to approximately a 0.1% probability of false detection.

Two LNRT sets are considered:

- Test set 1: MS 4 with gross errors of -20σ and 15σ added to active power flow measurement p_{6-11} and voltage measurement v_{d1}, respectively.
- Test set 2: MS 4 of Table I with gross errors of -15σ and 20σ added to voltage measurements v_4 and v_{d2}, respectively.

The two largest magnitudes of the normalized residuals of each cycle are shown in Table 6.16. The measurement with the highest normalized residual is removed from the MS at the end of each cycle and a new SE is conducted with the updated MS. After two estimation cycles, the erroneous measurements are successfully identified as bad data.

Table 6.16: AC/HVDC ISE – Normalized residual tests for the IEEE 14-bus system.

Test Set 1						
Cycle	1		2		3	
Meas.	p_{6-11}	v_{d1}	v_{d1}	v_{d2}	q_{1-2}	p_{1-5}
$\lVert \boldsymbol{r}_N \rVert_\infty$	19.9829	10.9854	10.9854	10.9489	1.7312	1.6894
Test Set 2						
Cycle	1		2		3	
Meas.	v_{d2}	v_4	v_4	δ_4	p_{1-5}	v_{d1}
$\lVert \boldsymbol{r}_N \rVert_\infty$	15.9780	13.4706	13.4720	9.0196	1.6932	1.582

6.5.4.2 IEEE 30-bus test system

To further demonstrate the efficacy of the proposed method, the HSE algorithm is applied to a modified version of the IEEE 30-bus test system (Figure 6.15). Lines 1-2 and 4-6 are substituted with two CSC-HVDC links. RTUs are located at buses 3, 5, 7, 13, 20, 24, and 30, while PMUs are placed at buses 1, 2, 4, 6, 10, 12, 15, 18, and 27. There are 42 RTU and 98 PMU measurements, as well as 10 zero injection buses (9, 22, 25, 27, and 28). Only one DC measurement (v_{di}) is taken for each DC line, and all measurements are assumed with random noise. The estimation process converges in 3 iterations, with average *MAE* equal to 1.422×10^{-3} and 2.696×10^{-1} for magnitudes and angles, respectively, and an average CPU time of 43.5 ms, obtained from 500 MC simulations. The above estimation results are presented in the box plots of Figure 6.16–Figure 6.19, along with the true values obtained from a power flow solution. Observe that the interquartile range is around 5×10^{-3} and 5×10^{-1} for AC voltage magnitudes and angles, respectively, which is acceptable with the given $e_{\max}$ values. It is also apparent that the median is equally close to the first and third quartiles, indicating that the distribution of the estimated states has no skew. The maximum number of outliers of the estimated states, after 500 simulation runs, is only 7 (1.4%) and 11 (2.2%) for magnitudes (bus 29) and angles (bus 13), respectively.

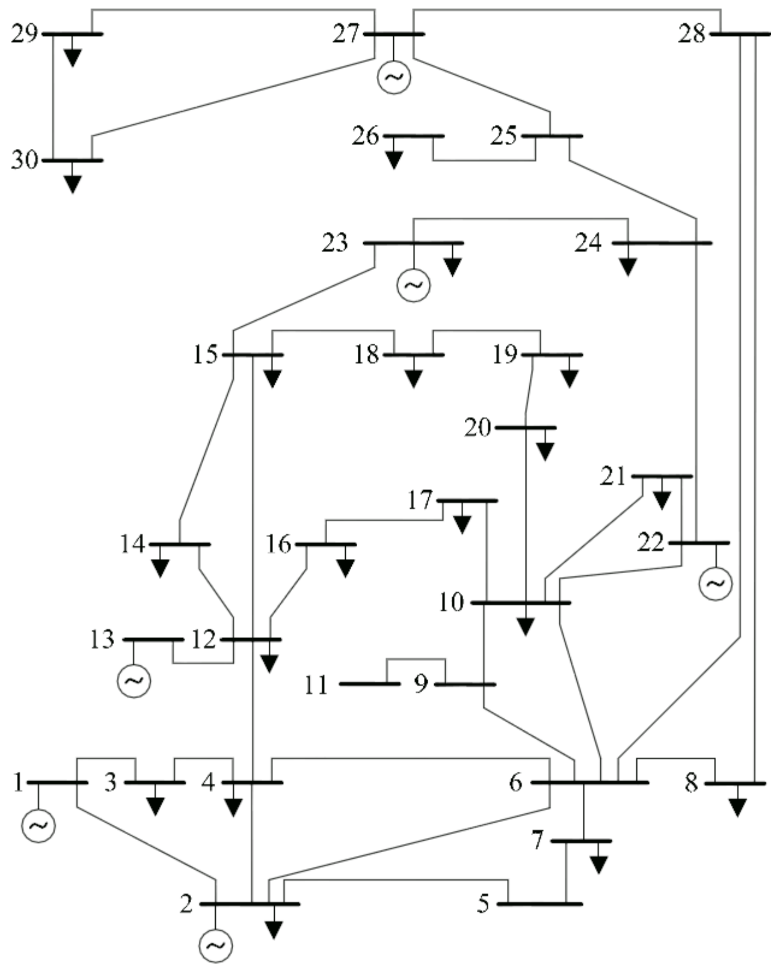

Figure 6.15: IEEE 30-bus test system single-line diagram.

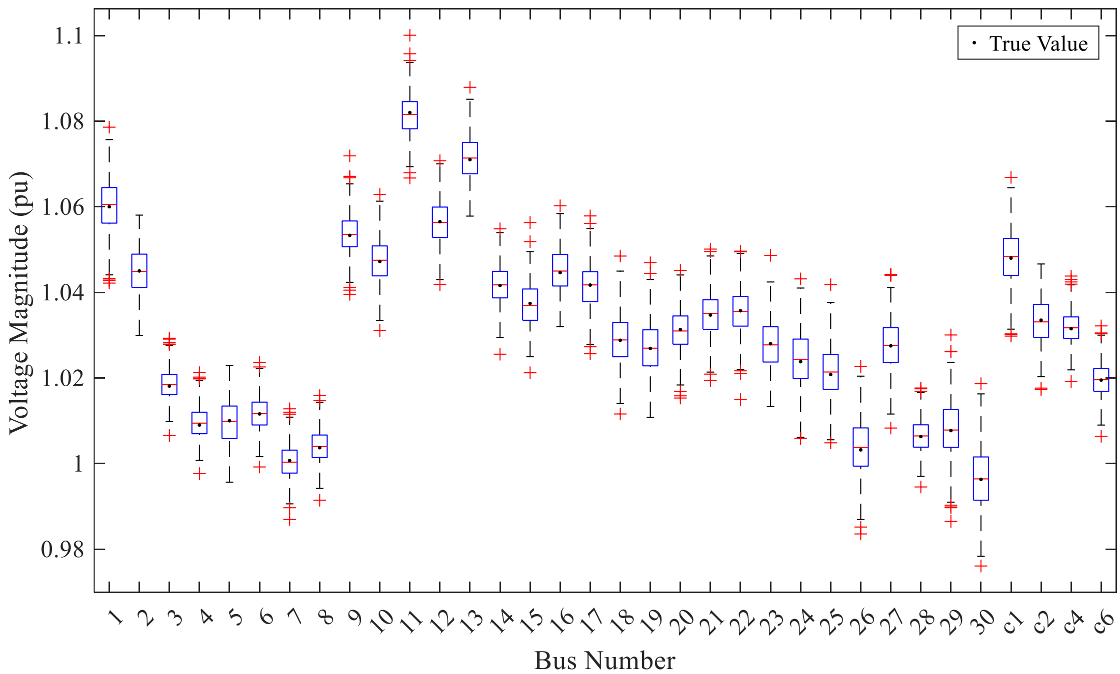

Figure 6.16: IEEE 30-bus system – Estimated voltage magnitudes of AC buses.

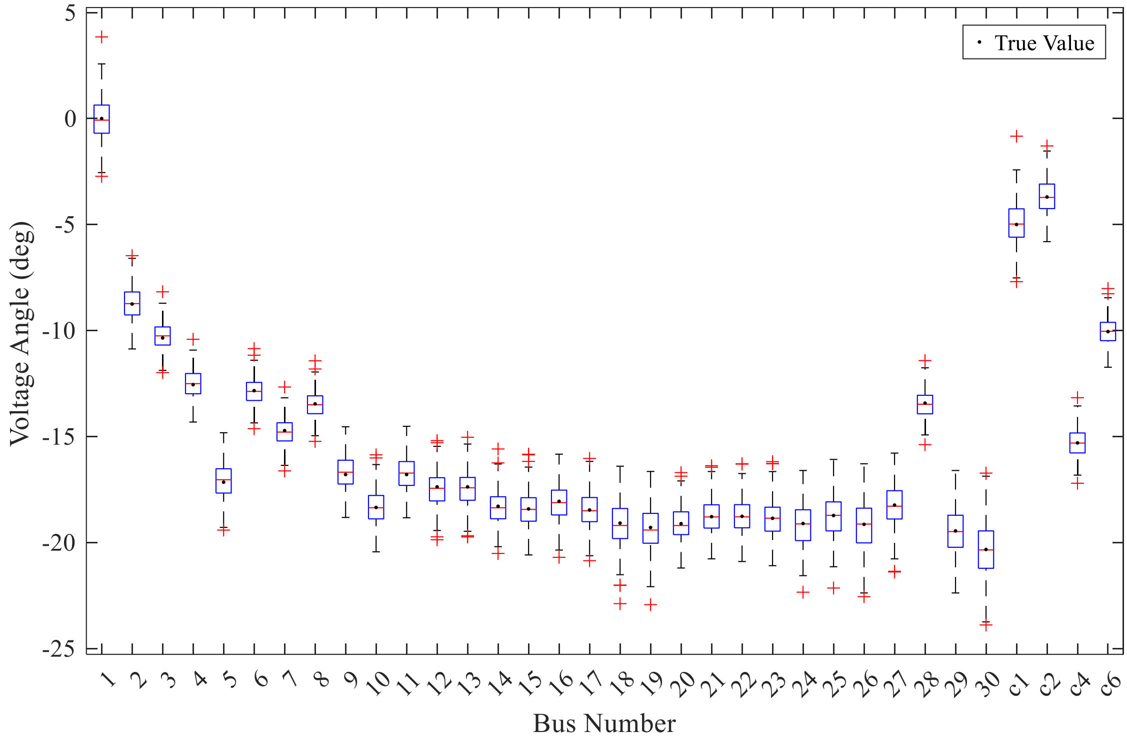

Figure 6.17: IEEE 30-bus system – Estimated voltage phase angles of AC buses.

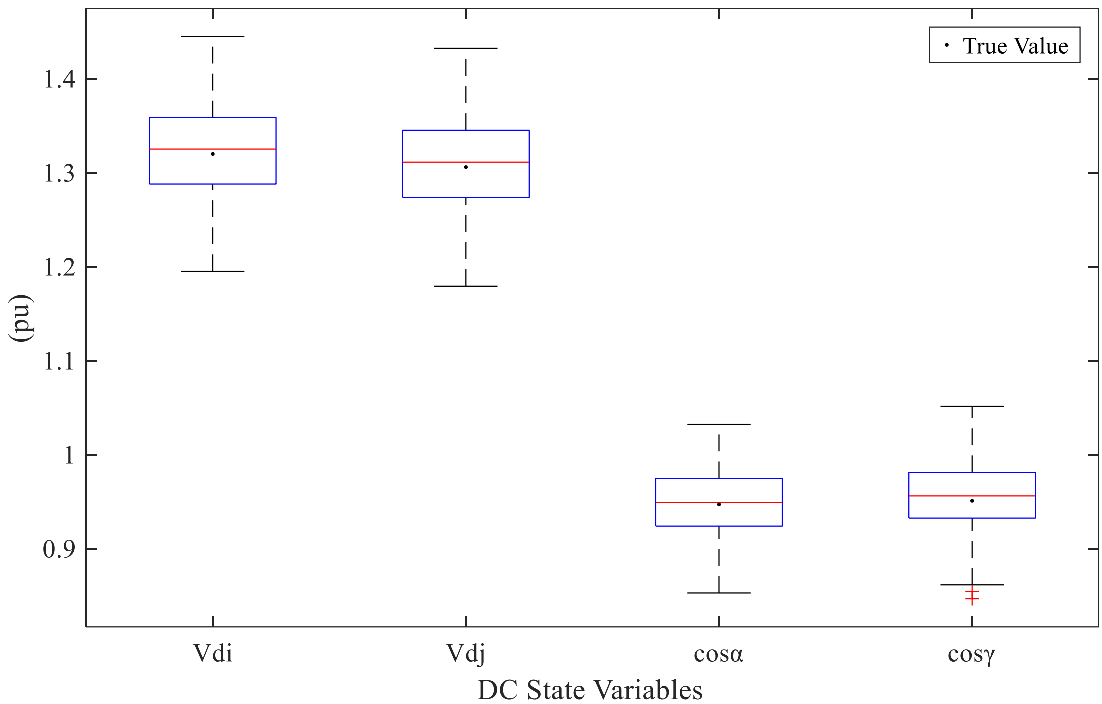

Figure 6.18: IEEE 30-bus system – Estimated DC states for HVDC link 1-2.

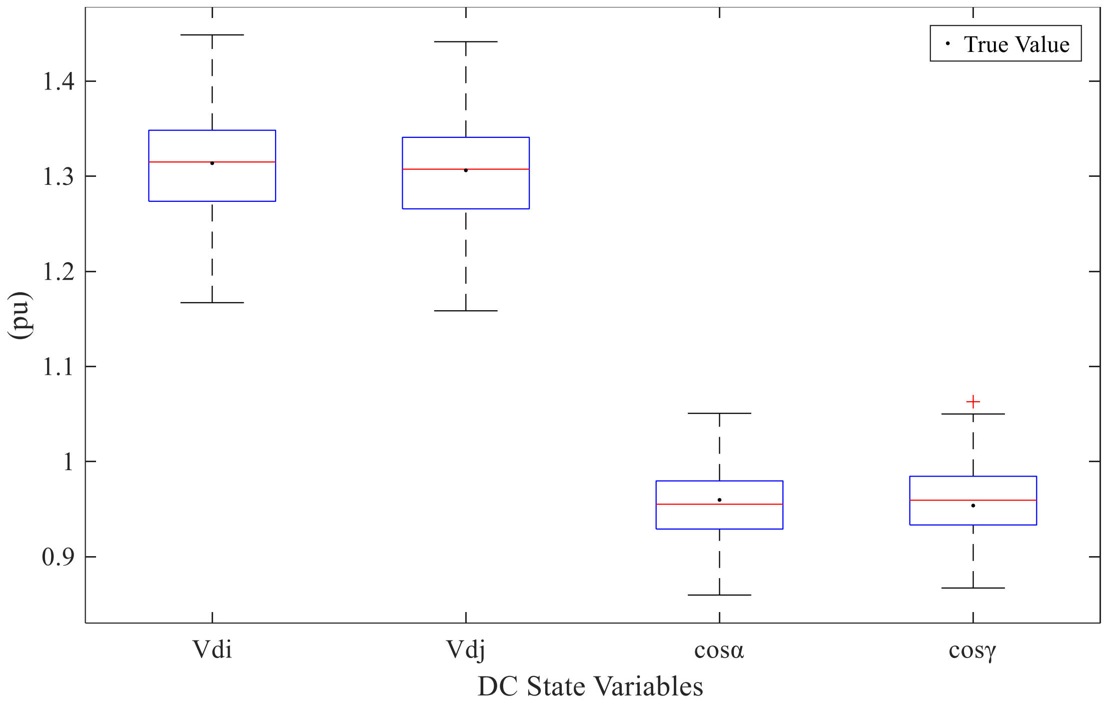

Figure 6.19: IEEE 30-bus system – Estimated DC states for HVDC link 4-6.

6.5.5 Inclusion of current injection measurements in HSE

To test the various combinations of PMU current measurement configurations, numerical studies are conducted on the IEEE 118-bus transmission system [211] and on the UKGDS 95-bus distribution benchmark system (Figure 6.20) [216]. To obtain the true system state vector, the Newton-Raphson load flow is solved using the MATPOWER toolbox [212]. A total of 500 MC trials is carried out for each test system.

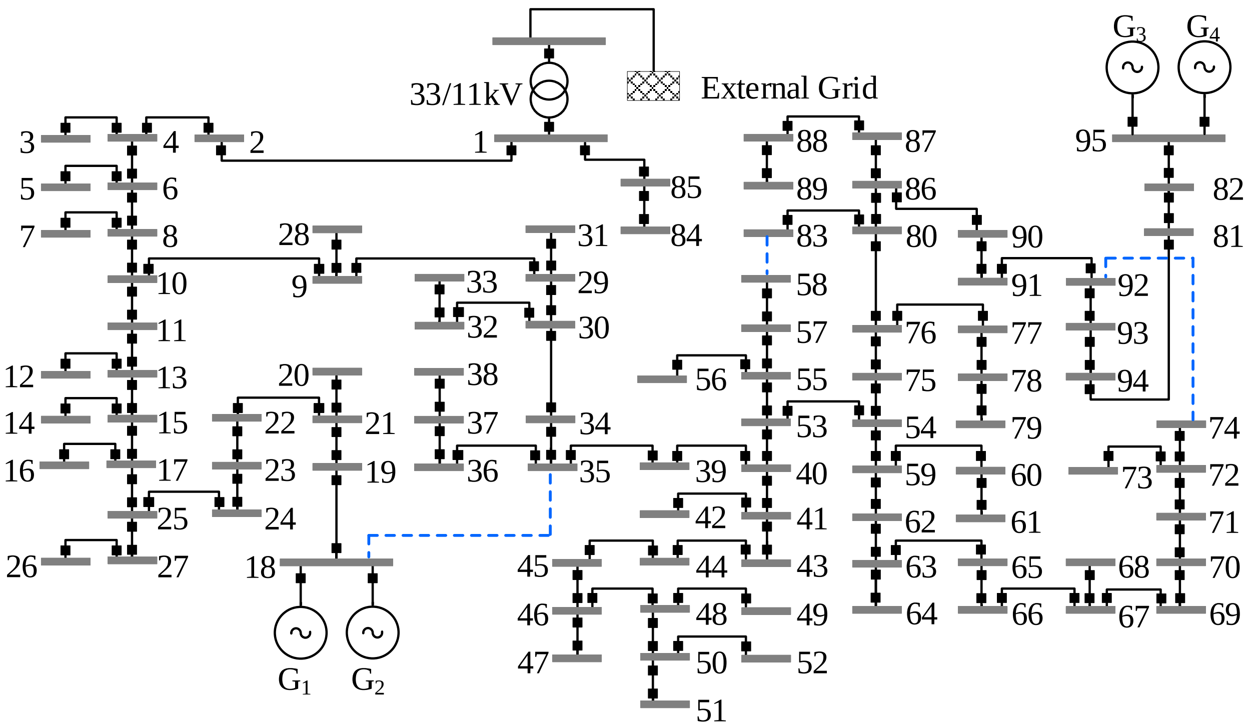

Figure 6.20: UKGDS 95-bus distribution benchmark system [216].

6.5.5.1 Measurement configuration

Initially, we determine which buses are equipped with SCADA and which ones with PMUs. The related information for both systems is provided in Table 6.17. As observed, 25 PMUs are assumed to be installed at the IEEE-118 system, while 30 PMUs are placed at the UKGDS 95-bus grid, which is a realistic scenario provided that low-cost PMUs are deployed. For the 118-bus transmission system, it is assumed that for each SCADA-monitored bus, the bus voltage magnitude and power injection, along with power flows recorded over all incident branches, are measured. For the 95-node feeder, the voltage magnitude of the slack bus and the power flows at the feeder head are telemetered, along with real-time voltage and injection data of PV buses 18 and 95. A bus voltage phasor and a complex current flow or injection measurement are obtained from each available PMU.

6.5.5.2 Evaluation of simulation results

In the sequel, we compare the HSE results obtained from utilizing three different configurations of PMU current measurements. The simulation scheme, applied to both test systems, is described below. We consider three configurations for the available PMU measurements. In the first configuration (C1), each PMU measures a single line current phasor of an incident branch. In the second one (C2), each PMU measures the complex current injection at the corresponding bus. In the third one (C3), half of the deployed PMUs (chosen randomly) record current flow phasors, while the other half measure complex current injections. The convergence threshold is set to $\varepsilon = 10^{-4}$ for all simulations.

The obtained accuracy ($Macc$) and convergence ($Mconv$) metrics, as well as the required iterations and total HSE execution time (averaged based on the conducted MC trials) for both systems, are provided in Table 6.18.

Regarding the IEEE-118 bus system, the usage of C3 outperforms the other two configurations, yielding better accuracy and convergence metrics. Moreover, using C2 is more advantageous than C1 in terms of both precision and convergence. The CPU time and number of iterations remain the same for all cases. Hence, configuring PMUs to record a mix of line current flows and bus current injections is the most efficient solution to boost HSE performance.

Concerning the UKGDS 95-bus network, the obtained results are less straightforward. Considering the accuracy aspect, the introduction of current injections into the MS by using C2 and C3, improves both $Macc_V$ and $Macc_S$. In fact, exclusively measuring current injections via C2 leads to better HSE accuracy. As for the convergence rate, the corresponding metrics become slightly worse in the case of C2 and C3, while the CPU time and iterations remain unchanged for all configurations. Therefore, the convergence properties practically are unaffected.

For both systems, the positive impact of utilizing current injection data on HSE accuracy is confirmed. Additionally, the convergence metrics are favorably affected in the case of the IEEE-118 system. Given the moderate size of the tested systems and the high number of PMUs considered, these findings are noteworthy; they suggest that the use of current injection synchrophasors, either exclusively or in combination with current flows, can comprise an effective scheme to leverage PMU measurements for HSE purposes.

6.5.5.3 Conclusions

Numerical studies conducted on two test systems were used to assess the utilized HSE methodology, focusing on accuracy and convergence metrics. The findings reveal that the type of current measurements (flow or injection) significantly influences the quality of SE. Notably, incorporating current injections into SE proves advantageous for enhancing accuracy. Furthermore, a brief analysis of practical considerations related to PMU installation suggests that measuring injected currents at buses is more convenient and cost-effective than measuring line flows at the power distribution level.

Therefore, relying solely on current flow measurements from PMUs is a limited approach. Instead, careful planning of PMU-based current metering schemes is essential to ensure high-quality SE.

Table 6.17: Measurement configuration for the 95- and 118-bus test systems.

Network	Measurements			
	SCADA-measured buses	PMU-measured buses	No. of SCADA measurements	No. of PMU measurements
IEEE 118-bus	3,8,11,12,17,21,22,27, 31,32,34,35,40,45,49,53,56, 62,65,72,73,75,77,80,85,86, 91,92,94,102,105,106,110	1,6,10,15,19,23,28,33,42, 44,46,51,54,59,61,69,70, 78,82,89,96,100,101,103, 107	375	100
UKGDS 95-bus	1, 18, 95	3,7,12,16,19,22,24,28, 32,34,37,39,43,49,52,56, 58,61,64,66,68,69,74,77, 79,81,83,87,90,94	11	120

Table 6.18: ISE accuracy and convergence metrics for different current measurement configurations.

Metric	IEEE 118-bus			UKGDS 95-bus		
	C1	C2	C3	C1	C2	C3
$Macc_V$ ($\times 10^{-3}$ pu)	4.50	4.20	4.00	5.10	2.20	2.80
$Macc_S$ ($\times 10^{-2}$ pu)	8.70	7.90	7.60	2.20	0.30	0.80
$Mconv_J$ ($\times 10^{-4}$ pu)	0.76	0.47	0.39	3.98	4.46	4.40
$Mconv_V$ ($\times 10^{-6}$)	2.17	1.93	1.61	3.73	3.81	3.79
$Mconv_\delta$ ($\times 10^{-6}$ rad)	4.17	4.54	3.05	0.05	0.14	0.10
Iterations	4.00	4.00	4.00	3.00	3.00	3.00
CPU time (ms)	17.00	17.00	17.00	7.00	7.00	7.00

7. Forecasting-aided State Estimation using Multi-source, Multi-rate Measurements

The application of DSE to quasi-steady state operating conditions, where changes in the power system are driven mainly by slow load fluctuations and gradual adjustments in generation, leads to the formulation of FASE. In this context, generators and other controllers can rapidly accommodate these slow variations, resulting in negligible changes in dynamic states [62]. FASE methods provide significant enhancement over SSE by incorporating predictive information about the system's state evolution, linking successive snapshots of the system state through a state space model, leveraging both measured and forecasted data. By integrating such data into the estimation process, FASE increases the robustness and accuracy of the classic SSE, particularly in situations with poor data redundancy or when the system is operating under quasi-steady conditions, whilst maintaining relatively low implementation complexity and computational requirements compared to DSE.

FASE approaches employ variants of the Kalman filter (KF), within the Bayesian framework, to combine real-time measurements with a linear state transition model informed by prior knowledge of the system's states accumulated over time and calculate an optimal state estimate. This process typically involves two stages: prediction (time update) and correction (measurement update). Various KF techniques – including the extended Kalman filter (EKF), unscented Kalman filter (UKF), cubature Kalman filter (CKF), and ensemble Kalman filter (EnKF) – can be used, each using a different approach to propagate state statistics [62].

Pioneering work on FASE methods utilizing multi-rate measurements is presented in [151], combining the concepts of unscented filtering and SE. Works [157], [160], address the issue of missing measurements over unreliable communication networks using EKF-based and CKF-based FASE methods, respectively. Various FASE methods focus on time-alignment of different data sources: in [153] an EKF-based algorithm is used for time-alignment of measurements, while [217], [154] propose the use of the Rauch–Tung–Striebel (RTS) smoothing algorithm, to reduce the effects of time skewness. Works [165], [218] make use of KF-based prediction of SCADA measurements to conduct SE with a limited number of PMUs between SCADA scans. Neural network-based FASE method [219] utilizes deep reinforcement learning to optimally predict slow-rate SCADA measurements and integrate them with real-time PMU data.

So far, the approaches that aim to integrate asynchronous SCADA and PMU measurements into FASE, have not necessarily prioritized ease of implementation within the EMS, requiring either substantial modifications to existing SSE software or necessitating entirely new implementations. Furthermore, the joint processing of SCADA and PMU data can lead to numerical issues, due to significant differences in measurement accuracy. Aiming to partially alleviate these drawbacks, several multi-stage (also referred to as sequential or post-processing [9]) FASE approaches have been proposed, where state information from separate PMU- and SCADA-based estimators is inferred in the form of pseudo-measurements or *a priori* information [164], [155]. In [146], PMU and SCADA data are processed by separate estimators, and a UKF-based data fusion framework is used to optimally combine the results.

In this context, this Chapter introduces a multi-stage EKF-based FASE method applicable to partially PMU-observable systems, which enhances EKF performance in the presence of multi-rate data, while requiring minimal modifications to the existing SSE framework. The key contributions of this work are outlined as follows [220]:

1) *Prediction (time update) step*: Traditional EKF implementations rely predominantly on fixed prediction-based state transition models, often limiting their responsiveness to real-time conditions. In contrast, the proposed method leverages the linear relationship between PMU-observable states

and real-time PMU measurements to continuously update the state transition model. This approach relies on multi-sensor data fusion theory to provide an optimal *a priori* estimate of the PMU-observable states, based on both forecasts and available PMU data.

2) *Forward correction (measurement update) step*: In typical FASE implementations, PMU and SCADA measurements are processed jointly, necessitating substantial modification or replacement of existing SE software. In the proposed method, the *a priori* state information, along with the synchrophasor measurements, are processed separately from the SCADA measurements, in two distinct stages of the SE process. This approach leaves the conventional SCADA-based SSE software unmodified and requires minimal interaction between the separate SE stages, simplifying integration into the EMS.
3) *Backward correction step*: Addressing the prevalent challenge of measurement asynchronization, the proposed approach incorporates a backward correction stage based on a fixed-interval smoothing technique. Fixed-interval smoothing has not been widely explored for power system FASE, while the RTS smoother employed in prior works generally imposes several strict assumptions of quasi-steady-state operating conditions and requires multiple matrix inversions. The MBF smoothing algorithm implemented in this work, significantly enhances computational efficiency and reduces reliance on operational assumptions [221]. Additionally, updating state transition model parameters after each FASE execution using the MBF algorithm provides a viable method for leveraging future measurements to reduce estimation errors injected by the EKF prediction models.

Finally, as demonstrated via extensive numerical simulations on IEEE benchmark networks, the proposed FASE method surpasses conventional EKF and RTS smoother-based approaches in accuracy, with computational requirements comparable to those of traditional SSE techniques.

7.1 Conventional FASE problem

By neglecting the dynamics of the system under quasi-steady operating conditions, the FASE approach linearizes the state transition model, resulting in the following discretized state space representation [75]:

$$\begin{aligned} \boldsymbol{x}_{k+1} &= \boldsymbol{F}_k \boldsymbol{x}_k + \boldsymbol{g}_k + \boldsymbol{w}_k \\ \boldsymbol{z}_k &= \boldsymbol{h}_k(\boldsymbol{x}_k) + \boldsymbol{e}_k \end{aligned} \tag{7.1}$$

where subscript k denotes the discrete time step t_k, $\boldsymbol{F}_k \in \mathbb{R}^{n \times n}$ is the diagonal state transition matrix for transition $t_k \to t_{k+1}$, vector $\boldsymbol{g}_k \in \mathbb{R}^n$ captures the trend of the state trajectory, $\boldsymbol{h}_k : \mathbb{R}^n \to \mathbb{R}^m$ is the vector of nonlinear functions relating the measurement vector $\boldsymbol{z}_k \in \mathbb{R}^m$ to the state vector $\boldsymbol{x}_k \in \mathbb{R}^n$, with $n < m$, random vectors $\boldsymbol{e}_k$ and $\boldsymbol{w}_k$ are the independent Gaussian measurement and transition errors, respectively, with $E(\boldsymbol{w}_k) = E(\boldsymbol{e}_k) = 0$, $Cov(\boldsymbol{w}_k) = \boldsymbol{Q}_k$ and $Cov(\boldsymbol{e}_k) = \boldsymbol{R}_k$. The state vector $\boldsymbol{x}_k$, can be expressed in either polar or rectangular coordinates, as $\boldsymbol{x}_k = \left[\boldsymbol{V}_k^T \ \ \boldsymbol{\delta}_k^T\right]^T$ or $\boldsymbol{x}_k = \left[\boldsymbol{V}_{\mathrm{R},k}^T \ \ \boldsymbol{V}_{\mathrm{I},k}^T\right]^T$, respectively, where $\boldsymbol{V}_k$, $\boldsymbol{\delta}_k$ are the vectors of magnitudes and angles, and $\boldsymbol{V}_{\mathrm{R},k}$, $\boldsymbol{V}_{\mathrm{I},k}$ are the vectors of real and imaginary parts of bus voltage phasors.

The state transition matrix $\boldsymbol{F}_k$ and the trend vector $\boldsymbol{g}_k$, are the parameters of the transition model, conventionally derived from historical information. A prevalent technique for determining these parameters is Holt's two-parameter exponential smoothing regression method, owing to its straightforward implementation [75]. Adopting the state space model (7.1) and Holt's forecasting method, the FASE problem is solved using the EKF, in two steps.

- *Prediction step*: Let $\hat{\boldsymbol{x}}_k$ and $\boldsymbol{P}_k$ be the *a posteriori* estimates of the state vector and its covariance matrix, respectively, at time t_k. By applying the conditional expectation operator on (7.1), the *a priori* estimate of the state vector $\tilde{\boldsymbol{x}}_{k+1} := \hat{\boldsymbol{x}}_{k+1|k}$ and its covariance matrix $\tilde{\boldsymbol{P}}_{k+1}$ are given by:

$$\begin{aligned} \tilde{\boldsymbol{x}}_{k+1} &= \boldsymbol{F}_k \hat{\boldsymbol{x}}_k + \boldsymbol{g}_k \\ \tilde{\boldsymbol{P}}_{k+1} &= \boldsymbol{F}_k \boldsymbol{P}_k \boldsymbol{F}_k^T + \boldsymbol{Q}_k \end{aligned} \tag{7.2}$$

- *Correction step*: Using the measurement vector $\boldsymbol{z}_k$ and the *a priori* (forecasted) state vector $\tilde{\boldsymbol{x}}_k$, the estimated state vector $\hat{\boldsymbol{x}}_k$ may be obtained by solving the following WLS optimization problem with objective function $J(\boldsymbol{x}_k)$ [75]:

$$\hat{\boldsymbol{x}}_k := \arg\min_{\boldsymbol{x}_k} J(\boldsymbol{x}_k) = \left[\boldsymbol{z}_k - \boldsymbol{h}_k(\boldsymbol{x}_k)\right]^T \boldsymbol{R}_k^{-1}\left[\boldsymbol{z}_k - \boldsymbol{h}_k(\boldsymbol{x}_k)\right] + \left(\tilde{\boldsymbol{x}}_k - \boldsymbol{x}_k\right)^T \tilde{\boldsymbol{P}}_k^{-1}\left(\tilde{\boldsymbol{x}}_k - \boldsymbol{x}_k\right) \tag{7.3}$$

The Kalman gain $\boldsymbol{K}_k \in \mathbb{R}^{n\times m}$ and the covariance matrix of $\hat{\boldsymbol{x}}_k$ $\boldsymbol{P}_k = E\left[(\boldsymbol{x}_k - \hat{\boldsymbol{x}}_k)(\boldsymbol{x}_k - \hat{\boldsymbol{x}}_k)^T\right]$ are obtained by evaluating $\boldsymbol{K}_k = \tilde{\boldsymbol{P}}_k \boldsymbol{H}_k^T\left(\boldsymbol{H}_k \tilde{\boldsymbol{P}}_k \boldsymbol{H}_k^T + \boldsymbol{R}_k\right)^{-1}$ and $\boldsymbol{P}_k = \left(\boldsymbol{I}_{n\times n} - \boldsymbol{K}_k \boldsymbol{H}_k\right)\tilde{\boldsymbol{P}}_k$ at $\hat{\boldsymbol{x}}_k$, where $\boldsymbol{H}_k$ is the Jacobian matrix of $\boldsymbol{h}_k(\cdot)$.

7.2 Formulation of the proposed FASE algorithm

Assuming m_s SCADA measurements (bus voltage magnitudes, branch power flows, and bus power injections), m_p PMU measurements (bus voltage and branch current phasors) provided by PMUs, and m_z zero injections, the state space model at instant t_k is given by:

$$\begin{aligned} \boldsymbol{x}_{k+1} &= \boldsymbol{F}_k \boldsymbol{x}_k + \boldsymbol{g}_k + \boldsymbol{w}_k \\ \boldsymbol{z}_{s,k} &= \boldsymbol{h}_{s,k}(\boldsymbol{x}_k) + \boldsymbol{e}_{s,k} \\ \boldsymbol{z}_{p,k} &= \boldsymbol{h}_{p,k}(\boldsymbol{x}_k) + \boldsymbol{e}_{p,k} \\ \boldsymbol{0} &= \boldsymbol{c}_k(\boldsymbol{x}_k) \end{aligned} \tag{7.4}$$

where $\boldsymbol{z}_{s,k} \in \mathbb{R}^{m_s}$ represents the vector of SCADA measurements, $\boldsymbol{z}_{p,k} \in \mathbb{R}^{m_p}$ is the vector of PMU measurements, with $\boldsymbol{h}_{s,k}(\cdot)$ and $\boldsymbol{h}_{p,k}(\cdot)$ being the vector functions relating SCADA and PMU measurements to the state vector $\boldsymbol{x}_k \in \mathbb{R}^n$, respectively, $\boldsymbol{e}_{s,k} \in \mathbb{R}^{m_s}$ and $\boldsymbol{e}_{p,k} \in \mathbb{R}^{m_p}$ are the normally distributed SCADA and PMU measurement errors, with zero mean and diagonal covariance matrices $\boldsymbol{R}_{s,k}$ and $\boldsymbol{R}_{p,k}$, respectively, and $\boldsymbol{c}_k : \mathbb{R}^n \to \mathbb{R}^{m_z}$ denotes the vector of functions modeling zero current injections.

7.2.1 Proposed prediction step

In this study the power system is assumed to be completely SCADA-observable and partially PMU-observable. The propagation of the EKF one-step-ahead $\left(t_k \to t_{k+1}\right)$ predictions for the entire power system is accomplished via Holt's linear exponential smoothing method, which involves the forecast equation and two smoothing equations [75]:

$$\begin{cases} \tilde{\boldsymbol{x}}_{k+1} = \boldsymbol{A}_k + \boldsymbol{B}_k \\ \boldsymbol{A}_k = \alpha \hat{\boldsymbol{x}}_k + (1-\alpha)\tilde{\boldsymbol{x}}_k \\ \boldsymbol{B}_k = \beta(\boldsymbol{A}_k - \boldsymbol{A}_{k-1}) + (1-\beta)\boldsymbol{B}_{k-1} \end{cases} \tag{7.5}$$

where $\boldsymbol{A}_k$ and $\boldsymbol{B}_k$ are the estimates of the level and the trend of the state variables, respectively, α and β are the corresponding scalar smoothing parameters, with $(\alpha,\beta)\in[0,1]^2$. The level $\boldsymbol{A}_k$ is the weighted average of the *a posteriori* $\hat{\boldsymbol{x}}_k$ and *a priori* $\tilde{\boldsymbol{x}}_k$ state estimates. The trend $\boldsymbol{B}_k$ is a weighted average of the estimated trend based on the level change $\boldsymbol{A}_k-\boldsymbol{A}_{k-1}$ and the previous estimate of the trend $\boldsymbol{B}_{k-1}$. Via mathematical manipulations (7.5) becomes [75]:

$$\begin{cases}\tilde{\boldsymbol{x}}_{k+1}=\boldsymbol{F}_k\hat{\boldsymbol{x}}_k+\boldsymbol{g}_k\\ \boldsymbol{F}_k=\alpha(1+\beta)\boldsymbol{I}_{n\times n}\\ \boldsymbol{g}_k=(1+\beta)(1-\alpha)\tilde{\boldsymbol{x}}_k-\beta\boldsymbol{A}_{k-1}+(1-\beta)\boldsymbol{B}_{k-1}\\ \boldsymbol{A}_k=\alpha\hat{\boldsymbol{x}}_k+(1-\alpha)\tilde{\boldsymbol{x}}_k\\ \boldsymbol{B}_k=\beta(\boldsymbol{A}_k-\boldsymbol{A}_{k-1})+(1-\beta)\boldsymbol{B}_{k-1}\end{cases}\tag{7.6}$$

For the purposes of FASE, the application of Holt's method requires the smoothing parameters α and β to be optimally estimated. Generally, these values may be reliably obtained from an analysis of the trajectory of the system states, based on available historical data [222]. Assuming a sequence of n_H available historical data points $\{\boldsymbol{x}_k\}_{k=1}^{n_H}$, let the one-step-ahead forecast be $\tilde{\boldsymbol{x}}_k(\alpha,\beta)=\boldsymbol{A}_{k-1}+\boldsymbol{B}_{k-1}$. The forecasting error vector at time t_k is [223]:

$$\boldsymbol{e}_{F,k}(\alpha,\beta)=\boldsymbol{x}_k-\left(\boldsymbol{A}_{k-1}+\boldsymbol{B}_{k-1}\right)\tag{7.7}$$

The parameters α and β can be chosen to minimize the sum of squared forecasting errors (SSFE) weighted by a decaying factor to prioritize recent observations [223]. The resulting optimization problem is defined as:

$$\begin{aligned}&\min_{\alpha,\beta}\sum_{k=1}^{n_H}\gamma^{n_H-k}\left\|\boldsymbol{x}_k-\left(\boldsymbol{A}_{k-1}+\boldsymbol{B}_{k-1}\right)\right\|_2^2\\ &\text{s.t. } 0<\alpha<1\\ &\quad\;\; 0<\beta<1\\ &\quad\;\; \boldsymbol{A}_k=\alpha\hat{\boldsymbol{x}}_k+(1-\alpha)\tilde{\boldsymbol{x}}_k\\ &\quad\;\; \boldsymbol{B}_k=\beta(\boldsymbol{A}_k-\boldsymbol{A}_{k-1})+(1-\beta)\boldsymbol{B}_{k-1}\end{aligned}\tag{7.8}$$

with $\gamma\in(0,1)$ controlling the decay rate.

The limited availability of synchronized, high-resolution PMU data can be utilized to formulate a transition model that closely tracks the incremental changes of the subvector of PMU-observable states $\boldsymbol{x}_{p,k}\in\mathbb{R}^{n_p}$ across successive FASE executions.

When the state vector is expressed in rectangular coordinates, the linear PMU-based WLS problem closed form solution at time t_{k+1} is given by [113]:

$$\tilde{\boldsymbol{x}}_{PM,k+1}=\boldsymbol{G}_p^{-1}\boldsymbol{H}_p^T\boldsymbol{R}_p^{-1}\boldsymbol{z}_{p,k+1}\tag{7.9}$$

$$\tilde{\boldsymbol{P}}_{PM,k+1}:=Cov(\tilde{\boldsymbol{x}}_{PM,k+1})=\boldsymbol{G}_P^{-1}\tag{7.10}$$

where subscript p denotes the m_p PMU measurements and corresponding constant matrices $\boldsymbol{H}_p=\partial\boldsymbol{h}_p/\partial\boldsymbol{x}_p$ and $\boldsymbol{G}_p=\boldsymbol{H}_p^T\boldsymbol{R}_p^{-1}\boldsymbol{H}_p$, pertaining to the n_p PMU-observable states $\boldsymbol{x}_{p,k}$. $\tilde{\boldsymbol{x}}_{PM,k+1}$ denotes the optimal estimate of $\boldsymbol{x}_{p,k+1}$ obtained via (7.9). Note that heuristic or systematic selection algorithms (e.g., greedy selection, rank-revealing decompositions, or convex optimization methods) can be employed to identify the set of state variables that yield a numerically stable solution of (7.9) [224].This subset of PMU-observable states is determined at the start of the FASE process, and the associated matrices remain static unless the network topology or the PMU configuration change.

At transition $t_k \to t_{k+1}$, the transition model for the PMU-observable states depending on Holt's smoothing method is written as:

$$\boldsymbol{x}_{p,k+1} = \boldsymbol{F}_{PH,k}\boldsymbol{x}_{p,k} + \boldsymbol{g}_{PH,k} + \boldsymbol{w}_{PH,k} \tag{7.11}$$

with the *a priori* estimate of $\boldsymbol{x}_{p,k+1}$ given by:

$$\begin{cases} \tilde{\boldsymbol{x}}_{PH,k+1} = \boldsymbol{F}_{PH,k}\hat{\boldsymbol{x}}_{p,k} + \boldsymbol{g}_{PH,k} \\ \boldsymbol{F}_{PH,k} = \alpha(1+\beta)\boldsymbol{I}_{n_p \times n_p} \\ \boldsymbol{g}_{PH,k} = (1+\beta)(1-\alpha)\tilde{\boldsymbol{x}}_{PH,k} - \beta\boldsymbol{A}_{PH,k-1} + (1-\beta)\boldsymbol{B}_{PH,k-1} \\ \boldsymbol{A}_{PH,k} = \alpha\hat{\boldsymbol{x}}_{p,k} + (1-\alpha)\tilde{\boldsymbol{x}}_{PH,k} \\ \boldsymbol{B}_{PH,k} = \beta(\boldsymbol{A}_{PH,k} - \boldsymbol{A}_{PH,k-1}) + (1-\beta)\boldsymbol{B}_{PH,k-1} \end{cases} \tag{7.12}$$

with covariance matrix:

$$\tilde{\boldsymbol{P}}_{PH,k+1} := Cov(\tilde{\boldsymbol{x}}_{PH,k+1}) = \boldsymbol{F}_{PH,k}\boldsymbol{P}_{p,k}\boldsymbol{F}_{PH,k}^{T} + \boldsymbol{Q}_{PH,k} \tag{7.13}$$

Via (7.9)–(7.13), it is evident that $\tilde{\boldsymbol{x}}_{PM,k+1}$ and $\tilde{\boldsymbol{x}}_{PH,k+1}$ are uncorrelated Gaussian variables with known covariances. The Bar-Shalom-Campo formula is a well-known method for providing an optimal linear unbiased minimum variance estimate when combining two or more independent state estimates with known error covariance matrices [139], [140]. Thus, an optimal fusion estimate $\tilde{\boldsymbol{x}}_{p,k+1}$ and an associated covariance $\tilde{\boldsymbol{P}}_{p,k+1}$, which contain the combined information from both the temporal forecasting model and the PMU-based measurement model, can be calculated as follows:

$$\tilde{\boldsymbol{x}}_{p,k+1} = \tilde{\boldsymbol{P}}_{p,k+1}\left(\tilde{\boldsymbol{P}}_{PM,k+1}^{-1}\tilde{\boldsymbol{x}}_{PM,k+1} + \tilde{\boldsymbol{P}}_{PH,k+1}^{-1}\tilde{\boldsymbol{x}}_{PH,k+1}\right) \tag{7.14}$$

$$\tilde{\boldsymbol{P}}_{p,k+1} := Cov(\tilde{\boldsymbol{x}}_{p,k+1}) = \left(\tilde{\boldsymbol{P}}_{PM,k+1}^{-1} + \tilde{\boldsymbol{P}}_{PH,k+1}^{-1}\right)^{-1} \tag{7.15}$$

Thus, by rewriting (7.14), the fusion *a priori* state estimate is given by:

$$\tilde{\boldsymbol{x}}_{p,k+1} = \boldsymbol{F}_{p,k}\hat{\boldsymbol{x}}_{p,k} + \boldsymbol{g}_{p,k} \tag{7.16}$$

where:

$$\boldsymbol{F}_{p,k} = \tilde{\boldsymbol{P}}_{p,k+1}\tilde{\boldsymbol{P}}_{PH,k+1}^{-1}\boldsymbol{F}_{PH,k} \tag{7.17}$$

$$\boldsymbol{g}_{p,k} = \tilde{\boldsymbol{P}}_{p,k+1}\left(\tilde{\boldsymbol{P}}_{PH,k+1}^{-1}\boldsymbol{g}_{PH,k} + \tilde{\boldsymbol{P}}_{PM,k+1}^{-1}\tilde{\boldsymbol{x}}_{PM,k+1}\right) \tag{7.18}$$

This approach harnesses the properties of both estimates:

- The estimate $\tilde{\boldsymbol{x}}_{PM,k+1}$ leverages real-time measurement data to quickly capture recent transitions that adhere to the physical network equations.
- Holt's method provides a data-driven forecast informed by the temporal evolution of the states, capturing longer-term trends that may not be directly evident from the PMU measurements.

For the set of SCADA-only observable states $\boldsymbol{x}_{s,k} \in \mathbb{R}^{n_s}$, Holt's method yields:

$$\begin{cases} \tilde{\boldsymbol{x}}_{s,k+1} = \boldsymbol{F}_{s,k}\hat{\boldsymbol{x}}_{s,k} + \boldsymbol{g}_{s,k} \\ \boldsymbol{F}_{s,k} = \alpha(1+\beta)\boldsymbol{I}_{n_s \times n_s} \\ \boldsymbol{g}_{s,k} = (1+\beta)(1-\alpha)\tilde{\boldsymbol{x}}_{s,k} - \beta\boldsymbol{A}_{s,k-1} + (1-\beta)\boldsymbol{B}_{s,k-1} \\ \boldsymbol{A}_{s,k} = \alpha\hat{\boldsymbol{x}}_{s,k} + (1-\alpha)\tilde{\boldsymbol{x}}_{s,k} \\ \boldsymbol{B}_{s,k} = \beta(\boldsymbol{A}_{s,k} - \boldsymbol{A}_{s,k-1}) + (1-\beta)\boldsymbol{B}_{s,k-1} \end{cases} \tag{7.19}$$

with covariance matrix:

$$\tilde{\boldsymbol{P}}_{s,k+1} := Cov(\tilde{\boldsymbol{x}}_{s,k+1}) = \boldsymbol{F}_{s,k}\boldsymbol{P}_{s,k}\boldsymbol{F}_{s,k}^T + \boldsymbol{Q}_{s,k} \tag{7.20}$$

Finally, the prediction step of the entire power system –illustrated in Figure 7.1– can be written as:

$$\tilde{\boldsymbol{x}}_{k+1} = \boldsymbol{F}_k\hat{\boldsymbol{x}}_k + \boldsymbol{g}_k \Leftrightarrow$$

$$\begin{bmatrix} \tilde{\boldsymbol{x}}_{s,k+1} \\ \tilde{\boldsymbol{x}}_{p,k+1} \end{bmatrix} = \begin{bmatrix} \boldsymbol{F}_{s,k} & \boldsymbol{0} \\ \boldsymbol{0} & \boldsymbol{F}_{p,k} \end{bmatrix} \begin{bmatrix} \hat{\boldsymbol{x}}_{s,k} \\ \hat{\boldsymbol{x}}_{p,k} \end{bmatrix} + \begin{bmatrix} \boldsymbol{g}_{s,k} \\ \boldsymbol{g}_{p,k} \end{bmatrix} \tag{7.21}$$

$$\tilde{\boldsymbol{P}}_{k+1} := Cov(\tilde{\boldsymbol{x}}_{k+1}) = \begin{bmatrix} \tilde{\boldsymbol{P}}_{s,k+1} & \boldsymbol{0} \\ \boldsymbol{0} & \tilde{\boldsymbol{P}}_{p,k+1} \end{bmatrix} \tag{7.22}$$

The statistical properties of the process noise $\boldsymbol{w}_k$, used to quantify the accuracy of the adopted state transition model, are not as straightforward to estimate compared to those of the measurement noise, since this requires quantifying the impact of unmodeled dynamics and time discretization on the FASE results. According to [2], a good estimate of the variance of the process noise $w_k(i)$, pertaining to the i-th state variable $x_k(i)$, can be calculated over a specified window of state changes as:

$$Var\left(w_k(i)\right) = \left(\frac{\max\left\{ \left| \Delta\left(\Delta x_k(i)\right) \right| \right\}}{2} \right)^2, \; i = 1, 2, \ldots, n \tag{7.23}$$

where $\Delta x_k(i) = x_k(i) - x_{k-1}(i),\ \Delta\left(\Delta x_k(i)\right) = \Delta x_k(i) - \Delta x_{k-1}(i),\ 3 \le k \le n_W$, and n_W is the length of the data window.

In turn, the covariance matrix is:

$$\boldsymbol{Q}_k = diag\left\{ Var\left(w_k(1)\right)\ Var\left(w_k(2)\right) \cdots Var\left(w_k(n)\right) \right\} \tag{7.24}$$

with $\boldsymbol{w}_k = \left[\boldsymbol{w}_{s,k}^T \ \ \boldsymbol{w}_{PH,k}^T \right]^T$ and $\boldsymbol{Q}_k = \begin{bmatrix} \boldsymbol{Q}_{s,k} & \boldsymbol{0} \\ \boldsymbol{0} & \boldsymbol{Q}_{PH,k} \end{bmatrix}$.

Eq. (7.23) and (7.24) corroborate that matrix $\boldsymbol{Q}_k$ should contain low values while remaining relatively constant during consecutive FASE executions. Excessively large or fluctuating values in $\boldsymbol{Q}_k$ indicate that there may be significant difference between the forecasted states and the measurements, meaning that the forecasting model needs refinement and/or that the actual system states are changing rapidly, i.e., the assumption of quasi-steady operating conditions is not met.

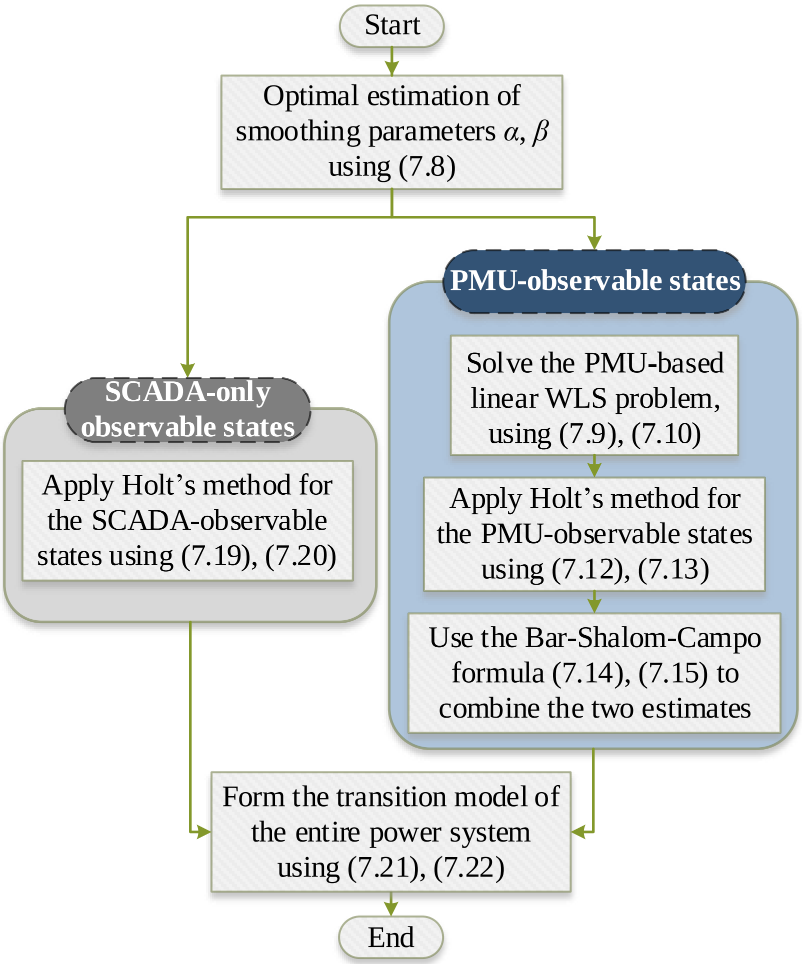

Figure 7.1: Flow diagram of the proposed prediction step.

7.2.2 *Proposed forward correction step*

The solution of the estimation problem (7.4) is obtained by applying the Hachtel's augmented matrix method [183]. The objective function is augmented with the weighted sum of the squared PMU measurement residuals $\boldsymbol{r}_{p,k}$, as well as of the *a priori* state information expressed via $\boldsymbol{r}_{f,k}$, and the constraints obeyed by $\boldsymbol{r}_{p,k}$, $\boldsymbol{r}_{f,k}$ and $\boldsymbol{c}_k(\boldsymbol{x}_k)$ are introduced, as follows:

$$\begin{aligned}
&\hat{\boldsymbol{x}}_k := \arg\min_{\boldsymbol{x}_k} aJ(\boldsymbol{x}_k) = a\boldsymbol{e}_{s,k}^T \boldsymbol{R}_{s,k}^{-1} \boldsymbol{e}_{s,k} + a\boldsymbol{r}_{p,k}^T \boldsymbol{R}_{p,k}^{-1} \boldsymbol{r}_{p,k} + a\boldsymbol{r}_{f,k}^T \tilde{\boldsymbol{P}}_k^{-1} \boldsymbol{r}_{f,k} \\
&\text{s.t. } \boldsymbol{r}_{p,k} = \boldsymbol{z}_{p,k} - \boldsymbol{h}_{p,k}(\boldsymbol{x}_k) \\
&\quad\ \ \boldsymbol{r}_{f,k} = \tilde{\boldsymbol{x}}_k - \boldsymbol{x}_k \\
&\quad\ \ \boldsymbol{c}_k(\boldsymbol{x}_k) = \boldsymbol{0}
\end{aligned} \tag{7.25}$$

Optimization problem (7.25) is solved via the method of Lagrange multipliers. The Lagrangian function at t_k is defined as follows:

$$\begin{aligned}
&\mathcal{L}(\boldsymbol{x}_k, \boldsymbol{r}_{p,k}, \boldsymbol{r}_{f,k}, \boldsymbol{\lambda}_k, \boldsymbol{\mu}_k, \boldsymbol{\xi}_k) = \\
&\quad a\boldsymbol{e}_{s,k}^T \boldsymbol{R}_{s,k}^{-1} \boldsymbol{e}_{s,k} + a\boldsymbol{r}_{p,k}^T \boldsymbol{R}_{p,k}^{-1} \boldsymbol{r}_{p,k} + a\boldsymbol{r}_{f,k}^T \tilde{\boldsymbol{P}}_k^{-1} \boldsymbol{r}_{f,k} + \boldsymbol{\lambda}_k^T \boldsymbol{c}_k(\boldsymbol{x}_k) \\
&\quad + \boldsymbol{\mu}_k^T \left[\boldsymbol{r}_{p,k} - \boldsymbol{z}_{p,k} + \boldsymbol{h}_{p,k}(\boldsymbol{x}_k)\right] + \boldsymbol{\xi}_k^T \left(\boldsymbol{r}_{f,k} - \tilde{\boldsymbol{x}}_k + \boldsymbol{x}_k\right)
\end{aligned} \tag{7.26}$$

where $\boldsymbol{\lambda}_k$, $\boldsymbol{\mu}_k$ and $\boldsymbol{\xi}_k$ are the Lagrange multipliers.

Iteratively solving the system of nonlinear equations derived from the first-order optimality conditions of (7.26) via the Gauss-Newton method, yields the following linear system at iteration (i):

$$\left[\begin{array}{cc:cc} a\boldsymbol{G}_{s,k}^{(i)} & \left(\boldsymbol{C}_k^{(i)}\right)^T & \left(\boldsymbol{H}_{p,k}^{(i)}\right)^T & \boldsymbol{I}_{n\times n} \\ \boldsymbol{C}_k^{(i)} & \boldsymbol{0} & \boldsymbol{0} & \boldsymbol{0} \\ \hdashline \boldsymbol{H}_{p,k}^{(i)} & \boldsymbol{0} & -a^{-1}\boldsymbol{R}_{p,k} & \boldsymbol{0} \\ \boldsymbol{I}_{n\times n} & \boldsymbol{0} & \boldsymbol{0} & -a^{-1}\tilde{\boldsymbol{P}}_k \end{array}\right]\left[\begin{array}{c} \Delta\boldsymbol{x}_k^{(i+1)} \\ \boldsymbol{\lambda}_k^{(i+1)} \\ \hdashline \boldsymbol{\mu}_k^{(i+1)} \\ \boldsymbol{\xi}_k^{(i+1)} \end{array}\right]=\left[\begin{array}{c} a\left(\boldsymbol{H}_{s,k}^{(i)}\right)^T\boldsymbol{R}_{s,k}^{-1}\Delta\boldsymbol{z}_{s,k}^{(i)} \\ -\boldsymbol{c}_k(\boldsymbol{x}_k^{(i)}) \\ \hdashline \Delta\boldsymbol{z}_{p,k}^{(i)} \\ \Delta\boldsymbol{z}_{f,k}^{(i)} \end{array}\right]\Leftrightarrow$$

$$\left[\begin{array}{c:c} \boldsymbol{G}_{sz,k}^{(i)} & \left(\boldsymbol{H}_{pf,k}^{(i)}\right)^T \\ \hdashline \boldsymbol{H}_{pf,k}^{(i)} & -a\boldsymbol{R}_{pf,k} \end{array}\right]\left[\begin{array}{c} \Delta\boldsymbol{x}_k^{(i+1)} \\ \boldsymbol{\lambda}_k^{(i+1)} \\ \hdashline \boldsymbol{\mu}_k^{(i+1)} \\ \boldsymbol{\xi}_k^{(i+1)} \end{array}\right]=\left[\begin{array}{c} a\boldsymbol{H}_{s,k}^T\boldsymbol{R}_{s,k}^{-1}\Delta\boldsymbol{z}_{s,k}^{(i)} \\ -\boldsymbol{c}_k(\boldsymbol{x}_k^{(i)}) \\ \hdashline \Delta\boldsymbol{z}_{p,k}^{(i)} \\ \Delta\boldsymbol{z}_{f,k}^{(i)} \end{array}\right] \tag{7.27}$$

where $\boldsymbol{H}_{s,k}$, $\boldsymbol{H}_{p,k}$, and $\boldsymbol{C}_k$ are the Jacobian matrices of $\boldsymbol{h}_{s,k}(\cdot)$, $\boldsymbol{h}_{p,k}(\cdot)$ and $\boldsymbol{c}_k(\cdot)$, respectively, $\boldsymbol{H}_{pf,k}=\begin{bmatrix} \boldsymbol{H}_{p,k} & \boldsymbol{0} \\ \boldsymbol{I}_{n\times n} & \boldsymbol{0} \end{bmatrix}$, $\boldsymbol{G}_{sz,k}=\begin{bmatrix} a\boldsymbol{G}_{s,k} & \boldsymbol{C}_k^T \\ \boldsymbol{C}_k & \boldsymbol{0} \end{bmatrix}$ and $\boldsymbol{R}_{pf,k}=\begin{bmatrix} \boldsymbol{R}_{p,k} & \boldsymbol{0} \\ \boldsymbol{0} & \tilde{\boldsymbol{P}}_k \end{bmatrix}$, with $\boldsymbol{G}_{s,k}=\boldsymbol{H}_{s,k}^T\boldsymbol{R}_{s,k}^{-1}\boldsymbol{H}_{s,k}$, $\Delta\boldsymbol{z}_{s,k}^{(i)}=\boldsymbol{z}_{s,k}-\boldsymbol{h}_{s,k}(x_k^{(i)})$, $\Delta\boldsymbol{z}_{p,k}^{(i)}=\boldsymbol{z}_{p,k}-\boldsymbol{h}_{p,k}(\boldsymbol{x}_k^{(i)})$, $\Delta\boldsymbol{z}_{f,k}^{(i)}=\tilde{\boldsymbol{x}}_k-\boldsymbol{x}_k^{(i)}$, and $\Delta\boldsymbol{x}_k^{(i+1)}=\boldsymbol{x}_k^{(i+1)}-\boldsymbol{x}_k^{(i)}$.

Solving for $\begin{bmatrix} \Delta\boldsymbol{x}_k^{(i+1)} \\ \boldsymbol{\lambda}_k^{(i+1)} \end{bmatrix}$, (7.27) yields:

$$\begin{bmatrix} \Delta\boldsymbol{y}_k^{(i+1)} \\ \boldsymbol{\lambda}_{y,k}^{(i+1)} \end{bmatrix}=\left(\boldsymbol{G}_{sz,k}^{(i)}\right)^{-1}\begin{bmatrix} a\left(\boldsymbol{H}_{s,k}^{(i)}\right)^T\boldsymbol{R}_{s,k}^{-1}\Delta\boldsymbol{z}_{s,k}^{(i)} \\ -\boldsymbol{c}_k(\boldsymbol{x}_k^{(i)}) \end{bmatrix} \tag{7.28}$$

$$\begin{bmatrix} \Delta\boldsymbol{u}_k^{(i+1)} \\ \boldsymbol{\lambda}_{u,k}^{(i+1)} \end{bmatrix}=\left(\boldsymbol{G}_{sz,k}^{(i)}\right)^{-1}\left(\boldsymbol{H}_{pf,k}^{(i)}\right)^T\left(a^{-1}\boldsymbol{R}_{pf,k}+\boldsymbol{H}_{pf,k}^{(i)}\left(\boldsymbol{G}_{sz,k}^{(i)}\right)^{-1}\left(\boldsymbol{H}_{pf,k}^{(i)}\right)^T\right)^{-1}\left(\begin{bmatrix} \Delta\boldsymbol{z}_{p,k}^{(i)} \\ \Delta\boldsymbol{z}_{f,k}^{(i)} \end{bmatrix}-\boldsymbol{H}_{pf,k}^{(i)}\begin{bmatrix} \Delta\boldsymbol{y}_k^{(i+1)} \\ \boldsymbol{\lambda}_{y,k}^{(i+1)} \end{bmatrix}\right) \tag{7.29}$$

$$\begin{bmatrix} \Delta\boldsymbol{x}_k^{(i+1)} \\ \boldsymbol{\lambda}_k^{(i+1)} \end{bmatrix}=\begin{bmatrix} \Delta\boldsymbol{y}_k^{(i+1)} \\ \boldsymbol{\lambda}_{y,k}^{(i+1)} \end{bmatrix}+\begin{bmatrix} \Delta\boldsymbol{u}_k^{(i+1)} \\ \boldsymbol{\lambda}_{u,k}^{(i+1)} \end{bmatrix} \tag{7.30}$$

Eq. (7.28)–(7.30) represent the iterative solution of (7.25), which can be obtained by employing a post-processing scheme, as reported in [184]. One observes that calculation of incremental correction $\Delta\boldsymbol{y}_k^{(i+1)}$ in (7.28), relies only on the SCADA measurement vector $\boldsymbol{z}_{s,k}$ and the zero injection information. The state vector incorporating the SCADA-based incremental correction $\Delta\boldsymbol{y}_k^{(i+1)}$ can be defined as $\boldsymbol{y}_k^{(i+1)}:=\boldsymbol{x}_k^{(i)}+\Delta\boldsymbol{y}_k^{(i+1)}$. By expressing the state vector $\boldsymbol{x}_k$ in rectangular coordinates, the PMU measurement model becomes linear, i.e., $\boldsymbol{H}_{pf,k}$ is a constant matrix, and thus we can write the incremental correction (7.29) as follows:

$$\begin{bmatrix} \Delta\boldsymbol{u}_k^{(i+1)} \\ \boldsymbol{\lambda}_{u,k}^{(i+1)} \end{bmatrix}=\left(\boldsymbol{G}_{sz,k}^{(i)}\right)^{-1}\boldsymbol{H}_{pf,k}^T\left(a^{-1}\boldsymbol{R}_{pf,k}+\boldsymbol{H}_{pf,k}\left(\boldsymbol{G}_{sz,k}^{(i)}\right)^{-1}\boldsymbol{H}_{pf,k}^T\right)^{-1}\begin{bmatrix} \boldsymbol{z}_{p,k}-\boldsymbol{H}_{p,k}\boldsymbol{y}_k^{(i+1)} \\ \tilde{\boldsymbol{x}}_k-\boldsymbol{y}_k^{(i+1)} \end{bmatrix} \tag{7.31}$$

For the iterative scheme (7.28)–(7.30), it holds that:

$$\Delta \boldsymbol{x}^{(i+1)} = \Delta \boldsymbol{y}^{(i+1)} + \Delta \boldsymbol{u}^{(i+1)} \Leftrightarrow \boldsymbol{x}^{(i+1)} = \boldsymbol{y}^{(i+1)} + \Delta \boldsymbol{u}^{(i+1)} \tag{7.32}$$

At the terminal iteration (t) where $\boldsymbol{y}^{(t)} := \hat{\boldsymbol{y}}$, $\boldsymbol{x}^{(t)} := \hat{\boldsymbol{x}}$ we can write:

$$\begin{bmatrix} \Delta \hat{\boldsymbol{u}}_k \\ \hat{\boldsymbol{\lambda}}_{u,k} \end{bmatrix} = \left(\boldsymbol{G}_{sz,k}^{(t)}\right)^{-1} \boldsymbol{H}_{pf,k}^T \left(a^{-1}\boldsymbol{R}_{pf,k} + \boldsymbol{H}_{pf,k} \left(\boldsymbol{G}_{sz,k}^{(t)}\right)^{-1} \boldsymbol{H}_{pf,k}^T \right)^{-1} \begin{bmatrix} \boldsymbol{z}_{p,k} - \boldsymbol{H}_{p,k}\hat{\boldsymbol{y}}_k \\ \tilde{\boldsymbol{x}}_k - \hat{\boldsymbol{y}}_k \end{bmatrix} \tag{7.33}$$

$$\begin{bmatrix} \hat{\boldsymbol{x}}_k \\ \hat{\boldsymbol{\lambda}}_k \end{bmatrix} = \begin{bmatrix} \hat{\boldsymbol{y}}_k \\ \hat{\boldsymbol{\lambda}}_{y,k} \end{bmatrix} + \begin{bmatrix} \Delta \hat{\boldsymbol{u}}_k \\ \hat{\boldsymbol{\lambda}}_{u,k} \end{bmatrix} \tag{7.34}$$

According to the analysis of Section 6.2.2, an equivalent SE formulation can be devised in which:

1) The effect of $\Delta \boldsymbol{u}_k^{(i)}$ on $\Delta \boldsymbol{x}_k^{(i)}$ is considered negligible for all iterations until the SCADA-based SSE has converged on its own. $\Delta \boldsymbol{y}_k^{(i)}$ and $\boldsymbol{\lambda}_{y,k}^{(i)}$ are calculated by the conventional SSE iterations, until convergence, which is attained when $\left\| \Delta \boldsymbol{y}_k^{(i)} \right\|_\infty \le \varepsilon$, where ε is the convergence threshold, yielding $\hat{\boldsymbol{y}}_k$ and $\hat{\boldsymbol{\lambda}}_{y,k}$.
2) In a post-processing step, as $\boldsymbol{H}_{p,k}$ is constant, $\Delta \hat{\boldsymbol{u}}_k$ can be calculated non-iteratively using (7.33), and $\hat{\boldsymbol{x}}_k$ is then given by (7.34).

According to the above analysis, we can formulate a non-iterative post-processing step to incorporate the PMU measurements $\boldsymbol{z}_{p,k}$, and the state predictions $\tilde{\boldsymbol{x}}_k$, as:

$$\begin{bmatrix} \Delta \hat{\boldsymbol{u}}_k \\ \hat{\boldsymbol{\lambda}}_{u,k} \end{bmatrix} = \boldsymbol{G}_{sz,k}^{-1} \boldsymbol{H}_{pf,k}^T \left(\boldsymbol{R}_{pf,k} + \boldsymbol{H}_{pf,k} \boldsymbol{G}_{sz,k}^{-1} \boldsymbol{H}_{pf,k}^T \right)^{-1} \begin{bmatrix} \boldsymbol{z}_{p,k} - \boldsymbol{H}_{p,k}\hat{\boldsymbol{y}}_k \\ \tilde{\boldsymbol{x}}_k - \hat{\boldsymbol{y}}_k \end{bmatrix} \tag{7.35}$$

$$\begin{bmatrix} \hat{\boldsymbol{x}}_k \\ \hat{\boldsymbol{\lambda}}_k \end{bmatrix} = \begin{bmatrix} \hat{\boldsymbol{y}}_k \\ \hat{\boldsymbol{\lambda}}_{y,k} \end{bmatrix} + \begin{bmatrix} \Delta \hat{\boldsymbol{u}}_k \\ \hat{\boldsymbol{\lambda}}_{u,k} \end{bmatrix} \tag{7.36}$$

where all Jacobian matrices are evaluated at the SCADA-based estimate $\hat{\boldsymbol{y}}_k$.

The forward transition step of the proposed FASE is presented in the flowchart of Figure 7.2. In the first stage, the algorithm iteratively calculates $\hat{\boldsymbol{y}}_k$ and in the second stage, uses (7.35) and (7.36) to calculate $\Delta \hat{\boldsymbol{u}}_k$ (PMU-based correction) and the final state vector $\hat{\boldsymbol{x}}_k$. Upon convergence of the forward correction step, $\boldsymbol{K}_k = \tilde{\boldsymbol{P}}_k \boldsymbol{H}_k^T \left(\boldsymbol{H}_k \tilde{\boldsymbol{P}}_k \boldsymbol{H}_k^T + \boldsymbol{R}_k \right)^{-1}$ and $\boldsymbol{P}_k = \left(\boldsymbol{I}_{n\times n} - \boldsymbol{K}_k \boldsymbol{H}_k \right) \tilde{\boldsymbol{P}}_k$ are evaluated at $\hat{\boldsymbol{x}}_k$, with $\boldsymbol{H}_k = \begin{bmatrix} \boldsymbol{H}_{s,k} \\ \boldsymbol{H}_{p,k} \end{bmatrix}$ and $\boldsymbol{R}_k = \begin{bmatrix} \boldsymbol{R}_{s,k} & \boldsymbol{0} \\ \boldsymbol{0} & \boldsymbol{R}_{p,k} \end{bmatrix}$.

7.2.3 Proposed backward correction step

After the EKF has been used to propagate the state statistics forward in time and compute estimates based on arriving measurements, the results are processed by the MBF smoother in a backward correction step, to refine the estimates throughout a specific time interval.

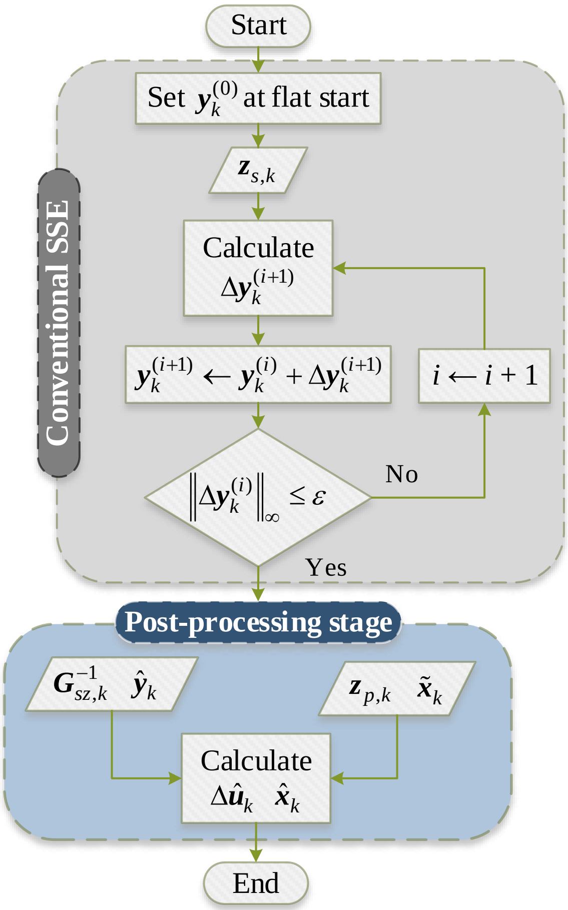

Figure 7.2: Flow diagram of the proposed forward correction step.

The MBF algorithm is a fixed interval smoother, derived from the RTS algorithm [221], [225]. Let the MBF smoother be applied to an interval $[t_1,\ t_N]$ with N available measurement vectors, at instants $t_1, t_2, \ldots, t_N$. Note that the dimension of the measurement vector at each instant may vary. After completing the EKF forward correction step at t_N, the MBF backward correction starts from t_N and proceeds backwards in time for $k = N-1, N-2, \ldots, 1$, to recursively calculate the filter variables $\hat{\boldsymbol{\Phi}}_k$ and $\hat{\boldsymbol{\varphi}}_k$ [221]:

$$\begin{cases} \tilde{\boldsymbol{\Phi}}_k = \boldsymbol{H}_k^T \boldsymbol{N}_k^{-1} \boldsymbol{H}_k + \boldsymbol{S}_k^T \hat{\boldsymbol{\Phi}}_k \boldsymbol{S}_k \\ \hat{\boldsymbol{\Phi}}_k = \boldsymbol{F}_k^T \tilde{\boldsymbol{\Phi}}_{k+1} \boldsymbol{F}_k \\ \hat{\boldsymbol{\Phi}}_N = \boldsymbol{0} \\ \tilde{\boldsymbol{\varphi}}_k = -\boldsymbol{H}_k^T \boldsymbol{N}_k^{-1} \left(\boldsymbol{z}_k - \boldsymbol{h}_k(\tilde{\boldsymbol{x}}_k) \right) + \boldsymbol{S}_k^T \hat{\boldsymbol{\varphi}}_k \\ \hat{\boldsymbol{\varphi}}_k = \boldsymbol{F}_k^T \tilde{\boldsymbol{\varphi}}_{k+1} \\ \hat{\boldsymbol{\varphi}}_N = \boldsymbol{0} \end{cases} \tag{7.37}$$

where $\boldsymbol{N}_k = \boldsymbol{H}_k \tilde{\boldsymbol{P}}_k \boldsymbol{H}_k^T + \boldsymbol{R}_k$, $\boldsymbol{S}_k = \boldsymbol{I}_{n\times n} - \boldsymbol{K}_k \boldsymbol{H}_k$.

In [154], it is found that increasing the length of the smoothing interval, i.e., the number of backward time steps, yields quickly diminishing improvements to SE results for the recursive RTS smoothing algorithm. Thus, to maintain the complexity of the smoothing process at a minimum and ensure near-real-time monitoring of the system, we consider a single backward transition $t_{k+1} \rightarrow t_k$. The corresponding recursive scheme for the smoothing interval $[t_k, t_{k+1}]$ is written as:

$$\hat{\boldsymbol{\Phi}}_k = \boldsymbol{F}_k^T \boldsymbol{H}_{k+1}^T \boldsymbol{N}_{k+1}^{-1} \boldsymbol{H}_{k+1} \boldsymbol{F}_k \tag{7.38}$$

$$\hat{\boldsymbol{\varphi}}_k = -\boldsymbol{F}_k^T \boldsymbol{H}_{k+1}^T \boldsymbol{N}_{k+1}^{-1} \left(\boldsymbol{z}_{k+1} - \boldsymbol{h}_{k+1}(\tilde{\boldsymbol{x}}_{k+1}) \right) \tag{7.39}$$

The smoothed state vector and its covariance matrix (denoted by superscript s) at time step t_k can then be calculated by substituting (7.38) and (7.39) in the following equations:

$$\begin{cases} \boldsymbol{P}_k^s = \boldsymbol{P}_k - \boldsymbol{P}_k \hat{\boldsymbol{\Phi}}_k \boldsymbol{P}_k \\ \hat{\boldsymbol{x}}_k^s = \hat{\boldsymbol{x}}_k - \boldsymbol{P}_k \hat{\boldsymbol{\varphi}}_k \end{cases} \tag{7.40}$$

The proposed backward transition step is presented in the flowchart of Figure 7.3. Two significant properties of the proposed method may be observed here:

1) The MBF smoother uses quantities directly from the forward correction step ($\boldsymbol{F}_k$, $\boldsymbol{H}_{k+1}$, and $\boldsymbol{N}_{k+1}^{-1}$), avoiding matrix inversions in the backward pass. Instead, it relies exclusively on matrix multiplications, which are computationally efficient, particularly because the matrices involved are sparse. The sparsity of these matrices is preserved throughout the backward correction step, ensuring that the computational cost $O(n_{nz})$ scales with the number of non-zero elements n_{nz}. This property greatly improves the performance of the proposed FASE algorithm as compared to the RTS smoother ($\sim O(n_{nz}^2)$ for sparse matrices) and is valid even if the covariance matrix $\tilde{\boldsymbol{P}}_k$ is ill-conditioned, which can occur under rapid changes in system states or significant mismatch between the state transition model of the EKF and the real-time measurements.

2) Considering that $\boldsymbol{F}_k$ is derived from Holt's method, the smoothed estimates of vectors $\boldsymbol{A}_k = \left[\boldsymbol{A}_{s,k}^T \;\; \boldsymbol{A}_{PH,k}^T \right]^T$ and $\boldsymbol{B}_k = \left[\boldsymbol{B}_{s,k}^T \;\; \boldsymbol{B}_{PH,k}^T \right]^T$ of (7.6) may be obtained after calculating $\hat{\boldsymbol{x}}_k^s$, as follows:

$$\begin{cases} \boldsymbol{A}_k^s = \alpha \hat{\boldsymbol{x}}_k^s + (1-\alpha) \tilde{\boldsymbol{x}}_k^s \\ \boldsymbol{B}_k^s = \beta(\boldsymbol{A}_k^s - \boldsymbol{A}_{k-1}) + (1-\beta) \boldsymbol{B}_{k-1} \end{cases} \tag{7.41}$$

This, in turn, means that during the next transition $t_{k+1} \rightarrow t_{k+2}$ the corresponding parameters $\boldsymbol{A}_{k+1}$ and $\boldsymbol{B}_{k+1}$ will be calculated using $\boldsymbol{A}_k^s$ and $\boldsymbol{B}_k^s$ by:

$$\begin{cases} \boldsymbol{A}_{k+1} = \alpha \hat{\boldsymbol{x}}_{s,k+1} + (1-\alpha) \tilde{\boldsymbol{x}}_{s,k+1} \\ \boldsymbol{B}_{k+1} = \beta(\boldsymbol{A}_{k+1} - \boldsymbol{A}_k^s) + (1-\beta) \boldsymbol{B}_k^s \end{cases} \tag{7.42}$$

This way, if one observes the trajectory of system states across a certain period, apart from enhancing the accuracy of the k-th FASE solution by leveraging any available data at t_{k+1}, the smoothed state vector $\hat{\boldsymbol{x}}_k^s$ is also propagated forward in time, through the state transition model (7.6).

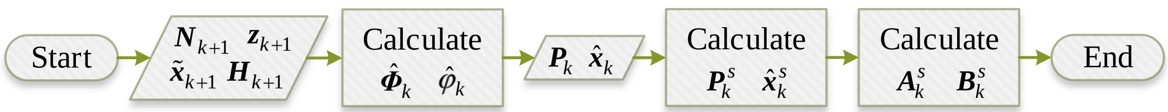

Figure 7.3: Flow diagram of proposed backward correction step.

7.3 Proposed FASE framework

The following assumptions are made regarding the execution of the FASE algorithm in the EMS, as illustrated in Figure 7.4, with respect to the discretized time:

- The first assumption is that the existing conventional SSE runs periodically in the EMS and utilizes SCADA measurements with random delays. This SSE is augmented with additional capabilities as per Subsection 7.2.2, effectively becoming a sequential hybrid FASE (HFASE) method. This HFASE is assumed to be executed in T_{HFASE} intervals, based on the requirements of the operators and the computational capabilities of the EMS.
- At the time of HFASE execution, the SCADA measurements utilized may or may not have been updated in the T_{HFASE} interval. This randomness applies to each SCADA measurement individually, meaning that the dataset of SCADA measurements can contain both recent measurements, as well as outdated information that does not describe the current operating conditions of the network. Contrariwise, PMU measurements can be safely assumed to be updated at each and every discrete time step, as 50 fps (or 60 fps, depending on nominal system frequency) are now the norm for PMU reporting rates. Thus, at the time of HFASE execution, the PMU measurements are assumed to form a complete snapshot of the quasi-steady operating conditions.
- In between successive HFASE executions, it is possible to solve a non-iterative PMU-based FASE (PFASE), based on the limited PMU information and the state forecasts provided by the state transition model of the EKF, which are necessary to achieve full observability. The PFASE is a PMU-based linear WLS state estimator with the inclusion of the EKF predictions [81], [130], and serves as a complementary way to exploit the available PMU measurements between HFASE executions. In the forward correction step, the PFASE closed-form solution is given by:

$$\left[\begin{array}{c|c} a\boldsymbol{H}_{p,k}^{T}\boldsymbol{R}_{p,k}^{-1}\boldsymbol{H}_{p,k}+a\tilde{\boldsymbol{P}}_{k}^{-1} & \boldsymbol{C}_{k}^{T} \\ \hline \boldsymbol{C}_{k} & \boldsymbol{0} \end{array}\right]\begin{bmatrix} \hat{\boldsymbol{x}}_{k} \\ \hat{\boldsymbol{\lambda}}_{k} \end{bmatrix}=\begin{bmatrix} a\boldsymbol{H}_{p,k}^{T}\boldsymbol{R}_{p,k}^{-1}\boldsymbol{z}_{p,k}+a\tilde{\boldsymbol{P}}_{k}^{-1}\tilde{\boldsymbol{x}}_{k} \\ \boldsymbol{0} \end{bmatrix} \tag{7.43}$$

PFASE can be executed at fixed T_{PFASE} intervals, which, without loss of generality, are assumed to remain constant and equal to $\Delta t_k = t_{k+1} - t_k$ (Figure 7.4). The execution frequency of PFASE depends on the PMU reporting rates, the size of the network, and the computational capabilities of the EMS.

The flowchart of the complete proposed FASE framework is illustrated in Figure 7.5.

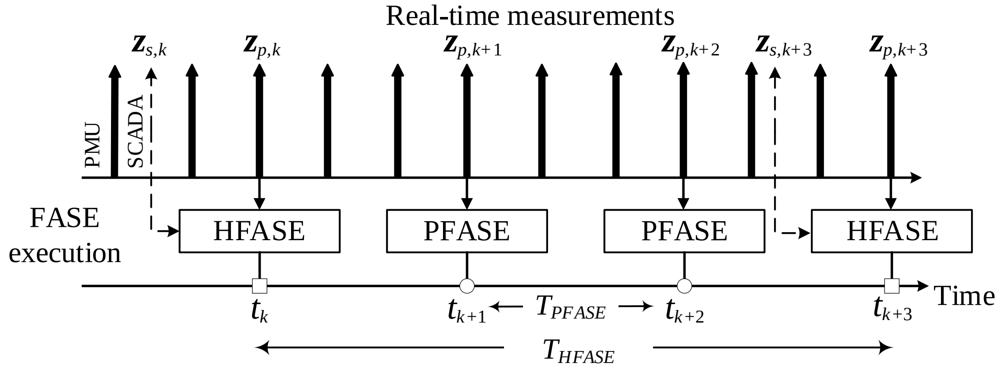

Figure 7.4: Sequence of measurement arrivals and FASE executions in the EMS.

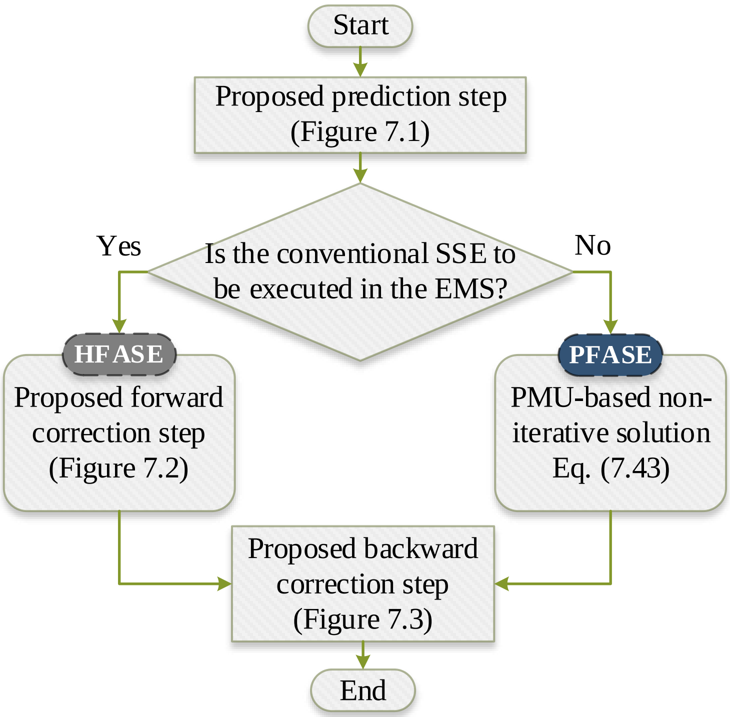

Figure 7.5: Flow diagram of the complete FASE framework.

7.4 Numerical simulations and results

The accuracy, convergence, and computational efficiency of the proposed FASE scheme are evaluated through numerical simulations conducted on the IEEE 14-, 118-, and 300-bus test systems [211]. The quasi-steady operating conditions of the networks, i.e., the slow fluctuation of the power system demand and generation, are simulated by varying the loads at randomly selected buses at each time step t_k. Load variations are applied within a band of ±30% of the base case value, with a mean fluctuation of ±0.5% at each transition. The generator participation factors, calculated for the base case of each network, are used to adjust the generator outputs to meet the load changes. This approach avoids the overload of the swing bus and provides more realistic system operation. The true system state vector is obtained by solving the Newton-Raphson load flow at each time step using the MATPOWER toolbox [212], and all the algorithms in question are implemented in MATLAB. A total of 500 MC trials is carried out for each system, with each trial spanning 200 discrete time steps.

7.4.1 Measurement and parameter configuration

The SCADA (PMU) measurements associated with a network bus consist of bus voltage magnitudes and power injections (bus voltage phasors), along with power flows (current phasors) recorded over all incident branches. Table 7.1 lists the MSs considered for each test system, providing the SCADA and PMU measurement locations in the form of SCADA- and PMU-measured buses, the SCADA measurement redundancy $r_{SCADA} = m_s/n$, as well as the values of parameters α and β of the prediction step, calculated from offline simulations using (7.8). The information of Table 7.1 is also visualized in Figure 7.6 and Figure 7.7, which illustrate the measurement type and redundancy at each bus of the IEEE 14- and 118-bus systems. Finally, Table 7.2 provides the PMU-unobservable buses of each test system, given the PMU measurement allocation of Table 7.1.

The true measurement values are derived from a power flow solution and are then corrupted with random additive Gaussian noise, so that the actual measured values are given by:

$$\boldsymbol{z}_k^{meas} = \boldsymbol{z}_k^{true} + \boldsymbol{v}_k \odot \boldsymbol{\sigma} \tag{7.44}$$

where $\boldsymbol{z}_k^{true}$ is the true measurement vector derived from the load flow solution at t_k, $\boldsymbol{v}_k$ is a $\mathcal{N}(\boldsymbol{0}, \boldsymbol{I})$ random vector, and $\boldsymbol{\sigma}$ is the vector of measurement standard deviations, with the following values [2], [113]:

- for SCADA measurements, $\sigma_{SCADA} = 0.01$ pu,
- for PMU magnitude measurements, $\sigma_{PMU_M} = 0.001$ pu,
- for PMU angle measurements, $\sigma_{PMU_A} = 0.35$ mrad.

Both voltage and current phasors are represented in rectangular coordinates, to linearize the PMU measurement model [113]. As the phasor measurements are converted from polar to rectangular form, their corresponding standard deviations need to be reevaluated according to error propagation theory [184].

Table 7.1: FASE simulations – Measurements and parameters for the IEEE test systems.

IEEE Network	SCADA buses	PMU buses	SCADA meas.	PMU meas.	r_{SCADA}	α	β
14-bus	2, 4, 6, 8-10	3, 5, 14	58	22	2.071	0.97	0.15
118-bus	2-4, 7, 8, 11, 12, 16, 17, 21, 22, 27, 28, 31, 32, 34, 35, 40, 41, 44-46, 48-50, 53, 56, 57, 62, 65, 72, 73, 75, 77, 78, 80, 84-87, 91, 92, 94, 95, 101, 102, 105-107, 109-111	1, 6, 19, 23, 33, 42, 51, 54, 59, 61, 69, 70, 89, 96, 100, 103	506	176	2.144	0.92	0.08
300-bus	1-3, 9, 11, 15, 17, 21, 23, 26, 27, 33, 37, 41, 43, 44, 47, 49, 51, 53, 55, 57, 61, 63, 70-73, 76, 77, 79, 80, 84, 97, 98, 102-105, 108, 109, 114, 119-121, 124-126, 135-137, 139, 140, 143, 153-157, 159, 161-163, 170, 172, 173, 177-179, 182-184, 188-190, 196-199, 203-206, 208, 209, 211, 213-218, 222-225, 227-236, 238, 239, 241-243, 245-250, 281, 552, 562, 609, 7023, 7024, 7039, 7071, 7130, 7139, 7166, 9002-9004, 9021, 9025, 9026, 9043, 9051-9055, 9071, 9072, 9121	5, 8, 10, 14, 20, 25, 38, 52, 58, 89, 91, 92, 94, 107, 112, 122, 123, 138, 141, 145, 146, 148, 149, 152, 167, 171, 176, 180, 181, 185, 186, 191, 200-202, 207, 220, 221, 319, 320, 322-324, 526, 528, 531, 664, 1190, 1200, 7001-7003, 7011, 7012, 7017, 7044, 7049, 7055, 7057, 7061, 7062, 9022, 9024, 9031-9038, 9041, 9042, 9533	1283	420	2.138	1.00	0.06

Table 7.2: FASE simulations – Regions unobservable by PMUs in each test system.

IEEE Network	PMU-unobservable buses	Total unob-servable buses
14-bus	7, 8, 10, 11, 12	5
118-bus	4, 8-14, 16, 17, 21, 26-31, 35, 36, 38, 39, 43-46, 48, 50, 57, 66, 67, 72, 73	52
300-bus	4, 16, 34-36, 39, 40, 42, 46, 47, 53, 54, 71, 73, 74, 76-78, 80, 81, 84, 88, 98, 100, 109, 113, 117, 118, 127-129, 132, 134, 135, 139, 142, 151, 154-156, 158-166, 168, 170, 182, 183, 189, 190, 193, 195-197, 203, 205, 208, 209, 212-216, 219, 222, 224, 226-247, 249, 250, 281, 552, 562, 609, 1201, 2040, 7023, 7039, 7071, 7130, 7139, 7166, 9001, 9005-9007, 9012, 9023, 9025, 9026, 9043, 9051, 9052, 9054, 9055, 9071, 9072, 9121	122

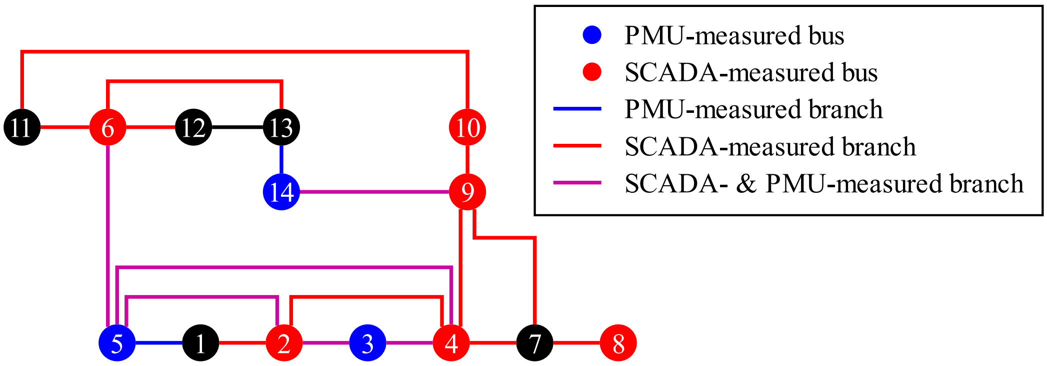

Figure 7.6: Measurement configuration for the IEEE 14-bus network.

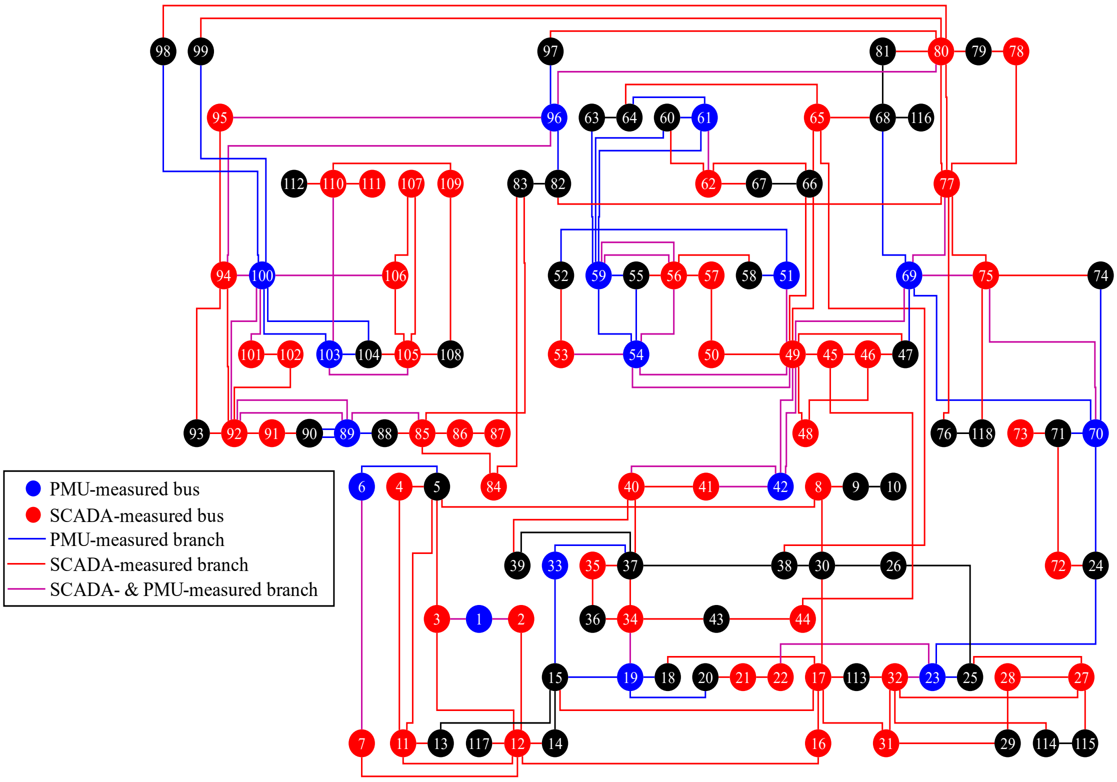

Figure 7.7: Measurement configuration for the IEEE 118-bus network.

7.4.2 *FASE initialization*

At time t_1, it is assumed that a conventional hybrid SSE is carried out, and thus a first estimate of the state vector is available, to be utilized in the prediction step of transition $t_1 \rightarrow t_2$. The corresponding covariance matrix $\boldsymbol{P}_1$ can be initialized as $\boldsymbol{P}_1 = Cov(\hat{\boldsymbol{x}}_1) = \boldsymbol{G}_1^{-1}(\hat{\boldsymbol{x}}_1)$, the trend vector $\boldsymbol{g}_1$ is initialized at $\boldsymbol{g}_1 = \boldsymbol{0}$, and $\boldsymbol{A}_1 = \hat{\boldsymbol{x}}_1$, $\boldsymbol{B}_1 = \boldsymbol{0}$. At t_2, $\boldsymbol{g}_2$ and $\boldsymbol{A}_2$ are calculated via (7.6), with $\boldsymbol{B}_2 = \boldsymbol{A}_2 - \boldsymbol{A}_1$.

7.4.3 *Comparison metrics*

To assess the performance of FASE algorithms in offline simulations, the mean absolute error (MAE) of voltage magnitudes and phase angles can be calculated as [213]:

$$MAE = \frac{1}{n}\sum_{i=1}^{n} | x_k^{true}(i) - \hat{x}_k(i) | \tag{7.45}$$

where $x_k^{true}(i)$ is the true value of the i-th state variable obtained by the power flow solution, and $\hat{x}_k(i)$ is its corresponding estimation. In the following, the MAE_V and MAE_A metrics correspond to voltage magnitude and angle states, respectively.

The $Macc_V$ metric is utilized to capture the effect of both magnitude and angle errors in a norm metric, and is defined as [213]:

$$Macc_V = \left\| \tilde{\boldsymbol{V}}_k^{true} - \tilde{\boldsymbol{V}}_k^{est} \right\|_2 = \left(\sum_{i=1}^{N} \left| \tilde{V}_{i,k}^{true} - \tilde{V}_{i,k}^{est} \right|^2 \right)^{\frac{1}{2}} \tag{7.46}$$

where $\tilde{V}_i^{true}$ and $\tilde{V}_i^{est}$ are the true and estimated complex phasor voltages of bus i, reported in p.u., and N is the total number of buses.

To determine each method's capability of estimating the complex power flow on each branch, the $Macc_S$ metric is computed as [213]:

$$Macc_S = \sqrt{\sum_{i=1}^{M} \left| \tilde{S}_{f,k}^{true}(i) - \tilde{S}_{f,k}^{est}(i) \right|^2 + \left| \tilde{S}_{t,k}^{true}(i) - \tilde{S}_{t,k}^{est}(i) \right|^2} \tag{7.47}$$

where the summation index i ranges over all the M network branches, $\tilde{S}^{true}$ and $\tilde{S}^{est}$ are the true and estimated complex power flows, and the sending and receiving ends of each branch are denoted by subscripts f and t, respectively.

7.4.4 Evaluation of simulation results

In the following, the performance of the proposed FASE method, referred to as the MBF method for convenience, is compared with the conventional EKF method [75] and the RTS method [217]. All three methods use the same optimally estimated smoothing parameters α and β, based on (7.8). In all RTS and MBF simulations, a single backward correction step is applied. The state vector $\boldsymbol{x}$ is expressed in rectangular coordinates, and a convergence threshold of $\varepsilon = 10^{-4}$ is used for all iterative algorithms.

Each set of MC trials is conducted for a different integer value of $T_R = \frac{T_{HFASE}}{T_{PFASE}}$, ranging from 1 (ideal scenario) to 20 (worst-case scenario), to gain a better understanding of how each method behaves under varying assumptions of SE execution in the EMS. As the value of T_R increases, the T_{HFASE} interval becomes larger, with T_{PFASE} remaining constant and equal to $\Delta t_k = t_{k+1} - t_k$. Of course, T_{PFASE} could be set equal to a multiple of Δt_k, and the parameters of the state transition model should then be adjusted accordingly to account for the potentially larger changes in state variables between consecutive PFASE executions. The graphs of Fig. 6 show how the MAE_V and MAE_A metrics change with respect to T_R. The analysis reveals that the proposed MBF method handles time skew in SCADA measurements more effectively. This becomes particularly evident for larger values of T_R, demonstrating the ability of the proposed state transition, model in combination with the MBF smoother, to effectively utilize available state predictions and measurements to fill in inconsistent SCADA information. In order to explicitly show the contribution of each stage of the proposed MBF method to the accuracy of the state estimate, Figure 7.11–Figure 7.13 juxtapose its MAE metrics with those of the *a* *priori* estimate of the state vector, obtained according to Subsection 7.2.1, as well as of the *a posteriori* estimate of Subsection 7.2.2, prior to the application of the MBF smoothing algorithm.

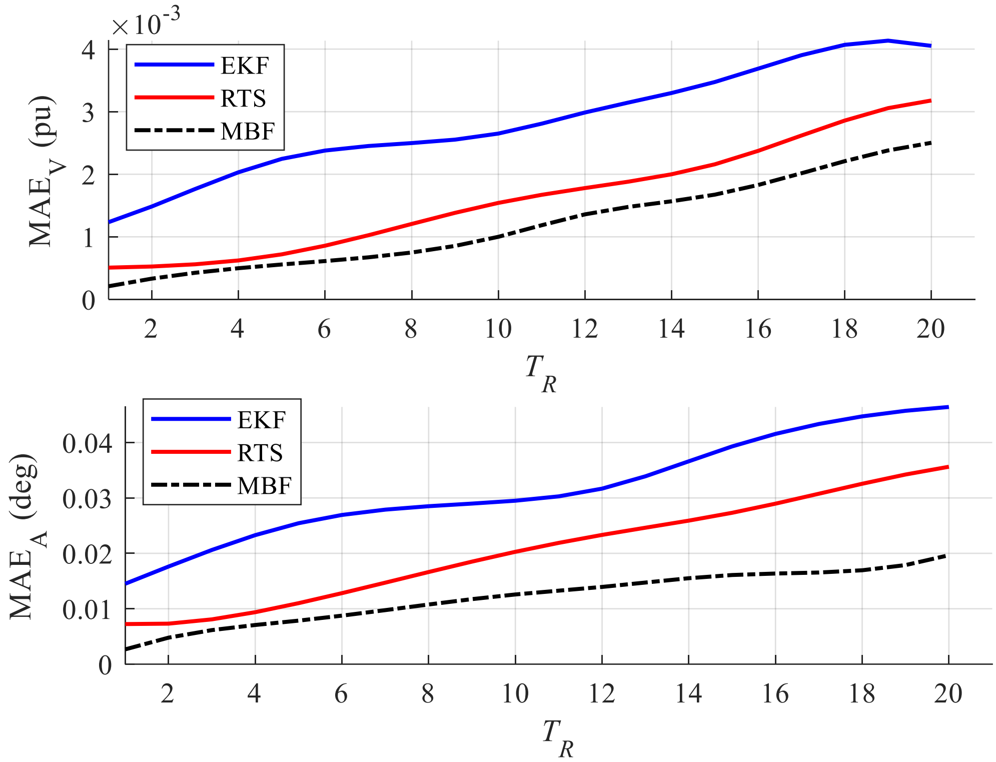

Figure 7.8: IEEE 14-bus system – MAE of the EKF, RTS and MBF methods for various values of T_R.

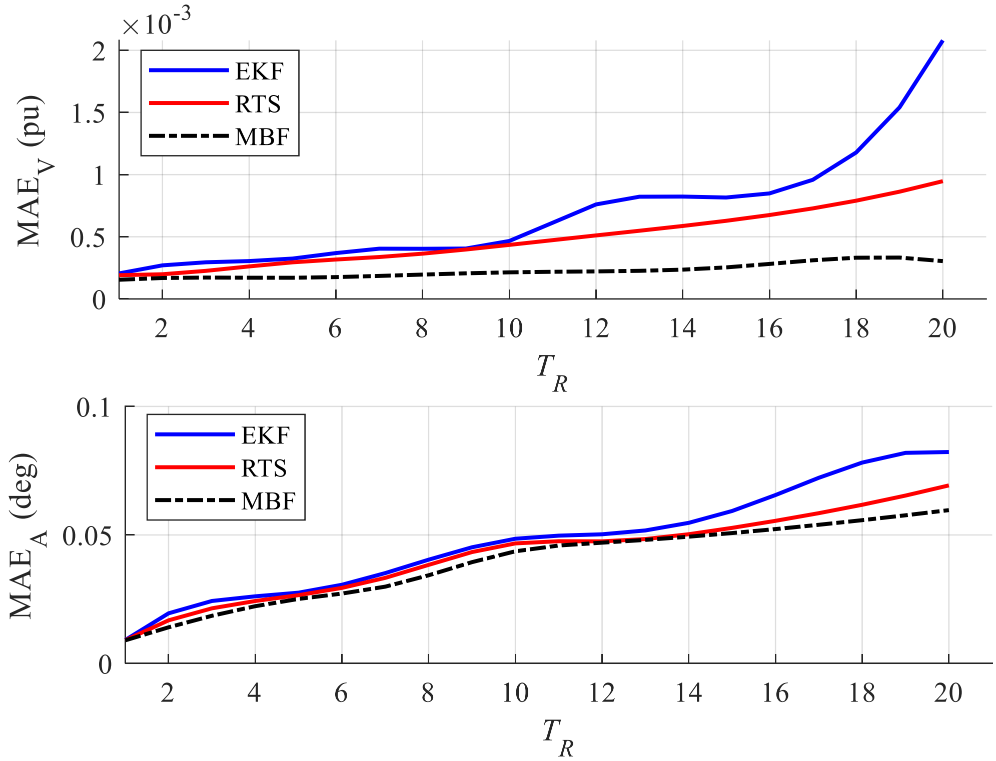

Figure 7.9: IEEE 118-bus system – MAE of the EKF, RTS and MBF methods for various values of T_R.

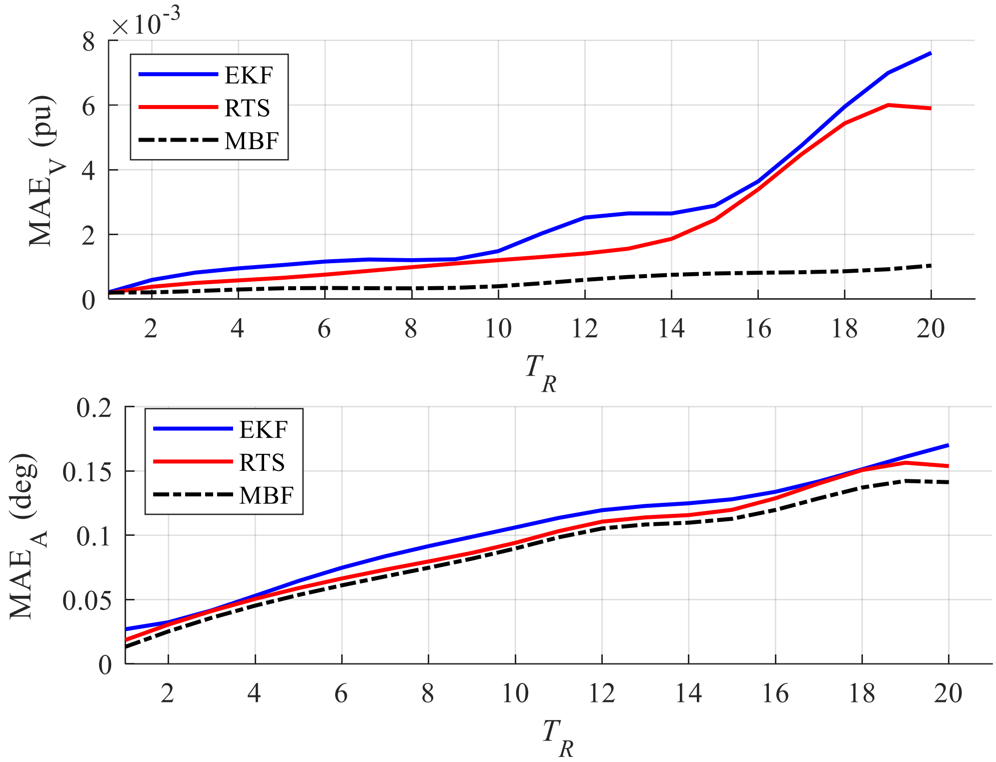

Figure 7.10: IEEE 300-bus system – MAE of the EKF, RTS and MBF methods for various values of T_R.

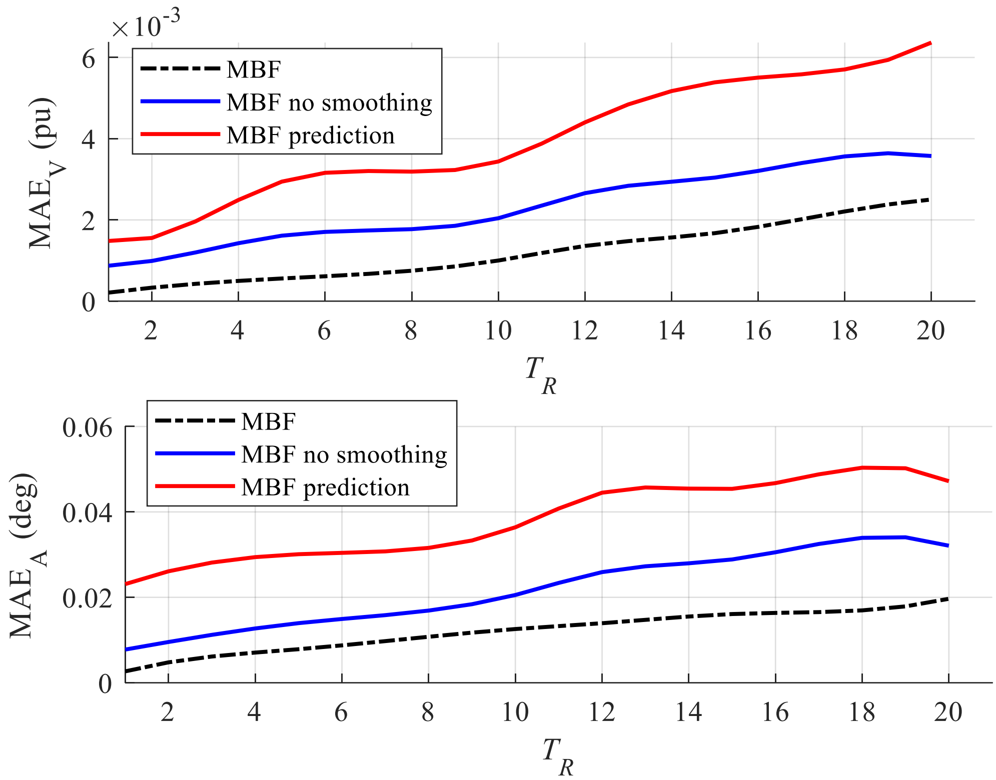

Figure 7.11: IEEE 14-bus system – MAE of the predicted and the estimated states using the MBF method without the backward correction (smoothing) step, for various values of T_R.

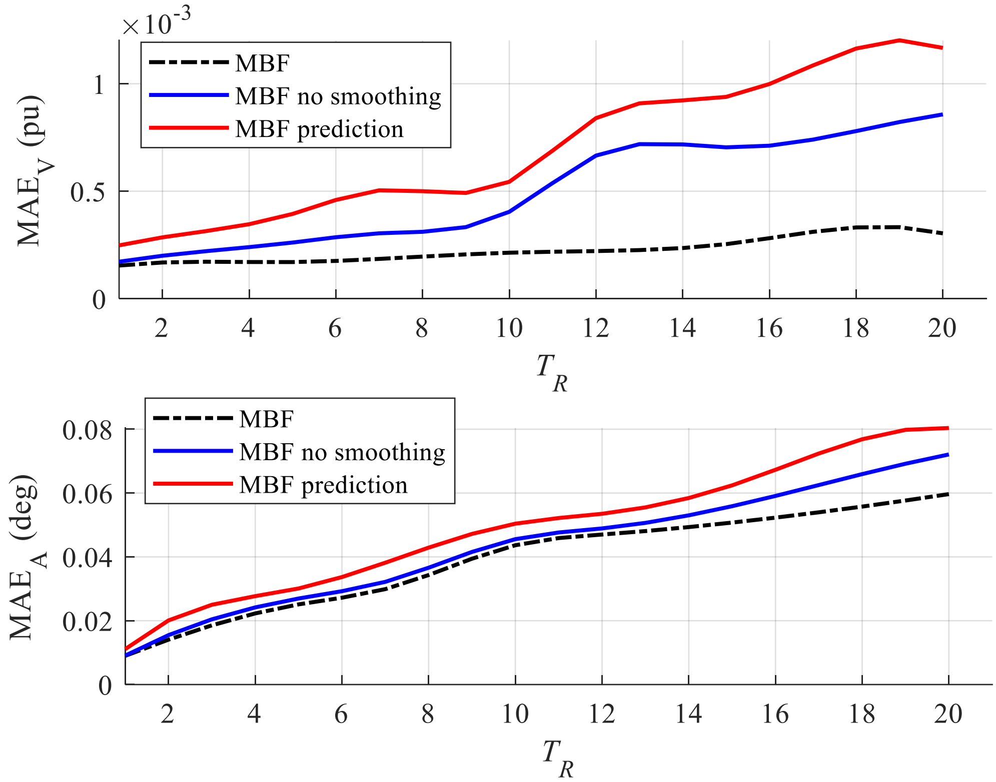

Figure 7.12: IEEE 118-bus system – MAE metrics of the predicted and the estimated states using the MBF method without the backward correction (smoothing) step, for various values of T_R.

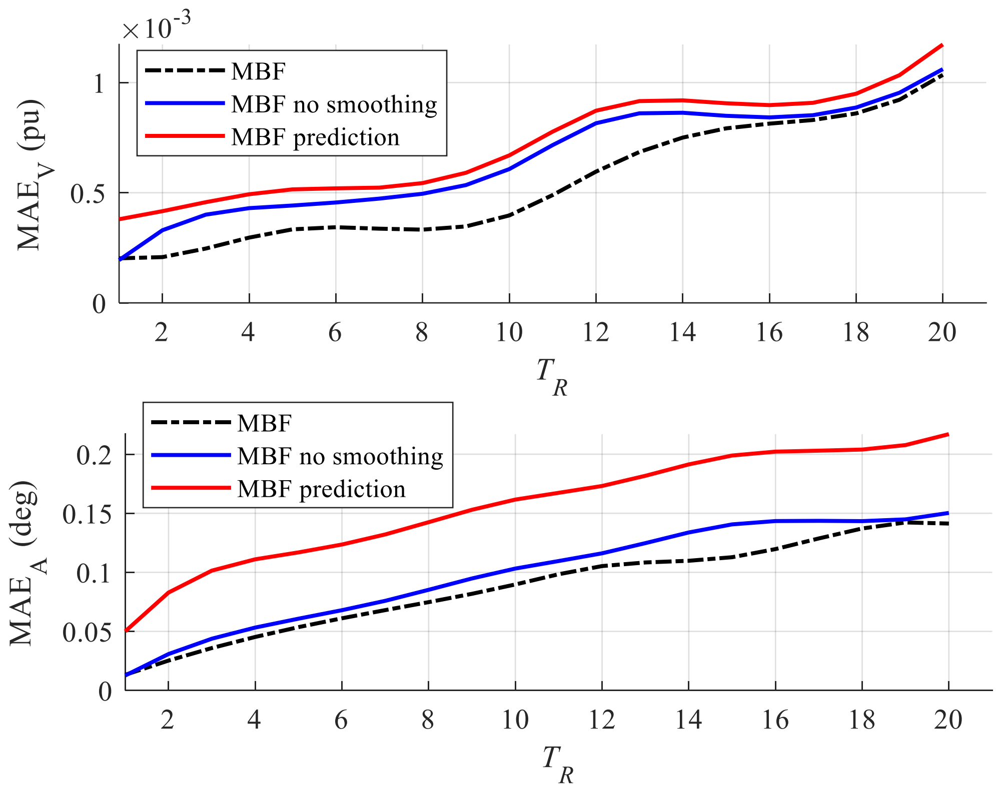

Figure 7.13: IEEE 300-bus system – MAE metrics of the predicted and the estimated states using the MBF method without the backward correction (smoothing) step, for various values of T_R.

Table 7.3 summarizes the MAE, $Macc_V$ and $Macc_S$ accuracy metrics averaged over the MC trials of the EKF, RTS, and the proposed MBF estimators, as well as the average total time required by each algorithm to process the MS, including the application of the fixed-interval smoothing algorithms (RTS or MBF). The computation times of the backward correction (smoothing) steps are also provided separately for easier comparison. It is observed that the proposed MBF method consistently produces the most accurate results for all test systems. More specifically, we may deduce the following:

- As expected, both RTS and MBF methods utilizing a backwards smoothing technique provide more accurate state estimates compared to the standard EKF approach.
- Substantial improvements over the EKF method are obtained using the proposed MBF algorithm. Metrics MAE_V, MAE_A, and $Macc_V$ decrease by 68%, 30.5%, and 34.5% on average, respectively, across all simulations. Compared to the RTS method, the MBF algorithm achieves improvements of 50%, 19%, and 20% in MAE_V, MAE_A, and $Macc_V$, respectively.
- The proposed algorithm is also found to provide a more reliable estimation of branch power flows, as its $Macc_S$ values are lower for all simulations. With a base value of 100 MVA, the $Macc_S$ values provided by the MBF method in p.u. correspond to a maximum deviation of 3.2%, 2.1%, and 3.4% from the true total branch power flow for the 14-, 118-, and 300-bus systems, respectively.
- The HFASE step of the MBF method incurs a slight increase in computation time for the 14- and 118-bus systems compared to the other methods, primarily due to the computational cost of calculating the transition matrix. However, for the larger 300-bus system, the MBF method achieves significantly lower HFASE execution times, as the EKF and RTS algorithms require more iterations to converge as T_R increases. The PFASE stage exhibits no significant differences in execution time among the three methods. Notably, the time required for the backward filtering (correction) step is substantially reduced with the MBF smoothing algorithm, owing to the properties discussed in Subsection 7.2.3. Note that calculation of vectors $\boldsymbol{A}_k^s$ and $\boldsymbol{B}_k^s$ is included in the smoothing stage of the proposed method. From a practical standpoint, the MBF method effectively handles the rapid arrival of PMU data (25–50 frames/s) for the 14- and 118-bus systems, enabling more frequent PFASE executions between consecutive HFASE stages. For larger networks, such as the 300-bus system, parallelization techniques may be required to achieve desired performance, particularly for the RTS and MBF methods [161].

It is also important to investigate the performance of the proposed method in terms of its capability to provide reliable state estimates for the PMU-unobservable buses. For this purpose, Figure 7.14–Figure 7.16 illustrate the average MAE metrics of the states unobservable by PMUs, calculated over the 500 MC simulations, with $T_R = 10$, for both the RTS and MBF methods, and all three test systems. One observes that the MAE values of the PMU-unobservable states for the MBF method are only slightly larger than the averages of Figures Figure 7.8–Figure 7.10, and overall lower than those of the RTS. This is attributed to the refined state transition model proposed in Subsection 7.2.1, as well as the propagation of the smoothed transition model parameters, described in Subsection 7.2.3, neither of which are employed by the RTS approach.

Table 7.3: Accuracy and performance metrics of FASE methods.

Metric	IEEE 14			IEEE 118			IEEE 300		
	EKF	**RTS**	**MBF**	**EKF**	**RTS**	**MBF**	**EKF**	**RTS**	**MBF**
MAE_V ($\times 10^{-3}$ pu)	2.80	1.60	1.50	10.30	4.00	1.70	2.00	1.60	0.86
MAE_A ($\times 10^{-2}$ deg.)	3.10	2.04	1.18	3.77	3.16	3.07	9.70	8.89	8.52
$Macc_V$ ($\times 10^{-2}$ pu)	1.32	0.92	0.87	16.66	6.49	2.83	7.50	6.31	5.47
$Maccs_S$ (pu)	0.10	0.09	0.09	6.61	2.63	0.92	21.51	19.09	16.87
HFASE time (ms)	5.40	5.99	8.30	23.20	21.50	25.84	200	194.90	177.80
PFASE time (ms)	2.20	2.49	2.40	8.30	9.00	10.24	42.80	51.10	55.00
Smoother time (ms)	–	0.19	0.10	–	1.40	0.84	–	12.90	9.80

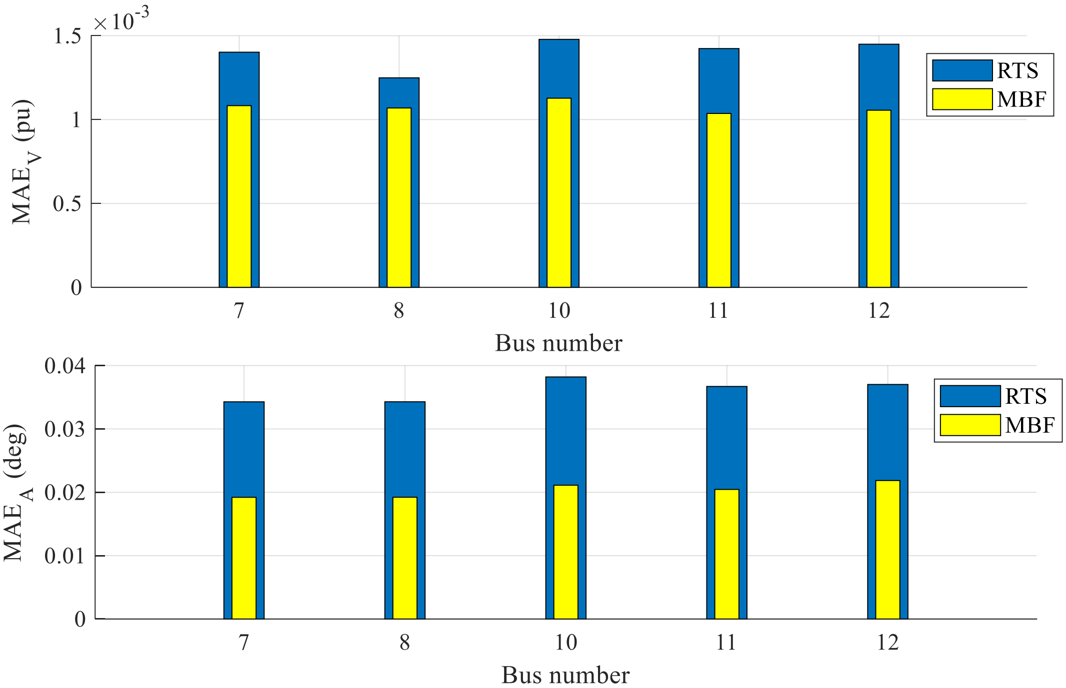

Figure 7.14: IEEE 14-bus system – MAE metrics of states unobservable by PMUs.

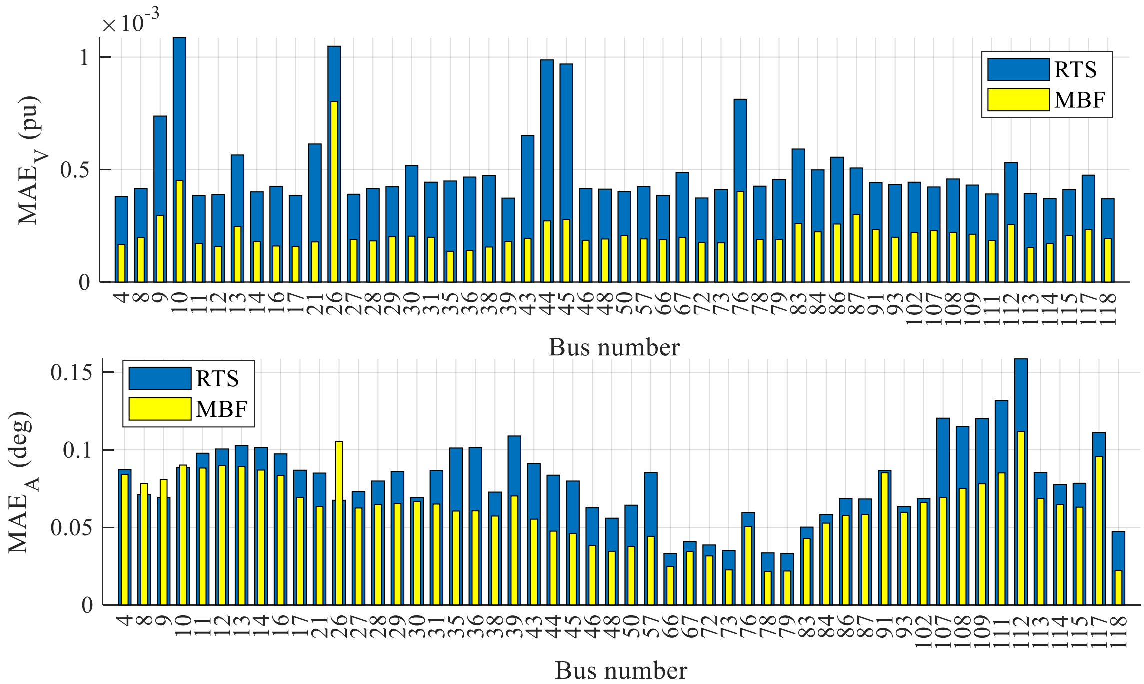

Figure 7.15: IEEE 118-bus system – MAE metrics of states unobservable by PMUs.

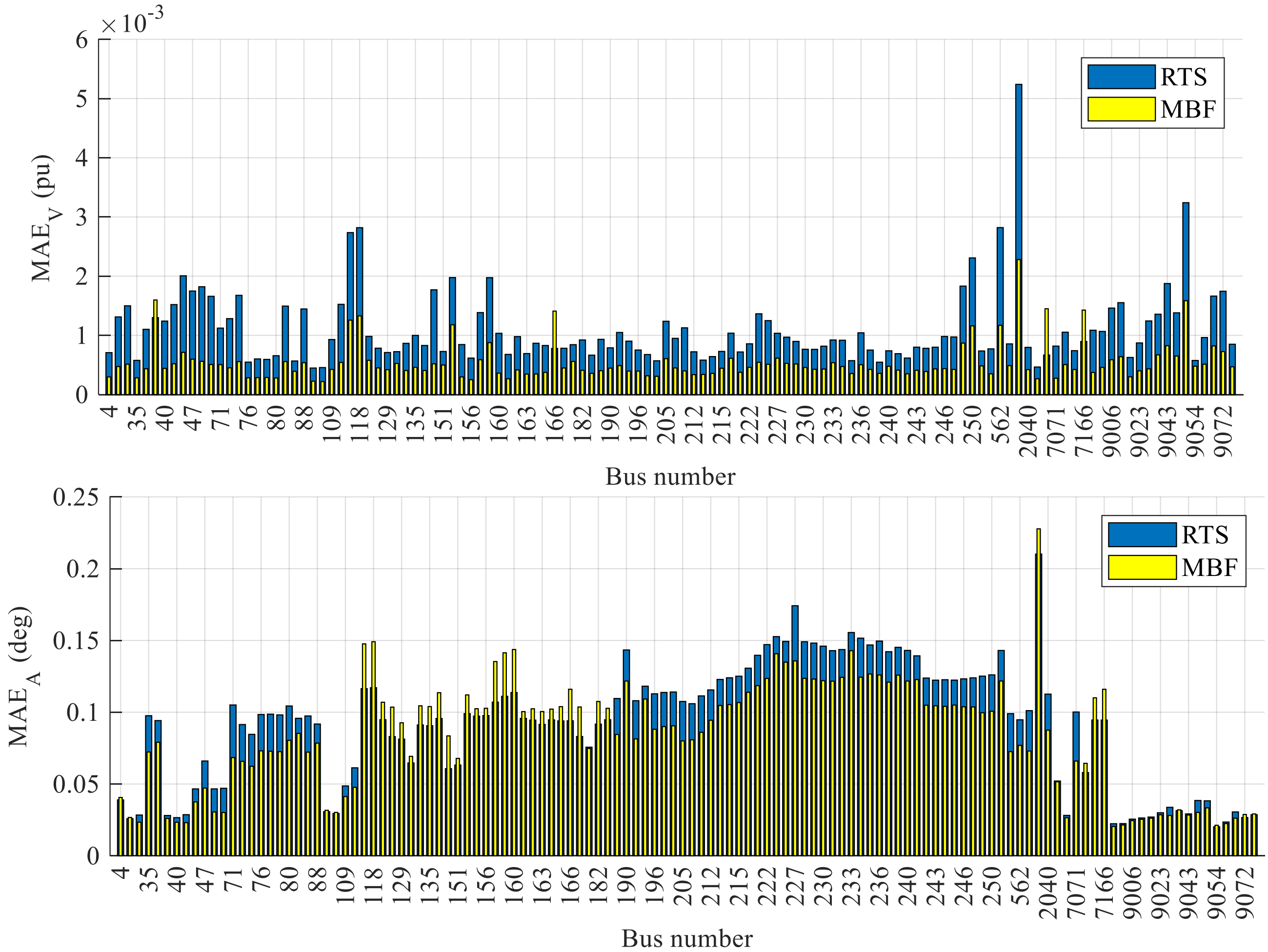

Figure 7.16: IEEE 300-bus system – MAE metrics of states unobservable by PMUs.

Finally, the performance of the three FASE methods in question is also tested under an abrupt disturbance of the quasi-steady system operating conditions. Figure 7.17 presents the $Macc_V$ metrics of the three methods for each test system, specifically focusing on the occurrence of a sudden generator outage at instant t_{100}, with respect to $T_R = 1, 2, ..., 20$. It is interesting to observe that the EKF exhibits significantly less reliable performance in comparison to the RTS and MBF methods, even for small values of T_R. It is also found that the smoothing-algorithm-based methods display similar trends in their $Macc_V$ values with respect to T_R; however, the MBF consistently delivers superior estimation accuracy over the RTS. This improved performance of the proposed method can be attributed to its enhanced prediction step, which effectively incorporates real-time measurements, thereby enabling a dynamic adjustment of the state transition model in response to evolving system conditions.

7.5 Summary

This Chapter presented a novel and practical EKF-based FASE framework designed to address the challenges of processing SCADA measurements with random delays and synchronized PMU data. The proposed framework leverages Hachtel's augmented matrix method to enhance the state estimation process without requiring modifications to the existing SCADA-based SE process. The HFASE stage integrates phasor data and *a priori* state information into the conventional SE via a non-iterative post-processing phase, while the linear PFASE stage utilizes synchrophasor data and state predictions between consecutive HFASE executions.

The framework adapts the conventional FASE state transition model using real-time information derived from the optimal fusion of PMU-based and forecasting-based state estimates. An additional backward correction step based on the MBF fixed-interval smoothing algorithm is incorporated into the EKF of both HFASE and PFASE formulations, mitigating errors caused by measurement time skew. Comprehensive numerical simulations on IEEE test systems validate the efficacy of the proposed method, demonstrating superior performance compared to other FASE approaches. Overall, the proposed framework offers a practical, scalable, and computationally efficient enhancement to conventional state estimation algorithms, addressing critical challenges posed by multi-source, multi-rate measurements in modern power systems.

This study lays the groundwork for future research to further improve the robustness and applicability of the framework. The integration of bad data detection and identification algorithms should be explored to further enhance the robustness of the framework. Additionally, investigating the application of the UKF as an alternative to the EKF could address the challenges posed by non-Gaussian measurement noise and enhance the framework's applicability to more complex system dynamics.

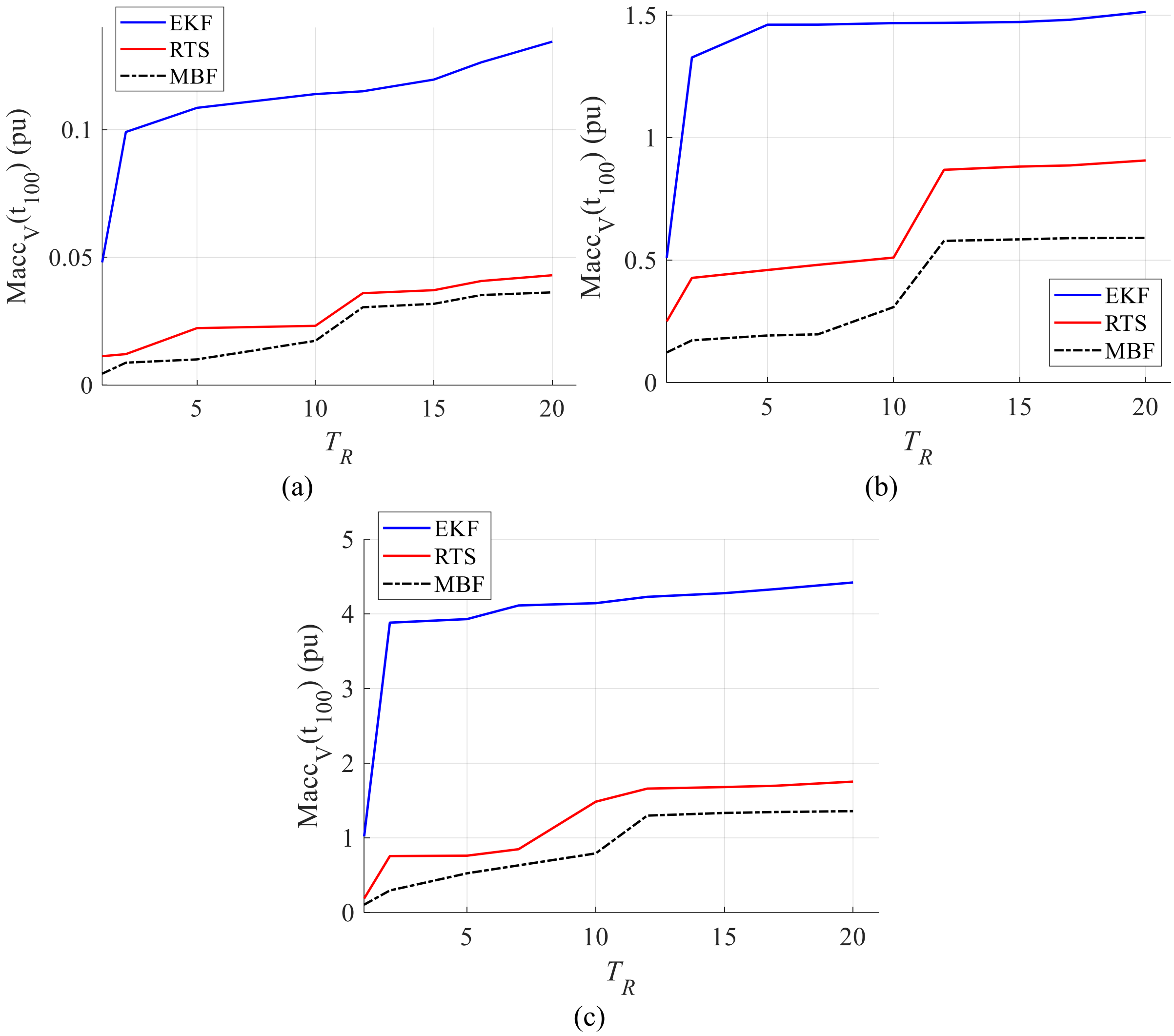

Figure 7.17: $Macc_V$ metrics of the EKF, RTS and MBF methods with generator outage at t_{100} for various values of T_R: (a) 14-bus system; (b) 118-bus system; (c) 300-bus system.

8. BAD DATA PROCESSING IN STATE ESTIMATION

Accurate state estimation relies on effectively detecting, identifying, and eliminating erroneous measurements. Measurement errors can stem from various sources, including:

- Random errors: caused by meter inaccuracies or communication noise, typically mitigated through redundancy in measurements.
- Systematic errors: biases, drifts, or incorrect meter connections can cause significant deviations. Telecommunication failures or interference may also corrupt data.
- Topology errors: incorrect network topology information can mislead the estimator, complicating error detection. These errors are handled by the network parameter estimation process, which is outside the scope of the thesis.

While some anomalies are easily detected through plausibility checks (e.g., negative voltage values or improbable bus current imbalances), others require advanced detection techniques. The WLS-based SE method, processes measurement residuals post-estimation to identify suspicious data based on their statistical properties.

Bad data can manifest in different ways, depending on the number, location, and relationships between erroneous measurements:

1) Single bad data: a single measurement exhibits a large error.
2) Multiple bad data: multiple measurements are erroneous, whose residuals can be strongly or weakly correlated. Strongly correlated measurements are those whose errors affect the estimated value of each other significantly, causing the valid one to also appear in error when the other contains a large error. Estimates of measurements with weakly correlated residuals are not significantly affected by the errors of each other. When measurement residuals are strongly correlated their errors may or may not be conforming. Conforming errors are those that appear consistent with each other. Multiple bad data can therefore occur in three distinct patterns:
   - Non-interacting: errors in weakly correlated measurements, where residuals remain largely independent.
   - Interacting, non-conforming: errors in strongly correlated measurements that appear inconsistent with one another.
   - Interacting and conforming: consistent gross errors in measurements with strongly correlated residuals.

The degree of interaction between measurement residuals, as determined by their sensitivity to measurement errors, provides valuable insights for error detection. In this Chapter, we will explore the techniques used in WLS-based SE to handle various forms of bad data, and develop bad data detection and identification algorithms appropriate for the hybrid SE methods proposed in Chapters 6 and 7.

8.1 Properties of measurement residuals

Let $\boldsymbol{x}$ and $\hat{\boldsymbol{x}}$ be the true and the estimated state vector, respectively, and $\delta\boldsymbol{x} := \boldsymbol{x} - \hat{\boldsymbol{x}}$. The measurement residuals can be expressed as follows:

$$\boldsymbol{r} := \boldsymbol{z} - \hat{\boldsymbol{z}} = \boldsymbol{z} - \boldsymbol{h}(\hat{\boldsymbol{x}}) \tag{8.1}$$

Expanding $\boldsymbol{h}(\boldsymbol{x})$ in a first-order Taylor series around $\hat{\boldsymbol{x}}$, yields:

$$\boldsymbol{h}(\boldsymbol{x}) = \boldsymbol{h}(\hat{\boldsymbol{x}}) + \boldsymbol{H}(\hat{\boldsymbol{x}})\delta\boldsymbol{x} \tag{8.2}$$

Substituting (8.2) into (8.1), yields:

$$\boldsymbol{r} = \boldsymbol{z} - \boldsymbol{h}(\boldsymbol{x}) + \boldsymbol{H}(\hat{\boldsymbol{x}})\delta\boldsymbol{x} = \boldsymbol{e} + \boldsymbol{H}(\hat{\boldsymbol{x}})\delta\boldsymbol{x} \tag{8.3}$$

Let us recall the solution of the NE, using the iterative scheme (4.70):

$$\boldsymbol{G}(\boldsymbol{x}^{(i)})\Delta\boldsymbol{x}^{(i)} = \boldsymbol{H}^T(\boldsymbol{x}^{(i)})\boldsymbol{R}^{-1}\left(\boldsymbol{z} - \boldsymbol{h}(\boldsymbol{x}^{(i)})\right) \tag{8.4}$$

which can be rewritten as:

$$\boldsymbol{G}(\boldsymbol{x})\left(-\delta\boldsymbol{x}\right) = \boldsymbol{H}^T(\boldsymbol{x})\boldsymbol{R}^{-1}\left(\boldsymbol{z} - \boldsymbol{h}(\boldsymbol{x})\right) \tag{8.5}$$

and, thus:

$$\delta\boldsymbol{x} = -\boldsymbol{G}^{-1}(\boldsymbol{x})\boldsymbol{H}^T(\boldsymbol{x})\boldsymbol{R}^{-1}\boldsymbol{e} \tag{8.6}$$

Using (8.6), eq. (8.3) yields:

$$\boldsymbol{r} = \left(\boldsymbol{I} - \boldsymbol{H}(\boldsymbol{x})\boldsymbol{G}^{-1}(\boldsymbol{x})\boldsymbol{H}^T(\boldsymbol{x})\boldsymbol{R}^{-1}\right)\boldsymbol{e} \tag{8.7}$$

Matrix $\boldsymbol{K} = \boldsymbol{H}\boldsymbol{G}^{-1}\boldsymbol{H}^T\boldsymbol{R}^{-1}$ is often called the *hat matrix*. A rough idea about the local measurement redundancy around a given meter can be obtained, by checking the corresponding row entries in matrix $\boldsymbol{K}$. A large diagonal entry relative to the off-diagonal elements in $\boldsymbol{K}$, will imply that the estimated value corresponding to that measurement is essentially determined by its measured value, i.e., the local redundancy is poor.

The measurement residuals can be expressed as follows:

$$\boldsymbol{r} = \left(\boldsymbol{I} - \boldsymbol{K}\right)\boldsymbol{e} = \boldsymbol{S}\boldsymbol{e} \tag{8.8}$$

Matrix $\boldsymbol{S}$ is the residual sensitivity matrix and represents the sensitivity of the measurement residuals to the measurement errors.

WLS estimation assumes that the measurement errors are distributed according to a Gaussian distribution given as below:

$$\boldsymbol{e} \sim \mathcal{N}\left(\boldsymbol{0}, \boldsymbol{R}\right) \tag{8.9}$$

Using the linear relation between the measurement residuals and errors given by (8.8), the mean and the covariance, and hence the probability distribution of the measurement residuals can be obtained as follows:

$$E(\boldsymbol{r}) = \boldsymbol{S}E(\boldsymbol{e}) = \boldsymbol{0} \tag{8.10}$$

$$Cov(\boldsymbol{r}) = \boldsymbol{\Omega} = E[\boldsymbol{r}\boldsymbol{r}^T] = \boldsymbol{S}\boldsymbol{R}\boldsymbol{S}^T = \boldsymbol{S}\boldsymbol{R} \tag{8.11}$$

Therefore:

$$\boldsymbol{r} \sim \mathcal{N}\left(\boldsymbol{0}, \boldsymbol{\Omega}\right) \tag{8.12}$$

The off-diagonal elements of the residual covariance matrix $\boldsymbol{\Omega}$ can be used to identify those strongly versus weakly interacting measurements.

8.2 Bad data detection and identification

Power systems include various types of measurements distributed across the network without a consistent topological pattern. The influence of each measurement on the state estimation depends not only on its value but also on its location. Measurements can be categorized as follows [38]:

- Critical measurement: A measurement whose removal renders the system unobservable. The corresponding column in the residual covariance matrix $\boldsymbol{\Omega}$ is identically zero, and its residual is always zero.

- Redundant measurement: A non-critical measurement. Only redundant measurements can exhibit nonzero residuals.
- Critical pair: A pair of redundant measurements whose simultaneous removal causes the system to become unobservable.
- Critical k-tuple: A set of k redundant measurements whose collective removal results in system unobservability. No subset of fewer than k measurements within this group is critical. The corresponding k columns in the residual covariance matrix $\mathbf{\Omega}$ are linearly dependent.

Bad data detection determines whether the MS contains erroneous data, while identification aims to locate the specific faulty measurements. The ability to detect and identify bad data depends on the measurement configuration within the system. Bad data can be detected only if removing the affected measurement does not make the system unobservable. Thus, bad data in critical measurements is inherently undetectable. A single bad measurement can be uniquely identified if:

1) It is not critical, and
2) it does not belong to a critical pair.

Bad data processing algorithms must account for these fundamental limitations. When the above conditions are met, single bad data can be detected and identified using the methods described in subsequent sections.

8.2.1 Bad data detection using the Chi-squares test

One common method for bad data detection is the Chi-squares or χ^2-test. Once bad data are successfully detected, they must be identified and either removed or corrected to ensure an unbiased state estimate.

Considering a set of k independent random variables $X_1, X_2, ..., X_k$ where each X_i is distributed according to the standard normal distribution:

$$X_i \sim \mathcal{N}(0,1) \tag{8.13}$$

The random variable Y defined as:

$$Y = \sum_{i=1}^{k} X_i^2 \tag{8.14}$$

will follow a χ^2 distribution with k degrees of freedom, i.e.

$$Y \sim \chi_k^2 \tag{8.15}$$

The degrees of freedom k represent the number of independent variables in the sum of squares. This value will decrease if any of the X_i variables form a linearly dependent subset.

Now, let us consider the function $f(\boldsymbol{x})$ written in terms of the measurement errors:

$$f(\boldsymbol{x}) := \sum_{i=1}^{m} R_{ii}^{-1} e_i^2 = \sum_{i=1}^{m} \left(\frac{e_i}{\sqrt{R_{ii}}} \right)^2 = \sum_{i=1}^{m} (e_i^N)^2 \tag{8.16}$$

where e_i is the i-th measurement error, R_{ii} is the diagonal entry of the measurement error covariance matrix and m is the number of measurements. Variables e_i^N follow the standard normal distribution:

$$e_i^N \sim \mathcal{N}(0,1) \tag{8.17}$$

In a power system, since at least n measurements will have to satisfy the power balance equations, at most $m-n$ of the measurement errors will be linearly independent. Thus, $f(\boldsymbol{x})$ will follow a χ^2 distribution with $k = m-n$ degrees of freedom (df).

A plot of the χ^2-probability density function (pdf) is shown in Figure 8.1. The area under the pdf represents the probability of finding X in the corresponding region, for example:

$$\Pr\{X \geq x_t\} = \int_{x_t}^{\infty} \chi^2(u)du \tag{8.18}$$

represents the probability of X being larger than a certain threshold x_t. This probability decreases with increasing values of x_t, due to the decaying tail of the distribution. Choosing a confidence of p, the threshold x_t can be set such that:

$$\Pr\{X \geq x_t\} = 1 - p \tag{8.19}$$

The threshold $x_t = \chi^2_{m-n,p}$ represents the largest acceptable value for X that will not imply any bad data. If the measured value of X exceeds this threshold, then with probability p, the measured X will not have a χ^2 distribution, i.e., presence of bad data will be suspected.

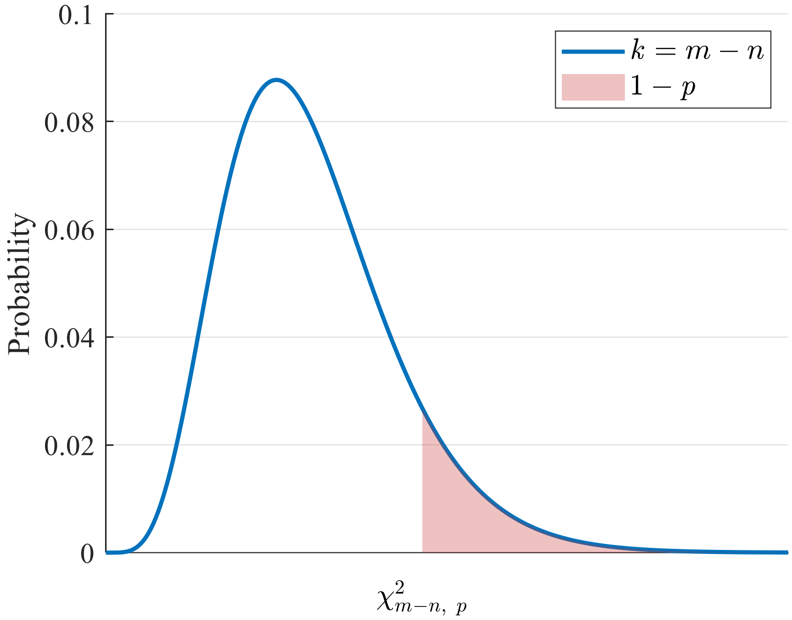

Figure 8.1: Chi-squared probability density function.

A bad data detection test, referred to as the Chi-squares test, can be devised based on the properties of the χ^2 distribution, as follows:

1) Solve the WLS estimation problem and compute the objective function:

$$J(\hat{\mathbf{x}}) = \sum_{i=1}^{m} \frac{[z_i - h_i(\hat{\mathbf{x}})]^2}{\sigma_i^2}$$

2) Look up the value from the Chi-squares distribution table corresponding to a detection confidence with probability p (e.g., 95%) and $k = m - n$ degrees of freedom. This value is the threshold $x_t = \chi^2_{m-n,p}$, such that $p = \Pr\{J(\hat{\mathbf{x}}) \leq \chi^2_{m-n,p}\}$.
3) Check if $J(\hat{\mathbf{x}}) \geq \chi^2_{m-n,p}$. If yes, then bad data is suspected, else the MS is assumed free of bad data.

8.2.2 *Bad data detection using normalized residuals*

The approximation of measurement errors by residuals in (8.16) may result in the Chi-squares test failing to detect certain bad data cases. A more accurate approach involves the use of normalized residuals, where the residual of measurement z_i is divided by the square root of the corresponding diagonal element of the residual covariance matrix:

$$r_i^N := \frac{|r_i|}{\sqrt{\Omega_{ii}}} = \frac{|r_i|}{\sqrt{R_{ii}S_{ii}}} \tag{8.20}$$

The normalized residual vector $\boldsymbol{r}^N$ will then have a standard normal distribution:

$$r_i^N \sim \mathcal{N}(0,1) \tag{8.21}$$

The largest normalized residual can be compared against a statistical threshold to determine the presence of bad data. This threshold is selected based on the desired detection sensitivity. If a single bad data point exists in the MS – and it is neither critical nor part of a critical pair – the largest normalized residual will correspond to the erroneous measurement. This property can also hold in some multiple bad data scenarios, particularly when the problematic measurements are weakly correlated, i.e., non-interacting. Using (8.8) it can be proven that the normalized residual for the erroneous measurement k is expected to be the largest among all residuals from error-free measurements, i.e.:

$$r_j^N \le r_k^N,\ j = 1,2,\ldots,m \tag{8.22}$$

The inequality becomes a strict equality when measurements j and k form a critical pair, as their corresponding columns in the residual sensitivity matrix $\boldsymbol{\Omega}$ are linearly dependent. In such cases, the normalized residuals are always equal, making it impossible to identify which measurement is erroneous, even though bad data can still be detected. The same limitation applies to any subset of $k-1$ measurements within a critical k-tuple: errors can be detected but not uniquely identified.

8.2.3 Bad data identification using the Largest Normalized Residual Test

Upon detection of bad data in the MS, their identification can be accomplished by further processing of the residuals. The characteristics of normalized residuals in the presence of a single bad measurement can be used to design a detection and elimination test known as the Largest Normalized Residual Test (LNRT) or $r_{\max}^N$-test. The procedure involves the following steps:

1) Solve the WLS estimation and obtain the elements of the measurement residual vector:

$$r_i = z_i - h_i(\hat{\boldsymbol{x}}),\ i = 1,2,\ldots,m$$

2) Compute the normalized residuals:

$$r_i^N := \frac{|r_i|}{\sqrt{\Omega_{ii}}},\ i = 1,2,\ldots,m$$

3) Find k such that r_k^N is the largest among all $r_i^N,\ i = 1,2,\ldots,m$.
4) If $r_k^N > c$, then the k-th measurement will be suspected as bad data. Else, stop, no bad data will be suspected. Here, c is a chosen identification threshold, for instance 3.0.
5) Eliminate the k-th measurement from the MS and go to step 1.

Implementing the LNRT may require multiple identification and elimination cycles. Each cycle includes two computationally intensive steps:

- Compute normalized residuals using the diagonal elements of the residual covariance matrix $\boldsymbol{\Omega} = \boldsymbol{SR} = \boldsymbol{R} - \boldsymbol{HG}^{-1}\boldsymbol{H}^T$. Note that only the diagonal entries of $\boldsymbol{\Omega}$ are required, which can be efficiently calculated by exploiting the already calculated Cholesky factorization of matrix $\boldsymbol{G}$ and the sparse structure of $\boldsymbol{H}$.

- Suppress the measurement with the largest normalized residual, then repeat the state estimation process. Instead of actually removing the bad measurement, its estimated error can be subtracted to correct it, as described below. The measurement corrupted with large error can be written as:

$$z_i^{bad} = z_i + e_i$$

where z_i^{bad} is the measured value, z_i is the true value and e_i is the gross error associated with the i-th measurement. Using the linearized residual sensitivity relation of (8.8), the residual of the bad measurement and the corresponding error can be approximated by:

$$r_i^{bad} = z_i^{bad} - h_i(\hat{x}) \simeq S_{ii} e_i \Rightarrow e_i \simeq \frac{R_{ii}}{\Omega_{ii}} r_i^{bad}$$

Subtracting the error e_i from the bad measurement yields:

$$z_i \simeq z_i^{bad} - \frac{R_{ii}}{\Omega_{ii}} r_i^{bad} \tag{8.23}$$

State estimation can be repeated after correcting the bad measurement. This yields an approximate state estimate comparable to that obtained by removing the measurement entirely. However, when the linear residual sensitivity model fails to capture the impact of large errors, the approximation may be inaccurate. In such cases, iterative correction is necessary to reduce the residual error.

It should also be noted that the performance of the LNRT depends on the type and configuration of bad data. Its behavior under different scenarios is summarized below:

- Single bad data: The LNRT reliably identifies the erroneous measurement, provided it is not critical and its removal does not introduce new critical measurements.
- Multiple bad data:
  1) Non-interacting: If $S_{ik} \simeq 0$, measurements *i* and *k* are non-interacting. In this case, even with gross errors appearing simultaneously in both measurements, the LNRT can identify the bad data sequentially, one at a time.
  2) Interacting, non-conforming: If S_{ik} is large, then measurements *i* and *k* are interacting. However, if their errors are inconsistent, the LNRT may still correctly identify the bad data.
  3) Interacting, conforming: When interacting measurements have consistent (conforming) errors, the LNRT may fail to identify either measurement as bad.

8.3 Bad data handling in ISE and PSE methods

In this Section, the process of bad data analysis will be explicitly formulated for the HSE methods proposed in Section 6.2. For all SE implementations, the measurement residual vector can be defined as:

$$\boldsymbol{r} = \begin{bmatrix} \boldsymbol{r}_s \\ \boldsymbol{r}_p \end{bmatrix} = \begin{bmatrix} \boldsymbol{z}_s - \boldsymbol{h}_s(\hat{\boldsymbol{x}}) \\ \boldsymbol{z}_p - \boldsymbol{h}_p(\hat{\boldsymbol{x}}) \end{bmatrix} \tag{8.24}$$

and the vector of normalized residuals is given by:

$$\boldsymbol{r}^N = \frac{|\boldsymbol{r}|}{\sqrt{diag(\boldsymbol{\Omega})}} \tag{8.25}$$

8.3.1 Bad data analysis for the ISE algorithm

Denoting the true and the estimated state vectors by $\boldsymbol{x}$ and $\hat{\boldsymbol{x}}$ respectively, we define $\boldsymbol{\delta x} = \boldsymbol{x} - \hat{\boldsymbol{x}}$.

The measurement function $\boldsymbol{h}(\boldsymbol{x})$ can be expressed as a function of $\boldsymbol{\delta x}$ by expanding $\boldsymbol{h}(\boldsymbol{x})$ in a first-order Taylor series around $\hat{\boldsymbol{x}}$:

$$\boldsymbol{h}(\boldsymbol{x}) = \begin{bmatrix} \boldsymbol{h}_s(\boldsymbol{x}) \\ \boldsymbol{h}_p(\boldsymbol{x}) \end{bmatrix} = \begin{bmatrix} \boldsymbol{h}_s(\hat{\boldsymbol{x}}) \\ \boldsymbol{h}_p(\hat{\boldsymbol{x}}) \end{bmatrix} + \begin{bmatrix} \boldsymbol{H}_s(\hat{\boldsymbol{x}}) \\ \boldsymbol{H}_p(\hat{\boldsymbol{x}}) \end{bmatrix} \boldsymbol{\delta x} \tag{8.26}$$

The error vector $\boldsymbol{e}$ can be partitioned as follows:

$$\boldsymbol{e} = \begin{bmatrix} \boldsymbol{e}_s \\ \boldsymbol{e}_p \end{bmatrix} = \begin{bmatrix} \boldsymbol{z}_s - \boldsymbol{h}_s(\boldsymbol{x}) \\ \boldsymbol{z}_p - \boldsymbol{h}_p(\boldsymbol{x}) \end{bmatrix} \tag{8.27}$$

Substituting (8.26) for $\begin{bmatrix} \boldsymbol{h}_s(\hat{\boldsymbol{x}}) \\ \boldsymbol{h}_p(\hat{\boldsymbol{x}}) \end{bmatrix}$ in (8.24) yields:

$$\boldsymbol{r} = \begin{bmatrix} \boldsymbol{r}_s \\ \boldsymbol{r}_p \end{bmatrix} \simeq \begin{bmatrix} \boldsymbol{z}_s - \boldsymbol{h}_s(\boldsymbol{x}) + \boldsymbol{H}_s(\hat{\boldsymbol{x}})\boldsymbol{\delta x} \\ \boldsymbol{z}_p - \boldsymbol{h}_p(\boldsymbol{x}) + \boldsymbol{H}_p(\hat{\boldsymbol{x}})\boldsymbol{\delta x} \end{bmatrix} = \begin{bmatrix} \boldsymbol{e}_s + \boldsymbol{H}_s(\hat{\boldsymbol{x}})\boldsymbol{\delta x} \\ \boldsymbol{e}_p + \boldsymbol{H}_p(\hat{\boldsymbol{x}})\boldsymbol{\delta x} \end{bmatrix} \tag{8.28}$$

Using the iterative Gauss-Newton method, the following system of linear equations is to be solved at each iteration (i):

$$\begin{bmatrix} a\boldsymbol{G}_s(\boldsymbol{x}^{(i)}) & \boldsymbol{C}^T(\boldsymbol{x}^{(i)}) & \boldsymbol{H}_p^T(\boldsymbol{x}^{(i)}) \\ \boldsymbol{C}(\boldsymbol{x}^{(i)}) & \boldsymbol{0} & \boldsymbol{0} \\ \boldsymbol{H}_p(\boldsymbol{x}^{(i)}) & \boldsymbol{0} & -a^{-1}\boldsymbol{R}_p \end{bmatrix} \begin{bmatrix} \Delta\boldsymbol{x}^{(i+1)} \\ \boldsymbol{\lambda}^{(i+1)} \\ \boldsymbol{\mu}^{(i+1)} \end{bmatrix} = \begin{bmatrix} a\boldsymbol{H}_s^T(\boldsymbol{x}^{(i)})\boldsymbol{R}_s^{-1}\Delta\boldsymbol{z}_s^{(i)} \\ -\boldsymbol{c}(\boldsymbol{x}^{(i)}) \\ \Delta\boldsymbol{z}_p^{(i)} \end{bmatrix} \tag{8.29}$$

It has already been proven in Section 6.2 that the above expression is equivalent to:

$$\begin{bmatrix} -\boldsymbol{\delta x} \\ \boldsymbol{\lambda} \end{bmatrix} = \begin{bmatrix} -\boldsymbol{\delta y} \\ \boldsymbol{\lambda}_y \end{bmatrix} + \begin{bmatrix} -\boldsymbol{\delta u} \\ \boldsymbol{\lambda}_u \end{bmatrix} \tag{8.30}$$

$$\begin{bmatrix} -\boldsymbol{\delta y} \\ \boldsymbol{\lambda}_y \end{bmatrix} = \begin{bmatrix} a\boldsymbol{G}_s & \boldsymbol{C}^T \\ \boldsymbol{C} & \boldsymbol{0} \end{bmatrix}^{-1} \begin{bmatrix} a\boldsymbol{H}_s^T\boldsymbol{R}_s^{-1}\boldsymbol{e}_s \\ \boldsymbol{0} \end{bmatrix} = \begin{bmatrix} \boldsymbol{E}_1 & \boldsymbol{E}_2^T \\ \boldsymbol{E}_2 & \boldsymbol{E}_3 \end{bmatrix} \begin{bmatrix} a\boldsymbol{H}_s^T\boldsymbol{R}_s^{-1}\boldsymbol{e}_s \\ \boldsymbol{0} \end{bmatrix} \tag{8.31}$$

$$\begin{bmatrix} -\boldsymbol{\delta u} \\ \boldsymbol{\lambda}_u \end{bmatrix} = \boldsymbol{G}_{sz}^{-1}\boldsymbol{H}_{pz}^T \left(a^{-1}\boldsymbol{R}_p + \boldsymbol{H}_{pz}\boldsymbol{G}_{sz}^{-1}\boldsymbol{H}_{pz}^T \right)^{-1} \left(\boldsymbol{e}_p + \boldsymbol{H}_p\boldsymbol{\delta y} \right) \tag{8.32}$$

where $\boldsymbol{\delta y} = \boldsymbol{y} - \hat{\boldsymbol{y}}$, and $\boldsymbol{\delta u} = \boldsymbol{u} - \hat{\boldsymbol{u}}$.
According to [226], (8.31) yields:

$$-\boldsymbol{\delta y} = a\boldsymbol{E}_1\boldsymbol{H}_s^T\boldsymbol{R}_s^{-1}\boldsymbol{e}_s \tag{8.33}$$

Observing that:

$$\boldsymbol{G}_{sz}^{-1}\boldsymbol{H}_{pz}^T = \begin{bmatrix} \boldsymbol{E}_1 & \boldsymbol{E}_2^T \\ \boldsymbol{E}_2 & \boldsymbol{E}_3 \end{bmatrix} \begin{bmatrix} \boldsymbol{H}_p^T \\ \boldsymbol{0} \end{bmatrix} = \begin{bmatrix} \boldsymbol{E}_1\boldsymbol{H}_p^T \\ \boldsymbol{E}_2\boldsymbol{H}_p^T \end{bmatrix} \tag{8.34}$$

$$\boldsymbol{H}_{pz}\boldsymbol{G}_{sz}^{-1}\boldsymbol{H}_{pz}^T = \boldsymbol{H}_p\boldsymbol{E}_1\boldsymbol{H}_p^T \tag{8.35}$$

we obtain:

$$-\boldsymbol{\delta u} = \boldsymbol{E}_1\boldsymbol{H}_p^T \left(a^{-1}\boldsymbol{R}_p + \boldsymbol{H}_p\boldsymbol{E}_1\boldsymbol{H}_p^T \right)^{-1} \left(\boldsymbol{e}_p + \boldsymbol{H}_p\boldsymbol{\delta y} \right) \tag{8.36}$$

Substituting (8.33) into (8.36) gives:

$$-\boldsymbol{\delta u} = \boldsymbol{E}_1\boldsymbol{H}_p^T\left(a^{-1}\boldsymbol{R}_p + \boldsymbol{H}_p\boldsymbol{E}_1\boldsymbol{H}_p^T\right)^{-1}\left(\boldsymbol{e}_p - a\boldsymbol{H}_p\boldsymbol{E}_1\boldsymbol{H}_s^T\boldsymbol{R}_s^{-1}\boldsymbol{e}_s\right) \tag{8.37}$$

Given that $-\boldsymbol{\delta x} = -\boldsymbol{\delta y} - \boldsymbol{\delta u}$:

$$\boldsymbol{\delta x} = -a\left(\boldsymbol{E}_1 - \boldsymbol{E}_1\boldsymbol{H}_p^T\left(a^{-1}\boldsymbol{R}_p + \boldsymbol{H}_p\boldsymbol{E}_1\boldsymbol{H}_p^T\right)^{-1}\boldsymbol{H}_p\boldsymbol{E}_1\right)\boldsymbol{H}_s^T\boldsymbol{R}_s^{-1}\boldsymbol{e}_s - \boldsymbol{E}_1\boldsymbol{H}_p^T\left(a^{-1}\boldsymbol{R}_p + \boldsymbol{H}_p\boldsymbol{E}_1\boldsymbol{H}_p^T\right)^{-1}\boldsymbol{e}_p \tag{8.38}$$

Setting:

$$\boldsymbol{A}_1 = a\left(\boldsymbol{E}_1 - \boldsymbol{E}_1\boldsymbol{H}_p^T\left(a^{-1}\boldsymbol{R}_p + \boldsymbol{H}_p\boldsymbol{E}_1\boldsymbol{H}_p^T\right)^{-1}\boldsymbol{H}_p\boldsymbol{E}_1\right) \text{ and } \boldsymbol{A}_2 = \boldsymbol{E}_1\boldsymbol{H}_p^T\left(a^{-1}\boldsymbol{R}_p + \boldsymbol{H}_p\boldsymbol{E}_1\boldsymbol{H}_p^T\right)^{-1},$$

equation (8.38) becomes:

$$\boldsymbol{\delta x} = -\boldsymbol{A}_1\boldsymbol{H}_s^T\boldsymbol{R}_s^{-1}\boldsymbol{e}_s - \boldsymbol{A}_2\boldsymbol{e}_p \tag{8.39}$$

Substituting (8.39) into (8.28) yields:

$$\begin{bmatrix}\boldsymbol{r}_s\\ \boldsymbol{r}_p\end{bmatrix} \simeq \begin{bmatrix}\boldsymbol{e}_s - \boldsymbol{H}_s\left(\boldsymbol{A}_1\boldsymbol{H}_s^T\boldsymbol{R}_s^{-1}\boldsymbol{e}_s + \boldsymbol{A}_2\boldsymbol{e}_p\right)\\ \boldsymbol{e}_p - \boldsymbol{H}_p\left(\boldsymbol{A}_1\boldsymbol{H}_s^T\boldsymbol{R}_s^{-1}\boldsymbol{e}_s + \boldsymbol{A}_2\boldsymbol{e}_p\right)\end{bmatrix} = \begin{bmatrix}\boldsymbol{I} - \boldsymbol{H}_s\boldsymbol{A}_1\boldsymbol{H}_s^T\boldsymbol{R}_s^{-1} & -\boldsymbol{H}_s\boldsymbol{A}_2\\ -\boldsymbol{H}_p\boldsymbol{A}_1\boldsymbol{H}_s^T\boldsymbol{R}_s^{-1} & \boldsymbol{I} - \boldsymbol{H}_p\boldsymbol{A}_2\end{bmatrix}\begin{bmatrix}\boldsymbol{e}_s\\ \boldsymbol{e}_p\end{bmatrix} \tag{8.40}$$

Given that $\boldsymbol{r} = \boldsymbol{S}\boldsymbol{e}$ it is obvious that:

$$\boldsymbol{S} = \begin{bmatrix}\boldsymbol{I} - \boldsymbol{H}_s\boldsymbol{A}_1\boldsymbol{H}_s^T\boldsymbol{R}_s^{-1} & -\boldsymbol{H}_s\boldsymbol{A}_2\\ -\boldsymbol{H}_p\boldsymbol{A}_1\boldsymbol{H}_s^T\boldsymbol{R}_s^{-1} & \boldsymbol{I} - \boldsymbol{H}_p\boldsymbol{A}_2\end{bmatrix} \tag{8.41}$$

and thus:

$$\boldsymbol{\Omega} = Cov(\boldsymbol{r}) = \boldsymbol{S}\boldsymbol{R} = \begin{bmatrix}\boldsymbol{R}_s - \boldsymbol{H}_s\boldsymbol{A}_1\boldsymbol{H}_s^T & -\boldsymbol{H}_s\boldsymbol{A}_2\boldsymbol{R}_p\\ -\boldsymbol{H}_p\boldsymbol{A}_1\boldsymbol{H}_s^T & \left(\boldsymbol{I} - \boldsymbol{H}_p\boldsymbol{A}_2\right)\boldsymbol{R}_p\end{bmatrix} \tag{8.42}$$

with $\boldsymbol{R} = \begin{bmatrix}\boldsymbol{R}_s & \boldsymbol{0}\\ \boldsymbol{0} & \boldsymbol{R}_p\end{bmatrix}$.

The complete bad data detection, identification and removal process for the proposed ISE method is presented in Algorithm 8.1.

8.3.2 Bad data analysis for the PSE method

For the PSE method of Subsection 6.2.2, the bad data detection and identification process can be split into two distinct stages. For the 1st estimation stage, the classic bad data detection method for equality-constrained WLS-based SE [226] is implemented. For the 2nd estimation stage, using (8.36) we obtain:

$$-\boldsymbol{\delta u} = \boldsymbol{E}_1\boldsymbol{H}_p^T\left(a^{-1}\boldsymbol{R}_p + \boldsymbol{H}_p\boldsymbol{E}_1\boldsymbol{H}_p^T\right)^{-1}\left(\boldsymbol{e}_p + \boldsymbol{H}_p\boldsymbol{\delta y}\right) \tag{8.43}$$

Given that $\boldsymbol{\delta y} = \boldsymbol{y} - \hat{\boldsymbol{y}} = \boldsymbol{0}$, (8.43) becomes:

$$-\boldsymbol{\delta u} = \boldsymbol{E}_1\boldsymbol{H}_p^T\left(a^{-1}\boldsymbol{R}_p + \boldsymbol{H}_p\boldsymbol{E}_1\boldsymbol{H}_p^T\right)^{-1}\boldsymbol{e}_p \tag{8.44}$$

and the measurement residual vector is given by:

$$\boldsymbol{r}_p \simeq \boldsymbol{e}_p + \boldsymbol{H}_p \boldsymbol{\delta x} \underset{\boldsymbol{\delta y}=\boldsymbol{0}}{\overset{\boldsymbol{\delta x}=\boldsymbol{\delta y}+\boldsymbol{\delta u}}{=}} \boldsymbol{e}_p - \boldsymbol{H}_p \boldsymbol{E}_1 \boldsymbol{H}_p^T \left(a^{-1}\boldsymbol{R}_p + \boldsymbol{H}_p \boldsymbol{E}_1 \boldsymbol{H}_p^T\right)^{-1} \boldsymbol{e}_p$$
$$= \left(\boldsymbol{I} - \boldsymbol{H}_p \boldsymbol{E}_1 \boldsymbol{H}_p^T \left(a^{-1}\boldsymbol{R}_p + \boldsymbol{H}_p \boldsymbol{E}_1 \boldsymbol{H}_p^T\right)^{-1}\right) \boldsymbol{e}_p = \boldsymbol{S}_p \boldsymbol{e}_p \tag{8.45}$$

Therefore, we have:

$$\boldsymbol{\Omega}_p = Cov(\boldsymbol{r}_p) = \boldsymbol{S}_p \boldsymbol{R}_p = \left(\boldsymbol{I} - \boldsymbol{H}_p \boldsymbol{E}_1 \boldsymbol{H}_p^T \left(a^{-1}\boldsymbol{R}_p + \boldsymbol{H}_p \boldsymbol{E}_1 \boldsymbol{H}_p^T\right)^{-1}\right) \boldsymbol{R}_p \tag{8.46}$$

The complete bad data detection, identification and removal process for the proposed PSE method is presented in Algorithm 8.2.

Algorithm 8.1: Bad data analysis for the proposed ISE algorithm.

1) Solve the WLS estimation problem and compute the objective function $J(\hat{\boldsymbol{x}}) = \sum_{i=1}^{m} \frac{[z_i - h_i(\hat{\boldsymbol{x}})]^2}{\sigma_i^2}$

2) Obtain threshold value $x_t = \chi^2_{m-n,p}$ corresponding to a detection confidence with probability p (> 99%) and $k = m - n$ degrees of freedom, such that $p = \Pr\{J(\hat{\boldsymbol{x}}) \le \chi^2_{m-n,p}\}$.

3) Check if $J(\hat{\boldsymbol{x}}) \ge \chi^2_{m-n,p}$. **If** yes, then bad data is suspected, **else** the MS is assumed free of bad data, and the algorithm terminates.

4) **If** there are suspect measurements:

- **a.** Obtain the elements of the measurement residual vector: $\boldsymbol{r} = \begin{bmatrix} \boldsymbol{r}_s \\ \boldsymbol{r}_p \end{bmatrix} = \begin{bmatrix} \boldsymbol{z}_s - \boldsymbol{h}_s(\hat{\boldsymbol{x}}) \\ \boldsymbol{z}_p - \boldsymbol{h}_p(\hat{\boldsymbol{x}}) \end{bmatrix}$
- **b.** Calculate $\boldsymbol{A}_1$, $\boldsymbol{A}_2$, and the diagonal elements of $\boldsymbol{\Omega}$ from (8.42).
- **c.** Compute the normalized residuals: $\boldsymbol{r}^N = \frac{|\boldsymbol{r}|}{\sqrt{diag(\boldsymbol{\Omega})}}$.
- **d.** Find k such that r_k^N is the largest among all r_i^N, $i = 1, 2, ..., m$. **If** $r_k^N > 3$, then the k-th measurement will be flagged as bad data.
- **e.** Attempt to correct the k-th measurement: $z_k \leftarrow z_k^{bad} - \frac{R_{kk}}{\Omega_{kk}} r_k$ and go to Step 1.

8.4 Bad data handling in the proposed FASE method

When state forecasting schemes are implemented in SE, one can use the forecasted state variables to calculate the forecasted measurements and use innovation analysis to determine if the measurement dataset contains erroneous information, before the forward correction step [227]. The innovation vector is given by:

$$\boldsymbol{v}_{k+1} = \boldsymbol{z}_{k+1} - \tilde{\boldsymbol{z}}_{k+1} = \boldsymbol{z}_{k+1} - \boldsymbol{h}(\tilde{\boldsymbol{x}}_{k+1}) \tag{8.47}$$

Note that $\boldsymbol{v}_{k+1}$ is approximately a white Gaussian process with zero mean and covariance matrix:

$$\boldsymbol{N}_{k+1} := Cov(\boldsymbol{v}_{k+1}) = \boldsymbol{R}_{k+1} + \boldsymbol{H}_{k+1} \tilde{\boldsymbol{P}}_{k+1} \boldsymbol{H}_{k+1}^T \tag{8.48}$$

At time step (k+1), the i-th component of the normalized innovation vector is calculated as:

$$v^N(i) := \frac{|v(i)|}{\sqrt{N(i,i)}}, \ i = 1,2,\ldots,m \tag{8.49}$$

and is tested against an adopted anomaly detection threshold c, which for the Gaussian distribution is set to 3.

Algorithm 8.2: Bad data analysis for the proposed PSE algorithm.

1) Stage 1: SCADA-based equality-constrained WLS estimation problem

a. Solve the WLS SE and compute the objective function $J_s(\hat{\boldsymbol{y}}) = \sum_{i=1}^{m_s} \frac{[z_{s,i} - h_{s,i}(\hat{\boldsymbol{y}})]^2}{\sigma_i^2}$

b. Obtain threshold value $x_t = \chi^2_{m_s-n,p}$ corresponding to a detection confidence with probability p (> 99%) and $k = m_s - n$ degrees of freedom, such that $p = \Pr\{J(\hat{\boldsymbol{y}}) \le \chi^2_{m_s-n,p}\}$.

c. Check if $J(\hat{\boldsymbol{y}}) \ge \chi^2_{m_s-n,p}$. **If** yes, then bad data is suspected, **else** the MS is assumed free of bad data, and the algorithm terminates.

d. If there are suspect measurements:

i) Obtain the elements of the measurement residual vector: $\boldsymbol{r}_s = \boldsymbol{z}_s - \boldsymbol{h}_s(\hat{\boldsymbol{y}})$.

ii) Calculate the diagonal elements of $\boldsymbol{\Omega}_s := Cov(\boldsymbol{r}_s) = \boldsymbol{R}_s - \boldsymbol{H}_s\boldsymbol{E}_1\boldsymbol{H}_s^T$.

iii) Compute the normalized residuals: $\boldsymbol{r}_s^N = \frac{|\boldsymbol{r}_s|}{\sqrt{diag(\boldsymbol{\Omega}_s)}}$.

iv) Find k such that $r_{s,k}^N$ is the largest among all $r_{s,i}^N$, $i = 1,2,\ldots,m_s$. **If** $r_{s,k}^N > 3$, then the k-th measurement will be flagged as bad data.

v) Attempt to correct the k-th measurement: $z_{s,k} \leftarrow z_{s,k}^{bad} - \frac{R_{s,kk}}{\Omega_{s,kk}} r_{s,k}$ and go to Step a.

2) Stage 2: PMU-based correction

a. Calculate the measurement residual vector: $\boldsymbol{r}_p = \boldsymbol{z}_p - \boldsymbol{h}_p(\hat{\boldsymbol{x}})$

b. Calculate the diagonal elements of $\boldsymbol{\Omega}_p = \left(\boldsymbol{I} - \boldsymbol{H}_p\boldsymbol{E}_1\boldsymbol{H}_p^T\left(a^{-1}\boldsymbol{R}_p + \boldsymbol{H}_p\boldsymbol{E}_1\boldsymbol{H}_p^T\right)^{-1}\right)\boldsymbol{R}_p$.

c. Compute the normalized residuals: $\boldsymbol{r}_p^N = \frac{|\boldsymbol{r}_p|}{\sqrt{diag(\boldsymbol{\Omega}_p)}}$.

d. Find k such that $r_{p,k}^N$ is the largest among all $r_{p,i}^N$, $i = 1,2,\ldots,m_p$. **If** $r_{p,k}^N > 3$, then the k-th measurement will be flagged as bad data. **Else**, the PMU measurements are free of bad data, and the algorithm terminates.

e. Attempt to correct the k-th measurement: $z_{p,k} \leftarrow z_{p,k}^{bad} - \frac{R_{p,kk}}{\Omega_{p,kk}} r_{p,k}$ and go to Step a.

Innovation analysis thus provides an *a priori* assessment of measurement quality. If the normalized innovation of a measurement is below a given threshold c, the measurement is considered consistent and its quality flag is set to 1. Otherwise (i.e., if the $\boldsymbol{v}^N$-test is positive), the measurement is marked as suspicious, with quality flag set to 0. In the context of the proposed FASE method (Section 7.2), innovation analysis can be applied to both SCADA and PMU data, though it is particularly useful for SCADA measurements, as they are affected by time skewness and are forecasted using only the conventional Holt's transition model, without incorporating additional real-time information. Conversely, the prediction step for PMU-observable states combines forecast and real-time data, mitigating the effect of inaccurate forecasts or erroneous PMU readings.

If no anomaly is detected, the forward correction step proceeds as described in Subsection 7.2.2. If any of the forecasts are unavailable or deemed invalid through the $\boldsymbol{v}^N$-test, then they are excluded from this correction step. After the filtering step, residual analysis is conducted to generate *a posteriori* quality flags. Measurements with a negative LNRT result are flagged as valid (flag = 1), while those with a positive result are flagged as bad (flag = 0).

By combining *a priori* (innovation-based) and *a posteriori* (residual-based) flags, an integrated anomaly diagnosis can be performed when forecasts are available. The diagnosis framework identifies three types of anomalies:

1) Gross measurement errors (bad data),
2) Bad data smearing effect,
3) Sudden shifts of the system operating point.

The diagnosis scheme uses a threshold of two or more suspicious normalized innovations (above c) to indicate a possible sudden change in system operating conditions. The following cases may arise:

1) No suspicious normalized innovations and negative residual tests: No bad data present; all quality flags set to 1.
2) One suspicious normalized innovation: in this case, suppose that the i-th measurement associated to $v^N(i) > c$ is *a priori* indicated as BD. The residual analysis complements the diagnosis with three possibilities:
   a) No suspicious residuals: occurs only if the bad measurement is critical. Due to limited redundancy, the residual test cannot detect bad data in such measurements. The innovation analysis alone flags the measurement as bad (flag = 0).
   b) One suspicious residual: the LNRT confirms that the i-th measurement is BD (flag=0).
   c) Multiple suspicious residuals: indicates bad data smearing. The initially flagged i-th measurement will have the highest residual and is confirmed as bad (flag = 0); others are likely false positives.
3) Two or more suspicious normalized innovations: in this situation, the results of the residual analysis lead to two possibilities:
   a) No suspicious residuals: suggests a sudden system change (e.g., in bus injections or topology), rendering forecasts invalid. In this case (positive $\boldsymbol{v}^N$-test and negative $\boldsymbol{r}^N$-test) only the *a priori* information (forecasts) is inconsistent. Affected measurements are flagged with 2, indicating forecast inconsistency rather than bad data.
   b) Suspicious residuals present: confirms multiple bad measurements. Those flagged by both innovation and residual tests are confirmed as bad (flag = 0). Residual-only outliers not matched by innovation flags are considered valid but affected by smearing (flag = 1).

Figure 8.2 presents the process of bad data detection and identification for the proposed FASE method. Table 8.1 summarizes the steps involved with the assignment of quality flag values to the measurements. For measurements confirmed as bad (flag = 0), as both measured and forecasted values are available, the FASE can either attempt to correct the measurement using (8.23), or replace it with its forecasted value – an option often favored for its computational simplicity.

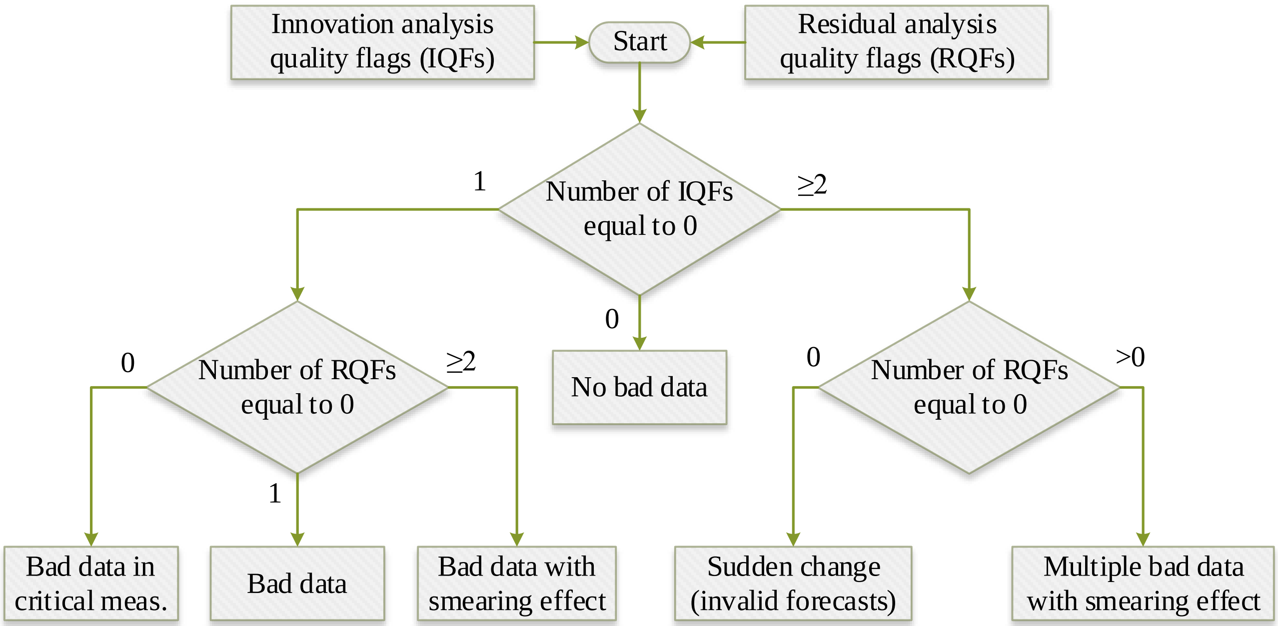

Figure 8.2: Bad data detection and identification flowchart for the proposed FASE method.

Table 8.1: Quality diagnosis of each measurement.

Quality flags			**Diagnosis**
Innovation analysis (IQF)	**Residual analysis (RQF)**	**Final**	
0	0	0	Measurement has gross error (bad data).
0	1	0 or 2	If this holds for only one measurement, then it is a critical measurement contaminated with large error (flag = 0). Else, there is an unexpected change in system states (flag = 2).
1	0	1	The measurement is valid and affected by bad data smearing.
1	1	1	The measurement is valid

9. Laboratory-scale PMU-based power system monitoring platform

The capability for large-scale, real-time power system simulation is essential for utilities to test, calibrate, and validate network performance across a wide range of scenarios and contingencies before deploying new technologies in mission-critical operations. This capability has become increasingly important with the adoption of smart grid technologies, which inherently alter the dynamic behavior and performance of the electric grid. Consequently, leading utilities are adopting integrated simulation frameworks to support the development, evaluation, and demonstration of emerging technologies. These frameworks enable comprehensive assessment of system performance in applications such as wide-area protection and control, renewable energy integration, and the coordination of distributed smart grid components [228], [229].

The advancement of modern real-time simulation hardware, collectively referred to as Real-Time Digital Simulators (RTDSs), has made it feasible to implement and test prototype technologies within controlled laboratory environments. Typically, an RTDS simulates electrical power systems in real time, enabling the testing of physical equipment, as well as software implementation and validation, through Hardware-in-the-Loop (HIL) and Software-in-the-Loop (SIL) configurations. These approaches provide a robust and reproducible framework for developing, validating, and certifying novel solutions [10].

Various synchrophasor applications – including SE, stability monitoring, and wide-area control algorithms – can be effectively designed, tested, and validated through the use of HIL and SIL architectures. Specifically, the testing of synchrophasor-based software applications with an RTDS enables utilities to visualize and analyze signals in real-time for validation purposes, assess performance under simulated conditions, and evaluate grid behavior using key power system metrics such as phase angle differences, grid stress levels, inter-area and local oscillations, voltage sensitivities, and frequency response characteristics. Compared to offline software-based simulation, HIL and SIL configurations offer several significant advantages:

1) *Model-based design flexibility*: Modern RTDS platforms support a wide spectrum of power system configurations, utilizing both generalized and highly detailed component models. Some platforms provide open development environments that allow for collaborative development among multiple stakeholders throughout various project stages.
2) *Improved efficiency, repeatability and test coverage*: PMU-based applications rely on precise, real-time data and must respond effectively to dynamic system conditions. RTDS platforms facilitate the creation of diverse operating scenarios, enabling comprehensive testing and broader coverage of potential events. Since system models can be modified in real time, testing is highly efficient and repeatable under controlled laboratory conditions.
3) *Interaction between RTDS, PMUs and other devices under test*: RTDS platforms feature multiple I/O modules that integrate external hardware through analog and digital interfaces and support communication protocols such as IEEE C37.118.2. These systems also provide continuous access to simulation data, allowing for detailed, real-time analysis and application-specific diagnostics.

In line with the preceding discussion, this chapter presents a laboratory-scale WAMS that utilizes commercial hardware and software. The proposed setup is designed for flexibility and scalability, supporting the integration and evaluation of user-developed synchrophasor-based applications. In this configuration, protection relays collect synchrophasor measurements from power systems simulated in real time using RTDS hardware. These measurements are streamed to a software-based PDC, which performs data aggregation and enables real-time monitoring of the simulated system. Two experimental use cases are explored:

1) The first use case integrates conventional measurements from virtual (software-based) RTUs with synchrophasor measurements from physical PMUs, for the implementation and real-time evaluation of the ISE algorithm proposed in Subsection 6.2.1.
2) The second deploys PMU-enabled SE algorithms for real-time monitoring of a transmission system and an Active Distribution Network (ADN).

9.1 Background

Digital Real-Time Simulation (DRTS) has been used in the power industry for over 25 years, and is a powerful tool for analyzing power system behavior under realistic and dynamic conditions [230]. Enabled by high-performance computing and parallel processing, DRTS solves power system differential equations in real time, an essential feature for evaluating time-sensitive applications, especially when interfacing with physical hardware [231]. Nowadays, DRTS plays a central role in rapid prototyping, novel monitoring and control scheme design, and education and training, highlighting its increasing relevance [232].

Different modeling approaches are used depending on the study objectives. Averaged models simplify power system behavior by representing complex elements with average values, thus providing computationally efficient representations for steady-state analysis and long-term planning (e.g., power flow studies, load flow analysis, and steady-state stability assessments), where the variation in system variables occurs over relatively long periods. Phasor-based simulation employs the phasor concept to represent power system dynamics, striking a balance between fidelity and computational speed, and making it suitable for medium-term stability analysis and control design. The phasor model is particularly effective for transient stability analysis and small-signal stability studies. Electromagnetic Transient (EMT) models provide a detailed representation of power system dynamics by considering the actual physical behavior of individual components, capturing high-frequency phenomena and fast transients with greater accuracy but at increased computational cost. EMT simulations are essential for analyzing power system responses to fast events such as faults, switching operations, and lightning strikes, and are primarily used for short-term or event-specific studies [231].

Two main types of DRTS exist in power system studies:

1) Fully digital simulation – also referred to as Software-in-the-Loop (SIL), Model-in-the-Loop (MIL), or Processor-in-the-Loop (PIL)) – simulates the entire system, including control, protection, and auxiliary components, without requiring external interfacing or physical inputs/outputs.
2) In Hardware-in-the-Loop (HIL) simulation, portions of the system are replaced by physical hardware connected through I/O interfaces (e.g., filters, ADCs/DACs, signal conditioners). HIL bridges the gap between the simulated and physical systems, enabling integrated testing of controls and communication layers.

Originally developed for aerospace applications, HIL simulation has since been adopted in automotive and industrial sectors. In the power systems domain, it was originally developed as a solution for flexibly testing control and protection schemes associated with HVDC projects [230]. HIL enables real-time interaction between simulated power networks and physical devices, offering a safe, flexible, and reproducible environment for testing and validation without the risks or costs of field deployment [233]. Thus, it is now widely used by utilities, research institutions, and consultants for testing protection schemes, control strategies, and device behavior under real-world conditions, in various general-purpose HIL test beds and cyber-physical platforms [229], [234]–[237].

9.1.1 *Real-time digital simulator capabilities [230], [233]*

As power systems transition from synchronous machines to converter-based generation, EMT simulations have become increasingly essential, due to their ability to capture system behavior across a wide frequency range, making them ideal for simulating modern grids. Phasor-based models often fall short in scenarios with increased RES penetration, yielding overly optimistic results by failing to capture fast dynamics or low-level converter controls.

Many EMT tools, including RTDSs, employ the Dommel algorithm for network solution, and use dedicated parallel processing hardware to execute simulations in real time. In the context of DRTS, the term *timestep* refers to the interval between successive output calculations of the EMT simulation, and defines the sampling frequency and determines the modeled signal frequency range. To maintain real-time performance, all network calculations must complete within each timestep. The timestep should be chosen based on the system dynamics under study and the desired fidelity of the results; for example, for protection and control testing, typical timesteps are 30–60 μs.

RTDSs designed for HIL testing consist of three main components:

1) Parallel processing hardware to execute real-time simulations.
2) Input/output (I/O) interfaces that enable closed-loop testing with physical devices.
3) Graphical user interface (GUI) that provides real-time interaction with the simulation and houses the power system modeling library.

As demand for real-time simulation grows, manufacturers must continuously advance the technology to improve fidelity, expand application range, simplify interfacing, and enhance usability. These improvements span across hardware capabilities, GUI features, and power system modeling tools. This evolution is critical given the rapid changes in power systems, such as the rise of converter-interfaced DERs, the increasing use of new communication protocols, and the decentralization of control architectures. Accurate modeling platforms that adapt to these trends are critical.

A key constraint in RTDS usage is the number of power system nodes that can be simulated per timestep. Each node contributes to the size of the network admittance matrix, which must be solved during each simulation cycle. Performing matrix decomposition dynamically at every timestep is computationally intensive but allows for the inclusion of non-linear elements and dynamic models without additional numerical interfaces. However, as the network size grows, the time required for matrix decomposition increases exponentially. Thus, simulator performance often limits model size. Users with limited hardware may need to simplify or reduce network models to fit within these constraints. Therefore, innovations that reduce processing demands while maintaining accuracy are of significant interest to the RTDS community.

In power-system research and practice, six vendors account for the vast majority of commercial DRTS/HIL installations:

- RTDS Technologies Inc. (Winnipeg, Canada):
  - RTDS Simulator (NovaCor series),
  - RSCAD software.
- OPAL-RT Technologies Inc. (Montréal, Canada):
  - XG Series real-time simulators (e.g. OP4512, OP4610XG, OP5705XG, OP5707XG),
  - eMEGASIM™, HYPERSIM®, ARTEMiS™ platforms.
- Typhoon HIL GmbH (Graz, Austria):
  - HIL Series (e.g. HIL 402, HIL 602, HIL 803),
  - TyphoonSim, Typhoon HIL Control Center.
- dSPACE GmbH (Paderborn, Germany):
  - SCALEXIO® real-time systems, MicroLabBox development units,

    - ConfigurationDesk and RTI configuration and implementation software.
- Speedgoat GmbH (Zürich, Switzerland):
    - Real-Time Target Machines under Simulink Real-Time (Baseline, Performance, Pulse, Mobile, Unit, Rack systems).

9.1.2 HIL and SIL testing of WAMPAC and synchrophasor applications

HIL simulation has become a valuable tool for studying different aspects of WAMPAC applications in modern power systems. PMUs, which serve as the cornerstone of these applications, are commonly integrated into HIL environments to support the development, testing, and validation of new tools. This approach enables early-stage certification and pre-commissioning evaluations under realistic conditions. The literature describes various HIL architectures designed for PMU integration, with the specific configuration typically chosen based on the test objectives, available infrastructure, cost constraints, and system complexity. Broadly, these configurations fall into three categories: basic setups with a single PMU as the device under test, platforms designed for rapid control or protection prototyping using PMUs, and implementations involving virtual PMUs. In line with these frameworks, this thesis focuses on laboratory environments that combine RTDS(s), physical and/or software-based (virtual) PMUs, software or hardware PDCs, and synchrophasor-driven applications [10], [228], [238]–[243].

Given the strict timing requirements of WAMPAC systems, latency and data delivery performance must be carefully assessed to ensure dependable operation [244]. Several studies have leveraged DRTS platforms in HIL configurations to assess operational delays, such as the affine modeling of communication latency in [245], [246], and the impact of quality-of-service degradation due to network conditions in [240]. These works use PMUs as the hardware under test to analyze how latency, packet loss, and data corruption affect synchrophasor-based applications. Communication delay impacts are further analyzed in [247]–[249], with emphasis on real-time performance of wide-area protection and monitoring systems. Further implementations of HIL and SIL setups have been employed to test protective schemes under transient conditions, support operator training, and facilitate cyber-physical security studies [250]–[253]. In one representative application [254], a Wide-Area Damping Controller (WADC) is validated using HIL by closing the control loop between the controller and a commercial excitation system (ABB Unitrol 1020), based on PMU measurements. Cybersecurity vulnerabilities, particularly Time Synchronization Spoofing Attacks (TSSA), are examined in [255], where a HIL setup emulates a GPS-based timing attack on a PMU. By spoofing time signals in real time, the study demonstrates how falsified synchrophasor data can lead to WAMPAC malfunctions, violating standard compliance and triggering erroneous trip signals. The experimental platform uses OPAL-RT, commercial PMUs, and PDCs, integrating both real and spoofed timing signals to assess the system's vulnerability and response.

In recent years, numerous laboratory-based studies have focused on the development and evaluation of synchrophasor-based monitoring and control algorithms. These efforts include real-time implementations of PMU-based inter-area oscillation mode estimation [256], [257], as well as voltage stability monitoring using both SIL and HIL platforms [258]–[261]. Under-frequency load shedding strategies based on synchrophasor data have been explored in [262], [263], while system inertia estimation techniques are presented in [264]. Islanding detection methods leveraging micro-PMU data have been explored in [265], alongside studies on power quality monitoring [266], and event detection using historical and real-time data streams [267], [268]. Wide-area control strategies, including damping controllers and protection schemes, have been developed and experimentally tested in [269]–[271]. Additionally, fault location and classification algorithms based on PMU data have been validated under HIL configurations in [272]–[275]. Cybersecurity aspects of WAMS have also been examined, from an algorithmic perspective, in [276]–[278].

Finally, a prominent application of DRTS concerns the validation of state estimation [279]–[286], as well as parameter identification [287] and topology estimation [288] algorithms, all of which leverage PMU measurements. In these studies, RTDS platforms either interface with physical PMUs or generate phasor data streams to simulate synchrophasor inputs. While hardware PMUs may be present in the test setup, the aim of such configurations is not to evaluate the metrological or communication performance of the PMUs themselves, as is the case in conventional HIL testing where the device under test is the primary focus. Rather, the objective is to assess and validate software-based monitoring or control algorithms that rely on PMU data. Notably, many of these algorithms operate in an open-loop configuration: for instance, SE or oscillation mode analysis tools process real-time measurements but do not feed any control signal back into the simulated system. Therefore, while such testbeds may adopt components of HIL or SIL architectures, they fall outside the strict definitions of these paradigms, as the hardware is not under test, and the software often does not close the control loop. Instead, these setups serve as measurement-driven algorithm validation environments, where the fidelity and timing of real-time data are crucial for assessing algorithmic performance under realistic operating conditions. This thesis adopts this perspective to support the systematic evaluation of synchrophasor-based monitoring and control functionalities.

9.2 Hardware and software overview

This Section outlines the structure and development process of the experimental synchrophasor network deployed at the Electric Energy Systems Laboratory of the School of Electrical & Computer Engineering at the National Technical University of Athens (NTUA). A complete schematic of the hardware configuration is provided in Figure 9.1.

Synchrophasor data in this setup is generated from current and voltage signals produced by a simulated power system running on the NovaCor RTDS. Accordingly, the RTDS and its companion simulation software RSCAD are introduced, and the simulated power system model and the method used to generate properly scaled analog outputs, which are necessary for feeding data into PMUs, are described. A description of the SEL-351A relays which are used here as PMUs, and their configuration are presented next, followed by a description of the PDC software used in this research. The section concludes with a description of the SEL-2407 satellite-synchronized clock, which provides GPS-based time signals for PMU synchronization. All essential configurations for the full synchrophasor network are included, making this section a practical reference for future users of the experimental testbed.

9.2.1 RTDS configuration

The RTDS used in this research is manufactured by RTDS Technologies Inc. and is designed specifically for real-time EMT simulations. The laboratory setup utilizes a single unit of the NovaCor™ [289] simulation hardware, powered by IBM®'s POWER8™ ten-core processor. A key feature of this platform is that it runs the simulation executable code directly on the processor without an intermediary operating system, enabling both high-speed execution and precise control over simulation tasks.

Typically, one processor core is dedicated to solving the power system network equations through nodal analysis, while the remaining cores handle the parallel computation of individual component models (for lines, transformers, machines, etc.). This architecture offers inherent scalability. First, the number of licensed processor cores dictates the size and complexity of the network that can be modeled. Second, for simulations exceeding this core-based capacity, the RTDS supports partitioning the network into multiple subsystems. These subsystems can run in parallel, exchanging data in real time via traveling-wave transmission line models, provided the travel time exceeds or equals the simulation timestep. This technique allows a subsystem to be simulated either on a separate NovaCor unit or on another core within the same hardware.

To interface with hardware PMUs, which expect analog inputs similar to those produced by physical VTs and CTs, the RTDS must convert its internal digital simulation signals into analog outputs. This is achieved using the 12 analog output channels on the front panel of the NovaCor chassis, and the Giga-Transceiver Analog Output (GTAO) card [290]. The RTDS is also equipped with a Giga-Transceiver Network Communication Card (GTNETx2) [291], for interfacing various network protocols, (TCP, UDP, IEC 61850, DNP3) with the RTDS. In the synchrophasor monitoring setup, the GTNET is used to acquire RTU measurement signals, derived from virtual voltage magnitude, active and reactive power meter components of RSCAD, and send them to a local workstation client over TCP. Figure 9.2 shows the front panel of the RTDS cubicle, with the analog outputs of the NovaCor simulator at the bottom of the picture, and the GTAO card, which is used to generate analog voltage signals corresponding to measured voltages and currents.

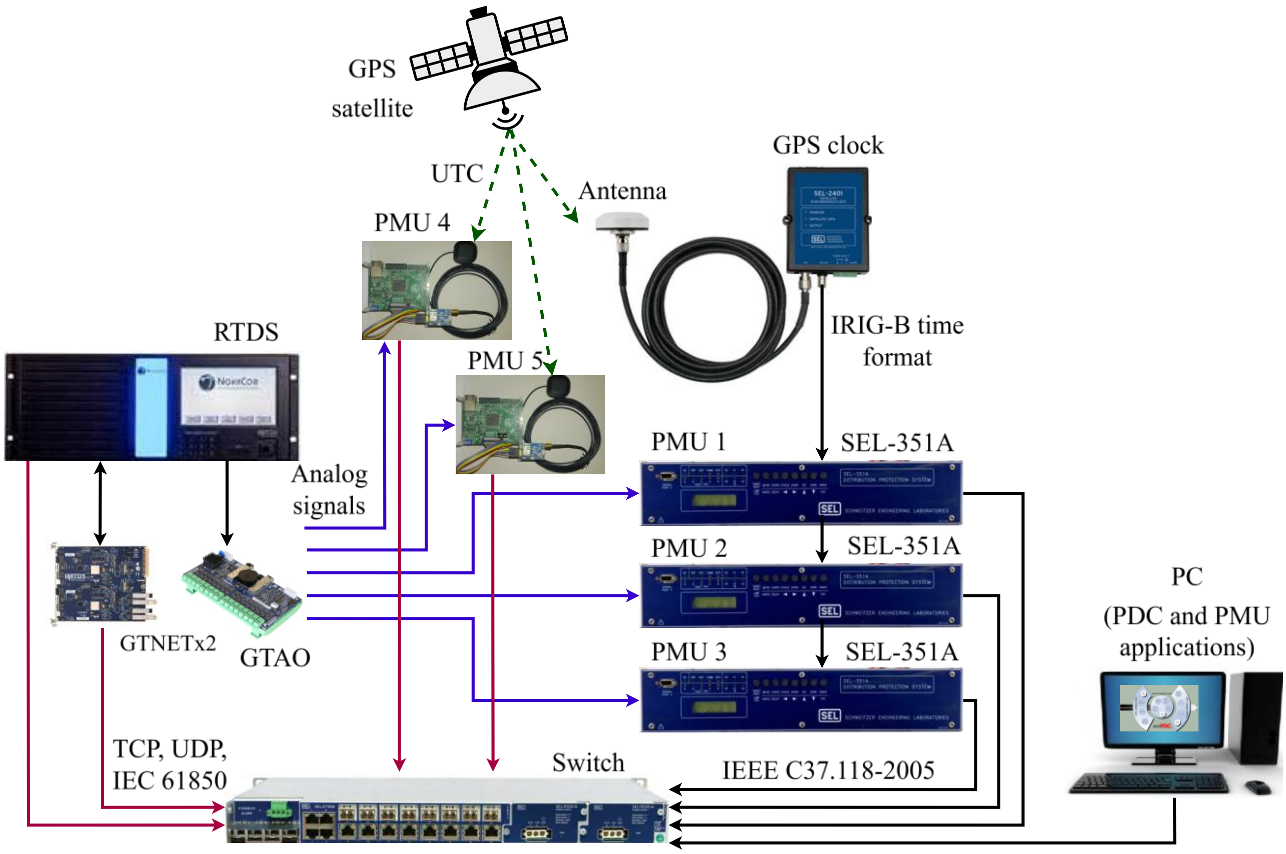

Figure 9.1: Schematic diagram of the laboratory hardware configuration.

Simulation design and operation are managed through the RSCAD software suite, which serves as the user interface for building, controlling, and analyzing simulations. RSCAD includes several integrated modules that support end-to-end simulation workflows without requiring third-party tools. The Draft module is used to construct simulation models using a comprehensive library of components that span power systems, control systems, protection, and automation domains. Users can configure the parameters for each component directly within this interface. Once the simulation model is complete, RSCAD automatically compiles the design into executable code and assigns simulation tasks to the appropriate processor cores. The compiled model is then uploaded to the NovaCor rack over an Ethernet connection. During execution, the Runtime module allows users to interact with the system in real time, by visualizing the real-time operation of the network and adjusting simulation parameters.

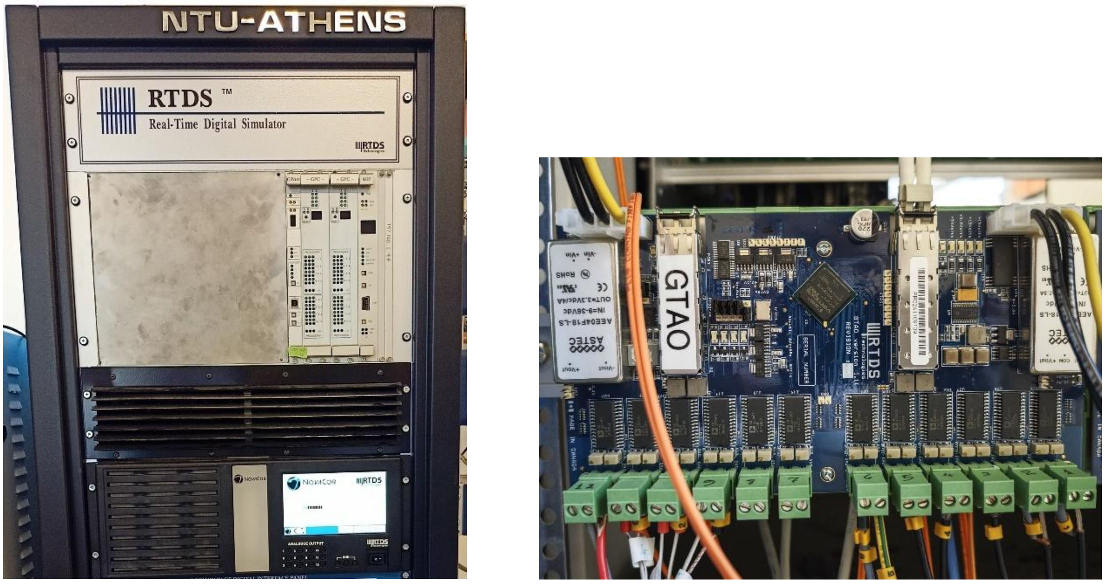

Figure 9.2: Laboratory setup of the RTDS (left) and GTAO expansion card (right).

9.2.2 Hardware PMUs

The laboratory configuration includes three SEL-351A [292] distribution feeder distance protection relays, depicted in Figure 9.3. In addition to their protection functions, these relays are capable of providing synchrophasor measurements when synchronized to a high-precision time source such as a GPS clock. The configuration of each relay begins with its Global Settings, which define parameters such as device location and identification, nominal frequency, number of setting groups, and the enabling and customization of synchrophasor output. All three relays are integrated into the local area network (LAN) via a 24-port Ethernet switch.


Figure 9.3: SEL-2730M switch and three SEL-351A PMUs.

The SEL-351A relays used in this study are equipped with one 3-phase voltage input and one 3-phase current input channel. Considering that the RTDS produces low-level analog signals (10 V_{max}) from the simulated cases, while the PMU voltage and current inputs are rated at 300V and 5A, respectively. As a result, these signals require either amplification or an alternative method of connection to be compatible with the relay inputs. To avoid external amplification, the laboratory configuration uses the low-level interface of the SEL-351A relays, which allows direct connection of the RTDS analog outputs and the GTAO card, to the relay input terminals via ribbon cables. Access to the low-level interface requires opening the front panel of the relay enclosure, as it is not exposed during standard operation. When this connection method is used, the analog inputs bypass the relay's internal instrument transformers, which normally scale down CT and VT outputs for internal A/D conversion. Therefore, it is essential to configure the RTDS analog output scaling appropriately to comply with the voltage levels of the low-level interface and ensure accurate signal representation. The following formulas are used to calculate the scaling factors for the analog measurement signal outputs of the RTDS:

- for voltage measurements: $V_{ph}^{meas} = \dfrac{V_{ph}}{VTR \times VSF}$,
- for current measurements: $I_{ph}^{meas} = \dfrac{I_{ph}}{CTR \times CSF}$,

where V_{ph}^{meas} (I_{ph}^{meas}) is the single-phase low-level voltage (current) measurement value fed to the PMU in V (A), V_{ph} (I_{ph}) is the single-phase voltage (current) value produced during the real-time simulation of the power system in V (A), *VTR* (*CTR*) is the voltage (current) transformer ratio set in the relay software settings, and *VSF* (*CSF*) is the voltage (current) scale factor for the low-level input module of the PMUs. For the SEL-351A devices *VSF* = 223.97 V/V and *CSF* = 110.6 A/V.

Relay settings and communication parameters are configured using AcSELerator QuickSet, the vendor-provided software tool. In the laboratory synchrophasor network, all synchrophasor data is transmitted over TCP/IP using the IEEE C37.118-2005 standard.

9.2.3 GPS-synchronized clock

All available PMUs need to be synchronized to a common time source, which is the UTC. The synchronization is achieved with the SEL-2401 [293] device, which is a satellite-synchronized clock that provides IRIG-B time-code format output for the SEL-351A relays. IRIG-B is a time data format consisting of one-second frame that contains 100 pulses divided into a number of fields. A PMU can decode the second, minute, hour and day fields and set its time clock after detecting valid time data in the IRIG-B time code.

The SEL-2401 is connected via a TNC coaxial connector to a GPS antenna that receives the UTC signal from at least four satellites. When the satellite clock is powered on, initially the IRIG-B outputs are disabled until the clock locks with satellites to prevent sending incorrect time to the PMUs. The GPS signal is then converted to IRIG-B time format with an average accuracy of ±100 ns and is sent through BNC cables to the PMUs. Note that the outputs of SEL-2401 exceed the required performance specifications established by the synchrophasor standard IEEE C37.118-2005.

9.2.4 Phasor data concentrators

PDCs play a central role in synchronized measurement systems, enabling the aggregation, time alignment, and real-time monitoring of high-resolution phasor data from geographically distributed PMUs across the grid. In this experimental setup, two types of PDCs are employed: the commercial SEL-5073 software PDC and the open-source openPDC platform. Both are used to collect, filter, and synchronize incoming data streams from PMUs. Their core functionalities and internal structures are illustrated in Figure 9.4. In accordance with the IEEE C37.118-2005 standard, PMUs act as servers, continuously streaming real-time phasor data over Ethernet to the software PDCs, which function as clients. Upon receiving these streams, the PDC aligns the data based on GPS-synchronized timestamps. It can also perform user-defined calculations, including real and reactive power, sequence component analysis, and other algebraic operations. The processed, time-aligned data is then re-broadcast at rates of up to 100 messages per second, making it available for downstream synchrophasor applications.

The PDC output streams support a variety of functions including system monitoring, real-time control, protection logic, and data archiving. Archiving options include both continuous recording and trigger-based recording. When trigger-based archiving is selected, users can define the conditions that initiate data capture, the duration of pre- and post-event recording, the maximum number of stored events, and data retention parameters. Additional configuration settings allow users to specify the output phasor format (polar or rectangular), angle units (degrees or radians), data formats such as CSV, Binary COMTRADE, or ASCII COMTRADE, and archive naming conventions and storage intervals. Configuration and diagnostic tools for each PDC are available via PDC Assistant (for the SEL-5073) and openPDC Manager (for openPDC).

9.2.5 Local Workstation

All software components used in this experimental setup are hosted on a general-purpose personal computer operating under the Windows platform. This workstation serves as the central node for managing simulation, data processing and algorithm testing tasks, and is networked with both the RTDS and the PMUs via LAN. It runs all critical software tools required for system operation and analysis, including: RSCAD (power system modeling and interfacing with the RTDS), PDCs (SEL-5073, openPDC), SEL-5078-2 SynchroWAVe Central, and MATLAB R2022a (PMU-based algorithm implementation and testing), as well as any user-specific synchrophasor applications under testing.

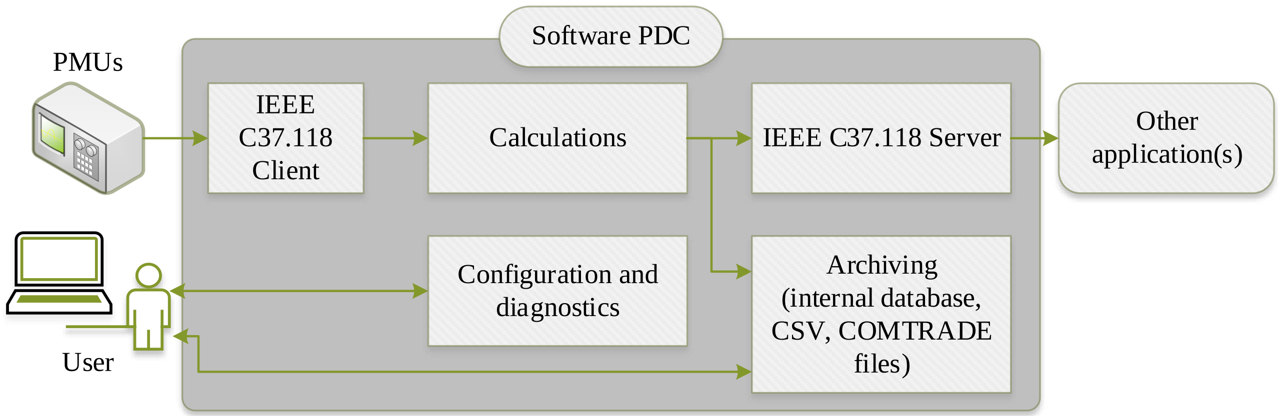

Figure 9.4: Diagram of software PDC functionalities.

9.3 Verification of synchrophasor measurements

This section presents the verification process carried out to ensure the correct configuration and functionality of the synchrophasor measurement network. The primary objective of these tests is to confirm that all components, including hardware PMUs, PDCs, and all associated software, are properly configured. Two key tools are employed: SEL-5078-2 SynchroWAVe Central, a dedicated synchrophasor visualization platform, and the built-in real-time status display available in the SEL-5073 PDC software. These tools are used to monitor system performance and assess the integrity of time-synchronized phasor data streams in real time.

The SEL-5073 interface provides critical diagnostic information regarding system operation. It displays the connection status of PMU inputs, network latency, the rate and consistency of data frame reception, and overall input/output activity. Figure 9.5 shows as an example of an input connections status produced by the SEL-5073 PDC during testing of the actual synchrophasor network, with PMU measurements collected from the IEEE 14-bus network simulated in the RTDS.

Meanwhile, SynchroWAVe Central provides a graphical interface for viewing live PMU data transmitted to the PDC. It interprets data stored in the PDC's internal relational database, converting it into user-friendly, real-time visualizations. The software connects directly to any PDC that complies with the IEEE C37.118 protocol and stores the incoming phasor data in its proprietary Historian database. Time-aligned measurements can then be displayed through SynchroWAVe Central's web-based dashboard in the form of dynamic plots and phasor diagrams.

In the representative example shown in Figure 9.6, the IEEE 14-bus system's real-time behavior is visualized during a simulation. The display includes live plots of frequency, bus voltages, and line current magnitudes, as measured by the PMU installed at Bus 1. A phasor scope illustrates the phase angles of all monitored voltages, using Bus 1 as the reference. To introduce dynamic behavior into the simulation, all loads in the RTDS model are configured using Dynamic Load components within RSCAD. This setup enables real-time external control of active and reactive power demand of each load through a MATLAB script. At a randomly selected point in the simulation, the reactive power load at Bus 2 is deliberately increased by the user. This event is immediately reflected in the SynchroWAVe Central interface, as shown in the captured screenshot (Figure 9.6), verifying the system's responsiveness and the synchrophasor network's integrity.

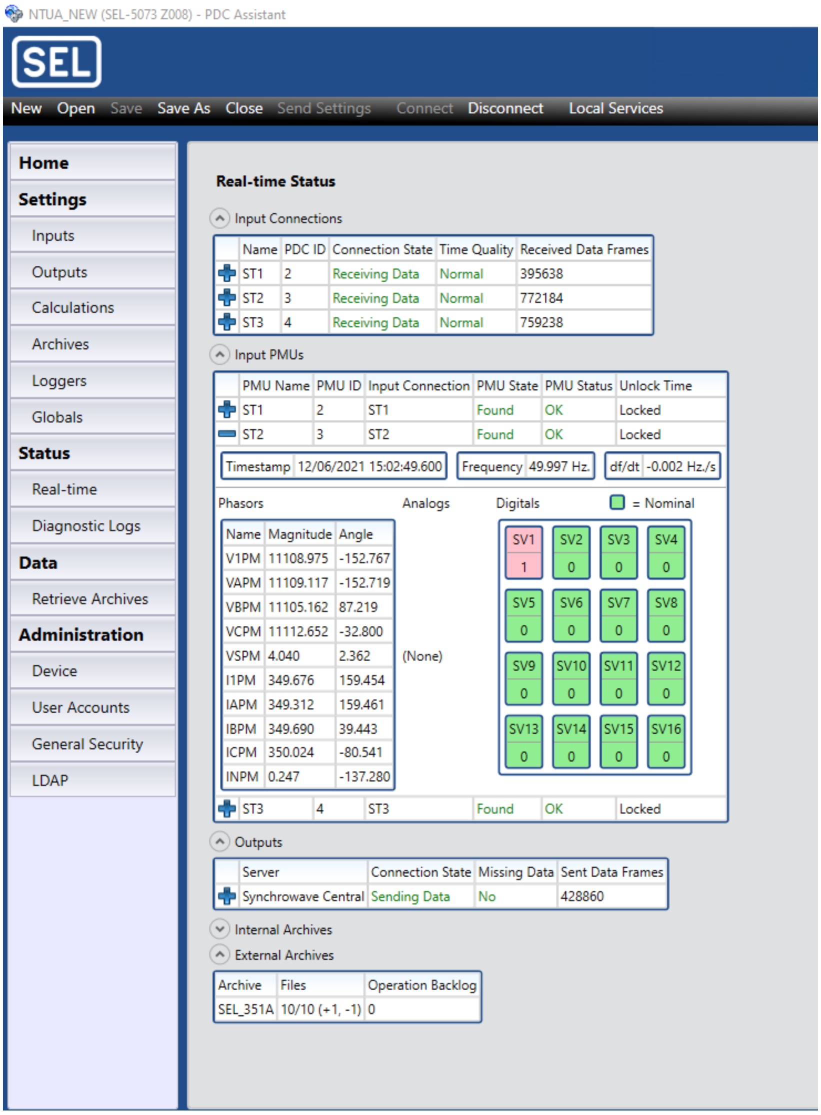

Figure 9.5: SEL-5073 PDC real-time status and diagnostics tab.

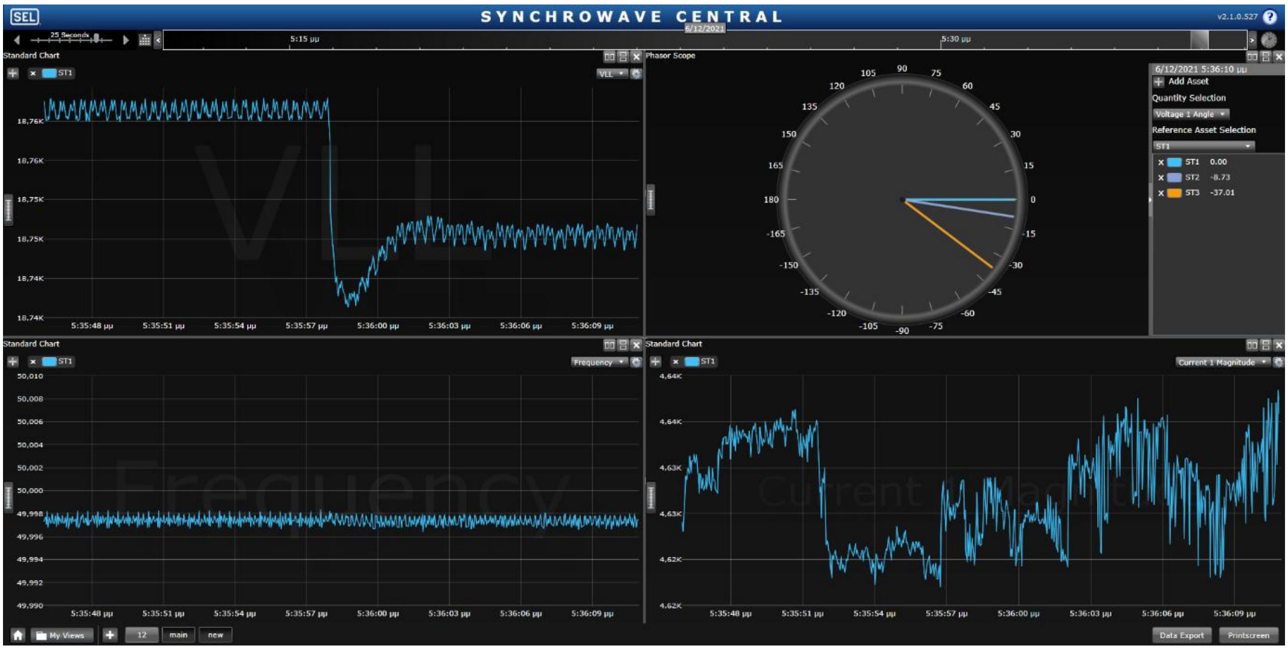

Figure 9.6: SynchroWAVe Central snapshot (voltage, frequency, current, phasor scope) during load variation at Bus 2 of the IEEE 14-bus network.

9.4 Online state estimation using PMU measurements

In the deployed laboratory setup, both hybrid and PMU-based SE algorithms are simulated in real time, and their performance is assessed using various metrics (see Subsection 6.5.2). The RTDS is used to emulate real-time operation of the IEEE 14-bus sub-transmission network, as well as a reduced 29-bus version of the 15-kV Active Distribution Network (ADN) of Kythnos island, Greece. Real-time data are received from the RTDS and the physical PMUs and used as inputs to the online SE algorithms. Finally, the SE results are presented via GUI, in the form of bus voltage phasors and line power flows on the SLD of the simulated system.

9.4.1 Online hybrid state estimation: IEEE 14-bus network

An online implementation of the ISE method proposed in Subsection 6.2.1, utilizing both virtual RTU and hardware PMU measurements, is developed and effectively validated in real-time, using the configurations presented in Figure 9.7 and Figure 9.8. The first implementation (Figure 9.7) utilizes the commercial software platform (SEL-5073 PDC) and relies on its internal database for exporting PMU measurements to the MATLAB-based SE algorithm, as well as the SynchroWAVe Central software for visualization purposes.

The second implementation is based solely on open-source tools. This setup utilizes openPDC (instead of SEL-5073) to collect PMU data, mongoDB for data storage and transfer between applications, and a python-based GUI that presents SE results in real-time on the SLD of the simulated network. The open-source openPDC software developed by Grid Protection Alliance (GPA) [294], is used. For the purposes of real-time applications, such as SE, openPDC has been configured to always supply the most recent measurements both to its internal database and to an external database (mongoDB). The use of a database to store the full set of PMU measurements offers the ability to retain historical data for future analysis, while simultaneously allowing real-time applications to query its contents. This role is fulfilled by mongoDB, an open-source, non-relational database. For real-time application development, minimizing data-lookup time is of paramount importance. To this end, mongoDB provides the “Change Streams” feature, which monitors the flow of data entering or exiting the database, enabling client applications to access updates in real time. Specifically, an application can be automatically notified by the database of any changes to its contents at the moment they occur. Thus, real-time applications communicating with mongoDB need not spend time polling for data, as they always have access to the latest records with minimal latency, leading to shorter execution times and reduced time-skew. Leveraging this capability, mongoDB is used as the data-transfer mechanism between openPDC and the state estimator.

The graphical user interface (GUI) serves as the HMI in the experimental setup and is intended to visualize the SE outputs, enabling the power-system operator to monitor network variations in real time. The GUI is implemented using Python's Tkinter library. The application's graphical interface consists of two independent windows. The first displays a dynamic SLD of the power system, on which the magnitude and angle of bus voltages, as well as active and reactive power flows of transmission lines and transformers, are updated in real time according to the latest SE results. To facilitate the identification of system disturbances, represented quantities change their display color to red if any predefined safety limits are violated. The second window allows oversight of the temporal evolution of the state variables, i.e., a real-time plot of the complex bus voltages versus time. In the open-source platform, the estimated state variables are stored in mongoDB and subsequently retrieved by the graphical display application.

Conventional measurements are recorded via software (virtual) RTUs implemented in RSCAD and are made available directly to the MATLAB-based SE process via TCP. PMU measurements are available to the estimator at 50 fps, while the conventional (RTU) measurements are updated every 2 seconds. The ISE process (Subsection 6.2.1) is executed automatically every 2 seconds, upon arrival of the RTU measurements, incorporating the most recent set of PMU data. It is noteworthy that the RTU measurements taken directly from the RTDS Runtime can be considered perfectly accurate (noise-free) compared to PMU device readings. Thus, Gaussian noise $rand \times \sigma_i$, $rand$ being a $\mathcal{N}(0,1)$ random number, is added to the RTU measurements obtained from the GTNET card of RTDS, in order to make them closely resemble real field measurements. The measurement uncertainties are assigned as described in Subsection 6.5.1.

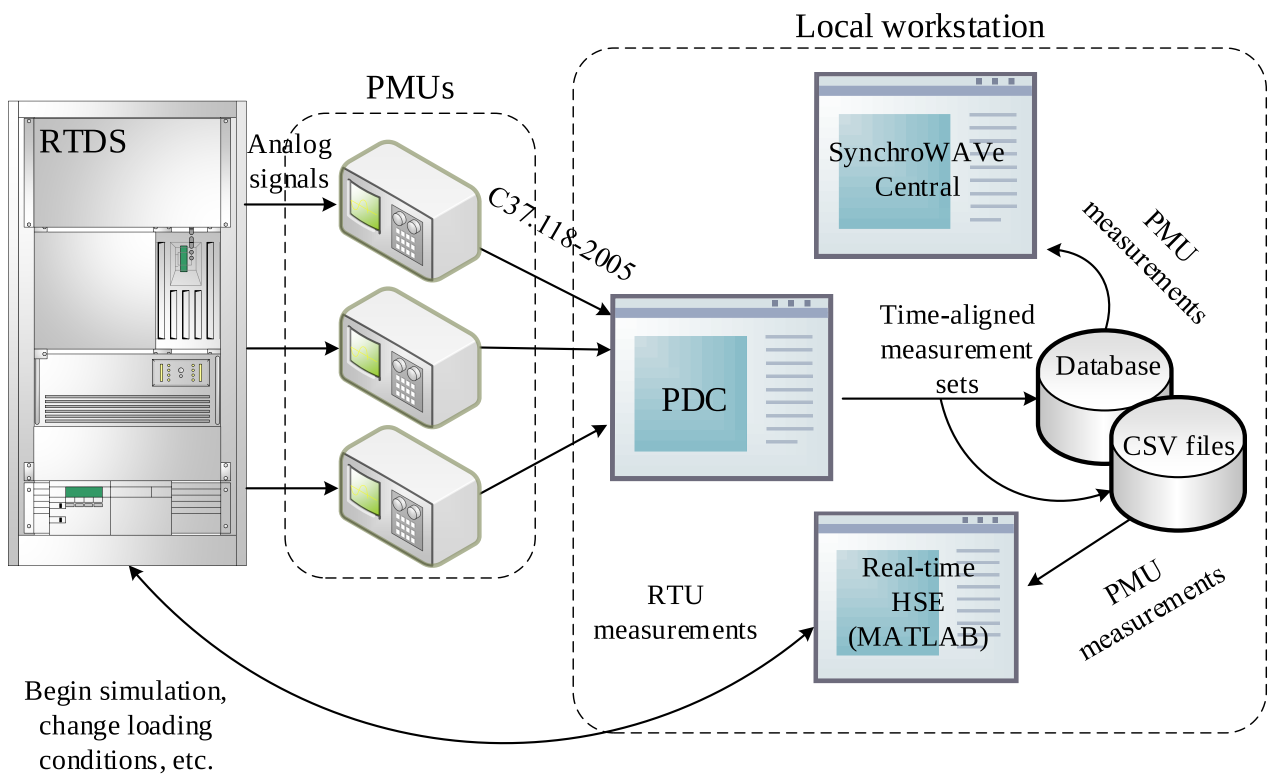

Figure 9.7: Data flow sequence for the real-time simulation of the ISE algorithm.

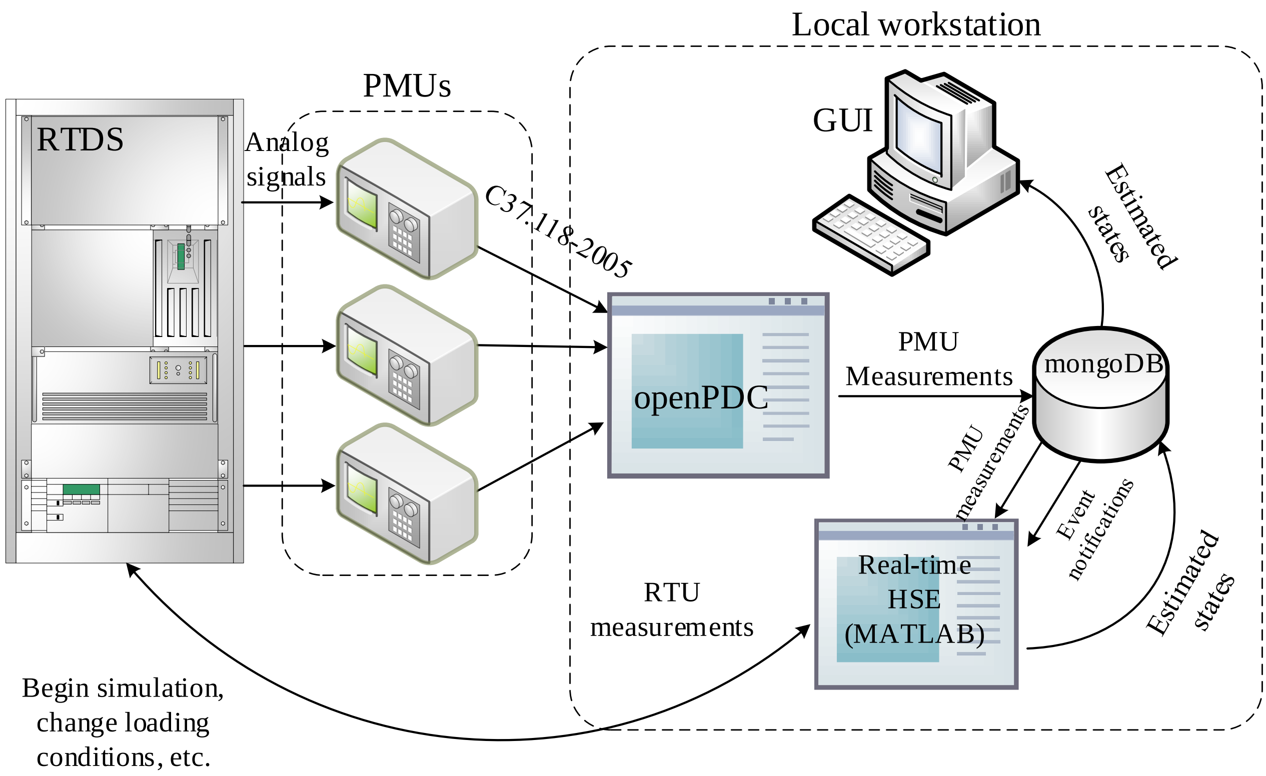

Figure 9.8: Alternative simulation setup of the ISE algorithm using open-source software.

A screenshot of the Draft module of RSCAD with the simulated IEEE 14-bus system is depicted in Figure 9.9. The IEEE 14-bus test system contains 11 loads, and 5 generation buses: 1, 2, 3, 6, and 8. The base case loading data for the IEEE 14-bus network and the two meter-placement schemes are presented in Table 9.1. A different MS is considered in each of the two ISE simulation setups:

- MS 1 (Figure 9.7): PMUs at buses 1, 3 and 5, lines 1-2, 3-4 and 5-6. RTUs at buses 2, 6, and 9.
- MS 2 (Figure 9.8): PMUs at buses 2, 6 and 8, lines 2-1, 6-11 and 8-7. RTUs at buses 3, 5 and 9.

Each set of PMU measurements forwarded to the PDC consists of the positive sequence voltage phasors at each monitored bus, and current phasors at each monitored line. Each set of RTU measurements includes the voltage magnitude and power injections at each RTU-measured bus, as well as power flow measurements over all incident branches.

In order to test the real-time static HSE implementation, 1000 Monte Carlo simulations are performed, both with and without bad data involved. Bad data detection, identification and removal are accomplished via Algorithm 8.1. The results of the ISE algorithm are compared with the true values provided by the RSCAD runtime in Table 9.2, which presents various performance metrics (see Subsection 6.5.2) obtained from the simulations. It should be noted that SE is performed without a reference bus, whereas the true states in the runtime are reported with Bus 1 as the reference. Hence, the estimation results are also presented using Bus 1 as the reference to enable direct comparison. A snapshot of the real-time supervisory application displaying the estimator results is shown in Figure 9.10.

As shown in Table 9.2, the ISE algorithm demonstrates strong performance across all evaluated accuracy metrics, considering the specified error parameters. The minimal difference observed between the results obtained with and without bad data indicates that the implemented algorithm is effective in detecting and rejecting gross measurement errors. The slightly elevated average execution time for the HSE in cases involving bad data can be attributed to the additional computational steps required for bad data processing.

Table 9.1: Online ISE – IEEE 14-bus network load data and measurement configuration.

Bus number	Type	Base Case Load		MS 1	MS 2
		P (MW)	Q (MVAr)	Sensor	Sensor
1	Slack	–	–	PMU	–
2	P-V	21.7	12.7	RTU	PMU
3	P-V	94.2	19.0	PMU	RTU
4	P-Q	47.8	−3.9	–	–
5	P-Q	7.6	1.6	PMU	RTU
6	P-V	11.2	7.5	RTU	PMU
7	P-Q	–	–	–	–
8	P-V	–	–	–	PMU
9	P-Q	29.5	16.6	RTU	RTU
10	P-Q	9.0	5.8	–	–
11	P-Q	3.5	1.8	–	–
12	P-Q	6.1	1.6	–	–
13	P-Q	13.5	5.8	–	–
14	P-Q	14.9	5.0	–	–

Table 9.2: Online ISE – Performance metrics.

Metric	MS 1		MS 2	
	No bad data	With bad data	No bad data	With bad data
MAE_V ($\times 10^{-3}$ pu)	1.00	1.50	1.20	1.25
MAE_A ($\times 10^{-1}$ deg.)	3.03	3.12	2.42	2.64
$Macc_V$ ($\times 10^{-2}$ pu)	1.47	1.50	1.06	1.28
ISE time (ms)	2.30	9.20	2.20	9.00

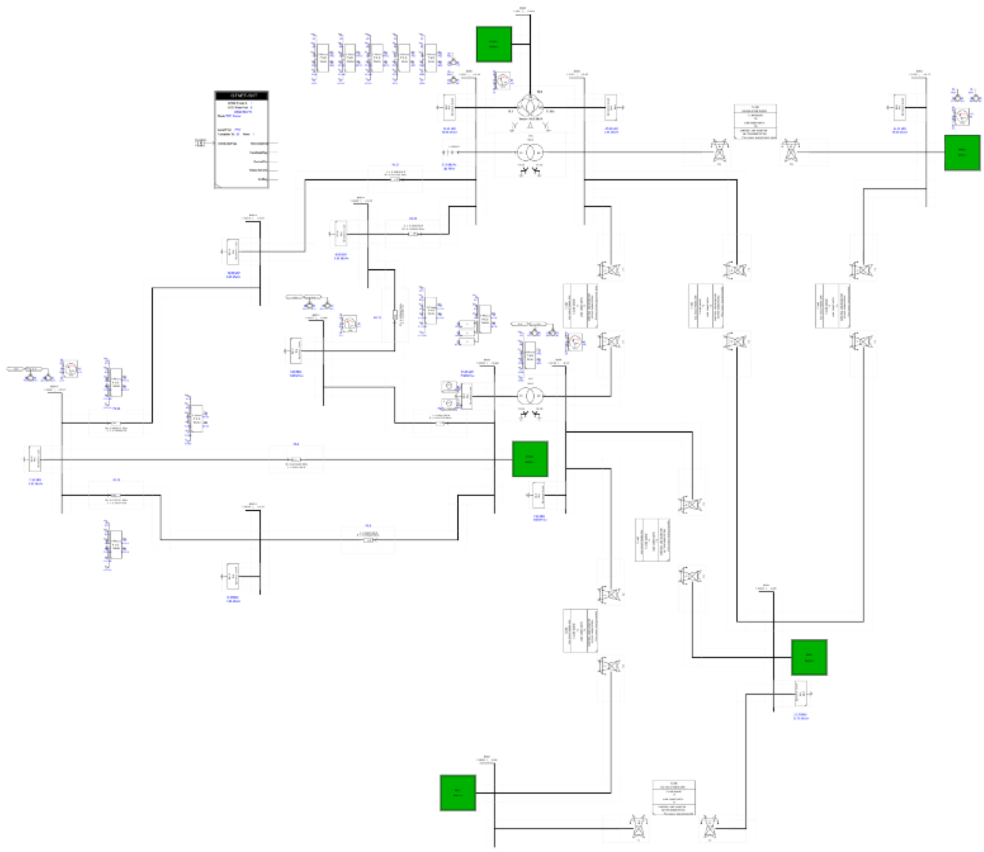

Figure 9.9: IEEE 14-bus system modeled in RSCAD.

An equally important parameter for real-time applications is latency – that is, the interval from the moment measurements are sent to the estimator until its results appear on the HMI. To calculate this duration, one must record the time when measurements occur and the time when the results are displayed on the computer screen, neglecting any transmission delay within the laboratory LAN. The difference between these two timestamps constitutes the time skew of the results relative to real time. The distribution of the supervisory application's time skew over 19,281 estimation cycles – having a mean skew of 120 ms – is presented in the plot of Figure 9.11.

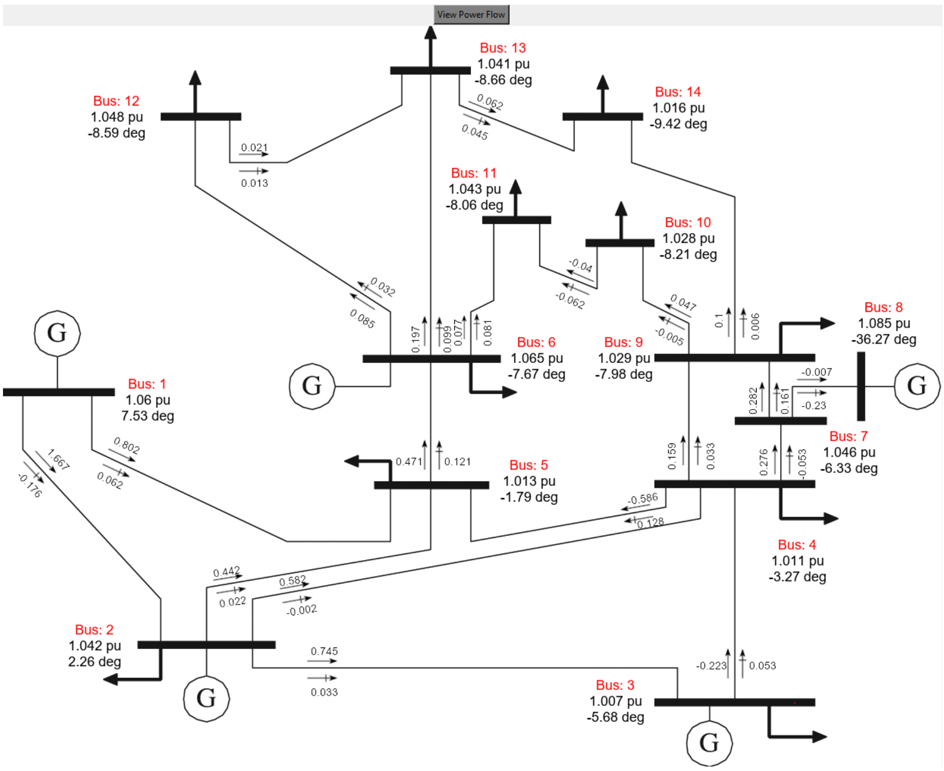

Figure 9.10: Graphical interface for monitoring bus voltages and line power flows.

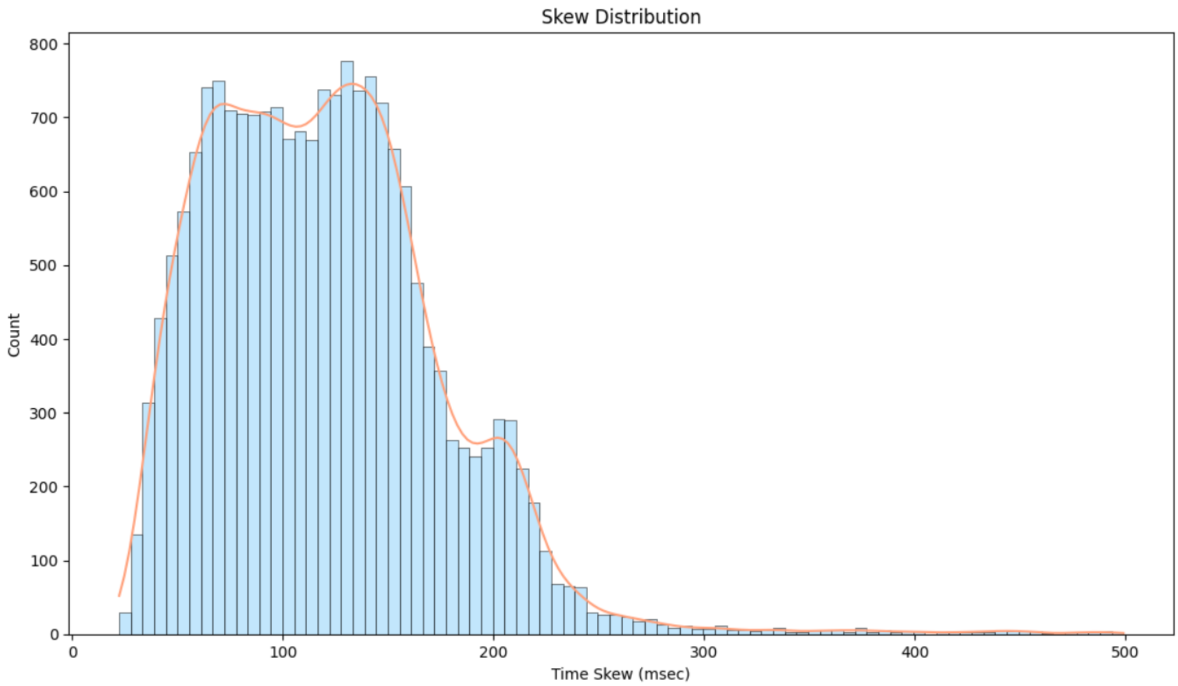

Figure 9.11: Histogram of the distribution of the ISE real-time application time skew.

9.4.2 *Online PMU-based state estimation: IEEE 14-bus network*

A MATLAB-based linear SE (LSE) algorithm is also implemented and validated using the devised test bed. The IEEE 14-bus system is simulated using the RTDS, while synchrophasors are recorded by the PMUs and collected via openPDC. The open-source MATLAB-based Synchrophasor Application Development Framework (SADF) software is then used as interface between openPDC and the real-time SE algorithm. During the simulations, the true state values are communicated from the RTDS to the MATLAB environment of the local workstation. Figure 9.12 illustrates the data flow diagram of the simulations.

In this setup we utilize the three commercial PMUs (SEL-351A), along with two low-cost prototype PMUs, presented in [295], resulting in a total of 5 hardware PMUs, each providing one 3-phase voltage and one 3-phase current phasor measurement channel. Thus, a maximum of 10 synchrophasors in total (5 voltage phasors and 5 currents) are available. However, these 10 phasor measurements are not sufficient to achieve complete observability for the 14-bus system. As the simulated network is symmetrical, i.e., phasor quantities are of equal magnitude and 120° apart in phase, and the impedances of the three-phase circuits are of equal magnitude and phase angle, we may utilize each measurement channel of the 5 hardware PMUs independently, to obtain a total of 3 voltage and 3 current phasor measurements from each device.

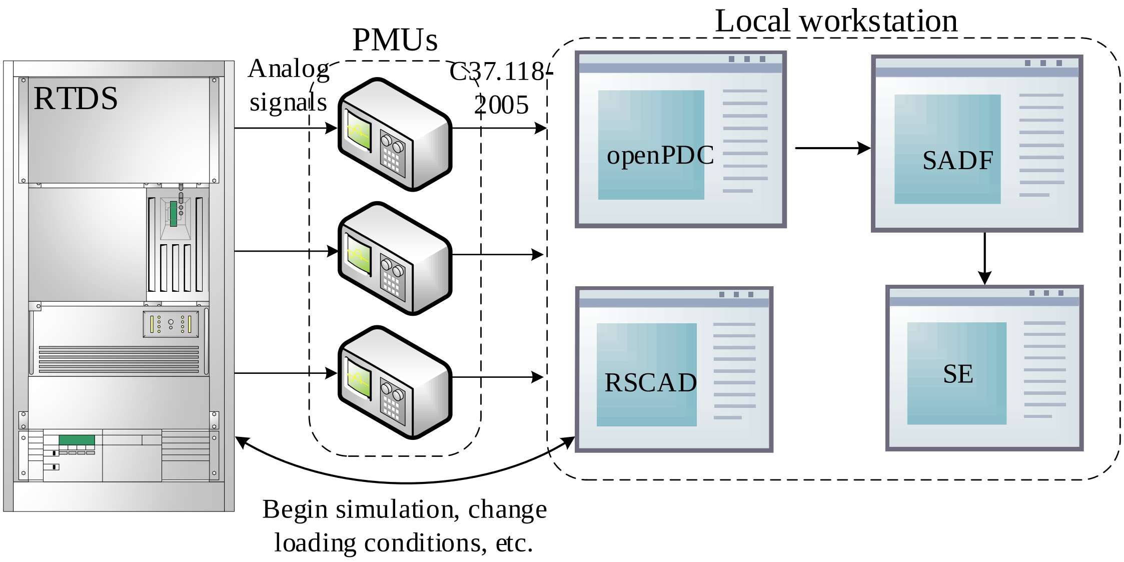

Figure 9.12: Data flow sequence for real-time PMU-based SE simulations.

To demonstrate the impact of PMU measurement redundancy to SE quality, we consider 2 MSs: MS 1 utilizes only 3 PMUs, while MS 2 uses measurements from all 5 available PMUs, as shown in Table 9.3. Each MS consists of:

- Complex voltages of phase A, at each monitored bus.
- Complex currents of phase A, at each monitored line.

To simulate the quasi-steady operating conditions, i.e., the slow fluctuation of the power system demand and generation through time, the load profile of the power system is varied within a band of ±10% of the base case value. This is accomplished by modeling all loads using the Dynamic Load component of RSCAD, which allows externally controlling the real and reactive power demand of each load during the simulation. Synchrophasor data obtained from the PMUs are aggregated by the openPDC, time-aligned, and forwarded to SADF at a reporting rate of 1 fps, so that they can be readily accessed by the MATLAB-based SE algorithm, whilst also being archived in a database for future use. The SE algorithm is implemented as a MATLAB callback function, which is executed automatically upon each new measurement acquisition. The total simulation time is 200 s, which means that the SE algorithm is executed 200 times.

From Table 9.4, it is evident that the SE algorithm provides a reliable estimate of the system states, for both MS 1 and MS 2, considering the given PMU measurement uncertainties. Even though the difference between the respective accuracy metrics of MS 1 and MS 2 is marginal, there seems to be some improvement to SE results with the addition of 16 PMU measurements. This improvement is of course expected to be more significant in larger systems, particularly in cases where there is low PMU measurement redundancy to begin with. The higher average execution time for MS 2 is due to the 16 additional measurements that need to be processed by the SE algorithm.

According to the box plots of Figure 9.13, for MS 1 the average interquartile range (IQR) is around 1.6×10^{-3} pu for voltage magnitudes, and 0.48° for voltage angles. Utilization of 16 additional PMU measurements in MS 2 (Figure 9.14), reduces the IQR to 1.4×10^{-3} pu and 0.36°, for voltage magnitudes and angles, respectively. For both MS 1 and MS 2, it is apparent that the median is equally close to the first and third quartiles, indicating that the distribution of the estimated states shows no significant skew. Finally, it appears that no more than 3 outliers are observed for each state variable, out of 200 simulations, validating that the standard deviations of the PMU measurements were selected appropriately.

Table 9.3: Online PMU-based SE measurement configurations.

MS	**Voltage Measurements (buses)**	**Current Measurements (lines)**	**Total no. of measurements**
MS 1	1,2,4,6,8,9,10,12,13	1-5,2-1,4-3,6-11,8-7, 9-14,10-9,12-13,13-14	36
MS 2	MS 1 and 3,5,11,14	MS 1 and 3-2,5-6, 11-10,14-9	52

Table 9.4: Online PMU-based SE accuracy and performance metrics.

Test Case	**Index**			
	MAE_V	MAE_A	$Macc_v$	Execution time
MS 1	1×10^{-3} pu	0.0143°	0.004 pu	1.5 ms
MS 2	8×10^{-4} pu	0.0131°	0.003 pu	2.3 ms

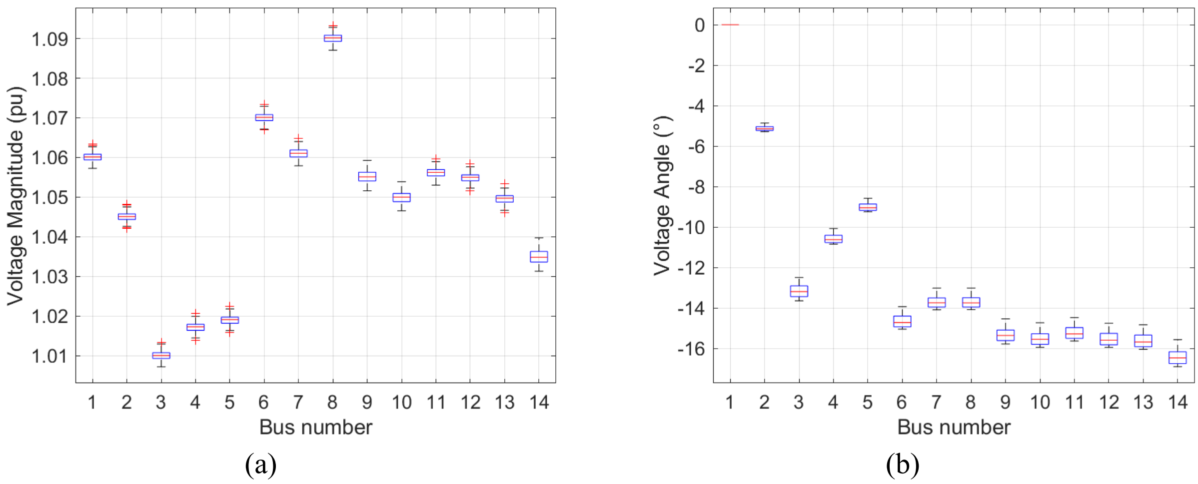

Figure 9.13: Box plots of online LSE results for MS 1: (a) voltage magnitudes, (b) voltage angles.

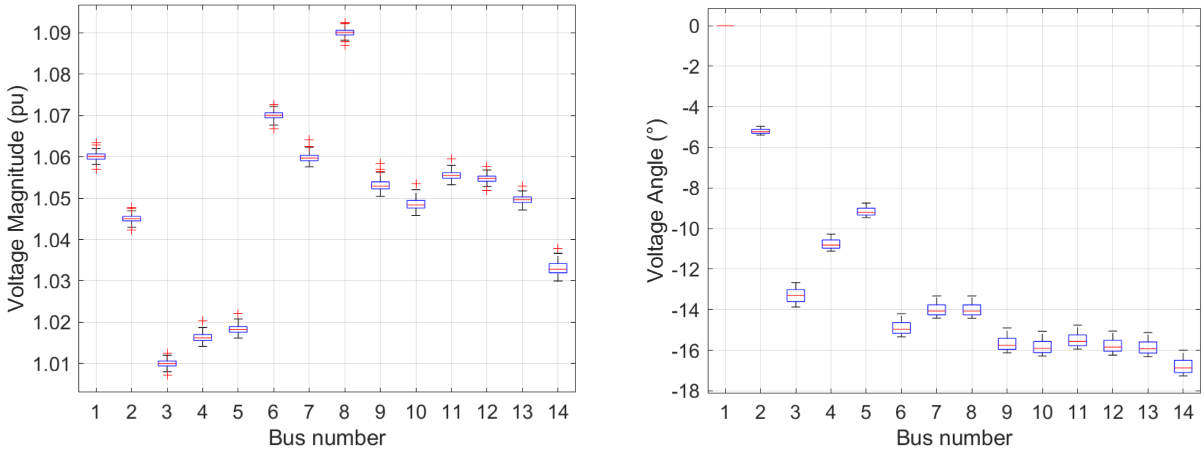

(a) (b)

Figure 9.14: Box plots of online LSE results for MS 2: (a) voltage magnitudes, (b) voltage angles.

9.4.3 HSE in active distribution grids: a case study for Kythnos island, Greece

Distribution system state estimation (DSSE) has become an undisputed necessity in ECCs for real-time monitoring and operation of ADNs, which are associated with bidirectional power flows, stochastic RES, load flexibility, and topology changes. In particular, isolated electrical systems and microgrids are among the main beneficiaries of the operation of state estimators. In this context, the implementation of DSSE tools is flourishing globally based on the long-standing academic research and field testing.

In traditional distribution networks (DNs), telemetry via SCADA typically reduced to the medium voltage (MV) busbar of primary substations, thus rendering all downstream buses unobservable unless a large number of pseudo-measurements – to the detriment of accuracy – was used. The ongoing upgrade of metering instrumentation of DNs initiated in the past decade, creates favorable conditions for implementing quality DSSE. Automated meter reading (AMR) systems and advanced metering infrastructure (AMI) based on smart meters deliver ample measurement data from customers. Following power transmission sector, synchrophasor technology gradually penetrates into distribution grids; distribution-level phasor measurement units (D-PMUs) can vitally boost the availability of actual measurements, thus expediting the consolidation of DSSE. Motivated by this promising perspective, this study showcases the exploitation of PMUs for HSE, using the ADN of Kythnos island as a testbed.

9.4.3.1 Active distribution network modelling

In order to implement the HSE algorithm in the SIL test bed, the non-interconnected 15-kV Kythnos distribution network is modeled in RSCAD and simulated on the RTDS. Principally, the full model of the Kythnos DN is represented by a 221-node grid, each one pertaining to one MV bus, and 220 branches, each one referring to one line connecting two buses. Due to hardware limitations imposed by the RTDS, the DSE simulations calculate the state estimates for a subnetwork of the Kythnos power system, comprising 29 buses and 28 branches. The network model includes the slack bus of the thermal power station (TPS), along with reduced versions of the 4 main distribution feeders (R21, R22, R23, and R24) originating from the TPS. The total number and type of each modeled bus is given in Table 9.5. The Kythnos distribution network modeled in RSCAD, is pictured in Figure 9.15.

Regarding the available measurements given the existing instrumentation of the DN, i.e., without any PMUs, the voltage magnitude at the MV busbar along with the power flows at the top of each feeder are the measurands acquired from the SCADA of the TPS. Also, real-time power injections at the PV sites are available, while virtual measurements convey error-free information about zero injection buses. It is noted that all power measurements refer to a pair of active and reactive injection or flow. In Table 9.7, a list of all measurement data utilized in the DSE simulations is provided. There is a total of 12 RTU and 36 PMU measurements. Each PMU was assumed to record two phasors (1 voltage and 1 current).

Table 9.5: Description of buses of the Kythnos network modeled in RSCAD.

Feeder	**No. of nodes with injections**			**Zero-injection buses**	**Total no. of buses**
	Slack bus	RES units	Load buses		
R21	1	0	3	3	7
R22	Common with R21	2	3	4	7
R23	Common with R21	1	3	5	8
R24	Common with R21	0	3	4	7
Aggregate	**1**	**3**	**12**	**16**	**29**

The standard deviation σ_i of measurement z_i, is given by the expression (6.98), which is repeated here for reasons of convenience:

$$\sigma_i \simeq \frac{e_{\max} z_i^{true}}{3}$$

where $e_{\max}$ is a percentage of maximum error about z_i, given according to Table 9.6.

The reason for assuming a relatively large measurement error in voltage angle measurements lies in the small differences between voltage angles of the Kythnos network, which is typical of distribution systems. As already mentioned, PMUs need near-perfect synchronization (<1 μs) with reference to UTC in order distinguish phase-angle differences lower than 0.02º. Taking into consideration the relatively low loading of each distribution feeder, it is safe to assume that voltage phase-angle measurement errors will correspond to a rather large percentage of the measured quantity. In general, by deriving the above $e_{\max}$ values from the accuracy level we expect to achieve for each measurement type, we are able to set realistic weights (standard deviations) for each measurement, which in turn greatly improves the accuracy of the HSE algorithm. The standard deviation and the value of a phase-angle measurement are expressed in radians. For all other measurements they are expressed in per-unit.

Table 9.6: Assumed maximum errors per measurement type for DN SE.

Measurement type	**$e_{\max}$ (%)**
Voltage magnitude at TPS (SCADA)	1
Power flows at TPS (SCADA)	2
Power injections from PVs	5
Phasor magnitudes (PMUs)	0.1
Phasor angles (PMUs)	1

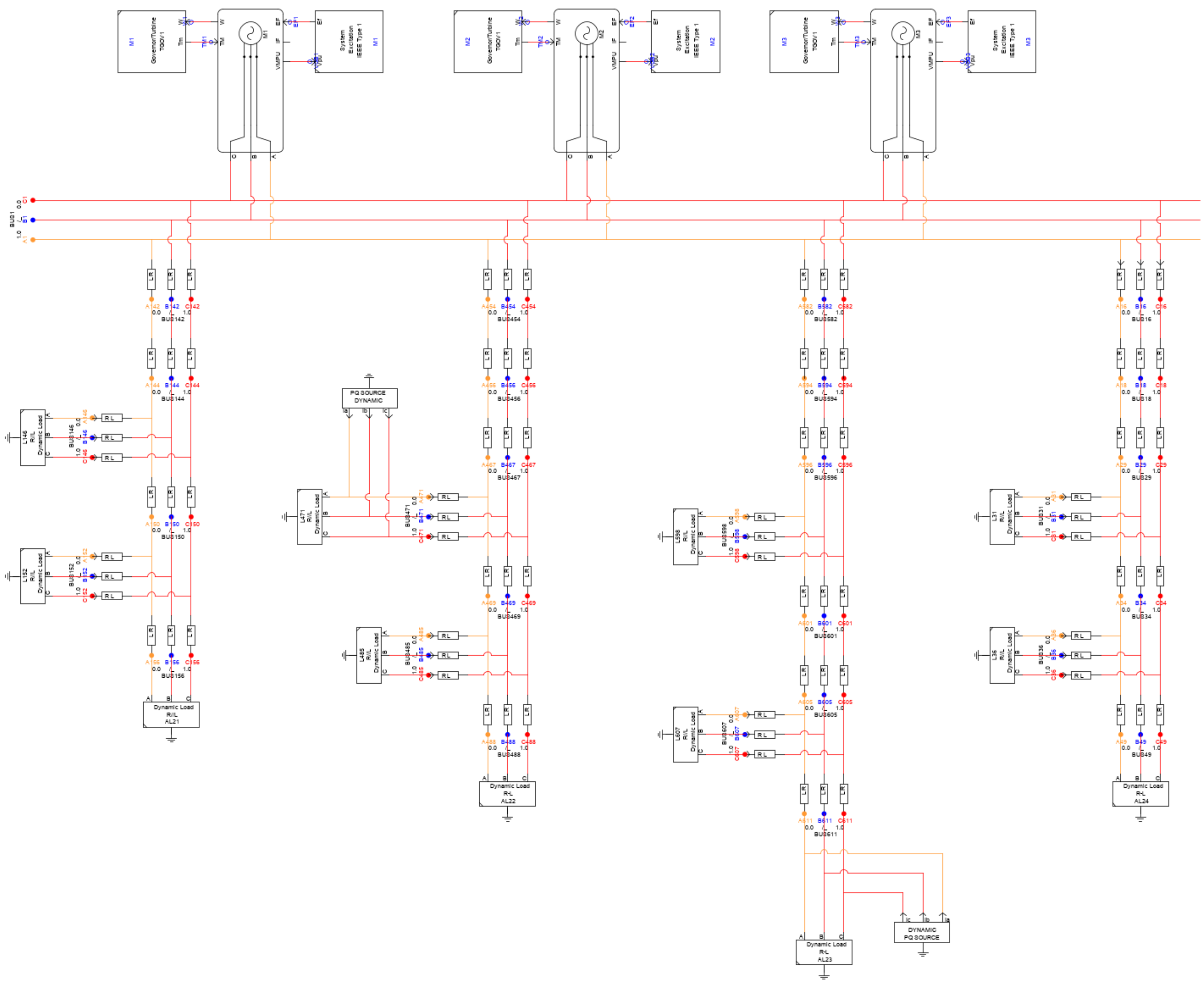

Figure 9.15: RSCAD Draft model of the 29-bus Kythnos network.

Table 9.7: Reduced Kythnos network – Type, number and source of measurements.

Network part	**Available Measurements**			**Location**
	Type	No.	Source	
Local TPS	Voltage phasor measurements	1	PMU #1	Bus 1
	Current phasor measurements	1	PMU #1	Line 1-16
Feeder R21	Voltage magnitude and power injections	1	RTU #1	Bus 156
	Voltage phasor measurements	2	PMUs #2 and #3	MV/LV buses 146, 152
	Current phasor measurements	2	PMUs #2 and #3	Lines 146-144, 152-150
	Zero current injections	3	Zero injection buses	Buses 142, 144, 150
Feeder R22	Voltage magnitude and power injections	1	RTU #2	Bus 488
	Voltage phasor measurements	2	PMUs #4 and #5	MV/LV buses 471, 485
	Current phasor measurements	2	PMUs #4 and #5	Lines 471-467, 485-469
	Zero current injections	4	Zero injection buses	Buses 454, 456, 467, 469
Feeder R23	Voltage magnitude and power injections	1	RTU #3	Bus 611
	Voltage phasor measurements	2	PMUs #6 and #7	MV/LV buses 598, 607
	Current phasor measurements	2	PMUs #6 and #7	Lines 598-596, 607-605
	Zero current injections	5	Zero injection buses	Buses 582, 594, 596, 601, 605
Feeder R24	Voltage magnitude and power injections	1	RTU #4	Bus 49
	Voltage phasor measurements	2	PMUs #8 and #9	MV/LV buses 31, 36
	Current phasor measurements	2	PMUs #8 and #9	Lines 31-29, 36-34
	Zero current injections	4	Zero injection buses	Buses 16, 18, 29, 34

For the purposes of this simulation, three different scenarios are considered, each under different loading conditions, based on past measurement datasets gathered during actual operating conditions of the Kythnos network. As regards the RES of the island, 3 photovoltaic (PV) units with total installed power of 240 kW are in operation. With the island's peak load for 2019 being approximately 3.5 MW, the following simulations are executed considering a peak load of 3.5 MW:

- **Case 1**: No RES generation combined with peak load.
- **Case 2**: Maximum RES generation, peak load.
- **Case 3**: 50% of maximum RES generation, 75% of peak load.

It is worth noting that the total RES generation of feeder R23 is considered as an aggregate active power generation on bus 611, simulating the existence of PV generation at downstream buses 679 and 892, which are not modeled in the reduced 29-bus system.

In short, the procedure of executing and validating the HSE algorithm is the following:

1) RTDS simulation of the DN is executed and measurements are obtained in real time, using the configuration of Figure 9.7. For comparison purposes, the PMU-based SE configuration of Figure 9.12 is also utilized, referred to as Linear State Estimator (LSE) for convenience.
2) The (hybrid or PMU-based) state estimator solution is produced (300 simulations for each steady-state test Case) and results are saved locally for further analysis. For the specific system conditions, the actual state vector is also obtained and stored from RSCAD.
3) Evaluation of the state estimator's accuracy and performance is conducted using various metrics.

Subsequently, all of the accuracy and performance metrics discussed above are derived as an average from 300 simulations for each operating Case, and are presented in Table 9.8 for the nonlinear ISE and the PMU-based LSE. Additionally, the results from the above simulations are depicted in the form of box plots, in order to examine the symmetry and skewness of the distribution of the state estimates. In the box plots of Figure 9.16 – 9.21, the estimation results of the ISE are presented for each simulation Case.

Table 9.8: Reduced Kythnos network – SE accuracy and performance metrics.

Metric	**System Loading**					
	Case 1		**Case 2**		**Case 3**	
	ISE	LSE	ISE	LSE	ISE	LSE
MAE_V (pu)	0.0026	0.0009	0.0027	0.0010	0.0028	0.0009
MAE_A (°)	0.0017	0.0023	0.0018	0.0021	0.0015	0.0021
$Macc_V$ (pu)	0.0209	0.0131	0.0217	0.0142	0.0207	0.0130
EEI	20.786	15.737	18.638	15.153	19.949	15.239
MAPE (%)	0.2625	0.0869	0.2682	0.0890	0.2783	0.0866
Time (ms)	2.7	0.9	2.7	1	2.8	0.9
Iterations	2	1	2	1	2	1

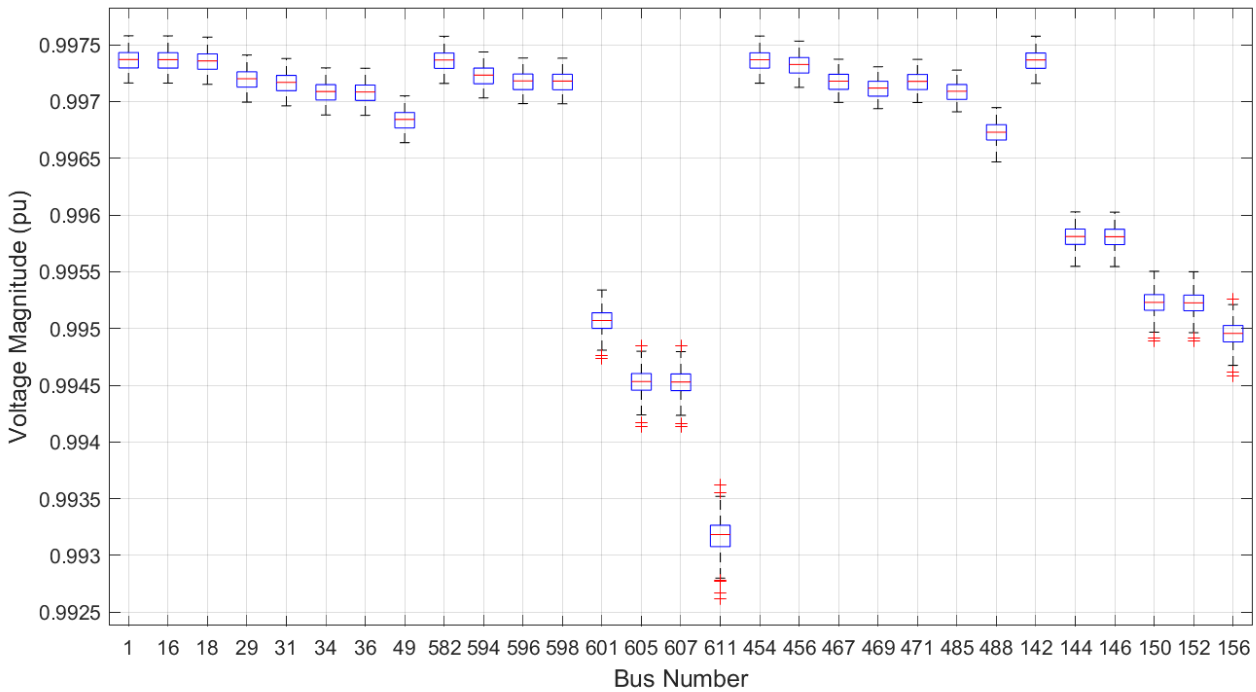

Figure 9.16: Kythnos DN ISE – Estimated bus voltage magnitudes for Case 1.

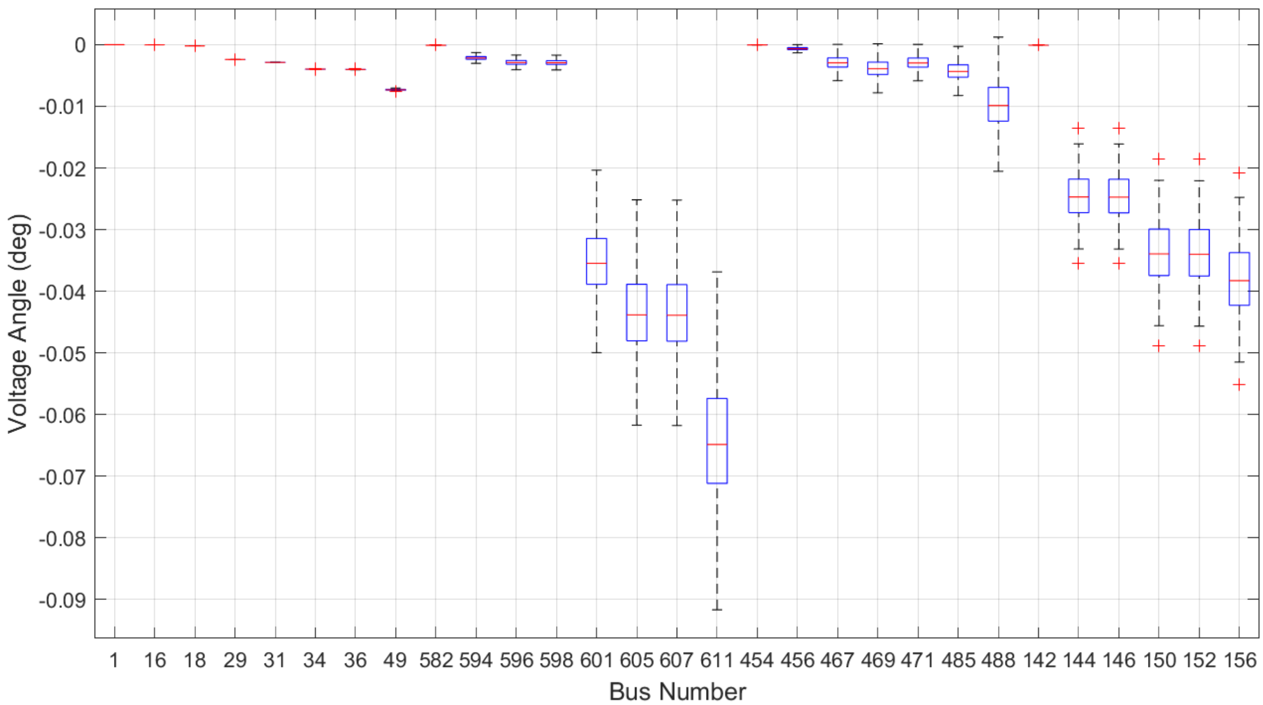

Figure 9.17: Kythnos DN ISE – Estimated bus voltage angle for Case 1.

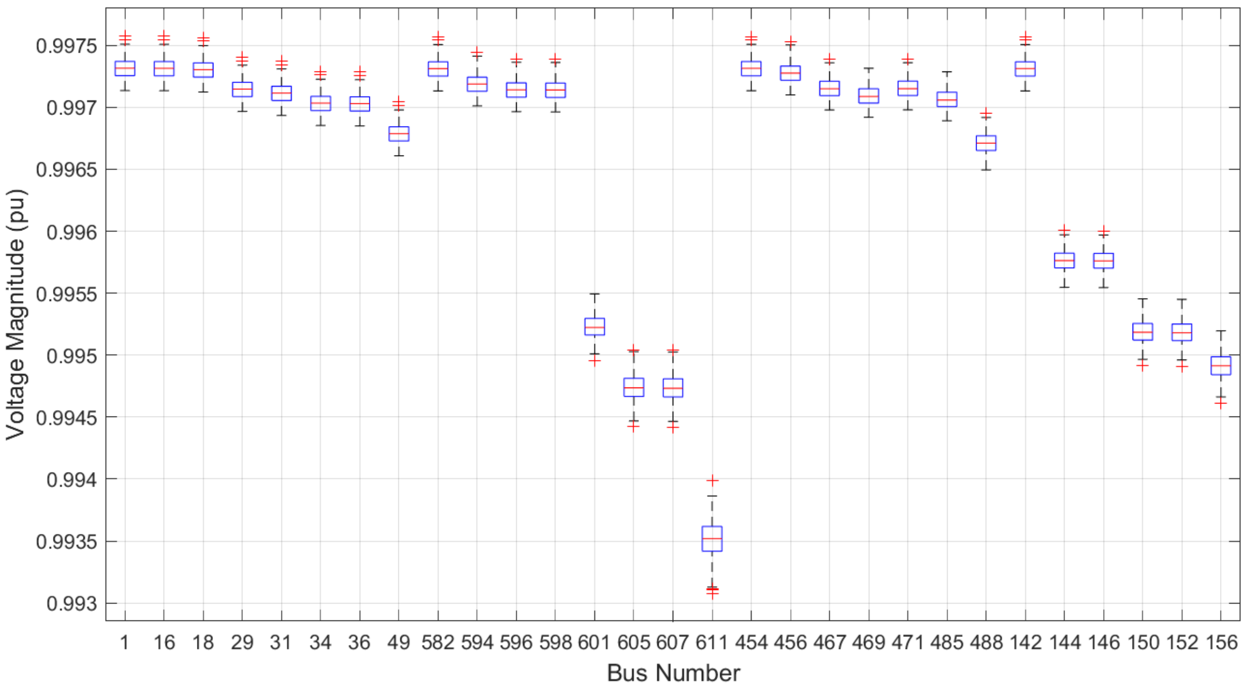

Figure 9.18: Kythnos DN ISE – Estimated bus voltage magnitudes for Case 2.

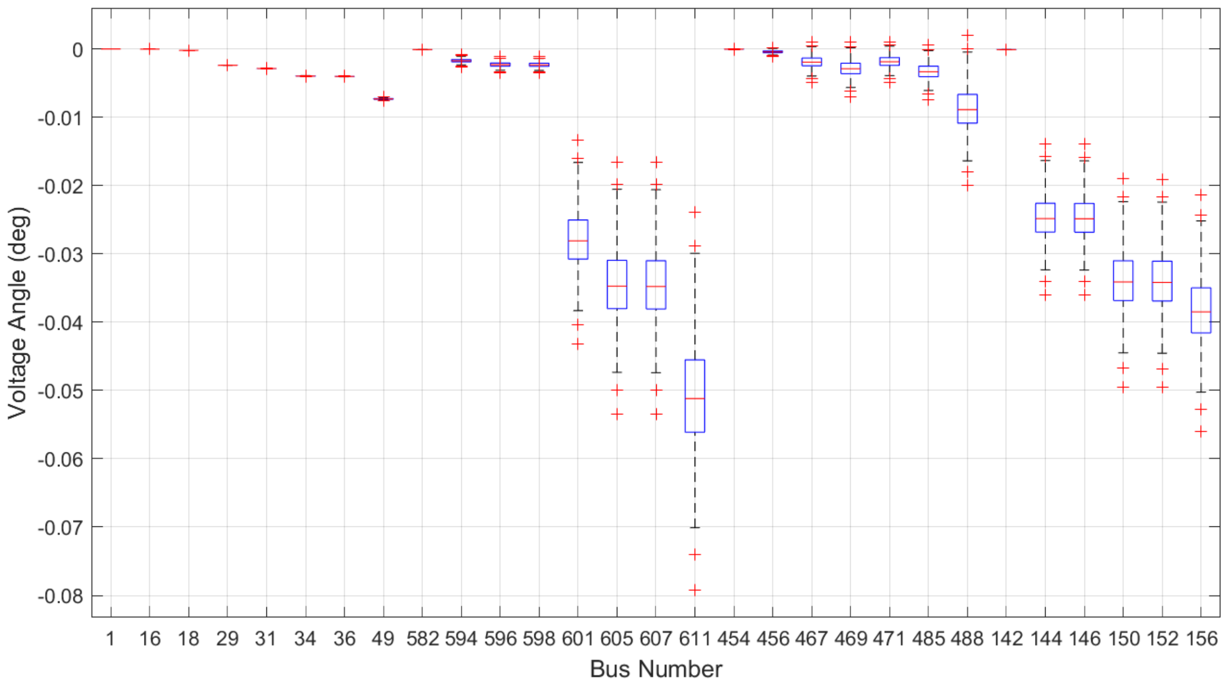

Figure 9.19: Kythnos DN ISE – Estimated bus voltage angles for Case 2.

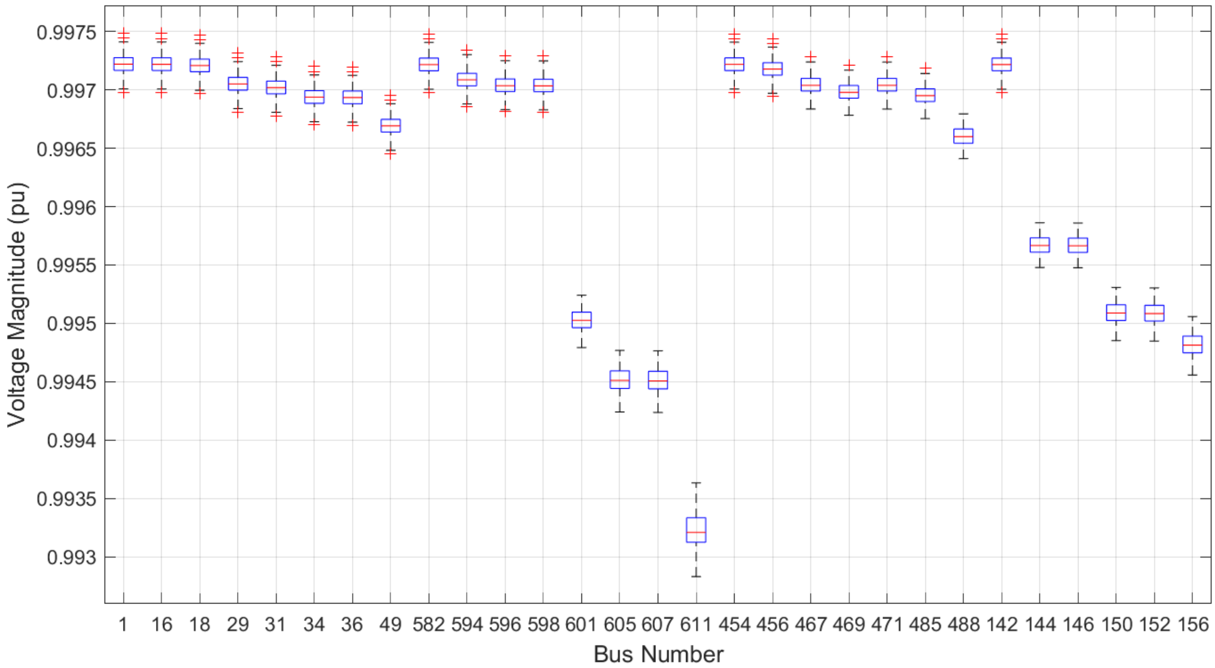

Figure 9.20: Kythnos DN ISE – Estimated bus voltage magnitudes for Case 3.

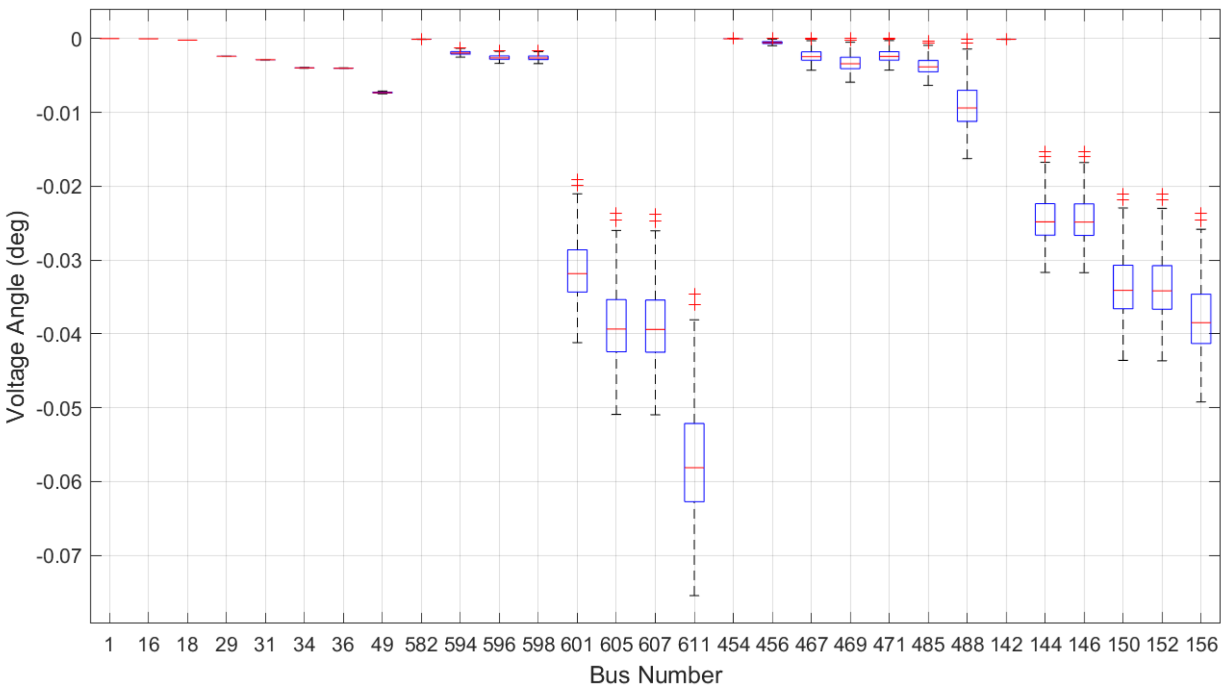

Figure 9.21: Kythnos DN ISE – Estimated bus voltage angles for Case 3.

9.4.3.2 Results evaluation

Judging by the accuracy metrics presented in Table 9.8, the following points are to be noted:

- According to MAE_V and MAE_A the proposed DSE algorithm can provide a reliable real-time snapshot of the power system states within a numerical tolerance of 3×10^{-3} pu and 2×10^{-3} degrees, for ISE, and 1×10^{-3} pu and 2×10^{-3} degrees for LSE, independently of simulation Case. The marginal improvement of the state estimate quality for the PMU-only SE over those of the HSE, is a direct result of utilizing only high-accuracy PMU measurements, instead of incorporating both PMU and RTU measurements. Note that the slight increase observed in MAE_A could be attributed to reduced measurement redundancy, as the PMU-only SE measurement quantity is reduced by 12, compared to the hybrid method.
- $Macc_V$ is of the order of 2×10^{-2} pu (1×10^{-2} pu) for hybrid (PMU-based) SE, which is acceptable considering the given meter uncertainties. Again, the accuracy metric shows minor improvement when only synchrophasors are considered. From the two Tables, it is also evident that $Macc_V$ is slightly higher for Case 2, which is expected, as according to literature estimation errors are usually larger for maximum loading conditions.
- The theoretical maximum value of EEI is:

  $$EEI_{\max}^{H} = \sum_{i=1}^{m_s+m_p}\left(\frac{3\sigma_i}{\sigma_i}\right)^2 = 9(m_s+m_p) = 9\times48 = 432\text{, for ISE, and}$$

  $$EEI_{\max}^{P} = \sum_{i=1}^{m_p}\left(\frac{3\sigma_i}{\sigma_i}\right)^2 = 9m_p = 9\times36 = 324\text{, for PMU-based LSE.}$$

  Notice that all EEI indices are very low, compared to their corresponding $EEI_{\max}$ values (~5% of $EEI_{\max}$), which essentially confirms the accuracy levels for both PMU and RTU measurements, as well as the good time quality (synchronization) of the obtained phasor angle measurements.
- Finally, the obtained *MAPE* values also aid in confirming the satisfactory quality of the state estimates, with an absolute difference of around 0.27% between estimated and true values of voltage magnitudes. This difference is even lower for the PMU-only SE module (~0.09%).

As far as the performance metrics are concerned, the ISE algorithm converges in 2 iterations, and requires approximately 2.8 ms of execution time, which is very efficient for a 29-bus system. As expected, the linear PMU-only SE converges even faster (~1 ms). The total execution time of the SE is of significant importance, as it should ideally be much lower than the measurement update period. In our case, this holds true for both PMU (20 ms) and RTU (2 s) measurements. It should be noted, however, that increasing the network size, i.e., simulating the entire 221-node Kythnos network, would naturally result in longer computation times and potentially a higher number of required iterations.

The statistical evaluation using box plots further validates the accuracy of the estimation results. Across all test cases, the interquartile range for voltage magnitude estimates is consistently around 10^{-4} pu, which is acceptable given the assumed measurement error bounds. A similar level of accuracy is observed for most voltage phase angle estimates, although slight degradation is noted at buses observable only through RTUs. Importantly, the symmetry of the box plots – where the median lies approximately equidistant between the first and third quartiles – suggests that the distribution of the estimated states demonstrates no significant skew. Furthermore, for all system states, the median aligns closely with the true values obtained from RSCAD. Given the near-identical median and mean values, this symmetry confirms that the implemented SE methods provide unbiased estimates of the system states. Finally, the number of outliers remains low for all Cases, being marginally higher for RTU-observable buses.

9.4.4 Conclusions

In this Chapter, a laboratory configuration for implementing and testing various synchrophasor applications has been presented. Physical PMUs and software PDCs were used to obtain measurements from power systems simulated in the RTDS, while hybrid and PMU-based SE algorithms were tested in real time. At this stage, we can deduce two major factors that should be taken into consideration when evaluating the SE results in terms of their accuracy and reliability, within the presented laboratory framework:

1) The measurement devices used (both hardware and software) are not connected to the simulated power system using VTs or CTs. As such, the measurement errors typically introduced by instrument transformers are not reflected in the current setup. As was clarified in Subsection 3.4, there are two sources of error in instrument transformers, namely ratio error and phase angle error. In a given transformer, the metering error is the combination of the two separate errors, which should realistically be around 0.5%, and 0.344º, for modern high-accuracy ITs. The overall metering error depends on the specific characteristics of the installed VTs/CTs and the error compensation algorithms implemented by the PMU manufacturer. In real-world systems, these errors contribute to small but non-negligible deviations in measurement accuracy, and, as they are absent from the laboratory results, they should be considered when extrapolating findings to field deployments.
2) The SEL-351A PMUs used in the laboratory setup benefit from ideal time synchronization conditions: all devices are placed in the same location, and share a common GPS antenna. This configuration ensures near-perfect synchronization accuracy, likely resulting in phase angle measurement errors that are even lower than those expected in field installations. According to IEEE C37.118-2011, phase angles should be ideally measured with an accuracy of around 0.02°, regardless of location of the PMUs. This is of course considered under perfect (low-latency) synchronization of the PMUs to the common time reference. That being said, in field conditions, synchronization delays and signal propagation effects often introduce additional errors, meaning that real-world phase angle measurements may be less precise than those recorded in the laboratory. Furthermore, in distribution systems, voltage phasor angles tend to differ by only very small margins, making them especially sensitive to synchronization errors. When applying WLS-based SE algorithms in such contexts, it is crucial to assign appropriate weights to phase angle measurements to ensure numerical stability and estimation accuracy.

10. Conclusions and Prospects

The entirety of the research carried out within the scope of this dissertation is presented in detail in Chapters 5 – 9. In this Chapter, a brief recap of the work is followed by a summary of the principal research findings. Finally, the research prospects regarding power system state estimators are noted, and a framework for future investigation is proposed.

10.1 Recapitulation and conclusions

The subject of this dissertation is the utilization of different measurement types with diverse characteristics for conducting power system static and dynamic state estimation. The main criteria for evaluating the performance of the proposed methods pertain to three main objectives: a) improving state estimation accuracy, b) being technically feasible within the existing EMS, c) forming a complete and viable framework for continuous, real-time operation. In this context, the methods developed in this thesis are essentially modified and enhanced versions of well-established WLS-based SSE and FASE techniques, which are implemented so as to satisfy the three aforementioned criteria.

After expanding on the background and motivations of the thesis in Chapter 1, the 2nd Chapter delves into the fundamental functionalities and elaborates on the typical architecture of modern SCADA/EMS systems. Chapter 3 then introduces the reader to the concept of synchrophasors and the broader WAMS, highlighting the role of PMUs as the backbone of enhanced, dynamic and reliable power system monitoring, and providing an overview of their functionalities. Chapter 4 performs an introduction into power system monitoring and, specifically, the basics of WLS state estimation. The derivation of the WLS formulation, along with all relevant mathematical modeling, in terms of power system components and measurement functions, and the different solution methods of the SE problem are provided here in detail, to serve as reference for the rest of the thesis. Chapter 5 specifies the focus of the thesis, that is, the exploration of novel HSE methods, by presenting a thorough literature review, and deducing several topics for future research.

The 6th Chapter presents the main body of research of the thesis into hybrid SSE methods, split into two parts: the first elaborates on the derivation of the proposed SE algorithms, and the second presents their application to IEEE benchmark transmission systems and to distribution networks reported in international studies. Here, the proposed methods refer to:

1) A novel multi-stage SSE framework, based on the Hachtel's augmented matrix formulation, for performing HSE with a limited number of PMU measurements.
2) An equality-constrained hybrid SSE formulation, for the inclusion of classic HVDC links into the SE process.
3) The investigation of the inclusion of current injection phasor measurements into HSE algorithms, focusing on its significance for distribution networks.

Chapter 7 continues with the contributions of this thesis, by presenting the detailed derivation of a multi-stage EKF-based hybrid FASE framework, which utilizes the modified Bryson-Frazier smoothing algorithm to refine the SE results, by calculating the temporal correlation of past and future measurements. Extensive simulations on IEEE benchmark transmission systems are leveraged to evaluate its performance, under varying system conditions. As bad data analysis is arguably one of the most important functionalities of a state estimator, Chapter 8 crucially addresses the formulation of bad data detection, identification and removal algorithms for the proposed HSE methods of Chapters 6 and 7.

Finally, Chapter 9 focuses on a more practical aspect of this research, by presenting the implementation process and utilization of a laboratory-scale platform built specifically to simulate the function of a synchrophasor network, from the power system to the actual PMU-based application. In the context of this work, the setup is used to test the real-time performance of hybrid and PMU-based SE algorithms presented in Chapters 4 and 6 of the thesis, on a transmission system, as well as on a reduced version of the distribution network of Kythnos island.

In light of the research work summarized above, the principal conclusions of this PhD dissertation are as follows.

10.1.1 Hybrid state estimation as reference

Based on the detailed literature review in Chapter 5, as the integration of PMUs increases, especially in transmission sector, it necessitates implementation of some form of hybrid SE, which leverages the recorded synchrophasor quantities as complementary information to the conventional SCADA measurements. The relevant literature on HSE is now quite mature, and it can be confidently stated that there has lately been a shift away from physics-driven towards data-driven methods. This is an expected and logical course, as there is an abundance of measurement points in power systems today, with monitoring tools such as WAMS collecting hundreds of data points each second. As the computational capabilities of modern hardware increase, it is highly likely that the HSE problem will eventually be infused with big data analytics and will move away from the model-based methods used thus far, such as the WLS formulation. Another key change to keep in mind is the decentralization of monitoring and control functions, as a result of substation digitalization. The concept of HSE as described and explored in this dissertation may become obsolete in the far future, as the centralized monitoring paradigm moves away from the ECC towards substation-based distributed SE. Nevertheless, for now, it is critical to continue enhancing the WLS model by leveraging synchronized phasor measurements together with conventional measurements, as it is the most widely adopted and reliable implementation of the SE algorithm.

10.1.2 Practical aspects of HSE

Although research on the integration of PMU data into SE now spans almost two decades, literature has focused mainly on its theoretical aspects. Seeing that in many ECCs, the SE software is now dated, having been developed for conducting SSE under SCADA information, with basic filtering and bad data detection functionalities, it is of utmost importance to fill this practical gap. The enhancement of SSE software with PMU measurements and additional capabilities, without altering it internally, which is often impractical or impossible as the software is usually proprietary, is a sound and viable way to modernize it and bring it up to speed with the dynamic nature of contemporary power networks. This is why in this dissertation, apart from enhancing the accuracy of WLS SE, there is also the focus of proposing practical algorithms, which attempt to avoid mixing the SCADA and PMU measurements, thus circumventing various implementation issues that were highlighted in the literature review of Chapter 5.

Furthermore, as mentioned in the Motivations of the thesis the inclusion of not only new measurement systems, but also increasingly deployed power system components, is crucial to the topic of SE. Under this premise, another practical aspect of SE explored in this thesis is the modeling of CSC-HVDC links for integration into the widely adopted WLS-based HSE. It should be noted that, although similar methods have been proposed in the literature, they do not devise as detailed a model of the HVDC link, and the formulated SE models are linearized to reduce computational complexity, at the cost of accuracy.

Last but not least, acknowledging that few suggestions have been made to the utilization of current injection phasor measurements, a scheme for including these PMU measurements in HSE is proposed, in terms of both the circuit-level measurement point, and the explicit mathematical modeling of these measurements in the SE model. Simulation results indicate that, for transmission networks, a combination of line flow and bus injection current phasors may yield better SE results in terms of accuracy and convergence, than exclusively allocating either type of current measurements to the available

PMUs. Furthermore, the proposed measurement scheme is highly applicable to distribution networks, in which case further research is necessary to solidify the impact of the different PMU configurations in SE performance, due to the inherent complexities of modern ADNs.

10.1.3 Details in implementation of FASE

Thus far, even though the concept of FASE, and of DSE in general, has been extensively studied, the relevant literature has not adequately addressed the actual implementation of FASE in a multi-source and multi-rate measurement environment. Furthermore, there are several key topics of interest for applying FASE methods that, to the best of the author's knowledge, have not been investigated: the origin and proper utilization of the historical information for constructing the state-forecasting (transition) model, the optimal selection of parameters for the Holt's model (many works simply mention calculating them "from offline simulations", without providing any further insights), as well as the proper weighting of the *a priori* state information in the SE problem, i.e., selection of the values of matrix $\boldsymbol{Q}$ (simply selecting "static, low values" of the order of 10^{-6} as proposed in several articles, not only diminishes the information provided by assigning proper uncertainties to the forecasted state variables, but is also found to negatively affect FASE results on several occasions). This PhD thesis attempts to cover all the aforementioned topics and thus serves as groundwork for future research endeavors on the topic of FASE.

10.1.4 Importance of DRTS in the deployment of synchrophasor applications

To improve the processes of conceptual design and validation of synchrophasor-based applications, this thesis suggests that DRTS architectures constitute a robust and cost-effective way to test novel methods prior to field deployment. Specifically, the most important HIL use cases include PMU compliance testing, WAMPAC application validation, and time synchronization spoofing studies. Regarding PMU functional testing, it can be expected that as synchrophasor applications evolve in scope and capabilities, there will be more demanding requirements on harmonic filtering, frequency response and sampling rate, which are not necessarily assessed in the standard PMU functional tests. An application-specific functional test can be easily implemented using an RTS. As for testing WAMPAC applications, the use cases show that DRTS provides confidence in deploying new applications and accelerating the development and validation process, thanks to its capability of simulating power network dynamics and its versatile interface to hardware devices and communication network. In addition, a validated system model could also be used directly in other studies, which would simplify the modeling tasks and accelerate a study's progress. From the cybersecurity perspective, a secure, fast and reliable synchrophasor data communication network is needed. An RTS can be part of a cyber-physical simulation setup to provide a closed-loop validation of the communication network reliability. Moreover, for educational purposes, real-time simulation can provide operators, researchers and students with adequate data to learn about the system behavior under different contingencies, with and without the actions of the synchrophasor-based applications.

For the purposes of SE and other open-loop, real-time monitoring applications (oscillations monitoring, voltage stability monitoring, etc.) DRTS is found to offer a very flexible and appealing alternative to offline software-based simulations. In this thesis, a versatile laboratory-scale platform consisting of an RTS, physical PMUs and software PDCs is used to validate HSE algorithms that were only tested using offline simulations (with data generated from power flow studies) in previous Chapters, utilizing open-loop DRTS. The findings confirm the performance of the proposed algorithms in a miniature WAMS, highlighting the nuances that have to be considered when conducting HSE or PMU-based SE in practice, particularly in distribution networks. In summary, it is concluded that DRTS can and should be used in multiple ways in tandem with PMUs, to test existing and develop novel synchrophasor applications.

10.2 Prospects and future research

Even though substantial progress has been made in the field of HSE, several critical challenges and open questions remain. In particular, the advancement of HSE is closely intertwined with emerging developments in adjacent domains, such as power-electronics-dominated grids, integrated energy systems, cyber-physical infrastructures, and the Internet of Things (IoT). These intersections present both opportunities and complexities that warrant deeper investigation. In light of this, the following directions are proposed to guide future research efforts:

1) *Measurement model*: Enhancing the HSE measurement model is a key area for future research. Traditional measurement models assume Gaussian, stationary, and uncorrelated noise, which is often invalid in real-world settings, with noise statistics becoming even more complex when multiple data sources are integrated. Additionally, the increasing integration of FACTS, HVDC, and DERs introduces new network modeling challenges, necessitating adjustments in both measurement models and parameter estimation techniques. Advanced mathematical formulations are needed to accommodate diverse combinations of system components and measurement data, broadening the scope of current SE modeling frameworks.
2) *State transition models*: Most of the existing DSE and FASE methods perform prediction by naive heuristics such as weighted averages of preceding time-series data. The optimality of these transition models is neither theoretically justified nor based on sufficient empirical evidence, limiting the performance especially with the uncertainty introduced by DERs. To obtain more reliable state estimates, state prediction and filtering must be made robust against the uncertainties inherent in power systems. Techniques like pattern recognition could help capture the effects of stochastic components, such as DERs. Multi-area, numerically robust, and efficient data-driven DSE methods represent promising directions for future exploration. Testing and validating DSE methods with real-world field data is also imperative, particularly under transient conditions where PMU accuracy can decline. To improve upon TSE and FASE methods, future research could consider simultaneous topology and parameter estimation, the correlation between different PMU channels and successive measurement scans, as well as more advanced techniques for state forecasting and state transition modeling.
3) *Network model uncertainty and estimation*: SE techniques operate under the assumption that the underlying network model is fully accurate. However, in practice, both topology errors and parameter inaccuracies are common and can significantly degrade estimation quality. This challenge is especially pronounced in distribution networks, where detailed and reliable system models are often incomplete or unavailable. To address this, there is growing potential in physics-informed, data-driven approaches that blend physical network knowledge with high-volume sensor data.
4) *Integration of data from RES*: One of the main drivers for advancing SE technologies is the growing variability introduced by renewable generation. Modern smart inverters are capable of reporting highly detailed measurements, offering a rich data source for enhanced observability. Additionally, under high renewable penetration, system states are often strongly linked to weather conditions such as solar irradiance, wind speed, and temperature. However, current SE methods rarely incorporate data from smart inverters or meteorological sources. Exploring ways to fuse these non-electrical data streams could significantly improve estimation accuracy – particularly in scenarios where electrical measurements alone are insufficient.
5) *Fusion of measurement data from different physical representations of the system*: As power systems increasingly integrate inverter-based resources, the influence of fast-switching dynamics becomes more prominent. Notably, phasor data from PMUs are based on RMS models, while sampled-value data from MUs, DFRs, and similar devices are derived from EMT models. Because

these models reflect different time scales and dynamic behaviors, integrating their respective data streams within a unified dynamic state estimation framework remains an open and critical research area.

6) *Universal frameworks for integrating heterogeneous measurements*: Most current approaches to integrating multiple types of measurements (e.g., SCADA with PMU or SCADA with AMI data) are highly case-specific. As more diverse and advanced sensors are deployed across the grid, such ad-hoc solutions will not scale to meet future needs. To enable robust and flexible state estimation, there is a clear need for generalized data fusion frameworks that can integrate any combination of measurement types, regardless of source or format.

Appendix A

In this Appendix, the mathematical expressions of the elements of the measurement Jacobian matrices of Chapter 4 are provided.

- Voltage and current magnitude measurements – state vector in polar coordinates:

$$\frac{\partial V_i}{\partial V_i} = 1 \tag{A.1}$$

$$\left.\begin{aligned}
\frac{\partial I_{ij}}{\partial V_i} &= \frac{C_{ij}V_i + V_j\left(E_{ij}\cos(\delta_i - \delta_j) + F_{ij}\sin(\delta_i - \delta_j)\right)}{\sqrt{C_{ij}V_i^2 + D_{ij}V_j^2 + 2V_iV_j\left(E_{ij}\cos(\delta_i - \delta_j) + F_{ij}\sin(\delta_i - \delta_j)\right)}} \\
\frac{\partial I_{ij}}{\partial V_j} &= \frac{D_{ij}V_j + V_i\left(E_{ij}\cos(\delta_i - \delta_j) + F_{ij}\sin(\delta_i - \delta_j)\right)}{\sqrt{C_{ij}V_i^2 + D_{ij}V_j^2 + 2V_iV_j\left(E_{ij}\cos(\delta_i - \delta_j) + F_{ij}\sin(\delta_i - \delta_j)\right)}} \\
\frac{\partial I_{ij}}{\partial \delta_i} &= \frac{V_iV_j\left(E_{ij}\cos(\delta_i - \delta_j) - F_{ij}\sin(\delta_i - \delta_j)\right)}{\sqrt{C_{ij}V_i^2 + D_{ij}V_j^2 + 2V_iV_j\left(E_{ij}\cos(\delta_i - \delta_j) + F_{ij}\sin(\delta_i - \delta_j)\right)}} \\
\frac{\partial I_{ij}}{\partial \delta_j} &= \frac{V_iV_j\left(E_{ij}\sin(\delta_i - \delta_j) - F_{ij}\cos(\delta_i - \delta_j)\right)}{\sqrt{C_{ij}V_i^2 + D_{ij}V_j^2 + 2V_iV_j\left(E_{ij}\cos(\delta_i - \delta_j) + F_{ij}\sin(\delta_i - \delta_j)\right)}}
\end{aligned}\right\} \tag{A.2}$$

- Active and reactive power flow measurements – state vector in polar coordinates:

$$\left.\begin{aligned}
\frac{\partial P_{ij}}{\partial V_i} &= 2t_{ij}^2(g_{sij} + g_{ij})V_i - t_{ij}t_{ji}V_j\left(g_{ij}\cos(\delta_{ij} + \Delta\varphi_{ij}) + b_{ij}\sin(\delta_{ij} + \Delta\varphi_{ij})\right) \\
\frac{\partial P_{ij}}{\partial V_j} &= -t_{ij}t_{ji}V_i\left(g_{ij}\cos(\delta_{ij} + \Delta\varphi_{ij}) + b_{ij}\sin(\delta_{ij} + \Delta\varphi_{ij})\right) \\
\frac{\partial P_{ij}}{\partial \delta_i} &= -t_{ij}t_{ji}V_iV_j\left(b_{ij}\cos(\delta_{ij} + \Delta\varphi_{ij}) - g_{ij}\sin(\delta_{ij} + \Delta\varphi_{ij})\right) \\
\frac{\partial P_{ij}}{\partial \delta_j} &= t_{ij}t_{ji}V_iV_j\left(b_{ij}\cos(\delta_{ij} + \Delta\varphi_{ij}) - g_{ij}\sin(\delta_{ij} + \Delta\varphi_{ij})\right)
\end{aligned}\right\} \tag{A.3}$$

$$\left.\begin{aligned}
\frac{\partial Q_{ij}}{\partial V_i} &= -2t_{ij}^2(b_{sij} + b_{ij})V_i + t_{ij}t_{ji}V_j\left(b_{ij}\cos(\delta_{ij} + \Delta\varphi_{ij}) - g_{ij}\sin(\delta_{ij} + \Delta\varphi_{ij})\right) \\
\frac{\partial Q_{ij}}{\partial V_j} &= t_{ij}t_{ji}V_i\left(b_{ij}\cos(\delta_{ij} + \Delta\varphi_{ij}) - g_{ij}\sin(\delta_{ij} + \Delta\varphi_{ij})\right) \\
\frac{\partial Q_{ij}}{\partial \delta_i} &= -t_{ij}t_{ji}V_iV_j\left(b_{ij}\sin(\delta_{ij} + \Delta\varphi_{ij}) + g_{ij}\cos(\delta_{ij} + \Delta\varphi_{ij})\right) \\
\frac{\partial Q_{ij}}{\partial \delta_j} &= t_{ij}t_{ji}V_iV_j\left(b_{ij}\sin(\delta_{ij} + \Delta\varphi_{ij}) + g_{ij}\cos(\delta_{ij} + \Delta\varphi_{ij})\right)
\end{aligned}\right\} \tag{A.4}$$

- Active and reactive power injection measurements – state vector in polar coordinates:

$$\left.\begin{aligned}
\frac{\partial P_i}{\partial V_i} &= 2G_{ii}V_i + \sum_{j\in a(i)} V_j\left(G_{ij}\cos\delta_{ij} + B_{ij}\sin\delta_{ij}\right)\\
\frac{\partial P_i}{\partial V_j} &= V_i\left(G_{ij}\cos\delta_{ij} + B_{ij}\sin\delta_{ij}\right)\\
\frac{\partial P_i}{\partial \delta_i} &= V_i\sum_{j\in a(i)} V_j\left(B_{ij}\cos\delta_{ij} - G_{ij}\sin\delta_{ij}\right)\\
\frac{\partial P_i}{\partial \delta_j} &= V_iV_j\left(G_{ij}\sin\delta_{ij} - B_{ij}\cos\delta_{ij}\right)
\end{aligned}\right\} \quad \text{(A.5)}$$

$$\left.\begin{aligned}
\frac{\partial Q_i}{\partial V_i} &= -2B_{ii}V_i + \sum_{j\in a(i)} V_j\left(G_{ij}\sin\delta_{ij} - B_{ij}\cos\delta_{ij}\right)\\
\frac{\partial Q_i}{\partial V_j} &= V_i\left(G_{ij}\sin\delta_{ij} - B_{ij}\cos\delta_{ij}\right)\\
\frac{\partial Q_i}{\partial \delta_i} &= V_i\sum_{j\in a(i)} V_j\left(G_{ij}\cos\delta_{ij} + B_{ij}\sin\delta_{ij}\right)\\
\frac{\partial Q_i}{\partial \delta_j} &= -V_iV_j\left(G_{ij}\cos\delta_{ij} + B_{ij}\sin\delta_{ij}\right)
\end{aligned}\right\} \quad \text{(A.6)}$$

- Voltage and current magnitude measurements – state vector in rectangular coordinates:

$$\left.\begin{aligned}
\frac{\partial V_i}{\partial V_{\mathrm{R},i}} &= \frac{V_{\mathrm{R},i}}{\sqrt{V_{\mathrm{R},i}^2 + V_{\mathrm{I},i}^2}}\\
\frac{\partial V_i}{\partial V_{\mathrm{I},i}} &= \frac{V_{\mathrm{I},i}}{\sqrt{V_{\mathrm{R},i}^2 + V_{\mathrm{I},i}^2}}
\end{aligned}\right\} \quad \text{(A.7)}$$

$$\left.\begin{aligned}
\frac{\partial I_{ij}}{\partial V_{\mathrm{R},i}} &= \frac{C_{ij}V_{\mathrm{R},i} + E_{ij}V_{\mathrm{R},j} - F_{ij}V_{\mathrm{I},j}}{\sqrt{C_{ij}\left(V_{\mathrm{R},i}^2 + V_{\mathrm{I},i}^2\right) + D_{ij}\left(V_{\mathrm{R},j}^2 + V_{\mathrm{I},j}^2\right) + 2E_{ij}\left(V_{\mathrm{R},i}V_{\mathrm{R},j} + V_{\mathrm{I},i}V_{\mathrm{I},j}\right) + 2F_{ij}\left(V_{\mathrm{I},i}V_{\mathrm{R},j} - V_{\mathrm{R},i}V_{\mathrm{I},j}\right)}}\\
\frac{\partial I_{ij}}{\partial V_{\mathrm{R},j}} &= \frac{D_{ij}V_{\mathrm{R},j} + E_{ij}V_{\mathrm{R},i} + F_{ij}V_{\mathrm{I},i}}{\sqrt{C_{ij}\left(V_{\mathrm{R},i}^2 + V_{\mathrm{I},i}^2\right) + D_{ij}\left(V_{\mathrm{R},j}^2 + V_{\mathrm{I},j}^2\right) + 2E_{ij}\left(V_{\mathrm{R},i}V_{\mathrm{R},j} + V_{\mathrm{I},i}V_{\mathrm{I},j}\right) + 2F_{ij}\left(V_{\mathrm{I},i}V_{\mathrm{R},j} - V_{\mathrm{R},i}V_{\mathrm{I},j}\right)}}\\
\frac{\partial I_{ij}}{\partial V_{\mathrm{I},i}} &= \frac{C_{ij}V_{\mathrm{I},i} + E_{ij}V_{\mathrm{I},j} + F_{ij}V_{\mathrm{R},j}}{\sqrt{C_{ij}\left(V_{\mathrm{R},i}^2 + V_{\mathrm{I},i}^2\right) + D_{ij}\left(V_{\mathrm{R},j}^2 + V_{\mathrm{I},j}^2\right) + 2E_{ij}\left(V_{\mathrm{R},i}V_{\mathrm{R},j} + V_{\mathrm{I},i}V_{\mathrm{I},j}\right) + 2F_{ij}\left(V_{\mathrm{I},i}V_{\mathrm{R},j} - V_{\mathrm{R},i}V_{\mathrm{I},j}\right)}}\\
\frac{\partial I_{ij}}{\partial V_{\mathrm{I},j}} &= \frac{D_{ij}V_{\mathrm{I},j} + E_{ij}V_{\mathrm{I},i} - F_{ij}V_{\mathrm{R},i}}{\sqrt{C_{ij}\left(V_{\mathrm{R},i}^2 + V_{\mathrm{I},i}^2\right) + D_{ij}\left(V_{\mathrm{R},j}^2 + V_{\mathrm{I},j}^2\right) + 2E_{ij}\left(V_{\mathrm{R},i}V_{\mathrm{R},j} + V_{\mathrm{I},i}V_{\mathrm{I},j}\right) + 2F_{ij}\left(V_{\mathrm{I},i}V_{\mathrm{R},j} - V_{\mathrm{R},i}V_{\mathrm{I},j}\right)}}
\end{aligned}\right\} \quad \text{(A.8)}$$

- Active and reactive power flow measurements – state vector in rectangular coordinates:

$$\left.\begin{aligned}
\frac{\partial P_{ij}}{\partial V_{\mathrm{R},i}} &= 2t_{ij}^2(g_{sij}+g_{ij})V_{\mathrm{R},i} - t_{ij}t_{ji}\Big[\big(g_{ij}\cos(\Delta\varphi_{ij})+b_{ij}\sin(\Delta\varphi_{ij})\big)V_{\mathrm{R},j} - \big(b_{ij}\cos(\Delta\varphi_{ij})-g_{ij}\sin(\Delta\varphi_{ij})\big)V_{\mathrm{I},j}\Big]\\
\frac{\partial P_{ij}}{\partial V_{\mathrm{R},j}} &= -t_{ij}t_{ji}\Big[\big(g_{ij}\cos(\Delta\varphi_{ij})+b_{ij}\sin(\Delta\varphi_{ij})\big)V_{\mathrm{R},i} + \big(b_{ij}\cos(\Delta\varphi_{ij})-g_{ij}\sin(\Delta\varphi_{ij})\big)V_{\mathrm{I},i}\Big]\\
\frac{\partial P_{ij}}{\partial V_{\mathrm{I},i}} &= 2t_{ij}^2(g_{sij}+g_{ij})V_{\mathrm{I},i} - t_{ij}t_{ji}\Big[\big(b_{ij}\cos(\Delta\varphi_{ij})-g_{ij}\sin(\Delta\varphi_{ij})\big)V_{\mathrm{R},j} + \big(g_{ij}\cos(\Delta\varphi_{ij})+b_{ij}\sin(\Delta\varphi_{ij})\big)V_{\mathrm{I},j}\Big]\\
\frac{\partial P_{ij}}{\partial V_{\mathrm{I},j}} &= t_{ij}t_{ji}\Big[\big(b_{ij}\cos(\Delta\varphi_{ij})-g_{ij}\sin(\Delta\varphi_{ij})\big)V_{\mathrm{R},i} - \big(g_{ij}\cos(\Delta\varphi_{ij})+b_{ij}\sin(\Delta\varphi_{ij})\big)V_{\mathrm{I},i}\Big]
\end{aligned}\right\} \quad \text{(A.9)}$$

$$\left.\begin{aligned}
\frac{\partial Q_{ij}}{\partial V_{\mathrm{R},i}} &= -2t_{ij}^2(b_{sij}+b_{ij})V_{\mathrm{R},i} + t_{ij}t_{ji}\Big[\big(b_{ij}\cos(\Delta\varphi_{ij})-g_{ij}\sin(\Delta\varphi_{ij})\big)V_{\mathrm{R},j} + \big(g_{ij}\cos(\Delta\varphi_{ij})+b_{ij}\sin(\Delta\varphi_{ij})\big)V_{\mathrm{I},j}\Big]\\
\frac{\partial Q_{ij}}{\partial V_{\mathrm{R},j}} &= t_{ij}t_{ji}\Big[\big(b_{ij}\cos(\Delta\varphi_{ij})-g_{ij}\sin(\Delta\varphi_{ij})\big)V_{\mathrm{R},i} - \big(g_{ij}\cos(\Delta\varphi_{ij})+b_{ij}\sin(\Delta\varphi_{ij})\big)V_{\mathrm{I},i}\Big]\\
\frac{\partial Q_{ij}}{\partial V_{\mathrm{I},i}} &= -2t_{ij}^2(b_{sij}+b_{ij})V_{\mathrm{I},i} - t_{ij}t_{ji}\Big[\big(g_{ij}\cos(\Delta\varphi_{ij})+b_{ij}\sin(\Delta\varphi_{ij})\big)V_{\mathrm{R},j} - \big(b_{ij}\cos(\Delta\varphi_{ij})-g_{ij}\sin(\Delta\varphi_{ij})\big)V_{\mathrm{I},j}\Big]\\
\frac{\partial Q_{ij}}{\partial V_{\mathrm{I},j}} &= t_{ij}t_{ji}\Big[\big(g_{ij}\cos(\Delta\varphi_{ij})+b_{ij}\sin(\Delta\varphi_{ij})\big)V_{\mathrm{R},i} + \big(b_{ij}\cos(\Delta\varphi_{ij})-g_{ij}\sin(\Delta\varphi_{ij})\big)V_{\mathrm{I},i}\Big]
\end{aligned}\right\} \quad \text{(A.10)}$$

- Active and reactive power injection measurements – state vector in rectangular coordinates:

$$\left.\begin{aligned}
\frac{\partial P_i}{\partial V_{\mathrm{R},i}} &= 2G_{ii}V_{\mathrm{R},i} + \sum_{j\in a(i)}\big(G_{ij}V_{\mathrm{R},j} - B_{ij}V_{\mathrm{I},j}\big)\\
\frac{\partial P_i}{\partial V_{\mathrm{R},j}} &= G_{ij}V_{\mathrm{R},i} + B_{ij}V_{\mathrm{I},i}\\
\frac{\partial P_i}{\partial V_{\mathrm{I},i}} &= 2G_{ii}V_{\mathrm{I},i} + \sum_{j\in a(i)}\big(B_{ij}V_{\mathrm{R},j} + G_{ij}V_{\mathrm{I},j}\big)\\
\frac{\partial P_i}{\partial V_{\mathrm{I},j}} &= -B_{ij}V_{\mathrm{R},i} + G_{ij}V_{\mathrm{I},i}
\end{aligned}\right\} \quad \text{(A.11)}$$

$$\left.\begin{aligned}
\frac{\partial Q_i}{\partial V_{\mathrm{R},i}} &= -2B_{ii}V_{\mathrm{R},i} - \sum_{j\in a(i)}\big(B_{ij}V_{\mathrm{R},j} + G_{ij}V_{\mathrm{I},j}\big)\\
\frac{\partial Q_i}{\partial V_{\mathrm{R},j}} &= -B_{ij}V_{\mathrm{R},i} + G_{ij}V_{\mathrm{I},i}\\
\frac{\partial Q_i}{\partial V_{\mathrm{I},i}} &= -2B_{ii}V_{\mathrm{I},i} + \sum_{j\in a(i)}\big(G_{ij}V_{\mathrm{R},j} - B_{ij}V_{\mathrm{I},j}\big)\\
\frac{\partial Q_i}{\partial V_{\mathrm{I},j}} &= -G_{ij}V_{\mathrm{R},i} - B_{ij}V_{\mathrm{I},i}
\end{aligned}\right\} \quad \text{(A.12)}$$

- Voltage magnitude and angle measurements – state vector in polar coordinates:

$$\frac{\partial V_i}{\partial V_i}=1 \text{ and } \frac{\partial \delta_i}{\partial \delta_i}=1 \tag{A.13}$$

- Real and imaginary current flow measurements:

$$\left.\begin{aligned}
\frac{\partial I_{\mathrm{R},ij}}{\partial V_i} &= t_{ij}^2\left((g_{sij}+g_{ij})\cos\delta_i-(b_{sij}+b_{ij})\sin\delta_i\right)\\
\frac{\partial I_{\mathrm{R},ij}}{\partial V_j} &= -t_{ij}t_{ji}\left(g_{ij}\cos(\delta_j-\Delta\varphi_{ij})-b_{ij}\sin(\delta_j-\Delta\varphi_{ij})\right)\\
\frac{\partial I_{\mathrm{R},ij}}{\partial \delta_i} &= -t_{ij}^2V_i\left((g_{sij}+g_{ij})\sin\delta_i+(b_{sij}+b_{ij})\cos\delta_i\right)\\
\frac{\partial I_{\mathrm{R},ij}}{\partial \delta_j} &= t_{ij}t_{ji}V_j\left(g_{ij}\sin(\delta_j-\Delta\varphi_{ij})+b_{ij}\cos(\delta_j-\Delta\varphi_{ij})\right)
\end{aligned}\right\} \tag{A.14}$$

$$\left.\begin{aligned}
\frac{\partial I_{\mathrm{I},ij}}{\partial V_i} &= t_{ij}^2\left((g_{sij}+g_{ij})\sin\delta_i+(b_{sij}+b_{ij})\cos\delta_i\right)\\
\frac{\partial I_{\mathrm{I},ij}}{\partial V_j} &= -t_{ij}t_{ji}\left(g_{ij}\sin(\delta_j-\Delta\varphi_{ij})+b_{ij}\cos(\delta_j-\Delta\varphi_{ij})\right)\\
\frac{\partial I_{\mathrm{I},ij}}{\partial \delta_i} &= t_{ij}^2V_i\left((g_{sij}+g_{ij})\cos\delta_i-(b_{sij}+b_{ij})\sin\delta_i\right)\\
\frac{\partial I_{\mathrm{I},ij}}{\partial \delta_j} &= -t_{ij}t_{ji}V_j\left(g_{ij}\cos(\delta_j-\Delta\varphi_{ij})-b_{ij}\sin(\delta_j-\Delta\varphi_{ij})\right)
\end{aligned}\right\} \tag{A.15}$$

REFERENCES

[1] U. Häger, C. Rehtanz, and N. Voropai, Eds., *Monitoring, Control and Protection of Interconnected Power Systems*, 1st ed. Berlin: Springer Berlin, Heidelberg, 2014.

[2] A. K. Singh and B. C. Pal, Eds., *Dynamic Estimation and Control of Power Systems*, 1st ed. London; San Diego, California: Elsevier Academic Press, 2019.

[3] M. Eremia, C.-C. Liu, and A.-A. Edris, Eds., *Advanced Solutions in Power Systems: HVDC, FACTS, and Artificial Intelligence*, 1st ed. Hoboken, New Jersey: John Wiley & Sons, Inc., 2016.

[4] A. Monti, Ed., *Phasor Measurement Units and Wide Area Monitoring Systems: From the Sensors to the System*, 1st ed. Amsterdam: Elsevier, 2016.

[5] M. S. Thomas and J. D. McDonald, *Power System SCADA and Smart Grids*. Boca Raton, Florida: CRC Press, Taylor & Francis Group, 2015.

[6] A. G. Phadke and J. S. Thorp, *Synchronized Phasor Measurements and Their Applications*, 1st ed. New York: Springer, 2008.

[7] J. Allemong, L. Radu, and A. Sasson, "A fast and reliable state estimation algorithm for AEP's new control center," *IEEE Trans. Power Appar. Syst.*, vol. PAS-101, no. 4, pp. 933–944, Apr. 1982.

[8] M. Kezunovic, S. Meliopoulos, V. Venkatasubramanian, and V. Vittal, *Application of Time-Synchronized Measurements in Power System Transmission Networks*, 1st ed. Berlin: Springer Cham, 2014.

[9] Z. Jin, P. Wall, Y. Chen, J. Yu, S. Chakrabarti, and V. Terzija, "Analysis of hybrid state estimators: accuracy and convergence of estimator formulations," *IEEE Trans. Power Syst.*, vol. 34, no. 4, pp. 2565–2576, Jul. 2019.

[10] S. Li, L. Zhang, J.-N. Paquin, J. Belanger, and L. Vanfretti, "Hardware-in-the-loop use cases for synchrophasor applications," in *2019 International Conference on Smart Grid Synchronized Measurements and Analytics (SGSMA)*, College Station, TX, USA, 2019, pp. 1–8.

[11] E. Handschin and A. Petroianu, *Energy Management Systems*. Berlin: Springer Berlin Heidelberg, 1991.

[12] E. Vaahedi, *Practical Power System Operation*, 1st ed. Piscataway, NJ: IEEE Press, 2014.

[13] G. Clarke, D. Reynders, and E. Wright, *Practical Modern SCADA Protocols*, 1st ed. Oxford: Elsevier Newnes, 2004.

[14] E. Padilla, *Substation Automation Systems: Design and Implementation*, 1st ed. Sussex: John Wiley & Sons, Ltd., 2015.

[15] C. P. Steinmetz, "Complex quantities and their use in electrical engineering," in *Proceedings of the International Electrical Congress*, 1893, pp. 33–74.

[16] A. G. Phadke, J. S. Thorp, and M. G. Adamiak, "A new measurement technique for tracking voltage phasors, local system frequency, and rate of change of frequency," *IEEE Trans. Power Appar. Syst.*, vol. PAS-102, no. 5, pp. 1025–1038, May 1983.

[17] A. G. Phadke, "Synchronized phasor measurements-a historical overview," in *IEEE/PES Transmission and Distribution Conference and Exhibition*, Yokohama, Japan, 2002, pp. 476–479.

[18] "IEEE 1344-1995(R2001) - IEEE standard for synchrophasors for power systems." IEEE, 30-Nov-1994.

[19] "IEEE C37.118-2005 - IEEE standard for synchrophasors for power systems." 21-Oct-2005.

[20] "IEEE C37.118.1-2011 - IEEE standard for synchrophasor measurements for power systems." IEEE, 28-Dec-2011.

[21] "IEEE C37.118.1a-2014 - IEEE standard for synchrophasor measurements for power systems -- Amendment 1: modification of selected performance requirements." IEEE, 30-Apr-2014.

[22] "IEEE C37.118.2-2011 - IEEE standard for synchrophasor data transfer for power systems." 28-Dec-2011.

[23] "IEEE/IEC 60255-118-1-2018 - IEEE/IEC International Standard - Measuring relays and protection equipment - Part 118-1: Synchrophasor for power systems - Measurements." Dec-2018.

[24] "IEEE C37.242-2021 - IEEE guide for synchronization, calibration, testing, and installation of phasor measurement units (PMUs) for power system protection and control." IEEE, 14-Oct-2021.

[25] "IEC 61869-1:2023 - Instrument transformers - Part 1: general requirements." 14-Jun-2023.

[26] H. Haes Alhelou, A. Y. Abdelaziz, and P. Siano, Eds., *Wide Area Power Systems Stability, Protection, and Security*, 1st ed. Cham, Switzerland: Springer, 2021.

[27] Yi Deng, Hua Lin, A. G. Phadke, S. Shukla, J. S. Thorp, and L. Mili, "Communication network modeling and simulation for wide area measurement applications," in *2012 IEEE PES Innovative Smart Grid Technologies (ISGT)*, Washington, DC, USA, 2012, pp. 1–6.

[28] P. Castello, C. Muscas, P. A. Pegoraro, G. M. Giannuzzi, P. Pau, C. Maiolini, and R. Zaottini, "An active phasor data concentrator suitable for control and protection applications," in *2019 International Conference on Smart Grid Synchronized Measurements and Analytics (SGSMA)*, College Station, TX, USA, 2019, pp. 1–7.

[29] R. Gore and M. Kande, "Analysis of wide area monitoring system architectures," in *2015 IEEE International Conference on Industrial Technology (ICIT)*, Seville, 2015, pp. 1269–1274.

[30] M. Patel, S. Aivaliotis, E. Allen, D. Bakken, L. Beard, and V. Bhaman, "Real-Time Application of Synchrophasors for Improving Reliability," North American Electric Reliability Corporation (NERC), Princeton, NJ, Final Report, Oct. 2010.

[31] G. Ledwich and A. Vahidnia, *Phasors for Measurement and Control*, 1st ed. Cham, Switzerland: Springer, 2021.

[32] A. Monticelli, *State Estimation in Electric Power Systems: A Generalized Approach*. Boston: Kluwer Academic Publishers, 1999.

[33] A. J. Wood, B. F. Wollenberg, and G. B. Sheblé, *Power Generation, Operation and Control*, 3rd ed. Hoboken, NJ: Wiley, 2014.

[34] F. Schweppe, "Power system static-state estimation, Part III: implementation," *IEEE Trans. Power Appar. Syst.*, vol. PAS-89, no. 1, pp. 130–135, Jan. 1970.

[35] Θ. Ξύγκης, "Βέλτιστη διαχείριση μετρήσεων για ενίσχυση παρατηρησιμότητας και ακρίβειας σε εκτιμητές κατάστασης συστημάτων ηλεκτρικής ενέργειας με ελλιπή δεδομένα," Διδακτορική Διατριβή, Εθνικό Μετσόβιο Πολυτεχνείο, Αθήνα, 2019.

[36] F. F. Wu, K. Moslehi, and A. Bose, "Power system control centers: past, present, and future," *Proc. IEEE*, vol. 93, no. 11, pp. 1890–1908, Nov. 2005.

[37] J. D. Glover, M. S. Sarma, and T. J. Overbye, *Power System Analysis and Design*, 6th ed. Boston, MA: CENGAGE Learning, 2016.

[38] A. Abur and A. Gómez Expósito, *Power System State Estimation: Theory and Implementation*. New York, NY: Marcel Dekker, 2004.

[39] F. C. Schweppe and E. J. Handschin, "Static state estimation in electric power systems," *Proc. IEEE*, vol. 62, no. 7, pp. 972–982, 1974.

[40] A. Garcia, A. Monticelli, and P. Abreu, "Fast decoupled state estimation and bad data processing," *IEEE Trans. Power Appar. Syst.*, vol. PAS-98, no. 5, pp. 1645–1652, Sep. 1979.

[41] O. Alsac, N. Vempati, B. Stott, and A. Monticelli, "Generalized state estimation," *IEEE Trans. Power Syst.*, vol. 13, no. 3, pp. 1069–1075, Aug. 1998.

[42] L. Holten, A. Gjelsvik, S. Aam, F. F. Wu, and W.-H. E. Liu, "Comparison of different methods for state estimation," *IEEE Trans. Power Syst.*, vol. 3, no. 4, pp. 1798–1806, Nov. 1988.

[43] F. F. Wu, "Power system state estimation: a survey," *Int. J. Electr. Power Energy Syst.*, vol. 12, no. 2, pp. 80–87, Apr. 1990.

[44] J. M. R. Munoz and A. G. Exposito, "A line-current measurement based state estimator," *IEEE Trans. Power Syst.*, vol. 7, no. 2, pp. 513–519, May 1992.

[45] A. Abur and A. G. Exposito, "Detecting multiple solutions in state estimation in the presence of current magnitude measurements," *IEEE Trans. Power Syst.*, vol. 12, no. 1, pp. 370–375, Feb. 1997.

[46] K. A. Clements, P. W. Davis, and K. D. Frey, "Treatment of inequality constraints in power system state estimation," *IEEE Trans. Power Syst.*, vol. 10, no. 2, pp. 567–574, May 1995.

[47] A. Simoes-Costa and V. Quintana, “A robust numerical technique for power system state estimation,” *IEEE Trans. Power Appar. Syst.*, vol. PAS-100, no. 2, pp. 691–698, Feb. 1981.

[48] G. N. Korres, “A robust method for equality constrained state estimation,” *IEEE Trans. Power Syst.*, vol. 17, no. 2, pp. 305–314, May 2002.

[49] A. Monticelli, “Electric power system state estimation,” *Proc. IEEE*, vol. 88, no. 2, pp. 262–282, Feb. 2000.

[50] L. Mili, M. G. Cheniae, N. S. Vichare, and P. J. Rousseeuw, “Robust state estimation based on projection statistics of power systems,” *IEEE Trans. Power Syst.*, vol. 11, no. 2, pp. 1118–1127, May 1996.

[51] P. J. Huber and E. M. Ronchetti, *Robust Statistics*, 2nd ed. Hoboken, NJ: Wiley, 2009.

[52] R. C. Pires, A. Simoes Costa, and L. Mili, “Iteratively reweighted least-squares state estimation through Givens Rotations,” *IEEE Trans. Power Syst.*, vol. 14, no. 4, pp. 1499–1507, Nov. 1999.

[53] R. A. Jabr, “Power system Huber M-estimation with equality and inequality constraints,” *Electr. Power Syst. Res.*, vol. 74, no. 2, pp. 239–246, May 2005.

[54] E. Kyriakides, S. Suryanarayanan, and G. T. H. Heydt, “State estimation in power engineering using the Huber robust regression technique,” *IEEE Trans. Power Syst.*, vol. 20, no. 2, pp. 1183–1184, May 2005.

[55] S. R. Eliason, *Maximum Likelihood Estimation: Logic and Practice*, 1st ed. Newbury Park, CA: SAGE Publications, Inc, 1993.

[56] K. Morrissey, “Fundamental Research Challenges for Distribution State Estimation to Enable High-Performing Grids,” New York State Energy Research and Development Authority, Final Report 18–37, May 2018.

[57] Power Systems Operations Committee/State Estimation Algorithms Working Group/Task Force on State Estimation Concepts and Terminology, “State Estimation Concepts and Terminology,” IEEE Power Energy Soc., Piscataway, NJ, PES-TR20, May 2016.

[58] G. H. Golub and C. F. Van Loan, *Matrix Computations*, 4th ed. Baltimore, MD: The Johns Hopkins University Press, 2013.

[59] A. Monticelli and A. Garcia, “Modeling zero impedance branches in power system state estimation,” *IEEE Trans. Power Syst.*, vol. 6, no. 4, pp. 1561–1570, Nov. 1991.

[60] J. Zhao, M. Netto, Z. Huang, S. S. Yu, A. Gomez-Exposito, S. Wang, I. Kamwa, S. Akhlaghi, L. Mili, V. Terzija, A. P. S. Meliopoulos, B. Pal, A. K. Singh, A. Abur, T. Bi, and A. Rouhani, “Roles of dynamic state estimation in power system modeling, monitoring and operation,” *IEEE Trans. Power Syst.*, vol. 36, no. 3, pp. 2462–2472, May 2021.

[61] Y. Liu, A. K. Singh, J. Zhao, A. P. S. Meliopoulos, B. Pal, M. A. bin M. Ariff, T. Van Cutsem, M. Glavic, Z. Huang, I. Kamwa, L. Mili, A. S. Mir, A. Taha, V. Terzija, and S. Yu, “Dynamic state estimation for power system control and protection,” *IEEE Trans. Power Syst.*, vol. 36, no. 6, pp. 5909–5921, Nov. 2021.

[62] J. Zhao, J. Qi, Z. Huang, A. P. S. Meliopoulos, A. Gomez-Exposito, M. Netto, L. Mili, A. Abur, V. Terzija, I. Kamwa, B. Pal, and A. K. Singh, “Power system dynamic state estimation: motivations, definitions, methodologies, and future work,” *IEEE Trans. Power Syst.*, vol. 34, no. 4, pp. 3188–3198, Jul. 2019.

[63] A. Debs and R. Larson, “A dynamic estimator for tracking the state of a power system,” *IEEE Trans. Power Appar. Syst.*, vol. PAS-89, no. 7, pp. 1670–1678, Sep. 1970.

[64] W. Miller and J. Lewis, “Dynamic state estimation in power systems,” *IEEE Trans. Autom. Control*, vol. 16, no. 6, pp. 841–846, Dec. 1971.

[65] Z. Huang, K. Schneider, and J. Nieplocha, “Feasibility studies of applying Kalman Filter techniques to power system dynamic state estimation,” in *2007 International Power Engineering Conference (IPEC 2007)*, 2007, pp. 376–382.

[66] E. Ghahremani and I. Kamwa, “Online state estimation of a synchronous generator using unscented Kalman filter from phasor measurements units,” *IEEE Trans. Energy Convers.*, vol. 26, no. 4, pp. 1099–1108, Dec. 2011.

[67] N. Zhou, D. Meng, Z. Huang, and G. Welch, “Dynamic state estimation of a synchronous machine using PMU data: A comparative study,” *IEEE Trans. Smart Grid*, vol. 6, no. 1, pp. 450–460, Jan. 2015.

[68] M. Netto and L. Mili, “A robust data-driven Koopman Kalman filter for power systems dynamic state estimation,” *IEEE Trans. Power Syst.*, vol. 33, no. 6, pp. 7228–7237, Nov. 2018.

[69] A. Rouhani and A. Abur, “Observability analysis for dynamic state estimation of synchronous machines,” *IEEE Trans. Power Syst.*, vol. 32, no. 4, pp. 3168–3175, Jul. 2017.

[70] J. Zhao, M. Netto, and L. Mili, “A robust iterated extended Kalman filter for power system dynamic state estimation,” *IEEE Trans. Power Syst.*, vol. 32, no. 4, pp. 3205–3216, Jul. 2017.

[71] J. Zhao and L. Mili, “A theoretical framework of robust H-infinity unscented Kalman filter and its application to pow-er system dynamic state estimation,” *IEEE Trans. Signal Process.*, vol. 67, no. 10, pp. 2734–2746, May 2019.

[72] S. Wang, J. Zhao, Z. Huang, and R. Diao, “Assessing Gaussian assumption of PMU measurement error using field data,” *IEEE Trans. Power Deliv.*, vol. 33, no. 6, pp. 3233–3236, Dec. 2018.

[73] D. Simon, *Optimal State Estimation: Kalman, H Infinity and Nonlinear Approaches*. Hoboken, N.J: Wiley-Interscience, 2006.

[74] N. Kumari, R. Kulkarni, M. R. Ahmed, and N. Kumar, “Use of Kalman Filter and Its Variants in State Estimation: A Review,” in *Artificial Intelligence for a Sustainable Industry 4.0*, S. Awasthi, C. M. Travieso-González, G. Sanyal, and D. Kumar Singh, Eds. Cham, Switzerland: Springer, 2021, pp. 213–230.

[75] M. B. Do Coutto Filho and J. C. S. de Souza, “Forecasting-aided state estimation—Part I: Panorama,” *IEEE Trans. Power Syst.*, vol. 24, no. 4, pp. 1667–1677, Nov. 2009.

[76] F. C. Schweppe and R. D. Masiello, “A tracking static state estimator,” *IEEE Trans. Power Appar. Syst.*, vol. PAS-90, no. 3, pp. 1025–1033, May 1971.

[77] K. Srinivasan and Y. Robichaud, “A dynamic estimator for complex bus voltage determination,” *IEEE Trans. Power Appar. Syst.*, vol. PAS-93, no. 5, pp. 1581–1588, Sep. 1974.

[78] D. M. Falcao, P. A. Cooke, and A. Brameller, “Power system tracking state estimation and bad data processing,” *IEEE Trans. Power Appar. Syst.*, vol. PAS-101, no. 2, pp. 325–333, Feb. 1982.

[79] K.-I. Nishiya, H. Takagi, J. Hasegawa, and T. Koike, “Dynamic state estimation for electric power systems—introduction of a trend factor and detection of innovation processes,” *Electr. Eng. Jpn.*, vol. 96, no. 5, pp. 79–87, 1976.

[80] K. Nishiya, J. Hasegawa, and T. Koike, “Dynamic state estimation including anomaly detection and identification for power systems,” *IEE Proc. C Gener. Transm. Distrib.*, vol. 129, no. 5, pp. 192–198, Sep. 1982.

[81] A. M. Leite Da Silva, M. B. Do Coutto Filho, and J. F. De Queiroz, “State forecasting in electric power systems,” *IEE Proc. C Gener. Transm. Distrib.*, vol. 130, no. 5, pp. 237–244, Sep. 1983.

[82] A. M. Leite da Silva, M. B. Do Coutto Filho, and J. M. C. Cantera, “An efficient dynamic state estimation algorithm including bad data processing,” *IEEE Trans. Power Syst.*, vol. 2, no. 4, pp. 1050–1058, Nov. 1987.

[83] A. P. Alves da Silva, V. H. Quintana, and G. K. H. Pang, “Solving data acquisition and processing problems in power systems using a pattern analysis approach,” *IEE Proc. C Gener. Transm. Distrib.*, vol. 138, no. 4, pp. 365–376, Jul. 1991.

[84] A. P. Alves da Silva and V. H. Quintana, “Pattern analysis in power system state estimation,” *Int. J. Electr. Power Energy Syst.*, vol. 17, no. 1, pp. 51–60, Feb. 1995.

[85] J. C. S. Souza, A. M. Leite da Silva, and A. P. Alves da Silva, “Data debugging for real-time power system monitoring based on pattern analysis,” *IEEE Trans. Power Syst.*, vol. 11, no. 3, pp. 1592–1599, Aug. 1996.

[86] J. C. S. Souza, A. M. Leite da Silva, and A. P. Alves de Silva, “Online topology determination and bad data suppression in power system operation using artificial neural networks,” *IEEE Trans. Power Syst.*, vol. 13, no. 3, pp. 796–803, Aug. 1998.

[87] K.-R. Shih and S.-J. Huang, “Application of a robust algorithm for dynamic state estimation of a power system,” *IEEE Trans. Power Syst.*, vol. 17, no. 1, pp. 141–147, Feb. 2002.

[88] S.-J. Huang and J.-M. Lin, “Enhancement of anomalous data mining in power system predicting-aided state estimation,” *IEEE Trans. Power Syst.*, vol. 19, no. 1, pp. 610–619, Feb. 2004.

[89] M. B. Do Coutto Filho, J. C. S. Souza, R. S. G. Matos, and M. Th. Schilling, “Revealing gross errors in critical measurements and sets via forecasting-aided state estimators,” *Electr. Power Syst. Res.*, vol. 57, no. 1, pp. 25–32, Jan. 2001.

[90] M. B. Do Coutto Filho, J. C. S. de Souza, and M. Th. Schilling, “Generating high quality pseudo-measurements to keep state estimation capabilities,” in *2007 IEEE Lausanne Power Tech*, 2007, pp. 1829–1834.

[91] M. Hassanzadeh, C. Y. Evrenosoğlu, and L. Mili, “A short-term nodal voltage phasor forecasting method using temporal and spatial correlation,” *IEEE Trans. Power Syst.*, vol. 31, no. 5, pp. 3881–3890, Sep. 2016.

[92] J. Zhao, G. Zhang, Z. Y. Dong, and M. La Scala, “Robust forecasting aided power system state estimation considering state correlations,” *IEEE Trans. Smart Grid*, vol. 9, no. 4, pp. 2658–2666, Jul. 2018.

[93] A. K. Sinha and J. K. Mondal, “Dynamic state estimator using ANN based bus load prediction,” *IEEE Trans. Power Syst.*, vol. 14, no. 4, pp. 1219–1225, Nov. 1999.

[94] “IEEE C37.1-2007 - IEEE standard for SCADA and automation systems.” 08-May-2008.

[95] V. Terzija, G. Valverde, D. Cai, P. Regulski, V. Madani, J. Fitch, S. Skok, M. M. Begovic, and A. Phadke, “Wide-area monitoring, protection, and control of future electric power networks,” *Proc. IEEE*, vol. 99, no. 1, pp. 80–93, Jan. 2011.

[96] S. Chakrabarti, E. Kyriakides, G. Ledwich, and A. Ghosh, “A comparative study of the methods of inclusion of PMU current phasor measurements in a hybrid state estimator,” in *IEEE PES General Meeting*, Minneapolis, MN, 2010, pp. 1–7.

[97] M. Kabiri and N. Amjady, “A new hybrid state estimation considering different accuracy levels of PMU and SCADA measurements,” *IEEE Trans. Instrum. Meas.*, vol. 68, no. 9, pp. 3078–3089, Sep. 2019.

[98] O. Darmis and G. Korres, “A survey on hybrid SCADA/WAMS state estimation methodologies in electric power transmission systems,” *Energies*, vol. 16, no. 2, Jan. 2023.

[99] M. Glavic and T. Van Cutsem, “Reconstructing and tracking network state from a limited number of synchrophasor measurements,” *IEEE Trans. Power Syst.*, vol. 28, no. 2, pp. 1921–1929, May 2013.

[100] N. M. Manousakis and G. N. Korres, “A hybrid power system state estimator using synchronized and unsynchronized sensors,” *Int. Trans. Electr. Energy Syst.*, vol. 28, no. 8, Aug. 2018.

[101] M. Asprou, S. Chakrabarti, and E. Kyriakides, “A two-stage state estimator for dynamic monitoring of power systems,” *IEEE Syst. J.*, vol. 11, no. 3, pp. 1767–1776, Sep. 2017.

[102] M. Gol and A. Abur, “A hybrid state estimator for systems with limited number of PMUs,” *IEEE Trans. Power Syst.*, vol. 30, no. 3, pp. 1511–1517, May 2015.

[103] M. Gol, “A decentralization method for hybrid state estimators,” *IEEE Trans. Power Syst.*, vol. 33, no. 2, pp. 2070–2077, Mar. 2018.

[104] R. J. Hamidi, H. Khodabandelou, H. Livani, and M. Sami-Fadali, “Hybrid state estimation using distributed compressive sensing,” in *2016 IEEE Power and Energy Society General Meeting (PESGM)*, Boston, MA, USA, 2016, pp. 1–5.

[105] J. Zhao, G. Zhang, K. Das, G. N. Korres, N. M. Manousakis, A. K. Sinha, and Z. He, “Power system real-time monitoring by using PMU-based robust state estimation method,” *IEEE Trans. Smart Grid*, vol. 7, no. 1, pp. 300–309, Jan. 2016.

[106] K. Sun, M. Huang, Z. Wei, J. Zhao, and G. Sun, “A real-time recursion correction hybrid linear state estimator using stream processing,” *IEEE Trans. Ind. Inform.*, vol. 19, no. 3, pp. 2317–2329, Mar. 2023.

[107] A. Dubey, S. Chakrabarti, A. Sharma, and V. Terzija, “Optimal utilisation of PMU measurements in power system hybrid state estimators,” *IET Gener. Transm. Distrib.*, vol. 13, no. 21, pp. 4978–4986, Nov. 2019.

[108] Q. Zhang, Y. Chakhchoukh, V. Vittal, G. T. Heydt, N. Logic, and S. Sturgill, “Impact of PMU measurement buffer length on state estimation and its optimization,” *IEEE Trans. Power Syst.*, vol. 28, no. 2, pp. 1657–1665, May 2013.

[109] V. Murugesan, Y. Chakhchoukh, V. Vittal, G. T. Heydt, N. Logic, and S. Sturgill, "PMU data buffering for power system state estimators," *IEEE Power Energy Technol. Syst. J.*, vol. 2, no. 3, pp. 94–102, Sep. 2015.

[110] Y. Chakhchoukh, V. Vittal, and G. T. Heydt, "PMU based state estimation by integrating correlation," *IEEE Trans. Power Syst.*, vol. 29, no. 2, pp. 617–626, Mar. 2014.

[111] J. Zhao, S. Wang, L. Mili, B. Amidan, R. Huang, and Z. Huang, "A robust state estimation framework considering measurement correlations and imperfect synchronization," *IEEE Trans. Power Syst.*, vol. 33, no. 4, pp. 4604–4613, Jul. 2018.

[112] T. S. Bi, X. H. Qin, and Q. X. Yang, "A novel hybrid state estimator for including synchronized phasor measurements," *Electr. Power Syst. Res.*, vol. 78, no. 8, pp. 1343–1352, Aug. 2008.

[113] G. N. Korres and N. M. Manousakis, "State estimation and bad data processing for systems including PMU and SCADA measurements," *Electr. Power Syst. Res.*, vol. 81, no. 7, pp. 1514–1524, Jul. 2011.

[114] G. Valverde, S. Chakrabarti, E. Kyriakides, and V. Terzija, "A constrained formulation for hybrid state estimation," *IEEE Trans. Power Syst.*, vol. 26, no. 3, pp. 1102–1109, Aug. 2011.

[115] S. K. Mallik, S. Chakrabarti, and S. N. Singh, "A robust regularized hybrid state estimator for power systems," *Electr. Power Compon. Syst.*, vol. 42, no. 7, pp. 671–681, May 2014.

[116] R. Khalili and A. Abur, "Iterative linear state estimation using a limited number of PMU measurements," in *2021 IEEE Madrid PowerTech*, Madrid, Spain, 2021, pp. 1–6.

[117] A. Jovicic and G. Hug, "Linear state estimation and bad data detection for power systems with RTU and PMU measurements," *IET Gener. Transm. Distrib.*, vol. 14, no. 23, pp. 5675–5684, Dec. 2020.

[118] A. S. Dobakhshari, S. Azizi, M. Abdolmaleki, and V. Terzija, "Linear LAV-based state estimation integrating hybrid SCADA/PMU measurements," *IET Gener. Transm. Distrib.*, vol. 14, no. 8, pp. 1583–1590, Apr. 2020.

[119] A. S. Dobakhshari, M. Abdolmaleki, V. Terzija, and S. Azizi, "Robust hybrid linear state estimator utilizing SCADA and PMU measurements," *IEEE Trans. Power Syst.*, vol. 36, no. 2, pp. 1264–1273, Mar. 2021.

[120] A. Jovicic, N. Codoni, and G. Hug, "Computationally efficient robust state estimation for power transmission systems with RTU and PMU measurements," in *2020 52nd North American Power Symposium (NAPS)*, Tempe, AZ, USA, 2021, pp. 1–6.

[121] A. Jovicic, M. Jereminov, L. Pileggi, and G. Hug, "A linear formulation for power system state estimation including RTU and PMU measurements," in *2019 IEEE PES Innovative Smart Grid Technologies Europe (ISGT-Europe)*, Bucharest, Romania, 2019, pp. 1–5.

[122] A. Jovicic, M. Jereminov, L. Pileggi, and G. Hug, "Enhanced modelling framework for equivalent circuit-based power system state estimation," *IEEE Trans. Power Syst.*, vol. 35, no. 5, pp. 3790–3799, Sep. 2020.

[123] X. Fan and D. Duan, "Decentralized multi-area state estimation with hybrid measurements," in *2017 IEEE Power & Energy Society General Meeting*, Chicago, IL, 2017, pp. 1–5.

[124] X. Li and A. Scaglione, "Robust decentralized state estimation and tracking for power systems via network gossiping," *IEEE J. Sel. Areas Commun.*, vol. 31, no. 7, pp. 1184–1194, Jul. 2013.

[125] A. Minot, Y. M. Lu, and N. Li, "A distributed Gauss-Newton method for power system state estimation," *IEEE Trans. Power Syst.*, vol. 31, no. 5, pp. 3804–3815, Sep. 2016.

[126] A. Sharma, S. C. Srivastava, and S. Chakrabarti, "An iterative multiarea state estimation approach using area slack bus adjustment," *IEEE Syst. J.*, vol. 10, no. 1, pp. 69–77, Mar. 2016.

[127] I. Dzafic, R. A. Jabr, and T. Hrnjic, "Hybrid state estimation in complex variables," *IEEE Trans. Power Syst.*, vol. 33, no. 5, pp. 5288–5296, Sep. 2018.

[128] I. Džafić and R. A. Jabr, "Real-time equality-constrained hybrid state estimation in complex variables," *Int. J. Electr. Power Energy Syst.*, vol. 117, May 2020.

[129] I. Dzafic, R. A. Jabr, and T. Hrnjic, "A complex variable perturbed Gauss-Newton method for tracking mode state estimation," *IEEE Trans. Power Syst.*, vol. 36, no. 3, pp. 2594–2602, May 2021.

[130] M. Zhou, V. A. Centeno, J. S. Thorp, and A. G. Phadke, "An alternative for including phasor measurements in state estimators," *IEEE Trans. Power Syst.*, vol. 21, no. 4, pp. 1930–1937, Nov. 2006.

[131] R. F. Nuqui and A. G. Phadke, "Hybrid linear state estimation utilizing synchronized phasor measurements," in *2007 IEEE Lausanne Power Tech*, Lausanne, Switzerland, 2007, pp. 1665–1669.

[132] K. Jamuna and K. S. Swarup, "Two stage state estimator with phasor measurements," in *2009 International Conference on Power Systems*, Kharagpur, India, 2009, pp. 1–5.

[133] S. Moshtagh and M. Rahmani, "Robust hybrid state estimation for power systems utilizing Phasor measurements units," *Electr. Power Syst. Res.*, vol. 196, Jul. 2021.

[134] N. Rathod, H. Patel, and S. Joshi, "Implementing two stage hybrid state estimation with various approaches," in *2020 International Conference on Smart Grids and Energy Systems (SGES)*, Perth, Australia, 2020, pp. 627–632.

[135] D. M. Bez, A. Simoes Costa, L. B. Ascari, and E. Z. Junior, "A block version of orthogonal rotations for improving the accuracy of hybrid state estimators," *IEEE Trans. Power Syst.*, vol. 35, no. 6, pp. 4432–4444, Nov. 2020.

[136] N. M. Manousakis, G. N. Korres, J. N. Aliprantis, G. P. Vavourakis, and G.-C. J. Makrinas, "A two-stage state estimator for power systems with PMU and SCADA measurements," in *2013 IEEE Grenoble Conference*, Grenoble, France, 2013, pp. 1–6.

[137] N. Kashyap, S. Werner, Y.-F. Huang, and T. Riihonen, "Power system state estimation under incomplete PMU observability—a reduced-order approach," *IEEE J. Sel. Top. Signal Process.*, vol. 8, no. 6, pp. 1051–1062, Dec. 2014.

[138] T. Yang, H. Sun, and A. Bose, "Transition to a two-level linear state estimator—Part II: Algorithm," *IEEE Trans. Power Syst.*, vol. 26, no. 1, pp. 54–62, Feb. 2011.

[139] Y. Bar-Shalom and L. Campo, "The effect of the common process noise on the two-sensor fused-track covariance," *IEEE Trans. Aerosp. Electron. Syst.*, vol. AES-22, no. 6, pp. 803–805, Nov. 1986.

[140] A. Simoes Costa, A. Albuquerque, and D. Bez, "An estimation fusion method for including phasor measurements into power system real-time modeling," *IEEE Trans. Power Syst.*, vol. 28, no. 2, pp. 1910–1920, May 2013.

[141] T. Wu, C. Y. Chung, and I. Kamwa, "A fast state estimator for systems including limited number of PMUs," *IEEE Trans. Power Syst.*, vol. 32, no. 6, pp. 4329–4339, Nov. 2017.

[142] L. B. Ascari, A. S. Costa, and V. Miranda, "Correntropy-based fusion strategy for incorporating PMU measurements into power system state estimation," in *2019 IEEE Milan PowerTech*, Milan, Italy, 2019, pp. 1–6.

[143] J. Zhao and L. Mili, "A framework for robust hybrid state estimation with unknown measurement noise statistics," *IEEE Trans. Ind. Inform.*, vol. 14, no. 5, pp. 1866–1875, May 2018.

[144] J. Ban, J. Im, Y.-J. Kim, and J. Zhao, "Decentralization of phasor-aided state estimation using local state vector extension," *IEEE Trans. Power Syst.*, vol. 36, no. 5, pp. 4645–4659, Sep. 2021.

[145] G. Cheng, Y. Lin, A. Abur, A. Gómez-Expósito, and W. Wu, "A survey of power system state estimation using multiple data sources: PMUs, SCADA, AMI, and beyond," *IEEE Trans. Smart Grid*, vol. 15, no. 1, pp. 1129–1151, Jan. 2024.

[146] M. Ghosal and V. Rao, "Fusion of multirate measurements for nonlinear dynamic state estimation of the power systems," *IEEE Trans. Smart Grid*, vol. 10, no. 1, pp. 216–226, Jan. 2019.

[147] M. A. Abooshahab, M. Hovd, E. Brekke, and X. Song, "A covariance consistent data fusion method for power networks with multirate sensors," in *2020 IEEE Conference on Control Technology and Applications (CCTA)*, Montreal, QC, Canada, 2020, pp. 807–814.

[148] S. Goleijani and M. T. Ameli, "Neural network-based power system dynamic state estimation using hybrid data from SCADA and phasor measurement units," *Int. Trans. Electr. Energy Syst.*, vol. 28, no. 2, Feb. 2018.

[149] S. Goleijani and M. T. Ameli, "A multi-agent based approach to power system dynamic state estimation by considering algebraic and dynamic state variables," *Electr. Power Syst. Res.*, vol. 163, pp. 470–481, Oct. 2018.

[150] J. Zhao, S. Wang, N. Zhou, R. Huang, L. Mili, and Z. Huang, "A new multi-scale state estimation framework for the next generation of power grid EMS," in *2019 IEEE Power & Energy Society General Meeting (PESGM)*, Atlanta, GA, USA, 2019, pp. 1–5.

[151] G. Valverde and V. Terzija, "Unscented Kalman filter for power system dynamic state estimation," *IET Gener. Transm. Distrib.*, vol. 5, no. 1, pp. 29–37, Jan. 2011.

[152] Y. Xiao, M. Lu, Z. Huang, Y. Wang, L. Lin, and C. Zhang, "Dynamic state estimation of power system considering asynchronous measurement," in *2020 International Conference on Electrical Engineering and Control Technologies (CEECT)*, Melbourne, VIC, Australia, 2020, pp. 1–6.

[153] A. M. Stankovic, V. Svenda, A. T. Saric, and M. K. Transtrum, "Hybrid power system state estimation with irregular sampling," in *2017 IEEE Power & Energy Society General Meeting*, Chicago, IL, 2017, pp. 1–5.

[154] S. J. Geetha, A. Sharma, and S. Chakrabarti, "Unscented Rauch–Tung–Streibel smoother-based power system forecasting-aided state estimator using hybrid measurements," *IET Gener. Transm. Distrib.*, vol. 13, no. 16, pp. 3583–3590, Aug. 2019.

[155] J. A. D. Massignan, J. B. A. London, C. D. Maciel, M. Bessani, and V. Miranda, "PMUs and SCADA measurements in power system state estimation through Bayesian inference," in *2019 IEEE Milan PowerTech*, Milan, Italy, 2019, pp. 1–6.

[156] B. Qu, Z. Wang, and B. Shen, "Fusion estimation for a class of multi-rate power systems with randomly occurring SCADA measurement delays," *Automatica*, vol. 125, Mar. 2021.

[157] L. Hu, Z. Wang, I. Rahman, and X. Liu, "A constrained optimization approach to dynamic state estimation for power systems including PMU and missing measurements," *IEEE Trans. Control Syst. Technol.*, vol. 24, no. 2, pp. 703–710, Mar. 2016.

[158] Z. Cheng, H. Ren, B. Zhang, and R. Lu, "Distributed Kalman filter for large-scale power systems with state inequality constraints," *IEEE Trans. Ind. Electron.*, vol. 68, no. 7, pp. 6238–6247, Jul. 2021.

[159] A. Sharma and S. R. Samantaray, "Power system tracking state estimator for smart grid under unreliable PMU data communication network," *IEEE Sens. J.*, vol. 18, no. 5, pp. 2107–2116, Mar. 2018.

[160] A. Sharma, S. C. Srivastava, and S. Chakrabarti, "A cubature Kalman filter based power system dynamic state estimator," *IEEE Trans. Instrum. Meas.*, vol. 66, no. 8, pp. 2036–2045, Aug. 2017.

[161] H. Karimipour and V. Dinavahi, "Extended Kalman filter-based parallel dynamic state estimation," *IEEE Trans. Smart Grid*, vol. 6, no. 3, pp. 1539–1549, May 2015.

[162] S. Goleijani and M. T. Ameli, "An agent-based approach to power system dynamic state estimation through dual unscented Kalman filter and artificial neural network," *Soft Comput.*, vol. 23, no. 23, pp. 12585–12606, Dec. 2019.

[163] Y. Sun and Y. Zhao, "Distributed cubature Kalman filter with performance comparison for large-scale power systems," *Int. J. Control Autom. Syst.*, vol. 19, no. 3, pp. 1319–1327, Mar. 2021.

[164] V. Kirincic, S. Skok, and V. Terzija, "A two-step hybrid power system state estimator," *Int. Trans. Electr. Energy Syst.*, vol. 25, no. 7, pp. 1158–1172, Jul. 2015.

[165] A. Dubey and S. Chakrabarti, "An unscented Kalman filter based hybrid state estimator considering conventional and PMU measurements," in *2016 IEEE 6th International Conference on Power Systems (ICPS)*, New Delhi, India, 2016, pp. 1–6.

[166] B. A. Alcaide-Moreno, C. R. Fuerte-Esquivel, M. Glavic, and T. Van Cutsem, "Electric power network state tracking from multirate measurements," *IEEE Trans. Instrum. Meas.*, vol. 67, no. 1, pp. 33–44, Jan. 2018.

[167] X. Qing, H. R. Karimi, Y. Niu, and X. Wang, "Decentralized unscented Kalman filter based on a consensus algorithm for multi-area dynamic state estimation in power systems," *Int. J. Electr. Power Energy Syst.*, vol. 65, pp. 26–33, Feb. 2015.

[168] J. A. D. Massignan, J. B. A. London Jr., and V. Miranda, "Tracking power system state evolution with maximum-correntropy-based extended Kalman filter," *J. Mod. Power Syst. Clean Energy*, vol. 8, no. 4, pp. 616–626, Jul. 2020.

[169] X. Bian, X. R. Li, H. Chen, D. Gan, and J. Qiu, "Joint estimation of state and parameter with synchrophasors—Part I: state tracking," *IEEE Trans. Power Syst.*, vol. 26, no. 3, pp. 1196–1208, Aug. 2011.

[170] Y. Wang, M. Xia, Q. Chen, F. Chen, X. Yang, and F. Han, "Fast state estimation of power system based on extreme learning machine pseudo-measurement modeling," in *2019 IEEE Innovative Smart Grid Technologies - Asia (ISGT Asia)*, Chengdu, China, 2019, pp. 1236–1241.

[171] F. Camoes, J. A. D. Massignan, V. Miranda, and J. B. A. London, "Sliding-priors for Bayesian information fusion in SCADA+PMU-based state estimation," in *2022 17th International Conference on Probabilistic Methods Applied to Power Systems (PMAPS)*, Manchester, United Kingdom, 2022, pp. 1–6.

[172] V. G. Švenda, A. M. Stanković, A. T. Sarić, and M. K. Transtrum, "Flexible hybrid state estimation for power systems with communication irregularities," *IET Gener. Transm. Distrib.*, vol. 14, no. 11, pp. 2111–2119, Jun. 2020.

[173] Y. Gu, Z. Yu, R. Diao, and D. Shi, "Doubly-fed deep learning method for bad data identification in linear state estimation," *J. Mod. Power Syst. Clean Energy*, vol. 8, no. 6, pp. 1140–1150, Nov. 2020.

[174] Y. Chen, H. Chen, Y. Jiao, J. Ma, and Y. Lin, "Data-driven robust state estimation through off-line learning and on-line matching," *J. Mod. Power Syst. Clean Energy*, vol. 9, no. 4, pp. 897–909, Jul. 2021.

[175] Z. Gao, S. Hu, H. Sun, J. Liu, Y. Zhi, and J. Li, "Dynamic state estimation of new energy power systems considering multi-level false data identification based on LSTM-CNN," *IEEE Access*, vol. 9, pp. 142411–142424, Oct. 2021.

[176] J. Kim, J.-H. Kang, J. Bae, W. Lee, and K.-K. K. Kim, "Distributed moving horizon estimation via operator splitting for automated robust power system state estimation," *IEEE Access*, vol. 9, pp. 90428–90440, Jun. 2021.

[177] G. Tian, Y. Gu, D. Shi, J. Fu, Z. Yu, and Q. Zhou, "Neural-network-based power system state estimation with extended observability," *J. Mod. Power Syst. Clean Energy*, vol. 9, no. 5, pp. 1043–1053, Jun. 2021.

[178] L. Wang, Q. Zhou, and S. Jin, "Physics-guided deep learning for power system state estimation," *J. Mod. Power Syst. Clean Energy*, vol. 8, no. 4, pp. 607–615, Jul. 2020.

[179] T. Chen, Y. Cao, L. Sun, X. Qing, and J. Zhang, "A distributed robust power system state estimation approach using t-distribution noise model," *IEEE Syst. J.*, vol. 15, no. 1, pp. 1066–1076, Mar. 2021.

[180] G. Cheng, Y. Lin, Y. Chen, and T. Bi, "Adaptive state estimation for power systems measured by PMUs with unknown and time-varying error statistics," *IEEE Trans. Power Syst.*, vol. 36, no. 5, pp. 4482–4491, Sep. 2021.

[181] Z. Sun, C. Liu, and S. Peng, "Maximum correntropy with variable center unscented Kalman filter for robust power system state estimation," *Entropy*, vol. 24, no. 4, Apr. 2022.

[182] M. J. Hossain and M. Naeini, "Multi-area distributed state estimation in smart grids using data-driven Kalman filters," *Energies*, vol. 15, no. 19, Sep. 2022.

[183] A. Gjelsvik, S. Aam, and L. Holten, "Hachtel's augmented matrix method - A rapid method improving numerical stability in power system static state estimation," *IEEE Trans. Power Appar. Syst.*, vol. PAS-104, no. 11, pp. 2987–2993, Nov. 1985.

[184] O. A. Darmis and G. N. Korres, "A hybrid power system state estimator under limited PMU availability," *IEEE Trans. Power Syst.*, vol. 39, no. 6, pp. 7166–7177, Nov. 2024.

[185] O. Darmis, G. Karvelis, and G. N. Korres, "PMU-based state estimation for networks containing LCC-HVDC links," *IEEE Trans. Power Syst.*, vol. 37, no. 3, pp. 2475–2478, May 2022.

[186] T. Xygkis, O. Darmis, and G. Korres, "Impact of current measurement configuration on power system state estimation," in *14th Mediterranean Conference on Power Generation Transmission, Distribution and Energy Conversion (MEDPOWER)*, Athens, Greece, 2024, pp. 1–6.

[187] J. R. Bunch and L. Kaufman, "Some stable methods for calculating inertia and solving symmetric linear systems," *Math. Comput.*, vol. 31, no. 137, pp. 163–179, 1977.

[188] E. Anderson, Z. Bai, C. Bischof, L. S. Blackford, J. Demmel, J. Dongarra, J. Du Croz, A. Greenbaum, S. Hammarling, A. McKenney, and D. Sorensen, *LAPACK Users' Guide*, 3rd ed. Society for Industrial and Applied Mathematics, 1999.

[189] W. F. Tinney, V. Brandwajn, and S. M. Chan, “Sparse vector methods,” *IEEE Trans. Power Appar. Syst.*, vol. PAS-104, no. 2, pp. 295–301, Feb. 1985.

[190] R. A. Horn and C. R. Johnson, *Matrix Analysis*, 2nd ed. New York, NY: Cambridge University Press, 2017.

[191] O. Saksvik, “HVDC technology and smart grid,” in *9th IET International Conference on Advances in Power System Control, Operation and Management (APSCOM 2012)*, Hong Kong, China, 2012, pp. 168–168.

[192] H. R. Sirisena and E. P. M. Brown, “Inclusion of HVDC links in AC power-system state estimation,” *IEE Proc. C Gener. Transm. Distrib.*, vol. 128, no. 3, pp. 147–154, May 1981.

[193] W. Li and L. Vanfretti, “Inclusion of classic HVDC links in a PMU-based state estimator,” in *2014 IEEE PES General Meeting | Conference & Exposition*, National Harbor, MD, USA, 2014, pp. 1–5.

[194] W. Li and L. Vanfretti, “A PMU-based state estimator considering classic HVDC links under different control modes,” *Sustain. Energy Grids Netw.*, vol. 2, pp. 69–82, Jun. 2015.

[195] A. A. Aljabrine, A. A. Smadi, Y. Chakhchoukh, B. K. Johnson, and H. Lei, “Resiliency improvement of an AC/DC power grid with embedded LCC-HVDC using robust power system state estimation,” *Energies*, vol. 14, no. 23, Nov. 2021.

[196] W. Li and L. Vanfretti, “A PMU-based state estimator for networks containing VSC-HVDC links,” in *2015 IEEE Power & Energy Society General Meeting*, Denver, CO, USA, 2015, pp. 1–5.

[197] E. A. Zamora-Cárdenas, C. R. Fuerte-Esquivel, A. Pizano-Martínez, and H. J. Estrada-García, “Hybrid state estimator considering SCADA and synchronized phasor measurements in VSC-HVDC transmission links,” *Electr. Power Syst. Res.*, vol. 133, pp. 42–50, Apr. 2016.

[198] V. Donde, X. Feng, I. Segerqvist, and M. Callavik, “Distributed state estimation of hybrid AC/HVDC grids by network decomposition,” *IEEE Trans. Smart Grid*, vol. 7, no. 2, pp. 974–981, Mar. 2016.

[199] X. Li, B. Han, K. Wang, G. Li, and X. Jiang, “State estimation for hybrid AC/DC power grids based on pseudo measurement modelling of converters,” in *2020 IEEE Power & Energy Society General Meeting (PESGM)*, Montreal, QC, Canada, 2020, pp. 1–5.

[200] R. Martínez-Parrales and C. R. Fuerte-Esquivel, “A new unified approach for the state estimation and bad data analysis of electric power transmission systems with multi-terminal VSC-based HVDC networks,” *Electr. Power Syst. Res.*, vol. 160, pp. 251–260, Jul. 2018.

[201] D. Tzelepis, V. Psaras, E. Tsotsopoulou, S. Mirsaeidi, A. Dysko, Q. Hong, X. Dong, S. M. Blair, V. C. Nikolaidis, V. Papaspiliotopoulos, G. Fusiek, G. M. Burt, P. Niewczas, and C. D. Booth, “Voltage and current measuring technologies for high voltage direct current supergrids: a technology review identifying the options for protection, fault location and automation applications,” *IEEE Access*, vol. 8, pp. 203398–203428, Nov. 2020.

[202] A. V. Meier, Merwin L Brown, R. Arghandeh, and E. M. Stewart, “Synchrophasor Monitoring for Distribution Systems -Technical Foundations and Applications,” NASPI Distribution Task Team, White Paper NASPI-2018-TR-001, 2018.

[203] S. Chakrabarti, E. Kyriakides, G. Ledwich, and A. Ghosh, “Inclusion of PMU current phasor measurements in a power system state estimator,” *IET Gener. Transm. Distrib.*, vol. 4, no. 10, pp. 1104–1115, Oct. 2010.

[204] S. K. Mallik, S. Chakrabarti, and S. N. Singh, “Analysis of ill-conditioning of hybrid state estimators in the presence of PMU measurements,” *Energy Convers. Econ.*, vol. 2, no. 1, pp. 35–44, Mar. 2021.

[205] M. Pau, P. A. Pegoraro, A. Monti, C. Muscas, F. Ponci, and S. Sulis, “Impact of current and power measurements on distribution system state estimation uncertainty,” *IEEE Trans. Instrum. Meas.*, vol. 68, no. 10, pp. 3992–4002, Oct. 2019.

[206] J. Li, M. Gao, B. Liu, and Y. Cai, “Forecasting aided distribution network state estimation using mixed µPMU-RTU measurements,” *IEEE Syst. J.*, vol. 16, no. 4, pp. 6524–6534, Dec. 2022.

[207] M. Mao, J. Xu, Z. Wu, Q. Hu, and X. Dou, “A multiarea state estimation for distribution networks under mixed measurement environment,” *IEEE Trans. Ind. Inform.*, vol. 18, no. 6, pp. 3620–3629, Jun. 2022.

[208] N. Vieyra, C. Angeles-Camacho, and P. Maya-Ortiz, “Design and implementation of a state estimator in a real distribution network,” *IET Gener. Transm. Distrib.*, vol. 17, no. 19, pp. 4329–4343, Oct. 2023.

[209] T. C. Xygkis and G. N. Korres, “Optimizing D-PMU deployment for distribution system state estimation,” in *2022 International Conference on Smart Grid Synchronized Measurements and Analytics (SGSMA)*, Split, Croatia, 2022, pp. 1–8.

[210] V. N. Giotopoulos and G. N. Korres, “A laboratory PMU based on third order generalized integrator phase-locked loop.”

[211] “Power Systems Test Case Archive - UWEE.” [Online]. Available: http://labs.ece.uw.edu/pstca/. [Accessed: 21-Dec-2024].

[212] R. D. Zimmerman, C. E. Murillo-Sánchez, and R. J. Thomas, “MATPOWER: steady-state operations, planning, and analysis tools for power systems research and education,” *IEEE Trans. Power Syst.*, vol. 26, no. 1, pp. 12–19, Feb. 2011.

[213] KEMA, “Metrics for determining the impact of phasor measurements on power system state estimation,” Eastern Interconnection Phasor Project, Mar. 2006.

[214] “Parallel Computing Toolbox Documentation.” [Online]. Available: https://www.mathworks.com/help/parallel-computing/index.html. [Accessed: 18-Jul-2023].

[215] “PSS®E: Robust Transmission Planning and Analysis,” *siemens.com Global Website*. [Online]. Available: https://www.siemens.com/global/en/products/energy/grid-software/planning/pss-software/pss-e.html. [Accessed: 08-Jan-2025].

[216] “IEEE PES Test Feeder - Resources.” [Online]. Available: https://cmte.ieee.org/pes-testfeeders/resources/. [Accessed: 24-Jul-2024].

[217] J. G. Sreenath, S. Chakrabarti, and A. Sharma, “Implementation of Rauch-Tung-Striebel smoother for power system dynamic state estimation in the presence of PMU measurements,” in *2015 IEEE Innovative Smart Grid Technologies - Asia (ISGT ASIA)*, Bangkok, Thailand, 2015, pp. 1–6.

[218] C. Cheng and X. Bai, “Robust forecasting-aided state estimation in power distribution systems with event-triggered transmission and reduced mixed measurements,” *IEEE Trans. Power Syst.*, vol. 36, no. 5, pp. 4343–4354, Sep. 2021.

[219] Y. Zhang, J. Zhao, D. Shi, and S. Chung, “Deep reinforcement learning-enabled adaptive forecasting-aided state estimation in distribution systems with multi-source multi-rate data,” in *2024 IEEE Power & Energy Society Innovative Smart Grid Technologies Conference (ISGT)*, Washington, DC, USA, 2024, pp. 1–5.

[220] O. Darmis and G. N. Korres, “Forecasting-aided power system state estimation using multisource multirate measurements,” *IEEE Trans. Instrum. Meas.*, vol. 74, pp. 1–15, 2025.

[221] G. J. Bierman, “Fixed interval smoothing with discrete measurements,” *Int. J. Control*, vol. 18, no. 1, pp. 65–75, Jul. 1973.

[222] G. E. P. Box, G. M. Jenkins, G. C. Reinsel, and G. M. Ljung, *Time Series Analysis: Forecasting and Control*, 5th ed. Hoboken, NJ: John Wiley & Sons, Inc, 2016.

[223] R. J. Hyndman, *Forecasting with Exponential Smoothing: The State Space Approach*. Berlin: Springer, 2008.

[224] T. C. Xygkis and G. N. Korres, “Optimized measurement allocation for power distribution systems using mixed integer SDP,” *IEEE Trans. Instrum. Meas.*, vol. 66, no. 11, pp. 2967–2976, Nov. 2017.

[225] H. E. Rauch, F. Tung, and C. T. Striebel, “Maximum likelihood estimates of linear dynamic systems,” *AIAA J.*, vol. 3, no. 8, pp. 1445–1450, Aug. 1965.

[226] F. F. Wu, W.-H. E. Liu, and S.-M. Lun, “Observability analysis and bad data processing for state estimation with equality constraints,” *IEEE Trans. Power Syst.*, vol. 3, no. 2, pp. 541–548, May 1988.

[227] M. Brown Do Coutto Filho, J. C. S. De Souza, and R. S. Freund, “Forecasting-aided state estimation—Part II: Implementation,” *IEEE Trans. Power Syst.*, vol. 24, no. 4, pp. 1678–1685, Nov. 2009.

[228] H. Chen, B. Bhargava, F. Habibi-Ashrafi, J. S. Park, and J. Castaneda, “Integration of RTDS with EPG synchrophasor applications for visualization and analysis of simulation scenarios at Southern California Edison,” in *2012 North American Power Symposium (NAPS)*, Champaign, IL, USA, 2012, pp. 1–5.

[229] P. Kotsampopoulos, D. Lagos, N. Hatziargyriou, M. O. Faruque, G. Lauss, O. Nzimako, P. Forsyth, M. Steurer, F. Ponci, A. Monti, V. Dinavahi, and K. Strunz, “A benchmark system for hardware-in-the-loop testing of distributed energy resources,” *IEEE Power Energy Technol. Syst. J.*, vol. 5, no. 3, pp. 94–103, Sep. 2018.

[230] K. Sidwall and P. Forsyth, “Advancements in real-time simulation for the validation of grid modernization technologies,” *Energies*, vol. 13, no. 16, p. 4036, Aug. 2020.

[231] M. R. Nasab, R. Cometa, S. Bruno, G. Giannoccaro, and M. L. Scala, “Power systems simulation and analysis: A review on current applications and future trends in DRTS of grid-connected technologies,” *IEEE Access*, vol. 12, pp. 121320–121345, 2024.

[232] P. C. Kotsampopoulos, V. A. Kleftakis, and N. D. Hatziargyriou, “Laboratory education of modern power systems using PHIL simulation,” *IEEE Trans. Power Syst.*, vol. 32, no. 5, pp. 3992–4001, Sep. 2017.

[233] M. D. Omar Faruque, T. Strasser, G. Lauss, V. Jalili-Marandi, P. Forsyth, C. Dufour, V. Dinavahi, A. Monti, P. Kotsampopoulos, J. A. Martinez, K. Strunz, M. Saeedifard, Xiaoyu Wang, D. Shearer, and M. Paolone, “Real-time simulation technologies for power systems design, testing, and analysis,” *IEEE Power Energy Technol. Syst. J.*, vol. 2, no. 2, pp. 63–73, Jun. 2015.

[234] V. Venkataramanan, P. S. Sarker, K. S. Sajan, A. Srivastava, and A. Hahn, “Real-time federated cyber-transmission-distribution testbed architecture for the resiliency analysis,” *IEEE Trans. Ind. Appl.*, vol. 56, no. 6, pp. 7121–7131, Nov. 2020.

[235] G. Lauss, Z. Feng, M. H. Syed, A. Kontou, A. D. Paola, A. Paspatis, and P. Kotsampopoulos, “A framework for sensitivity analysis of real-time power hardware-in-the-loop (PHIL) systems,” *IEEE Access*, vol. 10, pp. 101305–101318, 2022.

[236] G. Mehlmann, U. Kühnapfel, F. Wege, A. Winkens, C. Scheibe, S. Vogel, P. Noglik, M. Gratza, J. Richter, M. Weber, I. Burlakin, A. Kuri, T. Wagner, S. Hubschneider, R. Poppenborg, T. Heins, K. Förderer, A. Ulbig, A. Monti, V. Hagenmeyer, and M. Luther, “The Kopernikus ENSURE co-demonstration platform,” *IEEE Open J. Power Electron.*, vol. 4, pp. 987–1002, 2023.

[237] J. M. Riquelme-Dominguez, F. Gonzalez-Longatt, A. F. S. Melo, J. L. Rueda, and P. Palensky, “Cyber-physical testbed co-simulation real-time: Normal and abnormal system frequency response,” *IEEE Trans. Ind. Appl.*, vol. 60, no. 2, pp. 2643–2652, Mar. 2024.

[238] S. S. Biswas, Jeong Hun Kim, and A. K. Srivastava, “Development of a smart grid test bed and applications in PMU and PDC testing,” in *2012 North American Power Symposium (NAPS)*, Champaign, IL, USA, 2012, pp. 1–6.

[239] K. Diakos, Q. Wu, and A. H. Nielsen, “Phasor measurement unit and phasor data concentrator test with real time digital simulator,” in *2014 IEEE PES Asia-Pacific Power and Energy Engineering Conference (APPEEC)*, Hong Kong, 2014, pp. 1–5.

[240] A. C. Adewole and R. Tzoneva, “Co-simulation platform for integrated real-time power system emulation and wide area communication,” *IET Gener. Transm. Distrib.*, vol. 11, no. 12, pp. 3019–3029, Aug. 2017.

[241] M. Stifter, J. Cordova, J. Kazmi, and R. Arghandeh, “Real-time simulation and hardware-in-the-loop testbed for distribution synchrophasor applications,” *Energies*, vol. 11, no. 4, p. 876, Apr. 2018.

[242] T. Becejac and P. Dehghanian, “PMU multilevel end-to-end testing to assess synchrophasor measurements during faults,” *IEEE Power Energy Technol. Syst. J.*, vol. 6, no. 1, pp. 71–80, Mar. 2019.

[243] A. P. Hurtado, E. M. Carrasco, M. T. V. Martínez, M. Á. Oliván Monge, C. N. Dikaiakos, and Y. Z. Korkmaz, “Laboratory-scaled DEMO possibilities for testing WAMPAC solutions before field implementation,” in *2021 IEEE Madrid PowerTech*, Madrid, Spain, 2021, pp. 1–6.

[244] P. Castello, G. Gallus, P. A. Pegoraro, and S. Sulis, “Measurement platform for latency characterization of wide area monitoring, protection and control systems,” *IEEE Trans. Instrum. Meas.*, vol. 73, pp. 1–12, 2024.

[245] F. Zhang, Y. Sun, L. Cheng, X. Li, J. H. Chow, and W. Zhao, “Measurement and modeling of delays in wide-area closed-loop control systems,” *IEEE Trans. Power Syst.*, vol. 30, no. 5, pp. 2426–2433, Sep. 2015.

[246] D. Baltensperger, S. Sanchez, S. D'Arco, and K. Uhlen, "Assessing hardware in the loop approaches for wide-area monitoring control and protection devices," *IEEE Trans. Power Deliv.*, vol. 38, no. 4, pp. 2724–2734, Aug. 2023.

[247] H. Georg, S. C. Muller, N. Dorsch, C. Rehtanz, and C. Wietfeld, "INSPIRE: Integrated co-simulation of power and ICT systems for real-time evaluation," in *2013 IEEE International Conference on Smart Grid Communications (SmartGridComm)*, Vancouver, BC, Canada, 2013, pp. 576–581.

[248] V. P. Tran, S. Kamalasadan, and J. Enslin, "Real-time modeling and model validation of synchronous generator using synchrophasor measurements," in *2013 North American Power Symposium (NAPS)*, Manhattan, KS, USA, 2013, pp. 1–5.

[249] C. B. Vellaithurai, S. S. Biswas, and A. K. Srivastava, "Development and application of a real-time test bed for cyber–physical system," *IEEE Syst. J.*, pp. 1–12, 2015.

[250] M. La Scala, M. De Benedictis, S. Bruno, A. Grobovoy, N. Bondareva, N. Borodina, D. Denisova, A. J. Germond, and R. Cherkaoui, "Development of applications in WAMS and WACS: an international cooperation experience," in *2006 IEEE Power Engineering Society General Meeting*, Montreal, Que., Canada, 2006, p. 10 pp.

[251] S. Bruno, M. De Benedictis, and M. La Scala, "Integrating dynamic optimization methodologies with WAMS technologies," in *2007 IEEE Power Engineering Society General Meeting*, Tampa, FL, USA, 2007, pp. 1–8.

[252] T. Becejac, C. Eppinger, A. Ashok, U. Agrawal, and J. O'Brien, "PRIME: a real-time cyber-physical systems testbed: from wide-area monitoring, protection, and control prototyping to operator training and beyond," *IET Cyber-Phys. Syst. Theory Appl.*, vol. 5, no. 2, pp. 186–195, Jun. 2020.

[253] L. Kumar, S. Ahmed, L. Vanfretti, and N. Kishor, "Real-time testing of synchrophasor-based wide-area monitoring system applications acknowledging the potential use of a prototyping software toolchain," *Int. Trans. Electr. Energy Syst.*, vol. 2022, pp. 1–13, Jul. 2022.

[254] M. S. Almas, M. Baudette, and L. Vanfretti, "Utilizing synchrophasor-based supplementary damping control signals in conventional generator excitation systems," *Electr. Power Syst. Res.*, vol. 157, pp. 157–167, Apr. 2018.

[255] M. S. Almas, L. Vanfretti, R. S. Singh, and G. M. Jonsdottir, "Vulnerability of synchrophasor-based WAMPAC applications to time synchronization spoofing," *IEEE Trans. Smart Grid*, vol. 9, no. 5, pp. 4601–4612, Sep. 2018.

[256] M. Baudette, R. S. Singh, V. S. Peric, S. Lovlund, and L. Vanfretti, "'In silico' testing of a real-time PMU-based tool for power system mode estimation," in *2016 IEEE Power and Energy Society General Meeting (PESGM)*, Boston, MA, USA, 2016, pp. 1–5.

[257] R. S. Singh, H. Hooshyar, and L. Vanfretti, "Experimental real-time testing of a decentralized PMU data-based power systems mode estimator," in *2017 IEEE Power & Energy Society General Meeting*, Chicago, IL, 2017, pp. 1–4.

[258] A. Bidadfar, H. Hooshyar, M. Monadi, and L. Vanfretti, "Decoupled voltage stability assessment of distribution networks using synchrophasors," in *2016 IEEE Power and Energy Society General Meeting (PESGM)*, Boston, MA, USA, 2016, pp. 1–5.

[259] E. Ghahremani, A. Heniche-Oussedik, M. Perron, M. Racine, S. Landry, and H. Akremi, "A detailed presentation of an innovative local and wide-area special protection scheme to avoid voltage collapse: from proof of concept to grid implementation," *IEEE Trans. Smart Grid*, vol. 10, no. 5, pp. 5196–5211, Sep. 2019.

[260] F. Quintero-Zuluaga, P. Viana-Villa, D. Giraldo-Gomez, B. Arboleda, D. Villegas, M. Sanchez, C. Perez, and N. Duque, "Hardware in the loop design and testing of a PMU-based special protection scheme: Case study of Colombia-Ecuador interconnection," in *2020 IEEE PES Transmission & Distribution Conference and Exhibition - Latin America (T&D LA)*, Montevideo, Uruguay, 2020, pp. 1–6.

[261] H. Lee, A. K. Srivastava, V. V. G. Krishnan, S. Niddodi, and D. E. Bakken, "Decentralized voltage stability monitoring and control with distributed computing coordination," *IEEE Syst. J.*, vol. 16, no. 2, pp. 2251–2260, Jun. 2022.

[262] Y. Zuo, G. Frigo, A. Derviskadic, and M. Paolone, "Impact of synchrophasor estimation algorithms in ROCOF-based under-frequency load-shedding," *IEEE Trans. Power Syst.*, vol. 35, no. 2, pp. 1305–1316, Mar. 2020.

[263] M. Sun, G. Liu, M. Popov, V. Terzija, and S. Azizi, "Underfrequency load shedding using locally estimated RoCoF of the center of inertia," *IEEE Trans. Power Syst.*, vol. 36, no. 5, pp. 4212–4222, Sep. 2021.

[264] R. K. Panda, A. Mohapatra, and S. C. Srivastava, "Online estimation of system inertia in a power network utilizing synchrophasor measurements," *IEEE Trans. Power Syst.*, vol. 35, no. 4, pp. 3122–3132, Jul. 2020.

[265] G. P. Kumar and P. Jena, "Pearson's correlation coefficient for islanding detection using micro-PMU measurements," *IEEE Syst. J.*, vol. 15, no. 4, pp. 5078–5089, Dec. 2021.

[266] I. D. De Melo, J. L. R. Pereira, C. A. Duque, M. P. Antunes, L. R. Manso Silva, and M. A. De Souza, "Power quality monitoring using synchronized phasor measurements: An approach based on hardware-in-the-loop simulations," in *2019 IEEE Milan PowerTech*, Milan, Italy, 2019, pp. 1–6.

[267] E. Khaledian, S. Pandey, P. Kundu, and A. K. Srivastava, "Real-time synchrophasor data anomaly detection and classification using *Isolation Forest, KMeans, and LoOP*," *IEEE Trans. Smart Grid*, vol. 12, no. 3, pp. 2378–2388, May 2021.

[268] A. Meghwani, J. G. Sreenath, S. C. Srivastava, S. Chakrabarti, and A. Sharma, "Robust event detection using synchrophasor assisted forecasting-aided state estimation," in *2019 IEEE Power & Energy Society General Meeting (PESGM)*, Atlanta, GA, USA, 2019, pp. 1–5.

[269] A. Shrestha, V. Cecchi, and R. W. Cox, "A real-time platform for validating continuous wide-area control systems," in *2013 IEEE PES Innovative Smart Grid Technologies Conference (ISGT)*, Washington, DC, 2013, pp. 1–6.

[270] A. S. Musleh, S. M. Muyeen, A. Al-Durra, and H. M. Khalid, "PMU based wide area voltage control of smart grid: A real time implementation approach," in *2016 IEEE Innovative Smart Grid Technologies - Asia (ISGT-Asia)*, Melbourne, Australia, 2016, pp. 365–370.

[271] F. Zhang, L. Cheng, X. Li, and Y.-Z. Sun, "A prediction-based hierarchical delay compensation (PHDC) technique enhanced by increment autoregression prediction for wide-area control systems," *IEEE Trans. Smart Grid*, vol. 11, no. 2, pp. 1253–1263, Mar. 2020.

[272] Y. Bansal and R. Sodhi, "PMUs enabled Tellegen's theorem-based fault identification method for unbalanced active distribution network using RTDS," *IEEE Syst. J.*, vol. 14, no. 3, pp. 4567–4578, Sep. 2020.

[273] D. Sodin, M. Smolnikar, U. Rudež, and A. Čampa, "Precise PMU-based localization and classification of short-circuit faults in power distribution systems," *IEEE Trans. Power Deliv.*, vol. 38, no. 5, pp. 3262–3273, Oct. 2023.

[274] M. Dhinu Lal and R. Varadarajan, "Intelligent fault detection, compensation, and power management in microgrids: A synchrophasor-enhanced approach using fuzzy logic controllers and RTDS," *IEEE Access*, vol. 12, pp. 115465–115496, 2024.

[275] P. A. Pegoraro, C. Sitzia, A. V. Solinas, S. Sulis, D. Carta, and A. Benigni, "Improved fault detection and location method in three-phase distribution networks leveraging traceable PMU measurements," *IEEE Trans. Instrum. Meas.*, pp. 1–1, 2025.

[276] A. S. Musleh, H. M. Khalid, S. M. Muyeen, and A. Al-Durra, "A prediction algorithm to enhance grid resilience toward cyber attacks in WAMCS applications," *IEEE Syst. J.*, vol. 13, no. 1, pp. 710–719, Mar. 2019.

[277] B. Chen, S. Yim, H. Kim, A. Kondabathini, and R. Nuqui, "Cybersecurity of wide area monitoring, protection, and control systems for HVDC applications," *IEEE Trans. Power Syst.*, vol. 36, no. 1, pp. 592–602, Jan. 2021.

[278] T. Hagan, D. Senaratne, R. Meier, E. Cotilla-Sanchez, and J. Kim, "Implementing power system protection algorithms in a digital hardware-in-the-loop substation," *IEEE Open Access J. Power Energy*, vol. 10, pp. 270–282, 2023.

[279] M. Lixia, A. Benigni, A. Flammini, C. Muscas, F. Ponci, and A. Monti, "A software-only PTP synchronization for power system state estimation with PMUs," in *2011 IEEE International Instrumentation and Measurement Technology Conference*, Hangzhou, China, 2011, pp. 1–6.

[280] A. Sharma, S. C. Srivastava, and S. Chakrabarti, "Testing and validation of power system dynamic state estimators using real time digital simulator (RTDS)," *IEEE Trans. Power Syst.*, vol. 31, no. 3, pp. 2338–2347, May 2016.

[281] A. Dubey, S. Chakrabarti, and V. Terzija, "Testing and validation of a dynamic estimator of states in OPAL-RT real time simulator," in *2017 IEEE Power & Energy Society General Meeting*, Chicago, IL, 2017, pp. 1–5.

[282] H. Khazraj, A. C. Adewole, U. D. Annakkage, F. F. Da Silva, C. L. Bak, and A. D. Rajapakse, "Online synchrophasor-based dynamic state estimation using real-time digital simulator," in *2018 IEEE International Conference on Environment and Electrical Engineering and 2018 IEEE Industrial and Commercial Power Systems Europe (EEEIC / I&CPS Europe)*, Palermo, 2018, pp. 1–6.

[283] V. V. G. Krishnan, S. Gopal, R. Liu, Z. Nie, A. Srivastava, and D. Bakken, "Resilient information architecture platform for distributed linear state estimation," in *2018 IEEE Power & Energy Society General Meeting (PESGM)*, Portland, OR, 2018, pp. 1–5.

[284] V. Sarfi, A. Ghasemkhani, I. Niazazari, H. Livani, and L. Yang, "Decentralized dynamic state estimation with bimodal Gaussian mixture measurement noise," in *2019 North American Power Symposium (NAPS)*, Wichita, KS, USA, 2019, pp. 1–5.

[285] I. Mohammed, S. J. Geetha, S. S. Shinde, K. Rajawat, and S. Chakrabarti, "Modified re-iterated Kalman filter for handling delayed and lost measurements in power system state estimation," *IEEE Sens. J.*, vol. 20, no. 7, pp. 3946–3955, Apr. 2020.

[286] S. V. S. Chauhan and G. X. Gao, "Spoofing resilient state estimation for the power grid using an extended Kalman filter," *IEEE Trans. Smart Grid*, vol. 12, no. 4, pp. 3404–3414, Jul. 2021.

[287] A. Mitra, A. Mohapatra, S. Chakrabarti, and S. Sarkar, "Online measurement based joint parameter estimation of synchronous generator and exciter," *IEEE Trans. Energy Convers.*, vol. 36, no. 2, pp. 820–830, Jun. 2021.

[288] A. Srivastava, A. Dubey, and S. Chakrabarti, "An exhaustive search based topology error detection method and its validation in real time digital simulator," in *TENCON 2017 - 2017 IEEE Region 10 Conference*, Penang, 2017, pp. 534–539.

[289] "NovaCor," *RTDS Technologies*, 09-Jun-2022. [Online]. Available: https://knowledge.rtds.com/hc/en-us/articles/360034290474-NovaCor. [Accessed: 18-Apr-2024].

[290] "GTIO Cards," *RTDS Technologies*. [Online]. Available: https://knowledge.rtds.com/hc/en-us/articles/360034281234-GTIO-Cards. [Accessed: 13-Jan-2023].

[291] "GTNETx2: The RTDS Simulator's Network Interface Card," *RTDS Technologies*. [Online]. Available: https://knowledge.rtds.com/hc/en-us/articles/360034788593-GTNETx2-The-RTDS-Simulator-s-Network-Interface-Card. [Accessed: 13-Jan-2023].

[292] SEL Inc., "SEL-351A Protection System Instruction Manual." .

[293] SEL Inc., "SEL-2401 Instruction Manual." .

[294] "Grid Protection Alliance - openPDC." [Online]. Available: https://gridprotectionalliance.org/phasorPDC.html. [Accessed: 26-Feb-2024].

[295] V. N. Giotopoulos and G. N. Korres, "A laboratory PMU based on third order generalized integrator phase-locked loop," *IEEE Trans. Instrum. Meas.*, vol. 73, pp. 1–11, Apr. 2024.